UNIVERSITÀ di VERONA

Department of BIOTECHNOLOGY

Toward an effective use of microalgae: a study on *Chlamydomonas reinhardtii* to disentangle non photochemical quenching (NPQ) and to engineer ketocarotenoids biosynthesis

PhD student:
Perozeni Federico

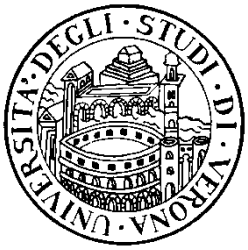

UNIVERSITÁ DEGLI STUDI DI VERONA

DIPARTIMENTO DI BIOTECNOLOGIE

SCUOLA DI DOTTORATO IN SCIENZE NATURALI ED INGEGNERISTICHE

DOTTORATO DI RICERCA IN BIOTECNOLOGIE
CICLO XXXII

Toward an effective use of microalgae: a study on *Chlamydomonas reinhardtii* to disentangle non photochemical quenching (NPQ) and to engineer ketocarotenoids biosynthesis

S.S.D: BIO04

Coordinatore:
Prof Matteo Ballottari

Supervisore:
Prof. Matteo Ballottari

Dottorando:
Federico Perozeni

Table of the contents

Summary ***1***

Chapter 1 ..... ***9***

Introduction 9

- Oxygenic photosynthesis 11
- Photosyntetic pigments 14
- The light absorption unit: PSI and PSII 16
- Photoinhibition and photoprotection 21
- The promising future of microalgae 26

Chapter 2 ..... ***31***

Investigation of non photochemical quenching (NPQ) mechanisms in green algae 31

- *In vitro* and *in vivo* investigation of chlorophyll binding sites involved in non-photochemical quenching in *Chlamydomonas reinhardtii* 35
- Molecular mechanisms of nonphotochemical quenching in the LHCSR3 protein of *Chlamydomonas reinhardtii* 49
- LHCSR3 is a nonphotochemical quencher of both photosystems in *Chlamydomonas reinhardtii* 63
- Identification of parallel pH- and zeaxanthin-dependent dissipation of excess energy in LHCSR3 in *Chlamydomonas reinhardtii* 81
- Identification of a plant-like Violaxanthin De-Epoxidase enzyme in the green alga Chlorella vulgaris reveals evolutionary divergency of photoprotective mechanisms in the green lineage 99
- Photosystem II antenna complexes CP26 and CP29 are essential for non-photochemical quenching in *Chlamydomonas reinhardtii* 119
- LHCSR Expression under *HSP70/RBCS2* promoter as a strategy to increase productivity in microalgae. 135

Chapter 3 ..... ***147***

Engineering ketocarotenoids biosynthesis in *Chlamydomonas reinhardtii* 147

- Functional analysis of photosynthetic pigment binding complexes in the green alga Haematococcus pluvialis reveals distribution of astaxanthin in Photosystems 149
- Turning a green alga red: engineering astaxanthin biosynthesis by intragenic pseudogene revival in *Chlamydomonas reinhardtii* 163

Conclusions ***181***

Appendix ***183***

- Encapsulation of Photosystem I in organic microparticles increases its photochemical activity and stability for ex vivo photocatalysis 185

Bibliography ***197***

Summary

Photosynthetic organisms can use solar energy to produce organic biomass starting from simple elements as CO_2 and water, releasing oxygen as side product. Algae are characterized by high growth rate, extremely rapid life cycle and intrinsic high photosynthetic efficiency. Moreover, microalgae can also be cultivated in a mixed autotrophic/heterotrophic condition, using reduced carbon sources. Several algal strains are characterized by high lipid accumulation or production of high value compounds. Thus, algae not only represent a valid alternative to plants, but they also play a central role considering the sustainability related to their cultivation. Wastewaters and flue gas can be used to ensure nutrients and CO_2 for carbon fixation, and, after biomass harvesting, water can be reused leading to a far lower consumption with respect to plants (especially in closed photobioreactor in which the evaporation is low). Unfortunately, algae evolved in conditions extremely different compared to actual industrial ones which involves 24/24 hours of high irradiance, strong shaking as well as high CO_2 concentration: all these elements ensure high photosynthetic rate and thus high biomass accumulation but make necessary a domestication of strains. Since this need became evident, engineers, biologists and biotechnologists had tried to overcome algae cultivation limitations in order to became it feasible and economically useful. From a biotechnological point of view several targets could be pointed.

Optimization of absorption/dissipation of light energy is one of the most interesting and explored. This thesis reports the use of several approaches to investigate the heat dissipation mechanisms (NPQ) in green algae, mainly focusing on the model organism *Chlamydomonas reinhardtii*. The results obtained reveal the molecular mechanisms of energy conversion from excitation energy into heat by the activity of specific pigment binding proteins called LHCSR (Light Harvesting Stress Related), going deep into details of the protein domains and pigments involved in the quenching process and the protein interaction network necessary for NPQ. In particular, the regulation of the accumulation of LHCSR proteins in *Chlamydomonas reinhardtii* revealed to be a successful genetic engineering strategy to improve biomass productivity.

Among the possible application of microalgae, one of the most promising one is their use as green factories to produce high value products: here, we report the metabolic engineering of *Chlamydomonas reinhardtii* as a bio-factory for ketocarotenoids production. The use of microalgae as host to produce high value metabolites, represents, indeed, an effective way to break down costs related to their cultivation with a potential high impact into the market. Astaxanthin is, currently, produce using *Haematococcus. lacustris* (recently renamed from *Haematococcus pluvialis*) in which, its accumulation causes a stop in growth. For that reason, in this thesis effects of astaxanthin accumulation of *H. lacustris* was investigated.

This thesis presents, with different approaches, a leap forward in microalgae domestication both trough enrichment of knowledge about NPQ and trough application of metabolic engineering to develop green bio-factories.

Chapter 2: Investigation of non photochemical quenching mechanisms in green algae

Light is fundamental for photosynthetic organism, ensuring charge separation in photosystems (PSI and PSII) which is the starting point for electron transport, proton motive force generation and NADPH and ATP production; but at the same time light can be extremely harmful. Indeed, plants and algae in their natural environment experiment changes in light intensity and quality: when the ability to harvest light exceeds the metabolic capacity to re-generate $NADP^+$ and ADP by Calvin Cycle photosynthetic apparatus undergoes overexcitation. In this condition, photosystems cannot properly dissipate energy through charge separation increasing the probability of energy transfer to oxygen generating toxic reactive oxygen species (ROS). To prevent photodamage induced by ROS, photosynthetic organisms developed a wide range of photoprotective mechanisms in which the heat dissipation of energy in a process called non-photochemical quenching (NPQ) is the most rapid and the one with the major role.

In this chapter, NPQ mechanism was studied in *Chlamydomonas reinhardtii*, model organisms for green algae. This process driven by LHCSR proteins was elucidated using different approaches.

Chapter 2 section 1

LHCSR3 pigments binding proprieties were investigated by generation of proteins mutated in specific chlorophyll binding sites and by their analysis both *in vitro* and *in vivo* using spectroscopic techniques as well as by complementation of *npq4 lhcsr1* mutant, lacking all the LHCSR subunits, showing a null NPQ. This allow to better understand spectroscopic proprieties of this protein and to identify chlorophylls and carotenoids involved in NPQ mechanism. The involvement of Chl a 613 in NPQ was shown. Despite a reduction of LHCSR3 quenching activity, the absence of this Chl was not enough to completely abolish NPQ suggesting the presence of multiple quenching sites cooperatively determining the overall quenching process.

Chapter 2 section 2

NPQ molecular mechanism was then investigated *in vitro* on refolded LHCSR3 by combination of picosecond time-resolved photoluminescence and femtosecond transient absorption in the visible and NIR spectral regions. Results obtained show the involvement of different mechanisms: radical cation formation, population of Car S1 state and aggregation-induced quenching. These mechanisms are always active but, they are further enhanced upon shifting to quenching conditions.

Chapter 2 section 3

The role of LHCSR1 and LHCSR3 was further investigated by measuring 77K fluorescence emission on whole cells in quenched or unquenched states. We showed that NPQ activation leads to energy quenching of also PSI in addition to well-known quenching on PSII. Both sites of quenching were further investigated by analyzing quenching properties of mutants affected on LHCSR proteins accumulation, state transition, as well as zeaxanthin accumulation. Results show a quenching mainly related to LHCSR3 at different sites: PSII complexes; LHC complexes bound to PSI; and LHCII “mobile” pool loosely connected to photosystems.

Chapter 2 section 4

The role of zeaxanthin, long debated in green algae, was here investigated *in vivo* by measuring quenching proprieties of mutants affected in zeaxanthin as well as LHCSR accumulation and *in vitro* by single molecule fluoresce spectroscopy. By combining these techniques, two individually quenching process were identified: the first controlled by pH, the second one by Car composition. Both *in vivo* and *in vitro* results showed the presence of a constitutive quenching in presence of zeaxanthin as reported for other LHC proteins.

Chapter 2 section 5

The role of xanthophyll cycle was investigated in the non-model microalga *C. vulgaris*. In this section we studied, in particular, the molecular details and functions of Vio to Zea conversion. Results show, differently to *C. reinhardtii,* the

presence of a plant-like violaxanthin de-epoxidase enzyme. Moreover, in *C. vulgaris* zeaxanthin accumulation was resulted to be is crucial for photoprotective quenching of both Photosystem I and II.

Chapter 2 section 6

In this section the role of other pigment binding proteins in the NPQ process was investigated, focusing on possible subunits interacting with the quenching subunits LHCSR. CP26 and CP29 roles both in light harvesting and in photoprotection in *Chlamydomonas reinhardtii* were here investigated. By CRISPR–Cas9 technology single and double mutants depleted of monomeric antennas were generated. Results reported show that the lack of CP29 and even more, the absence of both CP29 and CP26 negatively effects photosynthetic efficiency, state transition and photoprotection. Moreover, it is reported here as, differently to plants, PSII monomeric antennae resulted to be essential for NPQ induction.

Chapter 2 section 7

Finally, a biotechnological application of NPQ manipulation was proposed by generating *Chlamydomonas reinhardtii* strains with a low accumulation of LHCSR3 protein. These strains show, beside less NPQ, also a remodulation of the overall photosynthetic apparatus. The combined effect of these factors leads to a lower ROS formation. These strains can better face high light stress and use light energy thanks to a boosted photosynthetic electron transport and carbon fixation machinery improving light use efficiency and biomass production.

Chapter 3: Engineering ketocarotenoids biosynthesis in *C. reinhardtii*

Among all carotenoids, canthaxanthin, but in particular astaxanthin, show an extremely high antioxidant power; one of the highest in nature. Astaxanthin has multiple benefits on human system and it is proposed to play a central role in tumors treatment, in prevention of neurological and cardiovascular diseases and diabetes. Currently, natural astaxanthin world demand is satisfied by the green microalgae *Heaematococcus lacustris* but several constrains are related to the use of this alga, leading production and purification of astaxanthin extremely difficult and expensive. Moreover, accumulation of astaxanthin is coupled by the formation of a thick cell wall which reduce the bio-avability for human consumption.

In second part of this thesis we first investigate the effects of astaxanthin accumulation on *H.lacustris* photosynthetic apparatus and later, we show the possibility to use *Chlamydomonas reinhardtii* as bio-factory the production of ketocarotenoids.

Chapter 3 section 1

In these first section, with the aim of better understand the reason why the accumulation of astaxanthin causes in *H.lacustris* a growth stop, biochemical and spectroscopic properties of its pigment binding complexes responsible for light harvesting and energy conversion were investigated. We demonstrate as transition to astaxanthin rich cysts leads to destabilization of the Photosystems in which β-car was substituted by astaxanthin without improving their photoprotection.

Chapter 3 section 2

Here we report a biotechnological approach used to generate strains of *C. reinhardtii* accumulating astaxanthin and other ketocarotenoids. Normally, ketocarotenoids are not accumulated in this alga but by rescue of endogenous pseudo gene, its re-design and its overexpression it was possible to obtain a ketocarotenoids accumulation comparable to *H. lacustris* but without constrains related to cultivation and extraction.

Sommario

Gli organismi fotosintetici sono in grado di produrre zuccheri e ossigeno come prodotto secondario partendo da elementi semplici come CO_2 e acqua sfruttando l'energia luminosa. Tra questi, le alghe sono caratterizzate da un alto tasso di crescita, un ciclo di replicazione molto rapido nonché dalla capacità di crescere utilizzando fonti di carbonio ridotte (mixotrofia). Molti ceppi algali, inoltre, sono in grado di accumulare grandi quantità di lipidi o prodotti ad alto valore economico. Per questo motivo le alghe non solo rappresentano una valida alternativa alle piante ma, in quest'ottica, giocano un ruolo chiave se viene considerata la sostenibilità relativa alla coltivazione algale. Acque reflue o fumi di scarico possono essere utilizzati per fornire i nutrienti e la CO_2 necessari per la crescita e, in seguito alla raccolta della biomassa, l'acqua può essere nuovamente re-immessa nel sistema; in questo modo, soprattutto in fotobioreattori chiusi dove l'evaporazione è pressoché assente, il consumo è notevolmente ridotto rispetto alla coltivazione in campo aperto. Purtroppo, le microalghe, si sono evolute in un ambiente con condizioni estremamente diverse da quelle in cui vengono cresciute industrialmente. 24/24 ore di illuminazione, forte agitazione o rimescolamento e alte concentrazioni di CO_2 assicurano un elevato tasso di fotosintesi e dunque un'alta produzione di biomassa ma, al contempo, rendono necessaria una domesticazione dei ceppi microalgali. Da quando questo problema divenne evidente, ingegneri, biologi e biotecnologi hanno provato a superare le limitazioni inerenti alla coltivazione algale in modo da renderla economicamente vantaggiosa e attuabile. Da un punto di vista biotecnologico diversi target possono essere esplorati per raggiungere tale obiettivo.

L'ottimizzazione dell'energia luminosa assorbita/dissipata è, sicuramente, una delle strategie più esplorate. A tale proposito, in questa tesi, viene riportato l'utilizzo di diversi approcci per investigare il processo di dissipazione termica (NPQ) nelle alghe verdi, focalizzando maggiormente l'attenzione sulla specie modello *Chlamydomonas reinhardtii*. I risultati ottenuti esplorano i meccanismi molecolari della conversione dell'energia di eccitazione in calore ad opera di specifiche proteine in grado di legare pigmenti chiamate LHCSR. Proprietà strutturali di legame di pigmenti, così come la presenza di interattori, sono stati delucidati. La modulazione dell'accumulo di LHCSR in *Chlamydomonas reinhardtii* si è rivelata una strategia efficace per incrementarne la produttività.

L'utilizzo delle microalghe come bio-factory per la produzione di composti ad alto valore economico è, sicuramente, una delle strategie più promettenti per abbattere i costi relativi alla loro coltivazione. In questa tesi, viene proposta l'ingegnerizzazione di *Chlamydomonas reinhardtii* per la produzione di ketocarotenoidi. L'astaxantina viene attualmente prodotta utilizzando l'alga Heamatococcus lacustris in cui però, l'accumulo di tale molecola, causa un blocco della crescita cellulare; le ragioni sono state qui investigate.

Questa tesi rappresenta dunque un passo in avanti nella domesticazione delle microalghe sia approfondendo la conoscenza del meccanismo di NPQ sia fornendo un'applicazione pratica di ingegneria metabolica.

Capitolo 2 Studio del quenching non fotochimico in alghe verdi

La luce è fondamentale per gli organismi fotosintetici: permette infatti di effettuare la separazione di carica, punto di partenza per il trasporto elettronico, per la generazione della forza proton motrice e, dunque, per la produzione di ATP e NADPH. Allo stesso tempo, però, la luce può anche essere estremamente dannosa. Piante e alghe, infatti, nel loro ambienti naturali, sperimentano costantemente cambi in quantità e qualità della luce incidente: quanto la capacità di raccogliere

l'energia luminosa eccede quella di rigenerare $NADP^+$ e ADP tramite il ciclo di Calvin, l'apparato fotosintetico va incontro ad over-eccitazione. In tale condizione, la fotosintesi non può dissipare correttamente l'energia attraverso la separazione di carica aumentando le probabilità di trasferimento energetico all'ossigeno generando specie reattive dell'ossigeno (ROS), dannose per la cellula. Per prevenire il foto-danno indotto dai ROS, gli organismi fotosintetici hanno evoluto una serie di meccanismi foto-protettivi tra i quali, la dissipazione termica, in un processo chiamato quenching non fotochimico (NPQ), è il più rapido e quello che ricopre un ruolo maggiore.

In questo capitolo, il meccanismo di NPQ è stato studiato in *Chlamydomonas reinhardtii*, organismo modello per le alghe verdi. Tale processo, attuato dalle proteine LHCSR, è stato investigato utilizzando diversi approcci.

Capitolo 1 sezione 1

Le proprietà dei pigmenti legati a LHCSR3 sono state investigate tramite la generazione di proteine mutate in specifici siti di legame delle clorofille ed attraverso la loro analisi in un approccio combinato *in vivo/in vitro* mediante tecniche spettroscopiche e complementazione del mutante *npq4 lhcsr1*, privo delle proteine LHCSR e con un fenotipo di NPQ nullo. Questo approccio ha permesso di comprendere meglio le proprietà spettroscopiche di questa proteina e di identificare clorofille e carotenoidi coinvolti nel meccanismo di quenching. Viene mostrato come la clorofilla a 613 sia implicata nella dissipazione termica dell'energia ma, la sua rimozione, non è sufficiente a causare una totale disattivazione del meccanismo; ciò implica la presenza di molteplici siti di quenching con un effetto cooperativo.

Capitolo 1 sezione 2

Il meccanismo molecolare alla base della dissipazione termica è stato dunque studiato *in vitro* su LHCSR3 usando un approccio combinato di fotoluminescenza risolta nel tempo e assorbimento transiente nel visibile e NIR. I risultati mostrano il coinvolgimento di diversi meccanismi: formazione del radicale cationico, popolazione dello stato S1 dei carotenoidi e quenching indotto dall'aggregazione. Tali meccanismi sono sempre attivi ma sono ulteriormente incrementati in condizioni di quenching.

Capitolo 2 sezione 3

Il ruolo di LHCSR1 e LHCSR3 è stato ulteriormente studiato investigando le emissioni di fluorescenza a 77K di cellule intatte con o senza induzione del quenching. Abbiamo dimostrato come il meccanismo di NPQ provochi, oltre al ben conosciuto quenching del PSII, anche un quenching del PSI. Entrambi i siti di quenching sono stati investigati utilizzando mutanti affetti in accumulo di LHCSR, transizioni di stato o accumulo di zeaxantina mostrando che il quenching è per lo più legato a LHCSR3 ed avviene in diversi siti: supercomplesso del PSII, LHC legate al PSI e LHCII "mobili" legate ai fotosistemi.

Capitolo 2 sezione 4

In questa sezione, il ruolo della zeaxantina, a lungo dibattuto nelle alghe verdi, è stato studiato *in vivo* misurando le proprietà di quenching di mutanti affetti nell'accumulo di zeaxantina/LHCSR e *in vitro* tramite spettroscopia a singola molecola. Combinando queste tecniche, due diversi meccanismi di quenching sono stati identificati: il primo, controllato dal pH, il secondo dalla composizione dei carotenoidi. Entrambi gli approcci hanno identificato la presenza di un quenching costitutivo in presenza di zeaxantina come già riportato per altre proteine LHC.

Capitolo 2 sezione 5

Il ruolo del ciclo delle xantofille è stato investigato nell'alga non modello *Chlorella vulgaris*. Sono stati studiati il meccanismo e la funzione della conversione Vio-Zea mostrando, a differenza di *C. reinhardtii* la presenza di una violaxantina de-epossidasi omologa a quella delle piante superiori. Inoltre, in tale alga, la presenza di zeaxantina si è rivelata fondamentale per l'induzione del quenching di entrambi i fotosistemi.

Capitolo 2 sezione 6

In questa sezione sono stati investigati i ruoli di altre proteine in grado di legare pigmenti focalizzando l'attenzione sui possibili interattori di LHCSR: CP26 e CP29. Tramite la tecnologia CRISPR-Cas9 sono stati generati un mutante singolo e uno doppio mancanti delle antenne monomeriche. I risultati riportati mostrano come la mancanza di CP29, ed ancora di più la concomitante mancanza di CP29 e CP26, influisca negativamente sull'efficienza di fotosintesi, sulle transizioni di stato e sulla fotoprotezione. Viene inoltre mostrato come, a differenza delle piante superiori, le antenne monomeriche del PSII siano necessarie per l'induzione dell'NPQ.

Capitolo 2 sezione 7

Infine, viene proposta un'applicazione biotecnologica legata alla manipolazione dell'NPQ tramite la generazione di mutanti di *C. reinhardtii* con un ridotto accumulo di LHCSR3. Questi ceppi mostrano, oltre ad un ridotto livello di NPQ, una rimodulazione di tutto l'apparato fotosintetico. L'effetto combinato di tali fattori porta ad una minor produzione di ROS. Questi ceppi possono fronteggiare meglio lo stress da alta luce ed utilizzarne meglio l'energia grazie ad una catena di traporto elettronico maggiorata e ad una fissazione del carbonio implementata portando ad una maggior produzione di biomassa.

Capitolo 3 ingegnerizzazione della biosintesi dei chetocarotenoidi in *C. reinhardtii*

Tra tutti i carotenoidi, la cantaxantina, ma in particolare l'astaxantina, mostrano un elevato potere antiossidante: uno dei più alti in natura. L'astaxantina ha diversi benefici sull'uomo e, attualmente, ne viene proposto l'uso nel trattamento di tumori, nella prevenzione di malattie neurodegenerative e cardiovascolari e nel diabete. La richiesta mondiale di astaxantina viene soddisfatta mediante la coltivazione della microalga *Haematococcus lacustris* ma vi sono molte complessità legate al suo utilizzo. La produzione e la purificazione sono infatti estremamente complessi e costosi. Inoltre, in *H. lacustris*, l'accumulo di astaxantina è accompagnato dalla generazione di una spessa parete cellulare che ne limita la biodisponibilità per il consumo umano.

Nella seconda parte di questa tesi è stato prima investigato l'effetto dell'accumulo di astaxantina sull'apparato fotosintetico di *H. lacustris* e, in seguito, viene mostrata la possibilità di utilizzare ceppi ingegnerizzati di *C. reinhardtii* per la produzione di chetocarotenoidi.

Capitolo 3 sezione 1

In questa prima sezione, con lo scopo di chiarire le ragioni del blocco della crescita che avviene in *H. lacustris* in seguito all'accumulo di astaxantina, ne sono state caratterizzate le proprietà biochimiche e spettroscopiche dei complessi fotosintetici. Abbiamo dimostrato come la transizione tra fase verde e fase rossa porti ad una destabilizzazione dei fotosistemi in cui il β-Car viene sostituito dall'astaxantina senza però aumentarne la fotoprotezione.

Capitolo 3 sezione 2

Viene riportato un approccio biotecnologico per generare ceppi di *Chlamydomonas reinhardtii* in grado di accumulare astaxantina e altri chetocarotenoidi. Normalmente, questi, non sono accumulati in quest'alga ma, tramite il ripescaggio di uno pseudo gene endogeno, il suo re-design e la sua over espressione, è stato possibile ottenere una produzione di chetocarotenoidi paragonabile a quella di *H.lacustris* ma senza tutti i problemi legati alla coltivazione di quest'alga ed all'estrazione del prodotto.

Chapter 1

Introduction

Contents

Oxygenic photosynthesis **11**

Photosyntetic pigments **14**

The light absorption unit: PSI and PSII **16**

Photoinhibition and photoprotection **21**

The promising future of microalgae **26**

Oxygenic photosynthesis

Photosynthesis represents one of the most important chemical reaction on earth. Most organisms depend, directly or indirectly, from this process which allow the conversion of solar energy into chemical energy. Photosynthesis process is performed by plants, algae, mosses and some kind of bacteria. In oxygenic photosynthesis water is used as electron donor to reduce CO_2 to carbohydrates. This process involves light and generates oxygen as side product. The following, represents the overall equation of photosynthetic process:

$$nH_2O + nCO_2 + light \rightarrow (CH_2O)_n + nO_2$$

The whole process can be divided into light dependent (or only light phase) and independent phase (named also dark phase). The first is strictly connected to light while the latter can occur also in dark, exploiting ATP and NADPH generated during light phase. Light phase starts with sunlight absorption by photosynthetic pigments (chlorophyll and carotenoids) followed by energy transfer to the reaction center where charge separation occurs. Electron transfer from the primary electron donor (water) to electron acceptor ($NADP^+$) is coupled by a transmembrane proton gradient which allow to generate, beside reducing power, also free energy in the form of NADPH and ATP respectively.

Light reaction can be summarized by the following equations:

$$2\ NADP^+ + 2\ H_2O + light \rightarrow 2\ NADPH + O_2 + 2H^+$$

$$ADP + Pi + energy \rightarrow ATP$$

In dark reactions, ATP and NADPH produced during the light reactions are used to reduce CO_2 to the carbohydrate GAP (Glyceraldehyde-3-Phosphate). The process of can be summarized as following:

$$3\ CO_2 + 9\ ATP + 6\ NADPH \rightarrow GAP + 9\ ADP + 8\ Pi + 6\ NADP^+$$

The chloroplast

Both light dependent and light independent phases take place in specialized organelle called chloroplast. Its number ranging from one in unicellular algae to few hundred in vascular plants in which, moreover, depends on species, growth conditions and development stage.

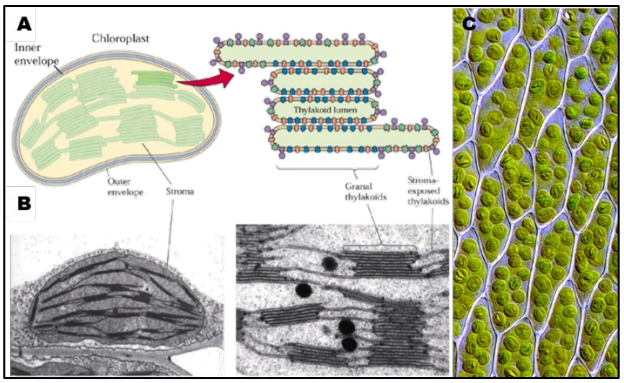

Figure 1 *A) Schematic representation of a chloroplast. Thylakoids are distinguished in grana and stroma lamellae. B) Electronic micrographs of a chloroplast. Images from C) Chloroplasts visible in Bryum capillare cells*

The chloroplast is present in all photosynthetic eukaryotes and it is characterized by the presence of two membranes (called together *envelope*): the first is highly permeable, while the latter contains specific transporters allowing a fine regulation of metabolites flux. *Envelope* membranes delimit a compartment named *stroma* which contains all the enzymes catalyzing dark reactions, plastidial DNA, RNA, ribosome, as well as a third membrane system: the *thylakoids*. Thylakoids membranes confine another compartment, the *lumen* and are organized into two different membrane domains: 1) cylindrical, stacked structure called *grana* and 2) region with no specific organization which interconnect grana membranes called *stoma lamellae*. Thylakoids membranes are keep stacked thanks to the presence of bivalent cations like Mg^{2+} which contrast the negative charge of these membranes [2].

The light phase

Light phase involves four protein complexes, all located into thylakoids membranes: photosystem II (PSII), cytochrome b6f, photosystem I (PSI) and ATP synthase **Figure 2**. These complexes catalyze the processes of light harvesting, electron transport and photophosphorylation converting light energy into free energy and reducing power (ATP and NADPH). Light reactions are catalyzed by two separate photosystems (PSI and PSII), while ATP synthase produces ATP exploiting the proton-motive force (*pmf*) that is formed by light reactions. The cytochrome-b6f complex mediates electron transport between PSII and PSI [3] and takes part in generating *pmf* for ATP formation. PSI and PSII bind pigments for light absorption. Energy,

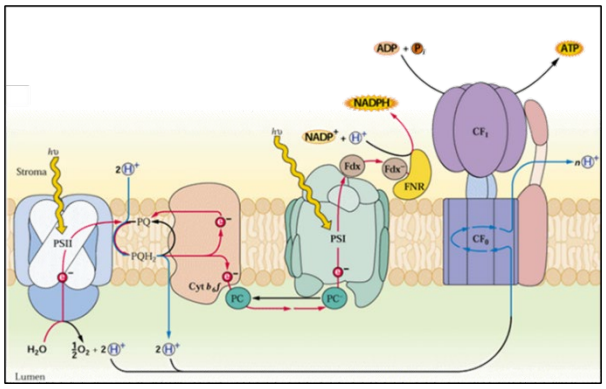

Figure 2 *Schematic representation of light reactions in photosynthesis. Organization of the major protein complexes in the thylakoid membrane is also shown.*

once harvested, is direct to reaction center in which excites two specialized reaction-center chlorophylls (special pair) which undergo charge separation. This event starts the translocation of one electron across thylakoids membrane through a series of cofactors. The energy required for the generation of NADPH cannot be provided by only one photon in the visible range of light: this is the reason why two photosystems act in series, as described in the so called Z-scheme [3] summarized in **Figure 3**. Oxidized special pair is then re-reduced by an electron coming from water oxidation. Four photons can oxidase completely two molecules of water to O_2 releasing four protons into the lumen. The electrons that have been extracted from water are translocated, through a quinone pool and the cytochrome-b6f complex, to plastocyanin, a small, copper-containing protein. In the cytochrome-b6f complex, the two electrons oxidation of a reduced quinone (PQH_2), that is bound at the luminal Qp site, results in the release of two protons to the lumen. Following a second reduction event at the Qn site, two protons are taken up from the stroma and the reduced quinone is released into the membrane (Q cycle **Figure 4**) [1]. Overall, the Q-cycle oxidizes two plastoquinols, reduces one plastoquinone, and

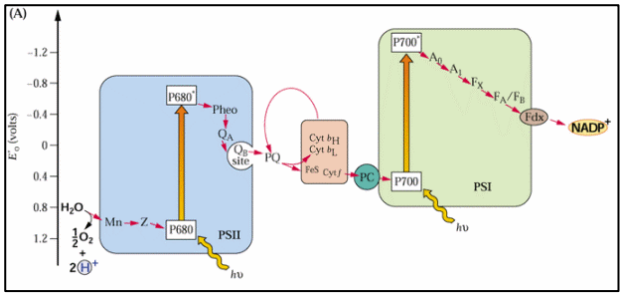

Figure 3 *The Z-scheme of Bendall and Hill. Cofactors involved in electron translocation between H2O and NADP+, and their redox potential, are indicated.*

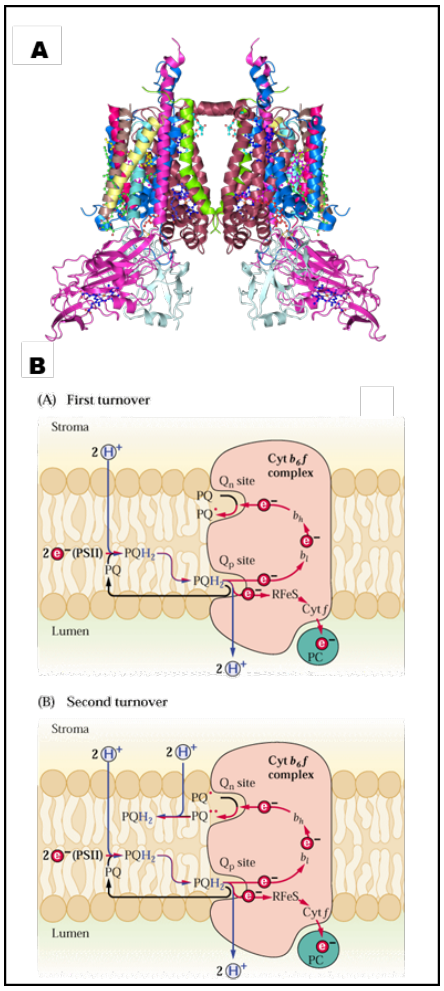

Figure 4 *A) 3D structure of cytochrome-b6f from Chlamydomonas reinhardtii 1 B) Schematic model of the proposed molecular mechanism of Q-cycle*

translocates 4 H+ for every 2 electrons transported to PSI forming, also, an electrochemical gradient across the membrane. Light energy absorbed by PSI induces the translocation of an electron from plastocyanin, in thylakoid lumen to ferredoxin, on the opposite side (stroma). Reduced ferredoxin can be used in several reactions, including, in the case of photosynthesis, NADPH production. *Pmf* produced during light phase steps is used by ATP synthase to produce ATP. This multimeric enzyme is composed by two main parts: a transmembrane region and a stromal region named CF_0 and CF_1 respectively **Figure 5**. Proton movement through CF0 is coupled to ATP synthesis/hydrolysis at sites in the -subunits of CF_1[4]. Light phase is an extremely efficient process; both photosystems operate with a very high quantum yield: for PSI it is proximal to 1 while for PSII is about 0.85.

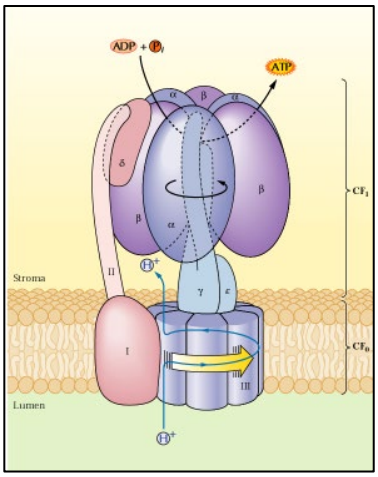

Figure 5 *representation of rotary and stationary subunits acting in ATP synthesis*

Alternative pathways

ATP/NADPH ratio significantly changes on the base of the metabolic status of cells. Several metabolic pathways such as nitrate assimilation, lipid, amino acids and pigments synthesis are in competition with the dark phase of photosynthesis for the use of ATP and NADPH, modifying the ATP/NADPH ratio. Alternative electron ways are important for balancing this ratio. For example, when the NADPH/NADP+ ratio is high, photosynthetic complex can operate in a different way generating only electro-chemical potential gradient used by ATPase to produce ATP without production of NADPH (PSII is not involved). This process, named cyclic electron flow, involves the reduction of ferredoxin following by electron transport to cyt b6f in order to reduce PC to reduce oxidized P700+ restoring the electron gap. In this way PSII is bay-passed; there is no production of NADPH and organisms can balance the ratios NADPH/NADP+ and ATP/NADPH [5]. Moreover, oxygen consumption in the chloroplast, also called chlororespiration, was defined as a respiratory electron transport chain in interaction with the photosynthetic apparatus. Chlororespiration includes a plastid terminal oxidase PTOX [6] which generate water by oxidation of plastoquinones.

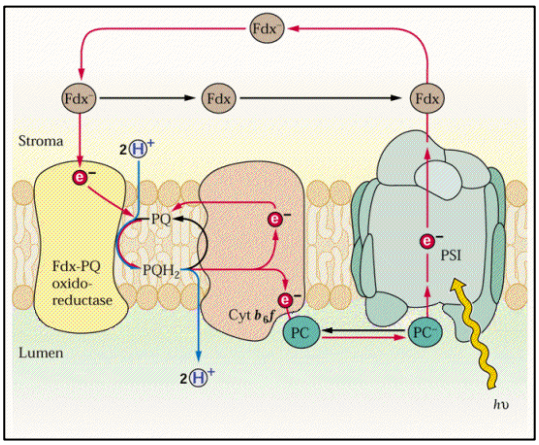

Figure 6 *Schematic representation of cyclic electron flow*

The dark phase.

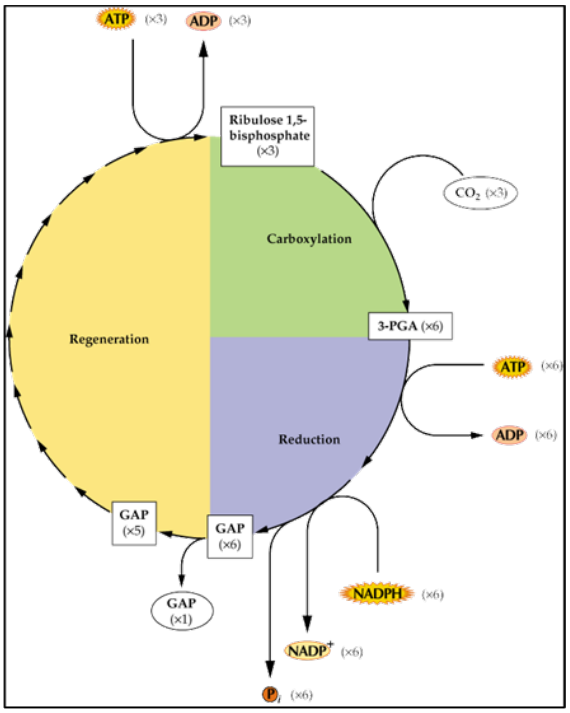

Figure 7 *schematic representation of Calvin Cycle showing 3 phases*

During the dark phase of photosynthesis, CO_2 is reduced to carbohydrates, using the ATP and NADPH produced during light reactions. RUBISCO is the enzyme responsible for CO_2 fixation to a molecule of ribulose-bisphospate producing two molecules of 3-phosophoglycerate. A series of reactions, indicated as Calvin cycle [7] allow the synthesis of one glyceraldehydes-phosphate (GAP) from three CO_2 molecules and the regeneration of Ribulose-5-phosphate (Ru5P). the whole cycle can be summarised with the following reaction:

$$3CO_2+3Ru5P+9ATP+6NADPH \rightarrow 6GAP+9ADP+6NADP^+ +8Pi$$

As show in **Figure 7** Calvin-Benson cycle can be divided into 3 main steps: (i) carboxylation, (ii) reduction, (iii) regeneration

Photosyntetic pigments

Light harvesting, charge separation and energy transfer are allowed by photosynthetic pigments. Two main classes are present in photosynthetic organisms: chlorophylls and carotenoids. These molecules can promote one electron to an excited state after interaction with a photon; The promotion to an exited state can occur only with specific energy of the photon (depending on its wavelength by Plank's law). According to level quantization, the excited state jump is allowed only if the photosynthetic pigment adsorbs a photon with the energy corresponding to the difference between the relaxed and the excited state. However, because of vibrational and rotational level the absorption take place in range of wavelength

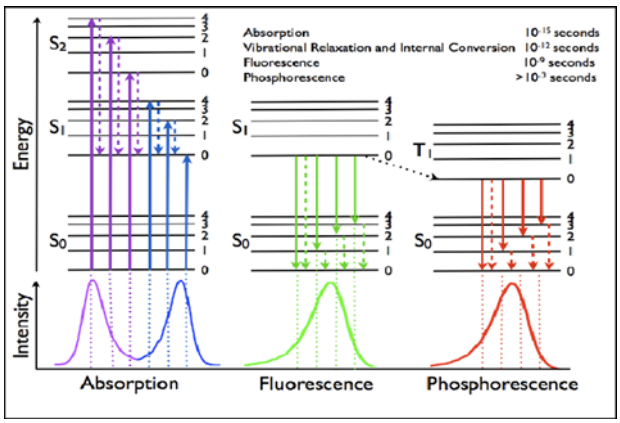

Figure 8 *Jablonski diagram representing energy levels and spectra. Solid arrows indicate radiative transitions as occurring by absorption (violet, blue) or emission (green for fluorescence; red for phosphorescence) of a photon. Dashed arrows represent non-radiative transitions (violet, blue, green, red)*

According to Jablonsky diagrams (**Figure 8**) the mechanisms which can be involved are:

- *Vibrational relaxation:* energy of the promoted electron is released as kinetic energy within the same molecule or other molecules. Time scale: 0.01 - 10 ps.
- *Internal conversion:* all energy is converted into heat in a non radiative decay. Time scale: 1ps.
- *Intersystem crossing*: energy is transferred by horizontal transfer from S_1 to T_1 by inverting electron spin. Triplet excited state molecules can react each other; as in the case of ROS (reactive oxygen species) formation after reaction with molecular oxygen. Time scale: 10ns – 1ms
- *Phosphorescence:* T_1 promoted electron can return to S_0 by spin inversion and photon long living emission. Time scale: 0.1ms – 10 s.
- *Fluorescence:* S_1 promoted electron energy is emitted as photon with a lower energy with respect to the one absorbed depending on vibrational loss of energy before emission (Stoke shift). Time scale: 1 – 100 ns.
- *Photochemistry:* in the case of exited chlorophylls, they undergo charge separation into reaction center. Time scale: 1ps
- *Excitonic transfer*: energy transfer between two different molecules causing the de-excitation of the first and the excitation of the latter. Time scale: 1 – 10 ps

The time in which each process takes place determines it probability upon the others.

Chlorophylls

The most abundant light-harvesting pigments are chlorophylls (Chls). In plants, algae and mosses five different types of Chls are present: the most widely distributed are Chl *a* and Chl *b*; Chl *c* (c_1, c_2 and c_3) and Chl *d* are present in red algae and cyanobacteria while Chl *f* was described only in cyanobacteria [8]. Their structure consists of a cyclic tetrapyrrole in which four nitrogen atoms coordinate a Mg atom and a long phytol chain esterified to the ring (except for Chlorophyll *c* which lacks the phytol chain) ([9]. Chl *a*, Chl *b*, Chl *d* and Chl *f* are almost identical, but they differ in their substitutions: Chl *a* has a methyl group on second pyrrole ring (**Figure 9**), Chl *b* has a formyl group [10]. Differently, Chl *d* has a methyl group on second pyrrole as Chl *a* but carries a formyl group on third pyrrole instead of a vinyl group [11] while Chl *f* has the same structure as Chl *a* except for a formyl group on first pyrrole [12]. Differently Chl *c* (*c1* and *c2*) show a peculiar structure completely absent of phytol tail [13]. Chlorophyll absorption

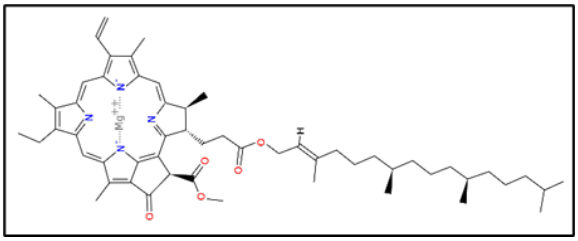

Figure 9 *structure of chlorophyll a*

spectra do not completely overlap each other increasing the spectral range of light that can be harvested by photosynthetic organisms. The absorption spectra of the Chls present two main bands: the Qy transition, around 670 and 640 nm for Chl *a* and Chl *b* respectively, and the Soret band which maximum is around 430 for Chl *a* and 460 nm for Chl *b*. A third absorption band, Qx, is also present around 580-640 nm; partly masked by the Qy vibronic transitions (**Figure 10**) [14]. Qy transition corresponds to the transition of an electron from S_0 to S_1 while Qx from S_0 to S_2 (**Figure 8**). Central Mg covers a key role in chlorophyll binding to proteins: in most cases it is bound by nucleophilic amino acids residues, like histidine; however chlorophylls can be also bound through water or lipid molecules [15]. In higher plants and green algae Chl *a* and Chl *b* are bound to different location: Chl *a* is present both in antennae and core complex while Chl *b* is present only in antennae proteins [16].

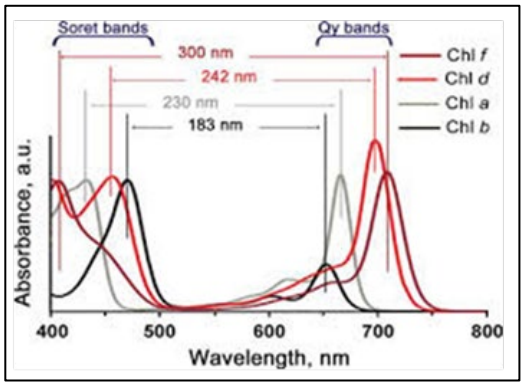

Figure 10 *Spectral comparison of isolated chlorophylls in acetone 80%*

Carotenoids

Carotenoids (Cars) are an extremely heterogeneous group containing several hundred of different molecular species [17]. Synthetized by plants, algae, bacteria and fungi, they play important roles in most of photosynthetic organisms; besides their light absorption function they are directly involved in photoprotection as well as photosynthetic apparatus assembly [18,19]. These pigments absorb light in the region between 400-500 nm (**Figure 11**), where Chls absorbance is limited thanks to π-electrons delocalization in the conjugated double bonds [20]. After light absorption from carotenoids, electrons are transferred from S_0 to S_2. The first excited singlet state S_1 cannot be populated from the ground state by photon absorption due to symmetry reasons. In higher plants and algae, Cars can be divided in two main groups: carotenes which are hydrocarbons with linear structure and cyclic groups at both the extremities and xanthophylls which are oxygenated derivatives of carotenes [21]. The major carotenoids associated with thylakoid membranes are the carotene β-Carotene (β-Car) and the xanthophylls Lutein (Lute), Violaxanthin (Viola), Neoxanthin (Neo) and Zeaxanthin (Zea). Carotenoids are non-covalently bound to the protein complexes, involving hydrophobic interactions [22]. Carotenes and xanthophylls show different localization: the firsts are bound especially to the core complex of both photosystems, while xanthophylls are mainly located in the antenna complexes [23,24].The absorption spectra of carotenoids are strongly red-shifted *in vivo*, compared to their spectra in organic solvents due to a lowering of the S_2 energy level, which has been ascribed mainly to protein environment. This effect is less visible in S_1 level which is less affected by the surrounding environment [25].

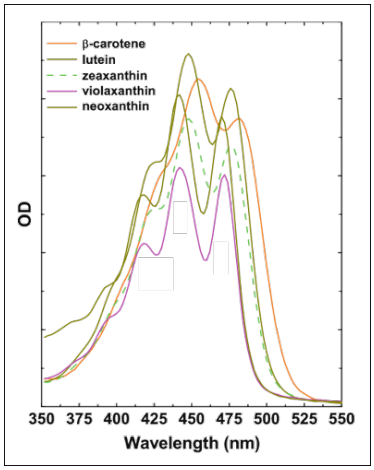

Figure 11 *Example of carotenoids absorption in acetone 80%*

Xanthophyll cycle

Xanthophyll cycle, observed in algae and higher plants, consists in a light-dependent reversible de-epoxidation of violaxanthin to zeaxanthin via the intermediate antheraxanthin (**Figure 12**). Constitutive accumulation of zeaxanthin, in *Arabidopsis,* decrease light use efficiency causing growth delay [26] thus a fine regulation of the xanthophyll cycle is crucial. The de-epoxidation reactions are catalyzed by violaxanthin de-epoxidase (VDE) [27,28], activated by acidification of the lumen upon high light exposure caused by excess of ATP synthase capacity to

produce ATP by proton transfer to stroma. Green alga *Chlamydomonas reinhardtii* has an atypical VDE (CVDE) not related to plant VDE but more related to lycopene cyclase from photosynthetic bacteria. The localization into thylakoids membrane of these two VDE is different: while plant VDE is located into thylakoid lumen, CVDE is located on the stroma side [29].

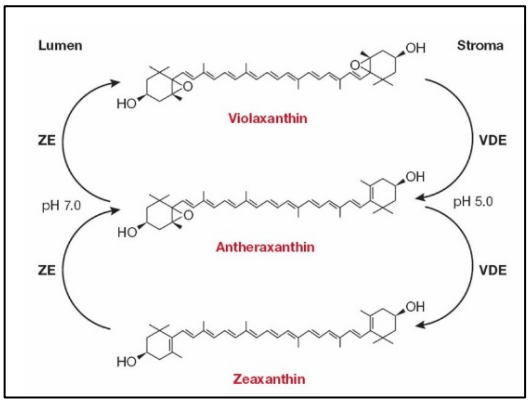

Figure 12 *schematic representation of plant xanthophyll cycle*

The light absorption unit: PSI and PSII

Photosystems (PSI and PSII) are complexes involved in light energy conversion into the chloroplast. They are trans-membrane multi-pigment-protein complexes, able to catalyze electron transport from donors located on the inner thylakoid surface to acceptors located on the stromal side. Distribution of PSI and PSII into thylakoids membranes is not homogenous: PSII is mainly located in grana membranes while PSI in stroma lamellae. The structure of PSI and PSII is different but in both complexes two moieties can identified: (a) a core complex, in which are located the chlorophyll special pair and the cofactors involved in charge separation and electron transport; an antenna system, responsible for light harvesting and energy transfer to the reaction center. Core complex acts as an energy trap due to its less energy with respect to antennae system; the energy is thus transfer from peripheral antenna towards reaction centers. Despite both core complex and antennae system bind chlorophylls and carotenoids, their distribution is different in between these two moieties: core complex binds only Chl *a* and carotenes while antenna proteins bind Chl *b* and xanthophylls. Important difference is also the localization of genes coding for core complex or antennae proteins: the firsts are mainly located into plastid genome while the latter are

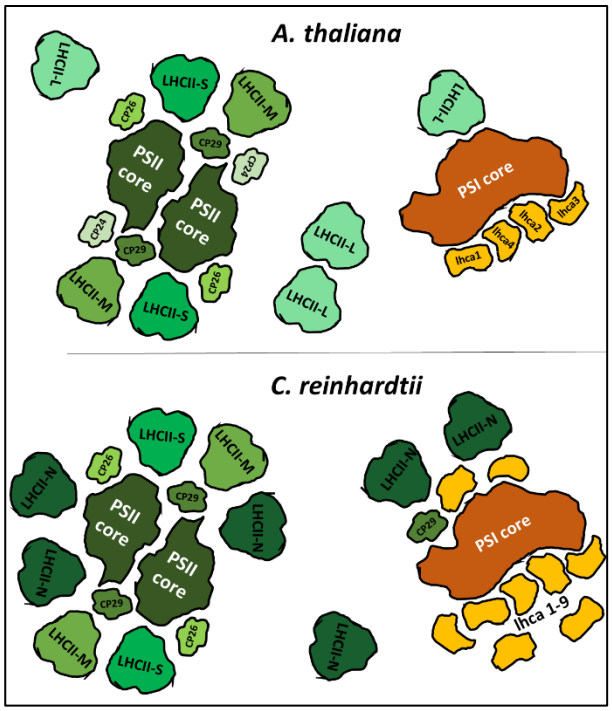

Figure 13 *Supramolecular organization of photosystems (PSI) and PSII with their light-harvesting complex (LHC) antenna proteins in higher plants (upper panel) and the green algae (lower panel). Core components and the antenna system of photosystem II are shown in green and components of the PSI–LHCI supercomplex in orange. Upon phosphorylation part of the PSII antenna can connect to PSI.*

coding by nucleus. Chloroplast genes for core complex proteins are highly conserved among oxygenic photosynthetic organisms; on the other side, genes coding for antenna proteins (Light Harvesting Complex) of PSI and PSII (LHCa and LHCb respectively) are diversified among different organisms [30]. Tic-Toc translocator system is responsible for the import of protein into chloroplast. Photosynthetic apparatus in green algae presents both similarities and differences compared to higher plants. As said before, core complexes are highly conserved and have a dimeric or monomeric structure for PSII and PSI respectively [31-34]. The antenna size of both PSI and PSII photosystems was shown to be larger in *C. reinhardtii* compared to higher plants (**Figure 13**) [35-37].

Photosystem I (PSI)

PSI function is to oxidize plastocyanin (Pc) or cyt *c6* and reduces ferredoxin (Fd), which eventually generates nicotinamide adenine dinucleotide phosphate (NADPH) via Fd-NADP-oxidoreductase (FNR). PSI is involved not only in linear electron transfer but also in cyclic electron transfer, which is required for the production of ATP without generation of NADPH. Energy harvested by antenna system is transferred to PSI reaction center. Here

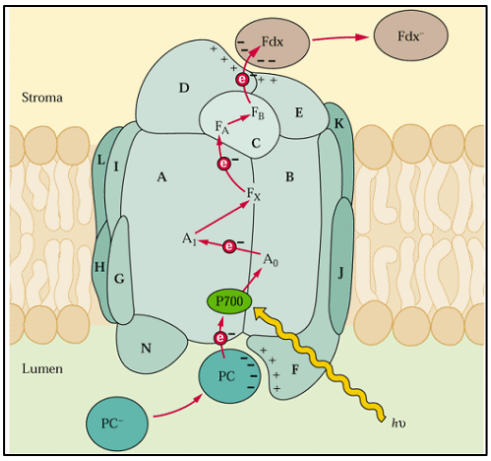

Figure 14 *Schematic model of photosystem I. Subunits organization and cofactors involved in electron transfer are indicated*

primary electron donor (P700) and several electron acceptors (A_0, A_1, F_X, F_A and F_B) convert it into redox energy with a quantum yield nearly 100% [38]. Oxidized P700 ($P700^+$) is reduced by Pc or cyt *c6* and the reduced F_B is oxidized by Fd. PSI is composed of a core complex (PSI core) and the antenna system responsible for light-harvesting (LHCI). PSI core is highly conserved from cyanobacteria to higher plants (although changes in small subunit composition exist, such as the loss of PsaM and PsaX and gain of PsaG, PsaH, PsaN and PsaO) consists in two homologous subunits (PsaA and PsaB), several single to triple transmembrane helix small subunits as well as three peripheral subunits (PsaC, PsaD and PsaE) (**Figure 14**). In total PSI core binds more than one hundreds pigments (90 Chlorophylls and 20 β-carotenes) [33,38,39].

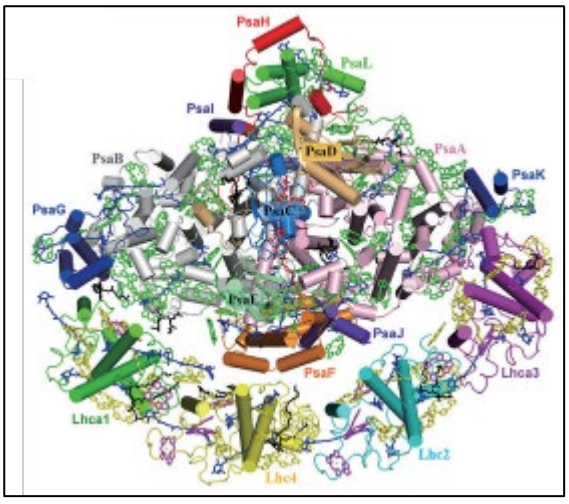

Figure 15 *overall structure of plant PSI-LHCI supercomplex; top view from stromal side*

Photosystem I (PSI) antenna system and supramolecular organization

While PSI remains conserved during 2.5 billion years evolution, its antenna system shows substantial differences in polypeptides composition and, as consequence, supramolecular organization. In higher plants Lhca 1-4 are the 4 polypeptides constituting the major components of PSI antenna system [40,41]. They are assembled into two dimers (Lhca1-Lhca4 and Lhca2-Lhca3), bound to core complex at PsaF/PsaJ site like a half moon belt, and stabilized by association with PsaG and PsaK, respectively [40,42,43] (**Figure 15**). Differently PSI of the green alga *Chlamydomonas reinhardtii* is associated with nine distinct LHCI proteins (Lhca1–9). The number of LHCI proteins in the *Chlamydomonas* PSI–LHCI supercomplex remains controversial but chemical crosslinking [34] and more recently cryo- EM [44] identify the presence of one copy of Lhca2-9 and two copy of Lhca1 for a total number of ten Lhca per core complex. Eight LHCIs are organized in two layers at one side of the PSI core, near PsaF/PsaJ. Each layer contains four LHCI proteins arranged in a crescent shape, forming the inner and outer LHCI belt. Other two Lhca are located close to PsaB, constituting the LHCI side layer (**Figure 16**). Higher plants PSI antenna complex is characterized by the presence of so called “red forms”: chlorophyll absorbing at lower energy with respect the reaction center [45]. “Red

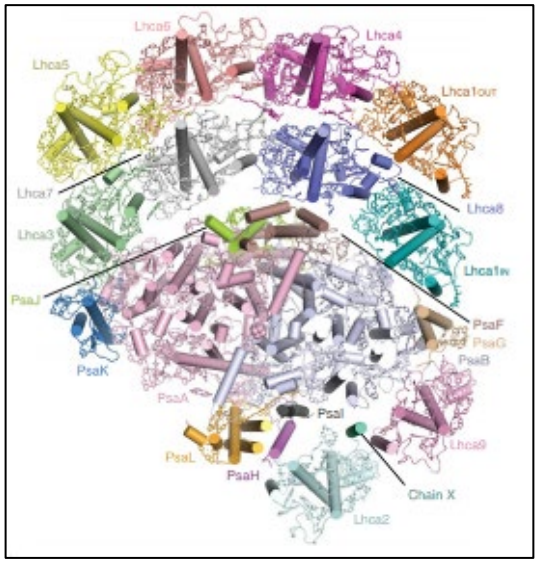

Figure 16 *The overall structure of Chlamydomonas PSI-LHCI, viewed from the stromal side. Membrane-extrinsic subunits PsaC, PsaD and PsaE are omitted for clarity*

forms" are present also in green algae but their spectra is blue shifted if compared to plants [46].

Photosystem II (PSII)

Evolution of PSII was crucial for the appearance of aerobic organisms. Photosystem II, in fact, is defined as a water–plastoquinone oxidoreductase; and catalyzes water oxidation generating oxygen. As for PSI, also in PSII two different moieties can be identified: a core complex in which primary photochemistry takes place which is surrounded by an antenna system. The mechanism of oxygen production involves the oxidation of two water molecules to make molecular oxygen (O_2) triggered by absorption of four light quanta. Primary electron donor are two coupled chlorophylls known as P680. An electron is translocated from P680 to the quinone Q_A followed by the reduction of a mobile quinone Q_B after the absorption of the first light quantum. After oxidation of nearby tyrosine (Y_Z) by $P680^+$ an electron is extracted from a cluster of four manganese (localized in the oxygen evolving complex), which binds two water molecules. Three extrinsic proteins of 33, 23 and 17 KDa (PsbO, PsbP and PsbQ) compose the oxygen evolving complex on the luminal side [47]. Having a calcium, a chloride and a bicarbonate ion as necessary cofactors. Upon an additional photochemical cycle, the doubly reduced QB (QB^{2-}) takes up two protons from the stroma to form QBH_2 and is released into the lipid bilayer; it will be then replaced by an oxidized plastoquinone from the lipid-free membrane pool. Two more photochemical cycle are required to provide to manganese cluster the four oxidizing equivalents needed for the oxidation of two water molecule producing O_2 [48].

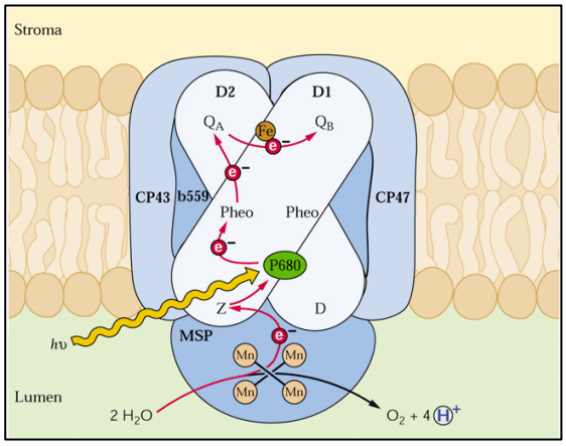

Figure 17 *Schematic model of photosystem I. Subunits organization and cofactors involved in electron transfer are indicated*

PSII core, as in the case of PSI core is highly conserved during evolution and it is composed by around 20 subunits. Among these, 4 large subunits D1, D2, CP43 and CP47 binds most of the pigments and co-factor needed. D1 (PsbA) and D2 (PsbD) are organized in a hetero dimer forming the reaction center in which charge separation occurs. On the other side CP47 (PsbB) and CP43 (PsbC) are bound to the two different sides of D1-D2 reaction center [49] forming the inner antenna of the core complexes and they funnel to the RC the light energy absorbed by themselves and transferred by the antenna proteins. Twelve small subunits surround the four large subunits (PsbE-Z) [50]. The function of all this subunits is still only partially clear but, mainly, they are involved in the PSII dimer stabilization and association of the antenna protein to the core [51]. PSII core of *Chlamydomonas reinhardtii* shows minor differences with respect to PSII core of cyanobacteria and higher plants. The small subunit PsbW is observed in the structure of PSII from green algae model organism as observed in plants [32,52] but not in cyanobacteria [53]. A transmembrane helix corresponding to the position of PsbW was also found in a red algal PSII [54]. Psb30 is another unique subunit found in the current Cr-PSII structure which is present in the structures of cyanobacterial [53,55] and red algal PSII [54] but absent in higher-plant PSII [32,52]. This reflects the intermediate feature of green algae PSII core between cyanobacteria and higher plants during evolution.

Antenna complex of PSII

The peripheral antennae of PSII is composed by six subunits in two different aggregation state: trimeric LHCII (major light harvesting complex) [56] and monomeric (minor antennae) [57]. All antenna proteins are encoded by nuclear genes and share a similar structure with three trans-membrane helixes. They also bind Chl *a*, Chl *b* and Cars in different stoichiometry and orientation that gives to each protein distinct spectroscopic properties. Higher plants and mosses show three types of monomeric antenna: CP29 (Lhcb4), CP26 (Lhcb5), and CP24 (Lhcb6) [58]. In *Chlamydomonas reinhardtii* only the minor antennas CP26 and CP29 are present while CP24 does not [59]. Minor antennae are named from their apparent mass in non-denaturing SDS gel [58]. CP29 (Lhcb4) is the largest among LHC proteins with its 256-258aa. It is necessary for PSII

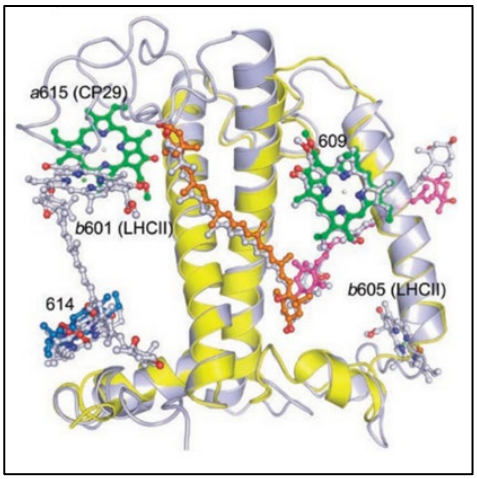

Figure 18 *Structural comparison between CP29 and LHCII (PDB1RWT). Both the apoprotein and pigments of LHCII are shown in gray. The apoprotein of CP29 is shown as a yellow ribbon, and its pigments are colored. Conserved pigments in the two structures are not shown*

organization [60], plays a bridging role in transferring the excitation energy from antenna system to reaction center [61] and it is also involved in photoprotection [62]. In *Chlamydomonas reinhardtii* CP29 is reported to be essential for state transition [63]. Crystal structure of spinach CP29 [64,65] shows the presence of 14 Chls and 3 Xanthophylls. The structural differences between CP29 and LHCII, especially their pigment composition and spatial arrangement, are at the base of their different functions. Besides its role as antenna and as bridge for energy transfer from LHCII and core complex, CP29 in response to high light undergoes changing in its energy regulation and quenching mechanisms [66,67] [68]. In *Chlamydomonas reinhardtii* CP29 binds 13 Chls and 3 carotenoids lacking Chl 614 found in plant CP29 (**Figure 18**).The Cr-CP29 possesses a shorter C terminus [33]; this C-terminal helix, in plants, interacts with the BC loop of CP24 strengthening the binding of Chl 614. The shorter C terminus of Cr-CP29 may be due to the absence of CP24, space occupied by the larger N-LHCII trimer, leading to a smaller space able to accommodate only a shorter C-terminal (**Errore. L'origine riferimento non è stata trovata.**). In *Arabidopsis thaliana*, Lhcb4 is present in three different isoforms (Lhcb4.1, Lhcb4.2 and Lhcb4.3).The latter isoform having a different expression profile, and a deletion in N-terminal domain leads recently to suggested being a distinct Lhcb antenna protein and renamed as Lhcb8 [69]. CP26 (Lhcb5) in *Arabidopsis* is a 243 amino acids polypeptide showing 48% identity with respect to LHCII and coordinating 13 Chls and 2-3 xanthophylls [57,70]. CP26 is a bridge in between CP43 and LHCII trimer-S [71]. In Cr-CP26, as in plants, 13 Chl binding sites and 3 carotenoid binding sites are found. However, the AC loop and EC loop of Cr-CP26 are longer than that of plant CP26 [33](**Figure 20**). These 2 extra regions can interact with S-LHCII trimer, forming unique interactions which contributes to the energy transfer.

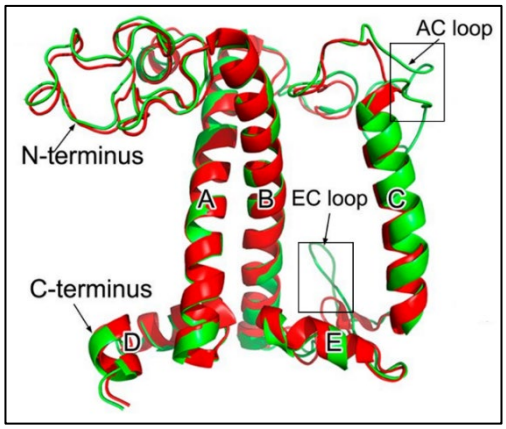

Figure 19 *Superposition of the cryo-EM structure of the CP26 apo-protein from C. reinhardtii with that from pea. The 2 extra loop regions in Cr-CP26 are highlighted with black boxes. Green: Chlamydomonas; red: pea*

CP24 (Lhcb6) with its 211 aa, due to the lack of the major part of C-terminal region, is the smallest of Lhc proteins. A total of 11 Chls and 3 xanthophylls are proposed bound [57]. CP24 is important in determining the structure and function of the PSII light-harvesting antenna, providing the linker for association of the M-trimer; that is necessary both for maximum quantum efficiency and for photoprotective dissipation of excess excitation energy [72]. Furthermore is suggest that CP24 has evolved later during evolution [73] to overcome limitations in PQ diffusion; in fact in higher plants size of grana stacks is higher with respect to green algae with possible negative effects on PQ mobility [74].

By genome and transcriptome data analysis, a new Lhcb protein similar to Lhcb5, named Lhcb7, was recently identified. Its contribution to the PSII antenna system is not clear: gene is rarely expressed and shows high relative expression levels in petals, sepals and in conditions of oxidative stress [69]. An additional Lhcb protein was first detected in the mosses *Physcopmitrella patens*., named Lhcb9. However, this antenna subunit did not fix in later stages of evolution and is restricted to mosses [75].

In higher plants three major LHCII proteins (type I-III) with five, four and one isoforms, respectively (LHCB1.1–1.5;

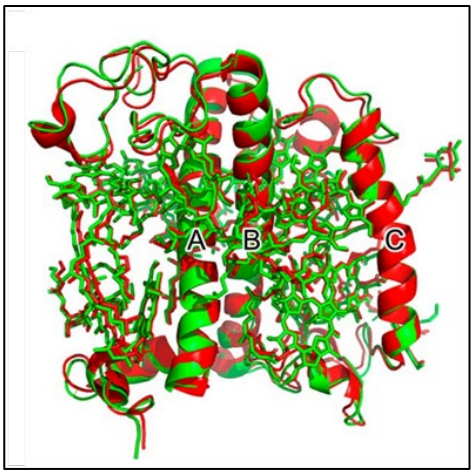

Figure 20*Superposition of the cryo-EM structure of an LHCII subunit from the S-LHCII trimer from C. reinhardtii with that from pea. Green: Chlamydomonas; red: pea*

LHCB2.1–2.4; LHCB3.1) composed the major antenna system. The three types are not equally distributed in trimers with Lhcb1 being the most abundant [41]. In *C. reinhardtii* nine genes encode for four major LHCII proteins (types I–IV) with five, one, two and one isoforms, respectively (LHCBM3, 4, 6, 8 and 9; LHCBM5; LHCBM2 and 7; LHCBM1) [63]. As in the case of monomeric antennae, in the trimeric complex, each monomer is formed by 3 transmembrane helixes (A, B and C). The N-terminal and the C-terminal are exposed respectively on the stromal and luminal spaces. In addition to the main transmembrane, two amphipathic helix, named D and E, are present on the C-terminal peptide and in the BC loop region respectively [15]. The Cr-LHCII trimers exhibited similar overall structures to that of higher plants in terms of the number and location of pigments as well as the protein secondary structure [33] (**Figure 21**). The whole trimerization region covers the amino-terminal domain, the carboxy terminus, the stromal end of helix B, several hydrophobic residues from helix C and the pigments and lipid bound to these parts of the polypeptide. Six Chl *a* (Chl 602 and Chl603 from each monomer) constitute the core of the trimer [15]. Each LHCII monomer binds 14 Chls and 4 Cars: 8 Chls *a*, 6 Chls *b*, 2 lutein, 1 violaxanthin and 1 neoxanthin. In addition, two different lipid molecules complete the LHCII structure: phosphatidyl glycerol (PG) and digalactosyl diacyl glycerol (DGDG) [15]. Inner carotenoids binding sites (L1 and L2) bind lutein while the outers V1 and N1 bind violaxanthin and neoxanthin respectively. In high light conditions, after violaxanthin conversion into zeaxanthin, V1 site can be occupied by the latter even if with different capacity among the 3 components of LHCII in plants. Lhcb3 shows higher zeaxanthin exchange rate with respect to other two [76]. Chlorophyll binding sites identified in LHCII from plants are also conserved in the nine *Chlamydomonas* Lhcbm proteins suggesting same number of chlorophylls bounded with only a possible change in Chl *a* or Chl *b* affinity considering Chl a/b ratio of these proteins [33,36].

Supramolecular organization of PSII

LHCII trimers associated with the PSII core can be distinguished into 3 types, namely S (strongly associated), M (moderately associated), and L (loosely bound), based on their position in the PSII–LHCII supercomplex and affinities with the core [49]. In *Chlamydomonas reinhardtii* L-type trimer was also named N type (N, naked) for the reason that this trimer was directly associated with the PSII core without involvement of any monomeric antenna [36]. The antenna size of PSII is larger in *C. reinhardtii* compared to higher plants [36] with around seven LHCII trimers for monomeric PSII core with respect to four in *A. thaliana* [51]. Structural models for higher plant PSII show the presence of a dimeric core (C_2), four LHCII trimers, two strongly bound (S) and two moderately (M) bound to the core; there are also present two monomeric copies each of CP29, CP26, and CP24 (**Figure 22**). S trimer are directly attached to CP43 core complex and can interact with CP29 to one PSII core monomer and with CP26 to the other core. M trimer are not directly in contact with CP47 but energy transfer occurs via CP24 and CP29 [61,77]. CP24 cannot transfer excitation energy directly to the core, because there are no Chls of CP47 located near CP24.

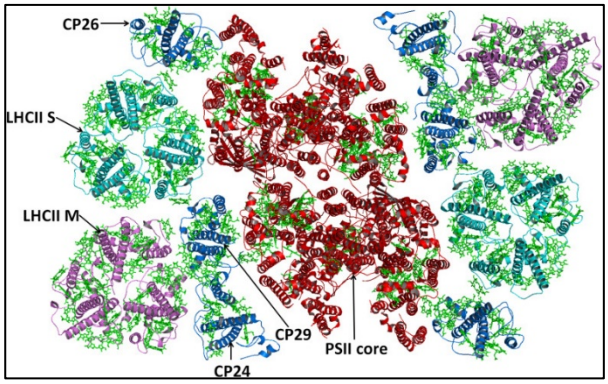

Figure 21 *Map of $C_2S_2M_2$. Architecture of PSII as seen from the stromal side of the membrane.*

This indicates that the transfer from trimer M and CP24 to the core occurs through CP29 [61]. As mentioned before, isolated PSII–LHCII supercomplexes contain from two to four LHCII trimers, depending on growth conditions, but biochemical quantification reveal the presence of about eight LHCII trimers per PSII core dimer. This implies the presence of a pool of unbound or very loosely bound LHCII (L-LHCII) that can connect to the PSII, forming the bigger $C_2S_2M_2L_{1\text{-}2}$ complexes [31,49]. In *Chlamydomonas reinhardtii* the overall structure of PSII–LHCII consists of 2 PSII core complexes (C_2), 2 strongly bound LHCII trimers (S-LHCIIs), 2 moderately bound LHCII trimers (M-LHCIIs), and 2 naked LHCII trimers (N-LHCIIs), forming a $C_2S_2M_2N_2$-type supercomplex (**Figure 23**). In addition, 1

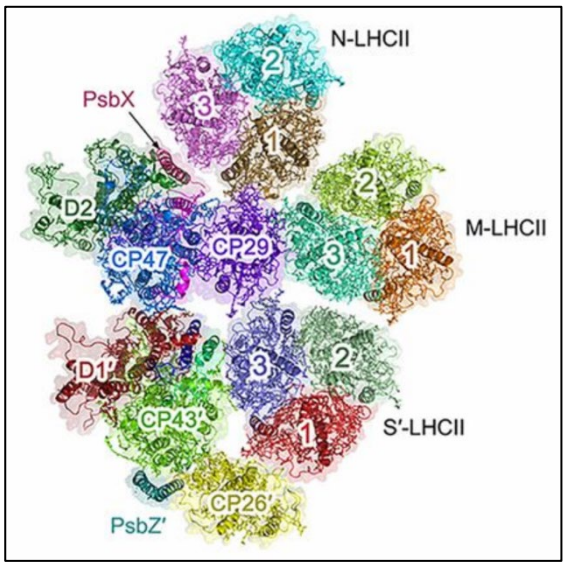

Figure 22 *Surface and cartoon representations of the local structure of Cr $C_2S_2M_2N_2$-type supercomplex including LHCII (S-LHCII, M-LHCII, and N-LHCII), CP26, CP29, D1, D2, CP43, CP47, PsbH, PsbI, PsbX, PsbW, and PsbZ, viewed from the stromal side*

CP26 subunit and 1 CP29 subunit are associated with each PSII core. S-LHCII and CP26 attach to the core directly at the CP43 side, whereas the M-LHCII trimer attaches to the core at the CP47 side through CP29. The N-LHCII trimer takes the position occupied by CP24 in plant PSII–LHCII [52], and attaches to the core at the CP47 side partially directly and partially through interactions with CP29. One distinct feature of the Cr-LHCII trimers is that its M-LHCII trimer is rotated counterclockwise by 60° relative to the position and orientation of M-LHCII in higher plants [33].

Photoinhibition and photoprotection

Photosynthetic organisms depend on sunlight harvesting to trigger photosynthetic reactions. However, light can be extremely harmful; its absorption can lead to the formation of reactive intermediates which can damage the thylakoids membranes in a photo-oxidation process called photoinhibition [78]. Photoinhibition occurs when the light harvested exceeds the metabolic ability to regenerate ADP and $NADP^+$. As light intensity increases, the rate of photosynthesis becomes saturated, but light in excess of what is required for the maximum photosynthetic rate (Pmax) is still absorbed (**Figure 24**). In this overexcited condition, the energy of exited chlorophylls cannot be properly used for photochemistry leading to the possible formation of dangerous molecules as oxygen reactive species [79,80]. Normally, excited pigments rapidly (<ps time scale) transfer the excitation energy to the reaction centers. However, upon saturation of the photosynthetic apparatus, singlet excited states of chlorophylls (^{1}Chl*) are not quenched by photochemistry and their concentration dramatically increase. ^{1}Chl* can be converted by intersystem crossing (ISC) into the long-lived triplet exited state chlorophyll (^{3}Chl). ^{3}Chls* (with lifetime about milliseconds) can react with triplet oxygen producing singlet oxygen ($^1O_2$) that is a highly reactive oxygen species (ROS) [81] [82]. $^1O_2$ causes oxidation of lipids [83], proteins and pigments [84]. Thylakoid membrane lipids, with their abundance in unsaturated fatty acid side chains, are highly susceptible of singlet oxygen attack [85]. PSII core is also a possible site in which ROS can be formed after charge recombination between $P680^+$ and Ph^- and consequent production of ^{3}P680. This could happens when Q_A is already reduced and electron transport is

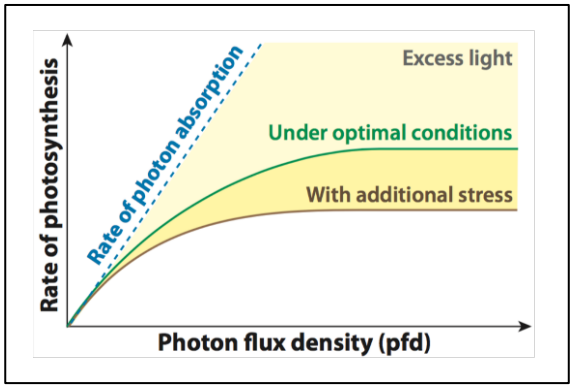

Figure 23 *Light response curves for photosynthesis compared with the rate of light absorption*

blocked; triplet P680 can react with oxygen forming ROS [86]. Production of singlet oxygen in the PSII reaction center causes damages especially at the D1 protein [78]. Differently, in PSI, $P700^+$ is more stable than $P680^+$ and behave as excitation quencher but ferredoxin can reduce oxygen to superoxide anion (O_2^-) [87,88]. ROS produced are able to damage key enzymes of photosynthetic carbon metabolism as well as subunits of PSI reaction center. Photosynthetic organisms evolved multiple strategies to limit ROS production and photoinhibition. These photoprotective strategies can classified on the base of the time required for their onset. Light stress can build up slowly (i.e. solar light that increase during day or with season alternance) or in a very short time (i.e. upon sun flecks) and for that reason several mechanisms with different time scale can be adopt by photosynthetic organisms (**Figure 25**).

Non photochemical quenching (NPQ)

Non photochemical quenching allows thermal dissipation of excess absorbed energy [89]. NPQ activation and modulation depends on thylakoid transmembrane ΔpH deriving from photosynthetic electron transport [90]. Thermal dissipation can be monitored as a light-dependent quenching of Chl fluorescence [91]. NPQ is a complex phenomenon and it involves several processes: energy-dependent feedback de-excitation quenching (qE) [92], state transition dependent quenching (qT) [93], zeaxanthin-dependent quenching (qZ) [94] and photo inhibitory quenching (qI) [95].

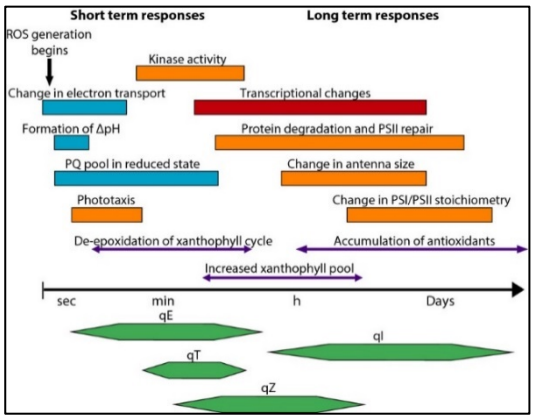

Figure 24 *Relative time scales of short-term and long-term responses to excess light in C.reinhardtii*

Energy dependent NPQ (qE)

qE is the component of NPQ most rapidly activated (in few seconds). It can be considered as a type of feedback regulation of the light-dependent reactions of photosynthesis sensing pH into thylakoids lumen and acting as consequence [95]. The requirement for acid pH is evidenced by the inhibition of qE by uncouplers such as nigericin. Moreover, mutants with lower qE levels allowed to uncovered, in some cases, defection in generation of the ΔpH [96]. It is worth mentioning that NPQ in cyanobacteria is an ON-OFF mechanism depending on photo-conversion of OCP only and it is independent of ΔpH [97].

There are three ways in which qE acts to protect from photo damage:

- decreasing the average lifetime of 1Chl* in PSII, thereby decreasing $^1O_2$ generation [78]
- prevent over-reduction of the electron carriers of the plastoquinone pool
- preventing over acidification of the thylakoid lumen [98] which can damage the oxygen-evolving complex and result in the release of the manganese cluster [99].

The ability to activate an NPQ response has been observed in all organisms performing oxygenic photosynthesis including cyanobacteria, algae and plants. Despite its widespread presence, NPQ has different features in different taxa. In cyanobacteria, NPQ depends on the presence of a soluble carotenoid-binding protein, OCP [100]. In eukaryotic algae and plants, NPQ is triggered by two different members of LHC protein family. In particular, light harvesting complex stress related (LHCSR) has been shown to be essential in green algae

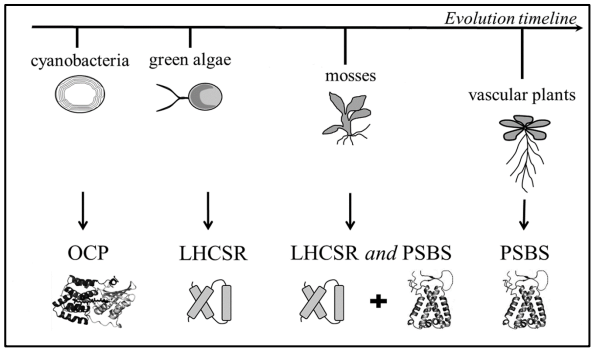

Figure 25 *Schematic representation of NPQ triggering protein from cyanobacteria to vascular plants*

[101]. On the other side, in vascular plants, NPQ depends on the presence PsbS [102] (**Figure 26**).

The role of zeaxanthin in qE is long time debated being different among taxa and being related to different protein activators. In *A. thaliana* the amount of zeaxanthin synthesized via the xanthophyll cycle is highly correlated with the level of qE [103]. Both using inhibitor like dithiothreitol that blocks zeaxanthin synthesis or using mutants that are unable to convert viola to zea a reduction in qE is evident [103,104]. Lutein has also been found to be implicated in qE activation. Mutants lacking lutein show less NPQ compared to wild type and, the double mutants of *A. thaliana* lacking lute and zeaxanthin, are totally impaired in qE activation [105]. Presence of zeaxanthin for qE activation, however, is not mandatory in green alga *Chlamydomonas reinhardtii*: *npq1* mutants, unable to convert violaxanthin into zeaxanthin, shows similar NPQ behavior [106].

Photoprotective proteins PSBS and LHCSR

Vascular plants sense low luminal pH and activate NPQ via PsbS. This protein has 4 trans-membrane helixes rather than 3 as in most members of LHC family [107] (**Figure 27**). The ability to sense pH is given by the presence of two protonatable glutamate residues exposed to the lumen [102,108]. The pigment-binding capacity of PsbS has been the subject of debate; data set it as a non-pigment-binding protein [109,110] but recently it has been shown that a chlorophyll molecule can be bound in a pocket on the luminal dimerization interface [111]. The molecular mechanism by which PsbS acts is not fully understood. Due to the probable absence of pigments, PsbS is unlikely itself primary site of quenching activity. Models rely on activation of a quenched state of LHCB proteins mediated by interaction of PsbS [112-114]. Recently two different mechanisms, both involving PsbS activation, which synergistically cooperate was proposed for LHCII major antennae and minor antennae [115]. Green algae possess PsbS gene even if for years the corresponding protein was not detected in any tested condition. Recently rapid and transient accumulation of PsbS was reported in green alga *Chlamydomonas reinhardtii* upon shift in high light conditions, with a maximum at 8 hours [116]. Despite that no clear role in photoprotection was attributable to

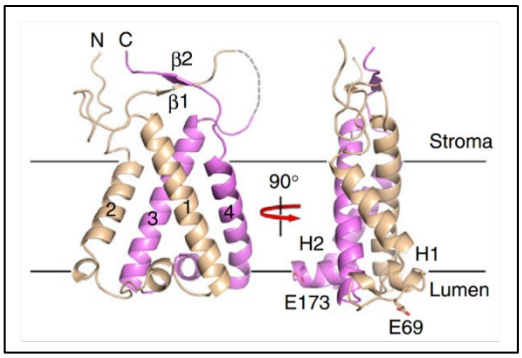

Figure 26 *Ribbon representation of PsbS viewed from the membrane plane*

PsbS in *C. reinhardtii* even though it showed the ability to increase NPQ [116]. Activation of NPQ in green algae is dependent on LHCSR proteins (Light Harvesting Complex Stress Related). LHCSR-like sequences have been identified in all eukaryotic algal groups, suggesting that algae rely on LHCSR-like proteins for NPQ. On contrary no LHCSR gene is present in any known vascular plant, but they have been identified in the moss *Physcomitrella patens* [75]. It is worth to note that, on contrary with respect to green algae, LHCSR in *P. patens* does not have an exclusive role in NPQ activation being necessary also the accumulation of PsbS even if with mutants its major role was shown [117].Three genes coding for LHCSR isoforms are present in *C. reinhardtii* genome: LHCSR3.1, LHCSR3.2 (coding for the same protein) and LHCSR1 coding for a polypeptide with 87% identity with respect to LhcSR3.1/LhcSR3.2 [118]. In some algal species, LHCSR is constitutively present [119], but in other species, such as *C. reinhardtii*, there are a linear correlation between light intensity, protein level and NPQ [101]. This linear correlation in *Chlamydomonas reinhardtii* has an exception: LHCSR1 is constitutively present even at low light levels [120] but its role in the overall NPQ mechanism is marginal if compared to LHCSR3 [101]. LHCSR protein is composed by three trans-membrane helices and can bind pigments, like other LHC proteins (**Figure 28**). Moreover, it has been found in dimeric forms in *C. reinhardtii* [106]. Comparing LHCSR sequence with other LHC protein it was possible to identify 6-8 conserved pigment-binding sites (6 are conserved while 2 are shifted) accordingly with stoichiometry analysis of *in vitro* reconstituted protein. Lutein and violaxanthin can respectively bind L1 and L2 sites. An additional xanthophyll can be bound to a third more peripheral site, V1 [106]. Analysis of *in vitro* refolded proteins underlines also the role of Chl *b* on protein stability: it can be replaced by

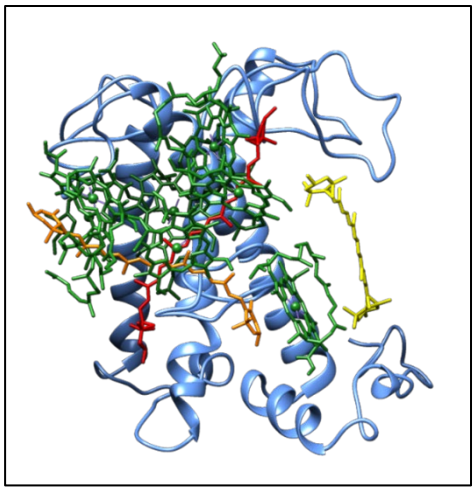

Figure 27 *LHCSR3 model built on LHCII crystal structure showing chlorophyll and carotenoids.*

Chl *a* but its absence causes a protein folding efficiency 20-fold lower [106]. Capability of binding pigments suggests that the protein can be direct site of energy quenching. This is clearly demonstrated by its short excited state lifetime, suggesting pigments positioning to determine an energy-dissipative form [106]. Sequence comparison of LHCSR proteins from different organisms revealed multiple protonatable sites suggesting an important role for them to sense pH variations. Mutation analysis on LHCSR3 from *Chlamydomonas reinhardtii* confirmed their importance in sensing pH and activating NPQ [121]. Interestingly, unlike other LHCSR homologous, *Chlamydomonas reinhardtii* LHCSR3 presents a C-terminal tail particularly rich in acidic residues (13 residues with respect to 4 in *P.patens* and 2 in *P. tricornutum*) hinting a possible different pH-sensing [121,122] (**Figure 29**). As in the case of PsbS, also LHCSR mediated quenching mechanism is not fully understood with several model proposed. Hypothesis

Figure 28 *LHCSR3 model built on LHCII crystal structure showing protonatable residues.*

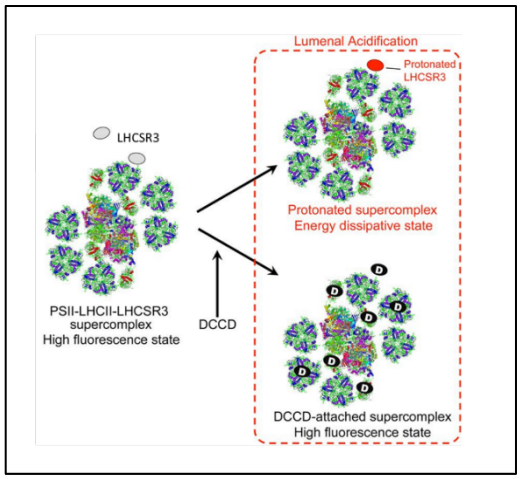

Figure 29 *A model for the induction of qE in C. reinhardtii. LHCSR3 expression under HL conditions and its binding to the PSII-LHCII supercomplex. After acidification of the thylakoid lumen supercomplex PSII-LHCII_LHCSR3 shifts to an energy dissipating state. This energy dissipation is inhibited by DCCD-binding.*

suggests that LHCSR regulates energy dissipation by, establishing reversible interactions induced by low luminal pH with other LHCB antenna proteins, in particular LHCBM1 [106,123,124]. Recently a possible role of LHCBM4-6-8 as docking site(s) for the interaction of the PSII antenna system with LHCSR3 was also reported. Model proposed by Tokutsu and co-authors involves LHCSR3 accumulation during excess light forming a PSII-LHCII-LHCSR3 supercomplex. The protonation of LHCSR3, which occurs upon luminal acidification directly modifies supercomplex conformation to form a quenching center [123].

Evolutionary reasons can explain differences between plants and algae NPQ triggers: when algae 450 Ma ago started land colonization, different environmental conditions forced them to evolve new NPQ induction mechanisms. Fast and more pronounced light fluctuations are common in the terrestrial environment so plants may have selected PsbS during their evolutive path instead of LHCSR, to face this problem. Comparison of NPQ amplitude at different actinic lights of *A. thaliana* and *C. reinhardtii* (**Figure 31**) showed that the alga activates and saturates NPQ activity at relative low light, in contrast with *A. thaliana* behavior, which responds proportionally to light intensity [125,126].

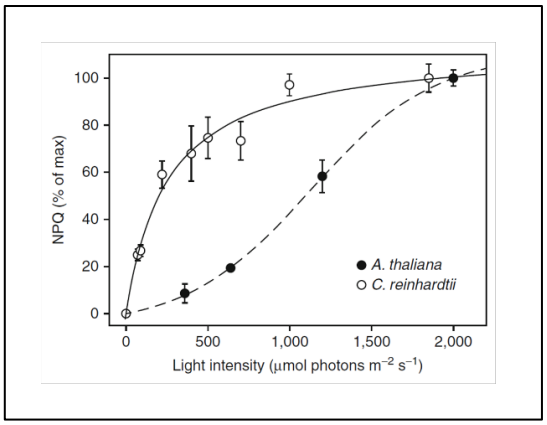

Figure 30 *Dependence of NPQ on actinic light intensity in C. reinhardtii and A. thaliana. Both organisms were acclimated to high light intensity*

Other NPQ components: qZ

In higher plants, zeaxanthin is known to trigger both qE and qZ, being the latter an NPQ component characterized by a slower rise over the course of few minutes as well as a slower relaxation over the course of tens of minutes [26,94]. qZ represents a zea-dependent NPQ component, which, except for the synthesis of zea, does not require a low luminal pH nor PsbS. Different models try to explain the mechanism by which the xanthophyll cycle induces dissipation of excess energy: they involve zeaxanthin directly by quenching ^{1}Chl* or indirectly by inducing structural changes in specific antenna complexes to a dissipative conformation [26,94].

Other NPQ components: qT

Considering in-series work of PSII and PSI, balance excitation of each photosystem is crucial to maintain efficient electron transport. Furthermore, PSII is more susceptible than PSI to photo-oxidation thus an excessive excitation of PSII can be extremely harmful. Photosynthetic organisms evolve a reversible mechanism triggered by a kinase/phosphatase system that responds to plastoquinone's redox state to move LHCII from PSII to PSI called state transitions. For example, in case of an insufficient absorption by PSI, the electrons transport chain would be blocked determining accumulation of reduced plastoquinones. This condition activates the kinase phosphorylating a LHCII sub-population which migrates to PSI, increasing its activity and reactivating electron transport chain. When the redox state of plastoquinones is restored, kinase is inactivated and, upon the action of a phosphatase, part of LHCII complexes return to PSII. Up to 80% of LHCII antennae are known to dissociate from PSII whenever state transition is triggered in *Chlamydomonas reinhardtii* [127,128] whereas in plants only 20% of LHCII antennae are involved [129].

Other NPQ components: qI

Protracted high light stress can irreversibly damage PSII core. Fortunately, PSII, is characterized by an efficient and dynamically regulated repair cycle [78]. In fact, photoinhibition occurs when the rate of damage outpaces the rate of repair determining the irreversible qI component of NPQ. qI determines a decrease in fluorescence emitted related to a decrease in abundance of PSII supercomplexes. By regulating PSII photoinhibition, involving PGR5 and Cyt b6f, electron flow to PSI can be regulated in order to protect it from damage, which is required, considering the absence of repairing mechanisms on it [130].

Alternative electron transport

Alternative electron transport mechanisms cooperate with NPQ acting as safety valves in condition of light excess [95].

- *Cyclic electron flow*: provides the extra ATP needed for carbon fixation and other cellular processes when the relative demand for ATP is higher than photosynthetic line can provide [5].
- *Chlororespiration*: provides a mechanism to prevent the complete oxidation of the plastoquinone pool in the dark, as well as to prevent its complete reduction in excess light. PTOX, a NADPH-dehydrogenase plastoquinol oxidase, operates the PQH_2 oxidation reducing oxygen to water. Electron flow from PSII to PTOX can drive ATP synthesis exploiting the proton gradient formed by PSII [131].
- *Mitochondrial respiration*: it has been shown to consume reducing power produced during the light phase of photosynthesis in order to restore the electron acceptor NADP+ [132].

Long-term photoprotective mechanisms

When photosynthetic organisms are exposed for a long time to high light stress conditions, long-term

photoprotective mechanisms are activated. These adaptations involve multiple processes, for instance the expression or repression of specific genes, but also chloroplast movement and modification of plant morphology. Reduction of antenna size by adjustment in LHC genes expression or LHC proteins degradation is one of these mechanisms [133]. In *A. thaliana*, upon a shift from low light to high light, LHCII major antenna proteins are strongly downregulated, decreasing the size of the PSII antenna [125]. Differently, *C. reinhardtii* acclimation to high light intensities causes a decrease in chlorophyll content per cell due to a reduction in photosystem number instead of antenna size reduction as in plants [126].

Photoprotective antioxidant molecules

Reactive species produced during photooxidative stress can be deactivated by several antioxidant molecules present in the chloroplast as ascorbate, glutathione, tocopherols and carotenoids [134]. Carotenoids are involved is several additional photoprotective mechanisms:

- *Modulation of triplet chlorophyll (^{3}Chl*) yield*: by excitation energy transfer from the triplet chlorophyll to carotenoid forming the carotenoid triplet (^{3}Car*). The triplet–triplet energy transfer from the triplet chlorophyll to carotenoid is possible because the triplet energy level of carotenoid is below the triplet energy level of chlorophyll [135,136]. The triplet carotenoid decays radiation-less into the ground state by heat dissipation.

- *Scavenging of ROS*: the excitation energy transfer from ROS to carotenoid generating triplet molecular oxygen ($^3O_2$) and the triplet excited state of carotenoid (^{3}Car*). As before, triplet carotenoid decays to ground state by heat dissipation [137].

- *Modulation of chlorophyll singlet excited states (^{1}Chl*) yield:* preventing over-excitation of reaction centers by quenching directly ^{1}Chl* states generating ^{1}Car* which decay by heat dissipation [138].

Tocopherols are thylakoid antioxidant molecules, free into the membrane, able to chemically scavenge $^1O_2$, O_2^- and $OH^\bullet$ [139].

Ascorbate is a soluble antioxidant molecule; it can prevent oxidative damage both by direct quenching of major ROS and as substrate for VDE and Ascorbate Peroxidase (APX) [140].

Glutathione has a key role in detoxifying $^1O_2$ and $OH^\bullet$. It is also involved in regeneration of both α-tocopherol and ascorbate [134].

The promising future of microalgae

Supply sustainably a growing world population with food, raw materials, and energy without worsening global pollution and climatic change is one of the biggest challenges of the twentieth century. Biomass, thus, plays an important role and photosynthetic organisms are a keystone being able to produce all the above-mentioned elements simply converting atmospheric carbon dioxide by exploiting solar energy. All photosynthetic organisms are, in principle, suitable for solar-driven biomass production but, despite the presence of pro and cons in using one instead the other, there are clear limits: availability of agricultural area is tricky and it will be always more considering desertification, erosion and industrialization. Microalgae are a promising way to overcome this limitation and the potential for bioeconomy exploiting these organisms is enormous.

Microalgae are photosynthetic organisms that grow in a range of aquatic habitats, including lakes, river, pounds, oceans, and even wastewater. They can tolerate a wide range of temperatures, salinities and pH values as well as different light intensities [141]. Chlorophyceae (green algae), include genera which are the most widely used for industrial applications, such as *Haematococcus*, *Chlorella*, *Dunaliella* and the model organism *Chlamydomonas reinhardtii*.

Beside the sole use for biomass accumulation, microalgae received increasing attentions for commercial cultivation for extraction of a wide range of products including recombinant protein, bioactive compounds and biofuels [142,143] as well as for use in wastewater treatments [144](**Figure 32**). Bio-refinery using a mono-species cultivation can thus produces a high variety of resources; moreover, residual biomass, after products extraction, can be easily used as livestock feed, as organic

fertilizer/biostimulant as well as used for energy production.

Several advantages in using microalgae instead of plants can be listed:

a) Microalgae can produce 5-10 times more biomass respect to the case of energy plants [145]. Considering plants, the theoretical maximal photosynthetic energy conversion efficiency is 4.6% for C3 and 6% for C4 plants, calculated based on the total initial solar energy and the final energy stored in biomass. On the other sides, microalgae theoretical photosynthetic efficiency is close to 8-10% with an harvest about 100 ton per hectare per year [145] with respect to 10 ton per hectare per year measured for sugar cane, best producing crops [146].

b) No valuable agricultural area is required. Microalgae can grow in wastelands, using wastewater or even sea water in the case of marine species. The possibility to use virtually any areas, implies that microalgae cultivation does not compete with resources for conventional food production.

c) Many microalgae species can be cultivated in mixotrophy conditions. In that case, beside photosynthesis, organic compounds are used as carbon source. Mixotrophic growth allows to harvest almost double biomass per liter per day respect phototrophic growth [147].

d) Different species can be selected for specific climate conditions. This is more difficult with conventional crops.

Applications and products

Microalgae are already used as food supplements for a long time. Proteins, vitamins, polyunsaturated fatty acids (PUFA) and antioxidant are only few of the substances which can be produced, for example, by the cyanobacterium Arthrospira [148] [149-151] or green alga *C. vulgaris* [151-153].

Another important application field is animal feed. Sustainable aquaculture has to be further expanded considering the overfishing of the ocean. Fishes are at the end of food chain, microalgae at the beginning; for that reason, finding and cultivation of algal strains able to feed

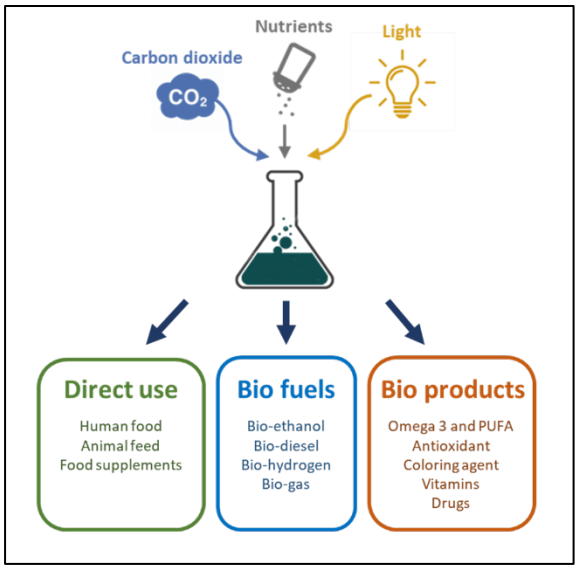

Figure 31 *Example of possible industrial products obtainable from microalgae*

fishes in an healthy way is the keystone to produce healthy fish for human feeding [154]. Besides fish feed, the use of microalgae for livestock feeding can be a possible alternative able to face the increased demand for meat [155].

Carotenoids represent the commercial product from microalgae with the highest market. They are mainly used as coloring agent in food, as aquaculture or poultry feed additives to impart color to farmed salmon or eggs yolks as well as components for cosmetics [156]. Carotenoids are also characterized by a strong antioxidant power making them extremely useful molecules in several biomedical application as anti-inflammatory [157]. Major carotenoids with health benefits on human which are produced in algae are β-carotene, astaxanthin, lutein, zeaxanthin and canthaxanthin. β-carotene, is responsible for the prevention of toxin build-up in the liver and have a preventative role in eye diseases [158]. Lutein and zeaxanthin play a significant role in eye health being predominant pigments in macula [159]. Canthaxanthin is reported to have positive effect in blood disorder diseases treatment [160]. Astaxanthin is one of the strongest natural antioxidants exhibits several-fold stronger antioxidant activity than vitamin E and β-carotene [161]. Astaxanthin has potential uses as an antitumor agent [162] as well as in prevention and treatment of neurological diseases and diabetes [163] [164]. It is worth to underline the way by which astaxanthin is currently produced at industrial level. Only few species of algae are able to produce this high value metabolite; among these, *H. lacustris* is the one

preferentially used [165]. *H. lacustris*, can accumulate astaxanthin up to 90% of total carotenoids and 4% of cell dry weight [166] upon stress conditions. Stress conditions cause stop of growth [167] as well as the formation of thick and resistant cell walls extremely recalcitrant to soft extraction methods [165]. Complexity of cellular changes, difficulty in cultivation as well as the need of strong extraction methods lead natural astaxanthin to be extremely expensive [168]. In *H. lacustris* astaxanthin is usually singly esterified with several fatty acids. (C18:3, C18:2, C18:1 and C16:0 are the most commonly). Doubly esterified astaxanthin was also found, although in lower concentrations compared to singly esterified astaxanthin[169].

Fatty acids and triglycerides (TAGs) find several industrial applications and microalgae perfectly integrate in this economy being the primary producers of lc-PUFAs [170]. Lc-PUFAs are important elements for human diet, currently supplied mainly by fish oil, which plays a crucial role as anti-inflammation molecules especially in allergic diseases treatment [171,172]. Oil from several microalgae, as *Nannochloropsis*, is starting to replace fish oil thanks to its far higher antioxidant power conferred also by carotenoids accumulation [173].

Finally, in last years, microalgae become an alternative source of biomass for replacing fossil fuels. Third generation biofuels, exploiting algae, are consider promising because these organism does not compete for arable land providing a solution for food vs fuel problem [174]. Carbon rich algae biomass can be fermented to bioethanol or biogas [175,176] or alternatively oil fraction can be trans-esterified to produce biodiesel [177]. Unfortunately, production of third generation biofuels is still far from being commercially viable [178]. Bio-hydrogen can be produced by microalgae but, although it is great promise for generating future sustainable energy, at the moment production is extremely low, difficult and expensive limiting its use on large scale [179].

Microalgae genetic engineering: state of the art and perspectives

'Green Revolution' of agriculture, over the past 50 years, based on breeding and phenotypic selection, allows successfully implement of crop productivity [180]. An industrial application of microalgae in order to be useful for providing biomass and bioproducts for growing population, needs, mandatorily, to take advantage of a domestication approach, analogous to that carried out for modern crops.

Genetic engineering has the potential to revolutionize microalgae industry overcoming current limitations and pulling the trigger on new applications. Manipulation of algal genome leads to the possibility to generate strains with desirable commercial traits by up/down regulation of endogenous genes or by transferring new genes from other organisms. Consolidation of transformation methods and developing of new technologies as CRISPR-Cas9 system both in model and in commercial microalgae, allows targeted manipulations bypassing 50 years of green revolution. Several cellular systems were efficiently manipulated resulting in an increased biomass/bioproducts accumulation.

Optimization of light penetration into high density culture with isolation of mutants having a truncated light-harvesting system shows higher productivity than the wild type for all of them in lab-scale [181-184]. This approach was successfully used also in algae with an industrial application as *Chlorella sorokiniana* [185] or *Nannochloropsis gaditana* [186].

NPQ is another proposed target to improve microalgae productivity considering results obtained in plants [187,188]. Positive results were obtained in cyanobacteria; here, deletion of OCP resulted in a 30% higher biomass [189]. Contrasting data were reported for *Chlamydomonas reinhardtii* leading this strategy to be only an hypothesis at the moment in this organisms [190 191].

Recently, biomass productivity as well as lipid yield increased up to 40% in the oleaginous *Nannochloropsis oceanica* by overexpressing endogenous RuBisCO activase was achieved [192].

Conferring competitive advantage over undesirable microorganisms, is crucial for open ponds cultivation affecting both productivity and maintenance costs. Best attempt in this direction was represented by the expression of PTXD gene coding for a phosphite dehydrogenase from *P. stutzeri* conferring the ability to use phosphite as P source. Phosphite cannot be utilized

by plants, fungi and most bacteria conferring advantages to transgenic algae [193].

Genetical engineering can be used not only to enhance productivity of microalgae manipulating cellular mechanisms but also to generate sustainable bio-factory. Several favorable characteristics lead algae to be platform for the expression of recombinant proteins: subcellular compartmentation, capacity of post-translational modification as well as sophisticated protein folding machinery [194,195]. Compared to other eukaryotic platforms to produce recombinant proteins, microalgae exhibit favorable properties such as inexpensive and easy cultivation, lack of human pathogens as well as facility to genetic manipulation [196]. Biotechnologically relevant recombinant proteins have been successfully secreted from *C. reinhardtii* [197,198] resulting in a physical separation of protein and algal biomass in a way similar to *E. coli* production method [199].

Chapter 2

Investigation of non photochemical quenching (NPQ) mechanisms in green algae

Contents

In vitro and in vivo investigation of chlorophyll binding sites involved in non-photochemical quenching in Chlamydomonas reinhardtii **33**

Molecular mechanisms of nonphotochemical quenching in the LHCSR3 protein of Chlamydomonas reinhardtii **47**

LHCSR3 is a nonphotochemical quencher of both photosystems in Chlamydomonas reinhardtii **61**

Identification of parallel pH- and zeaxanthin-dependent dissipation of excess energy in LHCSR3 in Chlamydomonas reinhardtii **79**

Identification of a plant-like Violaxanthin De-Epoxidase enzyme in the green alga Chlorella vulgaris reveals evolutionary divergency of photoprotective mechanisms in the green lineage **97**

Photosystem II antenna complexes CP26 and CP29 are essential for non-photochemical quenching in Chlamydomonas reinhardtii **117**

LHCSR expression under HP70/RBCS2 promoter as a strategy to increase productivity in microalgae **133**

2.1

In vitro and *in vivo* investigation of chlorophyll binding sites involved in non-photochemical quenching in *Chlamydomonas reinhardtii*

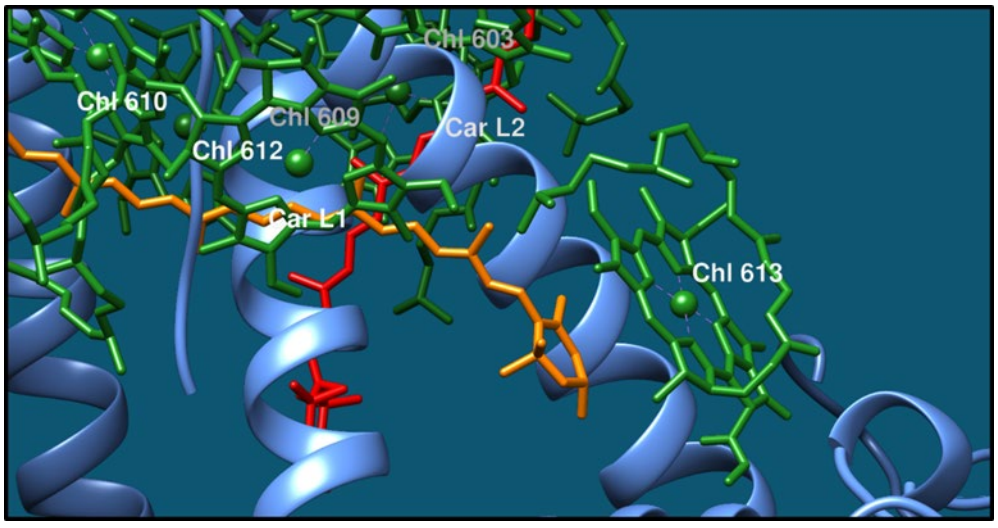

This section is based on the published article: Perozeni, F., Cazzaniga, S. & Ballottari, M. *In vitro* and *in vivo* investigation of chlorophyll binding sites involved in non-photochemical quenching in Chlamydomonas reinhardtii. Plant, cell & environment 42, 2522-2535, doi:10.1111/pce.13566 (2019).

Author Contributions: Ballottari M. conceived the work and wrote the paper. Perozeni F. performed all the experiments reported. Cazzaniga S. contributed to the selection and characterization of transformant strains and to the 77 K time-resolved fluorescence measurements. All authors analyzed the results, contributed to writing, and approved the final version of the manuscript.

In vitro and *in vivo* investigation of chlorophyll binding sites involved in non-photochemical quenching in *Chlamydomonas reinhardtii*

Federico Perozeni[1], Stefano Cazzaniga[1], Matteo Ballottari[1]

[1] Dipartimento di Biotecnologie, Università di Verona, Strada Le Grazie 15, 37134 Verona, Italy

Abstract:

Non-photochemical quenching (NPQ) of the light energy absorbed is one of the main photoprotective mechanisms evolved by oxygenic photosynthetic organisms to avoid photodamage, at a cost of reduced photosynthetic efficiency. Tuning of NPQ has been reported as a promising biotechnological strategy to increase productivity in both higher plants and unicellular microalgae. Engineering of NPQ induction requires the comprehension of its molecular mechanism(s), strongly debated in the last three decades with several different models proposed. In this work, the molecular details of NPQ induction were investigated at intramolecular level by *in vivo* and *in vitro* site-specific mutagenesis on chlorophyll binding sites of the Light-Harvesting Complex Stress-Related 3 (LHCSR3) protein, the pigment binding complexes identified as the quencher during NPQ induction in the model organism for green algae *Chlamydomonas reinhardtii*. The results obtained demonstrate a correlation between the quenching activity of LHCSR3 variants *in vitro* and the NPQ phenotypes observed *in vivo*. In particular, multiple quenching sites in LHCSR3 cooperatively dissipating the excitation energy were revealed with a peculiar role of Chl 613, a chromophore located a close distance to carotenoid binding site L1.

Introduction

Plants and algae in their natural environment are constantly exposed to rapid change in quality and intensity of light. When light is absorbed in excess, compared with the metabolic capacity to regenerate ADP and $NADP^+$, the precursor of ATP and NADPH, the photosynthetic apparatus incurs in overexcitation. In this condition, excitation energy at the level of photosystems cannot be properly used for the photochemical process, increasing the probability of energy transfer to oxygen-forming toxic reactive oxygen species (ROS) [104]. To prevent photodamage caused by ROS formation, a wide range of photoprotective mechanisms have been developed by oxygenic photosynthetic organisms [104]. Non-photochemical quenching (NPQ) is the most rapid one and leads to thermal dissipation of excitation energy in a non-radiative process [104,200-202]. NPQ has been observed and measured in several organisms, from cyanobacteria [100] to green algae [101,203], diatoms [204,205], mosses [117], and higher plants [102,104,206], being activated rapidly in seconds to minutes time scale with a feedback mechanism triggered by lumen acidification [101,108,121,122,207]. However, activation of non-radiative dissipative channel of excitation energy increases photoprotection properties at a cost of reduced photosynthetic efficiency: tuning of NPQ induction for a proper balance of photoprotection and photosynthetic efficiency has been reported as a strategy to increase biomass productivity in both higher plants [188] and microalgae [190]. The molecular details of NPQ induction in the different organisms have been extremely debated in the last three decades. Characterization of mutants selected for having an NPQ phenotype, allowed to identify light harvesting complexes (LHC) as the main quenching site during NPQ induction in eukaryotic photosynthetic organisms, with PSBS and LHCSR subunits as NPQ triggers, being able to sense the luminal pH [101,102,138,203]. In higher plants, NPQ induction is indeed activated by the thylakoid subunit PSBS, with a minor role of zeaxanthin accumulation upon high light exposure [101] [102,138] In the model organism for green algae, *C. reinhardtii* LHCSR1 and LHCSR3 proteins have been reported to be essential for NPQ induction, whereas the role of xanthophyll cycle is negligible, if any [106,208-210]. PSBS and LHCSR are present

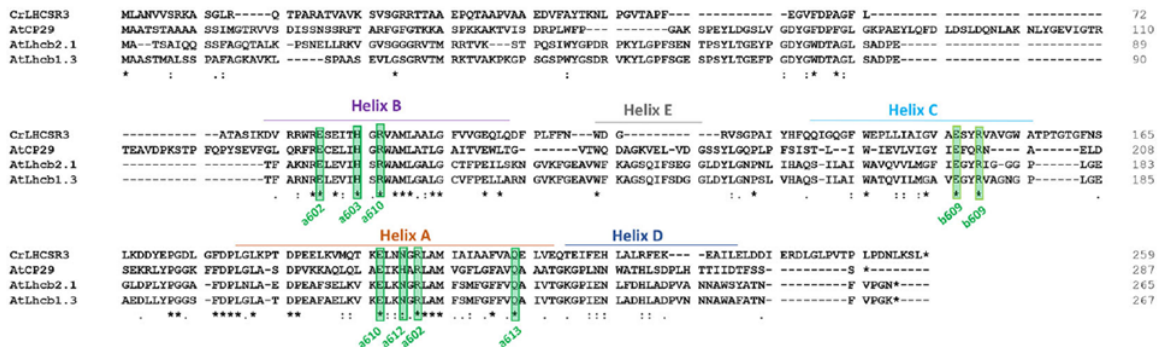

Figure 2.1.1 *Sequence alignment of LHCSR3 with CP29 and LHCII. LHCSR3 aminoacidic sequence aligned with CP29 and LHCII (Lhcb2.1 and Lhcb1.3) sequences from Arabidopsis thaliana: conserved chlorophyll binding residues are highlighted. In the case of Chl 602, 610, and 609, the glutamate residues involved in chlorophyll binding form an ion pair with an arginine residue indicated in the alignment for each case*

in the thylakoid membranes with protonatable residues exposed to the lumen side [108,121,122], being able to sense the luminal pH and activate NPQ upon acidification. However, the molecular mechanism by which these two proteins induce NPQ is different because PSBS is essentially a membrane subunit that does not bind pigments, whereas LHCSR subunits does [106,111]. PSBS is thus considered to induce other LHC proteins to switch to a dissipative state [211-213], whereas LHCSR subunits have been reported to be directly able to switch to dissipative state at low pH, being at the same time a sensor of the lumen pH and a quencher [121,122]. At intramolecular level, the detailed mechanism by which excitation energy is converted into heat it still under debate, with several mechanisms proposed. Most of the different mechanisms proposed suggest that, upon NPQ induction, LHC proteins switch to a quenched state where the chlorophyll (Chl) with the lowest energy level acts as a sink of excitation energy transferring it to a nearby carotenoid (Car), populating S_1 state or other carotenoid dark states where the quenching occurs [68,214,215]. Alternatively, excitation energy has been suggested to be quenched by formation of charge transfer state between a Chl dimer [216] or through the formation of a carotenoid radical cation [217]. In both cases, the formation of a quenching state requires a strong proximity between Chl and Car or between the Chl–Chl dimer. *In vitro* analysis on isolated and reconstituted LHC proteins was used to evaluate the role of the different chlorophyll binding sites to identify the molecular mechanisms for NPQ induction, resulting with identification of Chl 612 [68,216], Chl 613 [15,215], or Chl 603 [66] as the potential quenching sites, being the closest Chls to the inner Cars binding sites called L1 (Chl 612 and Chl 613) and L2 (Chl 603) and being involved in strong excitonic coupling with other Chl [15,64]. The identification and the characterization of binding chromophores is thus a keystone for the comprehension of quenching mechanism in LHC proteins. The quenching properties shared by different LHC proteins and the difficulties to mimic *in vitro* the quenching conditions where NPQ occurs, did not allow in the past to properly demonstrate which Chls bound to LHC are directly involved or not in the quenching mechanism. The intrinsic quenching properties of LHCSR, its peculiar role in NPQ induction in *C. reinhardtii*, and the availability of the *npq4 lhcsr1* mutant in *C. reinhardtii* depleted of all LHCSR subunits where no NPQ could be observed, allowing in this work to finally investigate the role of specific Chl binding sites *in vivo* by complementation of *npq4 lhcsr1* with LHCSR3 gene, specifically mutated on different residues responsible for Chl binding sites [106,218].

Results

Investigation of chlorophyll binding sites involved in NPQ in vitro

Identification of potential targets for site specific mutagenesis was obtained upon sequence alignment with other LHC proteins which structure with pigments bound are available, as in particular LHCII [15,64](**Figure 2.1.1**). As reported in **Figure 2.1.1**, six Chl binding sites were conserved in LHCSR3 compared with LHCII and CP29, namely, residues responsible for binding Chls 602, 603, 609, 610, 612, and 613 [106,218]. Other Chls proposed to be bound with LHCSR3 are the Chl 604, 608, and 611, which however are not coordinated by a specific residue, but rather by water or lipid molecules, making the obtainment of site-specific mutants for these Chl binding sites impossible. Chl 612 and Chl 613 were thus chosen for

	Chl tot	Chla/Chlb	Chla	Chlb	ΔChla	ΔChlb	Chl/car	Car tot	neo	viola	lute	beta-car
WT	7	7.06 ± 0.07	6.13 ± 0.06	0.87 ± 0.01	/	/	2.74 ± 0.08	2.55 ± 0.08	0.12 ± 0.17	1.49 ± 0.15	0.93 ± 0.06	0.01 ± 0.02
N200F	6	7.8 ± 0.17	5.32 ± 0.12	0.68 ± 0.01	0.81 ± 0.13	0.19 ± 0.02	2.61 ± 0.02	2.3 ± 0.02	0.05 ± 0.07	1.29 ± 0.16	0.94 ± 0.05	0.02 ± 0.01
Q231L	6	7.72 ± 0.24	5.31 ± 0.17	0.69 ± 0.02	0.82 ± 0.18	0.18 ± 0.02	2.69 ± 0.02	2.23 ± 0.02	0.1 ± 0.15	1.13 ± 0.1	0.99 ± 0.19	0.01 ± 0.01
H90F	6	5.94 ± 0.19	5.14 ± 0.17	0.86 ± 0.03	1 ± 0.018	0 ± 0.03	4.44 ± 0.98	1.35 ± 0.3	0.06 ± 0.08	0.39 ± 0.03	0.89 ± 0.14	0.01 ± 0.01

Table 2.1.1 *Pigment binding properties of recombinant LHCSR3 WT and mutant variants refolded in vitro. Pigments binding properties of LHCSR3 WT and mutant variants are reported considering eight chlorophylls bound by the following:*

mutagenesis analysis in LHCSR3 because of proximity with Car L1 site in both LHCII [15] and CP29 [64], whereas chlorophylls Chl 602 and 603 were chosen being the closest Chls to Car L2 [15,64] (**Figure 2.1.1**,**Table 2.1.2**).In addition, Chl 612 and Chl 603 are strongly coupled with Chl 610/611 and Chl 609 and/or Chl 602, respectively [15,64,218,219]. Finally, Chl 612 has been reported to be the Chl with the lowest energy level associated in most LHC protein, suggesting its potential role in quenching [219], whereas Chl 613 was proposed to be the reddest chlorophyll in LHCSR3 [218]. Mutated version of LHCSR3 subunit on Chl binding sites were thus obtained by substituting the polar residues responsible for Chl coordination with non-polar ones In particular, the following residues N200, Q213, E87, and H90 responsible for Chl 612, 613, 602, and 603 binding were mutated to F, L, V, and F, respectively (**Table 2.1.2**), as previously reported for other LHC proteins [220,221]. In the case of Chl 602, the double mutant E87V–R202L was also included in the set of LHCSR3 mutant because, as previously reported, the glutamate responsible for Chl 602 forms an ionic pair with an arginine on the opposite helix which destabilize the holoprotein if the latter is not mutated as well to a non-charged residue [221]. LHCSR WT and mutated version were first analyzed i*n vitro* upon protein expression in *E. coli*, followed by refolding with pigments to investigate the effect of the mutation introduced on the pigment binding properties of the protein complex. Among the LHCSR3 mutants reported in **Table 2.1.2**, either single or double mutants putatively affecting Chl 602 were not stable *in vitro* and no reconstituted holoproteins were obtained for these mutants. Pigment binding properties of refolded complexes were analyzed and reported in **Table 2.1.1**. Considering a stoichiometry of one lutein molecule per holocomplex [106], one Chl was found to be lost in mutant complexes. In particular, one Chl *a* was lost in H90F mutant, whereas a small partial loss of Chl *b* was also detected in the case of N200F and Q213L mutants (**Table 2.1.1**). The loss of Chl *b* upon mutations on Chl binding site located close to L1 has been reported previously for other LHC complexes, as in the case of LHCB1 from *Zea mays* [222] or LHCB5 from *Arabidopsis thaliana* [220]. In the case of mutant H90F, a strong reduction of Cars content and in particular violaxanthin was also evident: considering the preferential binding of violaxanthin to the inner Cars binding site L2 [106], this finding suggest a partial destabilization of L2 site upon mutation to closely located Chl 603 binding site. Reconstituted holoproteins were then analyzed by absorption spectroscopy (**Figure 2.1.3**): absorption spectra in the visible region were normalized considering the loss of one Chl molecule in H90F, N200F, and Q213L mutant compared with WT as previously described [221]. By subtracting the mutant to WT absorption spectra (**Figure 2.1.3 a-c**), it was possible to observe the spectral feature of the Chl lost: difference absorption spectra WT minus mutant were indeed characterized by a main peak in the 600–800 nm region at around 680 nm in all cases,

Table 2.1.2 *LHCSR3 mutant variants analyzed in vitro and in vivo. Mutated residues on LHCSR3 mutant variants herein investigated in vitro and in vivo are reported together with the chlorophyll binding site affected. For each chlorophyll binding site affected by mutation the closest carotenoid binding site, the distance in Å between the two conjugated π-systems of carotenoid and Chl, as reported in the case of CP29 and LHCII and the closest interacting chlorophylls are reported*

Mutation	Chl affected	Closest Car binding site	Closest distance beetween the two conjugated π-systems of carotenoid and Chl in CP29 and LHCII (Å)		Interacting Chls	*In vitro*	*In vivo*
N200F	Chl 612	L1	3.72	3.65	Chl 611/Chl 610	√	√
Q231L	Chl 613	L1	3.83	3.88		√	√
E87V.E87V/R202L	Chl 602	L2	3.58	3.41	Chl 603	Non stable	Non stable
H90F	Chl 603	L2	3.7	3.7	Chl 609	√	Non stable

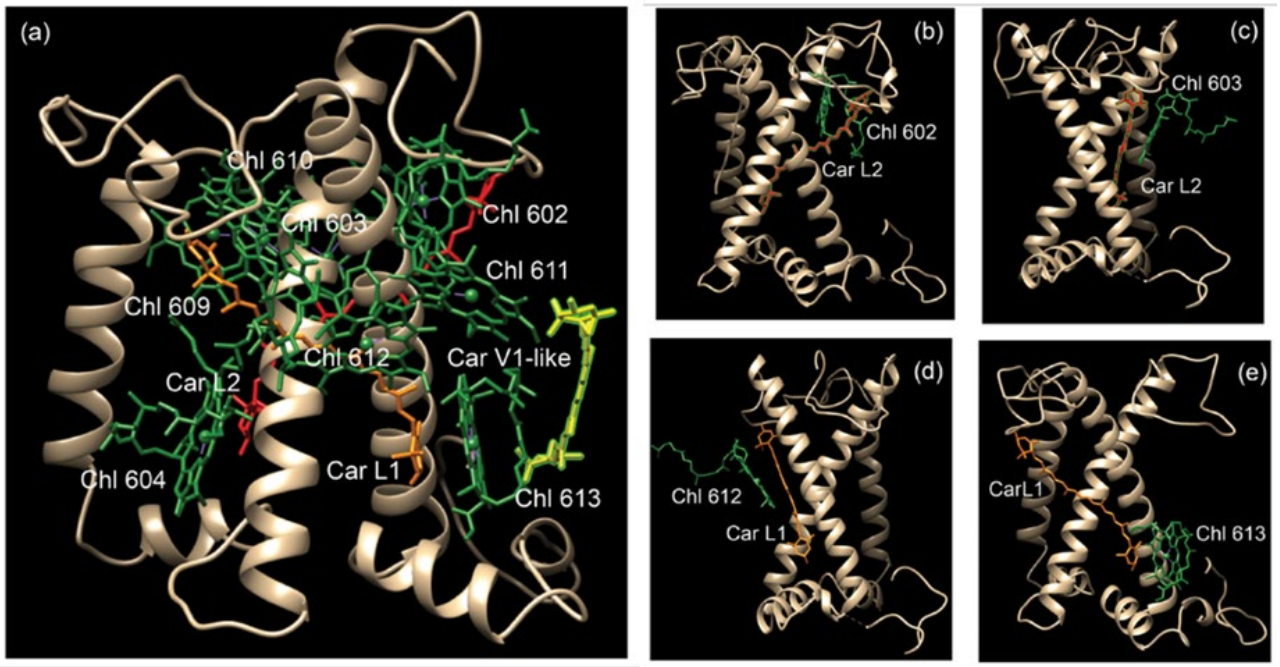

Figure 2.1.2 *Model structure of LHCSR3. (a) Structural model of LHCSR3 obtained by sequence alignment with CP29 (PDB n. 3PL9); (b) Chl 602, (c) Chl 603, (d) Chl 612, and (e) Chl 613 in LHCSR3 model*

confirming the predominant presence of Chl *a* in Chl 612, Chl 613, and Chl 603 binding site. In the case of N200F, a negative peak was also detected at 667 nm, suggesting that the mutation introduced also influenced the spectral features of other Chl in the complex, as likely the Chl 610 or Chl 611, located close to Chl 612. Fluorescence emission spectra were thus measured to determine the influence of the mutations introduced on the energy level of Chls, being the Chl with the lowest energy level the main final emitter. As reported in **Figure 2.1.3 d**, only in the case of mutant on Chl 612 binding site (N200F) a blue shift of fluorescence emission spectra was observed, indicating that the mutation affected the final emitter. These results suggest that Chl 612 is in LHCSR3, the Chl with the lowest energy associated, as reported for other LHC proteins [219], differently from a previous model based on excitation energy transfer measurement, which rather suggested that Chl 613 as the "reddest" chlorophyll in LHCSR3 complex [218]. Time-resolved fluorescence lifetimes analysis was thus performed at pH 7.5 and pH 5 to investigate the pH-dependent quenching properties of LHCSR mutants compared with WT. As reported in **Figure 2.1.4**, all mutants analyzed showed a slightly longer fluorescence lifetime at pH 7.5 compared with WT. A pH-dependent quenching was then observed for all samples, decreasing the pH to 5, with a reduced quenching activity in the case of the mutant on Chl 612 binding sites. However, it is worth to note that fluorescence lifetimes of LHCSR3 complexes in high detergent conditions were in all cases higher than 1 ns (**Table S 2.1.1**), even at pH 5, whereas *in vivo*, a quenching mechanism that can significantly quench the excited states of Chls should have a rate of few hundreds of ps^{-1}. For this reason, time-resolved fluorescence was also measured in WT and Chl binding sites mutants reducing the detergent concentration; in this condition proteins undergo clustering, in a condition closer to the *in*

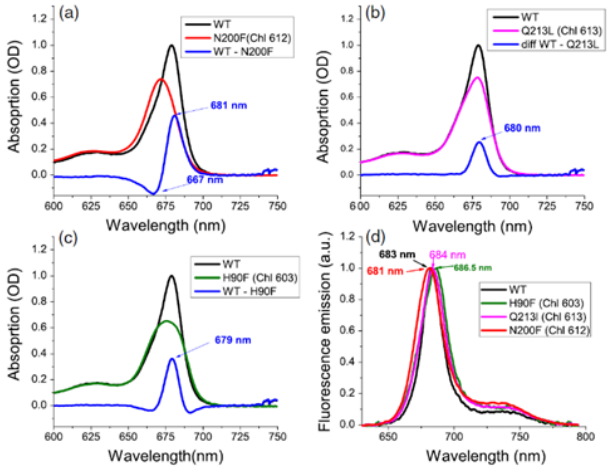

Figure 2.1.3 *Absorption and fluorescence emission spectra of LHCSR3 WT and mutants on chlorophyll binding residues. (a–c) Absorption spectra of WT and mutants on Chl 612 (a), Chl 613 (b), and Chl 603 (c). In each case, the absorption spectra were normalized considering the chlorophyll content in each complex. Difference spectra calculated subtracting the mutant absorption spectrum to the WT spectrum are also reported. (d) Fluorescence emission spectra of LHCSR3 WT and mutants on chlorophyll binding site upon excitation at 440 nm*

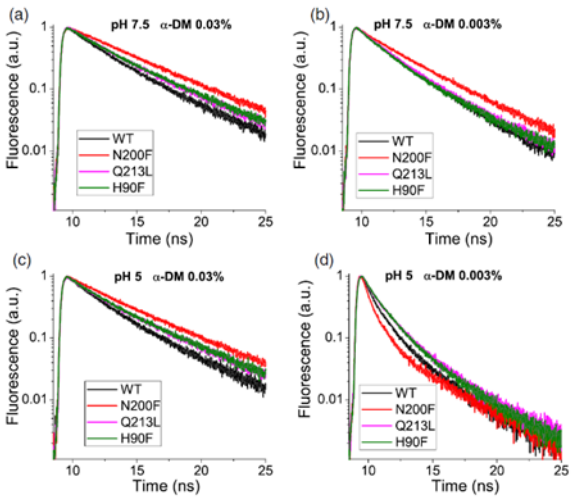

Figure 2.1.4 *Time-resolved fluorescence of WT and mutants on chlorophyll binding site. Fluorescence decay kinetics of WT (black), H90F (green),N200F (red), and Q213L (pink) mutants upon 447 nm excitation. Measurement were performed in Hepes buffer at pH 7.5 (a,b) or in MES buffer atpH 5 (c,d). Detergent (n-Dodecyl α-D-maltoside) concentration was set at 0.03% (a,c) or at 0.003% (b,d)*

vivo state where these proteins are immersed in the highly crowed thylakoid membranes, with a strong reduction of fluorescence lifetime [121,223]. At low detergent concentration, all samples were characterized by faster kinetics of fluorescence decay compared with the condition in high detergent, with a clear pH-dependent quenching for all LHCSR3 variants. Comparing the fluorescence decay kinetics of WT and Chl binding site mutants in the most quenched conditions at low detergent concentration and pH 5, only in absence of Chl 613 and Chl 603 a reduced quenching efficiency was observed in LHCSR3 mutated holoproteins (**Figure 2.1.4 d**), whereas in absence of Chl 612, an even stronger quenching was observed compared with the WT case.

Investigation of chlorophyll binding sites involved in NPQ *in vivo*.

Because these results obtained at low detergent *in vitro* might be influenced by uncontrolled aggregation event caused by the site-specific mutations introduced, the role of the different Chl binding residues herein investigated was then analyzed *in vivo* by complementation of *npq4 lhcsr1* mutant, lacking all LHCSR proteins [121], with WT and LHCSR3 gene mutated on Chl 612, Chl 613, Chl 602, and Chl 603 binding residues. The genomic sequence of

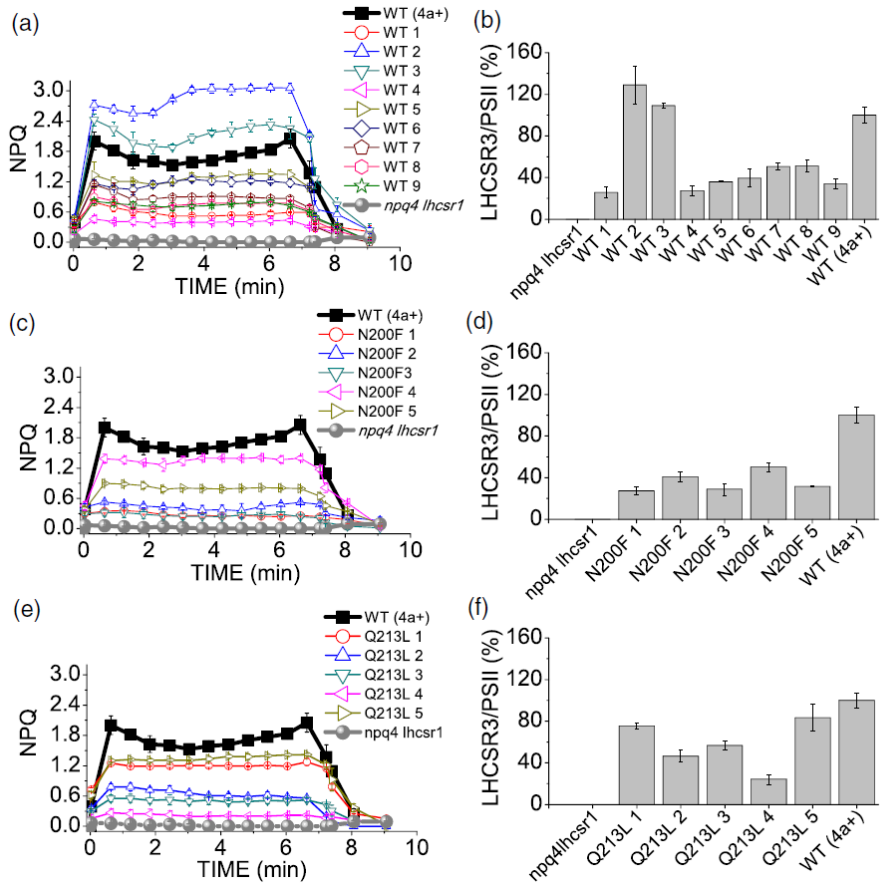

Figure 2.1.5 *Non-photochemical quenching (NPQ) phenotypes and accumulation of LHCSR3 in complemented lines. (a) NPQ induction kinetics and (b) LHCSR3 accumulation per PSII of Chlamydomonas reinhardtii WT (strain 4A+), npq4 lhcsr1 mutant, and transformant lines with LHCSR3.2 WT genomic sequence. (c) NPQ induction kinetics and (d) LHCSR3 accumulation per PSII of C. reinhardtii WT (strain 4A+), npq4 lhcsr1 mutant, and transformant lines with LHCSR3.2 N200F mutant variant (Chl 612 binding site). (e) NPQ induction kinetics and (f) LHCSR3 accumulation per PSII of C. reinhardtii WT (strain 4A+), npq4 lhcsr1 mutant, and transformant lines with LHCSR3.2 Q213L mutant variant (Chl 613 binding site)*

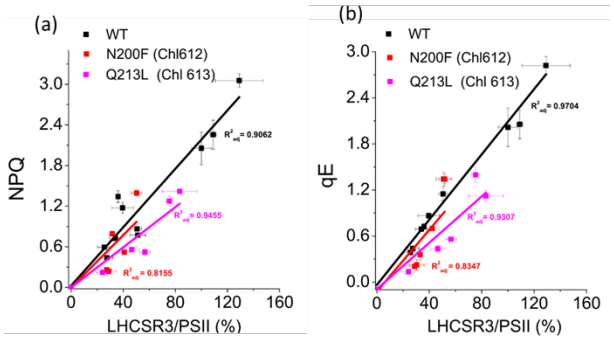

Figure 2.1.6 *Correlation between NPQ, qE, and LHCSR3 accumulation. (a) Linear regression of non-photochemical quenching and LHCSR3 content per PSII. (b) Linear regression of qE and LHCSR3 content per PSII. Nine and five biological independent lines were analyzed in the case of WT or mutants, respectively (three independent biological replicates for each line). Correlation coefficients are reported as adjusted R^2*

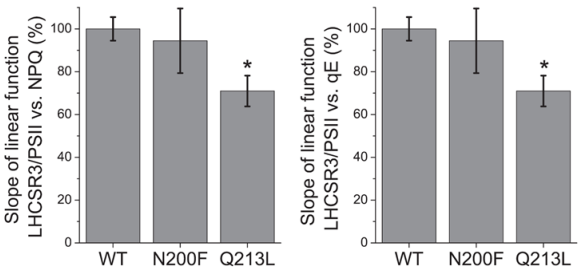

Figure 2.1.7 *LHCSR3 quenching efficiency in WT vs. N200F and Q213L mutants. LHCSR3 quenching efficiency is reported as the slope of the linear function correlating non-photochemical quenching (a) or qE (b) with the amount of LHCSR3 protein accumulated in each line as described in Figure 6*

LHCSR3, extended at 5′ UTR of 1000 bp and at 3′ of 300 bp in order to contain also the promoter and terminator regions, was inserted in the *npq4 lhcsr1* mutant. The expression of the inserted genes was thus under control of LHCSR3 endogenous promoter, which is upregulated in stressing conditions, as high light, as in the case of LHCSR3 gene in the WT background [120]. Upon high light acclimation of transformant lines, accumulation of LHCSR3 protein and NPQ induction curves were measured. As reported in **Figure S 2.1.1**, in the case of insertion of WT LHCSR3 gene sequence, lines with different levels of LHCSR3 were obtained. These differences are related to the different insertion sites of LHCSR3 gene, which can strongly influence gene expression. Consistently with the role of LHCSR3 in NPQ activation, complemented lines with different LHCSR3 level exhibited different kinetics of NPQ induction, with the lines with the highest LHCSR3 expression having an increased maximum NPQ induction compared with WT (**Figure 2.1.5**). Plotting maximum NPQ values or its rapidly reversible component qE [207], as a function of LHCSR3/PSII ratio, it was possible to observe in both cases a linear correlation between protein amount and level of energy dissipation (**Figure 2.1.6**), as previously reported for *C. reinhardtii* cells acclimated to different growth conditions [126]. In the case of single mutant E87V and double mutant E87V/R202L on Chl 602 binding site, 40 resistant lines to the selection marker (paromomycin) were obtained upon transformation but none were found accumulating a detectable amount of protein despite the insertion of LHCSR3 coding genes verified by PCR (**Figure S 2.1.2**). These results are consistent with the destabilization of protein induced by mutation of Chl 602 binding site observed *in vitro*. In the case of H90F mutant on Chl 603 binding site, among the 45 transformant strains carrying the LHCSR3.2 gene, none were found to accumulate a significant amount of LHCSR3 proteins (**Figure S 2.1.2**). Substitution of H90 residue with F is thus likely destabilizing LHCSR3 protein *in vivo*, even if *in vitro* mutant H90F can be refolded upon pigment addition. As a consequence of the absence of LHCSR3 accumulation, no NPQ induction could be detected transformant lines carrying E87V, E87V/R202L, or H90F LHCSR3 mutant variants. Differently, in the case of mutants on Chl 612 (N200F) or Chl 613 (Q213L) binding site, LHCSR3 accumulation could be detected by immunoblotting upon high light acclimation (**Figure S 2.1.1**), leading to NPQ induction (**Figure 2.1.5**). As in the case of WT, for both mutants on Chl 612 (N200F) or Chl 613 (Q213L) binding site, a liner correlation between maximum NPQ or qE and LHCSR3 protein quantity per PSII were observed (**Figure 2.1.6**). In the case of N200F mutants, the slope of the linear function was almost identical compared with WT (p value = .62 and .57 for NPQ and qE linear correlation with LHCSR3/PSII, respectively), ruling out a possible direct involvement of Chl 612 in quenching mechanism in LHCSR3. Rather, in the case of Chl 613, a significant reduction of ~30% (**Figure 2.1.7**) of the slope of the liner function correlating both NPQ (p value = .007) or qE (p value = .0427) and LHCSR3/PSII was observed. These results indicate that the absence of Chl 613 reduces the quenching efficiency of the protein even if this Chl is not strictly required for NPQ induction. In order to further investigate the role of the different Chl binding sites in LHCSR3 quenching activity, time-resolved fluorescence

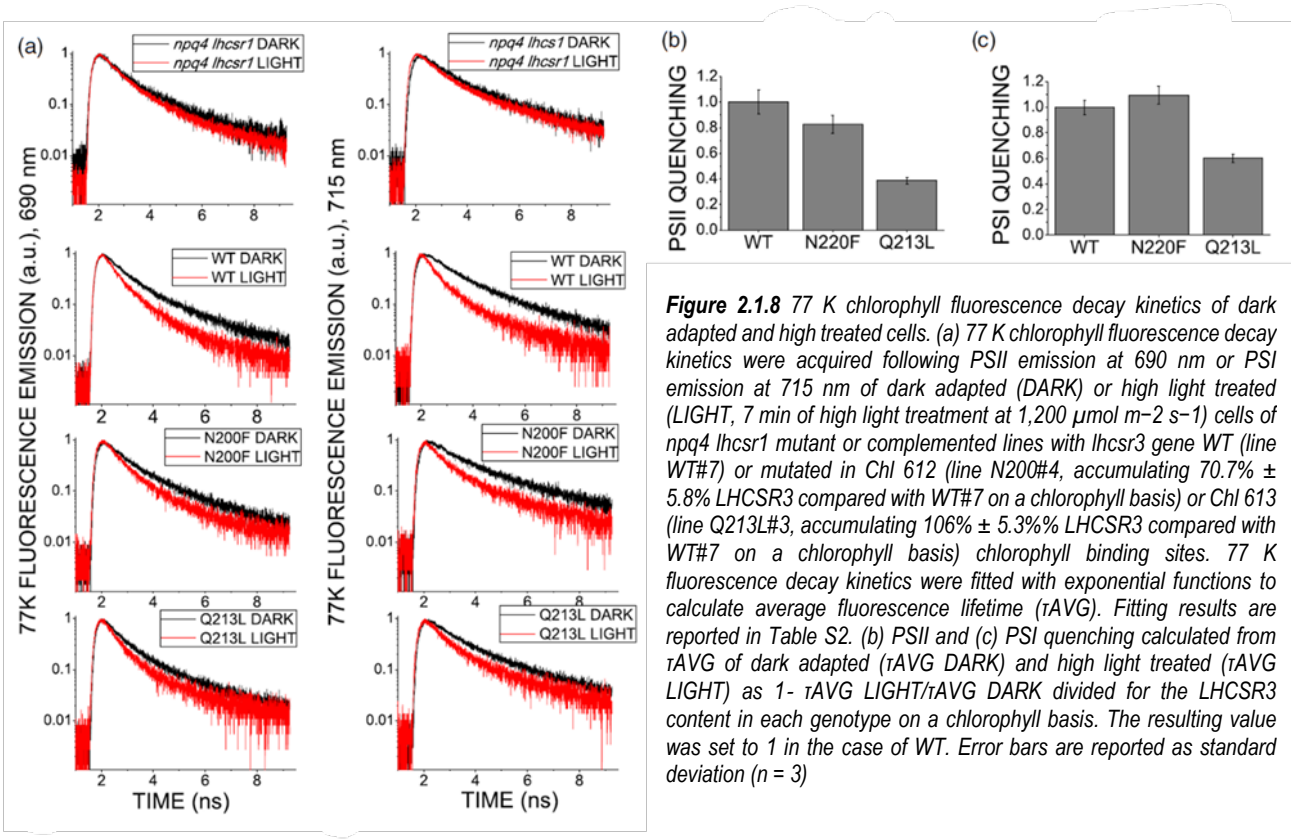

Figure 2.1.8 *77 K chlorophyll fluorescence decay kinetics of dark adapted and high treated cells. (a) 77 K chlorophyll fluorescence decay kinetics were acquired following PSII emission at 690 nm or PSI emission at 715 nm of dark adapted (DARK) or high light treated (LIGHT, 7 min of high light treatment at 1,200 µmol m−2 s−1) cells of npq4 lhcsr1 mutant or complemented lines with lhcsr3 gene WT (line WT#7) or mutated in Chl 612 (line N200#4, accumulating 70.7% ± 5.8% LHCSR3 compared with WT#7 on a chlorophyll basis) or Chl 613 (line Q213L#3, accumulating 106% ± 5.3%% LHCSR3 compared with WT#7 on a chlorophyll basis) chlorophyll binding sites. 77 K fluorescence decay kinetics were fitted with exponential functions to calculate average fluorescence lifetime (τAVG). Fitting results are reported in Table S2. (b) PSII and (c) PSI quenching calculated from τAVG of dark adapted (τAVG DARK) and high light treated (τAVG LIGHT) as 1- τAVG LIGHT/τAVG DARK divided for the LHCSR3 content in each genotype on a chlorophyll basis. The resulting value was set to 1 in the case of WT. Error bars are reported as standard deviation (n = 3)*

analysis was performed on whole cells before (DARK) and after (LIGHT) NPQ induction (**Figure 2.1.8**). Considering that chlorophyll fluorescence decay kinetics in whole cells are strongly influenced by photochemical quenching at the level of photosystems, the non-photochemical quenching activity of *npq4 lhcsr1* lines complemented with LHCSR3 WT, and mutant variants were investigated at 77 K in order to block photochemical reactions. Moreover, 77 K fluorescence emission enabled to discriminate between PSII and PSI emission peaks as widely reported in the literature [224]. Indeed, by measuring 77 K fluorescence decay kinetics on whole *C. reinhardtii* cells, LHCSR3 has been recently reported to be a quencher for both PSII supercomplexes and PSI antenna proteins [225]. Fluorescence decay kinetics reported in **Figure 2.1.8** demonstrate that both PSI (emission at 715 nm) and PSII (emission at 690 nm) are quenched upon NPQ induction in the lined complemented with WT or N200F and Q213L lhcsr3 genes, but not in *npq4 lhcsr1* (**Table S 2.1.1**). Because the quenching observed is related to the accumulation of LHCSR3 in the cell, the reduction of the average lifetime (τ_{AVG}) due to light treatment (1 - $\tau_{AVG\ LIGHT}/\tau_{AVG\ DARK}$) was normalized to the content of LHCSR3 on a chlorophyll basis (**Figure 2.1.8**), revealing a ~40% decrease of both PSII and PSI fluorescence quenching efficiency in the case of Q213L mutant.

Discussion

Molecular details of NPQ in LHC proteins have been strongly debated since decades: models proposed for excitation energy quenching in LHC proteins involve the formation of carotenoid radical cation [66], or the population of S1 [68] or other dark states [215] of carotenoids, or the formation of Chl–Chl charge transfer states in strongly coupled dimers [216]. Identification of Chl binding residues involved in thermal dissipation of the excitation energy is extremely important to disentangle the molecular details of NPQ. Structural details for LHCSR3 are not available yet: sequence alignment with other LHC proteins, which structure has been solved, allowed to identify the putative Chl binding residues [106,218] Chl 612, Chl 613, and Chl 603 are conserved in LHCSR3 (**Figure S 2.1.1**) and were identified as the Chl closest to Car (usually lutein) in carotenoid binding site L1, in the case of Chl 612 and Chl613, or to Car in L2 (lutein in LHCII, violaxanthin in CP29) in the case of Chl 603 [15,64]. Moreover, these Chls have been reported to be involved in strongly coupled Chls cluster, as in particular the Chl 610-Chl 611-Chl 612, Chl 613-Chl 614, and Chl 603-609 and/or Chl 603-602 clusters

[15,64,218]. For these reasons, any quenching mechanisms proposed up to now suggested a key role for one of these Chls [15,66,68,209,218,226]. The involvement of Chl 612, Chl 613, Chl 602, and Chl 603 in quenching properties of LHCSR3 was thus evaluated in this work *in vitro* and *in vivo*. *In vitro* spectroscopic analysis of LHCSR3 mutants on residues responsible for binding the aforementioned Chls demonstrated the presence of essentially Chl *a* in the Chl binding residue herein investigated, among which Chl 612 resulted to be the Chl with the lowest energy level associated, a conservative trait at least among LHC proteins constituting the peripheral antenna system of PSII [219]. Loss of Chl 612 clearly affected the final emitter of the complex (**Figure 2.1.3**) but measuring fluorescence lifetime in "quenching" conditions induced by aggregation state at low pH, mutant on Chl 612 was even more quenched compared with the WT (**Figure 2.1.4**). Because fluorescence decay kinetics *in vitro* at low detergent conditions might be influenced by possible aggregation dependent side effects due to the mutation introduced, *in vivo* quenching activity of LHCSR3 Chl binding sites were then studied. Mutation on Chl 612 binding site *in vivo* clearly demonstrates that, correlating NPQ and LHCSR3 protein level, in absence of Chl 612 the induction of NPQ was similar or even slightly stronger compared with the WT case, in agreement with the *in vitro* results. These results suggest that Chl 612 is not directly involved in NPQ induction *in vivo* in LHCSR3. Differently, in the case of Chl 613, a reduction of specific LHCSR quenching activity was evident (**Figure 2.1.4**,**Figure 2.1.6**,**Figure 2.1.7**,**Figure 2.1.8**), even if the loss of this Chl did not completely impair NPQ induction, in agreement with quenching analysis *in vitro*. Chl 613 binding site can thus be identified as a protein domain with a peculiar, but not exclusive, role in the quenching activity of LHCSR3 proteins. In the case of Chl 613, its location close to Car in L1 (**Table 2.1.2**) makes this Chl-Car interaction site suitable for energy transfer to Car S1 or other dark state. The absence of Chl 614 in LHCSR3 [218], being this Chl the sole Chl excitonically coupled with Chl 613 in other LHC proteins, rules out a possible Chl–Chl charge transfer state [216] as NPQ mechanism at Chl 613 site. Alternatively, the finding of LHCSR3 as a dimer attached to PSII supercomplex might suggest that Chl 613 interact with another Chl of the interacting monomer forming a potential Chl–Chl charge transfer site. By the way, the reduced but still significant quenching activity observed in LHCSR3 mutated on Chl 613 strongly suggest that indeed multiple quenching sites are present, which cooperatively dissipate the excitation energy. In the case of Car in L2, it was not possible to yield information *in vivo* on the role of Chl 602 or Chl 603, the closest Chls to this Car, because of impaired protein accumulation *in vivo* in this mutant. In this case, a possible structural role of Chl binding site located close to Car in L2 can be proposed for LHCSR3 homocomplex formation. Indeed, in the case of Chl 603 mutant a strong destabilization of L2 Cars binding site was evident (**Table 2.1.1**). It should also be noted that Cars in L2 site, Chl 602 and Chl 603 have been reported to be the main quenching site of Chl triplets [227], with a strong increase of ROS formation *in vitro* in mutants variants of LHC proteins depleted of this Chls. Upon high light exposure of transformant lines, for inducing protein accumulation, this mutated version of LHCSR3 could be rapidly degraded because of the generation of a high level of unquenched Chl triplets, and consequently ROS. The quenching efficiency of LHCSR3 mutated on Chl 603 was anyway investigated *in vitro*, observing a similar behavior compared with mutant on Chl 613 binding site. These results suggest that protein domain formed by Car in L2 and Chl 603 or Chl 602 is likely a quenching site, which cooperatively acts with other quenching sites, as Chl 613 and Car in L1 dimer, to dissipate excitation energy trapped by LHCSR3 protein. Chl 603 could be involved in energy transfer to Car in L2, or in formation of Car radical cation, as previously reported in the case of other LHC proteins [66,228], or even in formation of Chl-Chl charge transfer state. Finally, by measuring time-resolved fluorescence at 77 K in whole cells before and after NPQ induction, it was possible to investigate LHCSR3-dependent quenching not only on PSII fluorescence but also on fluorescence deriving from PSI (**Figure 2.1.8**). LHCSR3 dependent quenching of PSI fluorescence has been recently reported to be independent from state transitions activation and STT7 activity but specifically occurring at the level of LHC complexes bound to PSI [225]. The results obtained and reported in **Figure 2.1.8** demonstrates that PSI quenching is again affected, considering the LHCSR3 protein content, upon mutation on Chl 613 but not upon mutation on Chl 612. In conclusion, this works allowed to elucidate the molecular mechanisms for NPQ in LHCSR3 in *C. reinhardtii*, which consist into multiple quenching sites that

cooperatively dissipate the excitation energy harvested directly by LHCSR3 or received by other interacting chlorophyll-binding proteins [124,229,230]. A further hypothesis is that LHCSR3 might not be the direct quencher of excitation energy, but rather a pH-dependent trigger switching other LHC protein to a quenched state, as previously suggested in the case of PSBS in higher plants [211]. These results can thus be applied in engineering NPQ process to improve photosynthetic efficiency and biomass production properly tuning photoprotection properties of plant cells.

Materials and methods

Structural model for LHCSR3

Model of the LHCSR3 structure was obtained by using CP29 structure (PDB 3PL9) [64] as a reference as described in [121] and visualized by Chimera 1.13 software.

Site-specific mutagenesis

Site-specific mutagenesis was performed on identified Chl binding residues using QuikChange® Site-Directed Mutagenesis Kit according to the manufacturer's instructions [121].

LHCSR3 in vitro reconstitution

LHCSR3 cDNA was cloned in pET28-His vector for overexpression in *Escherichia coli* as reported previously [106], removing the coding sequence for the first 14 residues—being the predicted transit peptide for chloroplast localization—which is not present in the active protein *in vivo*. LHCSR3 apoprotein was purified from E. coli as reported in [218] and refolded in vitro as previously described [121 221]

Absorption and fluorescence steady state measurements

Absorption measurements were performed in the 350–750 nm region with a Cary 4000, Varian spectrophotometer. Steady state fluorescence measurements were performed with BeamBio custom device equipped with USB2000+ OceanOptics spectrometer and custom LED light sources for excitation.

Pigment analysis

Pigment analysis were performed by HPLC as described in [231]. Chl a/b and Chl/Car ratios were analyzed on pigment extracts in 80% acetone by spectral deconvolution with Chl and Cars absorption forms in organic solvent as previously reported [106 221].

In vivo complementation of *npq4 lhcsr1 C. reinhardtii* mutant

LHCSR3.2 gene (Cre08.g367400) was amplified from *C. reinhardtii* genomic DNA extracted as previously described described [121]. In order to amplify the entire promoter, the region to be cloned was extended by 1000 bp at its 5′ UTR. In contrast, at 3′ UTR, a 300 bp region was selected as hypothetical terminal region. Amplified DNA was then inserted in pBC1 vector as described [121]. *npq4 lhcsr1* mutant {Ballottari, 2016 #444}) was kindly gifted by Prof. Niyogi from UC Berkeley. Cells transformation and transformant selection were performed as previously described [121]. Transformed cells were plated in TAP medium in presence of paromomycin as selective marker. Resistant colonies were then transferred in TAP medium at 25°C in flask with white light (70 µE, 16 hr light/8 hr dark photoperiod). High light acclimation was induced in WT (4A+ strain), *npq4 lhcsr1* mutant and transformant lines by growing cells at 400 µE in HS medium as previously described [121].

NPQ analysis

NPQ induction curves were measured on *C. reinhardtii* WT, *npq4 lhcsr1* and transformant lines by using a closed-GFPCam-FC800 from Photon System Instruments (Czech Republic). NPQ analysis were performed on *C. reinhardtii* cultures in exponential phase acclimated to high light for 4 days. Measuring, saturating, and actinic light were respectively 7, 5000, and 1200 µmol m^{-2} s^{-1}.

Time-resolved fluorescence analysis

Time-resolved fluorescence analysis was performed with a Chronos BH ISS Photon Counting instrument with picosecond laser excitation at 447 nm operating at 50 MHz. Fluorescence emissions were recorded at 685 nm in the case of isolated LHCSR complexes or at 690 nm or 715 nm in the case of whole cells, with 4 nm bandwidth. Laser power was kept below 0.1 µW; 77 K fluorescence measurements were performed on previously frozen samples. In particular, whole cells were frozen in liquid nitrogen after 20 min of dark adaptation (DARK) and after 7 min of high light treatment at 1200 µmol m^{-2} s^{-1} (LIGHT); 77 K measurements were performed by using a cryostat (ISS) mounted on the Chronos BH ISS photon

counting instrument. Fluorescence decay kinetics were analyzed with ISS Vinci 2 software by fitting with bi-exponential or three-exponential functions. Amplitudes (Ai) and time constants (τi) retrieved from fitting results were then used to calculate average fluorescence lifetimes (τavg) as ΣAiτi/ΣAi. In the case of 77 K measurements on whole cells τavg calculated for dark adapted (τavg DARK) and for high light treated (τavg LIGHT) samples were used to calculate the parameter 1-(τavg LIGHT/τavg DARK) which is inversely proportional to the LHCSR3 quenching activity.

SDS-PAGE and western blots

SDS-PAGE was performed with a Tris-Tricine as reported in [232]. Western blots were performed as reported in [106] using α-HCSR3 and α-CP43 specific antibodies from Agrisera (AS14 2766 and AS11 1787, respectively).

Statistical analysis

All the data reported are the average of at least three biological replicates, with specific N value reported in the figure legends. Initial screening of transformant lines were performed for at least 50 positive colonies. At least five independent transformant lines were fully characterized for each LHCSR3 WT and mutant variant. Errors bars are reported as standard deviation. Linear regression reported were performed with OriginPro8.0 software. Statistical significance of linear regression was evaluated by F test in the "Compared dataset" function in OriginPro8.

Supporting information

	A_1	τ_1 (ns)	A_2	τ_2 (ns)	A_3	τ_3 (ns)	τ_{avg} (ns)
WT pH 7.5 0,03% α-DM	0,44	4,35	0,51	1,87	0,04	0,53	2,91
WT pH 5 0,03% α-DM	0,37	4,42	0,5	1,83	0,13	0,4	2,59
WT pH 7.5 0,003% α-DM	0,32	3,91	0,55	1,91	0,14	0,45	2,34
WT pH 5 0,003% α-DM	0,09	3,12	0,52	0,92	0,39	0,23	0,83
N220F pH 7.5 0,03% α-DM	0,84	4,87	0,13	1,38	0,03	0,5	4,3
N220F pH 5 0,03% α-DM	0,7	4,92	0,23	1,57	0,07	0,35	3,83
N220F pH 7.5 0,003% α-DM	0,53	4,31	0,28	1,82	0,19	0,33	2,87
N220F pH 5 0,003% α-DM	0,05	3,68	0,42	0,76	0,54	0,24	0,62
Q213L pH 7.5 0,03% α-DM	0,54	4,76	0,41	1,81	0,06	0,25	3,31
Q213L pH 5 0,03% α-DM	0,51	4,75	0,41	1,65	0,08	0,35	3,12
Q213L pH 7.5 0,003% α-DM	0,31	4,26	0,54	1,87	0,15	0,33	2,37
Q213L pH 5 0,003% α-DM	0,1	3,51	0,47	1,31	0,43	0,37	1,13
H90F pH 7.5 0,03% α-DM	0,58	4,82	0,38	1,75	0,04	0,48	3,47
H90F pH 5 0,03% α-DM	0,5	4,78	0,38	1,65	0,11	0,41	3,09
H90F pH 7.5 0,003% α-DM	0,28	4,3	0,56	1,79	0,16	0,4	2,27
H90F pH 5 0,003% α-DM	0,1	3,48	0,54	1,3	0,36	0,38	1,18

Table S 2.1.1 *Time resolved fluorescence analysis and average fluorescence decay lifetimes of LHCSR3 WT and mutant proteins refolded in vitro. Decay kinetics reported in the main text in Figure 4 were fitted with a three-exponential decay function Vinci 2 software from ISS. Amplitudes (Ai) and time constants (τi) are reported. Average fluorescence lifetimes (τavg) were calculated as ΣAiτi/ΣAi. Standard deviations are < 5% (n=3).*

PSII emission (690nm)		A1	τ1 (ns)	A2	τ2 (ns)	τavg (ns)	1-(τavg LIGHT/ τavg DARK)
WT#7	DARK	0,50	2,37	0,50	0,55	1,46	0,56
	LIGHT	0,40	1,53	0,60	0,35	0,80	
N200F#4	DARK	0,56	2,37	0,44	0,58	1,58	0,66
	LIGHT	0,46	1,78	0,54	0,41	1,04	
Q213L #3	DARK	0,50	2,25	0,50	0,46	1,35	0,72
	LIGHT	0,36	2,04	0,64	0,38	0,97	
npq4 lhcsr1	DARK	0,51	2,26	0,49	0,56	1,43	0,95
	LIGHT	0,37	2,66	0,63	0,61	1,37	
PSI emission (715nm)		A1	τ1 (ns)	A2	τ2 (ns)	τavg (ns)	1-(τavg LIGHT/ τavg DARK)
WT#7	DARK	0,56	2,81	0,44	0,79	1,93	0,52
	LIGHT	0,53	1,61	0,47	0,31	1,00	
N200F#4	DARK	0,69	2,94	0,31	0,75	2,25	0,61
	LIGHT	0,58	2,07	0,42	0,40	1,37	
Q213L #3	DARK	0,64	2,62	0,36	0,69	1,93	0,77
	LIGHT	0,49	2,49	0,51	0,52	1,49	
npq4 lhcsr1	DARK	0,56	2,74	0,44	0,76	1,88	0,89
	LIGHT	**0,60**	**2,44**	**0,40**	**0,52**	**1,68**	

Table S 2.1.2 *77K time resolved fluorescence analysis and average fluorescence decay lifetimes of LHCSR3 WT and mutant proteins refolded in vitro. High light acclimated npq4 lhcsr1 cells and complemented lines with LHCSR3 WT or mutants on Chl 612 (N220F) or Chl 603 (Q213L) were frozen in liquid nitrogen after 20 minutes of dark adaptation (DARK) and after 7 minutes of high light treatment at 1200 µmol m^{-2} s^{-1} (LIGHT). 77K fluorescence emission were then measured at 690 nm or 715 nm in order to follow PSII or PSI fluorescence respectively. Fluorescence kinetics were then fitted with a bi-exponential decay function Vinci 2 software from ISS: amplitudes (Ai) and time constants (τi) are reported. Average fluorescence lifetimes (τavg) were calculated as ΣAiτi/ΣAi. τavg calculated for dark adapted (τavg DARK) and for high light treated (τavg LIGHT) samples were then used to calculate the parameter 1-(τavg LIGHT / τavg DARK) which is inversely proportional to the LHCSR3 quenching activity. Standard deviations are < 10% (n=3).*

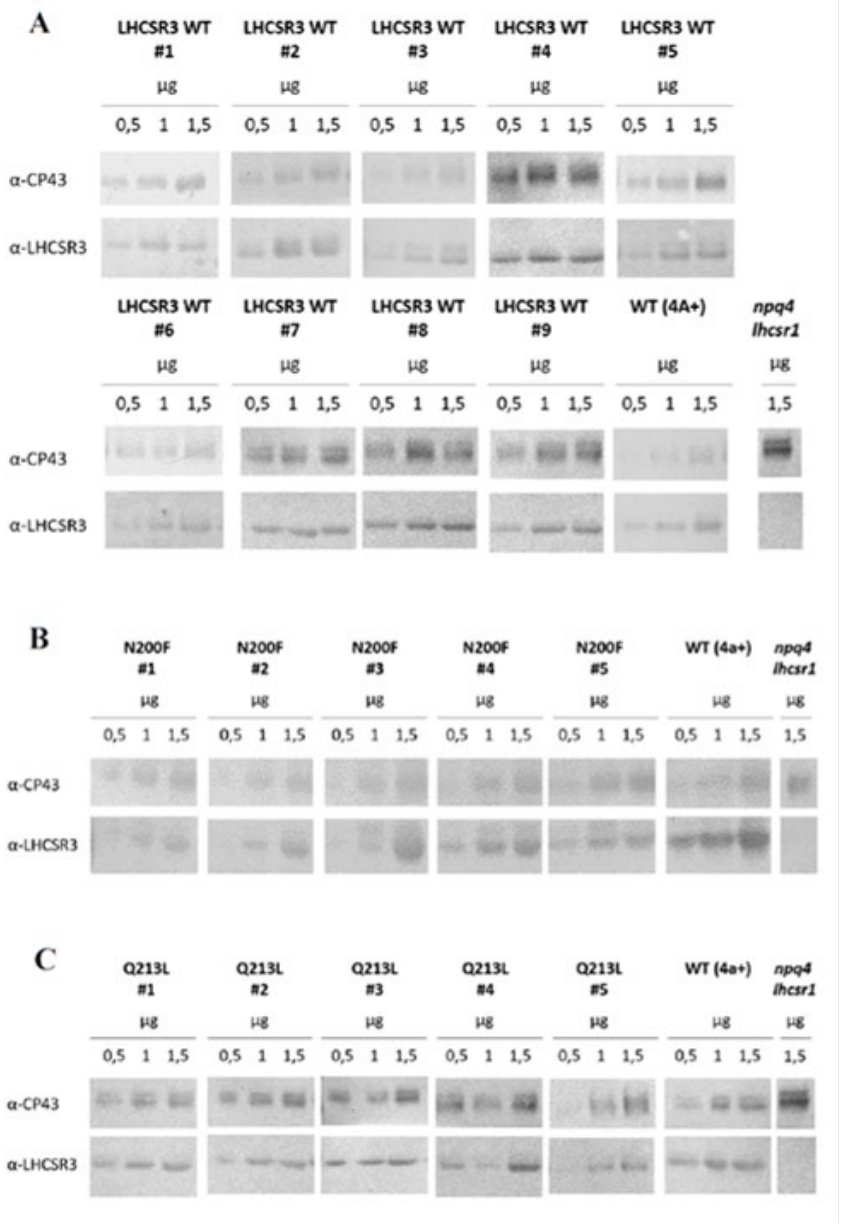

Figure S 2.1.1 Western blot analysis of LHCSR3 accumulation upon npq4 lhcsr1 complementation. Western blot analysis of LHCSR3 accumulation upon npq4 lhcsr1 complementation with LHCSR3.2 WT gene sequence (A) or mutated on CHl 612 (B) or 613 (C) chlorophyll binding sites. Sample were loaded in three replicates at different amount of chlorophylls. µg of loaded chlorophylls are indicated. Western blots were developed using antibodies specific for LHCSR3 and CP43, the latter as a marker for PSII.

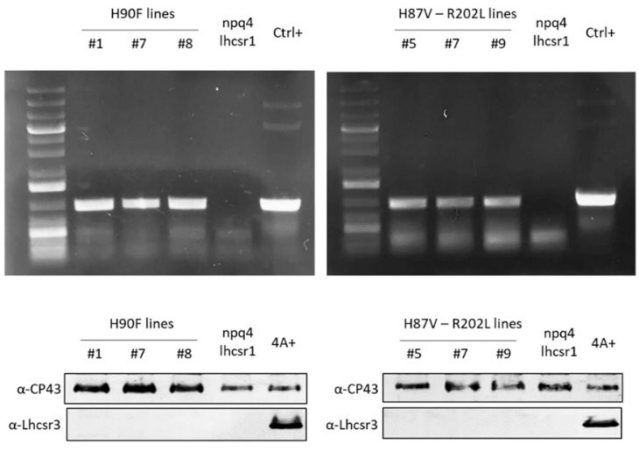

Figure S 2.1.2 *npq4 lhcsr1 transformation with H90F and H87V-R202L LHCSR3.2 mutant variant. The presence of genes coding for LHCR3 and resistance for paromomycin (AphVIII) in transformant strains were tested by PCR on genomic DNA extracted from colonies grown in selective plates. pBC1 vector used for transformation was used as positive control while genomic DNA extracted from npq4 lhcsr1 untransformed strain was used as negative control. Western blot on total protein extract is reported on the bottom, with WT 4A+ as positive control. Three independent lines for each mutation are reported as representative of the different resistant lines screened. 40 resistant lines to the selection marker (paromomycin) were obtained and verified for the presence of LHCSR3 coding sequence in the case of each mutant E87V and E87V-R202L on Chl 602 binding site while 45 transformant strains were obtained and verified in the case of H90F mutant on Chl 603 chlorophyll binding site*

2.2

Molecular mechanisms of nonphotochemical quenching in the LHCSR3 protein of *Chlamydomonas reinhardtii*

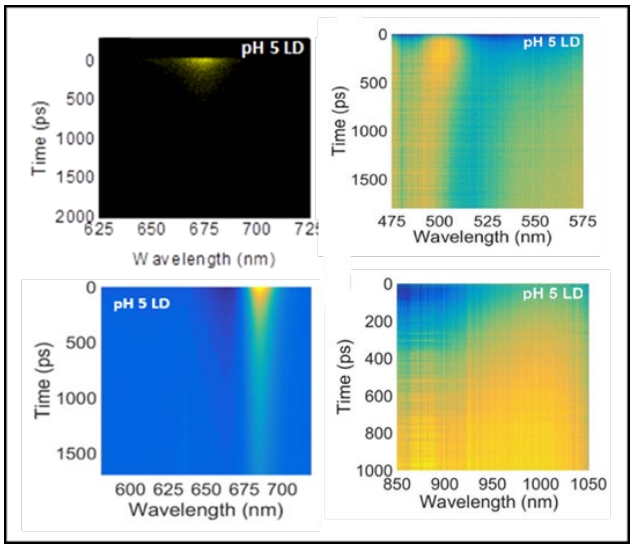

This section is based on the pubblished article: de la Cruz Valbuena, G. et al. Molecular Mechanisms of Nonphotochemical Quenching in the LHCSR3 Protein of *Chlamydomonas reinhardtii*. *The journal of physical chemistry letters* 10, 2500-2505, doi:10.1021/acs.jpclett.9b01184 (2019).

Author Contributions: Ballottari M., Cerullo G. and D'Andrea C. conceived the work and wrote the paper. **Perozeni F.** performed sample preparation and protein characterization. del la Cruz Valbuena G., Camargo F. V. A. and Borrego-Varillas R. performed all TA experiments. del la Cruz Valbuena G. with contribution of Perozeni F**.** performed PL measures. All authors analyzed the results, contributed to writing and approved the final version of the manuscript.

Molecular mechanisms of nonphotochemical quenching in the LHCSR3 protein of *Chlamydomonas reinhardtii*

Gabriel de la Cruz Valbuena[1], Franco V. A. Camargo[1], Rocio Borrego-Varillas[1], Federico Perozeni[2], Cosimo D'Andrea[1,3], Matteo Ballottari[2] and Giulio Cerullo[1]

[1] IFN-CNR, Department of Physics, Politecnico di Milano, P.za L. da Vinci 32, 20133 Milano, Italy
[2] Dipartimento di Biotecnologie, Università di Verona, Strada Le Grazie 15, 37134 Verona, Italy
[3] Center for NanoScience and Technology@PoliMi, Istituto Italiano di Tecnologia, via Pascoli 70/3, 20133 Milano, Italy

Abstract:

Photosynthetic organisms possess photoprotection mechanisms from excess light conditions. The fastest response consists in the pH-triggered activation of a dissipation channel of the energy absorbed by the chlorophylls into heat, called nonphotochemical quenching. In green algae, the pigment binding complex LHCSR3 acts both as a chlorophyll quencher and as a pH detector. In this work, we study the quenching of the LHCSR3 protein in vitro considering two different protein aggregation states and two pH conditions using a combination of picosecond time-resolved photoluminescence and femtosecond transient absorption in the visible and NIR spectral regions. We find that the mechanisms at the basis of LHCSR3 quenching activity are always active, even at pH 7.5 and low aggregation. However, quenching efficiency is strongly enhanced by pH and by aggregation conditions. In particular, we find that electron transfer from carotenoids to chlorophylls is enhanced at low pH, while quenching mediated by protein−protein interactions is increased by going to a high aggregation state. We also observe a weak pH dependent energy transfer from the chlorophylls to the S_1 state of carotenoids.

Photosynthetic organisms depend on the harvested sunlight to fuel their metabolic energy consumption. However, high-intensity illumination can be harmful to the organism. Under excess light conditions, the activity of the photosynthetic electron transfer chain saturates, inhibiting the photochemical relaxation of chlorophyll (Chl) singlet excited states (^{1}Chl*). These states can then undergo intersystem crossing to the Chl excited triplet state (^{3}Chl*), and the consequent formation of singlet oxygen ($^1O_2$*) causes photodamage or even cell death [233]. Photosynthetic organisms evolved a variety of photoprotection mechanisms to prevent such harmful effects: differential gene expression and metabolic changes act on the long-term [234], while at the molecular level short-term mechanisms are rapidly activated upon increased irradiances [235]. One of these short-term responses is called nonphotochemical quenching (NPQ) and consists in the opening of channels for safe dissipation of the excitation energy as heat. NPQ consists of several processes, the fastest of which is called energy-dependent quenching (qE) [235]. Several no mutually exclusive molecular mechanisms for qE were proposed, all involving activation of a fast (~ps) quenching process of ^{1}Chl*. Strong electronic coupling of two adjacent Chls was suggested to lead to the formation of a charge transfer state that dissipates energy [216]. All other qE mechanisms involve the interaction of Chls with carotenoids (Cars), which are suitable quencher molecules due to their low-energy short-lived dark states [236,237]. One is energy transfer from ^{1}Chl* to a lower energy excited dark state of the Car, such as S_1 [68,238,239] or the more recently proposed S_q [218], with short (~ps) lifetime; another is electron transfer from the Car to the photoexcited Chl, generating a Car radical cation and a Chl anion [66,217,240,241]; a third mechanism is Car-Chl excitonic coupling, with the coupled state acting as excitation quencher [214]. Often Cars quenching is related to the xanthophyll cycle (conversion of Car violaxanthin to zeaxanthin), which upregulates the NPQ process [102,242-244]. Previous studies demonstrated that qE is triggered by lumen acidification caused by saturation of the photosynthetic apparatus: Its onset thus requires both a sensor of the luminal pH and a quencher

for energy dissipation. In higher plants, the pH sensor is the non-pigment-binding protein PSBS [102,108], while other proteins from the light harvesting complex gene family are responsible for the energy dissipation process [66,68,216]. In algae, pigment binding complexes named Light Harvesting Complex Stress Related (LHCSR) [101] proteins are responsible for both pH detection and Chl quenching. In the model organism for green algae *Chlamydomonas (C.) reinhardtii* two LHCSR isoforms, LHCSR1 and LHCSR3, were observed to accumulate in the thylakoid membrane of the chloroplasts under excess illumination, with the latter being the main trigger for qE activation [101]. LHCSR are trihelical proteins with Chl *a*, Chl *b*, and Car molecules bound to the helices and acid functional groups attached facing the luminal part of the chloroplasts [106,218,245]. High light stress conditions generate a pH gradient across the thylakoid membrane, which is sensed by the acid groups of LHCSR3 and triggers its quenching activity [106,121,209,245]. The molecular quenching mechanisms in LHCSR proteins are still intensively studied and debated [121,218,243]. A zeaxanthin dependent and a zeaxanthin-independent quenching process were identified in the LHCSR1 from the moss *Physcomitrella (P.) patens*, involving, respectively, energy transfer to the Car S_1 state and formation of a Car radical cation [243]. Both quenching mechanisms, energy transfer to Car S_1 and Car radical cation formation, have been also recently observed *in vivo* in the microalga *Nannochloropsis oceanica* strictly related to the presence of both zeaxanthin and the complex LHCX1, homologous to LHCSR subunits [246]. Differently, in the case of *C. reinhardtii*, zeaxanthin has been demonstrated to be unnecessary for qE induction [106], opening the question about the quenching mechanisms underlying LHCSR3 activity *in vivo*. In this complex, a zeaxanthin-independent Car radical cation quenching mechanism was previously reported, being triggered at low pH [106]. However, this mechanism was measured *in vitro*, resulting in protein complexes with a fluorescence lifetime in the ns scale, incompatible with the strong quenching on tens to hundreds of ps time scales observed upon activation of LHCSR3-dependent quenching *in vivo* [246,247] or *in vitro* in isolated PSII-LHCII-LHCSR supercomplexes [209]. Recently, site directed mutagenesis [121] allowed to obtain *C. reinhardtii* LHCSR3 variants with reduced quenching activity and pH inducibility *in vivo*. However, similar reduced quenching efficiency *in vitro* was obtained only when partial aggregation of the protein was induced by reducing the detergent concentration [121]. It is known that qE induction *in vivo* is accompanied by a change in protein−protein interactions [113], so these results suggest that protein−protein interactions induced *in vitro* by partial aggregation could simulate the quenching conditions occurring *in vivo*, even if the neighboring interacting proteins are not exactly the same in both cases. In this work, we employ ultrafast optical spectroscopy to understand the quenching mechanisms in LHCSR3 under different pH and aggregation conditions. We detect the onset of quenching pathways in LHCSR3 *in vitro* by changing the pH from 7.5 (neutral) to 5 (acid medium) and by reducing the concentration of detergent from high to low. We identify distinct pH- and aggregation-dependent mechanisms that are responsible for the qE activity of the protein. LHCSR3 holoprotein was obtained upon pigment addition in an *in vitro* refolding process of recombinant apoprotein overexpressed in *E. coli*, as previously described [106]. The refolded protein was characterized by an absorption spectrum with a peak in the Chl Qy region at 679.2 nm (**Figure S 2.2.1**) and fluorescence peaking at 683 nm (**Figure S 2.2.2**), consistent with previous findings [106]. Pigment binding properties of the refolded complex are reported in **Table S 2.2.1**. To induce protein aggregation, the concentration of the detergent alpha-dodecyl maltoside (α-DM) was decreased from 0.03% to 0.003%. For simplicity, these conditions are referred to as high detergent (HD) and low detergent (LD) in the following. In principle, different pH conditions can induce different aggregation levels, so we tested the amount of aggregation using the fluorescence spectra at 77 K **Figure S 2.2.3** reveals the formation of oligomers characterized by increased far-red fluorescence only in the case of LD samples, with the strongest aggregate emission found in pH 5 LD. Hence, the HD samples act as controls for the

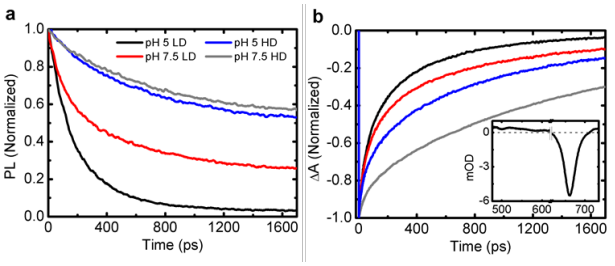

Figure 2.2.1 *LHCSR3 kinetics traces measured by (a) TRPL (pump at 430 nm, integrated from 650 to 760 nm), and (b) TA at 680 nm (pump at 630 nm). Inset: TA spectrum at 500 fs (pH 5 LD).*

effect of pH alone. We study the photophysics of the samples following photoexcitation of the Chls, combining time-resolved photoluminescence (TRPL), to determine the lifetime of ^{1}Chl*, and transient absorption (TA), to identify the formation and decay of dark excited states such as triplets, the Car S_1, and radical cation states. **Figure 2.2.1a** shows the normalized TRPL decay kinetics integrated over the 650−760 nm spectral range under different pH and aggregation conditions. The HD sample at pH 5 shows a faster decay compared to pH 7.5, a trend that is also present under LD conditions with even shorter lifetimes (see **Table S 2.2 2** for time constants obtained by biexponential fits). This confirms that both aggregation and pH play a role in the overall quenching mechanism, with the detergent concentration being the most important factor, as the pH 7.5 LD sample is more quenched than the pH 5 HD one. Similar behavior was observed in the related protein LHCSR1 from *P. patens* [248]. TRPL maps and spectra integrated over the entire temporal window of the experiment are reported in **Figure S 2.2.4** and **Figure S 2.2.5**, respectively. **Figure 2.2.1b** displays the TA kinetics at 680 nm of all samples (for TA maps and spectra in the visible, see **Figure S 2.2 6**, **Figure S 2.2 7Figure S 2.2.8**) following excitation at 630 nm. For all samples we used the same optical density and pump fluence, set at 6 μJ/cm^2 to minimize bimolecular annihilation effects [249] (see **Figure S 2.2.9** for fluence-dependent dynamics of all quenched samples). At early times, the TA spectra of all samples consist of a negative peak around 680 nm, due to ground state bleach (GSB) and stimulated emission (SE) of ^{1}Chl*a*, and a broad positive band from 470 to 600 nm corresponding to photoinduced absorption (PA) from ^{1}Chl*. The GSB/SE dynamics follow the same trend observed in TRPL: shorter lifetimes at low pH and LD, with the aggregation state prevailing. In the TA data a fast component is resolved in the pH 5 HD and LD samples, whereas in TRPL measurements this difference is not observed due to the lower temporal resolution (20 ps as compared to 100 fs). Most of the reported qE mechanisms involve interaction of the Chls with Cars. In our TA experiments, selective excitation of ^{1}Chl* ensures that any signal from the Car molecules must be due to an interaction with the photoexcited Chl. We thus focus on the 470−570 nm wavelength range (for TA maps and spectra, see **Figure S 2.2 7** and **Figure S 2.2.8b**) that contains the Car GSB (peaking at 500 nm) and the Car triplet−triplet PA (peaking at 510 nm) [237,250], besides the previously mentioned broad PA of the ^{1}Chl*. **Figure 2.2.2a,b** shows sequences of TA spectra for the most contrasting samples: pH 7.5 HD and pH 5 LD, respectively. At early times, a negative peak overlapped in the broad PA spectrum of ^{1}Chl* is evident at 500 nm in both samples; as it matches the 0−0 peak of the $S_0 \rightarrow S_2$ Cars transition, we assign it to Cars GSB. These results highlight coupling between Chls and Cars, previously observed [214,243] and assigned to an ultrafast electrochromic shift of the carotenoid in response to the presence of the excited state of the Chl *a*. In **Figure 2.2.2a,b** we observe a buildup of the Cars GSB over tens of picoseconds, which is a trend we find on the other samples too (**Figure 2.2.2c**). This is more strongly present in the low pH samples, with the Car GSB becoming strong enough to prevail over the Chl PA and cause a change of sign of the overall TA signal. On the nanosecond time scale, we observe in **Figure 2.2.2d** the formation of a PA band peaking at 510 nm, attributed to the absorption of ^{3}Car* [243]. This state is populated via triplet−triplet energy transfer from the Chl to the Car, following intersystem crossing (ISC) in the Chl, according to the scheme ^{1}Chl* → ^{3}Chl* → ^{3}Car* [248]. Therefore, a longer lifetime of the ^{1}Chl* state corresponds to a higher efficiency for the ISC process and to a higher ^{3}Car* signal. Consistently, the formation of the ^{3}Car* PA band in **Figure 2.2.2d** is more pronounced in the less quenched samples, with the highest triplet PA signal seen in pH 7.5 HD. The TA data in the Car region was adequately fitted with three time constants for all samples using a global analysis

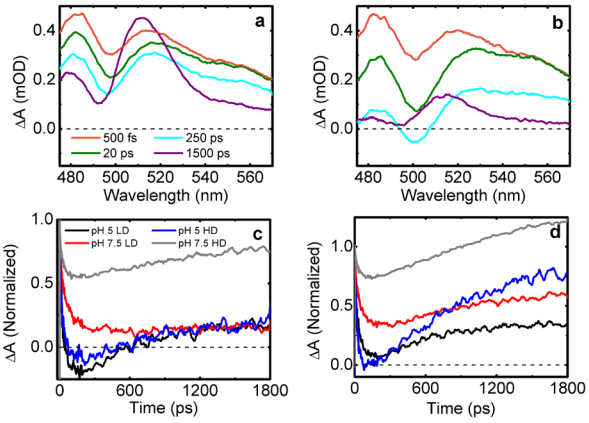

Figure 2.2.2 *TA of LHCSR3 exciting 1Chl* at 630 nm for (a) pH 7.5 HD and (b) pH 5 LD conditions. Kinetics measured at (c) 500 nm, showing the build-up of Car GSB and (d) 510 nm, showing the build-up of Car triplet-triplet PA.*

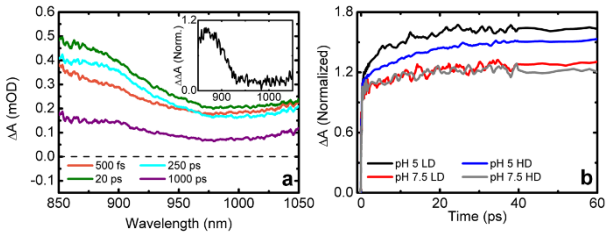

Figure 2.2.3 *(a) NIR TA spectra of LHCSR3 for the pH5 LD sample following Chl excitation at 630 nm. Inset: difference TA spectrum obtained by subtraction of the spectra at 20 ps and 500 fs. (b) TA kinetics at 880 nm normalized by their average value over the first 300 fs following excitation.*

	τ1 (ps)	τ2(ps)	τ3 (ps)
pH 7.5 HD	13.4 ± 0.1	106 ± 1	1559 ± 13
pH 5 HD	10.3 ± 0.1	81 ± 1	718 ± 6
pH 7.5 LD	11.3 ± 0.2	101 ± 1	684 ± 7
pH 5 LD	9.0 ± 0.1	69 ± 0.5	477 ± 2

Table 2.2.1 *Time constants from the global fit analysis of the TA data from 480 to 570 nm.*

routine (see **Figure S 2.2.10** for the quality of the fits) [251]. The fit results are summarized in **Table 2.2.1**, and decay-associated spectra (DAS) of all samples are shown in è **Figure S 2.2.11**. We assign the calculated time constants to a fast multiexponential buildup of the carotenoid GSB (~10 ps, τ_1; 70−100 ps, τ_2), followed by the rise of the triplet state in a longer time scale (480−1600 ps, τ_3), which becomes faster in the more quenched samples due to the shorter lifetime of the ^{1}Chl* state. Comparison between TA spectra in **Figure 2.2.1a** and **Figure 2.2.2c** reveals a correlation between the quenching activity of LHCSR3 and the build-up Car GSB, pointing to the involvement of Cars in the qE process. However, this observation does not provide conclusive evidence of the quenching mechanism as we cannot distinguish if the process is associated with energy or charge transfer from Chls to Cars. Careful inspection of the TA dynamics at 560 nm for the pH 5 samples (both HD and LD), shown in **Figure S 2.2.12**, reveals a weak increase of the PA signal. As this probe wavelength matches the peak of the characteristic intense $S_1 \rightarrow S_n$ PA band of Cars [248], this demonstrates the presence of a weak quenching channel for ^{1}Chl* via energy transfer to the Car S_1. This channel is activated solely at low pH since it is not observed in the pH 7.5 HD or LD samples. Because Cars radical cations absorb in the NIR spectral range, following previous studies [106,243], we can directly assess the presence of electron transfer to the photoexcited Chls by extending our TA probe to the 850−1050 nm spectral range. TA spectra at different pump−probe delays are reported in **Figure 2.2.3a** (see **Figure S 2.2.13** for the complete maps). At early times one observes a broad positive band, which is assigned to PA of the photoexcited Chl [217]; on a 20 ps time scale the signal shows a clear build-up, which is more pronounced at 880 nm with respect to 1050 nm. Since the Chl population decays on this time scale (**Figure 2.2.1**), the signal build-up must be associated with the formation of a new species. To estimate the spectrum of this species, we take the difference of the TA spectra recorded at 20 ps (when most of the build-up has occurred) and 500 fs. The resulting spectrum (**Figure 2.2.3a insert**) peaks at 870 nm, in excellent agreement with the PA spectrum of the lutein radical cation [252]. Due to our limited spectral coverage, we cannot exclude partial involvement of the other Car present in LHCSR3, violaxanthin, for which the radical cation PA peaks at 830 nm [252]. The TA dynamics at 880 nm, reported in **Figure 2.2.3b**, show that the Car radical cation is formed even at pH 7.5, and in similar amounts regardless of the detergent concentration. At pH 5 the formation of radical cation is enhanced, especially so for LD conditions. Global analysis of the NIR TA revealed three time constants for all samples (**Table 2.2.2** and **Figure S 2.2.14**), which were assigned to a fast multiexponential buildup of the Car radical cation (~10 ps, τ_1; ~70 ps, τ_2) followed by a longer decay (>400 ps, τ_3), which reflects both Car radical cation decay and Chl excited state decay. These observations correlate very well with the buildup of the Car GSB at 500 nm seen in **Figure 2.2.2c**. Therefore, we conclude that the buildup of the PA signal in the NIR and of the Cars GSB at 500 nm are predominantly associated with the formation of the Car radical cation, and that electron transfer from Car to Chl is an important quenching mechanism in LHCSR3 enhanced by pH and aggregation. Our results demonstrate the pH-dependent activation of electron transfer from Car to Chl in LHCSR3 and a concomitant weak excitation energy transfer to Car S_1. These findings can be compared to what has been recently reported *in vivo* in the case of LHCX1 from *N. oceanica* [246], where both quenching mechanisms were observed but only in the presence of zeaxanthin. Chl to Car energy transfer has been previously reported also *in vitro* for the LHCSR1 from *P. patens*, again only in the presence of zeaxanthin [243], or in the case of trimeric LHCII in aggregation conditions only

	τ1 (ps)	τ2(ps)	τ3 (ps)
pH 7.5 HD	9.7 ± 0.2	74.7 ± 3.1	906.9 ± 12,5
pH 5 HD	10.1 ± 0.1	56.4 ± 0.5	772.9 ± 2.9
pH 7.5 LD	20.0 ± 0.2	91.3 ± 4.4	559.2 ± 8.7
pH 5 LD	10.2 ± 0.1	56.0 ± 1.0	409.7 ± 1.1

Table 2.2.2 *LHCSR3 time constants obtained by a global fit of the data in the 880-1050 nm spectral range.*

[68]. The case of LHCSR3 from *C. reinhardtii* herein reported is peculiar since Car radical cation formation and Chl to Car S_1 energy transfer are both related to low pH and occur even in absence of zeaxanthin or aggregation. Electron transfer from Car to Chl is, however, further enhanced at pH 5 and LD conditions, where LHCSR3 activity was previously correlated to its *in vivo* activity [121]. The radical cation formation and the energy transfer to the Car S_1 are, however, insufficient to fully explain the quenching activity of LHCSR3. Indeed, these processes are, respectively, enhanced and activated at low pH, while our data consistently show that the pH 7.5 LD sample is more quenched than the pH 5 HD one. Hence, there must be an additional quenching mechanism related to protein−protein interactions occurring in the LD samples, the condition where a closer correlation was found with the i*n vivo* situation by analyzing the LHCSR3 activity in mutant variants [121]. Aggregation-dependent quenching mechanisms have been previously reported both *in vitro* and *in vivo* in the case of different LHC complexes in higher plants [68,216,226,253], being revealed by the appearance of far-red fluorescence in quenched leaves [114]. In the case of *C. reinhardtii* such far-red fluorescence was not detected in quenched cells [208]. However, we note that upon NPQ induction a strong LHCSR3-dependent reduction of PSI fluorescence was also recently reported [225], likely masking the possible appearance of aggregation-dependent far-red fluorescence. Considering the substoichiometric content of LHCSR3 per PSII [123], LHCSR proteins upon protonation likely change their conformation inducing a different interaction with other LHC subunits rather than forming oligomers themselves. In our LHCSR3 measurements, TRPL and TA data consistently show decay components for the ^{1}Chl* signal with hundreds of ps time constant in LD conditions, with increased amplitude at low pH (**Figure 2.2.1**), indicating the presence of a quenching mechanism related to aggregation and consequent protein−protein interactions. This is consistent with previous TRPL work on LHCSR1 from *P. patens* [248] showing in LD conditions the presence of a 80 ps decay component with a red-shifted emission spectrum, which was attributed to the formation of aggregates. In the case of LHCII aggregates *in vitro*, besides energy transfer to Car S_1, the main quenching mechanism proposed is the formation of a Chl−Chl charge transfer state,[216] which could also be at the basis of the strong quenching observed in the case of LD samples here. In conclusion, we presented a comprehensive characterization of the ultrafast photophysical mechanisms underlying qE in LHCSR3 using TRPL and TA in the visible and NIR regions with selective excitation of the Chls. The existence of signals attributable to the quenching species in all samples implies that the mechanisms of LHCSR3 quenching are always active, even at pH 7.5 and low aggregation. However, quenching efficiency is strongly enhanced by the pH and by aggregation conditions. In particular, we find that both energy transfer to the S_1 of Car and electron transfer from Car to Chl are enhanced at low pH, with the latter being further increased by aggregation, the condition where a strong correlation was found between *in vitro* LHCSR3 activity and *in vivo* NPQ induction [121]. Since *in vivo* the lumen acidification is the trigger for LHCSR-dependent quenching in *C. reinhardtii*, it is important to note that protein−protein interactions are also tuned upon protonation of different thylakoidal proteins occurring at low pH. In a final model we can thus propose that lumen acidification induces qE by switching LHCSR3 to a strongly quenched state correlated to increased charge transfer from carotenoids to chlorophylls and increased protein− protein interactions. Quenching mechanisms in LHC proteins appear to be differently distributed among LHC subunits, with different quenching species being formed in different subunits and/or in different conditions. Possible quenching species were indeed observed in all the different LHC proteins investigated up to now, opening the unsolved question of how it is possible for these complexes with a high pigment density to maintain a stable and efficient light harvesting function rather than always causing excitation energy quenching. Considering the strong effect of the distance between Chl−Chl and/or Chl−Car for the formation of quenching species, fine-tuning of protein conformation and pigment organization is

at the base of the light harvesting vs energy quenching activity of LHC subunits.

Material and methods

Sample preparation

LHCSR3 CDS was amplified from cDNA of High Light adapted *Chlamydomonas reinhardtii* and cloned into pETMHis as reported in [106]. LHCSR3 apoprotein, overexpress in BL21 *E. coli*, was recovered as inclusion body and refolded *in vitro* in presence of pigments as previously reported [106,218]. Absorption spectra were measured with Cary 60 UV-VIS spectrophotometer (Agilent). Fluorescence emission at 300K with excitation at 440 nm, 475 nm and 500 nm was used in order to evaluate correct folding of the protein looking at energy transfer between pigments. pH and detergent concentration were then adjusted as described in the following: in the samples used for time-resolved fluorescence analysis upon *in vitro* refolding LHCSR3 was diluted ten times with solutions composed by 20 mM Hepes pH 7.5 or 20mM MES pH 4.9, in order to reach pH of 7.5 o 5 respectively, and 0.03% α-DM only in the case of HD samples. The absence of detergent in the diluting solution used for LD samples yielded in those samples a final detergent concentration of 0.003%. In the case of samples used for transient absorption measurement upon *in vitro* refolding samples were concentrated to an OD/cm= 60 and detergent was removed in all cases by using BIO-RAD Bio-beads SM2. LHCSR3 samples were then diluted ten times in 20 mM Hepes pH 7.5 or 20mM MES pH 4.9, in order to reach pH of 7.5 o 5 respectively, and 0.03% α-DM or 0.003% α- DM in the case of HD or LD samples respectively. Aggregation state of LHCSR3 samples used for transient absorption measurements was investigated by 77K fluorescence as described in [121].

Time resolved photoluminescence

Time-resolved photoluminescence measurements were performed on sample concentrated at OD/cm 0.1 on an optical path-length of 0.3 cm using a Ti: sapphire laser (Chameleon Ultra II, Coherent) with a repetition rate of 80 MHz. The output was sent to a beta barium borate crystal (BBO) to get the final 430 nm excitation. A proper filter was used to remove the fundamental pulse. The detection system consisted in a streak camera (C5680, Hamamatsu) giving spectro-temporal matrices with spectral and temporal resolutions of ~1 nm and ~20 ps, respectively.

Transient absorption measurements

Transient absorption (TA) measurements were carried out on samples concentrated at OD/cm=6 on a 1 mm-path-length cuvette using a home-made pump-probe setup, based on a regeneratively amplified Ti:Sapphire laser (Libra, Coherent) at 800 nm wavelength with 100 fs pulse duration and 1 kHz repetition rate. A fraction of the fundamental wavelength was used to seed a non-collinear optical parametric amplifier (NOPA) delivering ~80 fs pulses at a central wavelength of 630 nm. The fluence was fixed at ≈ 6 μJ/cm2 to minimize bimolecular recombination. A broadband probe was obtained through white light continuum generation by focusing the fundamental pulses either in a 2 mm sapphire plate or 4 mm YAG crystal, plus appropriate filters to reject the remaining light at 800 nm. The spectrum generated covered respectively the visible (470-700 nm) or the infrared (850-1050 nm) range. After the sample, the transmitted probe was sent to a spectrometer (SP2150 Acton, Princeton Instruments) and detected using a linear image sensor driven and read out by a custom-built board from Stresing Entwicklungsburo. For each probe wavelength, the differential transmission (ΔT/T) was measured as a function of the pump-probe time delay. For the experiments reported here, the measurements were acquired at magic angle (54.7°) polarization. Before each measurement the beam profile of pump and probe beams was imaged at the overlap position using a camera, and the cross-sections obtained were used to calculate the fluence. All TA and TRPL measurements were performed with the sample at 10 degrees Celsius to avoid protein unfolding. The signal levels of different TA scans during the measurement time were compared to confirm that no sample degradation had taken place, which was not observed for any sample under these measurement conditions.

Data analysis

Spectro-temporal data matrices acquired were fitted globally using the Glotaran software program. The data

was fitted as a sum of exponential functions with a numerical deconvolution of the instrumental response function and a polynomial to describe the chirp. To study the excited state dynamics, a sequential and irreversible scheme was considered (A → B → C → D) with increasingly slower time constants. The fits were optimized until no systematic residuals were present both in the time and wavelength variables.

Supporting information

Pigment	Number	Standard deviation
Chls	8,00	
Chl a/Chlb	6,86	0,03
Chl a	6,98	0,03
Chl b	1,02	0,00
Chl/Car	3,27	0,15
Cars	2,44	0,11
Violaxanthin	1,60	0,14
Lutein	0,84	0,08

Table S 2.2.1 Pigments analysis of refolded LHCSR3 complexes. Chls: total number of chlorophylls total number of carotenoids per LHCSR3 complex; Cars: total number of carotenoids per LHCSR3 complex.

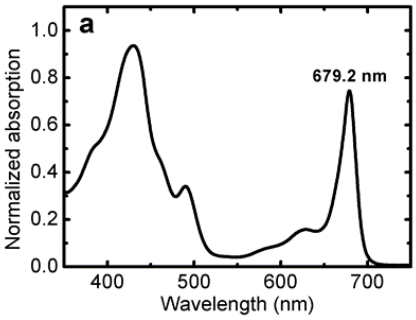

Figure S 2.2.1 *Steady-state absorption spectra of LHCSR3 at room temperature.*

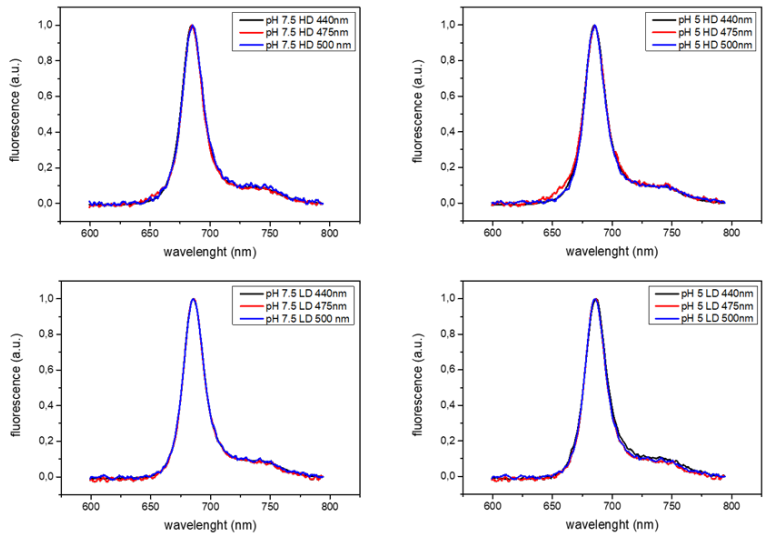

Figure S 2.2.2 *Fluorescence spectra of LHCSR3 complexes measured at room temperature at different excitation wavelengths (reported in each panel). (a) pH 7.5 HD (b) pH 5 HD (c) pH 7.5 LD (d) pH 5 LD.*

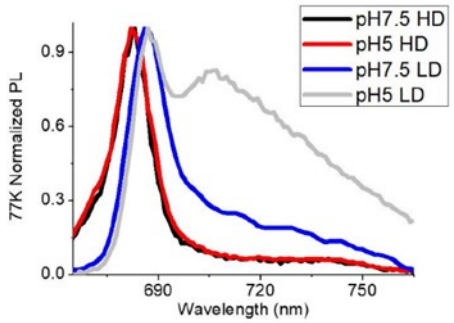

Figure S 2.2.3 fluorescence spectra of recombinant LHCSR3 at 77 K measured at pH 5 or 7.5 in the presence of 0.03% α-DM (HD) or 0.003% α-DM (LD).

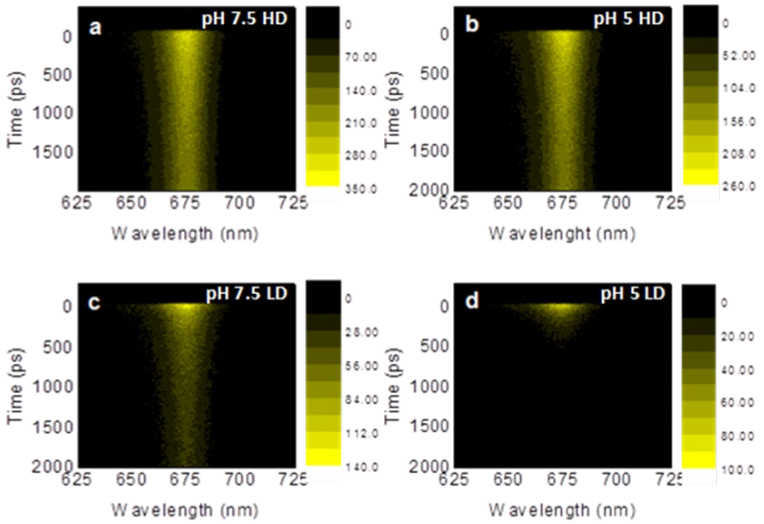

Figure S 2.2.4 *LHCSR3 TRPL maps (pump at 430 nm) of (a) pH 7.5 HD (b) pH 5 HD (c) pH 7.5 LD (d) pH 5 LD.*

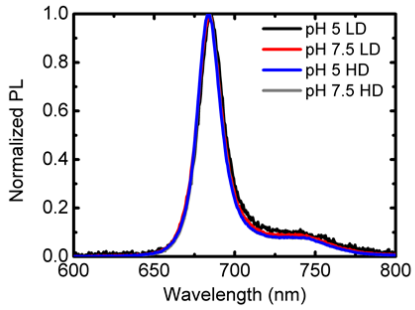

Figure S 2.2.5 *integrated TRPL spectra of LHCSR3 (pump at 430 nm, integration up to 1.8 ns).*

	A1 (%)	t1 (ps)	A2(%)	t2 (ps)	tavg (ps)
pH 7.5 HD	48	593	52	8132	4506
pH 5 HD	51	521	49	7574	3962
pH 7.5 LD	58	184	53	2655	1231
pH 5 LD	59	119	41	330	206

Table S 2.2 2 *time constants of LHCSR3 TRPL obtained by bi-exponential fits in the 650-760 nm spectral range.*

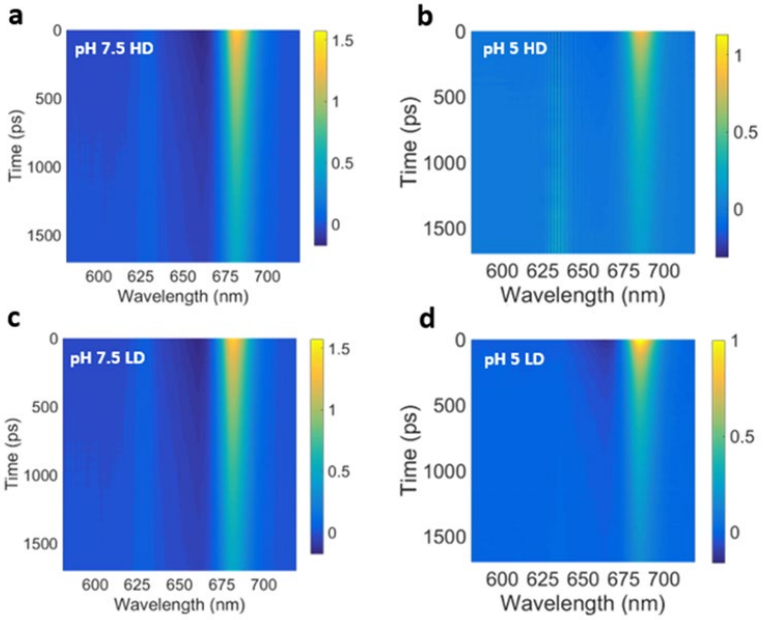

Figure S 2.2 6 *visible TA maps of LHCSR3 (pump at 630 nm) at: (a) pH 7.5 HD; (b) pH 5 HD; (c) pH 7.5 LD; (d) pH 5 LD.*

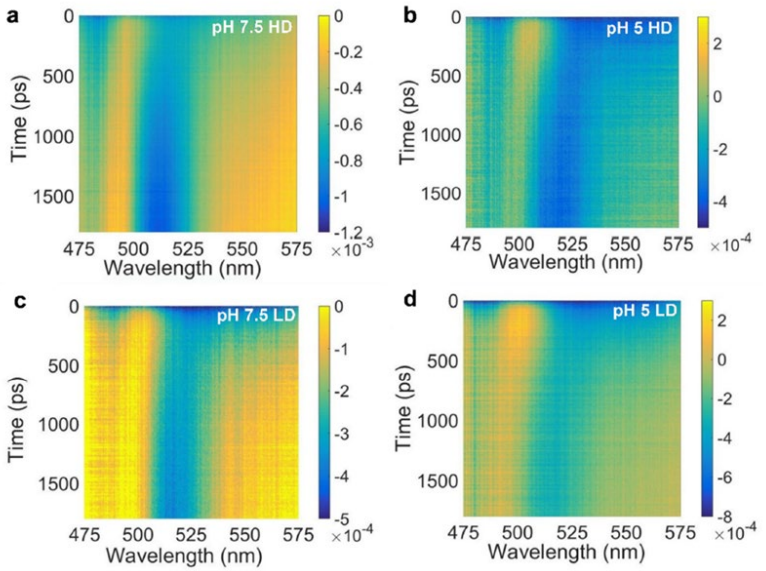

Figure S 2.2 7 *visible TA maps of LHCSR3 (pump at 630 nm) at: (a) pH 7.5 HD; (b) pH 5 HD; (c) pH 7.5 LD; (d) pH 5 LD.*

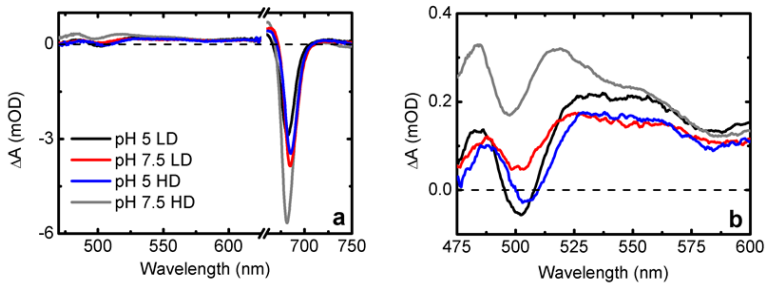

Figure S 2.2.8 *visible transient absorption spectra at 100 ps after excitation in (a) the whole spectral range. (b) Close up of the carotenoid region.*

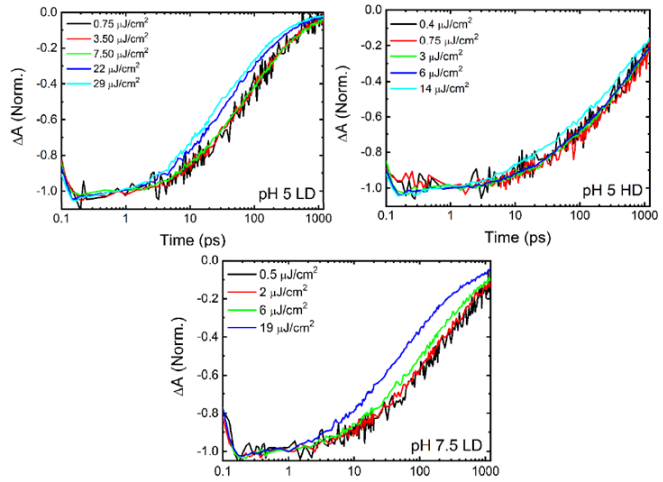

Figure S 2.2.9 *fluence dependent TA spectra of LHCSR3 at 680 nm for all quenched samples: at the excitation fluence of 6 μJ/cm2, used in the experiments, no singlet-singlet annihilation is detected for both samples at pH 5, while a very small amount of singletsinglet annihilation is present for the pH 7.5 LD sample.*

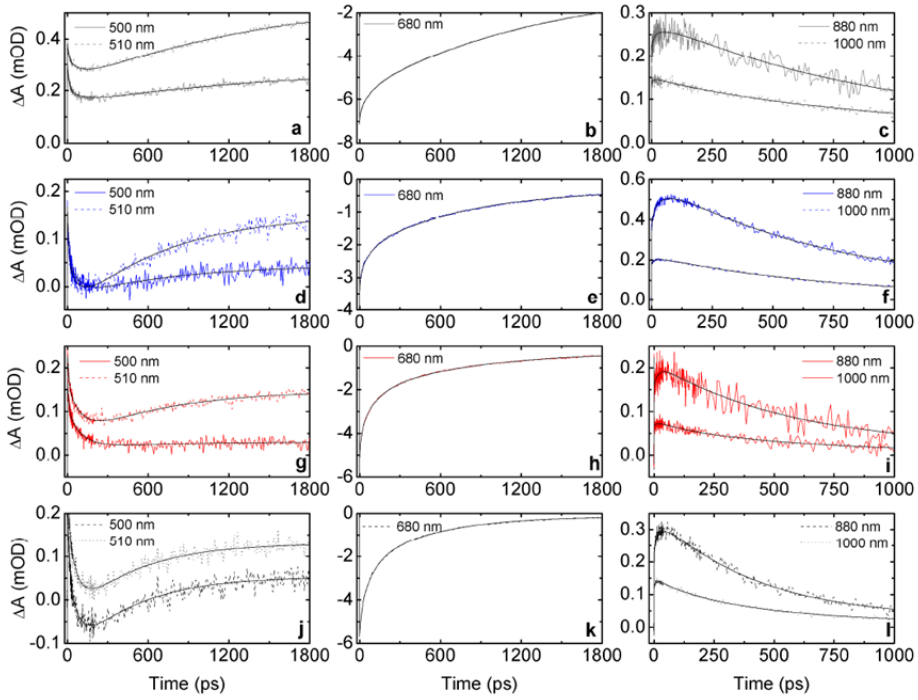

Figure S 2.2.10 *LHCSR3 TA kinetics at different wavelengths for (a-c) pH 7.5 HD (gray), (d-f) pH 5 HD (blue), (g-i) pH 7.5 LD (red) and (j-l) pH 5 LD (black). The black solid lines show the corresponding fits.*

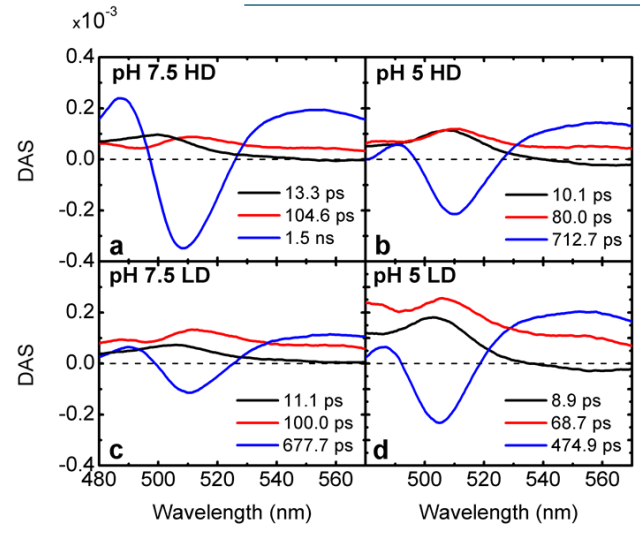

Figure S 2.2.11 *decay-associated spectra for the LHCSR3 visible TA data at (a) pH 7.5 HD, (b) pH 5 HD, (c) pH 7.5 LD and (d) pH 5 LD.*

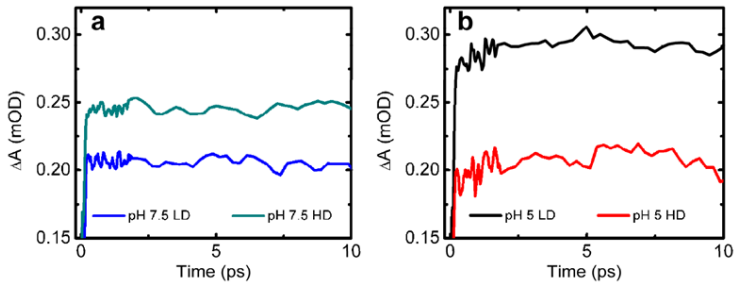

Figure S 2.2.12 *LHCSR3 TA kinetics at 560 nm in the first 10 ps for (a) pH 7.5 and (b) pH 5*

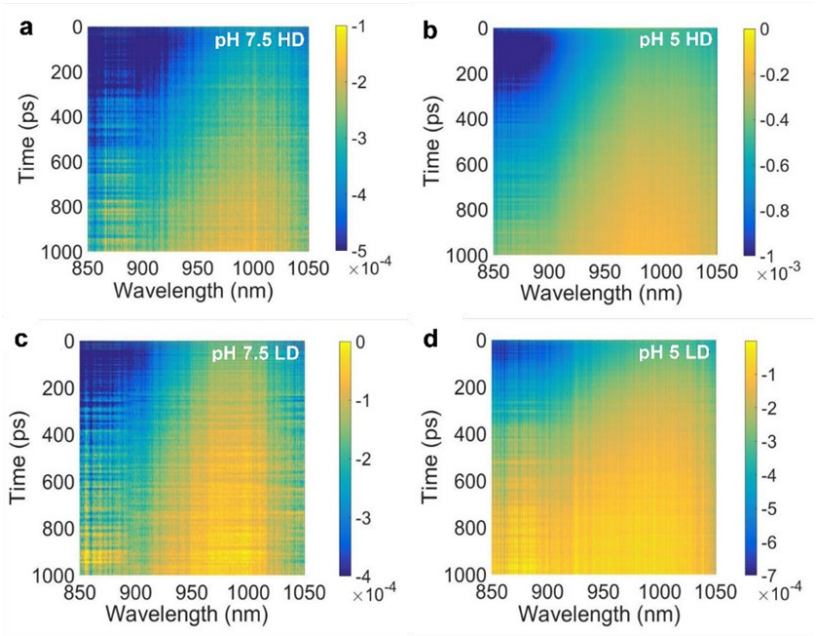

Figure S 2.2.13 *near infrared (NIR) transient absorption maps (pump at 630 nm) of (a) pH 7.5 HD (b) pH 5 HD (c) pH 7.5 LD (d) pH 5 LD.*

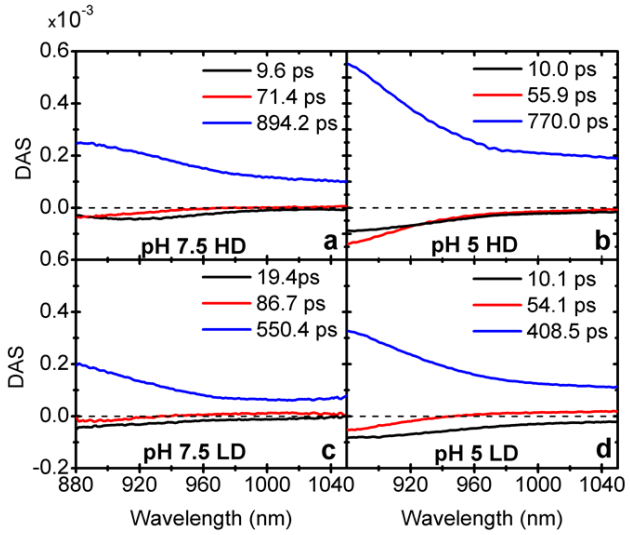

Figure S 2.2.14 *decay-associated spectra for the LHCSR3 NIR TA data at (a) pH 7.5 HD, (b) pH 5 HD, (c) pH 7.5 LD and (d) pH 5 LD*

2.3

LHCSR3 is a nonphotochemical quencher of both photosystems in *Chlamydomonas reinhardtii*

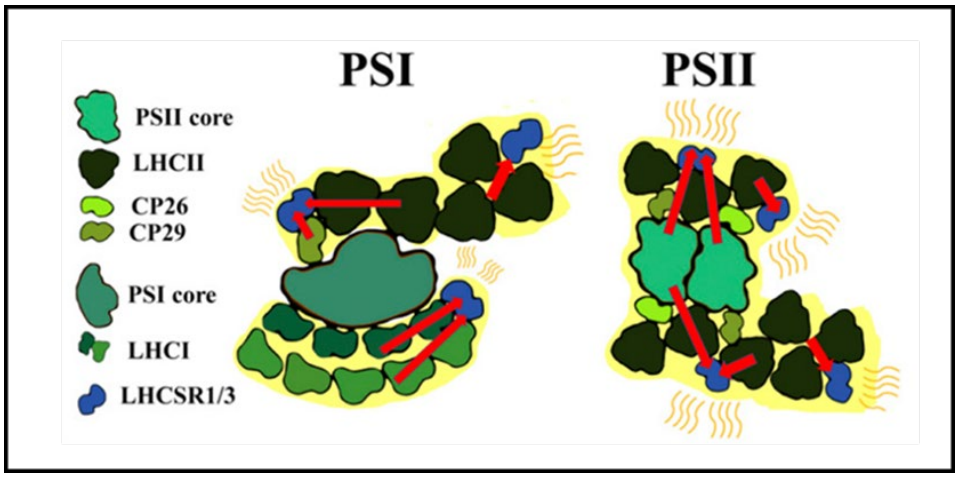

This section is based on the published article: Girolomoni, L. et al. LHCSR3 is a nonphotochemical quencher of both photosystems in Chlamydomonas reinhardtii. Proceedings of the National Academy of Sciences of the United States of America 116, 4212-4217, doi:10.1073/pnas.1809812116 (2019).

Author contributions: Ballottari M. and Bassi R. designed research; Girolomoni L., Cazzaniga S., Pinnola A., Perozeni F., and Ballottari M. performed research; Perozeni F. generated *npq4 lhcsr1* complemented mutants; Girolomoni L., Cazzaniga S., Perozeni F. and Ballottari M. analyzed data; Girolomoni L., Ballottari M., and Bassi R. wrote the paper.

LHCSR3 is a nonphotochemical quencher of both photosystems in *Chlamydomonas reinhardtii*

Laura Girolomoni[1], Stefano Cazzaniga[1], Alberta Pinnola[1,2], Federico Perozeni[1], Matteo Ballottari[1], and Roberto Bassi[1]

[1] Department of Biotechnology, University of Verona, 37134 Verona, Italy
[2] Department of Biology and Biotechnology, University of Pavia, 27100 Pavia, Italy

Abstract

Photosynthetic organisms prevent oxidative stress from light energy absorbed in excess through several photoprotective mechanisms. A major component is thermal dissipation of chlorophyll singlet excited states and is called nonphotochemical quenching (NPQ). NPQ is catalyzed in green algae by protein subunits called LHCSRs (Light Harvesting Complex Stress Related), homologous to the Light Harvesting Complexes (LHC), constituting the antenna system of both photosystem I (PSI) and PSII. We investigated the role of LHCSR1 and LHCSR3 in NPQ activation to verify whether these proteins are involved in thermal dissipation of PSI excitation energy, in addition to their well-known effect on PSII. To this aim, we measured the fluorescence emitted at 77 K by whole cells in a quenched or unquenched state, using green fluorescence protein as the internal standard. We show that NPQ activation by high light treatment in *Chlamydomonas reinhardtii* leads to energy quenching in both PSI and PSII antenna systems. By analyzing quenching properties of mutants affected on the expression of *LHCSR1* or LHCSR3 gene products and/or state 1–state 2 transitions or zeaxanthin accumulation, namely, *npq4* , *stt7*, *stt7 npq4* , *npq4 lhcsr1*, lhcsr3-complemented *npq4 lhcsr1* and *npq1*, we showed that PSI undergoes NPQ through quenching of the associated LHCII antenna. This quenching event is fast-reversible on switching the light off, is mainly related to LHCSR3 activity, and is dependent on thylakoid luminal pH. Moreover, PSI quenching could also be observed in the absence of zeaxanthin or *STT7* kinase activity.

Introduction

Photosystem II (PSII) and I (PSI) are pigment–protein complexes, located in the thylakoid membranes, composed of a core complex, hosting photochemical reactions, and a peripheral antenna system formed by Light Harvesting Complexes (LHC) [32,254]. PSI and PSII fuel a light-dependent electron transport chain from water to NADPH coupled with proton transport to the lumen driving ATP synthesis. ATP and NADPH are then used by the Calvin-Benson-Bassham cycle to reduce CO_2 into sugars. In excess light, the rate of Calvin-Benson-Bassham cycle reactions is saturated and ATP and NADPH are produced in excess compared with their metabolic demand, leading to ATPase limitation from lack of ADP substrate, which reduces the return of H^+ to the stroma compartment and causes lumen acidification. Lack of electron acceptors causes charge recombination in PSII with triplet chlorophyll (Chl) excited state formation and reaction with oxygen, forming toxic reactive oxygen species [104]. A major photoprotective mechanism, nonphotochemical quenching (NPQ), is activated when luminal pH drops, safely dissipating up to 80% of the excitation energy absorbed into heat [207]. In *Chlamydomonas reinhardtii*, NPQ activity requires LHCSR1 and LHCSR3 proteins, which are triggered to a quenching state on sensing low luminal pH [101]. Both LHCSR1 and LHCSR3 subunits are overexpressed on prolonged high-light (HL) treatment, whereas LHCSR1 expression depends on high CO_2 [101,120]. LHCSRs expression has been reported to be triggered by blue light, involving phototropins as photoreceptors that activate a signal transduction pathway leading to LHCSR3 accumulation [255]. LHCSR1 has been reported to be triggered by UV light through the activity of the UVR8 photoreceptor. LHCSR3 is accumulated to a far higher level than LHCSR1, making the former the major player in NPQ activity [190,208]. The *npq4* mutant lacks LHCSR3 and retains a low NPQ, which is abolished in *npq4 lhcsr1* also lacking *LHCSR1* [101,190]. In HL, violaxanthin is converted to zeaxanthin, a strong NPQ enhancer in plants [138,256] but not

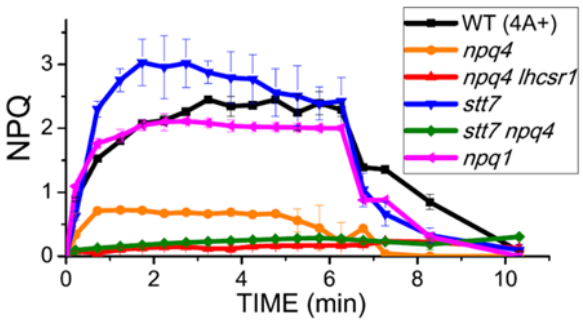

Figure 2.3.1 *NPQ induction kinetics measured at room temperature. Pulse-amplitude fluorometric time course at room temperature of WT and npq1, npq4, npq4 lhcsr1, stt7, and stt7 npq4 mutants. SDs are reported as error bars (n = 5).*

in *C. reinhardtii* (*npq1*) [106]. Photoprotection is also favored by reversible phosphorylation of PSII antenna subunits LHCII and CP29, on which they are released from PSII and connect to PSI, enhancing its cross-section and balancing PSI vs. PSII electron transport rates. This process, called state 1–state 2 transition, depends on the *STT7* kinase [257,258], which, in turn, is activated by interaction with Cytochrome b_6f complex on reduction of the PQ pool [259-261]. Despite *STT7* activity decreases under HL [260], a photoprotective effect of state transitions was reported based on enhanced photoinhibition observed in the *stt7 npq4* double mutant compared to *npq4* single mutant under HL [262]. Evidence for interaction between NPQ and state transitions relies on LHCSR3 being phosphorylated by *STT7* [106,263] and interacting with the mobile LHCII fraction [262,264]. However, *STT7*-independent phosphorylation sites have also been reported in LHCSR3 and LHCSR1 [263]. LHCSR3 was reported to interact with both PSI and PSII complexes [123,263,265], with phosphorylation negatively affecting LHCSR3 binding to PSI [263]. Phosphorylation of LHCSR3 and LHCII was reported not to affect NPQ [106]. Although both LHCSR1 and LHCR3 have been reported to be quenchers for LHCII and PSII complexes [208,230,264], their involvement in PSI photoprotection is still under debate. In the moss *Physcomitrella patens*, LHCSR1 was found to be localized in stroma membranes and to be a quencher of both photosystems [266]. Recently, LHCSR1 was reported to be involved in PSI quenching via excitation energy transfer from LHCII in *C. reinhardtii* [210]. In this work, we investigated the quenching properties of LHCSR proteins toward LHCII, PSII and PSI-LHCII complexes in *C. reinhardtii*.

Results

NPQ at Room Temperature

Although room temperature fluorescence analysis is effective as a probe for NPQ of PSII, the low quantum yield of PSI makes its fluorescence a poor signal. As reported in **Figure 2.3.1**, the *npq4* mutant showed low residual NPQ activity from LHCSR1 when the effect of excess light was measured at room temperature; that is, in conditions specific for detection of fluorescence from PSII. NPQ activity was further reduced in the double-mutant *npq4 lhcsr1*. NPQ induction of the *stt7* mutant was faster than in WT, and its amplitude was enhanced, suggesting *STT7* kinase is not essential for NPQ. Interestingly, *stt7 npq4* mutant exhibited lower NPQ compared with *npq4*, suggesting that the LHCSR1-dependent quenching might depend on *STT7* activity, despite the fact that LHCSR1 was not a *STT7* substrate. Analysis of WT vs. *npq1* mutant [203] showed NPQ was independent from zeaxanthin (**Figure 2.3.1**), in agreement with previous reports [106]. Because the amplitude of NPQ in *C. reinhardtii* is modulated by the amount of LHCSR subunits, their accumulation was quantified in the genotypes investigated by immunoblotting. LHCSR3 content per PSI or PSII was similar in WT, *npq1*, and *stt7* mutants. In WT and *npq1* strains, LHCSR3 appeared as a double band, related to the presence of the phosphorylated form, increasing its apparent molecular weight. The LHCSR3 phosphorylated form was lost in the absence of the *STT7* kinase. In *stt7* mutant, LHCSR1 accumulation was rather increased compared with WT, as in the case of *npq4* and *stt7 npq4* (**Figure S 2.3.1**).

Light-Dependent Quenching of PSII and PSI in *C. reinhardtii* Measured by 77 K Fluorescence Emission Spectra

PSI fluorescence contribution to the overall fluorescence emitted by *C. reinhardtii* can be investigated at 77 K, where the PSI photochemistry is essentially blocked and the fluorescence quantum yield is significantly increased [267]. Fluorescence emission spectra at the low temperature of the WT show two peaks, at 687 nm and 710 nm, which can be mainly attributed to PSII and PSI contribution, respectively. Spectral deconvolution with Gaussian forms allowed for extrapolating the contributions of the different

emitting components (**Figure S 2.3.2**): two Gaussians peaking at 684 and 694 nm can be associated with PSII-LHCII complexes, whereas the Gaussian form peaking at 712 nm can be associated with PSI contribution. The Gaussian component peaking at 735 nm was instrumental in compensating for deviation of the Chl fluorescence spectral form from Gaussian shape. These attributions were then confirmed by deconvolution analysis on 77 K fluorescence emission spectra obtained from mutants with a reduced amount of PSI (*psaB* mutant) [268] or depleted of PSII (*psbD* mutant) [269] or LHCI and LHCII complexes (*cbs3*)[270]. To investigate the role of LHCSR proteins in the quenching of PSI and PSII, *C. reinhardtii* cells from WT, *npq4* , *npq4 lhcsr1*, *stt7*, *npq1*, and *stt7 npq4* mutants were acclimated to HL (400 µE) for at least 10 generations to induce LHCSR1 and LHCSR3 expression in the genotypes in which the genes were expressed. Dark-adapted, HL-acclimated cells were added with green fluorescent protein (GFP) as the internal fluorescence intensity standard and split into aliquots for different treatments on which samples were rapidly frozen in liquid nitrogen and stored in the dark at 77 K until fluorescence measurements were performed. As reported in **Figure S 2.3.3**, HL treatment for 6 min with strong light (1,500 µE) did not change the GFP fluorescence emission spectrum or amplitude, enabling its use as internal standard, as previously reported [266]. Because a light-independent transthylakoidal ΔpH was previously reported to form in green algae, especially in the presence of high reducing power in the mitochondria [271], and to exclude any potential quenching on PSII or PSI in dark-adapted cells, 77 K fluorescence emission spectra were measured in the presence of the uncoupler nigericin, obtaining no significant effect on fluorescence emission spectra (**Figure S 2.3.4**). HL treatment gave a similar reduction of both PSI and PSII peaks in WT and *npq1* (**Figure 2.3.2a,b**). The quenching on PSI and PSII observed was confirmed by deconvolution of WT and *npq1* 77 K fluorescence emission spectra into Gaussian components, as described in **Figure S 2.3.2**, resulting into a reduced amplitude for both PSI and PSII spectral components (**Figure 2.3.3a,b**). In the case of *stt7*, the overall fluorescence emission of PSI was reduced in *stt7* mutant, likely as a result of the depletion of phosphorylated LHCII contributing to PSI emission in this mutant [262], where HL treatment caused a more evident quenching of the main

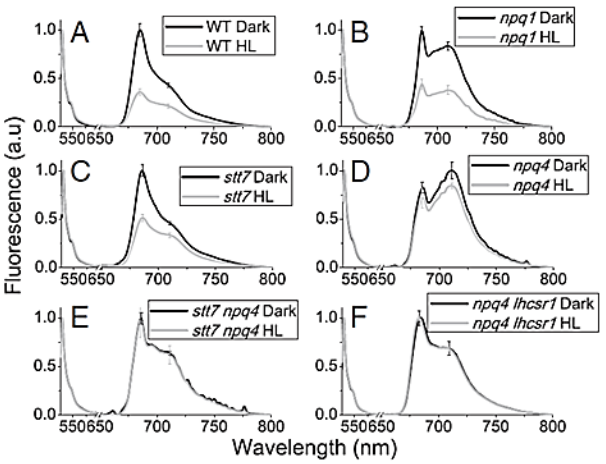

Figure 2.3.2 *Here, 77 K fluorescence emission spectra of C. reinhardtii WT (A) and npq1 (B), stt7 (C), npq4 (D), stt7 npq4 (E), and npq4 lhcsr1 (F) mutant cells normalized to GFP before and after HL exposure. Fluorescence emission spectra of C. reinhardtii were recorded for whole cells that were dark adapted (black) or HL treated (1,500 µE) for 6 min (gray). GFP was added as internal standard for normalization. SDs are reported as error bars (n = 4).*

peak (PSII), rather than on the 709-nm shoulder from PSI (**Figure 2.3.2c**). Gaussian deconvolution analysis, however, allowed for detection of decreased emission from PSI (**Figure 2.3.3c**), implying the onset of *STT7*-independent quenching on PSI. In the case of *npq4* a minor effect was detected on PSII components on HL treatment (**Figure 2.3.2d** and **Figure 2.3.3d**), whereas a more evident reduction of PSI contribution at 709 nm was observed (**Figure 2.3.2d**). These results suggest that both PSII and PSI quenching were still active in *npq4* where LHCSR1 is the only LHCSR subunit, even if to a reduced extent compared with WT. It is worth noting that the highest PSI/PSII fluorescence ratio was detected in *npq4*, consistent with previous findings [190,262]. This residual quenching on PSI was, however, almost absent in the double-mutant *stt7 npq4* (**Figure 2.3.2e** and **Figure 2.3.3e**). Both PSI and PSII quenching activities were absent in *npq4 lhcsr1* (**Figure 2.3.2f** and **Figure 2.3.3f**). To further investigate the possible role of LHCSR1 in PSI and PSII quenching, a genotype with only a LHCSR3 subunit was generated by complementation of the *npq4 lhcsr1* mutant with the lhcsr3.1 gene under the control of its endogenous promoter, as previously described [121]. Complemented lines, here called C-lhcsr3-4 and C-lhcsr3-24, were characterized by a similar level of LHCSR3 compared with WT, but no LHCSR1 (**Figure S 2.3.1**). The resulting NPQ at room temperature was similar to the WT with even a faster rise upon illumination and faster

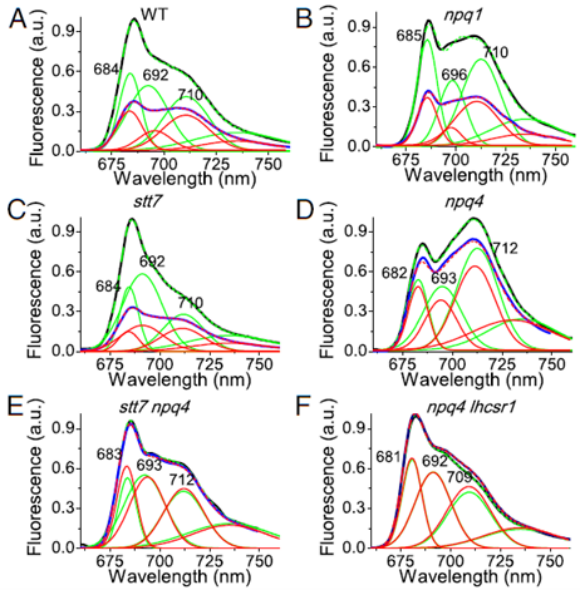

Figure 2.3.3 *Fluorescence emission spectra of dark-adapted (black) or HL-treated (blue) WT (A) and npq1 (B), stt7 (C), npq4 (D), stt7 npq4 (E), and npq4 lhcsr1 (F) mutant cells were reconstructed by spectral deconvolution with Gaussians: cumulative fit results are reported in dashed green (dark-adapted samples) or dashed red (HL-treated samples), whereas the different Gaussians used are reported in green (dark-adapted samples) or red (HL-treated samples). GFP was added as internal standard for normalization.*

recovery under low far-red light (**Figure S 2.3.5**), as previously reported [121]. In addition, 77 K fluorescence emission spectra demonstrated that both PSI and PSII contributions were quenched on HL treatment, even in absence of LHCSR1 in C-lhcsr3-4 and C-lhcsr3-24 lines obtaining similar results compared with WT (**Figure S 2.3.5**). To characterize the kinetics of quenching, 77 K fluorescence emission spectra were followed on HL treatment for 2, 4, and 6 min and after 2, 5, or 10 min of dark recovery in the presence of far red light. As reported in **Figure S 2.3.6**,**Figure S 2.3.7**,**Figure S 2.3 8**, HL treatment of WT, *stt7*, *npq1* and complemented lines C-lhcsr3-4 and C-lhcsr3-24 induced a progressive decrease of fluorescence emissions from both the main PSII peak (685 nm) and the PSI peak (709 nm). After 6 min of HL treatment cells were further incubated in the dark using a dim far-red light to maintain plastoquinone pool oxidized: their fluorescence emission almost recovered the amplitude of the dark-adapted cells (**Figure S 2.3.6**). Differently, *npq4* and *stt7 npq4* mutants only underwent a transient decrease of both 686-nm and 710/711-nm emission peaks during the first 4 min HL, whereas a slight reduction of the 711-nm peak was observed in the case of the *npq4* mutant only, with poor, if any, recovery in the dark (**Figure S 2.3.7**). No significant quenching could be

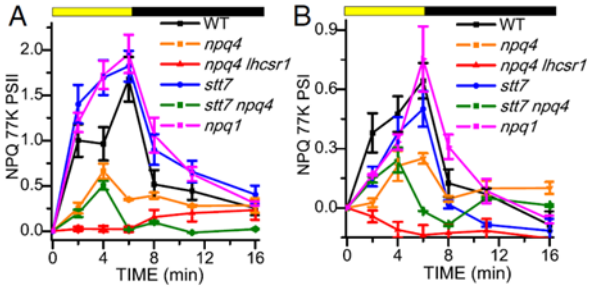

Figure 2.3.4 *Calculated NPQ induction kinetics at 77 K. The NPQ curves were calculated for PSII (A) and PSI (B) from the area of the sum of the Gaussians used for the fitting according to the formula (ADark−AX)/AX, where AX and ADark are, respectively, the amplitude at time X (AX) or at time 0 (ADark, dark-adapted samples) of the different Gaussians attributable to PSII or PSI. SDs are reported as error bars (n = 4).*

observed in the case of *npq4 lhcsr1* mutant, neither on 682-nm nor on 709-nm peaks (**Figure S 2.3.6d,e**). Rather, a minor reduction of a 682-nm peak was detected during dark recovery in the presence of far red light, possibly related to activation of PSII repair system. To reconstruct the kinetics of PSI and PSII quenching from the fluorescence emission spectra, spectral deconvolution into Gaussians components was performed, as described in **Figure 2.3.3**, for the 77 K fluorescence emission spectra obtained at different times of illumination or dark recovery. Fitting analysis on WT, C-lhcsr3-4 and C-lhcsr3-24, *stt7*, and *npq1* curves showed similar quenching kinetics for all the components retrieved, with the 692–696-nm component (PSII) showing the highest quenching amplitude on light treatment (**Figure S 2.3.9**,**Figure S 2.3.10**,**Figure S 2.3.11**,**Figure S 2.3.12**,**Figure S 2.3.13**). In *npq4* and *stt7npq4* mutants, small and virtually irreversible quenching effects were detected for the different components (**Figure S 2.3.14** and **Figure S 2.3.15**). In *npq4 lhcsr1*, instead, no quenching was observed in any component on HL treatment (**Figure S 2.3.16**). According to the amplitude of the PSII and PSI Gaussians, the quenching on PSII vs. PSI was estimated (**Figure 2.3.4**). The amplitude at time X (A_X) of the different Gaussians components was then used to calculate the quenching on PSI or PSII according to the formula $(A_{Dark}-A_X)/A_X$. PSII quenching estimated from Gaussian deconvolution was faster in *stt7*, *npq1*, and C-lhcsr3-4 and C-lhcsr3-24 lines compared with WT, while being strongly reduced in *npq4* and *stt7 npq4* mutants and negligible in *npq4 lhcsr1* (**Figure 2.3.4a** and **Figure S 2.3.17**), consistent with the NPQ kinetics at room temperature

(**Figure 2.3.1** and **Figure S 2.3.5**). PSI quenching was observed in WT, *stt7*, C-lhcsr3-4 and C-lhcsr3-24 lines and *npq1* strains, with a faster induction kinetic in the case of WT and C-lhcsr3-4 and C-lhcsr3-24 lines. PSI quenching was partially detectable in *npq4* and in *stt7 npq4* even if strongly reduced but absent in the *npq4 lhcsr1* mutant. These results imply that mainly LHCSR3 is involved in quenching of both PSI and PSII, whereas *STT7* activity and zeaxanthin have a minor effect. In the absence of LHCSR3, a small amount of LHCSR1- dependent quenching could be also measured.

77 K Fluorescence Excitation Spectra: PSI Quenching Is Specifically Located on Antenna Complexes

LHCSRs-dependent quenching can be active specifically on LHC antenna proteins, acting as an alternative trap for excitation energy, or on the whole PSI or PSII supercomplexes. To discriminate between these two possibilities, the fluorescence excitation spectra were measured for PSI (emission at 710 nm) or PSII (emission at 685 nm) in dark-adapted or HL-treated cells. In addition, 77 K excitation spectra were characterized by two main peaks: 435 nm (Chl *a*) and 480 nm (Chl *b*). Because LHC antenna proteins bind both Chl *a* and Chl *b*, whereas core complexes bind Chl *a* only, a preferential quenching of LHC antenna in HL is expected to yield excitation spectra with a decreased Chl *b* contribution. In WT, NPQ induction did not change the PSII excitation spectrum compared with a dark-adapted sample but reduced the Chl *b* peak in the PSI excitation spectrum (**Figure 2.3.5**). These results indicate that in the case of PSII, NPQ activation quenches the overall PSII-LHCII supercomplex, whereas in the case of PSI, the HL treatment specifically reduces the contribution of LHC complexes to the fluorescence emission of PSI. This observation was even more striking when the 480 nm/440 nm ratio observed in 77 K fluorescence excitation spectra was corrected for the partial overlapping of PSII and PSI emission at 710 nm, according to the Gaussian deconvolution of 77 K fluorescence emission spectra (**Table S 2.3 1**). Similar results were then obtained in the case of C-lhcsr3-4 and C-lhcsr3-24 or *npq1* (**Figure S 2.3.18** and **Figure S 2.3.19**). In the case of *stt7* mutant, HL treatment caused a decrease of Chl *b* contribution in PSI excitation spectrum,

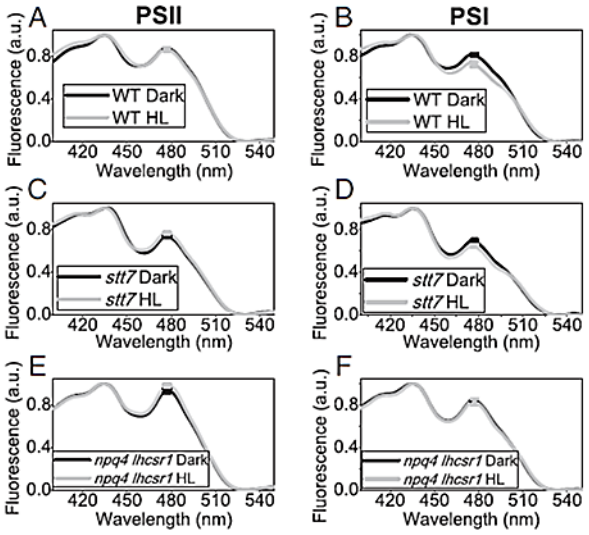

Figure 2.3.5 *Here, 77 K fluorescence excitation spectra were recorded measuring fluorescence emission at 685 nm (A, C, E), where mainly PSII emits, and 710 nm (B, D, F), where mainly PSII emits. Fluorescence excitation spectra were measured in the case of dark-adapted (black) and HL treated (gray) WT (A, B) and stt7 (C, D) and npq4 lhcsr1 (E, F) mutant cells and normalized to the Chl a contribution at 436 nm. SDs are reported as error bars (n = 4).*

although the decrease was smaller compared with that for WT (**Figure 2.3.5c,d**). No decrease in Chl **b** contribution was observed in *npq4 lhcsr1* (**Figure 2.3.5e,f**), *npq4*,and *stt7 npq4* (**Figure S 2.3.19**), consistent with LHCSR being involved in specifically quenching LHC proteins connected to PSI while homogeneously quenching the LHCII-PSII core pigment bed.

77 K Time-Resolved Analysis

Time-resolved fluorescence analysis at 77 K was performed on WT and *npq4 lhcsr1* strain in the dark-adapted state or on activating quenching by HL treatment. Fluorescence decay traces were then submitted to global analysis, as previously described [272], to identify the different associated spectral components and relative decay time constants. Four DAS (decay-associated spectral components) were required for best fit of the fluorescence decay maps (**Figure 2.3.6**). The first component (DAS 1) was characterized by a positive/negative DAS and a time constant of 32–47 ps: this component reflects the excitation energy transfer from LHC proteins to PSII and PSI core complex, which is not significantly affected by activation of NPQ mechanisms [273]. The second component (DAS 2) peaked in the 680–690-nm region, with a shoulder at 710 nm and a decay constant of 630 ps in dark-adapted WT and in *npq4 lhcsr1*. Differently, in the case of HL-treated WT, DAS 2 showed

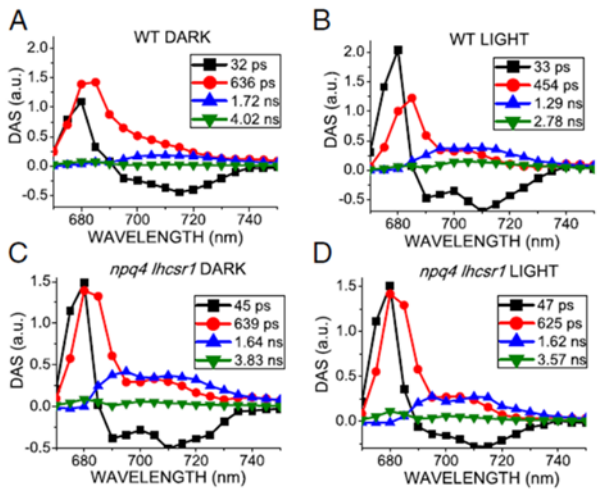

Figure 2.3.6 *Global analysis of time-resolved fluorescence kinetics at 77 K. Fluorescence decay kinetics of dark-adapted (A, C) or HL-treated (B, D) WT (A, C) and npq4 lhcsr1 mutant (B, D) were acquired at 77 K in the 670–750 nm range with 5 nm step and globally fitted with four exponentials. The DAS obtained are reported as normalized to the same total area for each sample, whereas the associated time constants are indicated in the legend. SD associated to time constants is less than 5% for each component.*

a shorter time constant of 454 ps. DAS 2 is principally related to PSII (680–690-nm emission), with a small contribution from PSI (emission at 710 nm), in agreement with reports of subnanosecond component at 77 K from both PSII and PSI [274]. The third DAS (DAS 3) showed a wide emission in the 690–740-nm, best-fitting PSI spectrum. The decay constant was 1.72 ns, reduced to 1.29 ns in HL. In the *npq4 lhcsr1* mutant, the decay constant of this DAS 3 was not significantly affected by light treatment. These results agree with a LHCSR-dependent activation of quenching mechanisms for both PSI and PSII on HL treatment. Finally, a small component (DAS 4) with a decay constant of 2.7–4 ns was observed in all samples: this component has been previously attributed to loosely bound LHCII and to the longest decay contribution from PSI at 77 K [274]. In WT, DAS 4 was shortened on HL exposure, from 4.01 to 2.70 ns. It should be noticed that the *npq4 lhcsr1* mutant also underwent a limited reduction in DAS 4 lifetime from 3.8 to 3.6 ns. DAS 4, however, was specifically decreased at 685 nm in WT compared to *npq4 lhcsr1* mutant, suggesting a preferential LHCSR-dependent quenching of loosely bound LHCII. Time-resolved fluorescence analysis was also performed on *stt7*, *npq1*, *npq4*, *stt7 npq4*, and C-lhcsr3-4 and C-lhcsr3-24 strains (**Figure S 2.3.20**). In the case of dark-adapted samples, global analysis yielded similar results compared with WT and *npq4 lhcsr1* genotypes. On HL treatment, only *stt7*, *npq1*, and C-lhcsr3-4 and C-lhcsr3-24 strains exhibited a shortening of the decay constants of DAS 2, DAS 3, and DAS 4, as in the case of WT. A minor shortening of decay constant of DAS 3 from 1.77 ns to 1.49 nm was also observed for *npq4*, in agreement with a minor quenching activity on PSI from residual LHCSR1.

Discussion

LHCSR3 and LHCSR1 are pigment-binding proteins involved in NPQ activation in *C. reinhardtii* [101,190,208,210]. NPQ measurements have been mainly based on room temperature fluorescence measurements monitoring changes of PSII fluorescence, whereas the low-fluorescence quantum yield of PSI prevents analysis in the presence of strong emissions by PSII. At 77 K, fluorescence quantum yield is high for both PSI and PSII, allowing for proper quantification of both emissions. Moreover, freezing samples in liquid nitrogen preserves the conformations previously induced by actinic light, thus allowing for spectral characterization of quenched states [266,275]. The direct involvement of LHCSR in activating quenching is evident from **Figure 2.3.2** and **Figure 2.3.3**, showing that HL was effective in reducing the amplitude of both PSII and PSI emissions in the presence of LHCSR subunits. Deconvolution of fluorescence emission spectra into Gaussian components allowed us to isolate the contributions of PSI from PSII and showed that both were quenched on HL treatment (**Figure 2.3.3**). Indeed, time-resolved fluorescence analysis, also at 77 K, on dark-adapted vs. HL-treated cells showed a strong reduction of time constants of both PSI and PSII in the presence of LHCSR subunits only (**Figure 2.3.6**). The activity of LHCSR subunits as quenchers for LHCII trimers of either components of PSII or PSI supercomplexes or loosely bound, is consistent with previous reports. LHCSR1 was found active vs. LHCII, either free or bound to PSI [208,210], whereas the LHCSR3 subunit was found to bind to both PSI and PSII in *C. reinhardtii* [123,263,265] and to be active in quenching purified PSII–LHCII supercomplexes [123]. Interestingly, the absence of LHCSR1 in C-lhcsr3-4 and C-lhcsr3-24 lines did not affect PSI or PSII quenching (**Figure S 2.3.17**), whereas only a partial quenching was observed on LHCSR1 up-regulation in *npq4* or *stt7 npq4* mutant (**Figure 2.3.4**). These results indicate that LHCSR3 is the major actor in PSI and PSII quenching,

whereas only a minor role, if any, can be attributed to LHCSR1. Nevertheless, the residual quenching observed in *npq4* and *stt7 npq4* indicates that LHCSR1 might be a quencher for both photosystems, even if with a much lower efficiency compared with LHCSR3. The increased quenching activity of LHCSR3 compared with LHCSR1 might be related simply to a dose effect and/or to some specific interactions with potential partners and/or to a specific intrinsic quenching activity. Quenching activity toward PSI or PSII by LHCSR3 differs: although the fluorescence excitation spectra of PSII-LHCII complex were similar in dark-adapted or HL-treated samples, suggesting homogeneous quenching in HL, a specific reduction of Chl *b* contribution to PSI emission was observed in the case of LHCSR3-dependent quenching of PSI (**Figure 2.3.5** and **Table S 2.3 1**). This result suggests that in the case of PSI, LHCSR3 subunits preferentially quench antenna proteins, rather than the PSI core complex. Both LHCSR1 and LHCSR3 have been previously reported to interact with the "mobile" fraction of LHCII preferentially involved in state transitions: LHCSR3 was suggested to modulate coupling/decoupling of this LHCII population to PSII [264] and LHCSR1 to modulate the excitation energy transfer from LHCII to PSI [210]. The results reported here are consistent with the above reports, highlighting a specific role of LHCSR subunits, and in particular LHCSR3, in quenching "mobile" LHCII trimers and thus reducing the fraction of LHC subunits involved in efficient energy transfer to PSI (**Figure 2.3.6**). At variance with results reported by Kosuge et al. [210], 77 K fluorescence excitation spectra and time resolved fluorescence analysis suggest that the LHCSR-dependent quenching on LHCII trimers does not correlate with increased excitation energy transfer to PSI. This interpretation is supported by several pieces of evidence: the Chl *b* contribution to PSI fluorescence emission was reduced, whereas an increased excitation energy transfer to PSI would be expected to increase the contribution of antenna proteins to PSI emission; the amplitude of the shortest DAS (DAS 1, ~30 ps), obtained by time-resolved fluorescence analysis from excitation energy transfer to PSI, did not increase on HL treatment, as expected from increasing the antenna size; time constants of DAS attributable to both PSII and PSI in WT dark-adapted cells were reduced on HL treatment, consistent with the onset of a quenching mechanism, rather than as a result of excitation energy transfer to the PSI reaction center; and PSI fluorescence was observed at 77 K, that is, with photochemical activity, if any, strongly reduced. This finding implies that the possible LHCSR-dependent quenching mechanism at room temperature should be extremely quick to compete with PSI photochemistry: a quenching conformation decaying in 80 ps was reported *in vitro* in the case of LHCSR1 from the moss *Physcomitrella patens* [248]. This time scale is consistent with competition with PSI photochemical traps, even if further investigation is required to properly evaluate this point. Nevertheless, we cannot fully rule out the possibility that LHCSR-dependent quenching might in part involve energy transfer to PSI reaction centers, as suggested by Kosuge et al. [210], or detachment of antenna proteins from the PSI core, which could account for the preferential loss of Chl *b* contribution to PSI excitation spectra (**Figure 2.3.5**). Kinetics of NPQ on PSII and PSI were reconstructed according to Gaussian deconvolution at different illumination times (**Figure 2.3.4**). Zeaxanthin accumulation on HL treatment had little effect on PSII quenching, whereas PSI quenching was only slightly affected in terms of decay kinetics (**Figure 2.3.4**). These results are consistent with a minor role, if any, of zeaxanthin in increasing the kinetic for activation of PSI quenching in *C. reinhardtii* [106]. In the case of *stt7* mutant, the absence of an active *STT7* kinase did not impair NPQ induction at the level of either PSI or PSII (**Figure 2.3.4**). Although LHCII phosphorylation is dependent on *STT7* activity and related to state transitions [258], LHCSR3 was also reported to harbor phosphorylation sites that are not substrates for *STT7*, and the binding of LHCSR3 to PSI was negatively

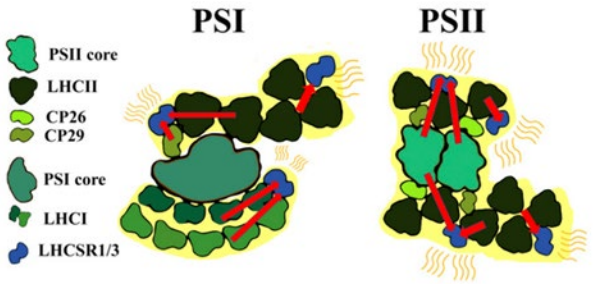

Figure 2.3.7 *Model for LHCSRs quenching on PSI and PSII. LHCSR1 and LHCSR3 interaction with PSI and PSII supercomplexes is schematically reported as a model for their quenching activity. LHCSR3 has the major role in quenching, whereas a residual LHCSR1 dependent quenching activity can be observed in the absence of LHCSR3. Red arrows indicate excitation energy transfer. Peripheral LHCII trimers loosely connected to PSI or PSII are also reported. In the model, the PSI and PSII subunits quenched by LHCR proteins are highlighted in yellow.*

affected by its phosphorylation [263]. The results presented here, together with previous findings, suggest that LHCSR3-dependent quenching of PSI occurs on LHC proteins bound to PSI-complex, which could be either identified as phosphorylated LHCII trimers or LHCI proteins (**Figure 2.3.7**), thus explaining the different Chl *b* contribution observed in fluorescence excitation spectra in *stt7* mutant on HL treatment. We conclude that in *C. reinhardtii*, LHCSR3 is involved in quenching both PSI and PSII by directly interacting both with PSII supercomplexes and with PSI-bound LHCII (**Figure 2.3.7**). Because in *C. reinhardtii*, photosystem II subunit S protein is only transiently expressed [116,211] and not detected in the conditions applied here (**Figure S 2.3.1**), LHCSR3 proteins appear to account for most or all NPQ activity, as shown by lack of quenching in *npq4 lhcsr1*. Quenching activity occurs at different sites: PSII complexes, where LHCSR3 was found docking to LHCII trimers or CP26 [230]; LHC complexes bound to PSI complexes; and a LHCII "mobile" pool loosely connected to photosystems (**Figure 2.3.7**). In the WT, on HL stress, PSII quenching rapidly occurred, whereas PSI quenching was slower (**Figure 2.3.4**), possibly as a result of a time lag for LHCSR-dependent detachment of LHCII proteins from PSI. The photoprotective relevance for the observed fluorescence quenching on PSI was confirmed by the strong PSI photoinhibition observed when PSI quenching was completely abolished in the *stt7 npq4* mutant [262].

Material and methods

Strains and Culture Conditions

C. reinhardtii cells were grown at 25 °C in flask with white light (70 µE; 16 h light/8 h dark photoperiod) in TAP medium. HL acclimation was induced by growing cells at 400 µE in HS medium. *npq4 lhcsr1* complementation was performed as described in [121].

NPQ Measurements at Room Temperature

NPQ measurements were performed with a PAM-101 (Waltz) with actinic and saturating light of 1,500 µE and 4,000 µE, respectively. The far-red LED was kept on during dark recovery. During dark adaptation, cells were shaken in HS medium.

Quenching Measurements at Low Temperature

In addition, 77 K fluorescence emission and excitation spectra were recorded using a Fluoromax3 (Horiba scientific) on whole *C. reinhardtii* cells dark-adapted or HL-treated (1,500 µE) as described in the text. GFP protein was added to the sample as internal standard for normalization of fluorescence emission spectra. Additional details on fluorescence spectra acquisition and analysis are reported on SI Appendix.

Time-Resolved Fluorescence

Time-resolved fluorescence measurements were performed at 77 K, using a Chronos BH ISS Photon Counting instrument with picosecond laser excitation at 447 nm operating at 50MHz. Laser power was kept below 0.1 µW. Fluorescence decay maps were then globally fitted with exponential functions, as previously reported [272], using Glotaran v.1.5.1 software [251] .

SDS/PAGE and Immunoblotting

SDS/PAGE and immunoblotting were performed as described in [106]. LHCSR1- and LHCSR3-specific antibodies (AS142819 and AS142766, respectively) were acquired from Agrisera company.

Quenching measurements at low temperature and Gaussians deconvolution of fluorescence emission spectra

Algal cells were washed twice with water and kept in dark for 1 hour; 1 µM of recombinant GFP was used as an internal standard. During dark adaptation cells were shacked in tap water at the concentration of 75 µg/ml of chlorophylls. When needed, nigericin was added in the dark 10 minutes before the measurements. The final concentration of nigericin was 15µM. Samples were collected before the illumination, after treatment with 1500 µE or following a 5-min recovery in the dark. All samples were frozen in liquid nitrogen. Fluorescence at low temperature were recorded using a Fluoromax3 equipped with an optical fiber (Horiba scientific). Emission spectra were performed by exciting the sample at 475 nm and recording emission from 500 to 800 nm, normalizing to the

GFP signal at 508 nm. Excitation spectra were performed by recording the emission derived from PSII at 685 nm and PSI at 709 nm for excitation in the 400- to 550-nm range. The contribution of PSI and PSII was evaluated through the deconvolution of the emission spectra using four Gaussians peaking at 681-685 (LHCII-PSII), 692-696 (PSII), 710-712 (PSI), and 735 nm (used for the fitting optimization) nm. The spectra analysis was performed using OriginPro 9.0 software (OriginLab

Supporting information

	685 nm emission			710 nm emission				
	480/440 nm ex	*dev.st*	% PSII	480/440 nm ex	*dev.st*	%PSI	480/440 nm ex PSI*	*dev.st*
WT *D*	0.875	*0.005*	95.4%	0.813	*0.009*	70.0%	0.786	*0.010*
WT *HL*	0.866	*0.014*	90.5%	0.728	*0.023*	80.1%	0.693	*0.027*
stt7 D	0.735	*0.009*	98.0%	0.693	*0.012*	65.2%	0.670	*0.015*
stt7 HL	0.769	*0.010*	95.6%	0.646	*0.011*	72.4%	0.600	*0.015*
npq4 lhcsr1 D	0.936	*0.016*	95.9%	0.843	*0.004*	75.9%	0.813	*0.016*
npq4 lhcsr1 HL	0.983	*0.013*	95.0%	0.828	*0.026*	79.2%	0.788	*0.029*
npq1 D	0.820	*0.006*	97.3%	0.774	*0.006*	77.4%	0.760	*0.008*
npq1 HL	0.819	*0.006*	88.7%	0.716	*0.006*	84.0%	0.697	*0.009*
npq4 D	0.920	*0.000*	94.2%	0.854	*0.012*	75.8%	0.833	*0.017*
npq4 HL	0.980	*0.021*	91.3%	0.856	*0.021*	74.7%	0.814	*0.030*
stt7 npq4 D	0.975	*0.005*	96.6%	0.823	*0.007*	67.5%	0.749	*0.009*
stt7 npq4 HL	0.982	*0.021*	97.7%	0.825	*0.050*	72.3%	0.765	*0.054*
C-lhcsr3-4 D	0.896	*0.020*	99.0%	0.822	*0.013*	60.9%	0.774	*0.024*
C-lhcsr3-4 HL	0.879	*0.022*	97.1%	0.753	*0.031*	69.2%	0.697	*0.038*
C-lhcsr3-4 D	0.890	*0.000*	97.8%	0.815	*0.006*	70.0%	0.783	*0.020*
C-lhcsr3-24 HL	0.915	*0.013*	88.4%	0.735	*0.011*	79.2%	0.687	*0.017*

Table S 2.3 1 *Contribution of Chl b to PSI and PSII fluorescence. Chl b and Chl a contribution to 685 and 710 nm emission were determined on the base of fluorescence excitation spectra reported in Figure 6 for WT, stt7 and npq4 lhcsr1, in Figure S18 for complemented lines C-lhcsr3-4 and Clhcsr3-24 and in Figure S19 for mutants npq4, npq1 and stt7 npq4 dark adapted (D) or high light treated (HL). The contribution of PSII or PSI emission to 685 or 710 nm fluorescence emission is reported as based on the Gaussians deconvolution reported in Figure 6 and Figure S12. Due to some overlapping of Gaussians attributed to PSI or PSII at 710 nm, the real 480/440 nm ratio in PSI excitation spectra (480/440 nm ex PSI*) was calculated by considering the contribution of PSII to 710 nm emission and the 480/440 nm ratio observed in the excitation spectra at 685 nm.*

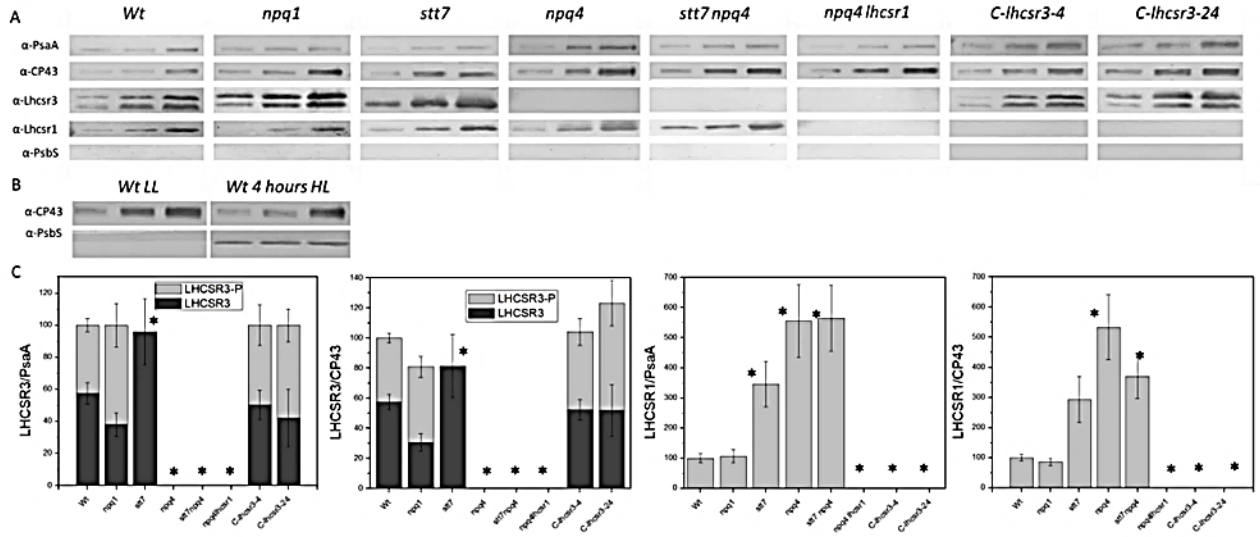

Figure S 2.3.1 *Accumulation of LHCSR subunits. Panel A: LHCSR1 and LHCSR3 accumulation in high light (400 µmol photons m^{-2} s^{-1}) acclimated WT, npq1, npq4, stt7, stt7 npq4, npq4 lhcsr1 mutants and npq4 lhcsr1 complemented lines with lhcsr3 gene (C-lhcsr3-4 and C-lhcsr3-24 lines) were investigated by immunoblotting using specific α-LHCSR1 and α-LHCSR3 antibodies recognizing respectively LHCSR1 (https://www.agrisera.com/en/artiklar/lhcsr1.html) or LHCSR3 (https://www.agrisera.com/en/artiklar/lhcsr3.html). Total protein extracts were loaded on SDS-PAGE on a chlorophyll basis loading 1, 0.5 and 0.25 µg of chlorophyll for each sample analysed. In the case of LHCSR3, both the phosphorylated (LHCSR3-P) and unphosphorylated form (LHCSR3, with lower apparent molecular weight) were detected by the α-LHCSR3 antibody. Specific antibodies recognizing PSI and PSII subunits PsaA and CP43 as described in (1) were also used to determine the PSI and PSII relative content respectively. In addition, PsbS accumulation was investigated using specific α-PsbS antibody (2), but no traces of this subunit were detected in the different strains herein analysed when acclimated to high light conditions. Panel B: positive control for PsbS detection. PsbS subunit was detected upon exposure of low light (LL) acclimated WT to 4 hours of high light (1200 µmol photons) as reported in (3). Panel C: relative LHCSR content was retrieved from immunoblots reported in Panel A by densitometry (in the case of LHCSR3, the amount of the phosphorylated and unphosphorylated forms were added up) and normalized to PSI or PSII content setting the LHCSR/PsaA or LHCSR/CP43 ratios to 100 in the case of WT. The LHCSR/CP43 and LHCSR/PsaA ratios obtained for the other genotypes were then normalized to the WT ratios. Data are expressed as mean ± s.d. (n = 3). The significantly different value from the WT are marked with an asterisk (*) (p<0,01).*

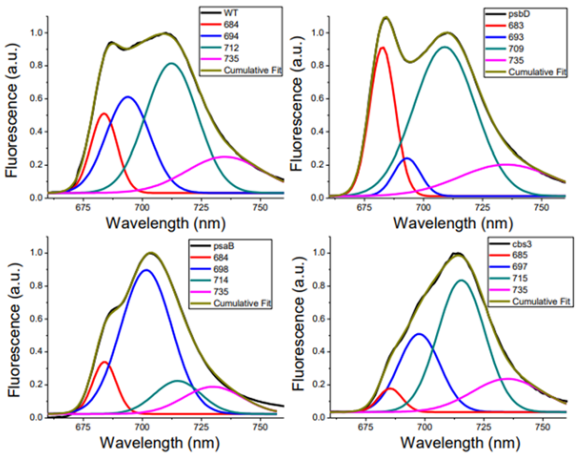

Figure S 2.3.2 *Fluorescence emission spectra of WT and of the mutant psbD, psaB and cbs Fluorescence emission spectra measured at 77K were analysed by spectral deconvolution with Gaussian forms to extrapolate the contribution of the different components. Differently from the other experiments reported in this work, the fluorescence emission spectra were measured from low light adapted strain (70 µE) grown in TAP mediumdue to high light sensitivity of the mutant strains herein investigated. In the case of WT, two Gaussians peaking at 684 and 694 nm can be associated to PSII-LHCII complexes, while the Gaussian form peaking at 712 nm can associated to PSI contribution. The last Gaussian function peaking at 735 nm was used for fitting optimization due to the red tail of chlorophyll emission forms. In the case of psbD mutant a strong reduction of the Gaussian peaking at 693 nm was evident, confirming its attribution to PSII supercomplexes. Fluorescence emission of psaB mutant was instead characterized by a strong reduction of the Gaussian peaking at 714 nm, which can be thus attributable to PSI-LHCI complex. The cbs3 mutant was instead characterized by a strong reduction of the 685 nm Gaussian, suggesting that this contribution is mainly related to LHC complexes which are bound to PSII-LHCII complex or free in the membrane.*

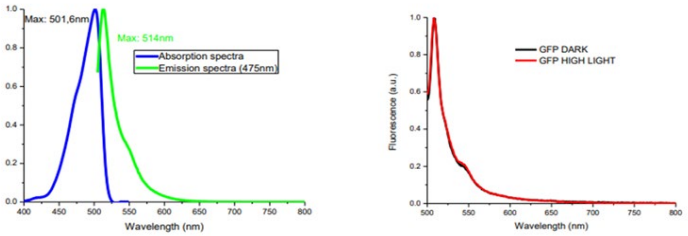

Figure S 2.3.3 *Absorption and emission spectra of Green Fluorescence Protein (GFP). Panel A: Absorption and emission spectra of GFP in water; emission spectrum wasrecorded exciting at 475nm. Panel B: emission spectra of GFP before and after high light treatment for 6 minutes at 1500 uE.*

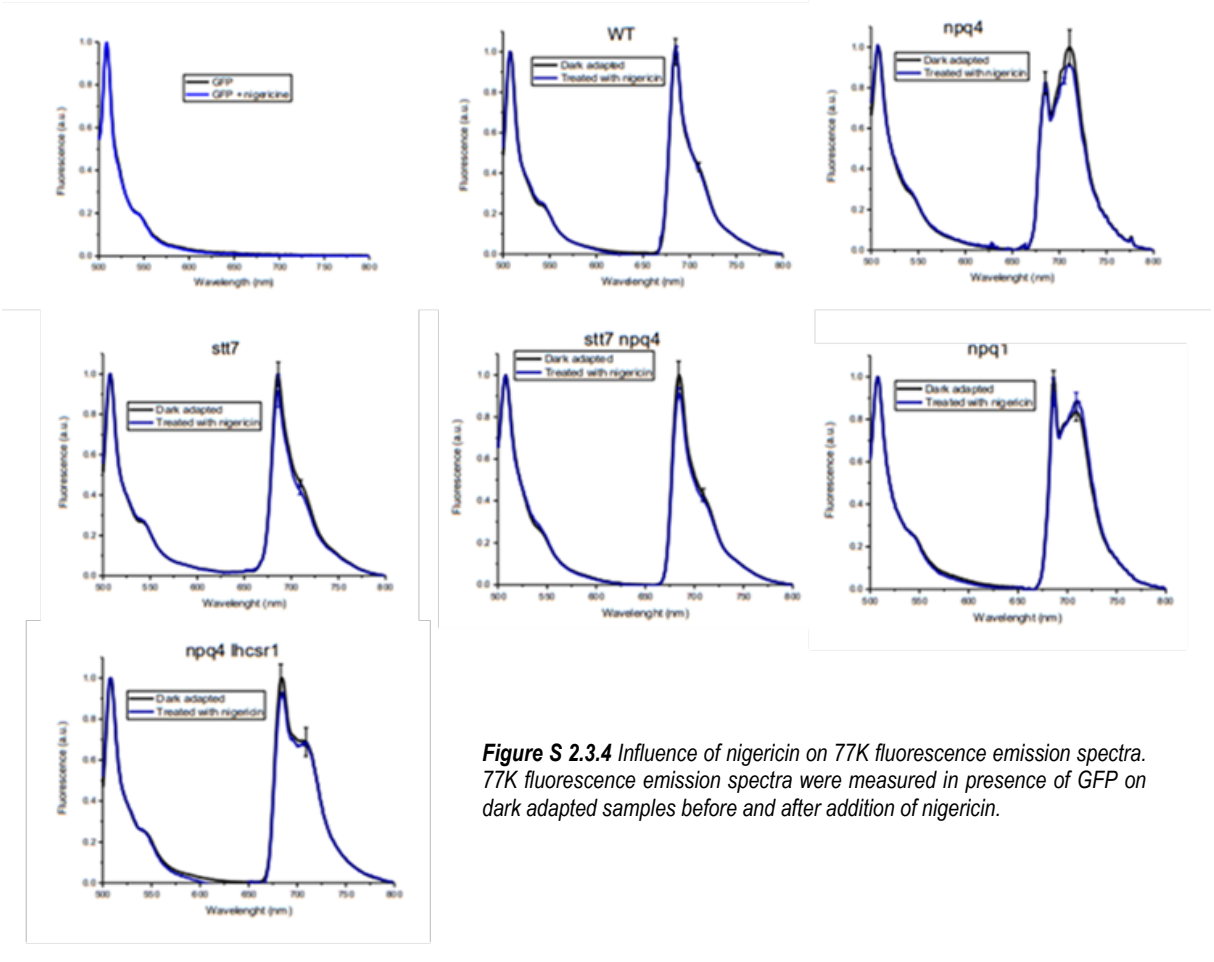

Figure S 2.3.4 *Influence of nigericin on 77K fluorescence emission spectra. 77K fluorescence emission spectra were measured in presence of GFP on dark adapted samples before and after addition of nigericin.*

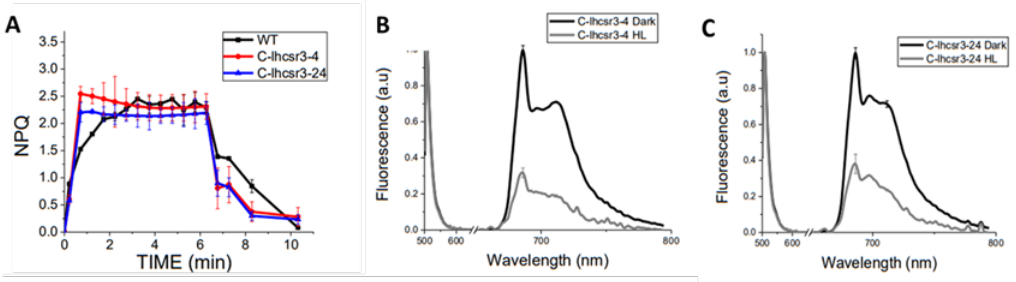

Figure S 2.3.5 *NPQ induction kinetics measured at room temperature and 77K fluorescence emission spectra of C-lhcsr3-4 and C-lhcsr3-24 complemented lines. Panel A: pulse-amplitude fluorometric time course at room temperature of C-lhcsr3-4 and C-lhcsr3-24 complemented lines compare to WT. Standard deviations are reported as error bars (n=5). Panel B/C: fluorescence emission spectra of C-lhcsr3-4 (B) and C-lhcsr3-24 (C) complemented lines recorded for whole cells dark adapted (black) or high light treated (1500 µE m^{-2} s^{-1}) for 6' (grey). GFP was added as internal standard for normalization. Standard deviations are reported as error bars (n=4).*

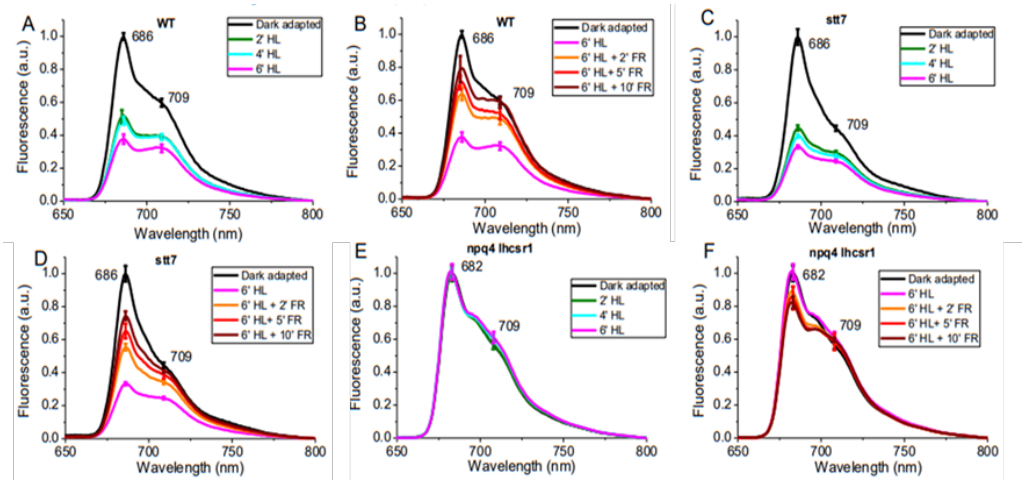

Figure S 2.3.6 *Changes in 77K florescence emission spectra during high light treatment and dark recovery. 77K fluorescence emission spectra of WT, npq4 lhcsr1 and stt7 mutants acquired for dark adapted samples or after different times of illumination (2', 4' and 6') followed by dark recovery in presence of far red light are reported normalized to GFP emission used as internal standard. Standard deviations are reported as error bars (n=4).*

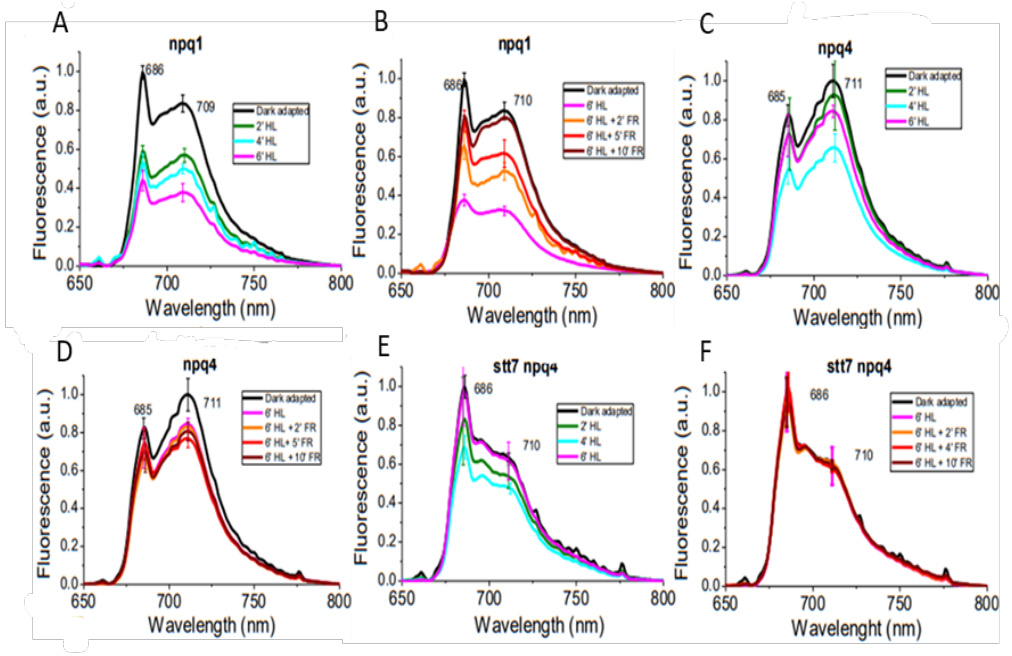

Figure S 2.3.7 *Changes in 77K florescence emission spectra during high light treatment and dark recovery in npq1, npq4 and stt7 npq4 mutants. 77K fluorescence emission spectra of WT, npq1, npq4 and stt7 npq4 mutants acquired for dark adapted samples or after different times of illumination (2', 4' and 6') followed by dark recovery in presence of far red light are reported normalized to GFP emission used as internal standard. Standard deviations are reported as error bars (n=4).*

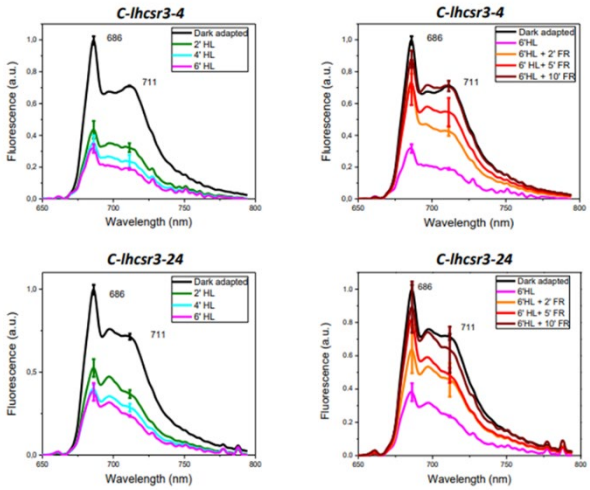

Figure S 2.3 8 *Changes in 77K florescence emission spectra during high light treatment and dark recovery in C-lhcsr3-4 and C-lhcsr3-24 complemented lines. 77K fluorescence emission spectra of C-lhcsr3-4 and C-lhcsr3-24 acquired for dark adapted samples or after different times of illumination (2', 4' and 6') followed by dark recovery in presence of far red light are reported normalized to GFP emission used as internal standard. Standard deviations are reported as error bars (n=4).*

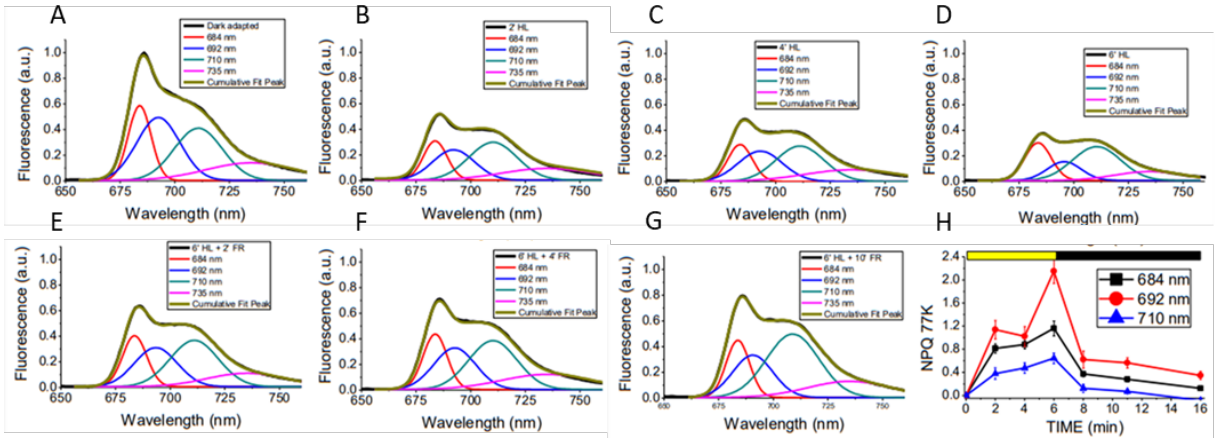

Figure S 2.3.9 *Deconvolution of fluorescence emission spectra from WT recorded at 77K. a) Dark adapted; b) treated for 2 minutes with high light; c) treated for 4 minutes with high light d) treated for 6 minutes with high light; e) treated for 6 minutes with high light and for 2 minutes with far red light; f) treated for 6 minutes with high light and for 5 minutes with far red light; g) treated for 6 minutes with high light and for 10 minutes with far red light; h) NPQ curve reconstruction using the area of the gaussian curves used for the fitting.*

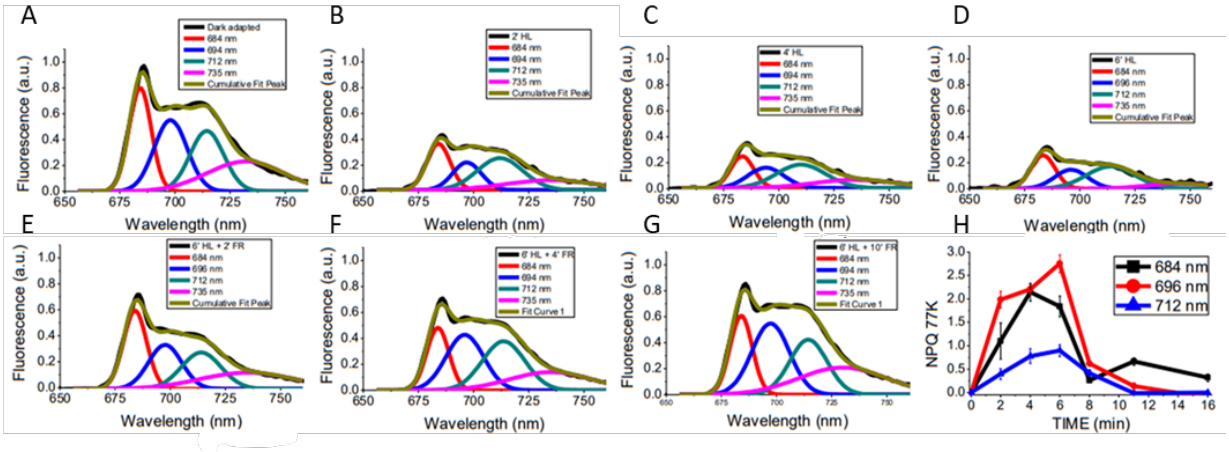

Figure S 2.3.10 *Spectra deconvolution of fluorescence emission spectra of C-lhcsr3-4 complemented line recorded at 77K. a) Dark adapted; b) treated for 2 minutes with high light; c) treated for 4 minutes with high light; d) treated for 6 minutes with high light; e) treated for 6 minutes with high light and for 2 minutes with far red light; f) treated for 6 minutes with high light and for 5 minutes with far red light; g) treated for 6 minutes with high light and for 10 minutes with far red light; h)NPQ curved reconstruction using the area of the gaussian curves used for the fitting*

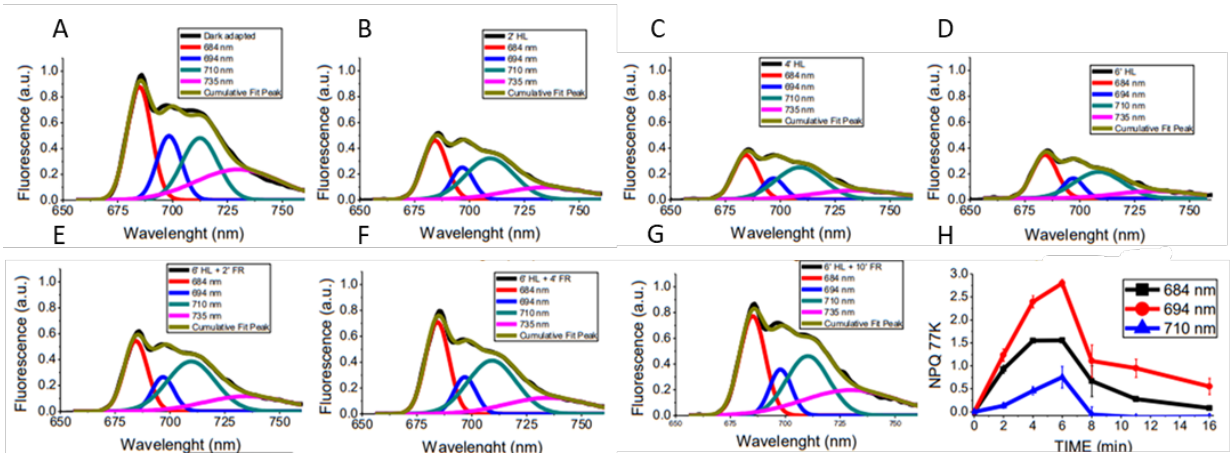

Figure S 2.3.11 *Spectra deconvolution of fluorescence emission spectra of C-lhcsr3-24 complemented line recorded at 77K. a) Dark adapted; b) treated for 2 minutes with high light; c) treated for 4 minutes with high light; d) treated for 6 minutes with high light; e) treated for 6 minutes with high light and for 2 minutes with far red light; f) treated for 6 minutes with high light and for 5 minutes with far red light; g) treated for 6 minutes with high light and for 10 minutes with far red light; h)NPQ curved reconstruction using the area of the gaussian curves used for the fitting*

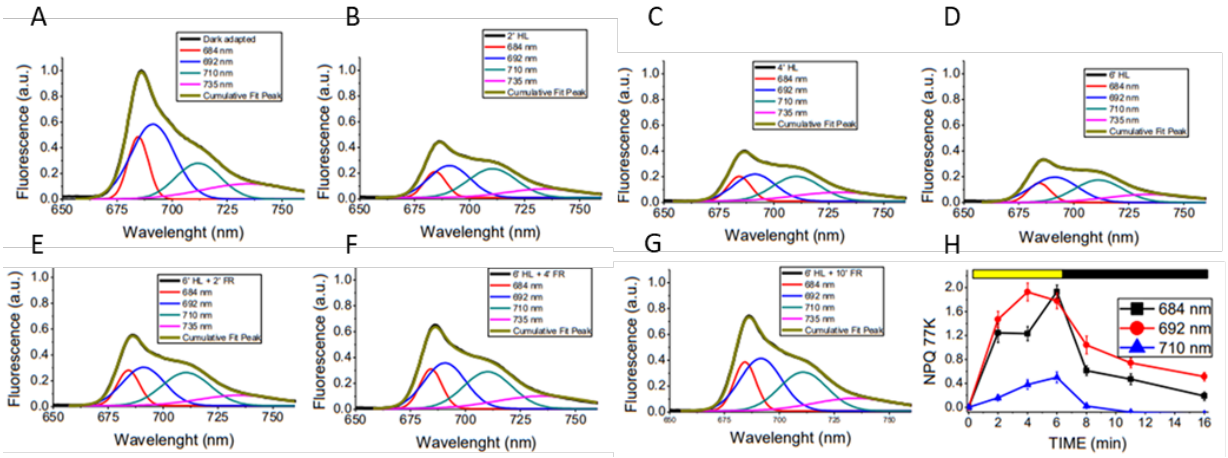

Figure S 2.3.12 *Spectra deconvolution of fluorescence emission spectra of stt7 mutant recorded at 77K. a) Dark adapted; b) treated for 2 minutes with high light; c) treated for 4 minutes with high light; d) treated for 6 minutes with high light; e) treated for 6 minutes with high light and for 2 minutes with far red light; f) treated for 6 minutes with high light and for 5 minutes with far red light; g) treated for 6 minutes with high light and for 10 minutes with far red light; h)NPQ curved reconstruction using the area of the gaussian curves used for the fitting*

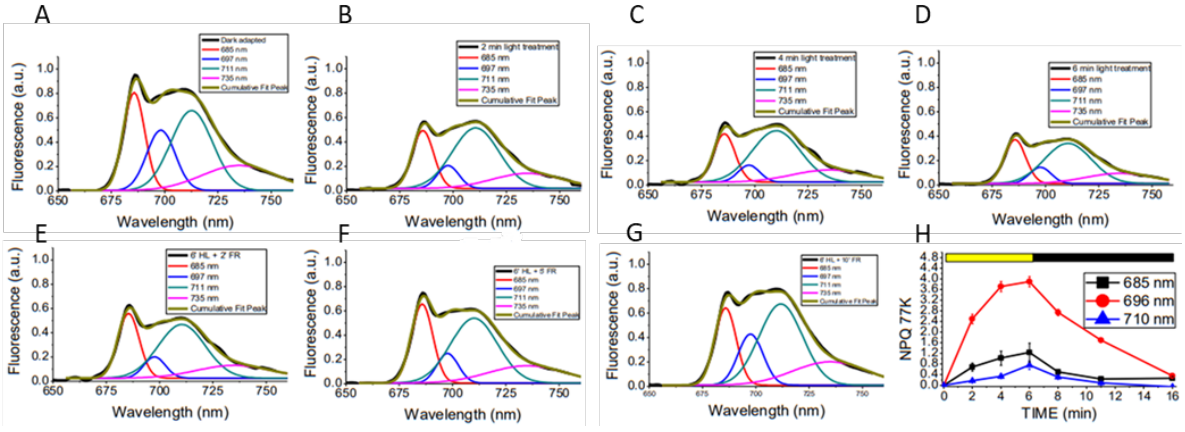

Figure S 2.3.13 *Spectra deconvolution of fluorescence emission spectra of npq1 mutant recorded at 77K. a) Dark adapted; b) treated for 2 minutes with high light; c) treated for 4 minutes with high light; d) treated for 6 minutes with high light; e) treated for 6 minutes with high light and for 2 minutes with far red light; f) treated for 6 minutes with high light and for 5 minutes with far red light; g) treated for 6 minutes with high light and for 10 minutes with far red light; h)NPQ curved reconstruction using the area of the gaussian curves used for the fitting*

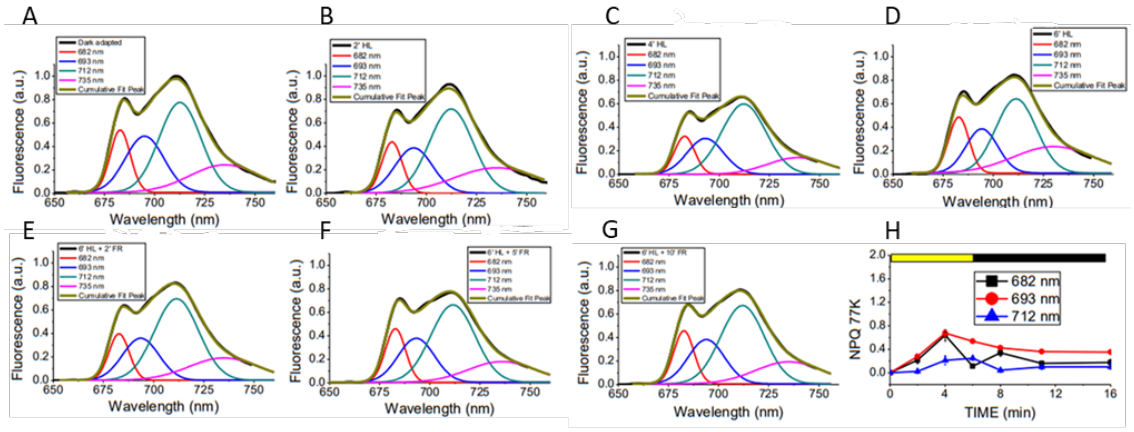

Figure S 2.3.14 *Spectra deconvolution of fluorescence emission spectra of npq4 mutant recorded at 77K. a) Dark adapted; b) treated for 2 minutes with high light; c) treated for 4 minutes with high light; d) treated for 6 minutes with high light; e) treated for 6 minutes with high light and for 2 minutes with far red light; f) treated for 6 minutes with high light and for 5 minutes with far red light; g) treated for 6 minutes with high light and for 10 minutes with far red light; h)NPQ curved reconstruction using the area of the gaussian curves used for the fitting*

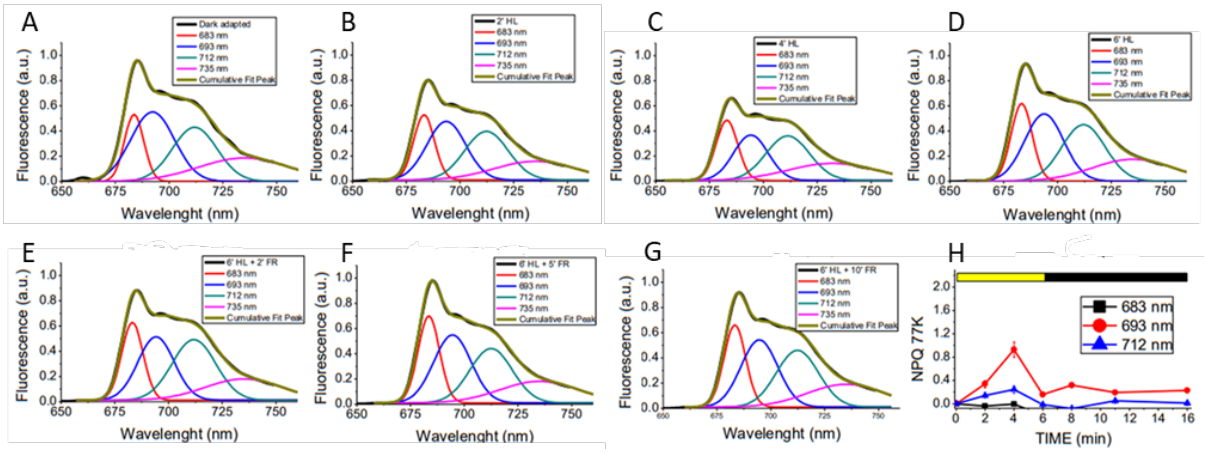

Figure S 2.3.15 *Spectra deconvolution of fluorescence emission spectra of stt7 npq4 mutant recorded at 77K. a) Dark adapted; b) treated for 2 minutes with high light; c) treated for 4 minutes with high light; d) treated for 6 minutes with high light; e) treated for 6 minutes with high light and for 2 minutes with far red light; f) treated for 6 minutes with high light and for 5 minutes with far red light; g) treated for 6 minutes with high light and for 10 minutes with far red light; h)NPQ curved reconstruction using the area of the gaussian curves used for the fitting*

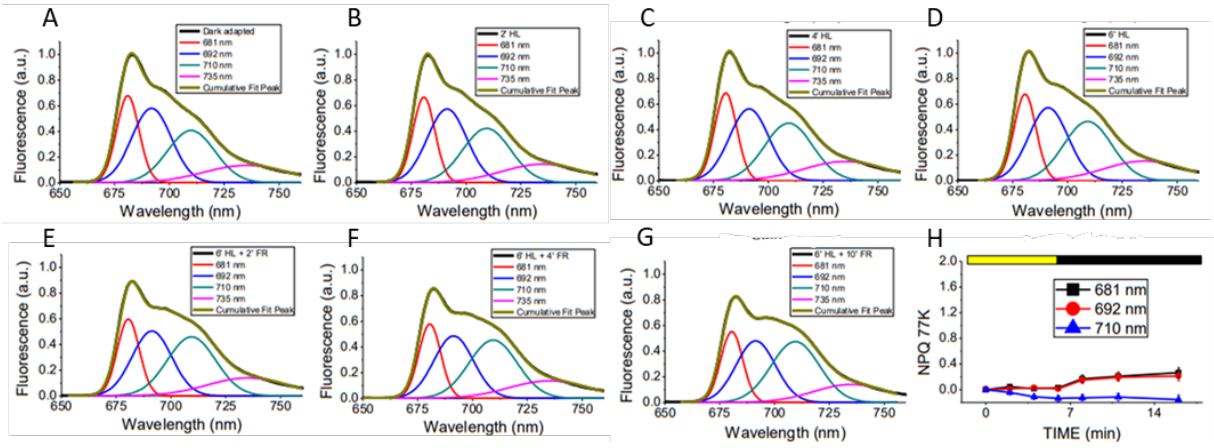

Figure S 2.3.16 *Spectra deconvolution of fluorescence emission spectra of npq4 lhcsr1 mutant recorded at 77K. a) Dark adapted; b) treated for 2 minutes with high light; c) treated for 4 minutes with high light; d) treated for 6 minutes with high light; e) treated for 6 minutes with high light and for 2 minutes with far red light; f) treated for 6 minutes with high light and for 5 minutes with far red light; g) treated for 6 minutes with high light and for 10 minutes with far red light; h)NPQ curved reconstruction using the area of the gaussian curves used for the fitting*

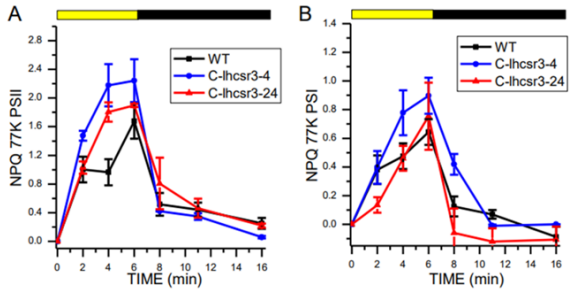

Figure S 2.3.17 *Calculated NPQ induction kinetics at 77K of C-lhcsr3-4 and C-lhcsr3-24 complemented lines. The NPQ curves were calculated from the area of the sum of the Gaussians used for the fitting according to the formula* $(A_{Dark} - A_X)/A_X$ *where* A_X *and* A_{Dark} *are respectively the amplitude at time X (AX) or at time 0* (A_{Dark}*, dark adapted samples) of the different Gaussians attributable to PSII or PSI. Standard deviations are reported as error bars (n=4).*

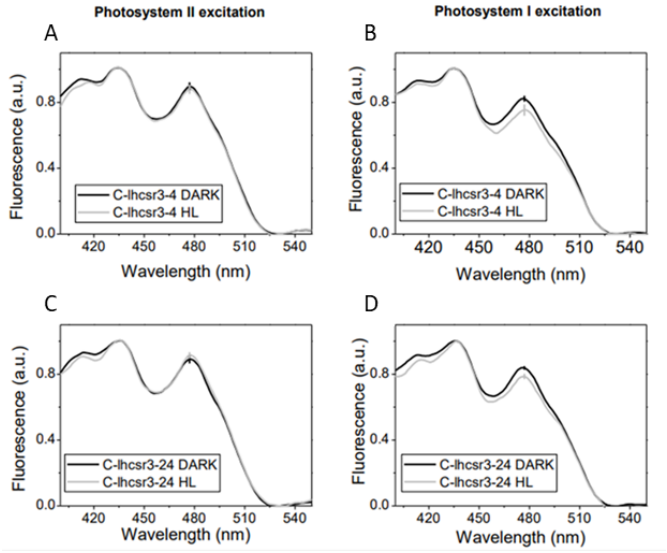

Figure S 2.3.18 *PSI and PSII excitation spectra in dark adapted and high light treated complemented lines C-lhcsr3-4 and C-lhcsr3-24. 77K fluorescence excitation spectra of PSI (fluorescence recorded at 710 nm) and PSII (fluorescence recorded at 685 nm) for dark adapted cells (black) and HL treated (grey) cells and normalized to the Chl a contribution at 436 nm. Standard deviations are reported as error bars (n=4).*

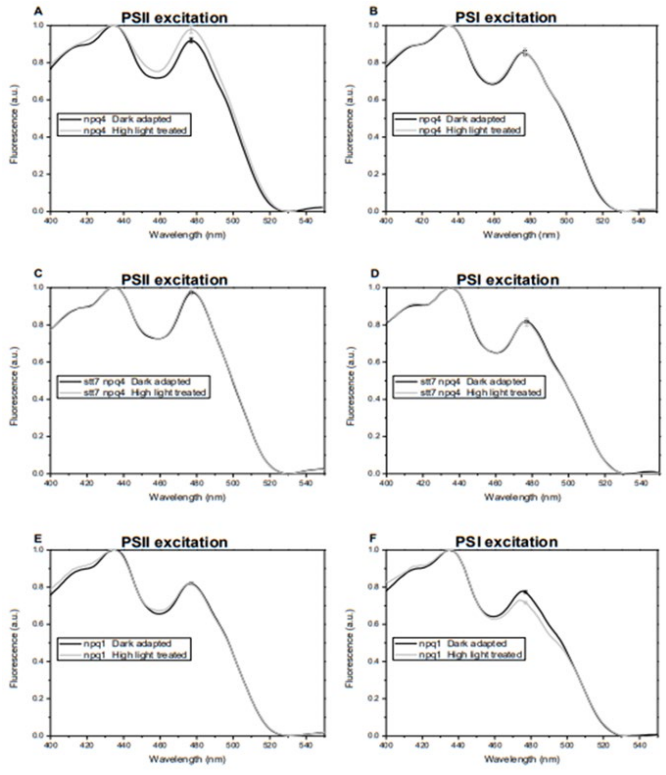

Figure S 2.3.19 *PSI and PSII excitation spectra in dark adapted and high light treated mutant strain npq4, stt7 npq4 and npq1. 77K fluorescence excitation spectra of PSI (fluorescence recorded at 710 nm) and PSII (fluorescence recorded at 685 nm) for dark adapted cells (black) and HL treated (grey) cells and normalized to the Chl a contribution at 436 nm. Standard deviations are reported as error bars (n=4). The increased Chl b contribution upon high light treatment in npq4 might suggest a partial degradation of Chl a binding core complexes during high light treatment in this strain or a preferential LHCSR1 quenching on PSII core subunits, even if minor as observed in Fig. 1 and Fig. 5. Other possible explanations of this finding are a possible reorganization of PSII supercomplexes during high light treatment in npq4 with release of Chl b binding antenna proteins with higher fluorescence quantum yield*

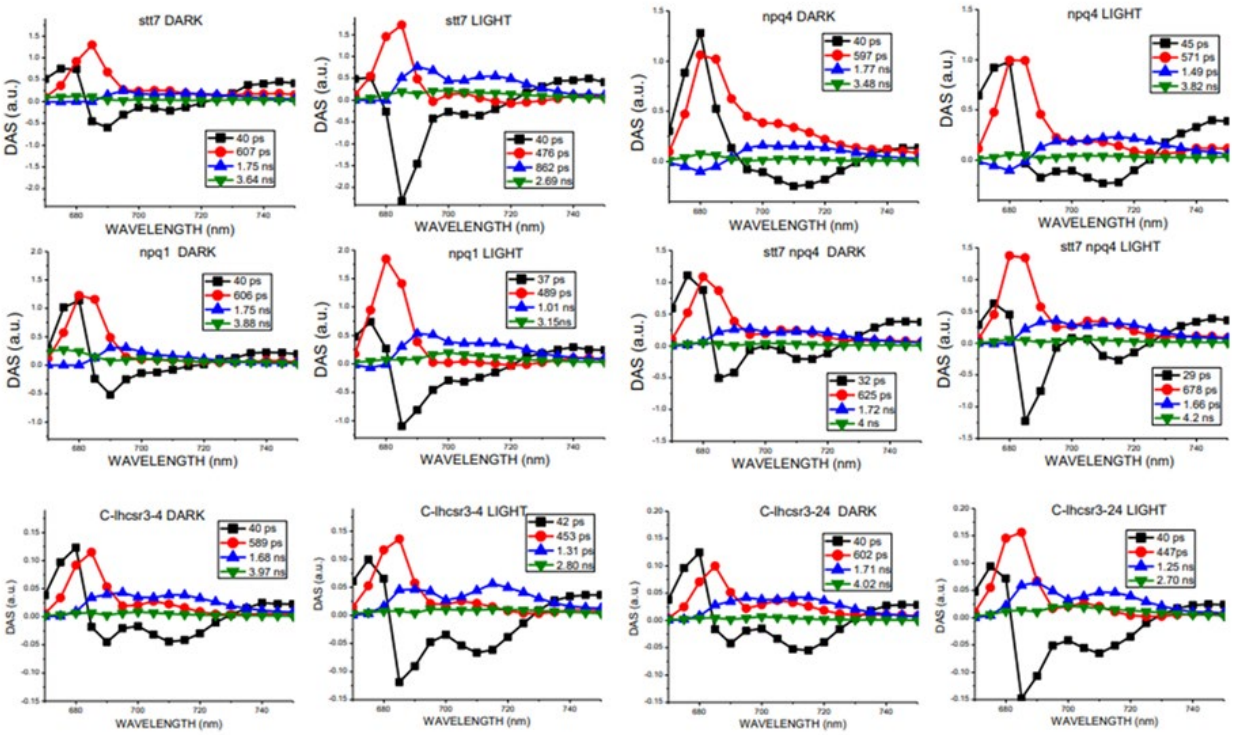

Figure S 2.3.20 *Global analysis of time resolved fluorescence kinetics at 77K of stt7, npq1, npq4, stt7 npq4 mutants and C-lhcsr3-4 and C-lhcsr3-24 complemented lines. Fluorescence decay kinetics of dark adapted or high light treated strains were acquired at 77K in the 670 – 750 nm range with 5 nm step and globally fitted with 4 exponentials. The decay associated spectra (DAS) obtained are reported normalized to the same total area for each sample, while the associated time constants are indicated the legend. Standard deviation associated to time constants is less than 5% for each component.*

2.4

Identification of parallel pH- and zeaxanthin-dependent dissipation of excess energy in LHCSR3 in Chlamydomonas reinhardtii

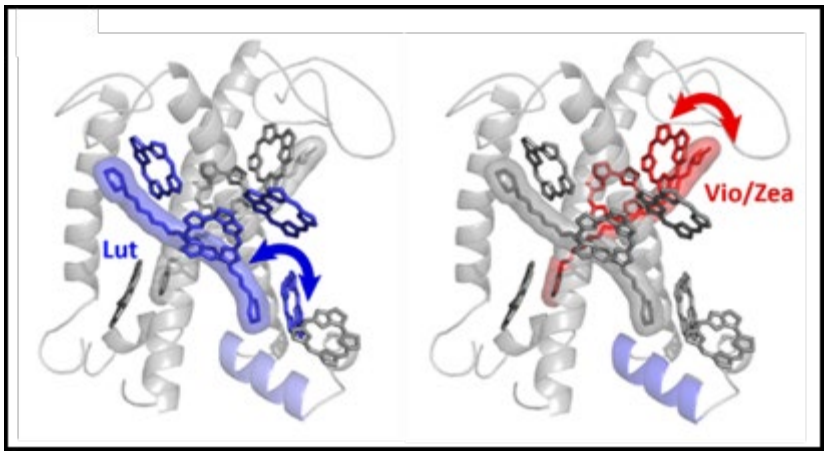

This section is based on the PNAS-submitted article: Troiano J. and Perozeni F. et al. Identification of parallel pH- and zeaxanthin-dependent dissipation of excess energy in LHCSR3 in Chlamydomonas reinhardtii."

Author contributions: * J.T. and F.P. contributed equally to this work. Ballottari M. Schlau-Cohen G.S. designed research; Perozeni F. and Zuliani L. performed *in vivo* characterization and prepare and characterized *in vitro* samples. Troiano J. and Moya R. performed single molecule spectroscopy. Baek K. generate *zep* mutant. Perozeni F., Zuliani L., Troiano J, Schlau-Cohen G.S. and Ballottari M. analyzed data and wrote the paper.

Identification of parallel pH- and zeaxanthin-dependent dissipation of excess energy in LHCSR3 in *Chlamydomonas reinhardtii*

Julianne M. Troiano[1], Federico Perozeni[2], Raymundo Moya[1], Luca Zuliani[2], Kwangryul Baek[3], EonSeon Jin[3], Stefano Cazzaniga[2], Matteo Ballottari[2], Gabriela S. Schlau-Cohen[1]

[1] Department of Chemistry, Massachusetts Institute of Technology, Cambridge MA 02139 USA
[2] Department of Biotechnology, University of Verona, 37134 Verona, Italy
[3] Department of Life Science, Hanyang University, Seoul, Korea.

Abstract

Under high light conditions, oxygenic photosynthetic organisms avoid photodamage by thermally dissipating excess absorbed energy, which is called non-photochemical quenching (NPQ). In green algae, a chlorophyll and carotenoid-binding protein, light-harvesting complex stress-related (LHCSR3), is the key gene product for NPQ. LHCSR3 detects changes in pH and serves as a site for quenching. Using a combined in vivo and in vitro approach, we identify two parallel, yet distinct quenching processes individually controlled by pH and carotenoid composition within LHCSR3 from Chlamydomonas reinhardtii. The pH-controlled quenching is removed in vitro within a mutant LHCSR3 that lacks the protonable residues responsible for sensing changes in pH. Constitutive quenching in zeaxanthin-enriched systems in vitro and in vivo shows zeaxanthin-controlled quenching, which is likely shared with other light-harvesting complexes. Both of these quenching processes prevent photodamage, and thus collectively provide distinct timescales and mechanisms of protection in a changing environment. Significance Statement Photosynthetic organisms survive despite changes in solar intensity. In oxygenic photosynthesis, organisms activate photoprotective pathways that safely dissipate excess energy to prevent the formation of damaging reactive oxygen species (ROS). While these pathways are critical for plant fitness, their inefficiencies limit biomass yields by up to 30%. The photoprotective pathways involve changes to pH and pigment composition for a large number of homologous proteins. Because of this complexity, disentangling the contributions and roles of individual parameters and 2 proteins has been challenging. Here, we combine *in vivo* and *in vitro* measurements to identify two parallel photoprotective pathways and their molecular origin, paving the way for optimization for improved crop yields.

Introduction

Sunlight is the essential source of energy for most photosynthetic organisms. In oxygenic photosynthesis, however, sunlight in excess of the organism's photosynthetic capacity can generate reactive oxygen species (ROS) that lead to cellular damage. To avoid damage, plants respond to high light by activating photophysical pathways that safely convert excess energy to heat, which is known as nonphotochemical quenching (NPQ) [276]. While NPQ allows for healthy growth, it also limits the overall photosynthetic efficiency under many conditions. If NPQ were optimized for biomass, simulations show that yields could improve by up to 30% [188]. However, critical information to guide optimization is still lacking, including the molecular origin of NPQ and the mechanism of regulation. Green algae are a sustainable alternative for biofuels [277] and livestock feed [278]. In *Chlamydomonas* (C.) *reinhardtii*, the model organism for green algae, quenching of excess energy occurs in light harvesting complex stress-related (LHCSR). LHCSR contains chlorophyll (Chl) and carotenoid (Car) held within its protein scaffold. Two isoforms of LHCSR, LHCSR1 and LHCSR3, are active in NPQ, although LHCSR3 is accumulated at higher levels and so has the major role.[101,120,123,208]. While the photophysical mechanism of quenching has not been determined, the primary proposals involve Chl-Car

interactions [68,279,280]. NPQ is triggered by a proton gradient across the thylakoid membrane that forms through a drop in luminal pH under excess light. The C-terminus of LHCSR3 contains a number of protonable residues exposed to the lumen that act as a pH sensor to trigger quenching [121,122]. The pH drop also activates the enzymatic conversion of the Car violaxanthin (Vio) to zeaxanthin (Zea) [281]. Along with LHCSR, other homologous light-harvesting complexes are likely involved in quenching [282]. In higher plants, Zea has been reported to be involved in NPQ induction by driving light harvesting complexes into a quenched state [66,283] and/or by mediating interaction between light-harvesting complexes and PsbS, non-pigment binding subunits essential for NPQ induction in vascular plants [284]. Similarly, Zea binding to LHCSR1 in the moss *Physcomitrella patens* and LHCX1 (a LHCSR homolog) in the microalga *Nannochloropsis oceanica* has been shown to be essential for NPQ [246,285]. Finally, in *C. reinhardtii*, a reduction of NPQ in the absence of Zea has been reported [203]. In contrast, recent work has shown Zea to be unnecessary for NPQ induction or related to highly specific growth conditions [106,286,287]. Thus, the contribution of Zea to quenching in green algae remains under debate. Because of the complexity of NPQ and the large number of homologous light-harvesting complexes, the individual contributions and mechanisms associated with LHCSR3, pH, and Zea have been challenging to disentangle, including whether they activate quenching separately or collectively. With the power of mutagenesis, the contribution of LHCSR3, and the dependence of this contribution on pH and Zea, can be determined. However, *in vivo* experiments leave the molecular mechanisms of LHCSR3 and its activation obscured. *In vitro* experiments, and particularly, single-molecule fluorescence spectroscopies, are a powerful complement to identify protein conformational states. A recent method to analyze single-molecule data, 2D fluorescence correlation analysis (2D-FLC) [288], quantifies the number of conformational states and their dynamics, including simultaneous, independent processes. Thus, the conformational states associated with NPQ can be resolved. Here, we apply a combined *in vivo* and *in vitro* approach to investigate NPQ in *C. reinhardtii*. We use mutagenesis, NPQ induction experiments, and fluorescence lifetime measurements on whole cells and single LHCSR3 complexes to show that pH and Zea can independently activate full quenching and prevent ROS accumulation. The pH-dependent quenching is controlled by protonable residues in the C-terminus of LHCSR3 as shown by mutagenesis to remove these residues. The Zea-dependent quenching is constitutive both *in vitro* and *in vivo*, and likely shared with other light-harvesting complexes. Based on the collective results, we find two likely quenching sites, i.e. Chl-Car pairs within LHCSR3, one regulated by pH and the other by Zea. The two quenching sites provide different time scales of activation and deactivation of photoprotection, allowing survival under variable light conditions.

Results

Roles of pH and Zea in quenching

To disentangle the individual contributions of LHCSR3, pH and Zea, both *in vivo* and *in vitro* measurements were performed on different *C. reinhardtii* genotypes. Wild type (WT) strains (4A+ and CC439), a strain depleted of LHCSR subunits (*npq4 lhcsr1*) [121], a strain unable to accumulate Zea due to knock out of the enzyme responsible for xanthophyll cycle activation [29] (*npq1*)[203], and a mutant constitutively accumulating Zea due to knock out of the zeaxanthin epoxidase enzyme (*zep*) were characterized *in vivo* [289]. To assess the ability of these phenotypes to undergo quenching of Chl fluorescence, the NPQ levels were measured after cells were acclimated to high light (HL, 500 µmol m^{-2} s^{-1}) for several generations to induce LHCSR3 expression (WT, *npq1*, and *zep* strains) and then exposed to strong light (2000 µmol m^{-2} s^{-1}) treatment for 60 minutes to induce maximum drop in luminal pH and Zea accumulation (WT, *zep*, and *npq4 lhcsr1* strains; data for xanthophyll cycle activation shown in **Figure S 2.4.1**). In the WT strains, the maximum NPQ level was reached after 10 minutes of illumination and fully recovered in the dark (**Figure 2.4.1 black**), despite a strong accumulation of Zea. The rapid recovery in the dark suggests that lumen acidification is the major trigger for NPQ. In the *npq4 lhcsr1* strain, which lacks LHCSR subunits, a null NPQ phenotype was observed (**Figure 2.4.1 purple**). These results confirm that LHCSR is responsible for NPQ in *C.*

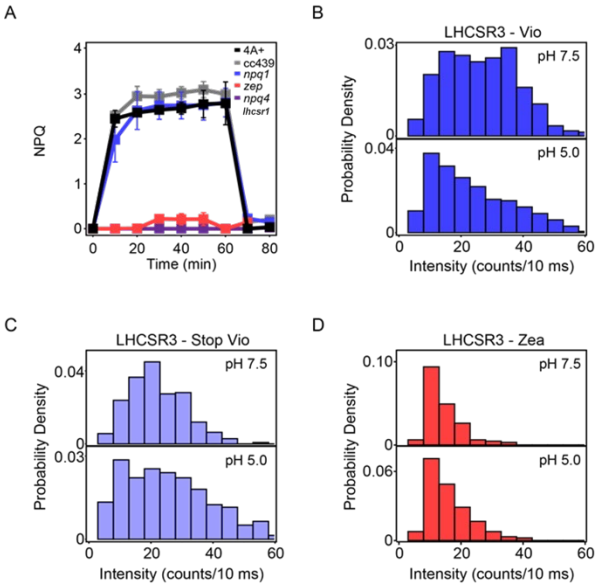

Figure 2.4.1 *Experimental studies of quenching mechanisms in vivo and in vitro. (A) NPQ induction kinetics measured upon 60 minutes of high light (15000 µmol $m^{-2}s^{-1}$) in vivo. Histograms of fluorescence intensities for individual LHCSR3 complexes containing Vio (B), stop mutant Vio (C) and Zea (D) at pH 7.5 (top) and pH 5.0 (bottom).*

reinhardtii. In the *npq1* strain, which lacks Zea, no reduction of the maximum level of NPQ was observed compared to the WT strain (**Figure 2.4.1 blue,black**). The similar level and timescales of onset and recovery for NPQ suggest a minor role, if any, for Zea in light-activated quenching. In the *zep* strain, which constitutively accumulates Zea, a strong reduction of the NPQ level was observed (**Figure 2.4.1 red**). To understand why, first accumulation of the LHCSR3 subunit was measured. However, similar LHCSR content was found in WT, *npq1* and *zep* strains (**Figure S 2.4.2**). Second, the extent of lumen acidification as compared to WT was measured. However, although acidification was reduced in the *zep* strain at low actinic light, it was similar at the higher irradiance used for measurement of NPQ (**Figure S 2.4.4**). In order to investigate the effect of pH and Zea at the level of the LHCSR subunit, single-molecule fluorescence was measured for individual LHCSR3 complexes (**Figure S 2.4.14**). Histograms were constructed of the intensity levels for LHCSR3 complexes with Vio at high and low pH, which mimic the cellular environment under low and high light conditions, respectively. As shown in **Figure 2.4.1b**, upon a decrease in pH from 7.5 to 5.0, the average fluorescence intensity of LHCSR3-Vio decreases as the quenched population increases, representing an increase in quenching of the excitation energy absorbed. This is consistent with the conclusion from the *in vivo* NPQ experiments that quenching can occur without Zea under high light conditions. Activation of LHCSR3 as a quencher has been suggested previously to be related to protonation of putative pH-sensing residues present at the C-terminus (**Figure S 2.4.10**). To assess the role of these protonable residues in pH-dependent quenching, a stop mutant lacking this protein portion was measured *in vitro* (**Figure S 2.4.11**, **Figure S 2.4.12**,**Table S 2.4.2**). Upon the same pH decrease that induced quenching in LHCSR3-Vio, the stop Vio complexes show similar fluorescence intensity (**Figure 2.4.1c**). This data shows that the stop mutants have lost the ability to activate quenching channels upon a pH drop, highlighting the sensing role of the protonable residues of the C-terminus of LHCSR3. Single-molecule measurements were also performed on LHCSR3 complexes with Zea at high and low pH. Under both conditions, as shown in **Figure 2.4.1d**, LHCSR3 complexes with Zea *in vitro* show decreased fluorescence intensity due to increased quenching. The pH-independence of these histograms is consistent with the NPQ measurements in the *zep* mutants where high light, and the associated pH drop in the lumen, does not change quenching levels. However, these measurements point to the existence of a constitutive quenching process in the presence of Zea, consistent with *in vivo* fluorescence lifetime measurements discussed below.

Identification of quenching sites in LHCSR3 *in vitro*

To further assess and quantify the contributions of pH and Zea in quenching in LHCSR3 *in vitro*, we used 2D-FLC to analyze the fluorescence data on single LHCSR3 complexes [290]. The 2D-FLC analysis identifies fluorescence lifetime states, which correspond to protein conformations with different extents of quenching, and quantifies the transition rates between the lifetime states, which correspond to switches between the protein conformations. To quantify the number of dynamical components, i.e. processes, between the two fluorescence lifetime states, a global fit of the auto- and cross-correlations for each sample provided the intensity of and the population in each state as well as the rate constants for the transitions between the quenched (low intensity, short lifetime) and active state (high intensity,

long lifetime). The best fits to the data were accomplished by including three dynamic components at different timescales (**Figure S 2.4.17**). Two of these components, one on a tens of microsecond timescale and the other on a hundred of microsecond timescale, would be hidden in traditional single-molecule analyses. These dynamic components likely arise from quenching of the Chl emitters, likely by a neighbouring Car. The third component is static at <0.01 s, which is attributed to unquenched emitters in the active state and partially photobleached complexes in the quenched state. The populations of the lifetime states and the rate constants for transitions can be used to construct illustrative free energy landscapes, which are shown in **Figure 2.4.2** for the two dynamic components. We examine the dependence on molecular parameters of these two components individually with the free energy landscapes associated with the slower component shown in **Figure 2.4.2a-c** and the landscapes associated with faster one in **Figure 2.4.2e-g**. **Figure 2.4.2a** and **Figure 2.4.2b** shows the pH-dependence of the free energy landscapes for the slower component in LHCSR3 containing Vio and Zea, respectively. In both cases, a decrease in pH from 7.5 to 5.0 stabilizes the quenched state. In LHCSR3 containing Vio, the quenched state is stabilized by a decrease in the transition rate from the quenched to the active state, corresponding to a higher barrier in the free energy landscape. In LHCSR3-Zea, the same decrease in the transition rate from the quenched to the active state is also accompanied by an increase in the transition rate from the active to the quenched state, further stabilizing the quenched state relative to the unquenched one. In the stop Vio sample however, no change in the population of the quenched state is observed upon a decrease in pH (**Figure 2.4.2c**), reflecting the expected pH-independence of the fluorescence. The bottom row of **Figure 2.4.2** shows the Zea-dependence of the free energy landscapes for the faster dynamic component at pH 5.0 and pH 7.5. At both pH levels, conversion from Vio to Zea stabilizes the quenched state via a decrease in the transition rate from the quenched to active state. At pH 5.0, the quenched state is further stabilized via an increase in the transition rate to the quenched state. This behaviour is not lost in the stop mutants, where the quenched state is still stabilized in the presence of Zea. The cross-correlation for every LHCSR3 sample begins above zero, which appears when multiple, independent dynamic components occur simultaneously (**Figure S 2.4.17**) [290]. For LHCSR3, this suggests that there are multiple Chl *a* emissive sites, where the dynamics of each give rise to a component. By considering the results of the 2D-FLC analysis along with previous structural, spectroscopic and theoretical work, we assign the dynamic components to likely sites within the LHCSR3 structure (**Figure 2.4.2d,h**). As shown in **Figure 2.4.2** and **Table S 2.4.2**, LHCSR3 from *C. reinhardtii* contains eight Chl molecules (7-8 Chl *a* and 0-1 Chl *b* molecules) and two Cars (one lutein (Lut) and one Vio or Zea). The Chl *a* molecules have the lowest energy levels and are the

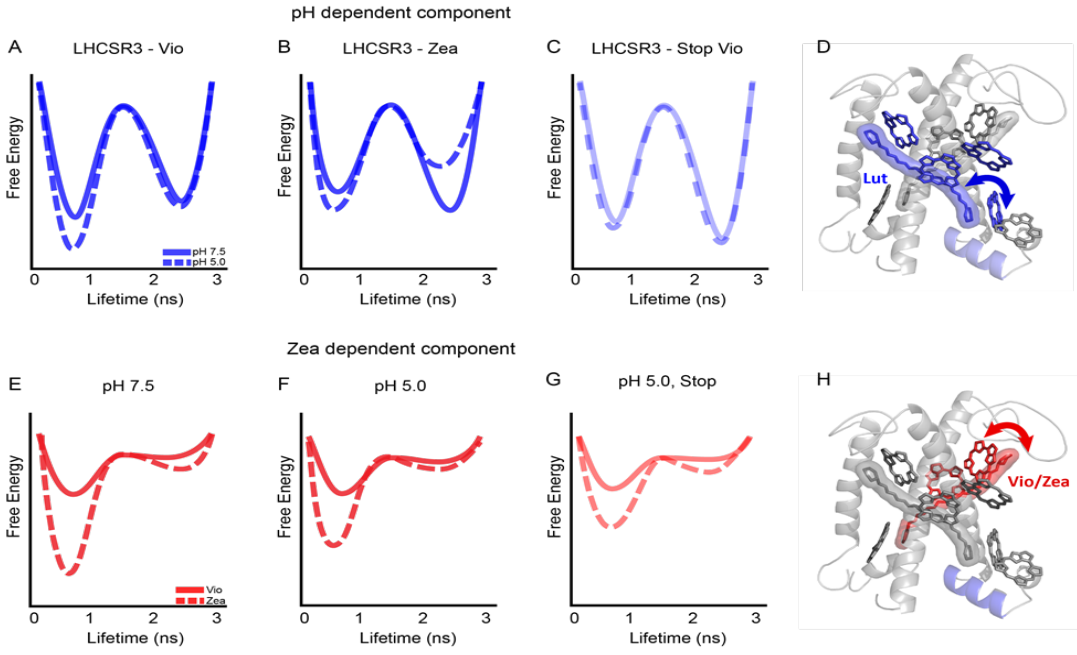

Figure 2.4.2 *Roles of pH and Zea on the dynamics of quenching in LHCSR3. Free energy diagrams (A-C and E-G) and structural model (D and H) for the effects of pH (top) and Zea (bottom) on protein dynamics.*

emissive sites that give rise to each component. Based on sequence comparison with LHCII and CP29, the conserved Chl *a* binding sites are the following; Chls *a* 602, 603, 609, 610, 612 and 613, with Chls *a* 604, 608 and 611 proposed as well [106,218]. Chl *a* 612 is strongly coupled with Chls *a* 610 and 611, while Chl *a* 603 is strongly coupled with Chl *a* 609 and/or Chl *a* 602 [15,64,218,219]. Previous spectroscopic analysis of LHCSR3 from *C. reinhardtii* has identified the likely binding sites of Lut and Vio/Zea within the structural model [106]. The two dynamic components that transition between the active and quenched states likely correspond to Chl-Car pairs, where the Car can quench the emissive Chl. These two components are both biased towards the quenched state in the LHCSR3 complexes. This is consistent with previous work where a quenching component was found to be active in LHCSR3, even at pH 7.5 [291]. Given that there are two Cars bound at the internal sites of LHCSR3, in close contact with different Chl pigments, it is likely that each Car is the major contributor for one of the components. The pH-dependent component is observed in both Vio and Zea samples, and so it is likely that this slower quenched-biased dynamic component (**Figure 2.4.2 top blue**) involves the Lut molecule. Both Chl *a* 612 (coupled to Chls *a* 610 and 611) and Chl *a* 613 have previously been proposed as quenching sites given their physical proximity to the Lut [68,218]. The Chl *a* 610-612 site contains the lowest energy Chl *a*, which are the primary emitters, and this site has been shown to be a major energy sink [292-294]. Additionally, computational results have shown that the interaction between the Lut site and Chl a 612 has large fluctuations [295]. This corresponds to the slower dynamics found for this component. However, recent *in vivo* and *in vitro* analyses found that the removal of Chl *a* 613 results in a reduction in LHCSR specific quenching, while removal of Chl *a* 612 only affected which Chl was the final emitter of the complex [296]. While either of these sites are potential quenching sites, it is likely that Chl *a* 613 plays the major role in pH-dependent quenching in LHCSR3 in *C. reinhardtii*. With a decrease in pH from 7.5 to 5.0, the equilibrium free energy difference for the pH dependent component is shifted toward the quenched state by over 200 cm-1 in Vio and over 500 cm-1 in Zea complexes. The specific conformational change upon protonation that leads to this stabilization remains undetermined. However, proposals in the literature include reduced electrostatic repulsion in the lumen-exposed domain causes a change in the distance and/or orientation between the helices [121] and an increase in protein-protein interactions [291]. These conformational changes could produce a displacement of Lut towards Chl *a* 613. Interestingly, there is little (< 30 cm^{-1}) to no change in the equilibrium free energy difference in the Vio or Zea stop mutant complexes (**Figure 2.4.2c** and **Table S 2.4.3**). In the stop mutants, this dynamic component remains slightly active-biased (**Figure 2.4.2c** and **Table S 2.4.3**). This demonstrates the functional role of the C-terminal tail in the structural changes that occur upon a change in pH and therefore in the quenching mechanism in LHCSR3. With conversion from Vio to Zea, the faster dynamic component, which is the Zea-dependent one, becomes further quenched-biased (**Figure 2.4.2 bottom red**). Given the likely binding site of Vio/Zea, this component is most likely the interaction of Vio/Zea with Chls *a* 602-603 [106,297,298]. MD simulations have shown this Car site to be highly flexible, sampling many configurations [215], which is consistent with the faster dynamics observed here. Upon substitution of Zea for Vio, the equilibrium free energy difference becomes further quenched-biased by over 550 cm^{-1} at pH 7.5 and over 300 cm^{-1} at pH 5.0. This result is consistent with a role of Zea in quenching in LHCSR3 that does not require a decrease in pH and therefore being unrelated to the light dependent NPQ observed *in vivo* in the WT that almost completely recovered in the dark (**Figure 2.4.1a**). In the stop mutant complexes, the equilibrium free energy differences for the Zea-dependent (faster) component is similar to the wild type samples (**Figure 2.4.2g**). This is consistent with the Vio/Zea-Chl *a* 602-603 site as the major contributor for the faster quenched-biased component. Although qualitatively similar, there is a small decrease (<200 cm^{-1}) in the stabilization of the quenched state upon Zea incorporation. This difference suggests that the C-terminal tail has an allosteric effect throughout the protein. The static component, which is assigned to unquenched emitters in the active state and partially photobleached ones in the quenched state, has a large contribution to the correlation profiles (**Table S 2.4.3**). The large amplitude is consistent with the low number of Cars available to interact with the Chls and thus the presence of several unquenched emissive Chl

a. Given the structural arrangement of the Cars and Chls, the static component is likely due to Chls 604, 608 and 609 that sit far from the Cars.

Analysis of *in vivo* quenching

Quenching mechanisms were further investigated *in vivo* by measuring fluorescence emission kinetics on whole cells acclimated to low or high light at 77K. Under these conditions, the photochemical activity is blocked and following the emission at 680 nm it is possible to specifically investigate the fluorescence kinetics of PSII, the main target of NPQ. Cells were either grown in low or high light, which determines the level of LHCSR protein (**Figure S 2.4.3**) and the fluorescence lifetime was recorded before and after exposure to 60 minutes of high light (1500 µE), which induces ΔpH and determines the level of Zea. These light conditions, combined with the genotypes generated, enabled studies that partially or fully separated the contributions of the different components of NPQ. Whole cell fluorescence lifetime traces show that LHCSR is necessary for NPQ in *C. reinhardtii*. WT and *npq1* cells grown in high light show a faster fluorescence decay, or an increase in quenching, after exposure to 60 minutes of high light (**Figure 2.4.3a gray bars**, fluorescence decays and fits to data shown in SI). For *npq4 lhcsr1* samples lacking LHCSR, similar fluorescence decay kinetics were measured regardless of light treatment (**Figure 2.4.3a purple**), comparable to the unquenched kinetics of WT cells. WT and *npq1*, which lacks Zea, cells grown in control light (low LHCSR content) remain unquenched, even after exposure to 60 minutes of high light (**Figure S 2.4.5**). These results are consistent with the NPQ measurements shown in **Figure 2.4.1**. Similar to WT, *npq1* cells grown in high light show a faster fluorescence decay after exposure to 60 minutes of high light (**Figure 2.4.3a**, **blue bars**). While the results from WT show a role for pH and/or Zea in light-induced quenching in LHCSR3, the results from the *npq1* strain shows that quenching can occur without Zea, i.e., induced by the pH drop alone. The *zep* mutant presented a similar decay among all samples regardless of HL or LL acclimation or light treatment that was much faster, or more quenched, compared to the decay of darkadapted WT (**Figure 2.4.3a red**, **Figure S 2.4.5**). These results indicate a constitutive quenching upon increased Zea

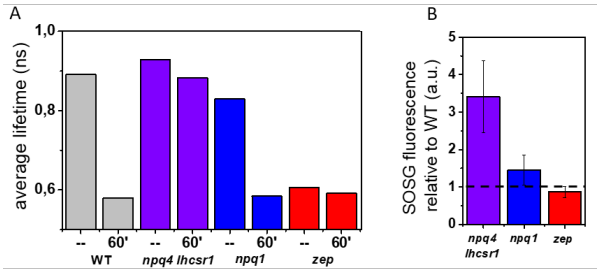

Figure 2.4.3 *Fluorescence lifetime decay of Chlamydomonas reinhardtii whole cells at 77K and singlet oxygen formation. (A) Fluorescence decay kinetics were measured on high light (600 µmol m^{-2} s^{-1}) acclimated samples. Each genotype was measured at a dark-adapted state (--) or after 60 minutes of high light treatment (2000 µmol m^{-2} s^{-1}, 60'). WT samples herein reported are 4A+ strain. Similar results were obtained in the case of CC439 strain. Fluorescence lifetime traces for all genotypes and light conditions are shown in Figure S5. (B) Singlet oxygen production rates for high light acclimated samples relative to WT (4A+ for npq1 and npq4 lhcsr1, cc439 for zep). Dotted line represents WT level at 1. Low light acclimated samples are shown in Figure S8.*

accumulation, consistent with the pH-independent quenching observed in the results in **Figure 2.4.1a,d**. However, the constitutive quenching observed in the *zep* mutant was unchanged in low vs. high light acclimated *zep* cells suggesting that the Zea dependent quenching observed in *zep* mutants is a more general process as opposed to one that occurs solely in LHCSR3.

Role of Zea and NPQ in photoprotection

The main function of quenching the Chl singlet excited states is to alleviate the excitation energy pressure on the photosynthetic apparatus, thereby preventing ROS formation and subsequent photoinhibition of their primary target, Photosystem II. Singlet oxygen is the main ROS species formed at the level of Photosystem II. In order to correlate the NPQ levels and quenching measured with ROS formation, singlet oxygen production was recorded in the different genotypes herein investigated. As expected from the low level of NPQ induction, *npq4 lhcsr1* demonstrated the highest level of singlet oxygen production, regardless of light treatment. Interestingly, the effect of Zea was almost negligible in HL acclimated samples (with a very high NPQ induction). Notably, the amount of singlet oxygen production (**Figure 2.4.3b**) was correlated with average lifetime (**Figure 2.4.3a**), i.e., inversely correlated with quenching, confirming that the quenching of Chl singlet excited states investigated here plays a role in photoprotection.

Discussion

This work leverages *in vivo* and *in vitro* experimental approaches to investigate NPQ mechanisms in *C. reinhardtii* and the molecular parameters responsible for their activation. In higher plants, both lumen acidification and Zea accumulation have been long understood to play a role in the induction of NPQ. While lumen acidification was thought to play a similar role in *C. reinhardtii*, here we demonstrate the impact of Zea accumulation, which had previously been elusive. We further identify the likely molecular mechanisms of both pH and Car composition. Both our *in vivo* and *in vitro* results point to pH and Zea controlling separable quenching processes. Full light-induced quenching upon lumen acidification in the *npq1* strain, which lacks Zea, and the full constitutive quenching in the *zep* strain, which is Zea-enriched, demonstrate two separate quenching mechanisms and induction processes *in vivo*. Likewise, the 2D-FLC analysis on single LHCSR3 complexes quantified two parallel dynamic components, or quenching sites, one of which is pH-dependent and the other Zea-dependent. For pH-dependent quenching, our 2D-FLC results, along with previous mutagenesis [296], point to Lut-Chl613 as the likely quenching site. Analysis of stop mutants that lack the protonable residues in the C terminus definitively shows that the C terminus controls quenching activity by pH-induced stabilization of the quenched conformation of LHCSR3. The 2D-FLC results show that removal of the C-terminal tail removes pH-dependent quenching, while leaving Zeadependent quenching nearly unaffected. Analogously, the WT LL grown strains, which lack LHCSR, also lack the ability for NPQ induction, supporting the critical role of the protonable residues unique to LHCSR in activating quenching. For Zea-dependent quenching, we observe a constitutive quenching process both *in vivo* and *in vitro* that we assign to the Vio/Zea-Chl *a* 602-603 site. Constitutive, as opposed to the typical inductive quenching, represents a distinct timescale and mechanism for the effect of Zea. The Zea-dependent quenching mechanism is described at the molecular level in the case of LHCSR3 but it likely shared with our LHC proteins: indeed, a strong reduction of fluorescence lifetime can be observed in whole cells in the case of *zep* mutant, even in LL acclimated cells where the amount of LHCSR3 is minimal (**Figure S 2.4.5**). This demonstrates that LHCSR subunits are not the sole quenching site where Zea-dependent quenching occurs. It is important to note that in the case of *zep* mutant, not only does Zea completely substitute Vio (de-epoxidation index is 1, **Figure S 2.4.1**), but also the Zea/Chl ratio is much higher compared to the ratio observed in WT or *npq4 lhcsr1*. This suggests an alternative possibility where the strong quenching observed in the *zep* mutant could be related to accumulation of Zea in the thylakoid membrane changing the environment where the photosystems and light-harvesting complexes are embedded, inducing the latter to a strong quenched state. While both possibilities allow for constitutive quenching in the presence of Zea, it is the constitutive quenching itself that is potentially the origin of the conflicting results in the literature. Taken together, the *in vivo* and *in vitro* results demonstrate that separate pH- and Zea-dependent quenching processes exist, and both provide efficient photoprotection. While *in vivo* measurements suggest that pH-dependent quenching is often dominant over Zea-dependent quenching, and correspondingly more efficient in photoprotection, the conformational states and pigment pairs likely responsible function in parallel via similar mechanisms. However, the timescales and induction associated with each quenching process are distinct; responsive pH-dependent quenching works in combination with the guaranteed safety valve of Zea-dependent quenching, potentially to protect against a rapid return to high light conditions.

Material and methods

Strains and culture conditions

C. reinhardtii WT (4A+and CC4349) and mutant strains (*npq1, npq4 lhcsr1* in 4A+ background, *zep* in CC4349 background) were grown at 24°C under continuous illumination with white LED light at 80 µmol photons m^{-2} s^{-1} (low light, LL) in high salts (HS) medium [299] on a rotary shaker in Erlenmeyer flasks. High light (HL) acclimation was induced by growing cells for 2 weeks at 500 µmol photons m^{-2} s^{-1} in HS.

SDS-PAGE Electrophoresis and Immunoblotting

SDS–PAGE analysis was performed using the Tris-Tricine buffer system [232]. Immunoblotting analysis were

performed using αCP43 (AS11 1787), αPSAA (AS06 172) and αLHCSR3 (AS14 2766) antibodies purchased from Agrisera (Sweden).

Violaxanthin de-epoxidation kinetics and pigment analysis

Violaxanthin de-epoxidation kinetics were performed illuminating the different genotypes with red light at 1500 µmol photons m^{-2} s^{-1} up to 60 minutes. Pigments were extracted in 80% acetone and analyzed by HLPC as described in [231].

NPQ measurements

NPQ induction curves were measured on dark adapted intact cells with a DUAL-PAM-100 fluorimeter (Heinz-Walz) at room temperature in a 1x1 cm cuvette mixed by magnetic stirring. Red saturating light of 4000 µmol photons m^{-2} s^{-1} and red actinic light of 1500 µmol photons m^{-2} s^{-1} were respectively used to measure Fm and Fm' at the different time points. NPQ was then calculated as Fm/Fm'-1.

LHCSR3 WT and Stop proteins refolding for *in vitro* analysis

pETmHis containing LHCSR3 CDS previously cloned as reported in [296] served as template to produce Stop mutant using Agilent QuikChange Lightning Site-Directed Mutagenesis Kit. Primer TGGCTCTGCGCTTCTAGAAGGAGGCCATTCT- and primer GAATGGCCTCCTTCTAGAAGCGCAGAGCCA were used to insert a premature stop codon to replace residue E231, generating a protein lacking 13 c-terminal residues. LHCSR3 WT and Stop protein were overexpressed in BL21 *E. coli* and refolded *in vitro* in presence of pigments as previously reported [106]. Fluorescence emission at 300K with excitation at 440 nm, 475 nm and 500 nm was used to evaluate correct folding as previously reported.

Single-molecule fluorescence spectroscopy

12 µM solutions of purified LHCSR3 complexes were stored at -80°C. Immediately prior to experiments, LHCSR3 samples were thawed over ice and diluted to 50 pM using buffer containing 0.05 wt% n-dodecyl-α-D-maltoside and either 20 mM HEPES-KOH (pH 7.5) or 40 mM MES-NaOH (pH 5.0). The following enzymatic oxygen-scavenging systems were also used: (1) 25 nM protocatechuate-3,4-dioxygenase and 2.5 mM protocatechuic acid for pH 7.5 and (2) 50 nM pyranose oxidase, 100 nM catalase and 5 mM glucose for pH 5.0 [300,301]. Diluted solutions were incubated for 15 minutes on Ni-NTA coated coverslips (Ni_01, Microsurfaces) fitted with a Viton spacer to allow LHCSR3 complexes to attach to the surface via their His-tag. The sample was rinsed several times to remove unbound complexes and sealed with another coverslip. Single-molecule fluorescence measurements were performed in a home-built confocal microscope. A fiber laser (FemtoFiber pro, Toptica; 130 fs pulse duration, 80 MHz repetition rate) was tuned to 610 nm and set to an excitation power of 350 nW (2560 nJ/cm^2 at the sample plane, assuming a Gaussian beam). Sample excitation and fluorescence collection were accomplished by the same oil-immersion objective (UPLSAPO100XO, Olympus, NA 1.4). The fluorescence signal was isolated using two bandpass filters (ET690/120x and ET700/75m, Chroma). The signal was detected using an avalanche photodiode (SPCM-AQRH-15, Excelitas) and photon arrival times were recorded using a time-correlated single photon counting module (Picoharp 300, Picoquant). The instrument response function was measured from scattered light to be 380 ps (full width at half maximum). Fluorescence intensity was analyzed as described previously using a change-point-finding algorithm [302].

2D Fluorescence lifetime correlation analysis

2D fluorescence lifetime correlation analysis was performed as detailed previously [290]. Briefly, we performed the following analysis. First, the total number of states exhibiting distinct fluorescence lifetimes was estimated from the 1D lifetime distribution. The lifetime distribution is determined using the maximum entropy method (MEM) to perform a 1D inverse Laplace transform (1D-ILT) of the 1D fluorescence lifetime decay [288]. Next, a 2D fluorescence decay (2D-FD) matrix was constructed by plotting pairs of photons separated by ΔT values ranging from 10^{-4} to 10 seconds. The 2D-FD matrix was transformed from t-space to the 2D fluorescence lifetime correlation (2D-FLC) matrix in Δ-space using a 2D-ILT by MEM fitting [288,303,304]. The 2D-FLC matrix is made up of two functions: the fluorescence lifetime distribution, A, and the correlation function, G. In practice, the initial fluorescence lifetime distribution, A_0, was estimated from the 2D-MEM fitting of the 2D-FD at

the shortest ΔT (10^{-4} s). Then the correlation matrix, G_0, was estimated at all ΔT values with A_0 as a constant. A_0 and G_0, along with the state lifetime values determined from the 1D analysis, were used as initial parameters for the global fitting of the 2D-FDs at all ΔT values. A was treated as a global variable and G was treated as a local variable at each ΔT (now G(ΔT)). The resulting fit provides the correlation function, G(ΔT). The correlation function was normalized with respect to the total photon number in each state. Each set of correlation curves (auto- and cross-correlation for one sample) were globally fit using the following model function:

$$G_{ij}^{s}(\Delta T) = q^2 J^2 I \cdot \sum_{x} \left(\left[\sum_{y \neq x} \{E_y \cdot \Phi_y \cdot R_y(\infty)\} + E_x \cdot \Phi_y \cdot R_x(\Delta T) \right] \cdot [E_x \cdot \Phi_x \cdot C_x] \right)$$

This equation accounts for multiple, independent emitters within one protein (multiple components). Here, x and y indicate the component number, i and j indicate the state (auto correlation for i=j, cross correlation for i≠j), q accounts for experimental factors such as the detection efficiency, filter transmittance, gain of the detector, etc., J is the laser power, and I is the total photon number proportional to the total measurement time. E, Φ, and C are diagonal matrices composed of the optical extinction coefficient, fluorescence quantum yield, and state population, respectively. R is a matrix element that is related to the rate matrix. The rate constants determined from the 2D-FLC analysis were used to calculate the free energies for each protein state. The rate constants for transitions between the quenched and active states are related to the free energies associated with both states through the Arrhenius equation:

$$k_{A \to Q} = A \exp\left(-\frac{E^*_{A \to Q}}{k_B T}\right) \quad [1]$$

$$k_{A \to Q} = A \exp\left(-\frac{E^*_{A \to Q}}{k_B T}\right) \quad [2]$$

Here, $k_{(Q \to A)}$ and $E^*_{(Q \to A)}$ ($k_{(A \to Q)}$ and $E^*_{(A \to Q)}$) are the rate constant and activation energy, respectively, for the transition from the quenched (Q) to the active (A) state. A is a constant, k_B is the Boltzmann constant, and T is the temperature. Upon equilibration of the Q and A states, the free-energy difference, ΔE^*, is given by the following equation:

$$k_{A \to Q} = A \exp\left(-\frac{E^*_{A \to Q}}{k_B T}\right) \quad [3]$$

Using the dynamic rates determined from the fits to the correlation function, we calculated ΔE^* at T = 300 K. The free-energy differences between the quenched and active states are shown as the energetic differences between the minima in the energy landscapes. The potential barriers were scaled by assuming the constant A in Equations [1] and [2] to be 1000, which was shown previously to be a reasonable estimate for LHCSR1 [290].

77K fluorescence

Low temperature quenching measures were performed according to [296]. Cells were frozen in liquid nitrogen after being dark adapted or after 60 minutes of illumination at 1500 µmol photons m^{-2} s^{-1} of red light. Fluorescence decay kinetics were then recorded by using Chronos BH ISS Photon Counting instrument with picosecond laser excitation at 447 nm operating at 50 MHz. Fluorescence emissions were recorded at 680 nm with 4 nm bandwidth. Laser power was kept below 0.1µW.

Supporting information

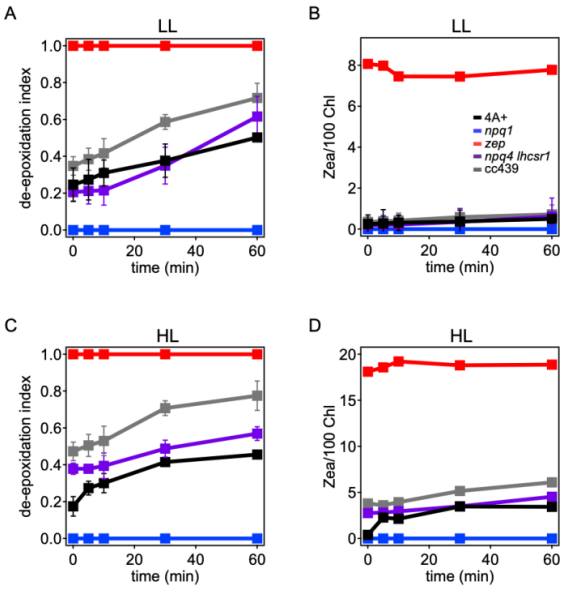

Figure S 2.4.1 *Violaxanthin de-epoxidation kinetics in Chlamydomonas reinhardtii WT and mutant strains. Violaxanthin de-epoxidation kinetics were measured upon 60 minutes of strong light treatment (red light 1500 µmol $m^{-2}s^{-1}$) of low light (LL) or high light (HL) acclimated cells. Panel A, C: de-epoxidation indexes at different time points. Panel B, D: zeaxanthin content per 100 chlorophylls.*

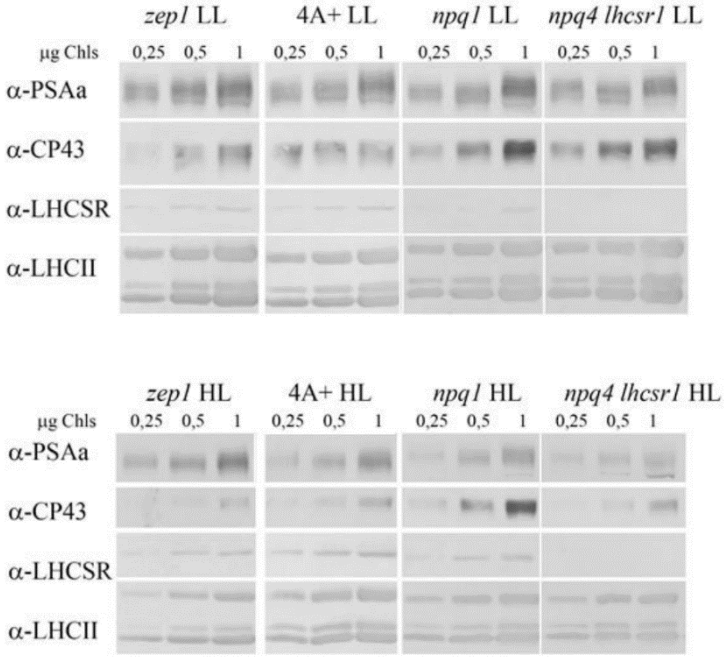

Figure S 2.4.2 *Immunoblot analysis of LHCSR3 accumulation in vivo. Total protein extracts from low Light (LL) or high light (HL) acclimated cells were loaded on a chlorophyll basis (µg of chlorophylls loaded are reported in the figure). Immunoblot analysis was performed using specific antibodies recognizing PsaA, CP43, LHCSR3 and al the LHCII subunits.*

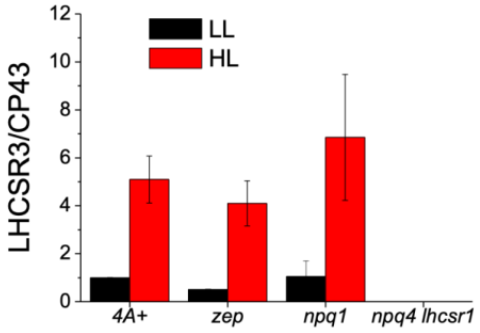

Figure S 2.4.3 *Quantification of LHCSR3 accumulation per PSII. Immunoblotting results were analyzed by densitometry. LHCSR3 content was then normalized to the amount of CP43 as a reference for PSII. The results obtained were then normalized to the 4A+ LL case.*

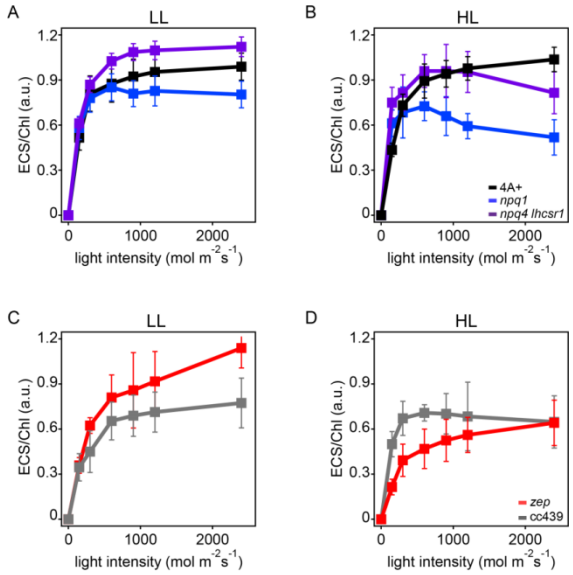

Figure S 2.4.4 *Electrochromic shift measurements at different light intensities in low light and high light acclimated Chlamydomonas reinhardtii cells. Electrochromic shift (ECS) measurements were performed in WT (4A+ and cc439) and mutant strains (npq4 lhcsr1, npq1 and zep) acclimated to low (Panel A and B) or high (Panel C, D) light. Genotypes having the same background are shown in the same Panel.*

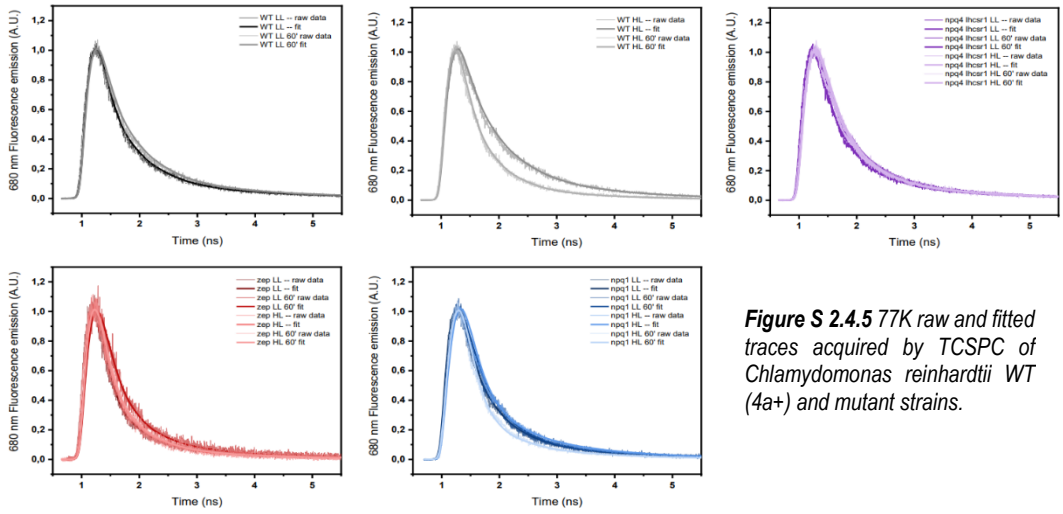

Figure S 2.4.5 *77K raw and fitted traces acquired by TCSPC of Chlamydomonas reinhardtii WT (4a+) and mutant strains.*

	τ1 (ns)	f1	τ2 (ns)	f2	τ3 (ns)	f3	Avg Time (ns)
WT LL --	0.04 ± 0.00	0.267 ± 0.003	0.451 ± 0.008	0.397 ± 0.005	1.77 ± 0.03	0.336 ± 0.00	0.786
WT LL 60'	0.04 ± 0.00	0.211 ± 0.002	0.471 ± 0.006	0.428 ± 0.004	1.78 ± 0.02	0.361 ± 0.00	0.851
WT HL --	0.04 ± 0.00	0.161 ± 0.003	0.479 ± 0.008	0.413 ± 0.006	1.61 ± 0.02	0.426 ± 0.00	0.891
WT HL 60'	0.04 ± 0.00	0.288 ± 0.004	0.373 ± 0.006	0.459 ± 0.005	1.57 ± 0.03	0.253 ± 0.00	0.58
zep LL --	0.04 ± 0.00	0.405 ± 0.005	0.403 ± 0.01	0.324 ± 0.006	1.93 ± 0.05	0.271 ± 0.00	0.67
zep LL 60'	0.039 ± 0.008	0.209 ± 0.009	0.334 ± 0.009	0.448 ± 0.008	1.58 ± 0.00	0.343 ± 0.008	0.7
zep HL --	0.04 ± 0.00	0.361 ± 0.006	0.381 ± 0.01	0.391 ± 0.007	1.79 ± 0.06	0.247 ± 0.00	0.606
zep HL 60'	0.04 ± 0.00	0.337 ± 0.006	0.364 ± 0.01	0.389 ± 0.007	1.59 ± 0.04	0.274 ± 0.00	0.592
npq 4 lhcsr1 LL --	0.04 ± 0.00	0.25 ± 0.002	0.456 ± 0.005	0.419 ± 0.003	2.16 ± 0.03	0.331 ± 0.00	0.917
npq 4 lhcsr1 LL 60'	0.04 ± 0.00	0.186 ± 0.002	0.465 ± 0.004	0.461 ± 0.003	2.06 ± 0.02	0.353 ± 0.00	0.95
npq 4 lhcsr1 HL --	0.04 ± 0.00	0.183 ± 0.002	0.42 ± 0.004	0.457 ± 0.003	2.02 ± 0.02	0.361 ± 0.00	0.929
npq 4 lhcsr1 HL 60'	0.04 ± 0.00	0.151 ± 0.004	0.401 ± 0.006	0.492 ± 0.004	1.9 ± 0.03	0.357 ± 0.00	0.883
npq1 LL -- 1	0.04 ± 0.00	0.224 ± 0.002	0.43 ± 0.004	0.459 ± 0.003	2.12 ± 0.02	0.317 ± 0.00	0.879
npq1 LL 60'	0.04 ± 0.00	0.152 ± 0.003	0.4 ± 0.007	0.519 ± 0.005	1.89 ± 0.04	0.33 ± 0.00	0.838
npq1 HL --	0.04 ± 0.00	0.0304 ± 0.002	0.254 ± 0.002	0.474 ± 0.002	1.43 ± 0.006	0.496 ± 0.00	0.829
npq1 HL 60'	0.04 ± 0.00	0.0792 ± 0.004	0.21 ± 0.002	0.573 ± 0.003	1.32 ± 0.01	0.348 ± 0.00	0.584

Table S 2.4.1 *77K time resolved fluorescence analysis and average fluorescence decay lifetimes of whole cells. Kinetics were fitted with a three-exponential decay function using Vinci 2 software from ISS. Fractions (fi) and time constants (τi) are reported. Average fluorescence lifetimes were calculated as Σfiτi.*

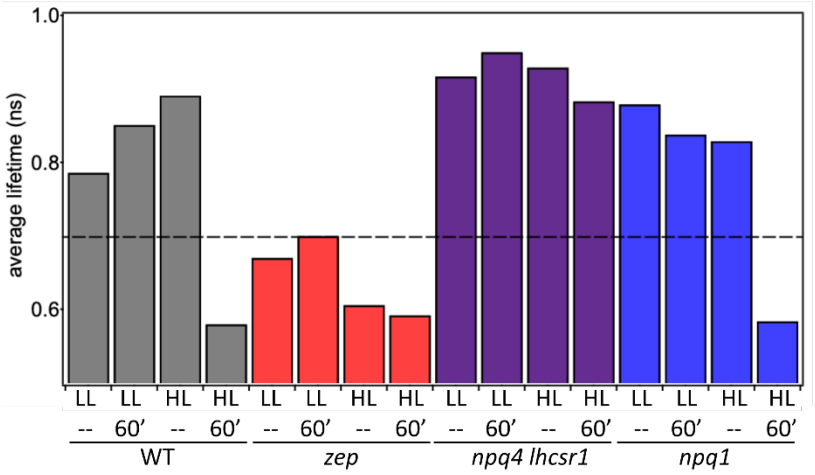

Figure S 2.4.6 Average fluorescence lifetime for WT (4A+) and mutant strains under all light conditions. Above dotted line is considered unquenched and below dotted line is considered quenched.

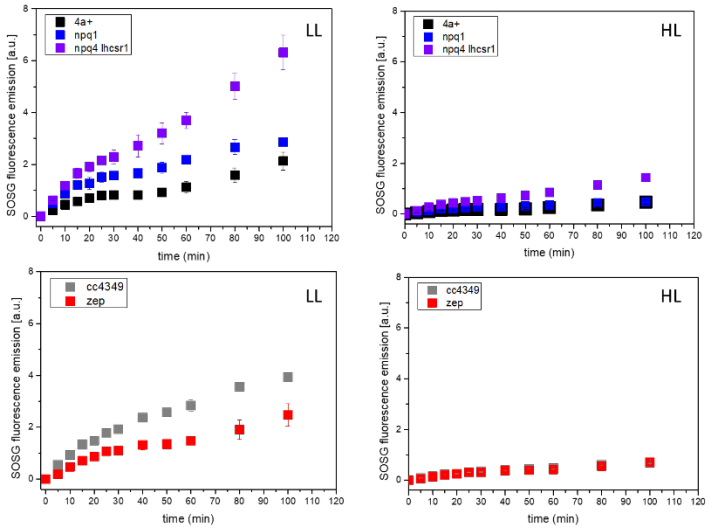

Figure S 2.4.7 Kinetics of singlet oxygen production in WT and mutant strains**.** Singlet oxygen production rate was measured by the singlet oxygen sensor green (SOSG) fluorescence probe. Low light (LL) or high light (HL acclimated samples were exposed to strong red light (2000 µmol $m^{-2}s^{-1}$) and singlet oxygen production rate was probed at the different time points by following SOSG fluorescence at 530 nm. Genotypes having the same background are shown in the same Panel.

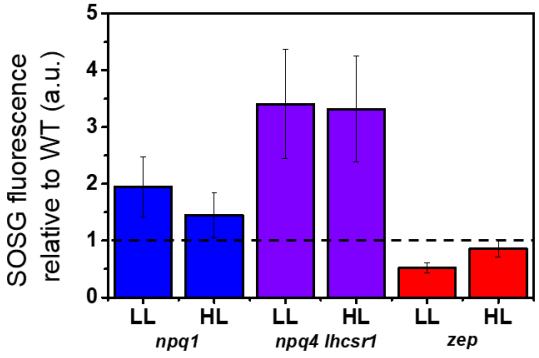

Figure S 2.4.8 *Singlet oxygen production in WT and mutant strains. Singlet oxygen production rate was measured by the singlet oxygen sensor green (SOSG) fluorescence probe. Low light (LL), left, or high light (HL) acclimated samples were exposed to strong red light (2000 µmol $m^{-2}s^{-1}$), right. Singlet oxygen production rates relative to WT (4A+ for npq1 and npq4 lhcsr1, cc439 for zep).*

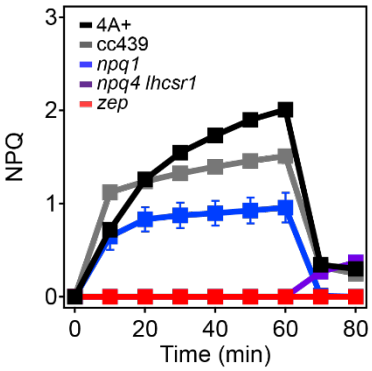

***Figure S 2.4.9* NPQ induction in low light acclimated Chlamydomonas reinhardtii cells.** NPQ induction kinetics measured upon 60 minutes of high light (2000 µmol $m^{-2}s^{-1}$) followed by 20 minutes of dark recovery.

```
                                                ▼
C. reinhardtii LHCSR3  KELNNGRLAMIAIAAFVAQELVEQTEIFEHLALRFEKEAILELDDIERDLGLPVTPLPDNLKSL   259
C. reinhardtii LHCSR1  KELNNGRLAMIAIAAFVAQELVEQTEIFEHLVLRFEKEVILELEDVERDLGLPLTPLPDNLKAI   253
Chlamydomonas sp ICE   KELNNGRLAMIAIAGFTVQELVDGQEIFEHLFVGAADEVVKELDDIERDLGISETPVPFPGF--   257
C. variabilis          KELNNGRLAMIGVAGFVLQELAVKRGIFEHLALYLEREAILEIEDLDPALNIALPTIP------   169
V. carteri             KELNNGRLAMIAIAAFVAQELVEQTEIFEHLFLRFEKEAILELDDIERDVGLPVTPLPSNLANL   254
B. natans              KELNNGRLAMLALAGFVAQELVNGKPILG-------------------------------------   185
B. prasinos            KELSHGRLAMVATAFFVAKELVTGNKIFPQFDLYPYQ-----------------------------   251
C. cryptica            KELQNGRLAMLAAAGFLAQEAVDGKGILEHFSS---------------------------------   199
P. Tricornutum         KELQNGRLAMLAAAGFMAQELVDGKGILEHLL----------------------------------   210
D. baltica             KELQNGRLAMLAAAGFLAQELVDGKGILEHLQA---------------------------------   209
U. linza               KELNNGRLAMIAVAGFVAQELVNKQGIIENLKASS-------------------------------   231
U. prolifera           KELNNGRLAMIAVAGFVAQELVNKQGIIENLKASS-------------------------------   230
P. Patens              KELNNGRLAMIAIAAFVAQELVSGEEIFVHLFKRLGL-----------------------------   244
A. ubliquus            KELNNGRLAMIAIAAFTVEELVSHQEIFEHPGAAL-------------------------------   227
                       ***.:*****:. * *  :* .    *:
```

Figure S 2.4.10 *Alignment of LHCSR-like proteins: protonatable residues are red written while insertion site for TAA mutation to generate STOP mutant is indicated by black arrow. Protein number for LHCSR-like proteins used for alignment are listed below: XP_001696064.1 Chlamydomonas reinhardtii LHCSR3, XP_001696125.1 Chlamydomonas reinhardtii LHCSR1, XP_002948670.1 Volvox carteri f. nagariensis, ADP89594.1 Chlamydomonas sp. ICE-L LHCSR2, XP_001768071.1 Physcomitrella patens LHCSR2, ABD58893.1 Acutodesmus obliquus, ADY38581.1 Ulva linza, ADU04518.1 Ulva prolifera, XP_005848576.1 Chlorella variabilis, XP_002178699.1 Phaeodactylum tricornutum, AHH80644.1 Durinskia baltica, AA05890.1 Bigelowiella natans, CCO66741.1 Bathycoccus prasinos.*

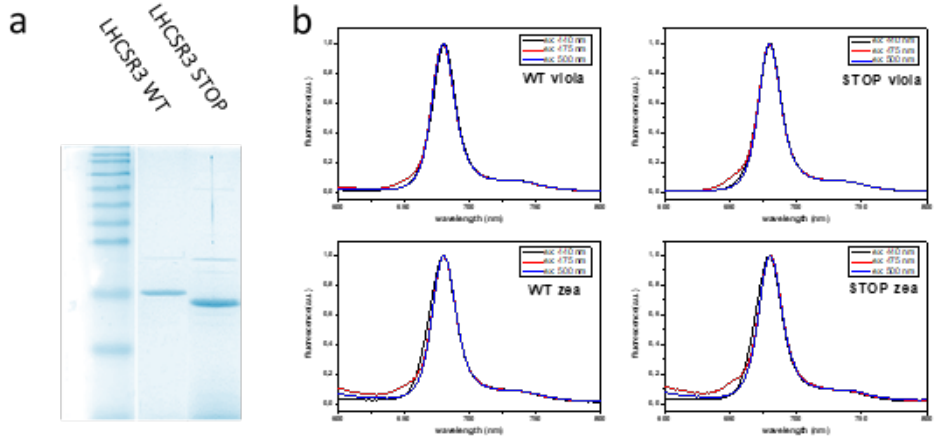

Figure S 2.4.11 ***Protein migration on gel and room temperature fluorescence of WT and STOP*** *(a) Coomassie brilliant blue stained SDS-page of LHCSR3 apo-protein separated on Tris-Glycine 12%. LHCSR3 STOP protein shows high mobility conferred by its shorter C-terminal with respect to LHCSR3 WT; (b) Fluorescence spectra of LHCSR3 complexes measured at room temperature at different excitation wavelengths (reported in each panel).*

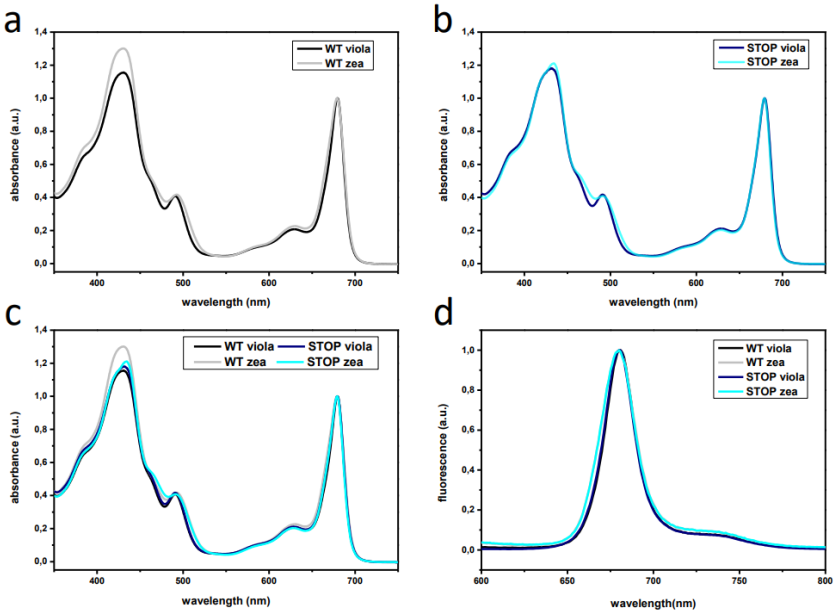

***Figure S 2.4.12* Absorption and fluorescence emission spectra of LHCSR3 WT and STOP**. (a-c) Absorption spectra of WT (a) or STOP (b) refolded with violaxanthin or zeaxanthin. (d) Fluorescence emission spectra of LHCSR3 WT and STOP mutant upon excitation at 440 nm with both violaxanthin and zeaxanthin pigments composition

	Total Chlorophylls	Chlorophyll a	Chlorophyll b	Chla/Chlb	Neoxanthin	Violaxanthin	Anteraxanthin	Lutein	Zeaxanthin	Total Carotenoids	Chl/Car
WT VIOLA	7	6,59 ± 0,00	0,41 ± 0,00	16,16 ± 0,16	0,00 ± 0,00	0,98 ± 0,00	0,09 ± 0,03	1,02 ± 0,02	0,08 ± 0,01	2,17 ± 0,02	3,22 ± 0,02
STOP VIOLA	7	6,38 ± 0,01	0,62 ± 0,01	10,33 ± 0,12	0,00 ± 0,00	0,99 ± 0,07	0,07 ± 0,02	0,95 ± 0,08	0,03 ± 0,04	2,04 ± 0,05	3,43 ± 0,08
WT ZEA	7	6,82 ± 0,01	0,18 ± 0,01	37,58 ± 2,82	0,00 ± 0,00	0,27 ± 0,00	0,00 ± 0,00	0,31 ± 0,04	1,41 ± 0,02	1,99 ± 0,03	3,51 ± 0,05
STOP ZEA	7	6,81 ± 0,00	0,19 ± 0,00	36,56 ± 0,35	0,00 ± 0,00	0,22 ± 0,00	0,00 ± 0,00	0,44 ± 0,47	1,09 ± 0,02	1,75 ± 0,00	3,99 ± 0,00

Table S 2.4.2 *Pigment binding properties of recombinant LHCSR3 WT and STOP refolded in vitro. Binding pigments are reported referred to 7 Chlorophyll.*

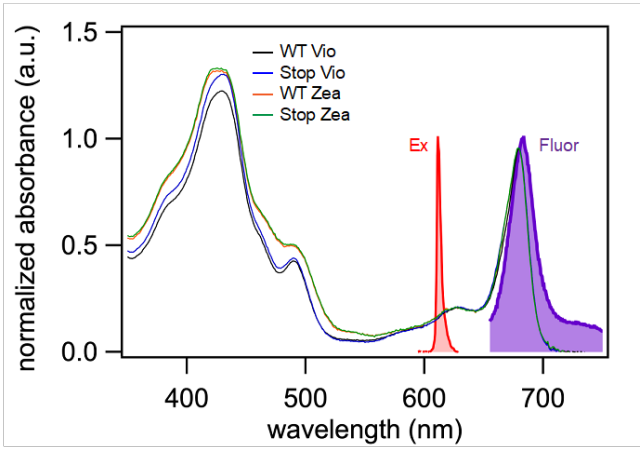

Figure S 2.4.13 *Room temperature absorption spectra of LHCSR3 with Vio (black) and Zea (orange) and stop mutant LHCSR3 with Vio (blue) and Zea (green) at pH 7.5. The intensity was normalized to the Qy peak at around 680 nm. Spectra of the excitation light (red) and the fluorescence of LHCSR3 with Vio at pH 7.5 (purple) are also shown.*

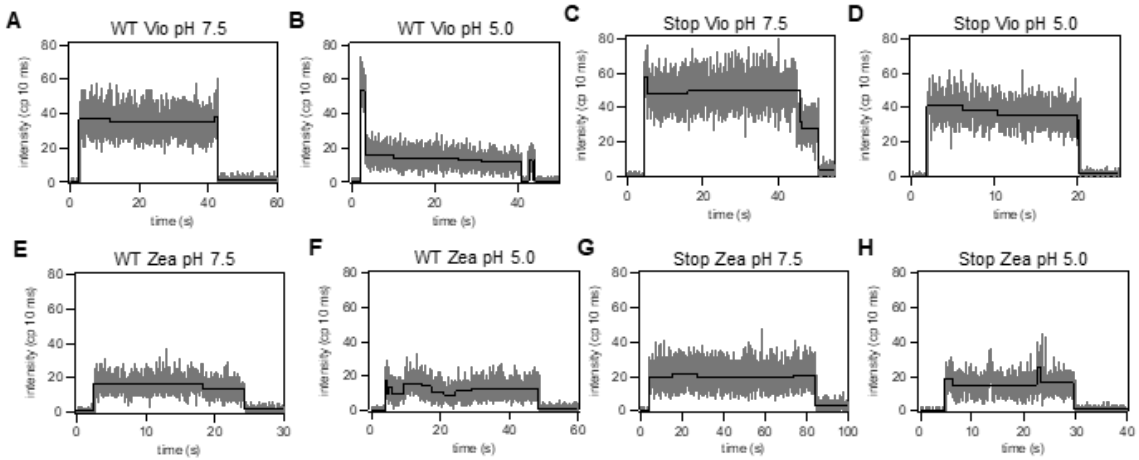

Figure S 2.4.14 *Representative fluorescence intensity traces. Fluorescence intensity traces for LHCSR3 complexes at pH 7.5 and 5.0. The intensity levels determined by the change-point-finding algorithm are shown in black.*

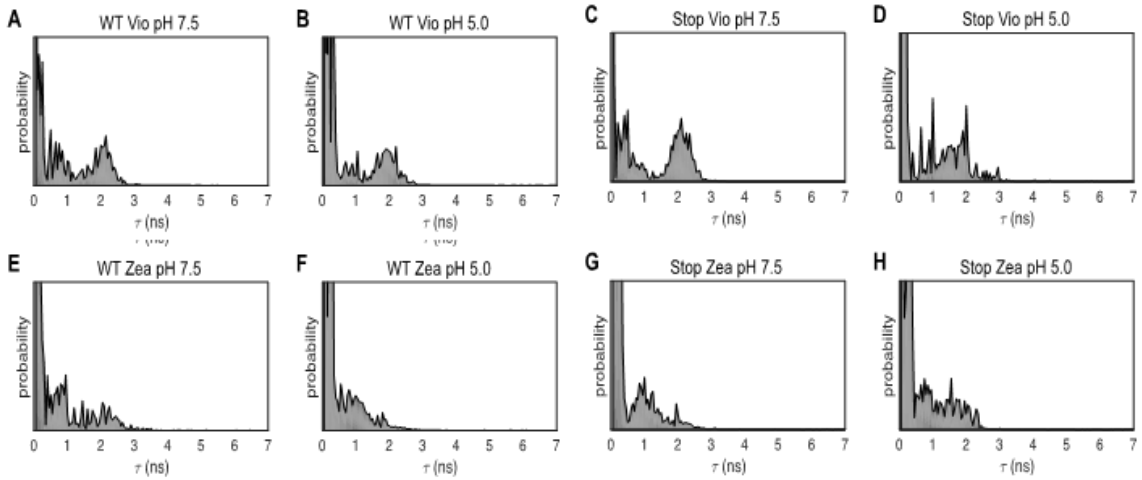

Figure S 2.4.15 *Lifetime distributions. Lifetime distributions for LHCSR3 determined using a one-dimensional inverse Laplace transform (1D-ILT) of the 1D fluorescence lifetime decay. Lifetime states identified from the 1D distribution were used as initial parameters in the fit to the 2D distributions.*

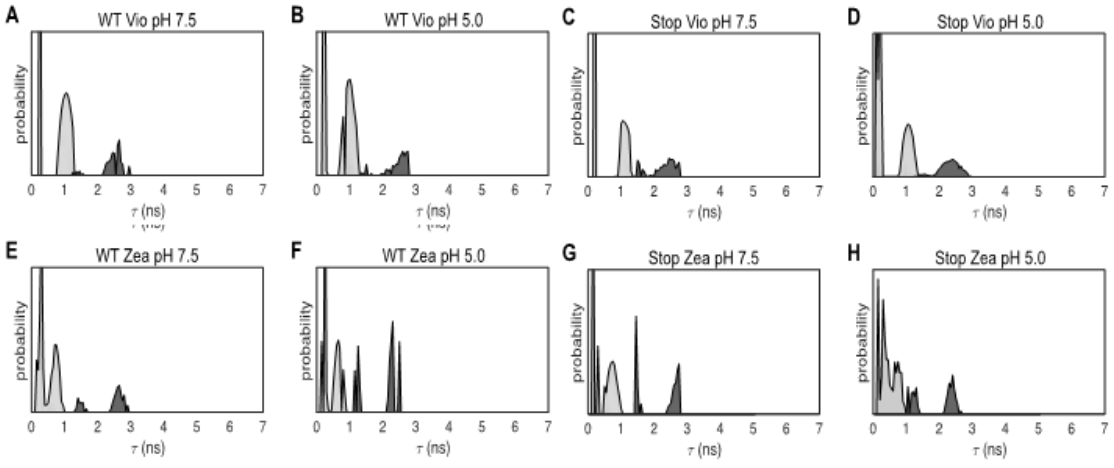

Figure S 2.4.16 *2D Lifetime distributions. Lifetime distributions for LHCSR3 complexes at pH 7.5 and 5.0 determined using the maximum entropy method (MEM) to perform a 2D-ILT.*

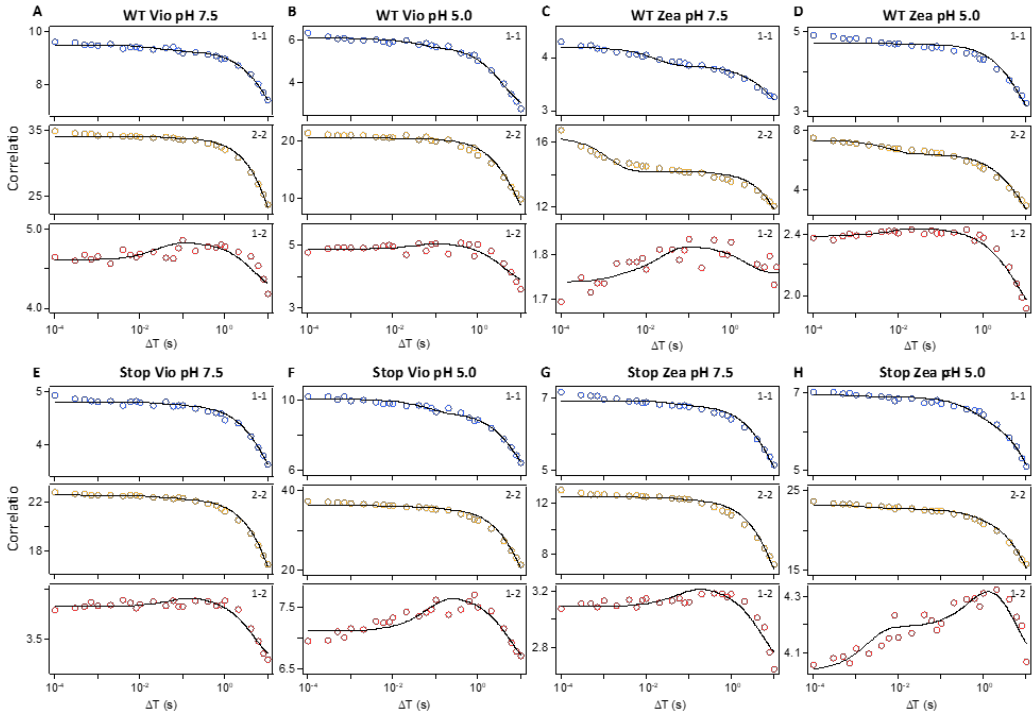

Figure S 2.4.17 *Correlation analysis of LHCSR3 complexes. Correlation function estimated from the 2D-FLC analysis of single LHCSR3 complexes with Vio at pH 7.5 (A) and pH 5.0 (B), Zea at pH 7.5 (C) and 5.0 (D), stop mutants with Vio at pH 7.5 (E) and pH 5.0 (F) and stop mutants with Zea at pH 7.5 (G) and pH 5.0 (H). The correlation curves for auto (1-1 and 2-2) and cross correlations (1-2) are shown in blue, yellow and red, respectively. The black line shows the fitting curve calculated using the model function given Methods.*

WT Vio

pH 7.5

Component	1		2		3	
Fluorescence						
Lifetime state	1	2	1	2	1	2
Lifetime	0.71	2.45	0.71	2.45	0.71	2.45
Intensity	0.10	0.10	0.080	0.32	0.18	0.13
Transition rates						
Lifetime state Final \ Initial	1	2	1	2	1	2
1	0.25	23	0.14	850	0.045	0.0017
2	15	0.25	230	0.23	< 0.001	0.039
Population	0.61	0.39	0.79	0.21	0.94	0.060
Free energy difference	90.0		278		587	

pH 5.0

Component	1		2		3	
Fluorescence						
Lifetime state	1	2	1	2	1	2
Lifetime	0.68	2.43	0.68	2.43	0.68	2.43
Intensity	0.083	0.049	0.074	0.21	0.0013	0.046
Transition rates						
Lifetime state Final \ Initial	1	2	1	2	1	2
1	0.27	23	0.22	780	0.49	0.0022
2	5.1	0.32	250	0.28	< 0.001	0.10
Population	0.83	0.17	0.72	0.28	0.95	0.050
Free energy difference	314		238		585	

WT Zea

pH 7.5

Component	1		2		3	
Fluorescence						
Lifetime state	1	2	1	2	1	2
Lifetime	0.47	2.35	0.47	2.35	0.47	2.35
Intensity	0.11	0.022	0.0076	1.0	0.091	0.23
Transition rates						
Lifetime state Final \ Initial	1	2	1	2	1	2
1	0.56	18	0.038	730	0.021	< 0.001
2	41	0.56	12	0.038	< 0.001	0.021
Population	0.31	0.69	0.98	0.020	0.42	0.58
Free energy difference	-166		857		-66	

pH 5.0

Component	1		2		3	
Fluorescence						
Lifetime state	1	2	1	2	1	2
Lifetime	0.44	1.97	0.44	1.97	0.44	1.97
Intensity	0.0073	0.13	0.060	0.41	0.046	0.020
Transition rates						
Lifetime state Final \ Initial	1	2	1	2	1	2
1	1.2	130	0.14	860	0.11	0.0031
2	25	0.33	53	0.23	< 0.001	0.11
Population	0.97	0.030	0.84	0.16	0.94	0.060
Free energy difference	342		581		712	

Stop Vio

pH 7.5

Component	1		2		3	
Fluorescence						
Lifetime state	1	2	1	2	1	2
Lifetime	0.49	2.27	0.49	2.27	0.49	2.27
Intensity	0.052	0.11	0.098	0.47	0.14	0.085
Transition rates						
Lifetime state Final \ Initial	1	2	1	2	1	2
1	0.28	6.0	0.17	1500	0.047	0.0014
2	13	0.26	320	0.25	< 0.001	0.027
Population	0.32	0.68	0.82	0.18	0.96	0.040
Free energy difference	-156		315		695	

pH 5.0

Component	1		2		3	
Fluorescence						
Lifetime state	1	2	1	2	1	2
Lifetime	0.53	2.20	0.53	2.45	0.53	2.20
Intensity	0.12	0.096	0.048	0.33	0.12	0.071
Transition rates						
Lifetime state Final \ Initial	1	2	1	2	1	2
1	0.23	5.2	0.12	870	0.10	0.0010
2	9.7	0.20	280	0.16	< 0.001	0.069
Population	0.35	0.65	0.75	0.25	0.95	0.050
Free energy difference	-129		233		649	

Stop Zea

pH 7.5

Component	1		2		3	
Fluorescence						
Lifetime state	1	2	1	2	1	2
Lifetime	0.46	2.17	0.46	2.17	0.46	2.17
Intensity	0.051	0.066	0.078	0.28	0.11	0.037
Transition rates						
Lifetime state Final \ Initial	1	2	1	2	1	2
1	0.29	6.7	0.15	1900	0.068	0.0017
2	9.9	0.29	270	0.15	< 0.001	0.066
Population	0.40	0.60	0.87	0.13	0.97	0.030
Free energy difference	-82		400		768	

pH 5.0

Component	1		2		3	
Fluorescence						
Lifetime state	1	2	1	2	1	2
Lifetime	0.46	1.90	0.46	1.90	0.46	1.90
Intensity	0.060	0.11	0.043	0.14	0.11	0.083
Transition rates						
Lifetime state Final \ Initial	1	2	1	2	1	2
1	< 0.001	0.56	1.7	470	0.050	0.0011
2	0.97	0.25	67	1.2	< 0.001	0.041
Population	0.37	0.63	0.88	0.12	0.90	0.010
Free energy difference	-114		406		466	

Table S 2.4.3 *Summary of dynamic properties estimated by the correlation fitting analysis. The fluorescence intensity and population of the initial and final state and the transition rates between these states for each component (blue, red, gray) were determined by global fitting of the correlation functions shown in Figure S12. The free-energy differences were given by Eq.[3] as described in the Methods. The fluorescence intensity is a relative intensity that is normalized by the total measurement time for each sample and by a scaling factor to set the maximum intensity to be 1.*

2.5

Identification of a plant-like Violaxanthin De-Epoxidase enzyme in the green alga Chlorella vulgaris reveals evolutionary divergency of photoprotective mechanisms in the green lineage

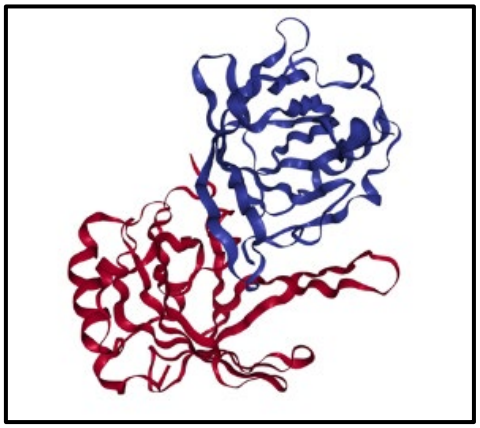

This section is based on New Phytologist: submitted article: Girolomoni L. et al. Identification of a plant-like Violaxanthin De-Epoxidase enzyme in the green alga Chlorella vulgaris reveals evolutionary divergency of photoprotective mechanisms in the green lineage

Author Contributions: Ballottari M. conceived the study, designed and supervised the experiments. Girolomoni L., Bellamoli F. and Cazzaniga S. performed or contributed to all the experiments herein reported. Cerullo G. and D'Andrea C. designed, coordinated and supervised the fluorescence lifetime measurements. Perozeni F.;D'Andrea C. and De la Cruz Valbuena G. performed fluorescence lifetime measurements. Ballottari M. wrote the manuscript with the contribution of Girolomoni L., Bellamoli F., Cazzaniga S., D'Andrea C. and Cerullo G.. All the authors discussed the results, contributed to data interpretation and commented on the manuscript.

Identification of a plant-like Violaxanthin De-Epoxidase enzyme in the green alga Chlorella vulgaris reveals evolutionary divergency of photoprotective mechanisms in the green lineage

Laura Girolomoni[1], Francesco Bellamoli[1], Gabriel de la Cruz Valbuena[2], Federico Perozeni[1], Cosimo D'Andrea[2,3], Giulio Cerullo[2], Stefano Cazzaniga[1], Matteo Ballottari[1*]

[1]Department of Biotechnology, University of Verona, Strada le Grazie 15, 37134 Verona, Italy
[2]IFN-CNR, Department of Physics, Politecnico di Milano, P.za L. da Vinci 32, 20133, Milano
[3]Center for NanoScience and Technology @PoliMi, Istituto Italiano di Tecnologia, via Pascoli 70/3, 20133, Milano, Italy.

Abstract

The xanthophyll cycle is the metabolic process by which the carotenoid violaxanthin is de-epoxidated to zeaxanthin, a xanthophyll with a crucial photoprotective role in higher plants and mosses. In green algae the role of zeaxanthin is still unclear and a peculiar violaxanthin de-epoxidating enzyme was found in the model organism *Chlamydomonas reinhardtii*. In this work we investigated the molecular details and functions of the xanthophyll cycle in the case of *Chlorella vulgaris*, one of the most considered green algae for industrial cultivation, where resistance to high light stress is a pre-requisite for sustainable biomass production. Identification of violaxanthin de-epoxidase enzyme in *Chlorella vulgaris* was performed by genome mining and *in vitro* analysis of the catalytic activity of the identified gene product. The photoprotective role of zeaxanthin was then investigated *in vivo* and in isolated pigment binding complexes. The results obtained demonstrate the functioning, even though with a different pH sensitivity, of a plant-like violaxanthin de-epoxidase enzyme in *Chlorella vulgaris*. Differently from *Chlamydomonas reinhardtii*, zeaxanthin accumulation in *Chlorella vulgaris* resulted to be crucial for photoprotective quenching of excitation energy harvested by both Photosystem I and II. These findings demonstrate an evolutionary divergence of photoprotective mechanisms among *Chlorophyta*.

Introduction

Photosynthetic organisms use light energy to produce chemical energy to fix CO_2 into organic biomass. Light energy, absorbed by Photosystems I and II, is used to fuel the photochemical reactions by which electrons are transported from electron donors, as water, to $NADP^+$. Light driven electron transport is coupled with a proton transport from stroma to lumen forming a transmembrane electrochemical gradient exploited by chloroplastic ATPase produce ATP. NADPH and ATP are then used to fix CO_2 into sugars by the Calvin-Benson cycle. The irradiance to which the photosynthetic machinery is exposed may undergo daily or seasonal changes: light may thus be limiting or in excess. In the latter case, the products of photosynthetic light phase, ATP and NADPH, are not fully consumed by the Calvin-Benson Cycle: the impaired regeneration of $NADP^+$ and ADP by carbon fixation reactions causes a saturation of the photosynthetic electron transport increasing the probability of excitation energy transfer from chlorophyll triplets to singlet oxygen forming the highly toxic reactive oxygen species (ROS) [104]. Several acclimation responses have been observed at different time scales in photosynthetic organisms exposed to different light regimes. Long term acclimation responses involve changes at the level of pigments and pigment binding complexes accumulation, which are only partially conserved among the different species [104]. The main short term photoprotection mechanism activated in oxygenic photosynthetic organisms is Non-Photochemical Quenching (NPQ) by which chlorophylls singlet excited states are dissipated into heat [202]. NPQ is composed by three different components, distinguishable by their kinetics. The fastest component activated upon

illumination is the pH- or energy-dependent component, called qE [92]. The mid-range component is qT, related to state transitions, a mechanism by which some antenna proteins of Photosystem II (PSII), upon phosphorylation, move to Photosystem I 74 (PSI) in order to balance the excitation pressure among the two Photosystems [305], while the longest component, is related to the photoinhibition of photosynthesis by PSII degradation, being called qI [90] and/or to a zeaxanthin dependent slow relaxing component called qZ [94]. Other mid-term adaptive responses involve chloroplasts movement to properly balance light absorption [306] and sun-tracking with specific movements of leaves [307]. The role of zeaxanthin in NPQ has been long debated, with different reports supporting its direct [246,66,115,217] or indirect [308] contribution to quenching. Moreover, a possible role of zeaxanthin in Photosystem I (PSI) quenching has been reported in *Arabidopsis thaliana* [228] even if this quenching mechanism has been negatively argued by Tian and coworkers [309]. In higher plants the xanthophyll cycle is triggered by luminal acidification and is mediated by the Violaxanthin De-Epoxidase (VDE) enzyme which is responsible of violaxanthin conversion into zeaxanthin in two de-epoxidation steps forming antheraxanthin as intermediate. Zeaxanthin is involved in singlet and triplet chlorophyll excited states quenching and in ROS scavenging [94,135,228,310,311]. VDE is a nuclear encoded protein activated by lumenal acidification, as a consequence of light phase saturation [312], and for its activity requires ascorbate to reduce the epoxy group with the consequent water production [242]. Previous studies revealed that the VDE activity is inhibited by dithiothreitol (DTT) which reduces one or more di-sulphide bonds formed by cysteine residues [28]. The protein sequence of the *A. thaliana* VDE contains three main domains: a cysteine rich region containing 13 residues, among which 12 conserved in different plant species, a catalytic site and a glutamate rich region [313]. Site directed mutagenesis experiments showed that in the catalytic domain the residues essential for the VDE activity are the Asp177 and the Tyr198 while the amino acids important for the structural organization are the Asp114, Arg138, His121 and the Tyr214 [314]. Moreover, four histidine residues (His121, His 124, His 169 and His 173 in the VDE sequence from spinach) have been reported to influence VDE catalytic activity [315] and its pH dependent binding to the thylakoid membranes [316]. The pH dependent activity of VDE was also proved by substituting the protonatable residues with aliphatic amino acids [317]. In microalgae, the role of xanthophyll cycle seems to be not homogeneous: in the model green *alga Chlamydomonas reinhardtii* zeaxanthin accumulation has been reported to be important for ROS scavenging but its role in NPQ induction is minor, if any [106,203,318]. Differently a partial de-epoxidized xanthophylls-dependent NPQ has been reported in some species belonging to green algae [318], brown algae [319], diatoms[320], *eustigmatophytes* [321] and *alveolata* [322]. In the diatoms *Phaeodactylum tricornutum* and *Thalassiosira pseudonana* genes encoding for a plant-like VDE have been reported being involved in de-epoxidation of the xanthophyll diadinoxanthin producing diatoxanthin, with this peculiar xanthophyll cycle being involved in NPQ induction [320]: in these photosynthetic heterokonts two additional VDE-like (VDL) or VDE-related (VDR) enzymes have been reported, even if their catalytic activity and their physiological role is still under debate [323]. In the case of *C. reinhardtii*, the catalytic violaxanthin de-epoxidation activity has been recently attributed to an enzyme, called CVDE, which is not related to the plant-VDE but to a lycopene cyclase from photosynthetic bacteria [29]. A similar CVDE enzyme has been more recently reported also in case of other green algae as *Volvox carteri* and *Chromochloris zofingiensis* [324]. This observation led to the hypothesis that green algae and plants evolved different VDE enzymes with implication on their regulation and functions [29]. In this work we investigated, *in vivo* and *in vitro*, the molecular details of the enzyme responsible for zeaxanthin accumulation in one of the most promising green algae for industrial cultivation, *Chlorella vulgaris* [325-329]. In particular, it has been recently reported that the molecular mechanisms involved in high light resistance are important biotechnological tool in order to improve biomass productivity in microalgae [330,331] and in particular in *C. vulgaris* [332]. We demonstrate that *C. vulgaris* undergoes a plant-like xanthophyll cycle and zeaxanthin is involved in quenching excitation energy absorbed by both PSI and PSII. The results obtained demonstrate a divergence in molecular mechanism and function of the xanthophyll cycle among green algae, probably associated to the different evolutionary pressure to which the different species were exposed in their different habitats. These results pave the way for better understanding of evolution

of photoprotective mechanisms in photosynthetic organisms, to improve photosynthetic efficiency by properly tuning energy dissipative pathways [188].

Results

Identification of VDE enzyme in *C. vulgaris*

C. vulgaris genomic and transcriptomic data were used to mine possible VDE and CVDE genes. Local BLAST analysis on *C. vulgaris* genome [325] was performed using the *A. thaliana* VDE sequence as query gave a positive result in the case of gene g7391, while the same analysis performed by using *C. reinhardtii* CVDE enzyme identified g3843 as putative homolog for CVDE in *C. vulgaris*. While in the case of CVDE limited information are available regarding the key residues involved in its catalytic function, the structure of catalytic domain and the functions of specific residues have been previously reported in the case of VDE[242,313-317]. The putative *C. vulgaris* VDE protein sequence was thus compared with VDE sequences from higher plants or other microalgae species. Multiple alignment (**Figure 2.5.1**) shows high similarity of *C. vulgaris* VDE with the other VDE sequences analysed in the case of the catalytic domain. N- terminal domain of *C. vulgaris* VDE is enriched in cysteine residues, a conserved feature compared to VDE sequences from all the organisms analysed. The multiple alignment also reveals the conservation in *C. vulgaris* of the key residues for catalytic activity (Asp177 and Tyr198) previously reported in the case of higher plants [314]. Important residues for the structural organization, Asp114, His121, Arg138 and Tyr214 are conserved in all the VDE sequences reported in **Figure 2.5.1**, while some variations can be observed in the case of the other His residues, His 124, His169 and His174 (corresponding in *A. thaliana* to the His168 and His173 previously investigated in VDE from spinach) reported to influence the catalytic activity [315] and VDE pH dependent binding to the thylakoid membranes [316]: His 124 is present only in higher plants, with the exclusion of *O. sativa*, His168 and His174 are conserved in higher plants, mosses and diatoms but not in the green algae *C. vulgaris* and *C. variabilis* where they are substituted with basic residues, as respectively lysine and an asparagine. Considering protonatable residues involved in pH sensing other variations are evident: Asp 114 is conserved in all the sequences analysed but not in *Phaeodactylum tricornutum*, Asp96 and Asp98 are conserved only in VDE sequence from higher plants, Asp206 is conserved only in land plants (**Figure 2.5.1**). These results open the question about a possible different pH dependence of *C. vulgaris* VDE enzyme compared to VDE enzymes from higher plants. higher plants.

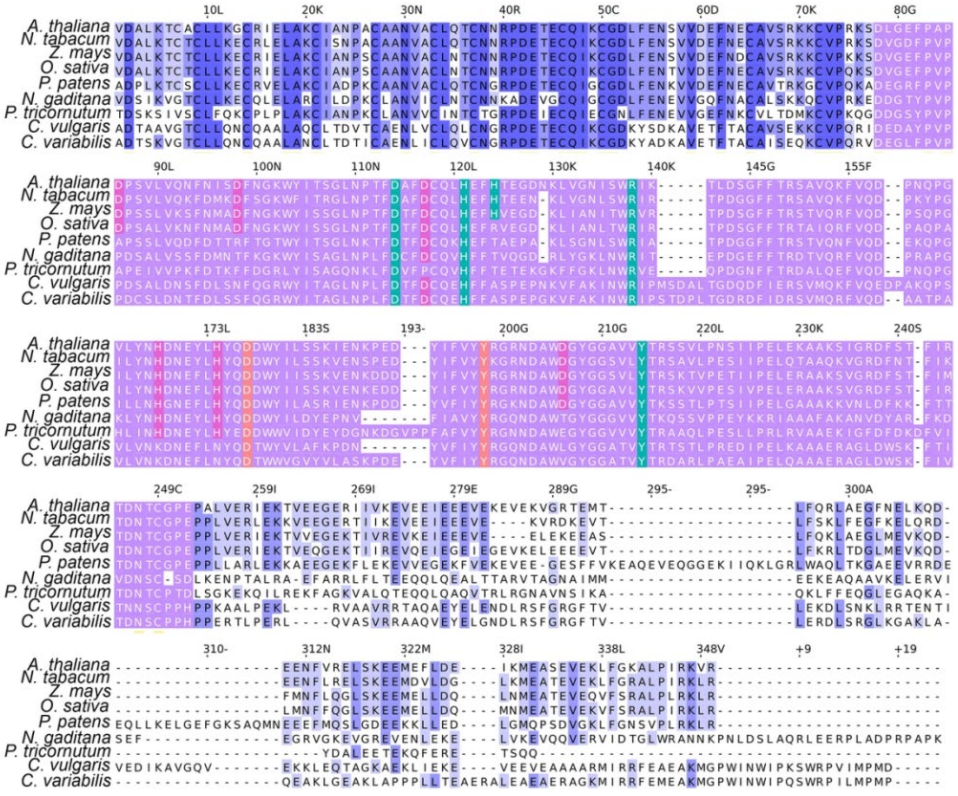

Figure 2.5.1 *Multiple alignment of VDE enzyme sequences. Multiple alignment of VDE sequences retrieved from Arabidopsis thaliana; Nicotiana tabacum; Zea mays; Oryza sativa; Physcomitrella patens; Nannochlopsis gaditana; Phaeodactylum tricornutum; Chlorella vulgaris and Chlorella variabilis. The domains organization is divided in three main regions: N-terminus region (1-76 in A. thaliana) is the cysteine rich region, the central region (77-252, in violet color) is the lipocalin domain and the C-terminus part is the glutamic rich region. In the lipocalin domain are evidenced the residues important for the catalytic activity (orange), for the structure organization (green) and for pH sensitivity*

Phylogenetic distribution of VDE and CVDE

To investigate the distribution of VDE among different photosynthetic organisms, a phylogenetic tree of putative VDE enzymes was then assembled. Protein sequences with VDE lipocalin domain identified by InterPro Scan were used to assemble a phylogenetic tree with *C. vulgaris* VDE. As reported in **Figure 2.5.2** VDE enzymes from *Streptophyta* clustered together while VDE enzymes being identified in some green algae, among which *C. vulgaris*, *Chlorella variabilis*, *Auxenochlorella prototechoides*, *Monoraphydium neglectum*, *Lobopshera incisa* and *Ostreococcus tauri*, and in organisms which plastids originated by a secondary symbiosis as diatoms, *Haptophyta, Ochrophyta* as *Nannochloropsis* sp., and photosynthetic *Alveolata* as *Chromera velia*. Separate and more divergent groups at the two ends of phylogenetic tree including VDE-like enzymes were also identified: a group of VDE-related (VDR) enzymes from organisms whose plastids originated by a secondary symbiosis, and at the opposite site a cluster including VDE-like enzymes from *Streptophyta* and *Chlorophyta*, with no VDE function reported yet. In order to investigate deeper the presence of VDE or CVDE enzymes in *Chlorophyta*, a more detailed analysis was performed among these organisms. Phylogenetic distribution of CVDE and its homolog CruP[29] among green algae is reported in **Figure S 2.5.1**, showing

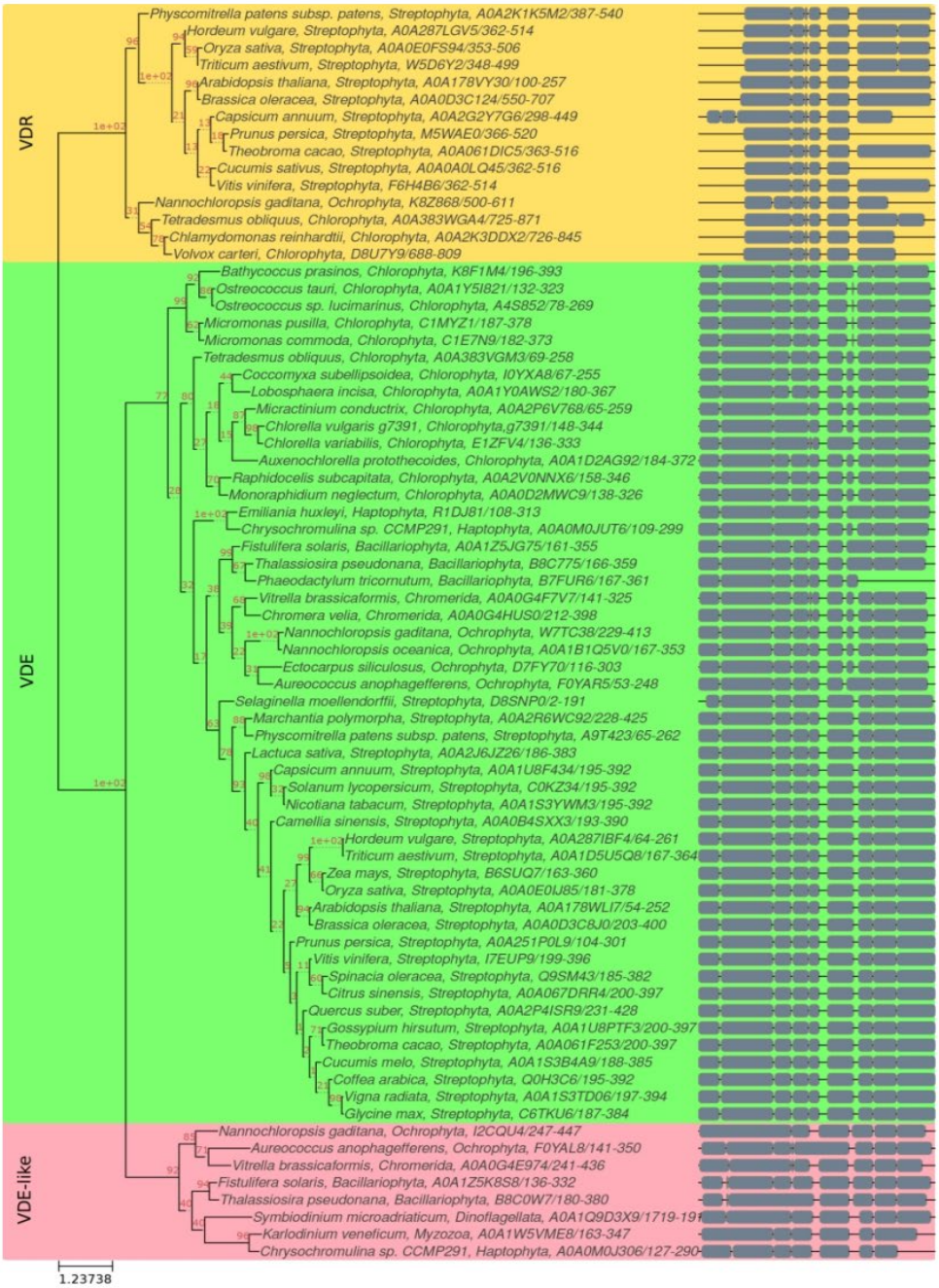

Figure 2.5.2 *Phylogenetic tree of VDE, VDR and VDE-like proteins. Phylogenetic tree was obtained by multiple alignment of protein sequences carrying a VDE lipocalin domain identified by InterPro (IPR010788). The units of branch length are residues substitution per site divided by the length of the sequence. Bootstrap values are reported in red.*

separate clusters for CVDE and CruP. The identification of VDE, VDR, CVDE genes among green algae species with complete genome available is reported in **Table S 2.5.1**: no VDE enzyme could be found in the *Volvocales* species herein analysed as *C. reinhardtii*, *Chlamydomonas eustigma*, *Gonium pectorale* and *Volvox carteri* where instead CVDE enzymes could be found in some cases VDR genes. Differently, in the case of the *Mamiellales* species only VDE enzymes could be found and no CVDE. *Sphaeropleales* species *Ostreococcus tauri*, *Ostreococcus lucimarinus*, *Micromonas commoda* and *Micromonas pusilla* were instead characterized for having both VDE and CVDE enzymes. A more variable situation could be observed in the case of *Trebouxiophyceae*: all the species analysed present a VDE gene, with the exception of *Chlorella sorokiniana*, where a VDR gene can be found, while CVDE genes could be identified only in the case of *Auxenochlorella protothecoides*, *Chlorella sorokiniana*, *Coccomyxa subellipsoidea* and *Chlorella vulgaris*. Even if further experimental work is required to investigate the violaxanthin de-epoxidation reactions in the different species herein reported, these results indicate a divergency among *Chlorophyta* of violaxanthin de-epoxidation catalysis during evolution.

In vitro de-epoxidation

The role of VDE and/or CVDE in xanthophyll cycle activation was investigated in *C. vulgaris* and *in vitro* and *in vivo*. Differently from CVDE, VDE enzymes from higher plants have been reported *in vitro* to catalyse violaxanthin de-epoxidation in thylakoids in presence of ascorbate and low pH, while DTT inhibits its activity [333]. *C. vulgaris*, spinach and *C. reinhardtii* thylakoids were exposed at pH 5.1 in presence of 20 mM ascorbate as reducing agent to activate VDE enzyme in presence or absence of 1 mM DTT. As reported in **Figure S 2.5.2**, substantial violaxanthin de-epoxidation was detectable already after 30 minutes in the case of spinach, while 4-8 hours were required to induce zeaxanthin formation in *C. vulgaris*. In both cases, a specific inhibitory activity of DTT was evident, causing no violaxanthin de-epoxidation (**Figure 2.5.3a**, **Figure S 2.5 3**). Differently, in the case of *C. reinhardtii* no violaxanthin de-epoxidation was observed in these conditions, in agreement with previous observation in this species, due to the absence of CVDE activity in the

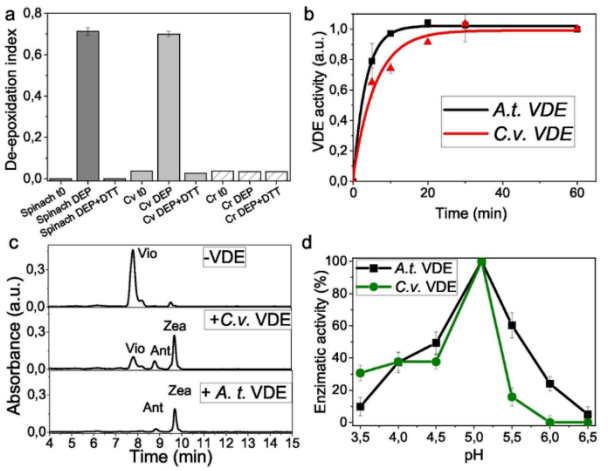

Figure 2.5.3 *In vitro violaxanthin de-epoxidation assay. (a) De-epoxidation index (D.I.) of thylakoids isolated from spinach, C. vulgaris (C.v.) and C. reinhardtii (C.r.) before (t0) or after (DEP) 1 hours (spinach) or 8 hours (C.v. and C.r.) at pH 5.1 in presence of ascorbate in order to induce violaxanthin de-epoxidation. De-epoxidation index obtained in presence of VDE inhibitor DTT is also reported. (b) VDE activity of recombinant C. vulgaris evaluated in vitro by measuring changes at 505 nm in carotenoid absorption spectrum due to violaxanthin conversion to zeaxanthin. The absoprtion at 540 nm were subtracted to the absorption at 505 nm; kinetics were normalized to 1 for the maximum activity observed. (c) Chromatogram related to HPLC pigment analysis after de-epoxidation in vitro assay in presence or absence of VDE enzymes from C. vulgaris (C.v.) or A. thaliana (A.t.). (d) VDE enzymatic activity during in vitro enzymatic assay at different pH, normalized to 100% in the case of the maximum value (pH 5.1). Standard deviations are reported as error bars (n=3).*

conditions tested [29]. Considering the inactivity CVDE *in vitro*, the possible activity of *C. vulgaris* CVDE was then investigated *in vivo*. *C. vulgaris* cells were exposed in presence or absence of the inhibitor DTT (1mM) to 2000 µmol photons m^{-2} s^{-1} for up to 40 minutes: as reported in **Figure S 2.5.4**, de-epoxidation index (D.I.) increased upon light exposure in absence of DTT, while cells treated with this inhibitor showed an almost impaired zeaxanthin accumulation, consistently with previous finding [318,334]. This result suggests a minor role of the DTT-insensitive CVDE xanthophyll cycle activation in *C. vulgaris*. In order to investigate the catalytic activity of the identified *C. vulgaris* VDE enzyme, its coding sequence was cloned in expression vector and overexpressed in *E. coli* as previously reported [314]. Recombinant protein was then purified from the soluble fraction of lysate bacterial cells through affinity column and used for evaluating its catalytic activity in presence of violaxanthin. *In vitro* enzymatic assay was performed at pH 5.1 in presence of violaxanthin and ascorbate following the changes in absorption spectrum (**Figure 2.5.3b**): in case of violaxanthin de-epoxidation, an increase of 500 nm absorption is expected

due to zeaxanthin formation [314]. *A. thaliana* VDE was used as positive control [314]. Increase of 505 nm absorption was indeed observed in presence of recombinant VDEs from both *A. thaliana* and *C. vulgaris*, but not in the negative control (no VDE added) suggesting violaxanthin de-epoxidation. Zeaxanthin accumulation in *A. thaliana* or *C. vulgaris* was then confirmed by HPLC analysis (**Figure 2.5.3c**). The pH dependence of *C. vulgaris* VDE was then investigated repeating the enzymatic *in vitro* assay at different pH after 60 minutes of incubation (**Figure 2.5.3d**). While for both *A. thaliana* and *C. vulgaris* VDE the optimum pH for de-epoxidation reaction was 5.1, the *C. vulgaris* subunit exhibited a reduced activity at higher pH compared to *A. thaliana* VDE. Considering the reduced content of protonatable residues involved in pH sensing in *C. vulgaris* VDE compared to *A. thaliana* VDE, the reduced activity of the former at higher pH suggests a possible cooperative regulation of pH sensing in this enzyme, partially affected in the *C. vulgaris* subunit (**Figure 2.5.1**).

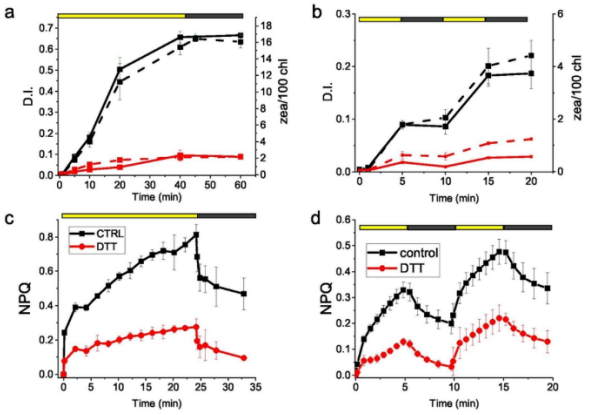

Figure 2.5.4 *VDE inhibition by DTT and role of zeaxanthin in NPQ induction. DTT inhibitor was added to whole cells in order to inhibit VDE catalytic activity. a,b) De-epoxidation index and zeaxanthin content normalized to 100 chlorophylls of cells treated in presence or absence of DTT for 40' with 2000 µmol photons m^{-2} s^{-1} followed with 20' of dark recovery (a) or illuminated for two consecutive cycles of 5' light followed by 5' of dark recovery (b). c,d) Effect of DTT on NPQ kinetics: NPQ induction kinetics in presence or absence of DTT upon illumination with 2000 µmol photons m^{-2} s^{-1} actinic light for 25' followed by 10' of dark recovery (c) or upon two consecutive cycles of 5' light followed by 5' dark. Standard deviations are reported as error bars (n=3).*

Role of zeaxanthin in NPQ induction in *C. vulgaris*

The specific role of zeaxanthin in NPQ induction was then studied by measuring NPQ in presence or absence of DTT, in order to inhibit VDE activity, under continuous light for 25 minutes, followed by dark recovery (**Figure 2.5.4a**), or upon a double cycle of illumination interrupted by 5 minutes of dark: in this way zeaxanthin accumulation is induced in the first cycle and its potential role in NPQ can be highlighted in the second cycle due to the long timing required for zeaxanthin epoxidation (**Figure 2.5.4b**). As reported in **Figure 2.5.4**, the presence of DTT caused a strong decrease of NPQ during both continuous light exposure or during both the first and second cycle of actinic light illumination, suggesting a key role of zeaxanthin for NPQ induction. Potential side effect of DTT can be excluded at the concentration used (1mM) as evidenced by the similar maximum quantum yield (Fv/Fm) of PSII in *C. vulgaris* kept in the dark in presence or absence of DTT for up to 30 minutes (**Figure S 2.5.4**), consistently with previous reports on isolated chloroplasts [335]. Differently, in the case of *C. reinhardtii*, the NPQ traces during the first and the second cycle were similar and no effect of DTT was evident (**Figure S 2.5.5**), confirming the minor role of zeaxanthin in this organism and the absence of CVDE inhibition by DTT [29]. The correlation between zeaxanthin accumulation and NPQ induction kinetics in *C. vulgaris* was then investigated at different actinic lights ranging from 200 µmol photons m^{-2} s^{-1} to 2500 µmol photons m^{-2} s^{-1} (**Figure S 2.5.6**). As shown in **Figure S 2.5.7**, an increase of the light intensities caused an increase of D.I. up to 0.6 at the highest irradiances. Similarly, higher actinic lights caused an increase of maximum amplitude of NPQ induction, with reduced recovery in the dark (**Figure S 2.5.7**). The possible relation between NPQ induction and zeaxanthin accumulation was thus investigated plotting the NPQ values measured at the end of the actinic light treatment and its components qE and qI (or qZ) as a function of the measured D.I. or zeaxanthin content (**Figure S 2.5.7**): an exponential asymptotic correlation could be drawn between D.I. and NPQ, qE or qI(qZ). Interestingly, in the case of qE the rate of the exponential asymptotic correlation function was higher compared to NPQ and qI/qZ, with the latter having the lowest rate. These results demonstrate that xanthophyll cycle activation is almost linearly correlated with the long relaxing component of NPQ, while relatively few molecules of zeaxanthin (and or anteraxanthin) are correlated with the activation of qE (**Figure 2.5.4**). irradiances.

Role of zeaxanthin in PSI quenching in *C. vulgaris*

NPQ analysis at room temperature allows to assess only quenching events at the level of PSII, being PSI fluorescence almost undetectable. In order to investigate a possible role of zeaxanthin in PSI photoprotection, emission of whole cells was investigated at 77K where photochemical reactions are blocked and PSI fluorescence can be measured [225]. As reported in **Figure 2.5.5**, by using green fluorescent protein (GFP) as internal standard, a light dependent decrease of both PSII (680-695 nm) and PSI (715 nm) emission peaks was evident, as previously reported in the case of *C. reinhardtii* [225]. In presence of DTT, inhibiting zeaxanthin accumulation, a less evident quenching of both PSII and PSI peaks was measured (**Figure 2.5.5**). Gaussians deconvolution of emission spectra allowed to retrieve PSII and PSI contributions of 77K emission spectra and to calculate the extent of light dependent quenching specifically for PSI and PSII. Consistently with NPQ measured at room temperature (**Figure 2.5.4**), in presence of DTT, PSII quenching was strongly reduced. Similarly, PSI quenching was also reduced, when VDE was inhibited, suggesting a role of zeaxanthin in PSI photoprotection.

Distribution and quenching properties of zeaxanthin in pigment binding complexes

Zeaxanthin distribution among pigment binding complexes was investigated inducing violaxanthin de-epoxidation *in vitro* in isolated thylakoids from *C. vulgaris* as reported in **Figure 2.5.3**. Pigment binding complexes were then separated by native Deriphat-PAGE electrophoresis (**Figure S 2.5.8**,**Figure S 2.5.9**,**Figure S 2.5.10**) [336] and zeaxanthin accumulation was investigated in eluted fractions by HPLC analysis. Only in the case of fractions corresponding to monomeric LHC, PSII core and PSI complexes detectable amount of zeaxanthin was found (**Table S 2.5.2**). In the case of monomeric LHC, sub-stoichiometric amount of zeaxanthin was found. Considering the similar absorption spectrum of monomeric (fraction A1/B1) and trimeric LHC (fraction A3/B3), likely monomeric LHC fractions were mainly composed by monomeric LHCII, where zeaxanthin has been reported to be accumulated in the highly unstable external V1 site [23,308]. The finding of zeaxanthin in PSII core is instead related to a contamination from residual antenna

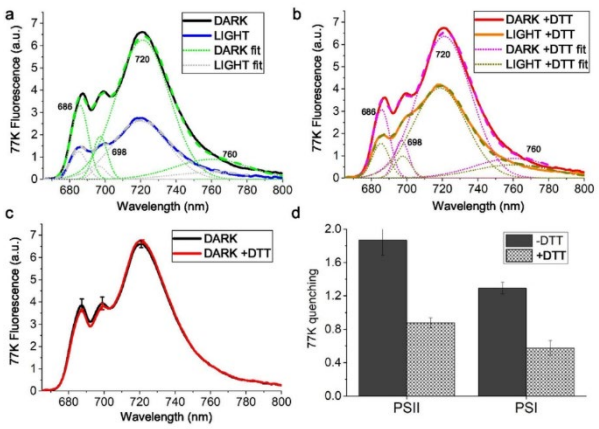

Figure 2.5.5 *PSI and PSII quenching measured at 77K. (a/b) Fluorescence emission spectra were recorded for C. vulgaris whole cells dark adapted (black/red) or high light treated (2000 µmol photons m^{-2} s^{-1}) for 6' (blue/orange) in absence (a) or presence (b) of VDE inhibitor DTT. GFP was added as internal standard for normalization. Fluorescence emission spectra were reconstructed by spectral deconvolution with Gaussians: different Gaussians used are reported in green (dark adapted samples, no DTT), pink (dark adapted samples with DTT), grey (high light treated samples, no DTT) or dark yellow (high light treated samples with DTT). Peaks of the different Gaussians are reported. (c) Comparison of dark adapted samples in presence or absence of DTT showing no major side effect due to the presence of the inhibitor. (d) Calculations of PSII and PSI quenching from the sum of the area of the Gaussians used for the fitting according to the formula (ADark–ALIGHT)/ALIGHT where ALIGHT and ADark are respectively the amplitude after light treatment or at time 0 of the different Gaussians attributable to PSII (peaking at 686 and 698 nm) or PSI (peaking at 720 nm). Standard deviations are reported as error bars (n=4).*

complexes bound, being xanthophyll binding sites absent in PSII core. Differently, in the case of PSI complex, almost two zeaxanthin molecules per PSI were detected, with a D.I. of 0.34. The accumulation of zeaxanthin in monomeric LHC complexes did not significantly affect their absorption or 77K fluorescence emission spectra, while in the case of PSI complex, a red shift in fluorescence emission was evident (**Figure S 2.5.5**). These results agree with those previously reported in the case of zeaxanthin binding in PSI isolated from a *A. thaliana npq2* mutant [228], a mutant constitutively accumulating this xanthophyll [138]. The quenching properties of zeaxanthin bound to monomeric LHC or to PSI complex were then investigated by time-resolved fluorescence analysis (**Figure 2.5.6**, **Figure S 2.5.11**,**Figure S 2.5.12**,**Figure S 2.5.13**). In the case of monomeric LHC the fluorescence decay kinetics were not significantly changed by the presence of zeaxanthin. In order to investigate a possible quenching effect of zeaxanthin bound to trimeric LHCII, milder solubilization of thylakoids were performed and pigment binding complexes were performed by ultracentrifugation in

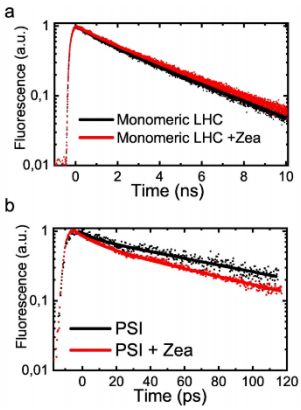

Figure 2.5.6 *Fluorescence decay kinetics of isolated monomeric LHC and PSI complexes with and without zeaxanthin. Monomeric LHC and PSI complexes were isolated from C. vulgaris thylakoid membranes before (black) or after (red) in vitro de-epoxidation to induce zeaxanthin accumulation. Fluorescence decay kinetics of monomeric LHC (a) were measured by TCSPC in the 0-10 ns time scale, while PSI complexes (b) were measured by Streak camera CCD in the 0-200 ps time scale.*

sucrose gradient, as procedure previously reported to partially maintain the occupancy of V1 site [23]: as reported in **Table S 2.5.2**, the LHCII trimers by this protocol were characterized by increased xanthophyll content with a D.I. of 0.53 in the case complex isolated from de-epoxidated thylakoids (LHCII-Zea). However, no significant zeaxanthin dependent quenching was detectable, comparing LHCII with or without zeaxanthin in V1 site (**Figure S 2.5.11**). Differently, in the case of PSI complex, a faster decay was evident in zeaxanthin binding sample. In particular, an average fluorescence lifetime of 75.5 ps was calculated in the case of PSI complex in absence of zeaxanthin, which decreased to 54.2 ps in zeaxanthin binding PSI (**Table S 2.5.3**). The 70 ps average fluorescence lifetime in zeaxanthin-free PSI is consistent with the previous data reported in the case of *C. reinhardtiii* [337], while the 30% reduction in average fluorescence lifetime observed in zeaxanthin binding PSI is consistent with the zeaxanthin dependent quenching previously observed in the case of zeaxanthin binding PSI from *A. thaliana* [228].

Discussion

This work identifies a plant-like VDE enzyme in *C. vulgaris* and relates its activity to the photoprotective mechanism NPQ of both PSI and PSII. *C. vulgaris* is one of the leading microalgae at industrial level due to the high growth rate and resistance to biotic and abiotic stresses [325,338-341]. Recently, further increase of productivity in this microalga has been reported by increasing its resistance to photooxidative stress [332]. Photoprotective mechanisms as NPQ have been reported as key targets for biotechnological manipulation of photosynthetic organisms assuring on one side enough photoprotection and, on the other side, higher photosynthetic efficiency [188]. Zeaxanthin has been associated with different photoprotective functions, from singlet and triplet chlorophyll excited state quenching to ROS scavenging in both higher plants and green algae [85,135,342]. However, the identification of CVDE, the gene product responsible for violaxanthin de-epoxidation in *C. reinhardtii*, revealed a divergence in the evolution in the green lineage of the enzyme carrying the VDE catalytic activity, being this enzyme not homologous to the VDE of *A. thaliana*, but more similar to a lycopene cyclase [29]. Moreover, CVDE is in the stromal side of thylakoid membranes and it is not activated by lumen acidification [29]. In the case of *Chlorophyta*, different distribution of VDE and CVDE could be found as reported in **Table S 2.5.1**, with both enzymes being found in the same genome only in the case of the *Spaeropleales* species herein investigated and in some *Chlorellales*, among which *C. vulgaris*. However, these *Trebouxiophyceae* CVDE-like genes appeared to be more phylogenetically distant compared to the other CVDE (**Figure S 2.5.1**), and the catalytic function of the encoded genes should be further analysed in detail. The divergence between CVDE and VDE, despite a similar catalytic activity, demonstrates the plasticity of the carotenoid biosynthetic pathway and divergent evolution of the involved key enzyme likely driven by their specific functions and interaction with the environment. In this work a violaxanthin de-epoxidase catalytic activity inducible at low pH was found in *C. vulgaris*, which allowed, using genome mining, to identify a conserved plant-like VDE enzyme in this member of the *Chlorophyta* group. Phylogenetic analysis reveals indeed that VDE sequences are widely distributed in higher and lower plants, while in unicellular algae, plant-like VDE sequences could be found only in some species among which some green algae, diatoms, *Haptophyta*, *Ochrophyta* as *Nannochloropsis sp.*, and photosynthetic *Alveolata* as *Chromera velia*. Other enzymes with lipocalin domains related to VDE can then be identified as VDR and VDE-like, but with possible different functions than violaxanthin de-epoxidation. In the case of *C. vulgaris* the VDE protein encoded by its genome resulted with a high level of identity compared to *A. thaliana* VDE (**Figure 2.5.1**). Only in the case of residues involved in protein sensitivity to pH, a partial conservation was found in *C. vulgaris* VDE compared to VDE from higher plants. Accordingly, the pH

dependent activation of *A. thaliana* and *C. vulgaris* VDE is different: despite a similar optimum at pH 5.1, the catalytic activity of the latter at higher pH is dramatically reduced compared to the former. This might be a consequence of the lower number of protonatable residues found in the lipocalin-like domain, considering a possible cooperative regulation of pH sensing in VDE given by the different protonatable residues (**Figure 2.5.1**). The activity of *C. vulgaris* VDE was completely inhibited by DTT *in vitro*, a condition where CVDE in *C. reinhardtii* was proven not to be active. Similarly almost complete inhibition of violaxanthin de-epoxidation could be observed *in vivo* in presence of DTT (**Figure S 2.5.4**): considering the insensitivity of CVDE for DTT [29], its possible role in the xanthophyll cycle activation in *C. vulgaris* appears to be minor. In higher plants, the fastest component of NPQ mechanism, qE, depends on the interaction of an LHC-like protein called PSBS with other LHC proteins [102,111,343]. Xanthophyll cycle activation has an important, though not crucial, role in higher plants in the induction of NPQ as observed in *npq1* and *npq2* mutants in *A. thaliana*, lacking VDE and zeaxanthin epoxidase (ZE): *npq2* showed faster NPQ kinetics while *npq1* was characterize by having a reduced NPQ phenotypes compared to WT but not zeroed [138]. Differently, in the case of *Physcomitrella patens* VDE activity has been reported to be essential for NPQ induction [285]. In microalgae, the role of de-epoxidized xanthophylls in the NPQ process is still unclear and highly species-specific [318]. In *C. reinhardtii*, mutants that are unable to accumulate zeaxanthin show an induction of NPQ similar to the WT[106,225], thus demonstrating that zeaxanthin does not have a specific role in NPQ in that organism. In *Phaeodactylum triconornutum* strains with a reduces level of diatoxanthin reflect lower induction of NPQ [320] The role of zeaxanthin was also studied in the stramenophile *Phaeomonas sp*. where NPQ level is correlated with its accumulation and is already active at dark [344], while in *Nannochloropsis oceanica* a mutant on VDE enzyme resulted in impaired NPQ induction [246]. In this work, a reduced NPQ phenotype was evident when VDE enzyme was partially inhibited demonstrating a role of zeaxanthin in NPQ induction in *C. vulgaris.* These results are in line with previous findings, where NPQ amplitude and /or kinetics were affected in *C. vulgaris* upon treatment with DTT [318,334]. Moreover, an exponential correlation between the induction of NPQ and zeaxanthin accumulation was found, suggesting that additional components are contributing to NPQ induction, especially at higher actinic lights. LHC-like proteins involved in quenching as PSBS and LHCSR, recently reported also in the case of *C. vulgaris* [325], or other LHCII proteins present indeed protonatable sites[345] [108,121,122] that could be responsible for the modulation of the extent of NPQ at different actinic light independently from the contribution of zeaxanthin. In *C. vulgaris*, zeaxanthin resulted to be involved also in PSI quenching (**Figure 2.5.5**,**Figure 2.5.6**) in both light dependent (**Figure 2.5.5**) and light independent mechanisms (**Figure 2.5.6**). Light dependent PSI quenching has been previously reported to be focused on its associated LHC antenna complexes and to be modulated by LHCSR subunits in *C. reinhardtii* by a zeaxanthin independent mechanism [210,225]. Differently, in the case of *C. vulgaris* inhibition of VDE activity caused a strong reduction of PSI light dependent quenching, suggesting a key role of zeaxanthin in this photoprotective mechanism, which however, form the data available, cannot be assessed as LHCSR dependent or independent (**Figure 2.5.5**). In the case of PSI, a light independent quenching was also observed mediated by zeaxanthin when zeaxanthin binding complexes were isolated from thylakoid membrane: this photoprotective mechanism is consistent with previous finding in PSI complexes isolated from *A. thaliana* mutant that constitutively accumulated zeaxanthin, the mutant *npq2* [138,228]. In PSI complexes isolated from *npq2*, all the violaxanthin binding sites were occupied by zeaxanthin: in the zeaxanthin binding complex isolated from *C. vulgaris* herein reported, a D.I. of 0.34 was observed with almost 2 zeaxanthin molecule per PSI complex which are likely bound to the external LHC antenna complexes [346]. When PSI complex was isolated from *A. thaliana* with a similar D.I. and zeaxanthin/PSI stoichiometry, no evident effect of zeaxanthin in PSI quenching was observed [309] suggesting a much higher influence of zeaxanthin in PSI quenching in *C. vulgaris* rather than *A. thaliana*. All these findings thus demonstrate the role of zeaxanthin in NPQ and excitation energy quenching in both PSII and PSI. Nevertheless, knock-out mutants on VDE, LHCSR and/or PSBS subunits in *C. vulgaris* are required to fully understand the relative role of these subunits in safe thermal dissipation of excitation energy absorbed by PSI and/or PSII. It is interesting to note that the similar relationship between NPQ and

zeaxanthin and the similar characteristics of the VDE enzyme in higher plants and *C. vulgaris* may be correlated with the capacity of this algae to form biofilms on land surface [347]. Living forming biofilm indeed increases the risk of being exposed to rapid light changes, as in the case of lower or higher plants [318]. However, it is important to note that other species known to live even in soils, as *C. reinhardtii*, has CVDE-dependent xanthophyll cycle and VDE enzyme can be found also in green algae living in planktonic form, including species as *Ostreoccus* or *Micromonas*, making not feasible a direct correlation between VDE evolution and the biofilm vs. planktonic living form of *Chlorophyta*. However, considering the minor role of zeaxanthin in NPQ in *C. reinhardtii* compared to the key role of zeaxanthin in *C. vulgaris* photoprotection it is possible to speculate that the latter evolved photoprotective mechanisms that have proved to be successful in the case of higher plants in which zeaxanthin has a central role. Accordingly to this evolutionary perspective, it was reported that mosses, the earliest photosynthetic organisms conquering the land, present a NPQ mechanism fully dependent on zeaxanthin accumulation [285]. Then, evolution of higher plants further tuned the dependency of photoprotection mechanisms toward xanthophyll cycle, which maintained a central role in photoprotection (**Figure S 2.5.10**) [85].

Material and methods

Strains and culture conditions

C. vulgaris (CCAP211/11P) and *C. reinhardtii* (4A+) cells were grown at 25°C in flask in shaker at 160rpm with a white light at 60 µE light conditions with a 16h light 8h dark photoperiod in BG-11 medium[348] or HS medium [349] respectively.

Arabidopsis thaliana genotypes and growth conditions

Arabidopsis thaliana Colombia-0 (Col-0) ecotype WT and *npq1* plants [138] were grown under controlled conditions at irradiance of 300 µmol photons m^{-2} s^{-1} with a 16:8h photoperiod, temperature of 23°C/20°C, day/night and 50–70% relative air humidity

VDE identification and phylogenetic analysis

Putative VDE genes were searched in the assembled *C. vulgaris* genome by BLAST search using *A. thaliana* VDE1 (AT1G08550) as query and *C. vulgaris* translated genome as database. All the sequences use for phylogenetic analysis were retrieved from Uniprot. Sequences carry a VDE lipocalin domain was retrieved from InterPro (IPR010788). Sequence alignment was obtained by MAFFD (version 7.394) software. The phylogenetic trees were generated using ClustalOmega with default parameters, trimAl for alignment cleaning and Phyml with 100 bootstraps, and rendered with ETE 3 toolkit [350].

VDE expression and purification

Total RNA from *C. vulgaris* was extracted from cell grown in high light using the Direct- zol™. RNA Miniprep Plus kit (Zymo Research). Transcript sequence was amplified from cDNA using specific primers designed on transcript g7391 (Supporting Information, Methods S1). Mature VDE coding sequence was cloned into pET28 expression vector removing the initial 28 amino acids putative signal peptide for the chloroplast. The signal peptide was calculated using ChloroP 1.1 tool. pQE60 construct for expression of *A. thaliana* VDE enzyme in *Escherichia coli* previously described [317,351] was kindly gifted by Prof. Tomas Morosinotto (University of Padua, Italy). Recombinant *A. thaliana* and *C. vulgaris* VDE were expressed in *E. coli* Origami™ 2(DE3) (Novagen) by inducing cells with 1mM isopropyl β-D-1-thiogalactopyranoside for 5 h at 37°C and purified as described in [314](Saga et al., 2010).

Pigment analysis

Pigments were extracted using dimethyl sulphoxide (DMSO) from whole cells and in acetone 80% from thylakoids and purified pigments binding complexes. In the case of pigments mixture used from VDE activity assays, carotenoids were extracted with diethyl ether inducing phase separation: the organic phase was collected, dried in a SpeedVac, and resuspended in 80% acetone for HPLC analysis [314]. DMSO or acetone extracts were then centrifuged and the supernatants analysed by HPLC as described in [231]. De-epoxidation index (D.I.) was

calculated from the concentration of zeaxanthin, anteraxanthin and violaxanthin as:

$$\frac{[Zea] + 0.5 * [Antera]}{[Zea] + [Antera] + [Viola]}$$

VDE activity assay

VDE activity was tested by adding pure violaxanthin as substrate in a de-epoxidation buffer as described in [314]. In particular, the de-epoxidation buffer was composed by 67 mM citrate buffer at pH 5.1, 60mM ascorbate, 6% methanol, 0.33 µM violaxanthin and 9µM MGDG. Violaxanthin and MGDG were mixed in methanol and then added to the de-epoxidation buffer. Violaxanthin de-epoxidation was monitored by measuring changes in absorption spectra in the 480-520 nm spectral region [314] and by HPLC analysis [231].

In vitro de-epoxidation on thylakoids

C. vulgaris and *C. reinhardtii* thylakoids were extracted from overnight dark-adapted cells by destroying them with glass beads directly in the de-epoxidation buffer (40mM MES pH 5.1, 330mM sorbitol, 5mM $MgCl_2$, 10mM NaCl 20mM ascorbate and BSA 0,5%). The inhibitor dithiothreitol (DTT) was added to the de-epoxidation buffer at a concentration of 1mM when indicated in the text. In the case of spinach, leaves were grinded in 0.4M NaCl, 5mM $MgCl_2$, 20mM Tricine/KOH pH 7.8 and 0.5% BSA, filtered through a 10µm filter, centrifuged at 10.000g and then resuspended in the in the de-epoxidation buffer. De-epoxidation reaction was then performed at 20°C up to 1 hour in the case of spinach and up to 8 hours in the case of *C. vulgaris* and *C. reinhardtii*. Pigments were then extracted using acetone 80% and analyzed by HPLC.

SDS-PAGE and western blotting

Total protein extracts were loaded into SDS-PAGE 12% gels as described in [352]. Western blot analysis was performed using antibody for *A. thaliana* VDE [125].

NPQ measurements

NPQ was calculated as (Fm-Fm')/Fm' [353] using a Dual PAM-101 (Waltz, Effeltrich, Germany). Fm is the maximum chlorophyll fluorescence emitted by dark adapted cells after 2 minutes treatment with far-red light-emitting diode (LED), Fm' is the maximum fluorescence measured upon exposure to actinic light or during dark recovery. Far red light was turn on also during dark recovery. A 5000 µE saturation pulse was used to induce Fm and Fm' while the intensity of the actinic lights used were reported in the results section.

77K quenching analysis

77K fluorescence emission was recorded as described in [225] on *whole C. vulgaris* cells dark adapted or high light treated (2000 µE). DTT was added as described in the text to inhibit VDE catalytic activity. GFP protein was added to the samples as internal standard for normalization of fluorescence emission spectra.

Thylakoid solubilization and pigments binding complexes purification

Pigment binding complexes were separated by Deriphat-PAGE as previously described [336] solubilizing thylakoid membranes with 0.8% n-Dodecyl β-D-maltoside [185]. Trimeric LHCII were also isolated by ultracentrifugation in sucrose gradient of thylakoid membranes solubilized in 0.6% n-Dodecyl α-D-maltoside as previously described [23].

Time-resolved fluorescence

Time-resolved fluorescence measurements were performed by Time-correlated Single Photon Counting (TCSPC) using a Chronos BH ISS Photon Counting instrument with picosecond laser excitation at 447 nm operating at 50 MHz. Laser power was kept below 0.1µW. Fluorescence emission was acquired at 690 nm with a bandwidth of 4 nm. In the case of PSI complexes, time-resolved fluorescence decay measurements were carried out using a femtosecond laser excitation at 440 nm operating at 80 MHz and a Streak Camera detection system, as reported in [228]. Fluorescence decay kinetics were obtained after integration over the whole emission spectrum and then fitted with exponential functions.

Supporting information

Figure S 2.5.1 *Phylogenetic tree of CVDE and CruP proteins. Phylogenetic tree was obtained by multiple alignment of protein sequences carrying a VDE lipocalin domain identified by InterPro (IPR010788). The units of branch length are residues substitution per site divided by the length of the sequence. Bootstrap values are reported in red*

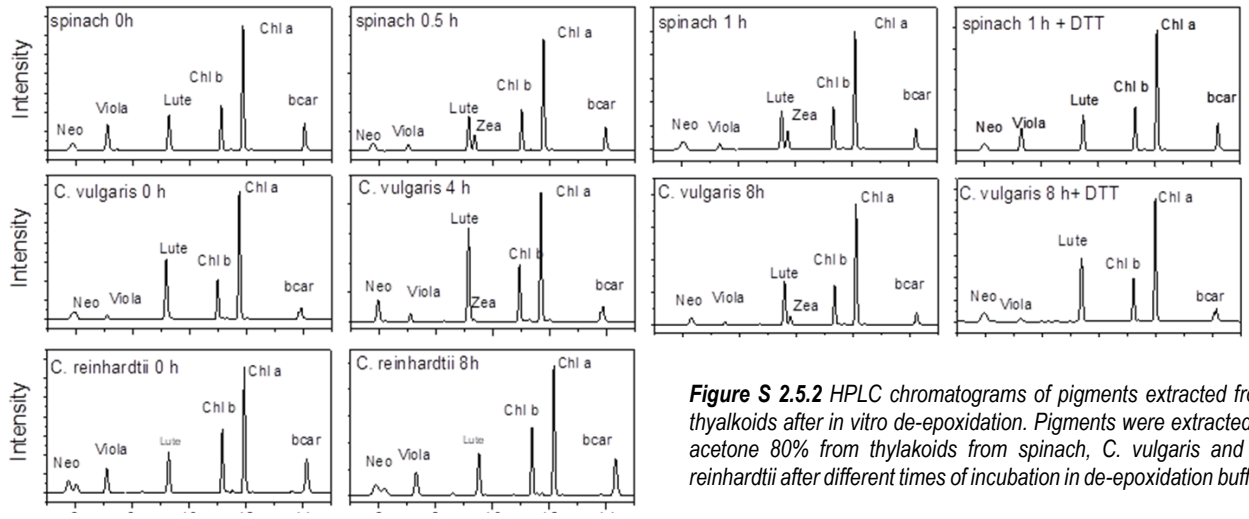

Figure S 2.5.2 *HPLC chromatograms of pigments extracted from thyalkoids after in vitro de-epoxidation. Pigments were extracted in acetone 80% from thylakoids from spinach, C. vulgaris and C. reinhardtii after different times of incubation in de-epoxidation buffer.*

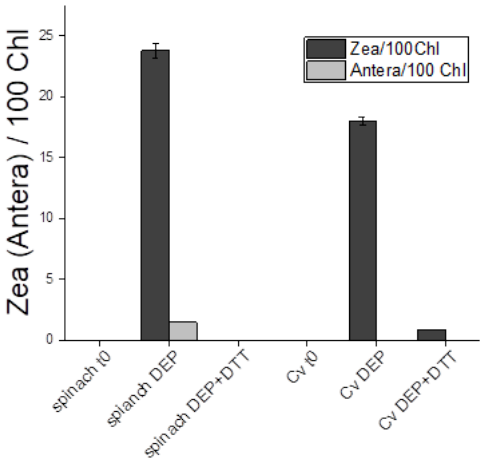

Figure S 2.5 3 *Zeaxanthin and anteraxanthin content in thylakoids after in vitro de-epoxidation Zeaxanthin and anteraxanthin content normalized to 100 chlorophylls in thylakoids isolated from spinach, C. vulgaris (C.v.) and C. reinhardtii (C.r.) before (t0) or after (DEP) 1 hours (spinach) or 8 hours (C.v. and C.r.) at pH 5.1 in presence of ascorbate in order to induce violaxanthin de-epoxidation.*

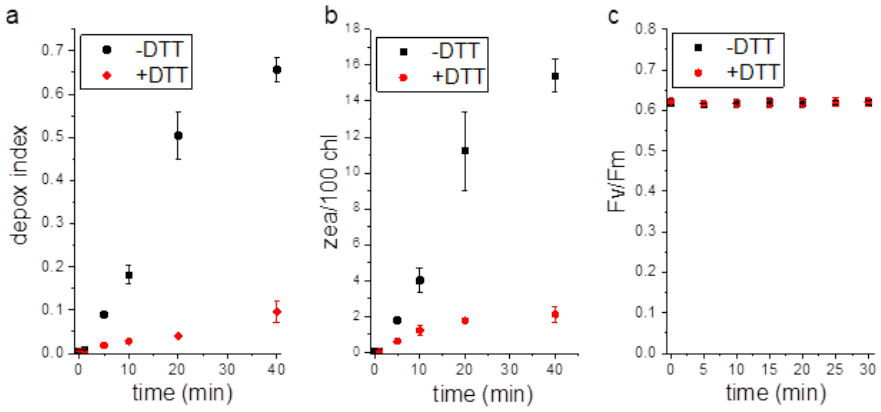

Figure S 2.5.4 *Effect of DTT on Chlorella vulgaris xanthophyll cycle and PSII fluorescence quantum yield. De-epoxidation index (a) and zeaxanthin content, normalized to 100 chlorophylls of C. vulgaris exposed to 2000 µmol photons m^{-2} s^{-1} light for up to 40'. (c) PSII fluorescence quantum yield (Fv/Fm) of dark-adapted C. vulgaris cells in presence or absence of DTT.*

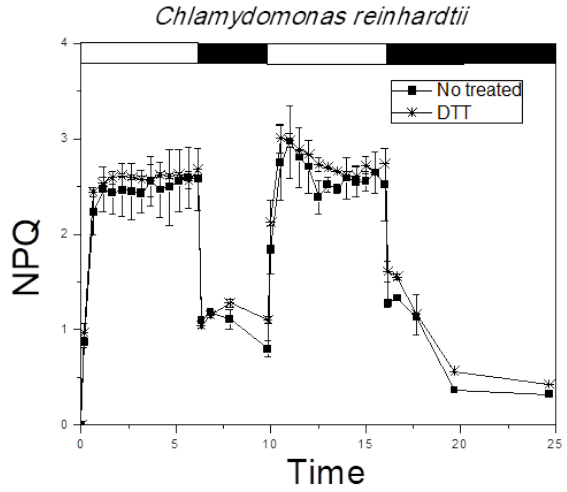

Figure S 2.5.5 *Effect of DTT on NPQ kinetics of Chlamydomonas reinhardtii. Two consecutive cycles of NPQ induction in C. reinhardtii cells acclimated to high light are reported. High light acclimated cells were used for this experiment since in C. reinhardtii high light acclimation is required for NPQ induction. An actinic light of 2000 µmol photons m^{-2} s^{-1} and a saturating light of 4000 µmol photons m^{-2} s^{-1} was applied for this measurement. Standard deviations are reported as error bars (n=3).*

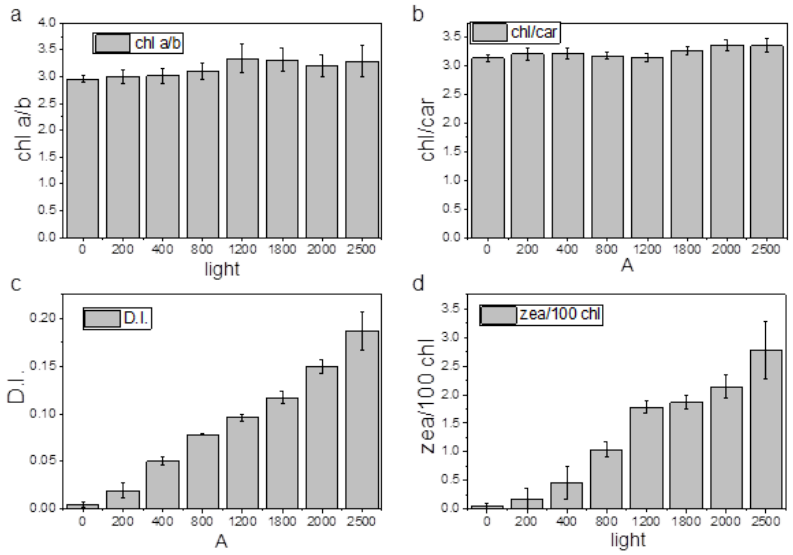

Figure S 2.5.6 *Pigment analysis on cells treated at different light intensities. HPLC analysis of pigments extracted from C. vulgaris cells dark adapted (T0) or treated for 6 minutes with different actinic lights (200, 400, 800, 1200, 1800, 2000 and 2500 µmol photons m^{-2} s^{-1}). (a) Chlorophyll (Chl) a/b ratio and (b) Chl/carotenoid (Car) ratio, (c) the de-epoxidation index (D.I.) calculated a (zeaxanthin + 0.5x antearaxanthin)/(violaxanthin+zeaxanthin +anteraxanthin) and (d) Zeaxanthin (Zea) /Car ratio. Errors bars are reported as standard deviation (n=3).*

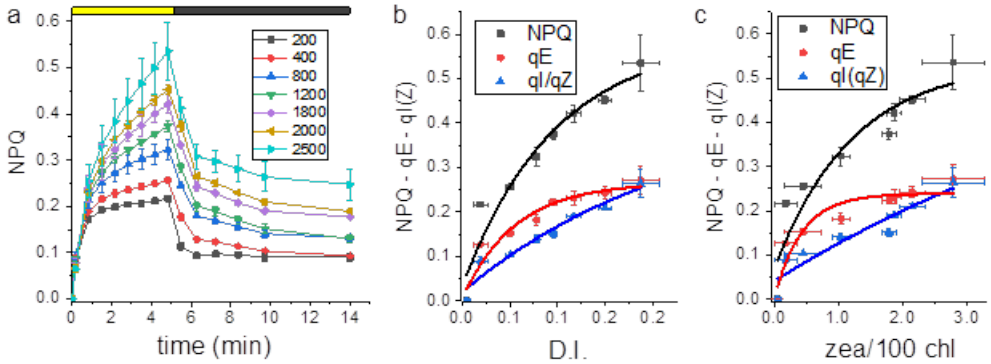

Figure S 2.5.7 *NPQ kinetics at different irradiances and their correlation with xanthophyll cycle. (a): NPQ induction curves measured by using an actinic light of 200, 400, 800, 1200, 1800, 2000 and 2500 µmol photons m^{-2} s^{-1}. (b, c): correlation of de-epoxidation index (b) zeaxanthin content normalized to 100 chlorophylls (c) with NPQ , qE, and qI(qZ). NPQ was measured at the end of the actinic light exposure, while its components qE was measured as the NPQ component decaying in two minute in the dark, and qI(qZ), measured as the residual NPQ component after 9 minutes of dark relaxation. Standard deviations are reported as error bars (n=3). de-epoxidation index (D.I.), measured as reported in Figure S4 at different light intensities.*

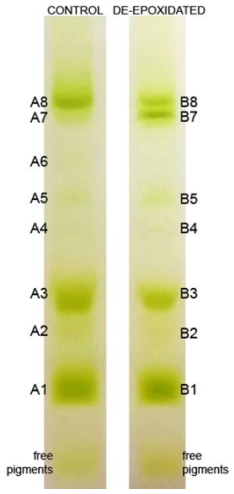

Figure S 2.5.8 *Native Deriphat-PAGE loaded with solubilized Chlorella vulgaris thylakoid membranes before and after in vitro de-epoxidation reaction. Isolated thylakoid membranes were loaded before and after in vitro de-epoxidation reaction in order to induce zeaxanthin accumulation. Thylakoid membranes were de-epoxidated as reported in Figure 3. The different protein bands retrieved were eluted from the acrylamide matrix and numbered as reported in the figure (A: control, B: de-epoxidated thylakoids).*

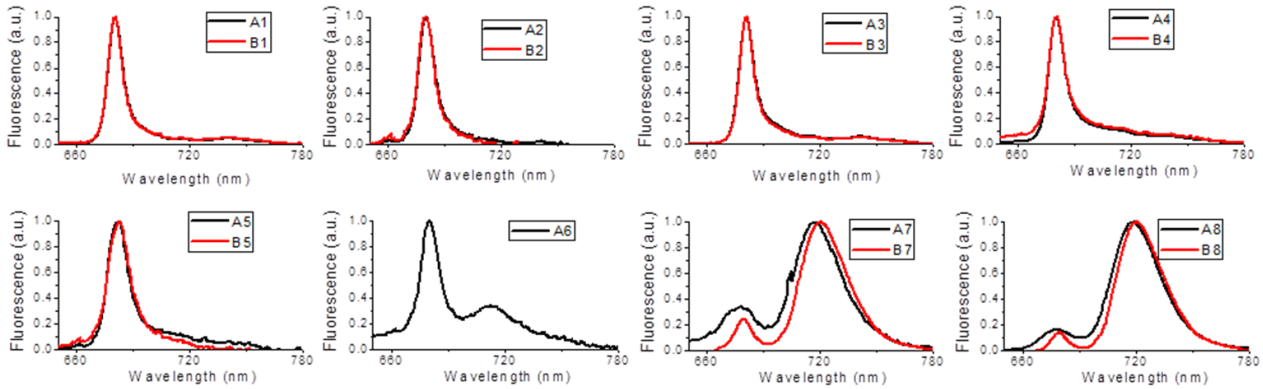

Figure S 2.5.9 *77K fluorescence emission of bands isolated from Deriphat-PAGE gel. 77K fluorescence emission spectra were measured with excitation at 475 nm on bands cut from Deriphat-PAGE gel as reported in Figure S5 and eluted from acrylamide matrix in Hepes 20mM pH 7.5, sucrose 0.1M and 0.03% α-dodecylmaltosyde. Fractions A1-8 and B1-8 were isolated from control or de-epoxidated thylakoids respectively. Fractions A1/B1, A2/B2, A3/B3 are respectively monomeric, dimeric and trimeric LHC; Fractions A4/B4 and A5/B5 are mainly composed by PSII core; A6 presents traces of PSI core, A7/B7 and A8/B8 are PSI complexes with different amount of LHCI, as previously reported in the case of C. reinhardtii.*

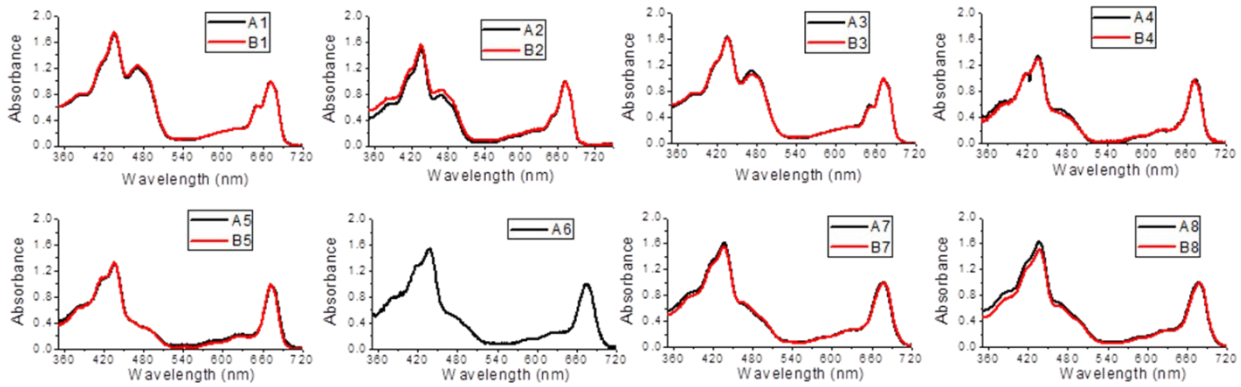

Figure S 2.5.10 *Absorption spectrum of bands isolated from Deriphat-PAGE gel. Absorption spectra in the visible region spectra were measured on bands cut from Deriphat-PAGE gel as reported in Figure S5 and eluted from acrylamide matrix in Hepes 20mM pH 7.5, sucrose 0.1M and 0.03% α-dodecylmaltosyde. Fractions A1-8 and B1-8 were isolated from control or de-epoxidated thylakoids respectively. Fractions A1/B1, A2/B2, A3/B3 are respectively monomeric, dimeric and trimeric LHC; Fractions A4/B4 and A5/B5 are mainly composed by PSII core; A6 presents traces of PSI core, A7/B7 and A8/B8 are PSI complexes with different amount of LHCI, as previously reported in the case of C. reinhardtii.*

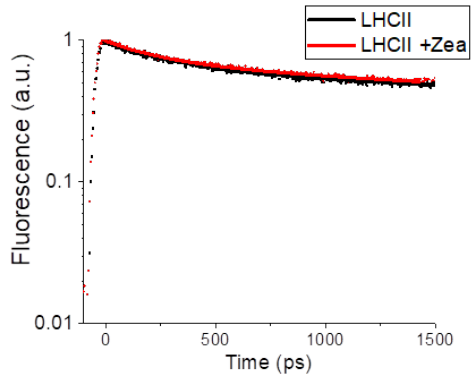

Figure S 2.5.11 *Fluorescence decay kinetics of LHCII complexes isolated from sucrose gradients. Fluorescence decay kinetics of LHCII complexes isolated from sucrose gradient loaded with solubilized thylakoid membranes isolated from C. vulgaris. LHCII+Zea sample was purified from thylakoid membranes which were previously de-epoxidated, Fluorescence decay kinetics were measured by Streak camera CCD in TR4 mode (0-2000ps scale).*

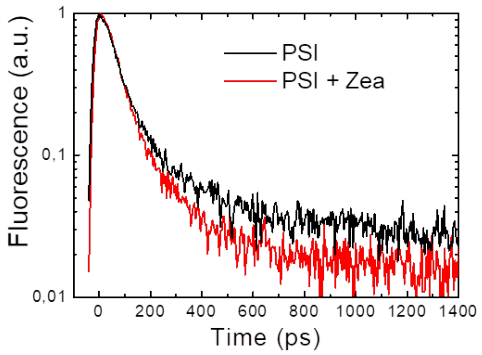

Figure S 2.5.12 *Fluorescence decay kinetics of PSI complexes in the ns timescale. Fluorescence decay kinetics of PSI complexes isolated from thylakoid membranes before (A8 in Deriphat-PAGE reported in Figure S5) and after (B8 in Deriphat-PAGE reported in Figure S5) in vitro de-epoxidation were measured by Streak camera CCD in TR4 mode (0-2000ps scale).*

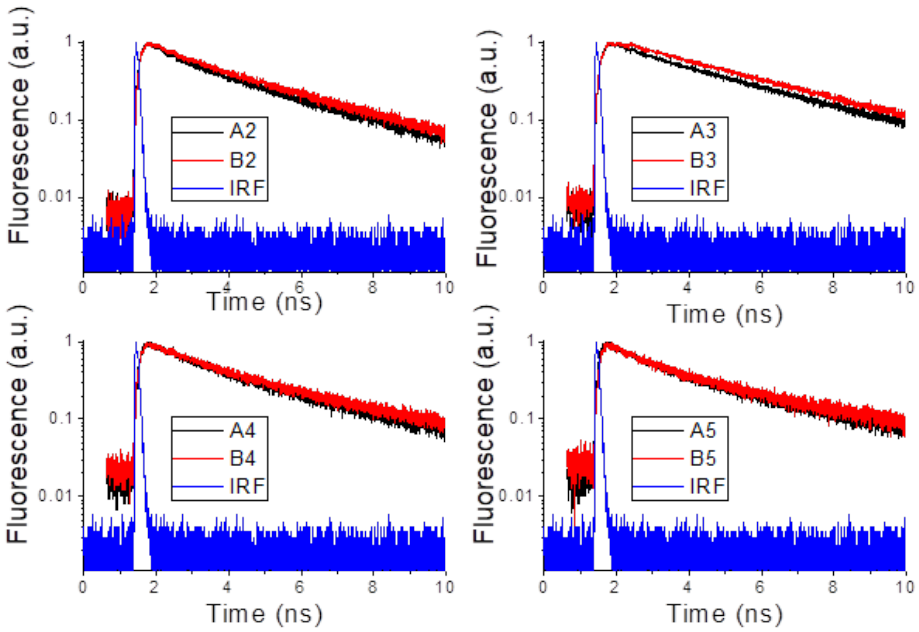

Figure S 2.5.13 *Fluorescence decay kinetics of A2/B2, A3/B3, A4/B4 and A5/B5 fractions isolated from Deriphat-PAGE gel. Fluorescence decay kinetics of A2/B2, A3/B3, A4/B4 and A5/B5 fractions eluted from Deriphat-PAGE reported in Figure S5 were measured by TCSPC. No traces of zeaxanthin were found in B2, B3, B4 and B5 fractions despite their isolation from de-epoxidated thylakoids.*

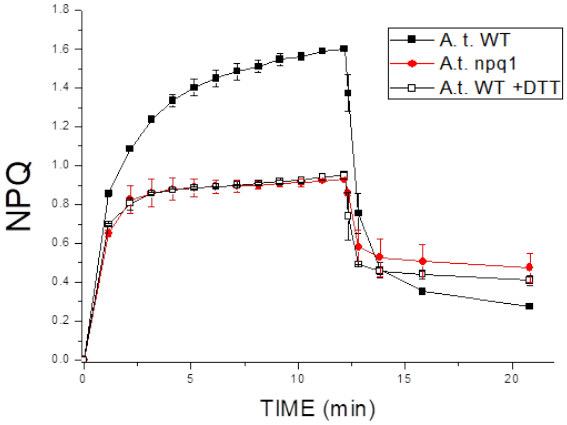

Figure S 2.5. 14 NPQ kinetics of Arabidopsis thaliana in presence or absence of zeaxanthin. NPQ induction of A. thaliana WT, npq1 and WT in presence of DTT are reported. npq1 is mutant on vde gene in A. thaliana. An actinic light of 1200 µmol photons m−2 s−1 and a saturating light of 4000µmol photons m−2 s−1 was applied for this measurement. Standard deviations are reported as error bars (n=3).

Species	VDE	VDR	cVDE	CruP
Auxenochlorella protothecoides	X	X	X	
Bathycoccus prasinos	X			X
Chlamydomonas eustigma		X	X	X
Chlamydomonas reinhardtii		X	X	X
Chlorella sorokiniana		X	X	X
Chlorella variabilis	X			
Coccomyxa subellipsoidea (strain C-169)	X		X	X
Gonium pectorale			X	X
Micractinium conductrix	X			X
Micromonas commoda (strain RCC299 / NOUM17 / CCMP2709)	X			
Micromonas pusilla (strain CCMP1545)	X			
Monoraphidium neglectum	X		X	X
Ostreococcus lucimarinus (strain CCE9901)	X			X
Ostreococcus tauri	X			X
Raphidocelis subcapitata	X		X	X
Tetradesmus obliquus	X	X	X	X
Volvox carteri f. *nagariensis*		X	X	X
Chlorella vulgaris	X		X	X

Table S 2.5.1 *Identification of VDE, VDR, CVDE or CruP in different Chlorophyta. The presence of plant-like VDE and/or CVDE was in different green algae was performed by BLAST search using as queries the protein or cDNA sequence of A. thaliana VDE or C. reinhardtii CVDE.*

	Chl	Chl a/b	Car	neo	viola	antera	lute	zea	b car	D.I.
A free pigments	100	4.20	33.19	2.02	2.44	n.d.	24.55	n.d.	4.18	0.00
A1	12	1.89	3.20	0.81	0.16	n.d.	2.18	n.d.	0.05	0.00
A2	14	2.48	2.15	0.33	0.19	n.d.	1.25	n.d.	0.39	0.00
A3	14	1.54	2.42	0.66	0.14	n.d.	1.62	n.d.	n.d.	0.00
A5	100	13.60	11.51	n.d.	0.81	n.d.	4.26	n.d.	6.44	0.00
A7	170	11.00	27.48	n.d.	2.64	n.d.	8.05	n.d.	16.79	0.00
A8	170	6.69	35.71	0.71	4.93	n.d.	15.79	n.d.	14.28	0.00
	Chl	**Chl a/b**	**Car**	**neo**	**viola**	**antera**	**lute**	**zea**	**b car**	**D.I.**
B free pigments	100	2.76	35.47	1.96	1.78	1.64	25.18	2.54	2.39	0.56
B1	12	1.91	3.49	0.98	0.06	n.d.	2.31	0.10	0.04	0.64
B2	14	2.23	3.05	0.70	0.14	n.d.	1.94	n.d.	0.26	0.00
B3	14	1.54	3.15	0.95	0.16	n.d.	2.05	n.d.	n.d.	0.00
B5	100	8.63	14.83	n.d.	0.41	n.d.	4.68	0.67	9.07	0.62
B7	170	5.40	29.03	n.d.	1.69	n.d.	10.22	1.19	15.91	0.41
B8	170	4.51	36.36	2.40	3.34	n.d.	14.93	1.73	13.96	0.34
	Chl	**Chl a/b**	**Car**	**neo**	**viola**	**antera**	**lute**	**zea**	**b car**	**D.I.**
LHCII	14	2.29	3.28	0.59	0.07	n.d.	2.56	n.d.	0.05	0.00
LHCII-ZEA	14	2.23	3.43	0.48	0.10	0.09	2.49	0.11	0.17	0.53

Table S 2.5.2 *HPLC analysis of isolated pigments binding complexes. Fractions isolated from Deriphat-PAGE loaded with solubilized control or in vitro de-epoxidated C. vulgaris thylakoids were analyzed by HPLC after pigment extraction by acetone 80%. LHCII isolated from sucrose gradient loaded with solubilized control or in vitro de-epoxidated C. vulgaris thylakoids are also reported indicated as LHCII (isolated from control thyalkoids) and LHCII+Zea (isolated from de-epoxidated thyalkoids. Chl: chlorophyll; Car: carotenoids; Neo: neoxanthin; viola: violaxanthin; lute: lutein; zea: zeaxanthin; b car: beta-carotene. Relative errors are below 15% for each value.*

	a1	τ1 (ps)	a2	τ2 (ps)	a3	τ3 (ps)	τav (ps)
A1	0.06	138.00	0.94	3070.00	n.d.	n.d.	2882.90
B1	0.05	121.00	0.95	3260.00	n.d.	n.d.	3094.53
A2	0.11	161.00	0.89	2820.00	n.d.	n.d.	2538.15
B2	0.08	136.00	0.92	2950.00	n.d.	n.d.	2726.18
A3	0.05	127.00	0.95	3220.00	n.d.	n.d.	3055.78
B3	0.03	57.60	0.97	3280.00	n.d.	n.d.	3194.96
A4	0.72	68.00	0.09	1110.00	0.18	3230.00	742.87
B4	0.74	61.20	0.10	1290.00	0.17	3610.00	771.44
A5	0.77	75.00	0.10	1290.00	0.13	3610.00	639.92
B5	0.73	75.00	0.11	1130.00	0.16	3790.00	785.26
A8	0.18	8.26	0.82	90.09	n.d.	n.d.	75.52
B8	0.34	11.60	0.66	76.57	n.d.	n.d.	54.22
LHCII	0.36	271.40	0.67	5146.98	n.d.	n.d.	3454.01
LHCII-Zea	0.32	273.57	0.64	5140.00	n.d.	n.d.	3508.58

Table S 2.5.3 *Fluorescence lifetimes of isolated pigments binding complexes. Fluorescence decay kinetics were fitted with 2 or 3 exponential functions. The amplitudes (a1-3) and time constant (t1-3) retrieved are reported with the average fluorescence lifetime (tAV) calculated as (A1*t1+A2*t2+A3*t3)/(A1+A2+A3)*

Primers used for *vde* transcript amplification from cDNA

Forward sequence (5' -3')	**Reverse sequence (5'-3')**
ATATAAAGCTTATGGCAGCTGCAGCACGC	ATATACTCGAGATCCATGGGCATGATGACTG

VDE transcript and protein sequences. Signal peptide is underlined.

>g7391.t1_protein

MQASRCTAAAVPAAPATNLPRCRRRVVRAAAARRPAASQQQRDADRQQEAQQPQQLGLTPLQKVATGAAGLLASAVLLTAPGSALAADT
AAVGTCLLQNCQAALAQCLTDVTCAENLVCLQLCNGRPDETECQIKCGDKYSDKAVETFTACAVSEKKCVPQRIDEDAYPVPPDSALDN
SFDLSNFQGRWYITAGLNPLFDTFDCQEHFFASPEPNKVFAKINWRIPMSDALTGDQDFIERSVMQKFVQEDPAKQPSVLVNKDNEFLN
YQDTWYVLAFKPDNYVFIYYRGQNDAWLGYGGATVYTRTSTLPREDIPELKAAAERAGLDWSKFTITNNSCPPHPPKAALPEKLRVAAV
RRTAQAEYELENDLRSFGRGFTVLEKDLSNKLRRTENTIVEDIKAVGQVEKKLEQTAGKAEKLIEKEVEEVEAAAARMIRRFEAEAKMG
PWINWIPKSWRPVIMPMD

>g7391.t1_transcript

ATGCAGGCCTCGAGGTGCACCGCAGCAGCCGTGCCAGCAGCCCCCGCCACAAACCTCCCGAGGTGCCGCCGGCGTGTGGTGCGGGCAGC
TGCAGCACGCCGCCCAGCCGCGTCTCAACAACAGCGCGATGCAGATAGGCAGCAGGAGGCACAACAGCCGCAGCAGCTGGGCCTGACCC
CACTGCAGAAGGTGGCAACTGGTGCGGCAGGCCTGCTAGCCTCTGCGGTCCTCCTCACGGCGCCTGGCTCAGCATTGGCGGCAGACACT
GCGGCTGTGGGCACGTGCCTGCTGCAAAACTGTCAAGCTGCGCTGGCCCAGTGCCTCACAGACGTCACCTGCGCGGAGAACCTGGTGTG
CCTGCAGCTGTGCAACGGCCGCCCAGACGAGACTGAGTGCCAGATCAAGTGTGGTGACAAGTATTCCGACAAGGCGGTGGAGACGTTCA
CTGCCTGCGCAGTCAGCGAGAAGAAGTGTGTCCCGCAGCGAATTGACGAGGATGCCTACCCCGTGCCACCAGACAGTGCACTTGACAAC
AGCTTCGATTTGTCGAACTTCCAGGGCCGCTGGTACATCACTGCTGGGCTAAACCCACTGTTCGACACATTCGACTGCCAGGAGCATTT
CTTTGCCAGCCCGGAACCAAACAAGGTGTTTGCCAAGATCAACTGGCGGATTCCCATGTCAGACGCTCTGACTGGGGATCAGGACTTCA
TTGAGCGGTCTGTGATGCAGAAGTTTGTGCAGGAGGACCCTGCCAAGCAGCCTTCTGTCCTAGTGAACAAGGACAACGAATTTTTGAAC
TACCAAGACACTTGGTATGTGCTAGCTTTCAAGCCTGACAACTACGTCTTCATCTACTATCGAGGCCAGAATGATGCGTGGCTGGGCTA
CGGCGGCGCTACTGTTTACACACGCACCTCGACCCTGCCTCGTGAGGACATTCCGGAGCTTAAGGCTGCAGCAGAGCGTGCGGGACTGG
ACTGGTCCAAGTTCACCATCACCAACAACAGCTGCCCACCTCACCCGCCCAAGGCAGCCCTGCCCGAGAAGCTGCGGGTGGCTGCGGTG
CGCCGTACTGCCCAGGCTGAATATGAGCTTGAGAACGATCTGCGCTCCTTTGGCCGAGGCTTCACCGTGCTAGAGAAGGATCTGTCAAA
TAAGCTGCGCCGCACTGAGAACACGATTGTGGAGGACATCAAGGCTGTGGGGCAGGTCGAAAAGAAGCTGGAGCAGACGGCGGGCAAGG
CAGAGAAGCTCATTGAGAAGGAGGTAGAAGAGGTGGAGGCAGCTGCGGCCCGCATGATTCGGCGCTTTGAGGCAGAGGCAAAGATGGGA
CCCTGGATCAACTGGATTCCCAAGAGCTGGCGGCCAGTCATCATGCCCATGGATTGA

2.6

Photosystem II antenna complexes CP26 and CP29 are essential for non-photochemical quenching in *Chlamydomonas reinhardtii*

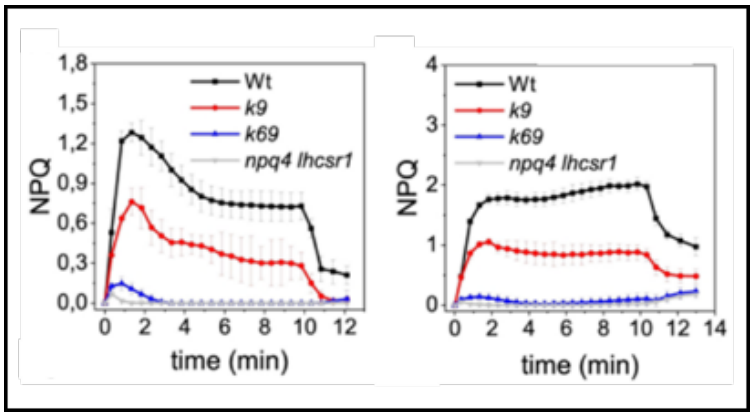

This section is based on the published article Cazzaniga, S. et al. Photosystem II antenna complexes CP26 and CP29 are essential for nonphotochemical quenching in Chlamydomonas reinhardtii. *Plant, cell & environment* 43, 496-509, doi:10.1111/pce.13680 (2020).

Author Contributions: Ballottari M. conceived the study, designed and supervised the experiments. Cazzaniga S. and Bellamoli F. performed or contributed to all the experiments herein reported with contribution of Perozeni F.. Kim M. Bellamoli F. Jeong J. and Lee S. generate CRISPR-Cas9 mutants coordinated by Jin ES. Cazzaniga S. Pompa A. Jin ES and Ballottare M. wrote the paper. All the authors discussed the results, contributed to data interpretation and commented on the manuscript.

Photosystem II antenna complexes CP26 and CP29 are essential for non-photochemical quenching in *Chlamydomonas reinhardtii*

Stefano Cazzaniga[1#], Minjae Kim[2#], Francesco Bellamoli[1#], Jooyoen Jeong[2], Sangmuk Lee[2], Federico Perozeni[1], Andrea Pompa[3,4], EonSeon Jin[2*], Matteo Ballottari[1*]

[1] Dipartimento di Biotecnologie, Università di Verona, Verona, Italy
[2] Department of Life Science, Hanyang University, Seoul, South Korea
[3] Dipartimento di Scienze Biomolecolari, Università degli studi di Urbino
[4] Istituto di Bioscienze e Biorisorse, Consiglio Nazionale delle Ricerche, Perugia, Italy

Abstract

Photosystems must balance between light harvesting to fuel the photosynthetic process for CO_2 fixation, and mitigating the risk of photodamage due to absorption of light energy in excess. Eukaryotic photosynthetic organisms evolved an array of pigment binding proteins called Light Harvesting Complexes (LHC) constituting the external antenna system in the Photosystems, where both light harvesting and activation of photoprotective mechanisms occur. In this work, the balancing role of CP29 and CP26 Photosystem II antenna subunits was investigated in *Chlamydomonas reinhardtii* using CRISPR–Cas9 technology to obtain single and double mutants depleted of monomeric antennas. Absence of CP26 and CP29 impaired both photosynthetic efficiency and photoprotection: excitation energy transfer from external antenna to reaction centre was reduced and state transitions were completely impaired. Moreover, differently from higher plants, Photosystem II monomeric antenna proteins resulted to be essential for photoprotective thermal dissipation of excitation energy by Non-photochemical quenching (NPQ).

Introduction

Photosynthesis is the process that provides the continuous energy income needed to maintain life on our planet [354]. The pigment binding complexes where light harvesting and primary photochemical reactions occur are named Photosystems. In oxygenic photosynthesis Photosystems I (PSI) and II (PSII) are similarly organized with a core complex, where the primary photochemical reactions occur, surrounded by an array of antennae[53]. Photosystems evolved their large array of antenna proteins in order to optimize light absorption within the visible region [219,355]. However, when too much excitation energy is absorbed and the electron transport chain becomes saturated, photodamage may occur with formation of reactive oxygen species (ROS)[356]. Within the photosynthetic machinery, due to the lower photosynthetic efficiency of PSII compared to PSI, PSII and its reaction centre have been indicated as the primary target of photoinhibition [357].

The peripheral antennae of PSII are in two different aggregation states: trimeric LHCII and monomeric CP29 (Lhcb4), CP26 (Lhcb5) and CP24 (Lhcb6), the latter found only in land plants [41,117]. All antenna proteins are pigment binding proteins encoded by nuclear genes and share a similar structure, with three trans-membrane domains and two amphipathic α-helices [15,30]. In *C. reinhardtii*, PSII supercomplex structure has been observed by electron microscopy, revealing two layers of antenna proteins surrounding a homodimeric core complex [358]: the inner layer is composed of CP29, CP26, and S-LHCII (S, strongly bound), forming with the core the C_2S_2 particle; the outer layer is made of M-LHCIIs (moderately bound) forming, together with C_2S_2, the $C_2S_2M_2$ complex. M-LHCIIs are expected to be connected to the core through CP29. In *C. reinhardtii,* an additional LHCII (N-LHCII) can be connected directly to the PSII core in the position occupied by CP24 in higher plants, forming the larger $C_2S_2M_2N_2$ complexes [358]. PSII antenna proteins are also involved in the state 1- state 2

transition [129] which regulates redistribution of excitation energy pressure between the two photosystems by disconnecting part of the LHCII trimers from PSII, which are then possibly transferred to PSI [63].

Photosynthetic organisms have evolved different mechanisms to protect themselves from harmful excess light, the fastest of which is the thermal dissipation of excitation energy by non-photochemical quenching (NPQ), a dissipative mechanism triggered by lumen acidification when the photosynthetic apparatus is saturated [91]. In *C. reinhardtii*, the LHCSR subunits (Light Harvesting Complex Stress Related) 1 and 3 are pigment binding LHC-like proteins that sense luminal pH and trigger NPQ switching to a dissipative state [101,225]. In vascular plants, LHCSR is substituted by the PSBS subunit which, however, does not bind pigments [108]. PSBS is also present in *C. reinhardtii* but it is accumulated only transiently upon high light or UV exposure and its contribution to NPQ is limited [116,211,359]. Both LHCSR proteins are overexpressed on prolonged high-light treatment but the molecular mechanisms at the base of NPQ and the interaction of LHCSR subunits with PSII supercomplexes are still not clear: LHCSR3 has been suggested to be bound to CP26 and/or to a LHCII trimer [230] suggesting a possible key role of monomeric subunits in the energy pathway from PSII to LHCSR subunits during NPQ induction. Moreover, it has been recently reported that phosphorylation of CP29 in *C. reinhardtii* is linked to LHCSR3 phosphorylation, being this process likely related to PSII assembly and repair in high light [360]. A knock-out mutant without monomeric subunits was obtained in *Arabidopsis thaliana,* showing only a slower NPQ induction [115,361]. In microalgae, only RNA interference mutants of *C. reinhardtii* with individual monomeric subunits knocked down are reported in literature, revealing a peculiar role of CP29 in state transitions [63], but the role on CP26 and CP29 in NPQ has never been investigated yet.

In this paper, we present the characterization of a *C. reinhardtii* double mutant, obtained with CRISPR–Cas9 technology, completely depleted of CP26 and CP29 subunits. This mutant presents reduced photosynthetic efficiency and impaired state transitions. Surprisingly, the lack of CP26 and CP29 completely abolishes NPQ induction even in presence of LHCSR1 and 3 subunits, implying that LHCSR needs the interaction with monomeric PSII antenna in order to perform its quenching function.

Results

Generation of *Chlamydomonas reinhardtii* mutants on monomeric CP26 and CP29 subunits

Monomeric PSII antenna mutants in *C. reinhardtii* were generated using CRISPR–Cas9 technology [289]. First, the cp29 gene (Cre17.g720250) was mutated by non-homologous end joining: two different sgRNA targets gave successful results leading to introduction of insertions or deletions (**Figure 2.6.1**, **Figure S 2.6.1**). The two selected mutant lines were named k9-1 and k9-2 (knock-out CP29 mutants). Thylakoid membrane polypeptides isolated from WT and k9 were separated on a denaturing gel (**Figure 2.6.1**). k9 mutants lacked the band corresponding to CP29 and the complete absence of the protein was confirmed by western blot analysis using a specific antibody (**Figure 2.6.1d**). The cp26 gene was subsequently targeted in WT and k9.2 strains: two lines selected (for hygromycin resistance) from WT background were named k6 mutants (for knock-out CP26), while the lines obtained from k9.2 background were named k69 (for knock-out CP26 CP29). SDS-PAGE and western blot analysis confirmed that both k6 and k69 mutants were completely depleted of CP26 (**Figure 2.6.1**). Surprisingly, both k6 and k69 lines also lacked the CP29 protein even if the gene was not targeted in k6 mutant strains (**Figure 2.6.1** and **Figure S 2.6.2**). In order to investigate if the absence of CP29 in k6 mutant was related to a transcriptional or post-transcriptional event, transcription profiles of lhcb4 and lhcb5 genes were investigated in WT and mutant lines. As reported in **Figure 2.6.1e** and **Figure S 2.6.3**, the transcription of cp29 and cp26 genes was not impaired in k6, k9 and k69 mutants compared to WT, suggesting that the absence of CP26 and CP29 accumulation was related to translation or post-translation events. Because k6 and k69 showed the same pattern of monomeric subunits and phenotype the following characterization was focused on k9 and k69 strains.

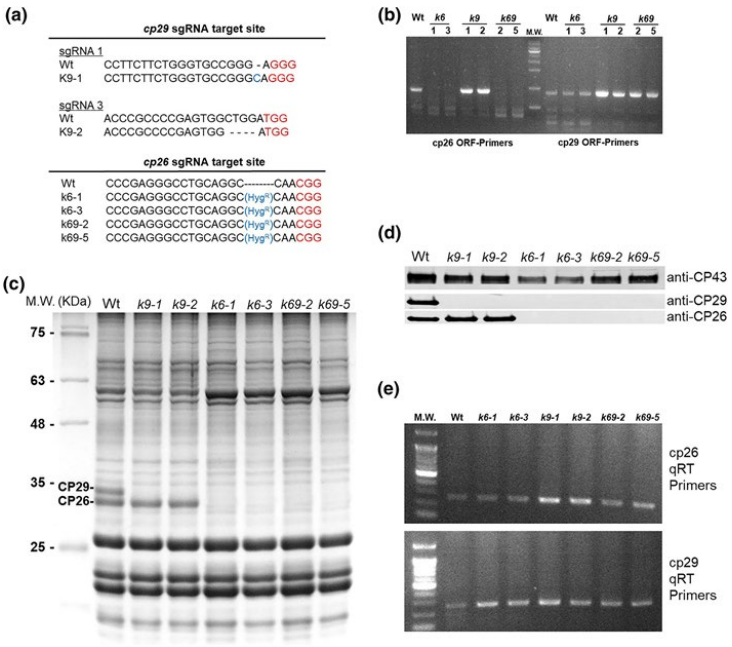

Figure 2.6.1 *CP26 and CP29 targeted gene disruption in Chlamydomonas reinhardtii by CRISPR/CAS9 genome editing. A, DNA sequence alignment of wild type (Wt) and mutants on cp26 (k6) and cp29 (k9) obtained by CRISPR/CAS9 genome editing. The 20-bp target sequence of sgRNA is reported before the red-colored PAM sequence. In the case of k9 mutant insertions (k9-1) or deletions were induced (k9-2) by non-homologous repair, while in the case of k6 mutant a CAS9 mediated hygromycin resistance cassette insertion was obtained in the target site. Double mutant k69 was obtained by hygromycin resistance cassette insertion in a k9 background. B, PCR amplification of cp26 and cp29 CDS sequences from Wt, k6, k9 and k69 cDNA. In the case of k6 and k69 mutants the cp26 CDS cannot be amplified due to hygromycin cassette insertion. C, SDS–PAGE analysis of Wt and mutant strains performed with the Tris-Tricine buffer system. 15 µg of Chl were loaded in each lane. Molecular weight (M.W.) markers are indicated on the left. CP26 and CP29 bands are marked. D, Immunoblot with specific antibodies directed against CP26 and CP29 on the same lanes of panel c. Immunoblot against CP43 was added as control of the loading. e, qRT-PCR on cp26 and cp29 genes in Wt and mutant strains. rack1 gene was used as control for qRT-PCR (see details in Supplementary information Figure S3).*

Pigments composition and stoichiometry of pigment-protein complexes

When grown in High salts (HS) medium [299] at 100 µmol m^{-2} s^{-1} , k9 and k69 showed a slight but not significant reduction of Chlorophyll (Chl) content compared to WT; the Chl/Carotenoid (Car) ratio was also similar in all the three genotypes (**Table 2.6.1**). Car composition determined by HPLC analysis was similar in the three genotypes with an increase of neoxanthin and violaxanthin and a decrease of β carotene in the k69 mutant (**Table 2.6.1**). In these growth conditions, no zeaxanthin accumulation was detected in any genotype. The Chl a/b ratio was remarkably affected by the absence of monomeric subunits, being reduced in k9 and even further decreased in k69 in comparison with WT (**Table 2.6.1** and **Figure 2.6.2a**), indicating a possible increment of PSII antenna proteins. In order to confirm this, we determined the relative amount of protein components of the photosynthetic apparatus by immunoblotting on LHCII, LHCI, CP43 (subunit of PSII core) and PSAA (subunit of PSI core) (**Figure 2.6.2b** and **Figure S 2.6.4**) [125]. Deletion of monomeric subunits had a strong effect on both PSII/PSI and LHCII/PSII ratios: in the k9 mutant there was a relative PSI increment of ~ 23% with respect to WT, while in the double mutant k69 the amount of PSI was more than doubled. The effect of CP26 and CP29 mutations on LHCII/PSII were even stronger: in k9, the LHCII amount was doubled while the k69 mutants showed a ~ 5-fold increase. The absence of CP26 and CP29 did not affect the PSI antenna since the LHCI/PSI ratio was the same as the WT. (**Figure 2.6.2b**and **Figure S 2.6.4**). The organization of pigment binding complexes was further analyzed by sucrose gradient upon solubilization of thylakoid membranes with dodecyl-α-d-maltoside (α-DM) (**Figure 2.6.2c**). Different green bands were resolved; from top to bottom the bands corresponded to LHC protein in monomeric state

Table 2.6.1 *Pigment content, Fv/Fm and PSII antenna size. All data were collected from cells grown in HS at 100 µmol photons m-2 s-1. PSII antenna size data are normalized to 1/T2/3 value of wild-type (Wt). Single carotenoid values are normalized to 100 chlorophylls. Data are expressed as mean ± SD. (n = 4). Values that are significantly different (Student's t-test, P < 0.05) from the Wt are marked with an asterisk (*). Data that are significantly different between k6 and k69 are marked with a circle (°). Chl: chlorophylls; car: carotenoids; neo: neoxanthin; viola: violaxanthin; anth: antheraxanthin; lute: lutein; zea: zeaxanthin; β-car: β-carotene.*

					Car/100 Chl					
	Chl, pg/cell	Chl a/b	Chl/Car	Fv/Fm	PSII Antenna Size, (au)	Neo	Viola	Anth	Lute	β-Car
Wt	1.55 ± 0.09	2.68 ± 0.03	2.92 ± 0.17	0.67 ± 0.07	100 ± 8	4.92 ± 0.05	4.79 ± 0.28	0.75 ± 0.35	15.26 ± 0.48	8.52 ± 0.10
k9	1.54 ± 0.17	2.34 ± 0.01*	2.91 ± 0.11	0.51 ± 0.09*	144 ± 25*	4.95 ± 0.01	5.43 ± 0.02*	0.61 ± 0.01	14.89 ± 0.02	8.49 ± 0.02
k69	1.41 ± 0.14	1.92 ± 0.10*,**	3.05 ± 0.06	0.43 ± 0.08*	258 ± 89*,**	5.83 ± 0.26*,**	6.56 ± 0.80*,**	0.29 ± 0.09*,**	14.0 ± 0.45*,**	6.11 ± 0.57*,**

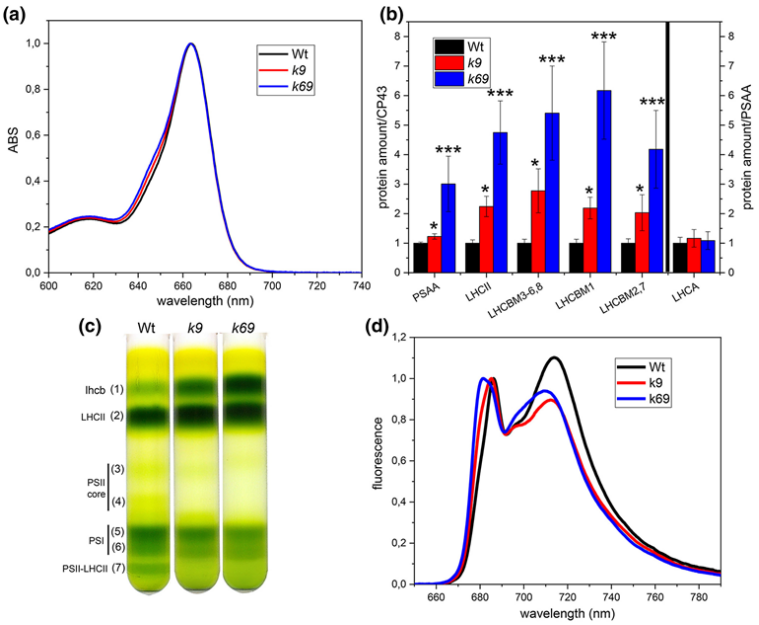

Figure 2.6.2 *Organization of thylakoid membranes. A, Absorption (Abs) spectra of acetone-extracted pigments from wild-type (Wt, black), k9 (red) and k69 (blue) cells. Spectra are normalized to the maximum of absorbance at 663 nm (Chl a absorption). The contribution of Chl b to absorption is visible at ~650 nm. B, Immunotitration of thylakoid proteins using specific antibodies against PSAA, LHCII and LHCA. Data were corrected for CP43 amount and normalized to Wt ratio. LHCA were corrected for PSAA amount. LHCII is shown as total amount (LHCII) or divided for three bands that are separated on the Tris-Tricine buffer system (see supplementary figure 2). Data are expressed as mean ± standard deviation (n = 4). Values that are significantly different (Student's t-test, P < 0.05) from the wild-type (WT) are marked with an asterisk (*). Date that are significantly different between k6 and k69 are marked with a circle (°). C, Sucrose density gradient fractionation of wild-type, k9 and k69 solubilized with 0.8% α-DM (dodecyl-D-maltopyranoside) Composition of the green bands is indicated on the left according to (Semchonok et al., 2017); Wt in black, k9 in grey and k69 in light grey. D, Low temperature fluorescence of Wt, k9 and k69 cells excited at 475 nm. Emission spectra are normalized at the maximum emission on PSII peak. All data were collected from algae grown in HS at 100 µmol photons m^{-2} s^{-1}.*

(fraction 1), trimeric LHCII (fraction 2), PSII core complex (fractions 3-4), PSI-LHCI (fractions 5-6) and PSII-LHCII supercomplex (fraction 7) [36]. In WT, the upper band contained CP29, CP26 and LHCII, monomerized by solubilization, while in k69 the band contained only the latter. The densitometry analysis of the band of the gradient confirmed the data from the immunotitration (**Figure S 2.6.5**) with an increment of the bands corresponding to antenna proteins (fractions 1 + 2) and a decrease of those corresponding to PSII core (fractions 5 + 6). The bands corresponding to PSII-LHCII supercomplex were absent in k9 and k69, indicating that in mutants these complexes were not assembled, or they were easily dissociated by solubilization.

The functional antenna size of PSII in WT and mutant strains was then determined by measuring fast chlorophyll florescence induction in presence of DCMU [362], being inversely proportional to the rise time. Mutants showed an antenna size increment of ~ 1.5-fold in k9 and 2.5-fold in the k69 double mutant with respect to WT (**Table 2.6.1** and **Figure S 2.6.6**), consistently with the increased LHCII content and decreased Chl a/b ratio measured in these strains.

Photosynthetic efficiency and state transition

Fluorescence induction analysis in dark-adapted cells [363] revealed a significant decrease of PSII (Fv/Fm) in mutants compared to WT (**Table 2.6.1**), suggesting that energy transfer from LHCII to PSII reaction center was less efficient in the absence of monomeric subunits. In particular, on a Chl basis a clear increase of F_0 was evident in the mutant strains (**Figure S 2.6.8**). Accordingly, 77K fluorescence emission spectra (**Figure 2.6.1d**) revealed a blue shift in the first peak from 686 nm in WT to 681 in k69 mutant, with a 680 nm shoulder evident also in k9 mutant: this 681 nm peak corresponds to light harvesting antennae unable to transmit their energy to PSII [364]. In order to evaluate how this defective connection affects photosynthetic complexes, microalgae were illuminated at different light intensities and PSII operating efficiency (ΦPSII), electron transport rate (ETR), and photochemical quenching (1-qL) were recorded (**Figure 2.6.3a-c**). Double mutant k69 showed a reduction of ΦPSII and ETR at all the lights tested; the single mutant k9 showed a reduction of these parameters with readings comprised between the WT and the double mutant values. The Q_A redox state of the three genotypes was similar after 20 minutes of illumination at all the lights tested. To further investigate the functional properties of the photosynthetic machinery in the monomeric antenna mutants, the light-saturation curve of photosynthesis, monitored as oxygen evolution, was measured on WT and mutant strains (**Figure 2.6.3d**). The rate of oxygen release was lower in the two mutants compared to WT at all light intensities tested and the slope of light saturation curve initial linear increase

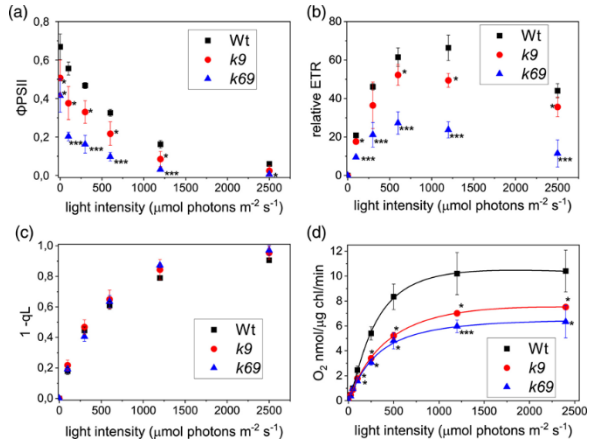

Figure 2.6.3 *Characterization of the photosynthetic electron flow. Dependence of the PSII operating efficiency (ΦPSII, A), relative electron transport rate (ETR, B), 1-qL (Estimates the fraction of PSII centres with reduced QA, C) and photosynthetic O2 evolution (D) on actinic light intensity for wild-type (Wt, black), k9 (red) and k69 (blue). Net photosynthetic rate data were fitted with Hill equation. Data are expressed as mean ± SD. (n >3). Values that are significantly different (Student's t-test, P < 0.05) from Wt are marked with an asterisk (*). Data that are significantly different between k6 and k69 are marked with a circle (°). All data were collected from algae grown in HS at 100 µmol photons m-2 s-1.*

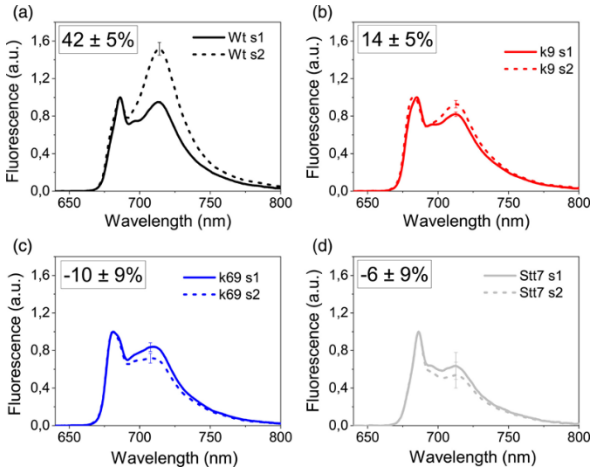

Figure 2.6.4 *State transitions. Low temperature fluorescence emission spectra of the cells of wild-type (Wt, A), k9 (B), k69 (C) and stt7 (D) after induction of state 1 (s1, solid line) or state 2 (s2, dashed line). The excitation wavelength was 475 nm and spectra are normalized to the maximum in PSII emission. Error bars are indicated on PSI maximum emission (n=4). The inset shows the estimation of state transition (see Materials and Methods section for details).*

was reduced (**Table S 2.6.1**). These data confirmed that the quantum yield of photosynthetic apparatus is impaired in these genotypes, especially in double mutant k69. Dark respiration was instead not affected by the absence of CP26 and CP29.

The roles of CP26 and CP29 in state transitions were then investigated by inducing state 1 and state 2 as previously described [365] using the stt7 mutant, unable to perform state transitions, as control [258]. In the WT in state I, fluorescence on PSII (max at 685 nm) and PSI (max at 714 nm) had similar intensities; when state II was induced, the fluorescence on PSI increased compared to the PSII value. The stt7 mutant was not able to increase the PSI fluorescence in state II. PSI fluorescence change in the two states in WT was 42 ± 5%: k69 double mutant was unable to perform state transitions as in the case of the negative control, stt7 mutant. Single mutant k9 retained a small fraction of state transitions but the mechanism was hampered (14 ± 5%) compared to WT. The defects in state transitions observed in the k9 and k69 mutant strains were not related to a different accumulation of the phosphorylating enzyme STT7, which was similarly accumulated in mutant strains compared to Wt (**Figure S 2.6.7**). The treatment inducing state II in WT caused in k9 mutant a shift of PSII emission from 686 to 681 nm, indicating that in k9 mutant, when state transitions are induced, LHCII detach from PSII complex but only a part of it is able to shift to PSI. In state II the shape of PSII emission was identical to k69 double mutant with a peak at 681 nm, suggesting that most of the LHCII trimers were already disconnected from PSII in both state I and II.

Non-Photochemical Quenching

The specific role of different PSII antenna in NPQ mechanism has long been debated [66,68,115,361]. We thus investigated the ability of WT, k9 and k69 to undergo quenching of Chl fluorescence upon exposure to excess light. *C. reinhardtii* needs to be adapted to high light conditions to fully activate NPQ mechanism; for this reason, WT and mutant strains were grown for 2 weeks at 500 µmol photons m^{-2} s^{-1} in autotrophy. After adaptation to high light, reduced Chl/cell and Chl/Car ratios were evident with no significant difference between WT and mutant strains (**Table S 2.6.2**). In the WT, the Chl *a* /*b* ratio was similar in the two growth condition (2.68 in low light vs 2.70 in high light) while in k9 and k69 a notable increase of Chl *a*/*b* ratio was measured: 1.92 in low light vs 2.48 in high light for k69 and 2.34 vs 2.55 for k9. This indicates that k9 and k69 mutants, in conditions of excess light, decrease their antenna content to a level similar to WT. As reported in **Table S 2.6.3** the Fv/Fm values of high light acclimated WT and mutant strain were consistent with the values

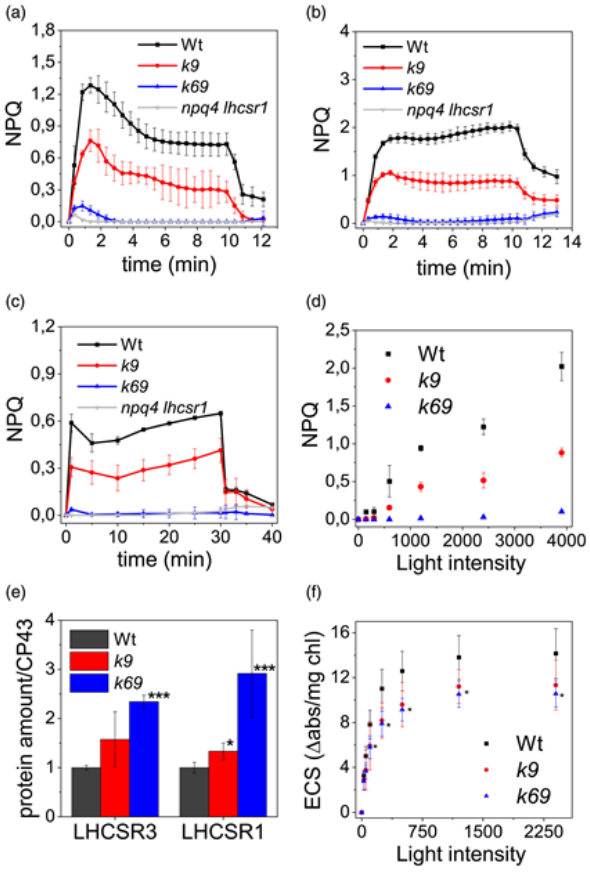

Figure 2.6.5 *Non photochemical quenching, LHCSR subunits accumulation and proton transport. Measurment of NPQ kinetic on wild-type (Wt, black), k9 (red), k69 (blue) and npq4 lhcsr1 (grey) cells using actinic lights of 1200 µmol photons $m^{-2}s^{-1}$(A) and 3900 µmol photons $m^{-2}s^{-1}$(B) for 10 minutes of illumination. (C) NPQ kinetic using actinic lights of 1200 µmol photons $m^{-2}s^{-1}$ for 30 minutes. (D) NPQ value after ten minutes of illumination at different actinic light intesities. (E) LHCSR and CP43 amounts were quantified by immunotitration. LHCSR/CP43 ratios were normalized to the Wt value. (F) Estimation of total proton motive force upon exposure to different light intensities, measured as electrochromic shift of carotenoid absorption spectrum (ECS). Data are expressed as mean ± SD (n=4). Values that are significantly different (Student's t-test, P < 0.05) from Wt are marked with an asterisk (*). Date that are significantly different between k6 and k69 are marked with a circle (°).*

observed in low light acclimated ones, demonstrating the presence of active PSII even when samples were acclimated to high irradiance. **Figure 2.6.5** shows the NPQ of the three genotypes: k9 mutant showed a halved NPQ value compared to WT while surprisingly k69 double mutant showed no NPQ like the *npq4 lhsr1* mutant, the only difference being that in the first minute k69 presented a transient NPQ rise (**Figure 2.6.5a**, **Figure S 2.6.9**). Even when NPQ induction was tested with longer illumination times or at higher actinic light (**Figure 2.6.5b-c**), the double mutant was still unable to activate NPQ while the k9 mutant was characterized by an intermediate phenotype (**Figure 2.6.5d**).

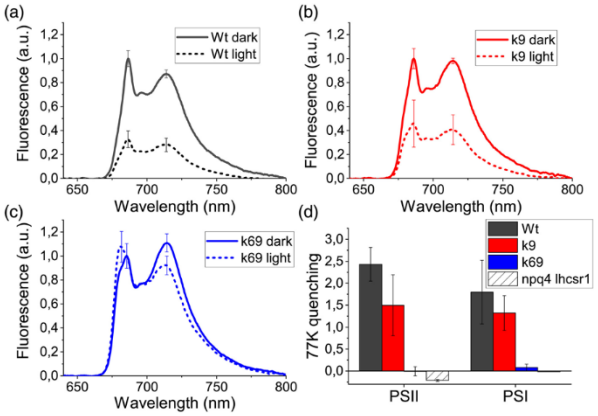

Figure 2.6.6 *Measurement of Quenching 77K Fluorescence Emission Spectroscopy. Low temperature fluorescence emission spectra of wild-type (A), k9 (B), k69 (C) dark adapted (dark) or illuminated for 10 minutes at 1200 µmol photons $m^{-2}s^{-1}$ (light) normalized to GFP signal (see material and methods for details). Cells were excited at 475 nm. (D) Calculated PSII and PSI quenching from the Gaussians used for fitting the two peaks according to the formula (ADark − Alight)/Alight, where ADark and Alight are, respectively, the amplitude of fuorescence emission in the dark and after illumination. Data are expressed as mean ± SD (n=4).*

The activation of NPQ in *C. reinhardtii* depends on lumen acidification and on accumulation of LHCSR proteins: we verified that both of these mechanisms were still active in mutants. LHCSR1 and LHCSR3 were present in mutants and their abundance, with respect to PSII core, was even higher than in WT (**Figure 2.6.5** and **Figure S 2.6.10**). The generation of an electrochemical proton gradient across thylakoid membranes was assessed using electrochromic shift (ECS)-induced absorbance changes at 520 nm (**Figure 2.6.5f**) [366,367]. The ECS, measured at the different light intensities, was similar between WT and k9 and only slightly reduced in the double mutant k69. Since LHCSR proteins were present and lumen acidification is not dramatically reduced, changes in NPQ activity are expected to reflect mainly an altered efficiency of quenching reactions in absence of CP29 and CP26. To confirm the absence of quenching in the monomeric antenna double mutant, NPQ induction was assessed with an alternative method, more specifically by looking at low temperature (77K) fluorescence prior to or at the end of actinic illumination using the Green Fluorescent Protein (GFP) as an internal standard for fluorescence emission spectra normalization [225] (**Figure 2.6.6**). 77K fluorescence also allowed the determination of PSI quenching, not detectable at room temperature with PAM measurement. In WT and k9 mutant, upon illumination, the amplitude of the fluorescence spectra decreased involving both PSII

and PSI components. In k69 double mutant PSII fluorescence emission did not decrease, while only a minor reduction was detected on PSI peak at ~710 nm. Deconvolution of the 77K fluorescence emission spectra with Gaussian functions allowed to distinctly evaluate the quenching on PSII and PSI (**Figure 2.6.6d**, **Figure S 2.6. 11**). This analysis confirmed the quenching of both PSII and PSI in WT and k9 while there was no significant quenching in the k69 double mutant, neither for PSII nor for PSI. These data point out that in *C. reinhardtii*, even if LHCSR subunits are present, NPQ of PSI and PSII cannot be activated in the absence of both CP26 and CP29.

Discussion

C. reinhardtii cp29 and cp26 genes were targeted by CRISPR–Cas9 technology to obtain mutants deprived of one or both PSII monomeric antenna subunits. The first surprising result in the characterization of these mutants was the phenotype of k6 lines, lacking not only CP26 but also CP29 subunit (Figure 1). Eight distinct k6 lines were analyzed and all confirmed that the deletion of CP26 also caused the loss of CP29, while the transcription of cp29 gene was not affected (Figure 1). These results imply that the loss of CP29 in k6 lines was related to translational or post-translational events: likely the removal of CP26 decreased CP29 stability in the PSII supercomplexes causing CP29 degradation. The inner layer of PSII antenna is composed of CP29, CP26, and S-LHCII, forming with the core the C_2S_2 particle [61]: the absence of CP26 could weaken the binding of S-LHCII to the core and the absence of this trimer could thereby destabilise the CP29 connection to the core. An analogue effect was noted for CP24 in higher plants, where CP29 knock-out plants lacked also CP24: CP24 and CP29 co-operate in binding M-LHCII (moderately bound) to the core, forming the $C_2S_2M_2$ complex [62]. The fact that CP26 was still present in k9 mutant could indicate that CP26 could, by itself, maintain a stable connection between S-LHCII and the core even in the absence of CP29. Alternatively, since CP26 is in an external position in the PSII supercomplex [36], it could be stabilized by the interaction with antennas of interacting neighbour PSII complexes.

The increase in F_0 and the blue-shift observed in the first peak of 77K fluorescence emission spectra indicate that, in the absence of CP26 and CP29, LHCII trimers are badly connected to PSII core and a larger fraction of absorbed energy is lost as fluorescence in the mutant instead of being efficiently harvested for photochemistry as already observed for monomeric antenna mutants in higher plants [62,361,368]. The defective connection of the PSII antenna in the mutant was also highlighted by the separation of photosynthetic complexes on a sucrose gradient, where the lower band, corresponding to PSII supercomplex, was essentially absent in the k9 and k69 mutants (**Figure 2.6.2**).

Both k9 and k69 mutants present an increased LHCII content and thus an increased functional antenna size of PSII: in the absence of monomeric subunits located at the interface between LHCII-M and LHCII-S, the excitation energy transfer from LHCII to PSII core is likely to be reduced, stimulating the partial compensatory increase of LHCII antenna amount. This is similar to what has been observed in plants in limiting light conditions, where LHCII accumulation is increased [369]. However, this strategy was only partially successful in the absence of CP29 and CP26: k69 mutant showed a ~5-fold increase in LHCII/PSII stoichiometry, but the functional antenna size was only increased by~ 2-fold with respect to WT. Moreover, it is worth to note that the functional antenna size of k9 and k69 might be overestimated as a consequence of the increased F_0 observed in these strains [362]. These findings thus demonstrate that in absence of CP26 and CP29 a significant fraction of trimers was not energetically coupled with PSII. Monomeric antenna proteins have thus a key role in *C. reinhardtii* in controlling excitation energy transfer from LHCII to the reaction center, as previously reported in the case of higher plants [219,361]. Values of PSII operating efficiency, relative ETR, ECS and oxygen evolution were lower at all light intensities tested: the absence of CP29 or both CP26 and CP29 caused a partial reduction of photosynthetic efficiency which could not be restored by the increased content of LHCII (**Figure 2.6.3**). Previous work showed that CP29 is involved also in state transitions [63] and more specifically in the docking of LHCII to PSI [365,370]. The results herein reported demonstrate that in *C. reinhardtii* both CP26 and CP29 are involved in state transitions [63], with a no-state transitions phenotype for the k69 mutant. Indeed, it has been shown that both subunits in state II condition are

phosphorylated and likely bind to PSI with LHCII trimers upon state 2 induction [371]. The results herein presented confirm the important role of monomeric antenna subunits in light harvesting and in preserving PSII photosynthetic efficiency. Similar evidence have already been reported in *A. thaliana* [115,361], even if the effects were more extreme in *C. reinhardtii* with respect to higher plant. The stronger difference observed when comparing *C. reinhardtii* and *A. thaliana* mutants depleted of monomeric CP26 and CP29 subunits is the NPQ phenotype. In an *A. thaliana* mutant without monomeric antennae, NPQ activation was slower in dark-to-light transition but after a few minutes of illumination the quenching was identical to WT [115,361]. In the case of *C. reinhardtii*, in the absence of CP29, an almost halved NPQ phenotype was detected, while the double mutant k69 presented a no-NPQ phenotype even after 30 minutes of illumination at high light intensity (**Figure 2.6.5**). In *C. reinhardtii* NPQ is thus totally dependent on the presence of PSII monomeric antenna subunits. The NPQ phenotype observed in k9 and k69 strains is not related to a different accumulation of LHCSR subunits, the NPQ triggers, because these subunits were rather increased in the absence of CP26 and CP29. Moreover, the absence of NPQ could not be due to a different LHCSR/antenna stoichiometry because in high light adapted cells, the difference in Chl *a*/*b* ratio between WT and k69 was only ~ 10%. k69 mutants exhibited also an impairment in state transitions induction and a slight reduction of the amount of zeaxanthin accumulated after two weeks in high light (**Table S 2.6.2**). However, these differences cannot be responsible for the no NPQ phenotype observed in absence of CP26 and CP29 subunits: both *stt7* and *npq1* mutants, impaired in state transitions and zeaxanthin accumulation, respectively, were reported with a similar NPQ compared to WT [203,225,262]. k69 mutant has reduced electron transport rates, oxygen evolution and proton gradient generation, but these alterations could eventually explain a slower kinetic of NPQ activation, but not its complete absence after prolonged illumination [361]. Besides, the highest actinic light used to induce NPQ was at least three times higher than the intensity needed to saturate photosynthesis, according to the oxygen evolution curves reported in **Figure 2.6.3**. The complete absence of NPQ in the absence of CP26 and CP29 is thus related to a specific role of monomeric subunits in the mechanism of NPQ and/or their interaction with LHCSR subunits. The NPQ phenotype in k9 and k69 mutant suggests that LHCSR subunits need to interact with CP26 and CP29 to act as quenchers upon NPQ induction, even if it could be excluded that CP29 and/or CP26 might be activated as quenchers themselves by LHCSR when it is protonated. It has been suggested that CP26 and a LHCII trimers are the docking sites of LHCSR3 on PSII. Our results demonstrate that in absence of CP29 a strong reduction of NPQ is evident, suggesting a direct interaction between LHCSR subunit and CP29, or an excitation energy transfer from CP29 to LHCSR subunits through a LHCII trimer. In absence of both CP26 and CP29 the NPQ induction is impaired demonstrating that the interaction between LHCSR3 and LHCII trimers is not sufficient to induce NPQ. Since we could not obtain a single mutant only without CP26, it is not possible to confirm if the NPQ of the double mutant was due to the absence of both subunits or to the absence of CP26 exclusively. Additional work is required to investigate the specific role of CP26. Considering the destabilization of PSII-LHCII supercomplexes in the absence of CP26 and CP29, an alternative possibility explaining the NPQ phenotype of k9 and k69 strains is an indirect role of CP26 and CP29, which absence might destabilize some other PSII subunits important for LHCSR1/3 binding as quenching activity, as reported in the case of PSBR [265].

Recent reports have pointed out that LHCSR also acts as quencher of PSI through the associated LHCII antennas [210,225]: this quenching component was also absent in k69. Considering that both CP26 and CP29 are involved in LHCII detachment from PSII and its migration toward PSI, it is possible that LHCSR-dependent quenching of LHCII, when detached from PSII and/or connected to PSI, may be also related to LHCSR interaction with monomeric antennas. Recently, a megacomplex composed by PSII, PSI, PSBS and LHCSR was reported in the case of *Physcomitrella patens* [372]: the formation of such megacomplexes in *C. reinhardtii* and their possible role in PSI quenching needs to be investigated by additional work. The specific role of CP26 and CP29 in state transitions and NPQ induction herein described reveals a strong difference in the function of monomeric antenna proteins among *A.*

thaliana and *C. reinhardtii*. In plant monomeric antenna are not essential for NPQ ,and their absence does not abolish state transitions [115,361], while in the latter both adaptive mechanisms require the presence of CP26 and/or CP29.

In conclusion, the data herein reported expands the understanding of the divergence between green algae and higher plants of light harvesting and photoprotection mechanisms. This could be the base for further research work to tune and increase microalgae biomass productivity to be used as food or energy source. Any effort toward microalgae domestication should likely avoid altering monomeric antenna subunits for their essential role in light conversion efficiency and photoprotective mechanisms.

Materials and methods

Strains and culture conditions

C. reinhardtii WT (CC503) and mutant strains were grown at 24°C in high salts (HS) medium [299] on a rotary shaker in Erlenmeyer flasks under continuous illumination with white LED light at 100 µmol photons m^{-2} s^{-1}. High light acclimation was induced by growing cells for 2 weeks at 500 µmol photons m^{-2} s^{-1} in HS.

Generation of Chlamydomonas reinhardtii mutants by CRISPR-CAS9 genome editing

Delivery of the DNA-free CRISPR-Cas9 RNP complex into cell was performed according to[289] and [373] with a few modifications. In brief, Cas9 protein (100 µg) (ToolGen, South Korea) and in vitro transcribed sgRNA (70 µg) which was synthesized by using GeneArt™ Precision gRNA Synthesis Kit following the manufacturer's protocol (Thermofisher, MA, USA) were mixed to form the RNP complex. The premixed RNP complex with and / or without *aph7* DNA cassette was introduced to the cells by Biorad Gene Pulser Xcell™ Electroporation system. (The *aph7* gene was prepared by PCR amplification from pChlamy3 vector with specific primer sets (F: ATGATTCCGCTCCGTGTAAATG, R: AGTACCATCAACTGACGTTACATTC).) After CRISPR-Cas9 transformation, cells were incubated in TAP liquid medium supplemented with 40 mM sucrose for 12 h and harvested for genotype characterization, or immediately diluted (2 × 10^3 cells) and plated on TAP medium containing 1.5% agar to obtain single colonies. In the case of *k9* mutant strains the colonies were screened by Fv/Fm fluorescence signal using a Walz Imaging PAM System (M-series). For the selection of CRISPR-Cas9 mediated antibiotic resistance knock-in derived mutants, cells were plated on TAP medium with hygromycin (25 µg/ml). Putative mutants screened were further analyzed by Sanger sequencing to confirm the indel mutations or antibiotic resistance insertion. In the case of knock-in mutants single insertion events were confirmed by Southern blot analysis.

Isolation of genomic DNA and complementary DNA preparation and quantitative reverse transcription PCR

Genomic DNA was extracted from *C. reinhardtii* using a protocol modified from [374]. Genomic DNA (20 µg) was digested with different restriction enzymes (NcoI and KpnI, TaKaRa, Kusatsu, Japan). The fragments were separated on a 0.8% agarose gel, transferred onto a positively charged nylon membrane (Hybond-N+, GE Healthcare, Chicago, IL, USA), and cross-linked using shortwave ultraviolet light (254 nm). The probe was designed to cover 467 bp of the Hygromycin resistance gene in pChlamy3 vector and was amplified from genomic DNA by PCR with the forward primer 5'-ATGATTCCTACGCGAGCCTG-3' and reverse primer 5'-ATCCGGCTCATCACCAGGTA-3'. The amplified probe was labeled with alkaline phosphatase using the Gene Images AlkPhos Direct Labeling and Detection System kit (GE Healthcare, Chicago, IL, USA). Labeling, hybridization, washing, and signal detection were conducted according to the manufacturer's protocol. Total RNA was extracted from cells in the exponential phase with RNeasy Plant Mini Kit (Qiagen, Hilden, Germany). Complementary DNA (cDNA) was synthesized from total RNA by using 2x reverse transcription master premix (ELPiS Biotech, Daejeon, Korea) and amplified using SYBR premix (TaKaRa, Kusatsu, Japan) in a Thermal Cycler Dice Real Time System TP 8200 (TaKaRa, Kusatsu, Japan). The gene for the 'Receptor For Activated C Kinase 1 (RACK1)' was used as a reference and was amplified with the forward

primer 5'-GGCTGGGACAAGATGGTCAA-3' and reverse primer 5'-GAGAAGCACAGGCAGTGGAT-3'.

Membrane preparation and fractionation

Thylakoid membranes were isolated as previously described [109]. Fractionation of pigment–protein complexes were performed starting from thylakoid membranes concentrated at0.5 mg/ml of Chls, solubilized with 0.8% α-DM and 10 mM HEPES, pH 7.8. Solubilized samples were then fractionated by ultracentrifugation in a 0.1–1 M sucrose gradient containing 0.06% α-DM and 10 mM HEPES, pH 7.8 (22 h at 280,000 g, 4 °C).

SDS-PAGE Electrophoresis and Immunoblotting

SDS–PAGE analysis was performed using the Tris-Tricine buffer system [232] followed by Coomassie blue staining. For immunotitration, thylakoid samples were loaded for each sample and electro-blotted on nitrocellulose membranes, then proteins were quantified with an alkaline phosphatase-conjugated antibody system. αCP26 (AS09 407), αCP29 (AS04 045), αCP43 (AS11 1787), αPSAA (AS06 172), αLHCSR1 (AS14 2819), αLHCSR3 (AS14 2766) and αSTT7 (AS15 3080); antibodies were purchased from Agrisera.

Pigment analysis

Chlorophyll and carotenoids content were analyzed by HLPC upon pigment extraction in 80% acetone as described in [231].

Spectroscopy and fluorescence

Absorption spectra of pigments, extracted from intact cells using 80% acetone buffered with Na_2CO_3, were measured with Jasco V-550 UV/VIS spectrophotometer. Spectra were fitted as previously described with different pigment absorption spectra [70]. Low temperature fluorescence spectra were performed on frozen samples with BeamBio custom device equipped with USB2000+ spectrometer (OceanOptics) and 475 nm LED light sources for excitation.

Photosynthetic parameters and NPQ measurements

Photosynthetic parameters ΦPSII, qL, ETR and NPQ were obtained by measuring with a DUAL-PAM-100 fluorimeter (Heinz-Walz) chlorophyll fluorescence of intact cells, at room temperature in a 1x1 cm cuvette mixed by magnetic stirring. ΦPSII, qL and ETR were measured and calculated according to [375,376] at steady-state photosynthesis upon 20 minutes of illumination. NPQ measurements were performed on dark adapted intact cells, with a saturating light of 4000 µmol photons m^{-2} s^{-1} and actinic lights from 150 to 3900 µmol photons m^{-2} s^{-1}. PSII functional antenna size was measured from fast chlorophyll induction kinetics induced with a red light of 11 µmol photons m^{-2} s^{-1} on dark-adapted cells (~ $2 \cdot 10^6$ cells/ml) incubated with 50 µM DCMU [362]. The reciprocal of time corresponding to two-thirds of the fluorescence rise ($\tau_{2/3}$) was taken as a measure of the PSII functional antenna size [362]. Proton motive force upon exposure to different light intensities was measured by Electrochromic shift (ECS) with MultispeQ v2.0 (PhotosynQ) according to [377]. State transitions were induced with the protocol present in [365]. State transition were estimated as (Fm_{PSIS2}- Fm_{PSIS1})/ Fm_{PSIS2} where Fm_{PSIS1} and Fm_{PSIS2} are the maximal PSI fluorescence in state 1 and state 2 respectively. The oxygen evolution activity of the cultures was measured at 25°C with a Clark-type O_2 electrode (Hansatech), during illumination with light from a halogen lamp (Schott). Samples of 1 ml cell suspension, $5x10^6$ cell/ml, not limited by the carbon supply.

77K fluorescence

Low temperature quenching measures were performed according to [225]. Cells were frozen in liquid nitrogen after being dark adapted or right after 10 minutes of illumination at 1200 µmol photons m^{-2} s^{-1}, and fluorescence emission spectra were recorded. GFP protein was added to all samples as an internal standard for fluorescence emission spectra normalization.

Statistics analysis

All the experiments herein described were performed at least on two independent lines for each mutant genotype in at least four independent biological experiments. Statistical analysis was performed by using two-sided Student's t-test.

Supporting information

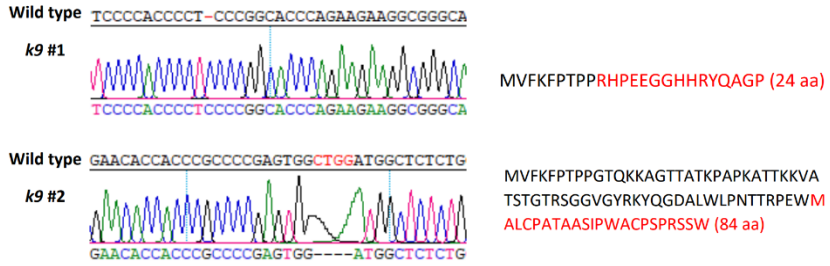

Figure S 2.6.1 *Chromatograms of ΔCP29 mutants at the cp29 locus and CP29 protein sequences predicted to be translated. Red color indicates disrupted region by indel mutation in the CP29 protein. WT CP29 protein is composed by 280 residues*

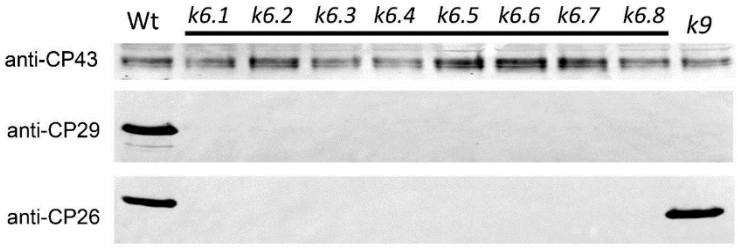

Figure S 2.6.2 *Absence of CP29 protein in k6 lines. Total protein extract for 8 different knock-out lines for CP26 (k6.1-k6.8) were loaded on SDS-page gel and checked for the presence of CP29 by immunoblot with specific antibody. Immunoblot against CP43 was added as control of the loading, immunoblot against CP26 to confirm that k6 strains were knock-out lines for CP26. Total protein extract from wild-type (Wt) and a k9 lines were added on the external lanes as control.*

A

Primer sequences

cp26_CDS_F: ATGCAGATCCAGGCTCTGTT

cp26_CDS_R: TTACAGGGTGGGGGTGCGCT

cp29_CDS_F: ATGGTGTTCAAGTTCCCCAC

cp29_CDS_R: TTAGAGCCCCTTGCCGTTGT

qRT_cp26_246F: AGTTCGACTCGTCGGTCTTC

qRT_cp26_246R: GGACGGTCAGCAGGTTGTAG

qRT_cp29_250F: CCGGTGTGTCTTGGGTTGAG

qRT_cp29_250R: TGCTTGATCTCAGCGGTCTT

qRT_RACK1_F: GGCTGGGACAAGATGGTCAA

qRT_RACK1_R: GAGAAGCACAGGCAGTGGAT

C

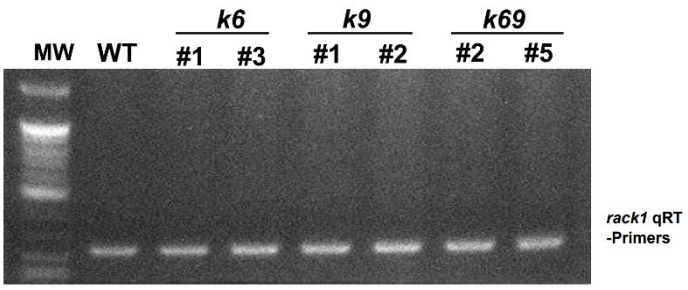

B

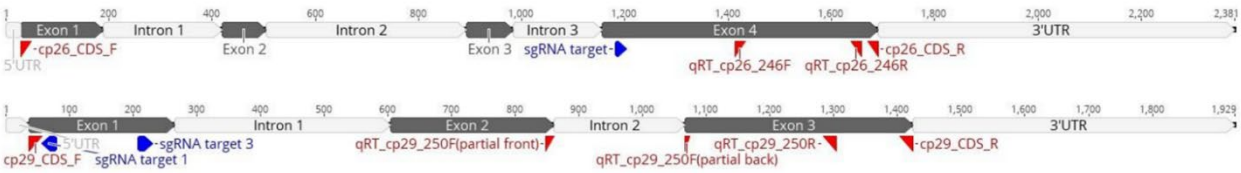

Figure S 2.6.3 *qRT-PCR on cp26,cp29 and rack 1 gene. a, Sequence of primers used for amplification of cp26 and cp29 CDS (Fig. 1b) and for cp26, CP29 and rack1 qRT-PCR. b, Scheme of primers pairing on cp26 and cp29 genes. sgRNA target are reported in blue color. c, qRT on rack1 gene used as loading control for qRT-PCR on cp26 and cp29 genes reported in Fig.1*

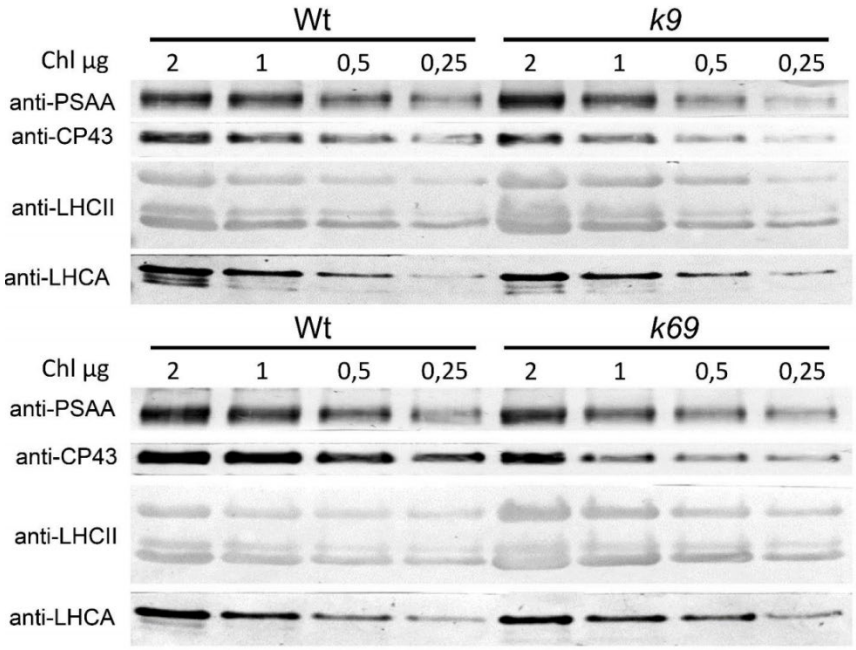

Figure S 2.6.4 *Polypeptide composition of thylakoid membranes. Image of two of the Western blot used for Immunotitration of thylakoid proteins in Fig. 2b. Specific antibodies against PSAA, CP43, LHCII and LHCA were used on cellulose on lanes loaded with 2, 1, 0.5 and 0.25 µg of Chls. On each gel wild-type (Wt) thylakoids were loaded in order to normalize the data.*

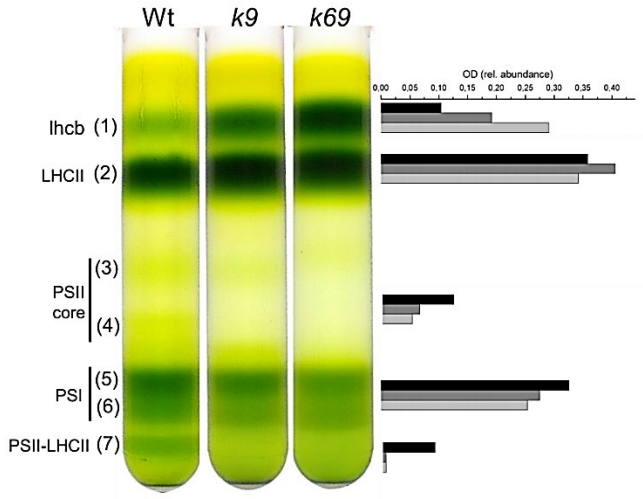

Figure S 2.6.5 *Densitometric analysis of sucrose gradients. Sucrose gradient loaded with solubilized thylakoids were analysed by densitometric analysis with GelPro extracting on green channel. Densitometric results are reported as optical density (OD) normalized to the total green of each gradient.*

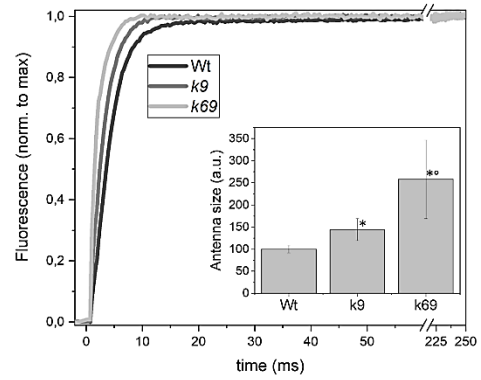

Figure S 2.6.6 *Functional PSII antenna size. Variable Chl fluorescence was induced with a weak red light of 11 µmol photons m^{-2} s^{-1}, on dark-adapted cells (about 2 · 106 cells/ml) in HS medium supplemented with 50 µM DCMU. The trace for wild-type (Wt, black), k9 (grey) and k69 (light grey) are the average of 40 curve for each genotype from four different experiments. The reciprocal of time corresponding to two-thirds of the fluorescence rise (1/τ2/3) is as a measure of the PSII functional antenna size and it is shown in the inset and in Table 1 normalized to the WT case, which was set to 100. Data are expressed as mean ± SD. Values that are significantly different (Student's t-test, P < 0.05) from the wild-type (WT) are marked with an asterisk (*). Date that are significantly different between k6 and k69 are marked with a circle (°).*

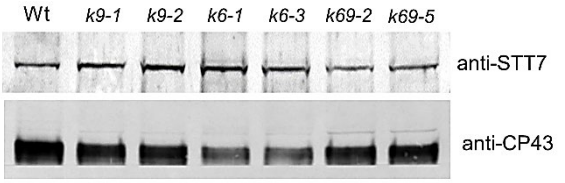

Figure S 2.6.7 *Western blot analysis of STT7 enzyme in Wt and mutant strains. Western blot were performed on STT7 kinase and CP43 used as loading control.*

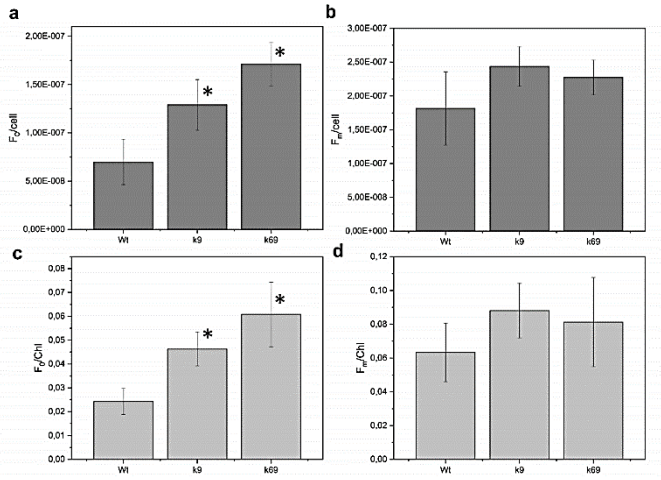

Figure S 2.6.8 *Quantification of minimal and maximum Chl fluorescence. The same amount of dark-adapted wild-type (Wt), k9 and k69 cells (2x10^6 cells/ml) was excited with same PAM light setting and minimal (F_0) and maximal (F_m) were recorded. After the measure Chl were extracted and quantified from all the sample. F_0 and F_m were normalized to cells (a,b for F_0 and F_m respectively) and Chl content (c,d for F_0 and F_m respectively). Data are expressed as mean ± SD. Values that are significantly different (Student's t-test, P < 0.05) from the Wt are marked with an asterisk (*).*

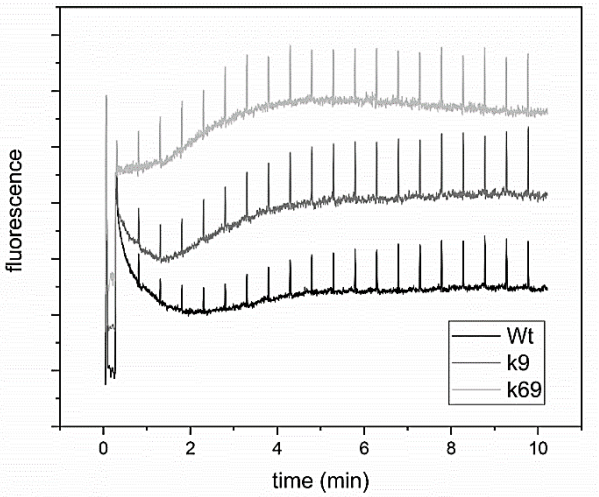

Figure S 2.6.9 *NPQ chlorophyll fluorescence. Example of fluorescence traces from wild-type (Wt black), k9 (grey) and k69 (light grey) obtained from NPQ measure using actinic light of 1200 µmol photons m^{-2} s^{-1}. Traces are vertically shifted to the same value of F_m.*

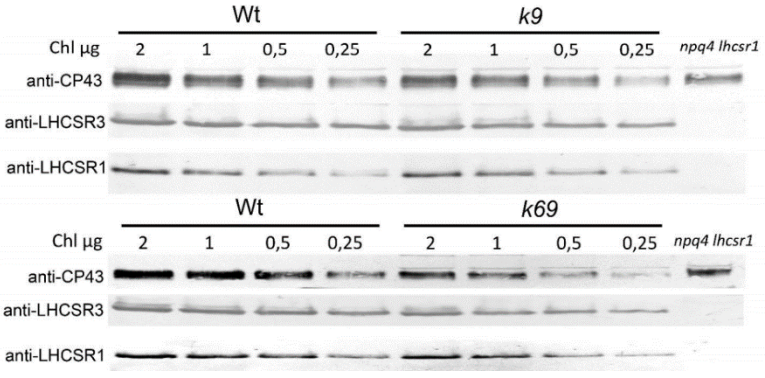

Figure S 2.6.10 *LHCSR quantification. Image of two of the Western blot used for immunotitration of thylakoid proteins in Fig. 5a. Specific antibodies against LHCSR3 and LHCSR1 were used on lanes loaded with 2, 1, 0,5 and 0,25 µg of Chl. On each gel wild-type (Wt) thylakoids were loaded in order to normalize the data. npq4 lhcsr1 thylakoid (1 µg of Chl) was loaded as negative control.*

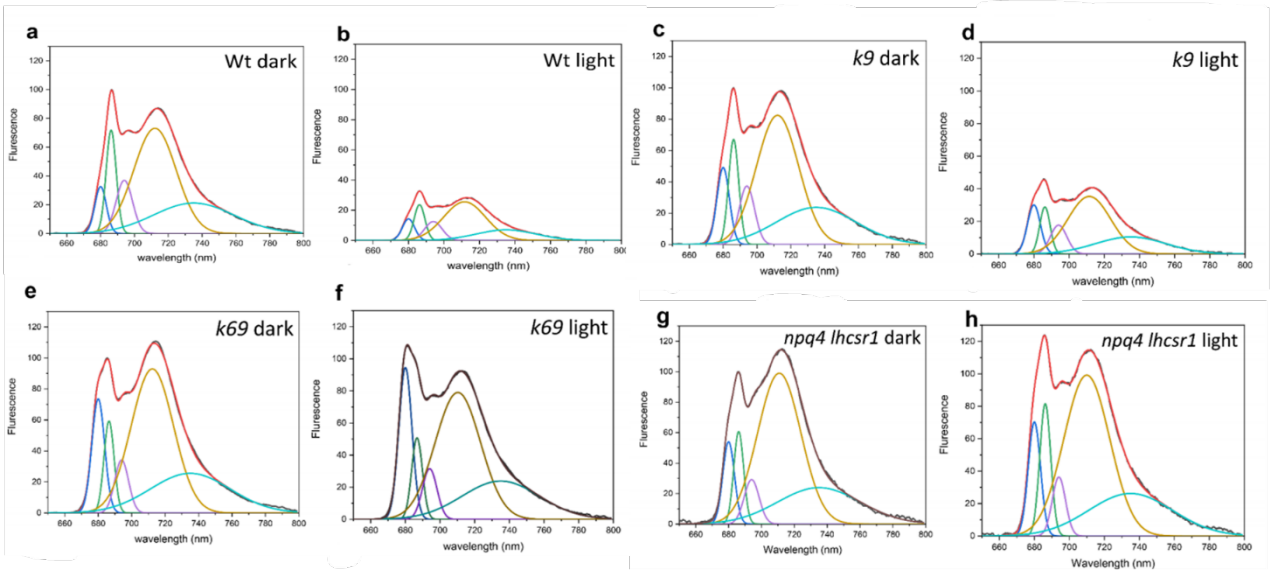

Figure S 2.6. 11 *77K fluorescence of WT and mutant strains. Low temperature fluorescence emission spectra of dark-adapted (dark) or light treated (light) wild-type (a,b), k9 (c,d), k69 (e,f) and npq4 lhcsr1(g,h) cells, shown if figure 7, were reconstructed by spectral deconvolution with Gaussians. Cumulative fit results are reported in red.*

	Wt	*k9*	*k69*
Respiration in the dark (O_2 mmol cell^{-1} min^{-1})	1.11 ± 0.25	1.10 ± 0.05	1.06 ± 0.21
Pmax (O_2 nmol ug chl^{-1} min^{-1})	10.47 ± 1.68	7.51 ± 0.24*	6.39 ± 1.32*
Half-saturation intensity (µmol m^{-2} s^{-1})	233 ± 23	247 ± 16	281 ± 21*°
Slope of linear increase (O_2 mmol cell^{-1} µmol m²)	1.32 ± 0.18	0.78 ± 0.18*	0.72 ± 0.30*

Table S 2.6.1 *Photosynthesis and respiration rates Parameters extrapolated from oxygen light saturation curves shown in Fig. 3d. Data are expressed as mean ± SD. (n >3). Values that are significantly different (Student's t-test, P < 0.05) from Wt are marked with an asterisk (*). Date that are significantly different between k6 and k69 are marked with a circle (°).*

				Car/100 Chl					
	Chl (pg)/ cell	**Chl a/b**	**Chl/Car**	**neo**	**viola**	**anth**	**lute**	**zea**	**β car**
Wt	1.28 ± 0.28	2.70 ± 0.07	2.13 ± 0.10	4.69 ± 0.21	4.07 ± 0.82	2.35 ± 0.41	24.22 ± 0.82	2.64 ± 1.09	8.97 ± 0.10
k9	1.25 ± 0.16	2.55 ± 0.12	2.19 ± 0.14	4.23 ± 0.14*	3.96 ± 0.52	2.71 ± 0.03	23.90 ± 0.03	2.53 ± 0.71	7.92 ± 0.17*
k69	0,98 ± 0.16	2.48 ± 0.15*	2.13 ± 0.14	4.65 ± 0.32	4.13 ± 0.23	1.69 ± 0.35*°	25,84 ± 0.90*°	1.71 ± 0.36	8.78 ± 0.97

Table S 2.6.2 *Pigment content of cell acclimated to 500 µmol photons m-2 s-1. Single carotenoids values were normalized to 100 chlororophylls. Data are expressed as mean ± SD. (n = 4). Values that are significantly different (Student's t-test, P < 0.05) from the wild-type (Wt) are marked with an asterisk (*). Date that are significantly different between k6 and k69 are marked with a circle (°). Chl: chlorophylls; car: carotenoids; neo: neoxanthin; viola: violaxanthin; anth: anteraxanthin; lute: lutein; zea: zeaxanthin; β-car: β-carotene.*

	Wt	*k9*	*k69*
Fv/Fm	0.67 ± 0.06	0.54 ± 0.06	0.46 ± 0.07

Table S 2.6.3 *Fv/Fm of cell acclimated to 500 µmol photons m-2 s-1. Photosystem II maximum quantum yield (Fv/Fm) measured in Wt and k9 and k69 mutant acclimated to high light (500 µmol photons m^{-2} s^{-1}). Data are expressed as mean ± SD. (n >3).*

2.7

LHCSR expression under HP70/RBCS2 promoter as a strategy to increase productivity in microalgae

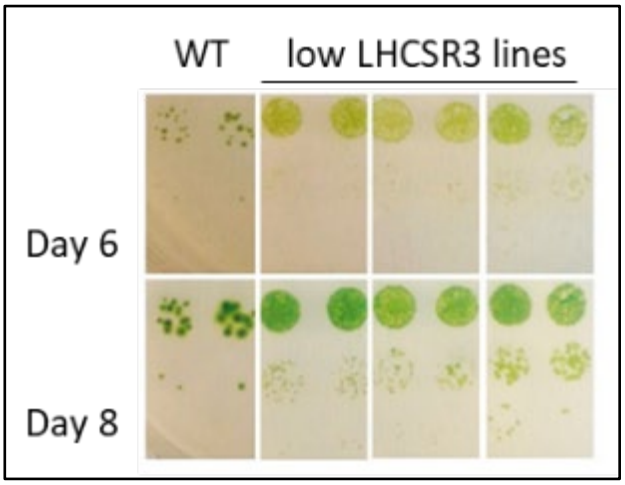

This section is based on the published article: Perozeni, F., Stella, G. R. & Ballottari, M. LHCSR Expression under HSP70/RBCS2 Promoter as a Strategy to Increase Productivity in Microalgae. *International journal of molecular sciences* 19, doi:10.3390/ijms19010155 (2018).

Author Contributions: Ballottari M. conceived and designed the experiments; Perozeni F. performed all the experiments; Stella GR. designed and obtained the vectors reported in Figure 1 and contributed to *npq4 lhcsr1* transformation. All the authors analyzed the data and contributing to writing the paper.

LHCSR Expression under *HSP70/RBCS2* promoter as a strategy to increase productivity in microalgae

Federico Perozenii[1], Giulio Rocco Stella[1] and Matteo Ballottari[1]

[1] Department of Biotechnology, University of Verona, 37134 Verona, Italy

Abstract

Biofuels or high value products. However, limited biomass productivity is commonly experienced in their cultivating system despite their high potential. One of the reasons for this limitation is the high thermal dissipation of the light absorbed by the outer layers of the cultures exposed to high light caused by the activation of a photoprotective mechanism called non-photochemical quenching (NPQ). In the model organism for green algae *Chlamydomonas reinhardtii*, NPQ is triggered by pigment binding proteins called light-harvesting-complexes-stress-related (LHCSRs), which are over-accumulated in high light. It was recently reported that biomass productivity can be increased both in microalgae and higher plants by properly tuning NPQ induction. In this work increased light use efficiency is reported by introducing in *C. reinhardtii* a *LHCSR3* gene under the control of *Heat Shock Protein 70*/*RUBISCO small chain 2* promoter in a *npq4 lhcsr1* background, a mutant strain knockout for all *LHCSR* genes. This complementation strategy leads to a low expression of *LHCSR3*, causing a strong reduction of NPQ induction but is still capable of protecting from photodamage at high irradiance, resulting in an improved photosynthetic efficiency and higher biomass accumulation.

Introduction

Photosynthetic organisms convert light energy into chemical energy to be used for carbon fixation to sustain cellular metabolism. Light harvesting occurs at the level of pigment binding protein complexes called Photosystem I (PSI) and II (PSII) [32,40]. Light energy absorbed by pigments bound to Photosystems causes formation of chlorophyll-excited states and energy transfer to reaction centers inducing charge separation and electron transport across thylakoid membranes. Light energy is thus used to extract electrons from water and transfer them to NADPH. This light dependent electron transport chain involves different electron acceptors and donors among which cofactors bound to PSII and PSI, plastoquinones, the protein complex Cytochrome b6f (Cyt b6f), plastocyanin, ferredoxin and ferredoxin-NADP$^+$ reductase enzyme [378-380]. Thylakoidal electron transport is coupled to the formation of a proton gradient across thylakoids which is then used to produce ATP by the chloroplast ATPase. Different photosynthetic organisms such as plants or algae must deal with rapid changes in sunlight quality and quantity which can be very dangerous for the photosynthetic apparatus [104,381]. Indeed, the formation of an excess of chlorophyll excited state can lead to saturation of the photosynthetic apparatus, with consequent increased probability of the population of triplet chlorophyll excited states with long lifetime (ms) which makes it possible to transfer energy to oxygen and form reactive oxygen species (ROS) [104]. Photosynthetic organisms have different photoprotective strategies to light changes, among which the thermal dissipation of the singlet chlorophyll excited states not quenched by photochemistry, in a mechanism known as non-photochemical quenching (NPQ)[202]. NPQ activation has been reported to be particularly important for de-excitation of PSII complexes with closed reaction centers, where photochemical reactions cannot properly consume excitation energy of the chlorophylls bound [200]. NPQ activation and in general regulation of photosynthetic reactions can be easily monitored *in vivo* by chlorophyll fluorescence measurement, a powerful tool to investigate the response of the photosynthetic apparatus to changing environments [382-384]. NPQ has been reported in all oxygenic photosynthetic organisms [100-102,385-387], but while in natural conditions it could be important for survival, NPQ activation decreases light use efficiency by opening a dissipative channel of the light energy absorbed. Indeed, recent studies have demonstrated that biotechnological manipulation of crops or microalgae cultures inducing a

reduction of NPQ activation or a faster recovery from dissipative state significantly increased photosynthetic efficiency and biomass production [190,388]. Increasing productivity in microalgae is a highly debated topic since microalgae have been proposed as a sustainable alternative for biofuels and food production, since these organisms have high potential photosynthetic efficiency, do no compete for arable land and can be cultivated using nutrient from wastewater [278,324,389-392]. In the model organism for green algae, *Chlamydomonas reinhardtii*, NPQ is triggered by the pigment-binding subunits LHCSR1 and LHCSR3, two LHC (light harvesting complex)-like Chl *a*/*b*-xanthophyll-binding proteins; these subunits have been reported to trigger NPQ induction on the basis of luminal pH, being able to significantly quench excitation energy present at the level of both PSI and PSII [101,121,122,190,208,266]. Both genes for LHCSR1 and LHCSR3 are transcriptionally regulated causing overaccumulation of these subunits in stress conditions [101,120]. Three genes encode LHCSR proteins in *C. reinhardtii*: two of them are closely related and encode the same product (LHCSR3) while the other one encodes the LHCSR1 subunit, which shows 82% identity to LHCSR3 [101]. All the different genes for LHCSR subunits in *C. reinhardtii* are transcriptionally controlled, depending on light, CO_2 concentration and calcium signaling[101,120,393]. Through random insertional mutagenesis, *npq4* mutant, a knockout mutant for both *LHCSR3.1* and *LHCSR3.2* genes, was obtained, accumulating only LHCSR1 subunit[101], while by TILLING (Targeting Induced Local Lesions IN Genomes) a knockout mutation for *LHCSR1* was added, obtaining the *npq4 lhcsr1* mutant which does not accumulate any LHCSR proteins [121,191]. These mutants revealed that even if both LHCSR subunits are active, LHCSR3 has a predominant role in NPQ induction (Peers *et al.*, 2009). Indeed, *npq4* mutant was characterized by a strong NPQ reduction associated with a significant increase in biomass productivity [190] while the *npq4 lhcsr1* showed similar growth rates compared to WT in continuous light conditions [191]. Interestingly, despite a ~60% reduction in NPQ induction, *npq4* was not more photo inhibited compared to WT, while *npq4 lhcsr1* mutant was characterized by the highest production of ROS [190]. These results suggested that it is possible to improve biomass production in *C. reinhardtii* reducing NPQ activation if a basal level of photoprotection is ensured by accumulation of some LHCSR subunits, such as LHCSR1 in the case of *npq4* mutant [190]. In this work, a different strategy to obtain strains with reduced NPQ and increased photosynthetic efficiency was addressed, by complementation of *npq4 lhcsr1* mutant with *LHCSR3* gene under control of a promoter obtained by fusion of *Heat Shock Protein (HSP70)* and *RUBISCO* small subunit *(RBCS) 2* promoters [394]. *LHCSR3* gene controlled by *HSP70/RBCS2* promoter is not strongly induced in high light resulting in a low expression of this gene and reduced NPQ compared to WT. This strategy could be indeed required for the biotechnological manipulation of other microalgae species inducing a basal accumulation of LHCSR subunits in mutants with NPQ phenotypes.

Results

Complementation of *npq4 lhcsr1* strain

C. reinhardtii strains with a constitutive expression of *LHCSR3* gene were obtained by complementation of *npq4 lhcr1* mutant with *LHCSR3* coding sequence under control of a promoter obtained fusing promoters of *HSP70* and *RBCS2* genes as previously reported[394] (**Figure 2.7.1**). In particular, two vectors were used for complementation differing in the presence of transit peptides: pSL18_HR contained LHCSR3 whole coding sequence, including its putative transit peptide, while in pSL18_HR_chloro LHCSR3 coding sequence was deleted of the first 42 nucleotides, corresponding to the putative 14 amino acids chloroplast transit peptide, according to ChloroP prediction [106], which were replaced by the RUBISCO small subunit transit peptide [395]. Transformed lines surviving antibiotic selection (**Figure S 2.7.2a**) were grown in high light conditions and screened for NPQ induction compared to the background strain. NPQ screening allowed the identification five lines transformed with pSL18_HR and one line transformed with pSL18_HR_chloro with an increased NPQ compared to *npq4 lhcsr1*, suggesting the accumulation of a functional LHCSR3 protein (**Figure S 2.7.2b**). LHCSR3 protein accumulation was then investigated by immunoblotting, confirming the presence of LHCSR3 protein in transformed lines with an increased NPQ phenotype compared to *npq4 lhcsr1* mutant (**Figure S 2.7.2c**). Three of these lines were then selected for the

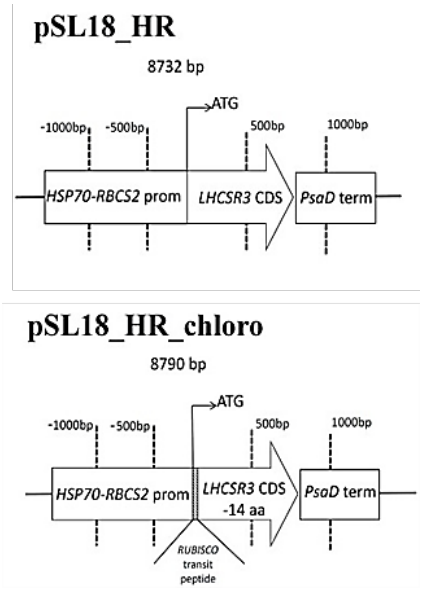

Figure 2.7.1 *Schematic maps of the vectors used for npq4 lhcsr1 transformation. LHCSR3 coding sequence (LHCSR3 CDS) was cloned in pSL18 vector under the control of promoter obtained by fusion of HSP70 and RBCS2 promoter (pSL18_HR). In the case of pSL18_hR_chloro, LHCSR3 coding sequence was truncated at the 5' in order to remove the codons coding for the first 14 aminoacids of the protein: chloroplast transit peptide was thus substituted with RUBISCO (rbcs) small subunit transit peptide. For both vectors PsaD terminator sequence was used as terminator.*

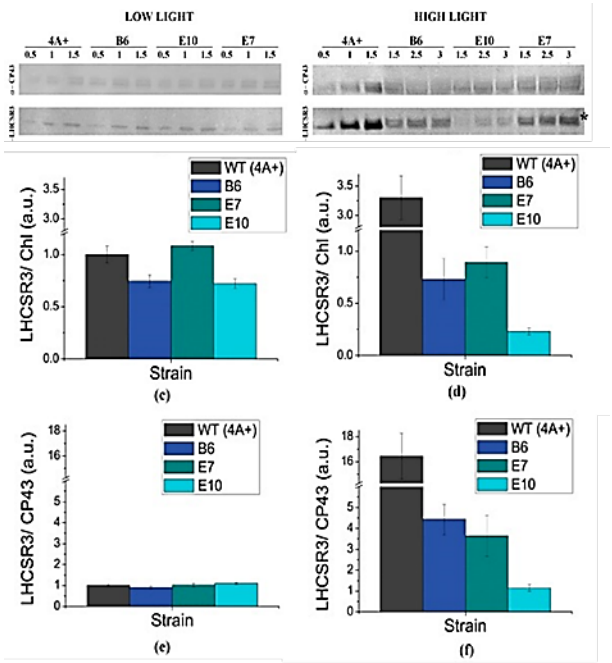

Figure 2.7.2 *Immunoblot analysis of LHCSR3 accumulation in transformed lines compared to WT (4A+) strain. (a,b): immunoblot analysis for strains grown in low light (a) or high light (b) using specific antibodies recognizing LHCSR3 and CP43 as a control for protein loading. Proteins extracted from WT and transformed lines were loaded at three different dilutions as reported in the figure. The phosphorylated form of LHCSR3 is indicated by *; (c–f): accumulation of LHCSR3 in low light and high light treated cells determined by densitometric analysis of filters reported in (a,b) respectively. LHCSR3 content was normalized to the chlorophyll (Chl) content (c,d) or to CP43 content (e,f). The amount of LHCSR3/Chl and LHCSR3/CP43 ratios were then normalized the ratios detected in WT cells grown in low light conditions. In the case of WT grown in high light conditions, LHCS3/Chl and LHCSR/CP43 ratios were normalized to the levels detected for WT cells grown in low light according to results reported in Figure S2. Values in (c, d, e, f) are indicated as arbitrary units (a.u.) with standard deviation reported as error bar (n = 3).*

following experiments: two lines transformed with pSL18_HR (lines E7 and E10) and one line transformed with pSL18_HR_cloro (line B6). LHCSR3 level in these complemented lines was quantified by immunoblotting in cells grown at low light (**Figure 2.7.2a**) or high light (**Figure 2.7.2b**) conditions, using the PSII subunit CP43 as control for loading. As reported in **Figure 2.7.2a**, in low light a transformed lines showed a LHCSR3 accumulation on chlorophyll basis (**Figure 2.7.2c**) or normalized to CP43 content (**Figure 2.7.2e**) comparable to the case of WT cells grown in the same conditions. In high light conditions, WT cells showed a strong increase of LHCSR3 accumulation compared to cells grown in low light both on a chlorophyll basis or upon normalization to CP43 content, leading to a strong increase of LHCSR3/PSII ratio, as previously reported [106,255] (**Figure 2.7.2b** and **Figure S 2.7.1**). Differently, transformed lines showed only a partial increase of LHCSR3 accumulation on a chlorophyll basis (**Figure 2.7.2d**) or per PSII (**Figure 2.7.2f**) in high light. In both low and high light conditions, E10 line showed a protein level slightly lower compared to the other transformed lines, which could be ascribable to a position effect. It is worth to note that in transformed lines, the phosphorylated form of LHCSR3, migrating at slightly higher apparent MW compared to the un-phosphorylated form[106,263], was particularly evident in high light-grown transformed lines, in agreement with the higher activity of the STT7 kinase in high light in mutants with reduced NPQ induction [262].

Pigment composition of transformed lines

Pigment composition of WT and transformed lines growing in low light or high light was investigated by HPLC analysis (**Table 2.7.1**) when cells reached the exponential growth phase. Chlorophyll content per cell was reduced in transformed lines, both in low light and high light, compared to WT. In addition, an increased Chl *a*/Chl *b* ratio and carotenoid content were measured in transformed lines in both light conditions. Chl/Car ratio was further reduced in transformed lines grown in high

		Chl/Cell	s.d.	Chl a/b	s.d.	Chl/Car	s.d.
low light	WT	2.16×10^{-6}	1.99×10^{-7}	1.86	0.01	3.93	0.02
	B6	1.42×10^{-6}	1.26×10^{-7}	3.22	0.01	2.46	0.01
	E7	1.40×10^{-6}	2.69×10^{-7}	3.24	0.03	2.50	0.02
	E10	1.29×10^{-6}	7.70×10^{-8}	3.24	0.10	2.49	0.06
high light	WT	7.29×10^{-7}	1.29×10^{-8}	1.49	0.04	2.48	0.20
	B6	3.87×10^{-7}	7.29×10^{-9}	2.43	0.07	1.39	0.06
	E7	4.38×10^{-7}	1.09×10^{-8}	2.53	0.03	1.15	0.03
	E10	4.17×10^{-7}	9.63×10^{-9}	2.59	0.05	1.07	0.03

Table 2.7.1 *Pigments analysis of transformed lines compared to WT. Chlorophyll content per cell, Chl a/b ratio, and Chl/Car ratio are reported with standard deviation (n = 4).*

light. It is interesting to note that the Chl/Car ratio of B6, E7 and E10 strains grown in low light is similar to the Chl/Car ratio of WT grown in high light, where the Chl/Car of transformed lines is further decreased. Intermediate values of Chl *a*/*b* ratio between WT and transformed lines were measured for the background strain *npq4 lhcsr1* grown in low light, while Chl *a*/*b* ratio in high light, Chl/Car ratio and Chl content per cell both in low light and high light were similar between WT and *npq4 lhcsr1* (**Table S 2.7.1**), suggesting the different pigment binding properties observed in transformed lines are independent from the genetic background but rather related to an adaptation process to the growing conditions likely related to reduced NPQ induction observed in these strains with consequent increased excitation pressure at the level of PSII. As reported in **Table S 2.7.2** the average cell size was not significantly different for transformed lines compared to WT, neither in low light nor high light conditions, suggesting that the reduced chlorophyll content per cell observed in transformed lines is likely dependent on adaptation processes occurring at the level of the chloroplast.

NPQ induction and LHCSR3 accumulation

NPQ induction kinetics of WT, *npq4 lhcsr1* mutant and complemented lines are reported in **Figure 2.7.3** for cells grown in low light or high light. Low light-acclimated WT cells were characterized by a lower NPQ induction compared to high light cells (**Figure 2.7.3a-b**) as previously reported, because of light dependent accumulation of LHCSR3 in *C. reinhardtii* [101,126].

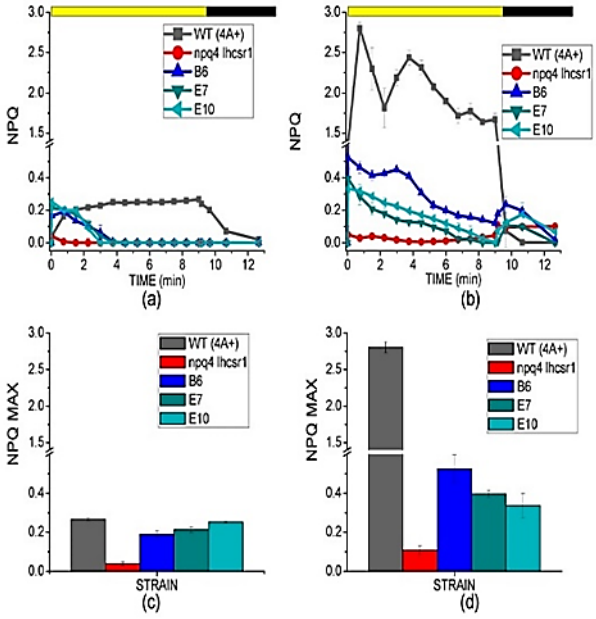

Figure 2.7.3 *NPQ kinetics and NPQ maximum induction.(a,b): NPQ kinetics measured in cells grown in low light (a) or high light (b) upon actinic light illumination (1200 µmol $m^{-2} \cdot s^{-1}$), and dark recovery. Yellow bar indicates the illumination period and the dark bar indicates the dark recovery;(c,d): maximum NPQ values detected for WT, transformed lines and their background npq4 lhcsr1 grown in low light (c) or high light (d) with standard deviation reported as error bar.*

Differently, *npq4 lhcsr1* mutant did not show any NPQ induction neither in low or high light, due to the absence of LHCSR subunits in this strain [121,190,191]. Complemented lines B6, E7 and E10 were characterized by an initial rise of NPQ induction during the first minute of measurement, followed by a decrease even if actinic light was still turned on. In low light, the maximum NPQ induction observed for WT and transformed lines was similar (**Figure 2.7.3c**), but while WT reached the maximum NPQ value at the end of the illumination period, complemented lines reached maximum NPQ induction after 30 s followed by a strong decrease in NPQ. A similar behavior was also observed in high light, with the maximum NPQ level observed in transformed lines only at the beginning of the measurement. Maximum NPQ level observed in the transformed line was thus much lower compared to WT (**Figure 2.7.3d**); the dependency of NPQ maximum induction vs. accumulation of LHCSR3 protein is reported in **Figure S 2.7.3**, suggesting a linear correlation between the amount of LHCSR3 per chlorophyll and the maximum NPQ value observed, which is in agreement with previous reports [126,190]. Moreover, NPQ in complemented lines decreases after few minutes in low light or seconds in high light; this result can be related to light-dependent activation of the Calvin cycle and de-saturation of

photosynthetic electron chain. In order to further elucidate this point, the accumulation of the different photosynthetic subunits was investigated by immunoblotting.

Composition of photosynthetic subunits

Accumulation of the major photosynthetic complexes was investigated by semiquantitative immunoblotting with specific antibodies targeting proteins representative of PSI, PSII, Cytb6f, ATPase and RUBISCO. In addition, immunoblotting analysis were performed using antibodies recognizing specifically the PSII antenna proteins CP29, LHCBM4/6/8 and an antibody recognizing all the different LHCII subunits (**Figure 2.7.4**)[229]. Transformed lines were characterized by a higher accumulation of RUBISCO compared to WT, either on a chlorophyll (**Figure 2.7.4**) or cell (**Figure S 2.7.4**) basis. Transformed lines were also characterized by a strong increase of Cyt f, α-ATPase, and PsaA on a chlorophyll basis accompanied by a reduced accumulation of CP43 compared to WT, resulting in an increased PSI/PSII, Cytb6f/PSII and ATPase/PSII ratio. Interestingly, on a cell basis, the accumulation of PsaA and ATPase was similar in WT and transformed lines, while CP43 was strongly reduced and Cyt f was increased in transformed lines (**Figure S 2.7.4**). These results suggest that the reduced NPQ activation observed in transformed lines causes a specific reduction of PSII accumulation on a cell basis, likely as a consequence of the increased excitation pressure due to reduced NPQ. In the case of PSII antenna proteins, on a chlorophyll basis CP29 and LHCII subunits decreased compared to WT, while LHCBM4/6/8 level was not significantly different. Considering the level of CP43, the stoichiometry LHCII/PSII was similar in WT and transformed lines, with the exception of LHCBM4/6/8 subunits which were increased per PSII. It is important to note that LHCBM4/6/8 was recently reported to have a minor role in light harvesting at the level of PSII but was rather involved in state transitions and light harvesting at the level of PSI [229]. Increased PSI/PSII ratio measured in transformed lines is consistent with the increase in Chl *a*/*b* ratio reported in **Table 2.7.1**, since Chl *a*/*b* ratio in the case of PSI is higher than the Chl *a*/*b* ratio observed in the case of PSII. The results obtained for transformed lines suggest an increased possible consumption of ATP and NADPH produced by light phase by carbon fixation, and at the same time a relative increase of electron acceptors downstream of PSII, as Cytb6f and PSI. Different accumulation of photosynthetic subunits likely allows dealing more efficiently with the increased excitation pressure on PSII due to reduced NPQ. Similar immunoblotting analyses were also performed comparing WT and *npq4 lhcsr1* to evaluate possible differences related to the background strain (**Figure S 2.7.5**); no differences were observed between WT and *npq4 lhcsr1*, with the only exception of a more evident reduction of LHCII content in *npq4 lhcsr1*. These results confirm that the different accumulation of photosynthetic subunits observed in transformed lines are related to the expression of the LHCSR3 subunit and not to their genetic background.

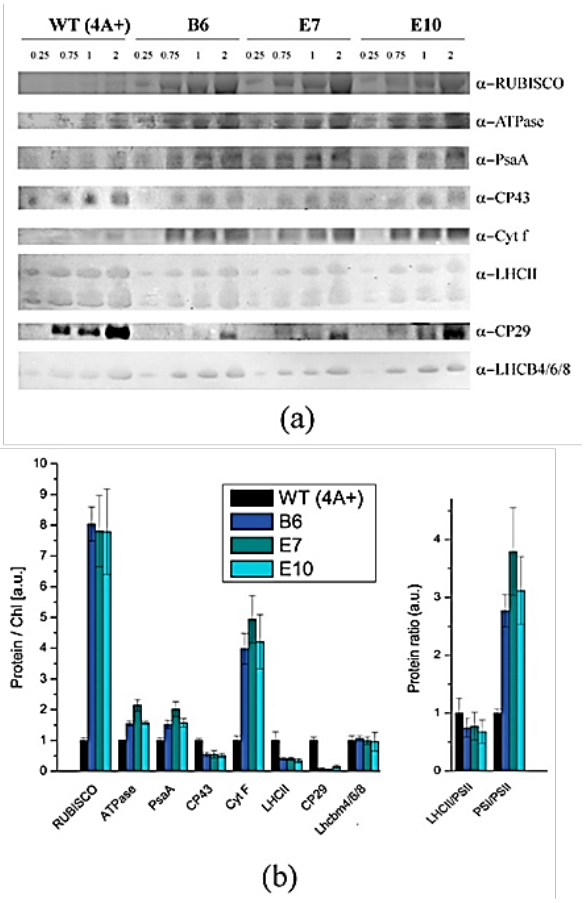

Figure 2.7.4 *Immunoblot analysis of photosynthetic subunit accumulation. (a): immunoblot analysis performed on WT and transformed lines proteins extract using specific antibodies for RUBISCO, ATPase β-subunit, PsaA, CP43, Cyt f, LHCII, CP29 and LHCBM4/6/8 subunits. Micrograms of chlorophylls loaded in each lane are reported on the top. (b): Immunoblot signals reported in panel A were analyzed by densitometry to determine the relative protein abundance. Each protein level was normalized to the WT protein level. LHCII/PSII and PSI/PSII ratio are also reported. Standard deviation is indicated as error bars (n = 4).*

Light dependent oxygen evolution vs. photoprotection

Photosynthetic activity of transformed lines compared to WT was evaluated measuring light-dependent oxygen evolution curves at different actinic light intensities (**Figure 2.7.5**). Transformed lines showed higher Pmax than WT, demonstrating an increasing light use efficiency for these strains. These data are consistent with improved light-dependent electron transport across thylakoids in transformed lines. Differently, dark respiration per cell was similar in transformed lines compared to WT. Increased photosynthetic activity of transformed lines characterized by reduced NPQ activation opens the question about the photoprotective properties of these strains. Singlet oxygen formation was thus followed *in vivo* upon exposure of cells to a strong red light by using a fluorescent probe called Singlet Oxygen Sensor Green [396], of which the fluorescence emission is linearly dependent on the concentration of singlet oxygen [311]. As reported in **Figure 2.7.6**, transformed lines were characterized by a similar or even less singlet oxygen production compared to WT, while their background strain *npq4 lhcsr1* was the strain with the highest singlet oxygen production. This data suggests that, as previously observed in the case of LHCSR1 accumulated at low level in *npq4* mutant, photoprotection provided by the small amount of LHCSR3 accumulated in WT was sufficient to preserve the photosynthetic apparatus from photoinhibition.

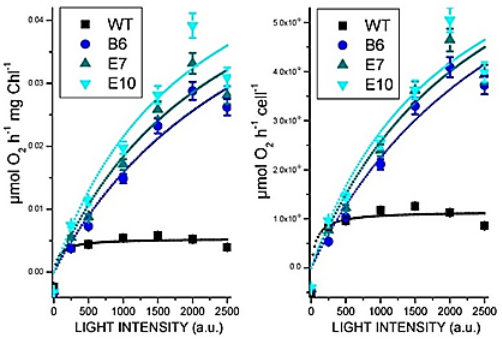

Figure 2.7.5 *Light saturation curves of photosynthetic oxygen evolution obtained from WT (4A+) and transformed lines. Data are reported on chlorophyll basis (a) or on a cell basis (b). Standard deviations are reported as error bars (n = 3).*

Biomass Productivity

Transformed lines with *LHCSR3* gene under control of the *HSP70/RBCS2* promoter were characterized by

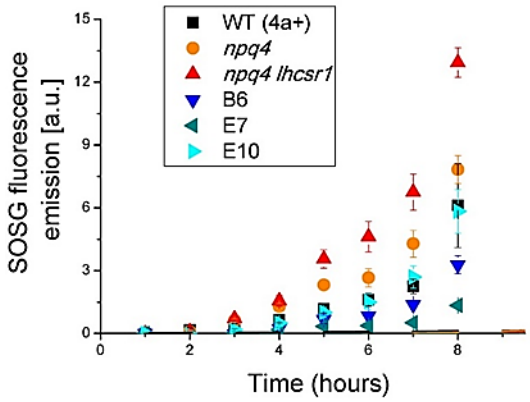

Figure 2.7.6 *Singlet oxygen production for WT and transformed lines. Singlet oxygen production was estimated from fluorescence emission of Singlet Oxygen Sensor Green (SOSG) probe. Data reported are the mean values of three independent biological replicates with standard deviations indicated as error bars.*

reduced NPQ induction compared to WT and increased photosynthetic activity (**Figure 2.7.5**) without suffering from photoinhibition (**Figure 2.7.6**). In order to prove a possible increased biomass productivity of transformed strain, growth performances in solid medium in high light was tested by spotting different cell concentrations for each genotype on HS medium (**Figure 2.7.7**) and comparing transformed lines to WT, *npq4* and *npq4 lhsr1* strains. As reported in **Figure 2.7.7**, *npq4* and transformed lines were characterized by a faster and increased growth compared to WT, while the lowest growth performance was detected for *npq4 lhcsr1* strain. Biomass productivity was then investigated in liquid medium by growing transformed lines in small scale photobioreactors (Multicultivator MC-1000-OD), at 400 µmol $m^{-2} \cdot s^{-1}$. As reported in **Figure 2.7.8a**, transformed lines grew faster than WT reaching higher cell density at the end of the growth curve (**Figure 2.7.8c**). Daily productivity was then estimated from the first derivate of the sigmoidal curves used to fit growth curves (**Figure 2.7.8b**), showing a ~35% higher maximal daily productivity in transformed lines compared to WT. Accordingly, dry weight of biomass collected at the end of the growth was increased in transformed lines by ~34% compared to WT (**Figure 2.7.8d**). Consistently, the specific growth rate (µ) calculated for transformed lines was increased by ~18% compared to WT (**Figure 2.7.8e**). It is worth to note that the specific growth rates reported in **Figure 2.7.8** are consistent with previous growth rates reported for *C. reinhardtii* [397-400]. Photosynthetic efficiency of WT and transformed cultures were then calculated

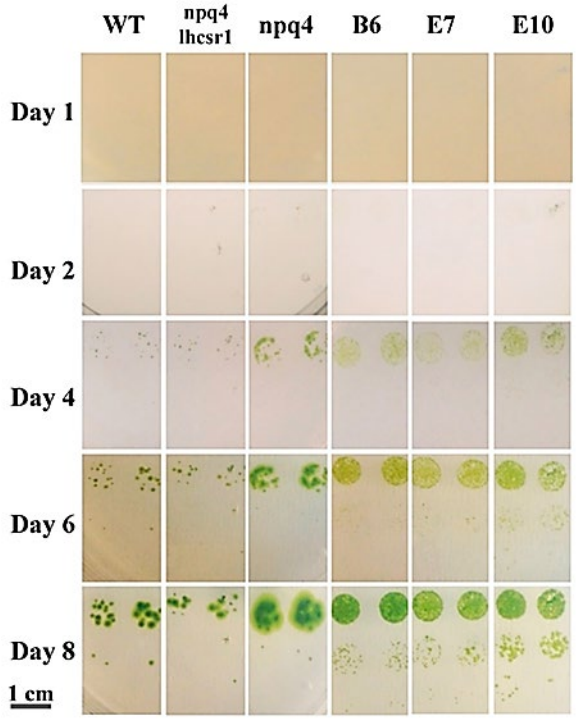

Figure 2.7.7 *Spot test for WT and transformed lines. Each genotype was spotted on solid minimum medium with three different cell amounts (10^2,10^3 and 10^4 cells). Scale bar is reported on bottom left.*

considering the total amount of photons received by the cultures and the energy stored as dry weight biomass at the end of growth curves; WT cells exhibited a photosynthetic efficiency of 3.4%, while transformed lines scored photosynthetic efficiencies of 4.4–4.7% (**Figure 2.7.8f**). While growth kinetics and biomass accumulation of *npq4 lhcsr1* was reported to be similar or lower compared to WT [191], complementation of *npq4 lhcsr1* mutant with *LHCSR3* gene under a constitutive promoter caused a significant increase of photosynthetic efficiency and biomass accumulation compared to WT.

Discussion

NPQ is a feedback photoprotective mechanism triggered in oxygenic photosynthetic organisms to decrease the risk of photoinhibition and cell death [104]. NPQ quenches chlorophyll singlet excited states reducing the probability of chlorophyll triplet formation and ROS production [401]. However, excitation energy quenched by NPQ is unavoidably loss for photochemical reactions, causing a decrease in photosynthetic efficiency [188,190]. Previous reports on the *npq4* mutant demonstrated that a reduced NPQ activation in the absence of LHCSR3 protein caused an increase of biomass accumulation compared to WT

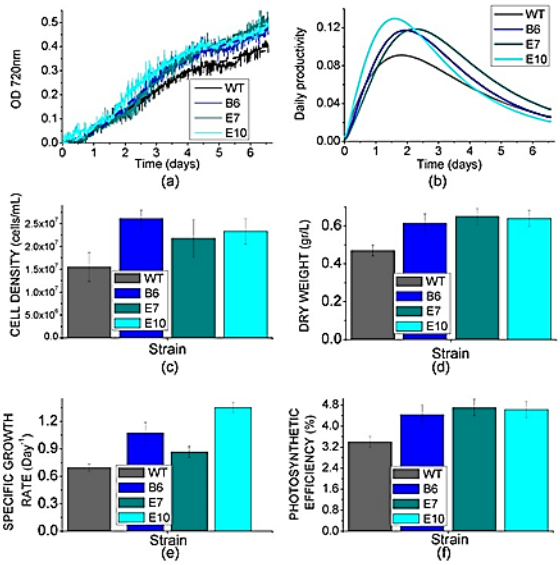

Figure 2.7.8 *Biomass productivity in photobioreactors. (a): growth curves of WT and transformed lines obtained by measuring the optical density (O.D.) at 730 nm. Growth curves were fitted with an exponential growth function; (b): daily productivity estimated from the first derivate of the fitting curves reported in (a); (c): cell density obtained at the end of the growth curve; (d): dry weight obtained at the end of the growth curve; (e): specific growth rate (μ) for WT and transformed lines; (f): photosynthetic efficiency of WT and transformed lines calculated from dry weight obtained at the end of growth curve. Mean value of three independent measurements are reported. Standard deviation is reported as error bars (n = 3).*

due to increased photosynthetic efficiency [190]; *npq4* mutant was reported to produce a similar level of singlet oxygen upon exposure to strong light compared to WT, despite strong reduction of NPQ, while the double mutant *npq4 lhcsr1* was more photo-inhibited than WT and *npq4* due to complete suppression of light-dependent NPQ activation [190]. It is worth to mention that a recent paper reported a similar biomass accumulation and CO_2 fixation upon continuous cultivation of *npq4* mutant and WT, while previous work reported an even stronger light susceptibility of *npq4* strain [101,262,402]. Contrasting results reported in the literature about the performances of *npq4* mutant are likely related to the different environmental conditions adopted for cultivation. In particular, the need for an efficient NPQ activation could be attenuated in the presence of high CO_2 content, resulting in a more active Calvin–Benson cycle as a sink for electrons transported during the light phase of photosynthesis. Moreover, the residual NPQ observed in *npq4* mutant depends on LHCSR1 subunit, the accumulation of which is strictly controlled at the transcriptional level by high light and high CO_2 content [120]. Residual NPQ observed in *npq4* mutant

is indeed related to LHCSR1 overexpression to partially counterbalance LHCSR3 absence and to ensure the minimum level of photoprotection required to sustain growth in high light condition [190]. In this work, we demonstrate a different strategy to increase photosynthetic efficiency by reducing NPQ, consisting of low expression of *LHCSR3* gene in absence of LHCSR1. Complementation of *npq4 lhcsr1* mutant with LHCSR3 genes under *HSP70/RBCS2* promoter (**Figure 2.7.1**) indeed resulted into accumulation of LHCSR3 protein similar to WT in LL conditions, but not in HL, where transformed lines were characterized by a strong reduction of LHCSR3, due to the strong light dependent transcriptional activation of the endogenous LHCSR3 gene in the WT (**Figure 2.7.4**). As reported in **Figure 2.7.6**, transformed lines with low NPQ induction were characterized by similar or even lower singlet oxygen production compared to WT, demonstrating that the excitation energy not quenched by NPQ could be successfully managed by the photosynthetic apparatus with, therefore, a 30% increase of biomass accumulation in transformed lines (**Figure 2.7.8**). Expression of LHCSR3 at low levels is thus a sufficient condition in *C. reinhardtii* to ensure enough photoprotection at least in the growth conditions herein tested, allowing for a higher photosynthetic efficiency (**Figure 2.7.5** and **Figure 2.7.8f**), because of reduced NPQ (**Figure 2.7.3**). We cannot exclude that more stress conditions, at higher irradiances, could impair the productivity of transformed lines, even if the singlet oxygen production of these strains illuminated with a strong light was similar or even lower than WT; additional experiments are required to elucidate the potential limits of this strategy to increase biomass productivity. It is interesting to note that NPQ induction curves of transformed lines were markedly different compared to WT, since the maximum NPQ level was observed only in the first minutes or seconds after exposure to actinic light, followed by a strong decrease. This result is likely related to light-dependent activation of Calvin cycle enzymes which consume NADPH and ATP, reducing the excitation pressure on PSII, when the CO_2 concentration is sufficient to provide a sink for photosynthetic light phase products. This hypothesis is sustained by the strong increase in RUBISCO enzyme observed in transformed lines compared to WT both on a chlorophyll or cell basis (**Figure 2.7.4** and **Figure S 2.7.4**), suggesting that the reduction in NPQ observed in transformed lines causes an enhanced Calvin–Benson cycle and a more general re-organization of the photosynthetic apparatus. Decrease in chlorophyll content was observed both in transformed lines coupled with increased Chl *a*/Chl *b* ratio and related to increased PSI/PSII ratio. Reduction of PSII content on a cell basis is likely the main reason for the reduced chlorophyll content observed in the case of transformed lines compared to WT (**Table 2.7.1**). The decreased PSII content on a cell basis is likely not related to PSII damage, since the oxygen evolution curves of transformed lines are characterized by a higher Pmax compared to WT, while in case of damaged PSII, the opposite would be expected. Rather, relative increase of PSI and Cytb6f compared to PSII content in transformed lines suggests a more efficient use of electrons coming from water splitting at the level of PSII. This adaptation strategy is likely adopted by transformed lines in order to improve oxidation of Q_A at the level of PSII reducing the risk of photoinhibition even in the presence of a strongly reduced NPQ activation. The higher resistance of transformed lines to ROS production can thus be explained as a combination of improved electron transport across thylakoid, increased electron sink due to relative increase of Calvin–Benson enzymes and reduced Chl/Car ratio (**Table 2.7.1**), with carotenoids being important photoprotective agents inducing chlorophyll triplets quenching and ROS scavenging [104]. In this scenario, transformed lines can better face high light stress and use light energy thanks to a boosted photosynthetic electron transport and carbon fixation machinery; the sum of these elements allows for improved light use efficiency and, thus, biomass accumulation. It is interesting to note that the different compositions of photosynthetic subunits in transformed lines are in line with what has been previously observed for *npq4* mutant compared to WT and for WT cells adapted to high light compared to low light grown cells. These results suggest that the reduction of NPQ observed in transformed lines induces cellular acclimation with a similar mechanism compared to WT cells exposed to increased irradiances due to the increased excitation pressure on photosystems when thermal dissipation of singlet chlorophyll excited states is reduced. The comparison between transformed lines with *LHCSR3* gene under *HSP70/RBCS2* promoter and their background, *npq4 lhcsr1* mutant, demonstrate how the

biochemical changes observed in transformed lines are not dependent on their background; the presence of LHCSR3 ensures a minimal level of photoprotection which allows the chloroplast to adapt the photosynthetic apparatus in order to exploit, as much as possible, the unquenched excitation energy. In addition, since LHCSR subunits have been previously reported to interact with both PSII and PSI [230,243,265], it cannot be excluded that LHCSR1 or LHCSR3 in *C. reinhardtii* could be required for this light-dependent adaptation process of the thylakoid membranes by controlling PSII and/or PSI stabilization in high light-treated cells; this possible hypothesis requires additional work to be elucidated. In summary, the results herein reported provide additional information on the relationship between NPQ and productivity in *C. reinhardtii*, suggesting that a possible strategy to improve light use efficiency and biomass productivity is controlling the expression of LHCSR3 gene by a promoter which is not strongly light inducible as in the case of its endogenous promoter, causing a strong reduction of NPQ induction in high light-treated cells. This strategy, herein reported for the model organism *C. reinhardtii*, could be transferred to other algal species, such as those with high commercial interest; in this case, knockout of potential high light-upregulated LHCSR-like genes could be obtained by genome editing or random mutagenesis, followed by complementation of LHCSR gene(s) under the control of a constitutive promoter. It is worth to mention that the relevance of NPQ induction in the natural environment is likely high, considering the ubiquitous identification of NPQ activation among oxygenic photosynthetic organisms. However, in artificial controlled conditions, as those experienced by microalgae in photobioreactors, tuning of NPQ can be a powerful tool to increase biomass productivity.

Materials and Methods

Chlamydomonas reinhardtii transformation

LHCSR3 coding sequence was obtained by PCR amplification of cDNA obtained from RNA extracted from high light treated 4A+ cells [106]. LHCSR3 coding sequence was then cloned in two vectors called pSL18_HR and pSL18_HR_chloro. Both vectors are derived from PSL18 vector [182] controlling the inserted sequence with a promoter obtained by fusion of heat shock protein 70 e RUBISCO small subunit promoters [394]. In the case of PSL18_HR_chloro the inserted LHSR3 coding sequence was deleted of the first 42 bases to remove the endogenous transit peptides, which was substituted by the transit peptide of RUBISCO small subunit[403]. *npq4 lhcsr1* strain [121] was transformed by electroporation as described in [182]. Selection of transformed colonies were performed in solid medium in presence of paromomycin.

Chlamydomonas reinhardtii cultivation

C. reinhardtii cells of strains 4A+, CW15, *npq4*, *npq4 lhcsr1* [101,190,404] and transformed lines were grown in minimum medium (HS medium) in flasks in control conditions (70 µmol $m^{-2} \cdot s^{-1}$; photoperiod of 16/8 h of light/dark). Growth analysis in liquid medium was performed in a small scale photobioreactors provided by Multi-Cultivator MC 1000 (Photon System Instruments, Brno, Czech Republic) as described in [190]. The samples were grown for one day at 70 µmol $m^{-2} \cdot s^{-1}$, and then at 400 µmol $m^{-2} \cdot s^{-1}$. Each experiment started with 5 × 10^5 cells/mL in minimal medium (HS medium) enriched with $NaHCO_3$ (0.5 g/L). Cell density in the Multi-Cultivator MC 1000 tubes was automatically monitored every ten minutes by measuring cell dependent scattering at 730 nm. The samplings for pigment analysis, immunoblotting, fluorescence and photosynthetic measurements were carried out on cultures in exponential growth phase. At the end of the exponential phase of growth, the cells were counted at the microscope using an improved Neubauer hematocytometer. Specific growth rates were calculated from liner regression of the exponential growth phase in logarithmic scale as described in [399]. Cell dry weight was measure upon drying biomass for 4 days at 60 °C. Spot test was performed spotting cells grown at 70 µmol $m^{-2} \cdot s^{-1}$ at mid-exponential phase. In particular, 10^2, 10^3 and 10^4 cells were spotted HS medium with 1% agar added; plates were then exposed to high light (400 µmol $m^{-2} \cdot s^{-1}$) for eight days.

Chlorophyll fluorescence and oxygen evolution measurement

A video imaging system designed for acquiring fluorescence (FluorCam 800MF by Photon System Instruments, Drasov, Czech Republic) was used for

screening transformed lines for a phenotype of increased NPQ compared to their background *npq4 lhcsr1*. NPQ was calculated as Fm/Fm'− 1 according to [202], where Fm is the maximum fluorescence emitted upon exposure to a saturating flash (3000 µmol $m^{-2}·s^{-1}$) of dark adapted cells, while Fm' is the maximum fluorescence emitted upon exposure to a saturating flash of cells exposed to actinic light (1200 µmol $m^{-2}·s^{-1}$). NPQ measurements were also performed using a PAM-110 fluorometer with a saturating light at 5000-µmol photons $m^{-2}·s^{-1}$ and actinic light of 1500 µmol photons $m^{-2}·s^{-1}$. Before measurements, cells were dark-adapted under stirring for at least 60 min at room temperature. Photosynthetic O_2 production was measured on whole cells at 25 °C using a Clark electrode for the liquid phase oxygen measurements (Oxy-Lab, Hansatech Instruments Ltd., Norfolk, UK) [190].

Pigment analysis

Pigments analysis were performed upon pigments extraction in 80% acetone and HPLC analysis as previously described [405].

SDS-PAGE analysis, immunoblot assays and western blotting quantifications

Protein extracted from whole cells were analyzed by SDS-PAGE electrophoresis on a 15% acrylamide gel with Tris-Tricine buffer system [232]. Immunoblot assays with antibodies against different polypeptides were performed as previously described [190,229].

Singlet Oxygen production

Singlet oxygen production was measured *in vivo* by exposing cells to a high red light (1500 µmol $m^{-2}·s^{-1}$) using Single Oxygen Sensor Green fluorescent probe [396] as described in [190].

Supplementary data

		Chl/cell	*s.d.*	Chl a/b	*s.d.*	Chl/Car	s.d.
Low light	**WT**	2.16E-06	*1.99E-07*	1.86	*0.01*	3.93	0.02
	npq4 lhcsr1	2.02E-06	*1.23E-07*	2.37	*0.01*	3.86	0.01
High light	**WT**	7.29E-07	3.29E-08	1.49	0.04	2.48	0.20
	npq4 lhcsr1	6.87E-07	4.28E-08	1.55	0.07	2.05	0.06

Table S 2.7.1 *Pigments analysis of npq4 lhcsr1 compared to WT. Chlorophyll content per cell, Chl a/b ratio, and CHl/Car ratio are reported with standard deviation (n=4).*

	Average diameter (µm)			
	Low light	*s.d.*	**High light**	*s.d.*
WT (4a+)	8.15	*1.91*	7.98	*2.47*
B6	6.58	*1.53*	10.57	*2.12*
E7	6.98	*1.55*	9.44	*2.81*
E10	6.80	*1.26*	9.13	*2.29*

Table S 2.7.2 *Average cell diameter of WT and transformed lines. Average diameter was calculated from cells grown in low light or high light conditions when cells were at the end of their exponential growth. Standard deviation is reported (n=40).*

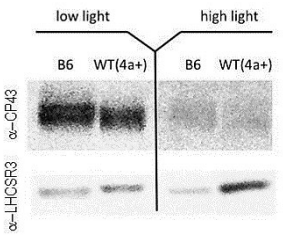

Figure S 2.7.1 *example of immunoblot analysis on protein extracts from WT and one transformed line grown in low light or high light loaded on the same filter. Immunoblotting was performed using specific antibodies recognizing LHCSR3 and CP43; 1,5 µg of chlorophylls was loaded for each lane.*

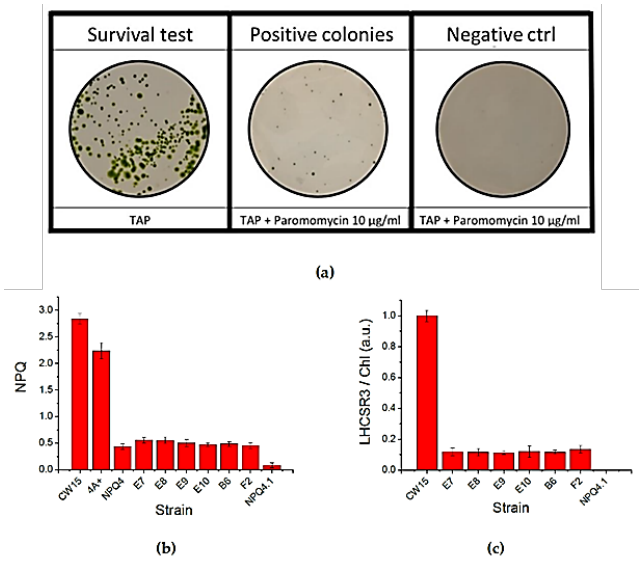

Figure S 2.7.2 *Screening of transformed lines expressing LHCSR3 protein in npq4 lhcsr1 background. (a): antibiotic selection in presence of paromomycin compared to survival test (no antibiotic added), and negative control (ctrl), where in the latter npq4 lhcsr1 cells not transformed were plated. (b): maximum NPQ induction observed in transformed lines upon high light adaptation for 5 five days compared to their background npq4 lhcsr1. Strains accumulating both LHCSR1 and LHCSR3 (CW15 and 4A+) or accumulating only LHCSR1 (npq4) are also reported for comparison. (c): LHCSR3 accumulation analyzed by immunoblotting reaction.*

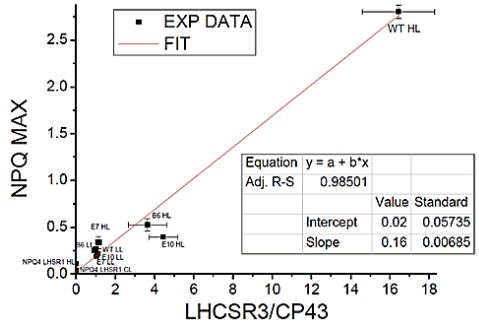

Figure S 2.7.3 *Linear correlation of LHCSR3 content per chlorophyll and maximum NPQ induction. In the graph the maximum NPQ measured for WT, npq4 lhcsr1 and transformed lines cultivated in low light (LL) or high light (HL) is reported as a function of LHCSR3 content per CP43 (Figure 2). Linear fit is reported on red. In the inset table the fitting parameter are indicated.*

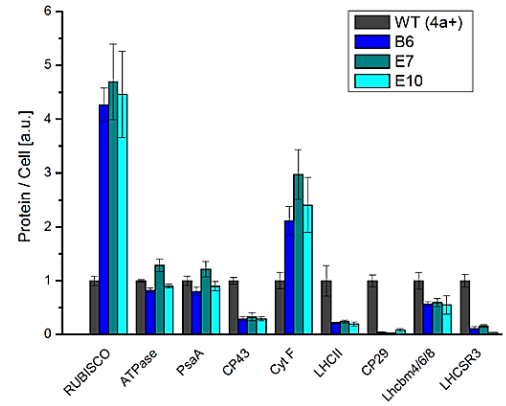

Figure S 2.7.4 *Immunoblot analysis of photosynthetic subunit accumulation normalized on a cell basis. Immunoblot signals reported in Figure 4 were analyzed by densitometry and reported normalized to the cell concentration. Standard deviation is indicated as error bars (n=4).*

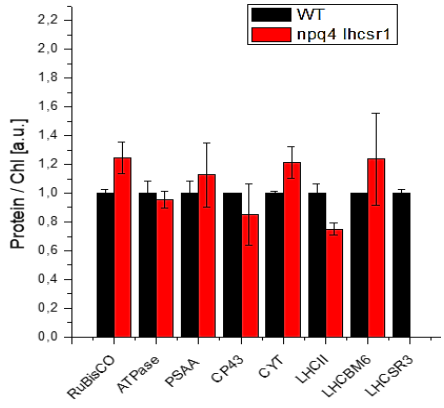

Figure S 2.7.5 *Immunoblot analysis of photosynthetic subunits accumulation in npq4 lhcsr1 compared to WT. immunoblot analysis performed on WT and tranformed lines using specific antibodies for RuBisCO, ATPase β-subunit, CP43, PsaA, Cyt b6, LHCII, LHCBM6, and LHCSR3. Immunoblotting results were analysed by densitometry in order to determine the relative protein abundance. Each protein level was normalized to the WT protein level.*

Chapter 3

Engineering ketocarotenoids biosynthesis in *Chlamydomonas reinhardtii*

Contents

Functional analysis of photosynthetic pigment binding complexes in the green alga Haematococcus pluvialis reveals distribution of astaxanthin in Photosystems **149**

Turning a green alga red: engineering astaxanthin biosynthesis by intragenic pseudogene revival in Chlamydomonas reinhardtii **163**

3.1

Functional analysis of photosynthetic pigment binding complexes in the green alga Haematococcus pluvialis reveals distribution of astaxanthin in Photosystems

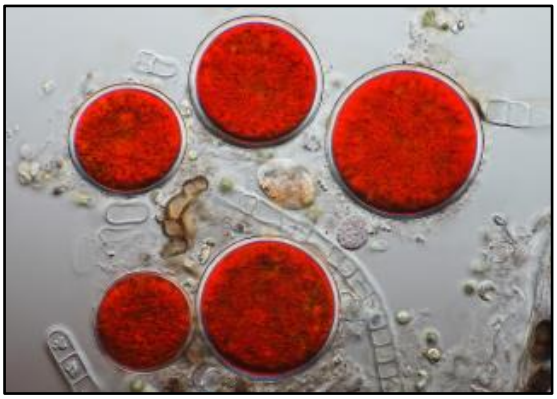

This section is based on published article: Mascia, F. *et al.* Functional analysis of photosynthetic pigment binding complexes in the green alga Haematococcus pluvialis reveals distribution of astaxanthin in Photosystems. *Scientific reports* **7**, 16319, doi:10.1038/s41598-017-16641-6 (2017).

Author contributions: Ballottari M. conceived the work and designed the experiments. Mascia F. and Girolomoni L. performed all the experiments. Cazzaniga S. contributed to experiments reported in Fig. 1-8. Perozeni F. contributed to isolation of pigment binding complexes (Fig. 1). D'Andrera C. and Cerullo G. coordinated the time resolved fluorescence analysis experiments. Mascia F., Ballottari M., Perozeni F., Bargigia. and D'Andrea C. performed the time resolved fluorescence analysis experiments (Fig. 6). Alcocer M., Bargigia I., Ballottari M., Cerullo G. and D'Andrea C. analyzed the fluorescence decay results by global analysis (Fig. 6). All the authors contributed to writing the manuscript. All the authors discussed the results and commented on the manuscript.

Functional analysis of photosynthetic pigment binding complexes in the green alga *Haematococcus pluvialis* reveals distribution of astaxanthin in Photosystems

Francesco Mascia[1], Laura Girolomoni [1], Marcelo J. P. Alcocer [2], Ilaria Bargigia[2], Federico Perozeni [1], Stefano Cazzaniga[1], Giulio Cerullo[3], Cosimo D'Andrea[2,3] & Matteo Ballottari [1]

[1]Dipartimento di Biotecnologie, Università di Verona, Strada Le Grazie 15, I-37134, Verona, Italy.
[2]Center for Nano Science and Technology @PoliMi, Istituto Italiano di Tecnologia, via Pascoli 70/3, 20133, Milano, Italy.
[3]IFN-CNR, Department of Physics, Politecnico di Milano, P.za L. da Vinci 32, 20133, Milano, Italy

Abstract

Astaxanthin is a ketocarotenoid produced by photosynthetic microalgae. It is a pigment of high industrial interest in acquaculture, cosmetics, and nutraceutics due to its strong antioxidant power. Haematococcus pluvialis, a fresh-water microalga, accumulates high levels of astaxanthin upon oxidative stress, reaching values up to 5% per dry weight. *H. pluvialis* accumulates astaxanthin in oil droplets in the cytoplasm, while the chloroplast volume is reduced. In this work, we investigate the biochemical and spectroscopic properties of the *H. pluvialis* pigment binding complexes responsible for light harvesting and energy conversion. Our findings demonstrate that the main features of chlorophyll and carotenoid binding complexes previously reported for higher plants or Chlamydomonas reinhardtii are preserved under control conditions. Transition to astaxanthin rich cysts however leads to destabilization of the Photosystems. Surprisingly, astaxanthin was found to be bound to both Photosystem I and II, partially substituting β-carotene, and thus demonstrating possible astaxanthin biosynthesis in the plastids or transport from the cytoplasm to the chloroplast. Astaxanthin binding to Photosystems does not however improve their photoprotection, but rather reduces the efficiency of excitation energy transfer to the reaction centers. We thus propose that astaxanthin binding partially destabilizes Photosystem I and II.

Introduction

Haematococcus pluvialis is a photosynthetic fresh-water microalga which accumulates a high level of the ketocarotenoid astaxanthin (up to 5% DW) [165,406-408]. Astaxanthin is mainly used as coloring agent in aquaculture but it has been also reported to be a strong antioxidant, preventing production of reactive oxygen species (ROS) and lipid peroxidation in solution and in several biologic systems [409-413]. Numerous studies have shown that astaxanthin has health-promoting effects in the prevention and treatment of various diseases such as cancers, chronic inflammations, metabolic syndrome, cardiovascular and gastrointestinal diseases, as well as enhancing the immune system and protecting the skin from radiation injury [414]. Astaxanthin cannot be manufactured in animals and therefore must be consumed in the diet. This carotenoid (Car) is thus of great interest for several industrial sectors and has a high market potential. Many studies have addressed the role of astaxanthin in *H. pluvialis* and the phenotypical characterization of this alga [165,406,408,415-420]. The lifecycle of *H. pluvialis* includes four phases and astaxanthin is accumulated only in the aplanospores phase, which is induced under stress conditions such as high light intensity, nutrient starvation, high salinity or low/high temperatures [165,419,421,422]. Astaxanthin production from *H. pluvialis* mass cultivation is commonly carried out in a two-stage batch culture; biomass production occurs in the first stage (green stage), while in the second stage (red stage) the cultures are stressed to induce astaxanthin accumulation [423]. Astaxanthin is accumulated mainly at the level of the endoplasmatic reticulum in the form of mono- and di-esters by using β-carotene as precursor [424]. While several reports focused on astaxanthin production and its application for humans as a nutraceutic, details regarding the role of this Car in *H. pluvialis* cells are still not complete [165,407,415,416,419,425-427]. The astaxanthin biosynthetic

pathway depends on carbon fixation by the photosynthetic process in the chloroplasts. During transition to astaxanthin rich cysts, Car biosynthesis is triggered and the plastids are degraded [428]. Photosynthetic processes are functionally divided in two phases; the light phase and dark phase. The light phase takes place in the thylakoid membranes, with light energy being harvested and converted into chemical energy in the form of NADPH and ATP. The subsequent dark phase is where NADPH and ATP are used in the stroma by Calvin-Benson cycle for enzymatic CO_2 fixation and reduction to carbohydrates. PSII and PSI are responsible for energy conversion, cytochrome b6f contributes to electron transport and proton translocation in the lumen, and ATPase catalyzes ATP synthesis using the energy derived from the transmembrane proton gradient. PSI and PSII are pigment binding proteins composed of a core complex and antenna proteins called Light Harvesting Complexes (LHC) [36,40,61,219]. The core complex binds chlorophyll (Chl) *a* and β-carotene, whilst the antenna proteins bind Chl *a*, Chl *b*, and xanthophylls [32,40]. Pigments bound by the photosystems absorb photons and transfer excitation energy to the reaction centers. In particular PSI was observed to trap excitation energy at the reaction center (RC) faster than PSII [355]. Higher plants and unicellular microalgae show some differences in both PSII and PSI supramolecular organization, with different stoichiometries of LHC proteins per PSI(II) core complexes. Four LHC subunits, called Lhca1-4, were found bound to PSI core complex of *A. thaliana*, while 7 to 9 different Lhca complexes were identified in the PSI-LHCI complexes from the green alga *Chlamydomonas reinhardtii*. In the case of PSII, the number of LHC complexes bound, called Lhcb, is more variable and depends on growth conditions [32,36,37,42,61]. Very little information is available regarding the photosynthetic complexes of the green alga *H. pluvialis* and how they are modulated during cyst formation and astaxanthin accumulation. Moreover, it is still under debate if astaxanthin accumulation has some photoprotective function at the level of the chloroplast [419,425,429,430]. The aim of this work is to characterize the photosynthetic complexes in *H. pluvialis* and the possible role of astaxanthin in the photosynthetic apparatus during acclimation to high light and transition to the red stage.

Results

Astaxanthin accumulation in *H. pluvialis*

Haematococcus pluvialis cells were grown in BG11 medium at 50 μE for 7 days (hereafter, referred as G/Green), at 400 μE for 3 days (hereafter, referred as O/Orange) and at 400 μE for 6 days (hereafter, referred as R/Red). As reported in **Figure 3.1.1**, a clear change in the culture color appeared under the three different growth conditions, from green, to brownish, to red for G, O and R conditions respectively. *H. pluvialis* cells grown were then observed in bright-field microscopy (**Figure 3.1.1b**). Cells grown in the G condition were round green cells with a distinct cell wall layer; in the O condition, cells became reddish, likely due to astaxanthin accumulation, but green chloroplasts were still visible; some cells in O and all cells R were characterized by a complete transition into a red stage, with strong astaxanthin accumulation. In this

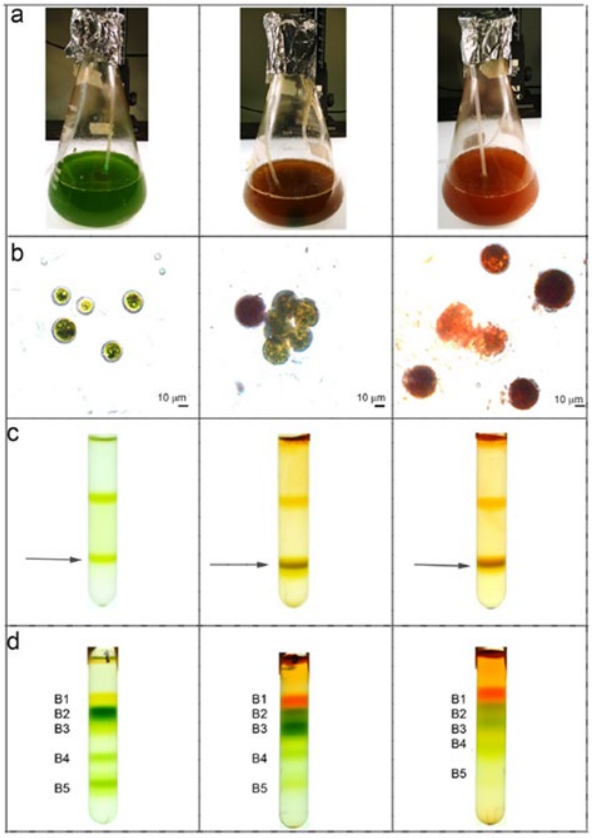

Figure 3.1.1 *Cell cultivation, membranes and pigment binding complexes isolation. Panel A: H. pluvialis cultures grown under 3 different stress conditions. Green: 50 μE for 7 days; Orange: 400 μmol $m^{-2}s^{-1}$ for 3 days; Red: 400 μmol $m^{-2}s^{-1}$ for 6 days. Panel B: microscope observation of cells grown as in Panel A. Panel C. isolation of plastid membranes from G, O and R cells. Purified membranes are indicated by the arrow. Panel D: Sucrose gradient ultracentrifugation separation of pigment binding complexes from plastid membranes solubilized in β-DM 1%.*

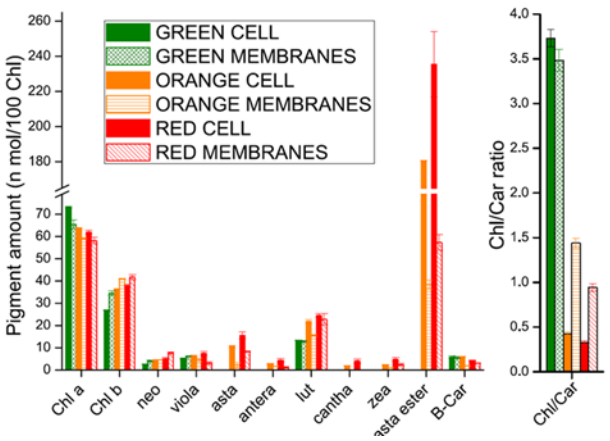

Figure 3.1.2 *Pigment analysis on H. pluvialis whole cells and isolated membranes. Pigment extracts were analyzed by HPLC. Pigment data were normalized to 100 chlorophylls. Chl: chlorophyll; Car: carotenoid; Neo: neoxanthin; Viola: violaxanthin; Lute: Lutein; Antera: anteraxanthin; Cantha: canthaxanthin; Zea: zeaxanthin; B-Car: β-carotene; Asta: astaxanthin; Asta ester: esterified forms of astaxanthin. Standard deviation (s.d.) are reported (n = 3).*

condition, partial cell degradation was also evident. Pigment composition was investigated by HPLC and reported in **Figure 3.1.2**. A strong reduction of chlorophyll to carotenoid (Chl/Car) ratio was observed in O and R cells with the higher Car accumulation in R cells. Astaxanthin esters were the predominant Car species found in O and R cells, while no traces of astaxanthin were found in G cells. Traces of canthaxanthin, a precursor of astaxanthin, were also found in O and R cells. Incidentally finding of Chls, β-carotene and xanthophylls in O and R cells suggested the residual presence of photosynthetic complexes, responsible for the photosynthetic activity previously reported for *H. pluvialis* during transition to the red stage [419]. Lutein and neoxanthin were more abundant on a Chl basis in O and R conditions, while beta-carotene was reduced in R cells. Since lutein and neoxanthin are bound only to LHC complexes, while beta-carotene is essentially bound only to PSI or PSII core subunits, the increased neoxanthin or lutein to beta carotene ratios imply a partial degradation of core subunits during high light exposure.

Isolation and characterization of pigment binding complexes of *H. pluvialis* in different growth conditions

Thylakoid membranes of G, O and R cells were isolated by mechanical cell disruption followed by selective centrifugations with a final purification step by ultracentrifugation in a sucrose step gradient. As reported in **Figure 3.1.1c**, membranes at similar sucrose densities were recovered from both G, O and R samples. Pigment composition of the purified membranes was then investigated by HPLC and reported in **Figure 3.1.2**. In O and R samples, the Chl/Car ratio was significantly reduced in purified thylakoid membranes as compared to whole cells. The observed reduction is mainly related to a strong decrease of astaxanthin, either in free or esterified forms, as compared to pigment extracts from whole cells. A reduction of β-carotene, anteraxanthin, zeaxanthin, canthaxanthin and lutein was also observed in O and R membranes as compared to whole cells, even if it was less pronounced when compared to astaxanthin. Since it has been reported that astaxanthin is accumulated only outside the plastids in *H. pluvialis* [424,425,428], the results obtained could be due to a co-purification of thylakoid membranes and astaxanthin rich oil droplets of similar densities. Since the presence of astaxanthin in thylakoid membranes has been reported for transgenic plants accumulating this Car [431-433], the possible presence of astaxanthin molecules bound to pigment binding complexes was investigated using treated membranes. Purified membranes were solubilized and the Chl binding complexes were isolated by ultracentrifugation in a sucrose gradient [434]. This ultracentrifugation step allowed a separation of the different photosynthetic complexes, based on their molecular density. Five bands (B1, B2, B3, B4, B5) were observed in every condition (G, O, R) (**Figure 3.1.1d**). B1-5 fractions were recovered and their absorption spectra investigated. The B1 band was composed of free pigments, as indicated by the Chl Qy absorption peak below 670 nm (**Figure S 3.1.1**). Absorption spectra of B2 and B3 fractions (**Figure 3.1.3a-b**) were similar in G, O and R conditions, resembling the features of LHC antenna proteins with two peaks in the Qy region attributable to Chl *a* (672 nm) and *b* (650 nm). Based on their molecular density, B2 and B3 were composed of monomeric and trimeric LHC proteins respectively. B4 spectra showed an almost complete absence of the 470 nm and 650 nm peaks (**Figure 3.1.3c**), which are both related to Chl *b*. This indicates a high Chl *a*/*b* ratio, and hints at the presence of PSII-core in this fraction. Comparing O B4 with G B4, it is possible to notice a decreased absorbance at ~470 nm coupled with an increased absorbance at ~530 nm, which suggests the presence of astaxanthin. B5 spectra (**Figure 3.1.3d**)

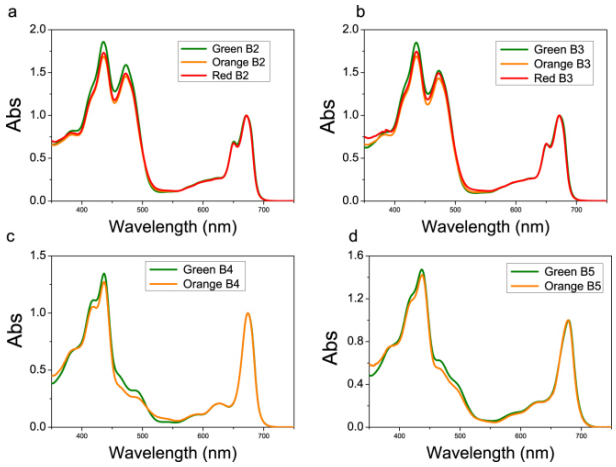

Figure 3.1.3 *Absorption spectra of pigment binding complexes isolated from H. pluvialis. Absorption spectra of B2, B3, B4 and B5 fraction (Figure 1 D) were normalized to the maximum absorption peak in the 600 nm and 700 nm region.*

reveal the predominance of Chl *a* with a maximum absorbance in the Qy region at 679 nm, although Chl *b* contributions at 650 and 470 nm were still present in a lower amount. B5 was thus likely composed of the PSI-LHCI supercomplex. PSII-core (B4) and PSI (B5) fractions from R were not harvested since the bands in sucrose gradient were fuzzier and not well defined, suggesting partial degradation of these complexes in these conditions. The protein composition of B2-B5 from G and O samples was subsequently investigated by SDS-PAGE (**Figure 3.1.4**). B2 and B3 were characterized by four bands migrating at around 30 kDa, as expected for LHC antenna proteins. Interestingly, the two bands at lower molecular weight (MW) were more abundant in B2 than in B3 for both G and O samples, suggesting the preferential monomeric state of some specific LHC proteins as in the case of CP26 and CP29 in *C. reinhardtii* [36,63]. In B4 fractions, PSII-core proteins such as CP43, CP47, D1, D2 and PsbO subunits were identified on the basis of their apparent MW [61]. In B5 fractions (PSI-LHCI), high MW bands (60–70 KDa) could be attributed to PsaA and PsaB, together with bands at low MW (<30 KDa) attributable to LHCI antenna proteins and other PSI core subunits. The pigment binding properties of the different isolated fractions were then analyzed by HPLC (**Table 3.1.1**). Pigment results from B2 and B3 fractions were normalized to 14 Chls, as previously reported for LHCII subunits from higher plants [15]. Chl *a*/Chl *b* ratios were similar in B2 and B3 fractions from G, O or R samples, while Chl/Car ratios were increased in O and R as compared to G. This was mainly due to a strong reduction in violaxanthin content which is likely related to reduced stability of the V1 site in the presence of zeaxanthin, as previously reported for LHC proteins isolated from higher plants [23,435]. Traces of zeaxanthin were indeed detected in B2 and B3 from O and R cells. Zeaxanthin accumulation at the V1 sites of the LHC protein is likely due to xanthophyll cycle activation during high light stress or zeaxanthin accumulation in O and R membranes as a precursor to astaxanthin [23,228,346,424]. The reduced stability of the V1 site in B2 and B3 complexes from O and R cells could also be the reason for the reduced content of lutein in these fractions as compared to B2 and B3 fractions from G samples. Since more than 2 luteins were found in B2 and B3 fractions, the extra lutein is likely bound to the peripheral site V1 [436], which however is partially empty in O and R samples. Astaxanthin was almost completely absent in LHC proteins, even if traces of this ketocarotenoid were present only in O/R B2 and B3 fractions. The possible affinity of LHCII complexes for astaxanthin has indeed been previously investigated by *in vitro* reconstitution [437]. B4 fractions were characterized by a high Chl*a*/Chl*b* ratio (>20), as expected for PSII-core. Traces of Chl *b*, neoxanthin and violaxanthin were also detected, and are likely to arise from the residual presence of antenna

	Chl	Chla/Chlb	Chl a	Chl b	Chl/Car	Neo	Viola	Asta	Antera	Lute	Zea	Asta ester	β-Car
GREEN B1	100	2.8	73.7	26.3	0.8	6.9	36.9	n.d.	n.d.	73.8	n.d.	n.d.	6.2
ORANGE B1	100	3.3	76.9	23.2	0.2	11.5	59.6	10.2	11.8	69.6	8.0	434.6	6.6
RED B1	100	4.2	80.9	19.1	0.1	12.0	105.2	17.8	23.1	91.4	14.7	1352.5	27.3
GREEN B2	14	1.6	8.6	5.4	4.0	0.7	0.7	n.d.	n.d.	2.7	n.d.	n.d.	n.d.
ORANGE B2	14	1.5	8.4	5.6	4.7	0.9	0.2	<0.1	n.d.	2.3	0.1	<0.1	<0.1
RED B2	14	1.5	8.4	5.6	4.5	0.9	0.2	<0.1	n.d.	2.4	0.1	0.1	<0.1
GREEN B3	14	1.7	8.8	5.2	3.8	0.7	0.8	n.d.	n.d.	2.8	n.d.	n.d.	n.d
ORANGE B3	14	1.5	8.5	5.5	4.8	0.8	0.3	<0.1	n.d.	2.3	0.1	n.d.	n.d.
RED B3	14	1.5	8.4	5.7	4.4	0.9	0.2	0.1	n.d.	2.3	0.1	0.1	n.d.
GREEN B4	72	22.6	68.9	3.1	4.3	0.3	1.0	n.d.	n.d.	3.3	n.d.	n.d.	12.1
ORANGE B4	72	29.4	69.6	2.4	6.3	0.6	0.6	0.6	n.d.	2.2	n.d.	1.9	5.4
GREEN B5	170	7.1	149.1	20.9	4.4	0.2	8.2	n.d.	n.d.	17.0	n.d.	n.d.	13.5
ORANGE B5	170	7.0	148.7	21.3	4.4	0.8	6.0	1.9	n.d.	18.0	1.0	0.9	10.6

Table 3.1.1 *Pigment analysis of isolated photosynthetic complexes. Pigment extracts were analyzed by HPLC. Pigment data from B2 and B3 fractions were normalized to 14 chlorophylls; pigments from B4 fractions were normalized to 72 chlorophylls; pigments from B5 fractions were normalized to 170 chlorophylls. Chl: chlorophyll; Car: carotenoid; Neo: neoxanthin; Viola: violaxanthin; Lute: Lutein; Zea: zeaxanthin; β-Car: β-carotene; Asta: astaxanthin; Asta ester: esterified forms of astaxanthin*

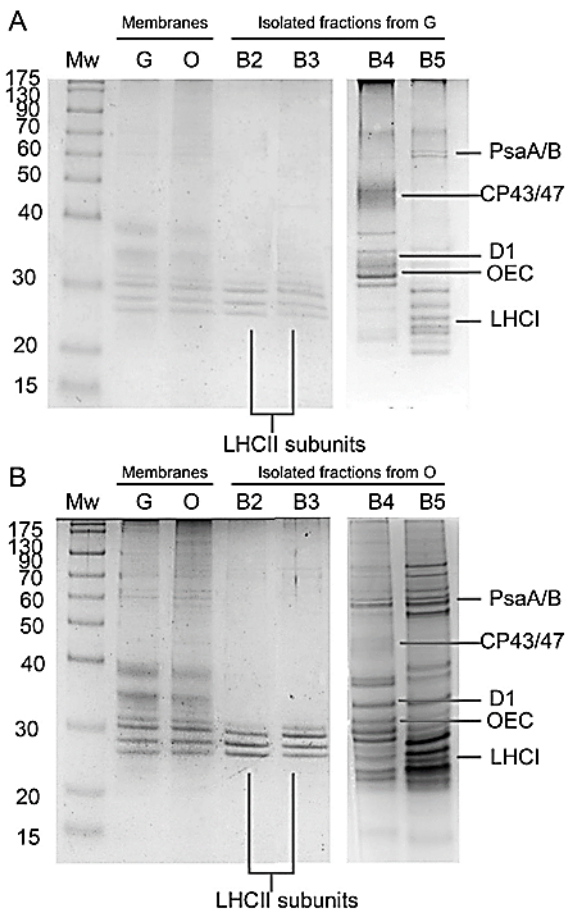

Figure 3.1.4 *SDS-PAGE of H. pluvialis purified membranes and isolated pigment binding complexes. Panel A: Isolated B2-5 fractions from Green cells (Figure 1) samples; Panel B: Isolated B2-5 fraction from Orange cells. SDS-PAGE gels loaded with isolated membranes and B2 B3 fractions were Coomassie stained while gel loaded with B4 and B4 were silver stained. Mw: molecular weight marker; G: proteins from "Green" cells grown at 50 µE; O: proteins from "Orange" cells grown at 400 µE for 3 days.*

proteins. The most evident difference between G and O of B4 fractions is a decrease in β-carotene which is partially replaced in O by astaxanthin. In particular ≈2.5 molecules of astaxanthin were bound by PSII-core in O, mainly in its esterified form. It is worth noting that violaxanthin and lutein were also found in decreased quantities in O B4 as compared to G B4. These xanthophylls are likely related to residual LHC proteins bound to B4, and it is not possible exclude a possible substitution of these pigment with astaxanthin in O B4. PSI-LHCI fractions (B5 fraction) were characterized by a Chl *a*/Chl *b* ratio of ≈7, an intermediate value between the Chl *a*/*b* ratio previously measured in the case of PSI-LHCI isolated from higher plants [355] and *C. reinhardtii* [337]. The lower Chl *a*/*b* ratio observed in *C. reinhardtii* is due to an increased content of Lhca proteins, with 7–9 Lhca subunits bound per reaction center as compared to the 4 Lhca subunits found in the case of *A. thaliana* [37,40,337,438]. In order to estimate the Lhca content associated to the PSI reaction center in *H. pluvialis*, we assumed 3.4 Cars per Lhca subunit as previously reported in the case of *A. thaliana* and *C. reinhardtii* [337] and 100 Chl *a* molecules per PSI core complex [42,43,254,439]. From the Chl *a*/*b* and Chl/Car ratios of the B5 fractions, we estimated 5 Lhca proteins per P700, with 14 Chls and 3.4 Cars bound by each subunit and 170 Chls bound by the PSI-LHCI complex. An intermediate value of Lhca content per PSI-LHCI complex in *H. pluvialis* as compared to higher plants and *C. reinhardtii* was then confirmed by PSI-LHCI functional antenna size measurement on whole cells (**Figure S 3.1.2**). Comparing B5 from G and O samples, a ~21% decrease in β-carotene content was evident, with a loss of ~2.9 molecules per P700. Conversely, ~2.8 astaxanthin molecules were found bound to each O B5 complex, suggesting a possible substitution of β-carotene with astaxanthin. A 28% decrease in violaxanthin was also observed in O B5 as compared to G B5, coupled with a rise in zeaxanthin, lutein and neoxanthin. A general re-organization of Car binding sites was thus evident in O samples even if the same total amount of Car was found in G or O B5 complexes. The markedly increased carotenogenesis observed in O cells leading to high accumulation of lutein, zeaxanthin and astaxanthin in thylakoid membranes is likely to be the reason for the different pigment binding properties of B4 and B5 complexes.

Excitation energy transfer in astaxanthin binding complexes

The functional properties of astaxanthin bound to photosynthetic complexes were initially investigated by fluorescence measurements at 77 K, where emission is mainly attributed to the lowest Chl excited states. When exciting Chl *a* at 440 nm, B2 and B3 fractions from G cells showed similar emission peaks at 680 nm and similar excitation spectra characterized by a high Chl *b* contribution (**Figure 3.1.1**). The traces of astaxanthin found in LHC proteins (**Table 3.1.1**) do not influence the fluorescence properties of these fractions. PSII-core fractions (B4) from both G and O samples were characterized by an emission spectrum peaking at 686 nm and an excitation spectrum almost absent of Chl *b* contribution, as expected for a PSII-core. Even in this

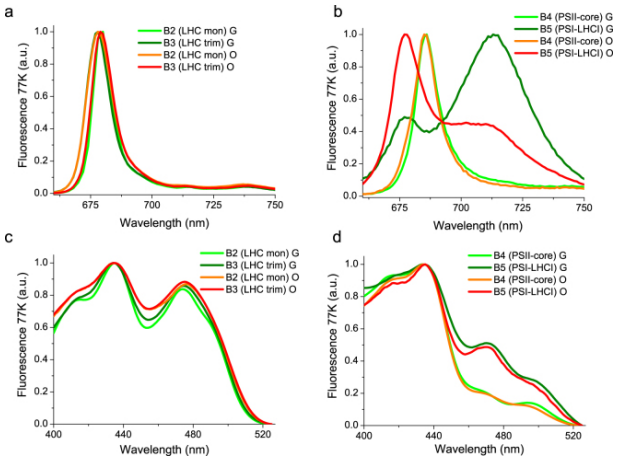

Figure 3.1.5 *77K Fluorescence emission and excitation spectra of isolated pigment binding complexes. Panel A/B:77K fluorescence emission spectra of B2-3 (Panel A) and B4-5 (Panel B) fractions, upon excitation at 440 nm. Panel C/D: 77K fluoresce excitation spectra of B2-3 (Panel C) and B4-5 (Panel D) fractions. Emission wavelengths were set at 680 nm for B2 and B3, 687 for B4 and 715 for B6 fractions.*

case, astaxanthin binding to PSII core did not influence the fluorescence properties of the complex. PSI-LHCI complex (B5) isolated from G cells presented two separated peaks; a major peak at 715 nm related to emission from the low energy Chls bound to the complex, and a minor peak at 680 nm associated to partially dissociated antenna proteins. In PSI-LHCI from O cells, the 680 nm emission peak was more dominant than the 715 nm peak, suggesting a higher proportion of detached LHCI subunits. The excitation spectra of the 715 nm emission peaks associated to the intact PSI-LHCI complex were similar for both G and O samples. Astaxanthin binding to the different complexes does not alter the energy of the emitting state but could be involved in a partial disconnection of LHC proteins from PSI core complex. Excitation energy transfer dynamics were subsequently investigated by time resolved fluorescence spectroscopy with a streak camera-based set up. Streak camera detection allows simultaneous acquisition of fluorescence decays at different wavelengths. The resulting datasets were analyzed by global analysis, resulting in decay associated spectra (DAS) for each sample – wavelength dependent amplitudes for each time-constant in a multi-exponential decay [272]. DAS identified in each sample were normalized to the total DAS amplitude of that sample. As reported in **Figure 3.1.6**, two components were sufficient to fit B2 and B3 decays, with a shorter redder component at ~200 ps ($DAS1_{B2/3}$) and a longer bluer component at ~4 ns ($DAS2_{B2/3}$). $DAS1_{B2/3}$ and $DAS2_{B2/3}$ could be assigned to two different LHC protein conformations with different non photochemical quenching properties, as previously reported [440]. DAS1 was higher in B2 than in B3 fractions and stronger in O than in G samples, indicating stronger quenching properties in B2 and in O samples. Accordingly, average fluorescence decay times (τ_{AV}) were shorter in B2 than in B3 fractions and in O than in G samples (**Figure 3.1.6**). The results obtained in the case of B2 and B3 are consistent with fluorescence decay kinetics of LHC monomers and LHCII trimers respectively [308,440]. The reduced τ_{AV} observed in the case of O fractions is unlikely to be related to the traces of astaxanthin or zeaxanthin bound to the complexes, but rather to varying protein compositions of these fractions induced by the different growth conditions and accumulation of protein subunits with stronger quenching properties [440]. In the case of B4 fractions, four DAS were identified. Differences were found mainly in the first two fast decaying $DAS1_{B4}$ and $DAS2_{B4}$, with decay constants of 8/22 ps, and 62/161 ps for Green/Orange B4 respectively. $DAS1_{B4}$ and $DAS2_{B4}$ amplitudes were similar in G samples, while in O samples $DAS2_{B4}$ had an increased weight as compared to $DAS1_{B4}$. $DAS3_{B4}$ and $DAS4_{B4}$ on the other hand exhibited similar time constants (300 ps and 4.4 ns respectively) in both G and O samples, with $DAS4_{B4}$ being more represented in O samples. $DAS1\text{-}4_{B4}$ identified for B4 are consistent with components previously reported for PSII core complexes, even if it is difficult to associate components unambiguously to Chl or protein moieties [441]. Only the weak 4.4 ns component ($DAS4_{B4}$), most clearly visible in the O sample, can be safely associated to partially detached antenna proteins or free Chls found in B4. A 77 ps τ_{AV} was calculated for B4 isolated from G cells, consistent with previous reports for PSII core [219]. The longer τ_{AV} determined in the case of B4 isolated from O cells (136 ps) suggests that excitation energy transfer to the PSII reaction center is partially disturbed in this complex. Four DAS components were also identified for the PSI-LHCI complexes (B5). In particular a short (5 ps) component, DAS1B5, with positive/negative amplitude was found in both G and O PSI-LHCI complexes and are attributed to energy equilibration within the complex [442]. The 13 ps $DAS2_{B5}$ found in B5 from G samples has been usually associated to emission from PSI-core. In the case of B5 from O cells, $DAS2_{B5}$ is characterized by time constant of

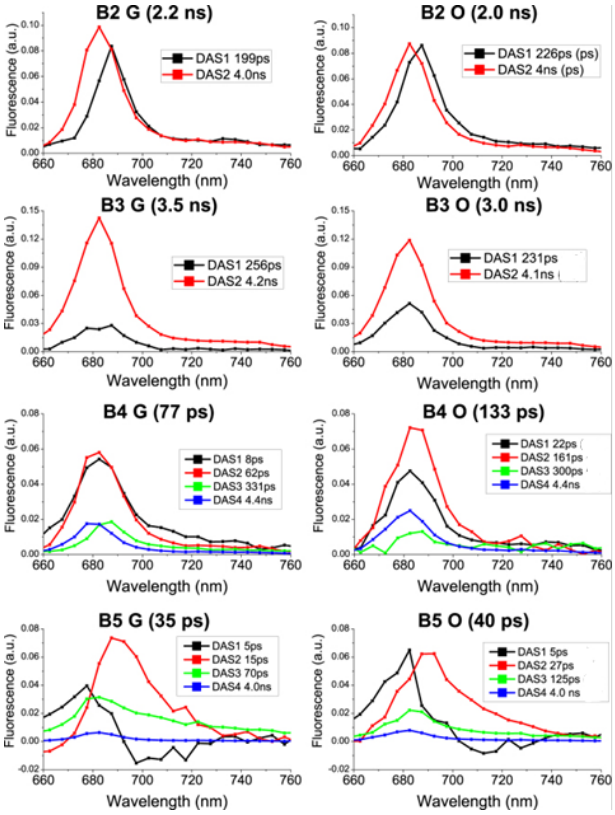

Figure 3.1.6 *Decay Associated Spectra (DAS) resulting from Global Analysis of fluorescence decay maps of isolated pigment binding complexes. 2D Streak camera maps were fitted with a multi-exponential decay function with a Global Analysis approach. The resulting wavelength dependent amplitudes, Ai (λ), are referred to as Decay Associated Spectra (DAS), with each DAS being associated with an exponential decay constant, τi. Decay Associated Spectra (DAS) of each sample are reported with associated decay constants indicated in the legend. Average fluorescence lifetimes for each sample is reported in brackets and calculated as ΣAiτi/ΣAi. Two exponential decay components were required to adequately fit the decay maps recorded for B2 and B3, whilst four were required for B4 and B5.*

27 ps which is longer than that in G samples and thus indicates an alteration of excitation energy transfer to the reaction center. $DAS3_{B5}$ found in the B5 fraction from G cells has a time constant of 70 ps and a spectrum which is more enriched in forms emitting above 700 nm. This component is related to energy transfer from peripheral LHCI complexes. In PSI-LHCI from O cells, the time constant associated with $DAS3_{B5}$ is increased to 125 ps whilst the DAS amplitude is reduced. This indicated some alterations in energy transfer from antenna complexes to the PSI reaction center. Finally, a small 4 ns component ($DAS4_{B5}$) was identified in both B5 fractions from G and O cells, and was attributed to detached antenna proteins as previously observed in PSI-LHCI preparations [228,337,355,442,443]. This ns component was almost 50% stronger in PSI-LHCI from O cells. Astaxanthin binding PSI-LHCI complexes from O cells were thus characterized by reduced excitation energy transfer to the reaction center from both the Chl moieties bound to the core complex and to the peripheral antenna proteins. They also contain a higher amount of partially disconnected LHCI proteins emitting in the ns time range, in agreement with the low temperature emission florescence spectra reported in **Figure 3.1.5**. In the case of PSI-LHCI, the photochemical efficiency (φPSI) of the complex can be estimated from the τ_{AV} (35 and 40 ps respectively for G and O samples), which in turn can be interpreted as the time required to transfer energy to the reaction center of the complex. φPSI calculated from PSI-LHCI τ_{AV} and disregarding the ns component, as previously reported [442], were in both cases higher than 98%. Inclusion of the ns component reduced the excitation energy transfer efficiency to 92% and 95% for the O and G samples respectively. Astaxanthin binding PSI-LHCI is thus characterized by a partial disconnection of LHCI proteins, whilst maintaining more than 90% of excitation energy transfer efficiency, as previously observed for PSI-LHCI complexes [337,355,444].

Photoprotective functions of astaxanthin in the plastids

The photoprotective role of astaxanthin bound to Chl binding subunits was evaluated by measuring $^1O_2$ production under high irradiance (2000 μmol $m^{-2}s^{-1}$) of red light (>600 nm) and application of a fluorescent probe (Singlet Oxygen Sensor Green, SOSG) whose fluorescence increases upon $^1O_2$ production [396]. The use of red light, which is absorbed only by Chls, enables selective investigation of the photoprotective role of astaxanthin without regard to its absorption properties [135,227]. As reported in **Figure 3.1.7**, after 30 minutes of illumination no significant differences were observed among G and O B2, B3 and B4 fractions (**Figure 3.1.7a-c**). In the case of PSI-LHCI complexes, O B5 showed a higher $^1O_2$ production than G B5 (**Figure 3.1.7d**). This can be explained by the presence of some antenna proteins in O B5 which transfer excitation energy less efficiently to the PSI reaction center, in agreement with 77 K steady state and time resolved fluorescence results: these antenna proteins are more prone to produce ROS upon high light illumination. In every case tested, no significant improvements in photoprotection were attributable to

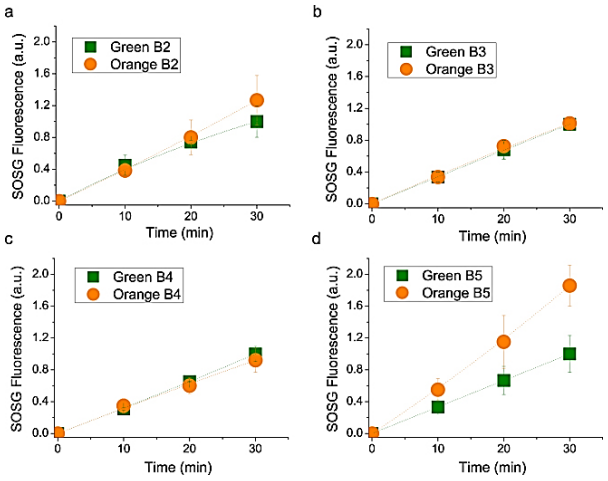

Figure 3.1.7 *Singlet oxygen production in isolated complexes upon red light treatment. Singlet oxygen production was indirectly determined following the increase of fluorescence of Singlet Oxygen Sensor Green (SOSG), a fluorescent probe increasing its fluorescence in presence of singlet oxygen. Isolated complexes were illuminated with red light at 2000 µmol $m^{-2}s^{-1}$. All data were normalized to chlorophyll content and to the SOSG fluorescence of the green samples after 30' of illumination. Standard deviations are indicated in both panels (n=3).*

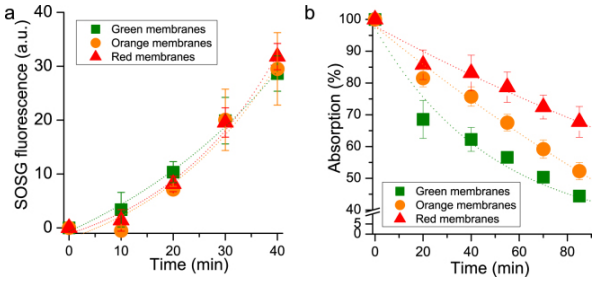

Figure 3.1.8 *Singlet oxygen production and chlorophyll photo-bleaching in isolated membranes. Panel A: singlet oxygen production indirectly determined following the increase of fluorescence of Singlet Oxygen Sensor Green (SOSG), a fluorescent probe increasing its fluorescence in presence of singlet oxygen. Isolated membranes were illuminated with red light at 6000 µmol $m^{-2}s^{-1}$. All data were normalized to chlorophyll content and to the SOSG fluorescence of green membranes after 30' of illumination. Panel B: chlorophylls photo-bleaching induced in isolated membranes upon illumination with white light at 6000 µmol $m^{-2}s^{-1}$. Standard deviations are indicated in both panels (n=3).*

astaxanthin binding. Since most of the astaxanthin was found not bound to Photosystems, the same SOSG analysis was performed on isolated membranes illuminated with red light at 6000 µmol $m^{-2}s^{-1}$ for 40 minutes (**Figure 3.1.8a**). Despite the huge amount of astaxanthin in O and R membranes, $^1O_2$ production comparable with G thylakoids was found after normalization to Chl content, suggesting a minor role of astaxanthin as scavenger of $^1O_2$. Moreover, astaxanthin in plastids could act as a light filter: in order to investigate this point, Chl bleaching was measured in these membranes upon white light treatment at 6000 µmol $m^{-2}s^{-1}$. As reported in **Figure 3.1.8b**, Chl absorption in G thylakoids was reduced by 60% after 80 minutes due to Chl degradation, while the O and R Chl bleaching kinetics were much slower, especially in the case of R samples. Astaxanthin thus improves photoprotection in thylakoid membranes only through its absorption properties, acting as a light filter.

Discussion

In this work, we presented the biochemical and spectroscopic properties of photosynthetic complexes responsible for light harvesting and energy conversion in *H. pluvialis*. In the case of cells grown in control conditions (G), monomeric and trimeric LHC proteins isolated from *H. pluvialis* present features consistent with previous report for LHC proteins purified from *A. thaliana* or *C. reinhardtii*. Interestingly, monomeric LHC proteins from *H. pluvialis* were characterized by a shorter fluorescence lifetime as compared to LHCII trimers. This finding is likely related to a somewhat different protein composition of B2 fractions as compared to B3 (**Figure 3.1.4**), with B2 containing some LHC proteins more abundant in monomeric form, such as the minor monomeric LHC subunits identified in *A. thaliana* (Lhcb4-6 subunits) and C. *reinhardtii* (CP26 and CP29) [219,440]. PSII core complexes were also isolated and analyzed, demonstrating conservation of pigment binding properties and similar biochemical and spectroscopic properties as compared to PSII cores purified from cyanobacteria or higher plants. The evolution of the photosynthetic process therefore mainly addressed the peripheral light harvesting complexes rather than core complexes [219,355]. In the case of PSI-LHCI, 77 K fluorescence demonstrates that *H. pluvialis* lacks Lhca proteins with so called "red-forms" which emit above 730 nm and are found in higher plants but not in green algae [337,355]. It is postulated that the absence of far red light in water did not lead microalgae to evolve LHC proteins which absorb above 700 nm. Chl *a*/*b* and Chl/Car ratios measured in the case of B5 fractions suggest the presence of 5 Lhca proteins per reaction center, however additional biochemical and structural work is required to support this hypothesis. Nevertheless, the PSI functional antenna size measured following P700 oxidation kinetics indicated an intermediate value between *A. thaliana* (4 Lhca per P700) [40] and *C. reinhardtii* (7/9 Lhca per P700) [37,337] (**Figure S**

3.1.2). *H. pluvialis* PSI-LHCI was characterized by a very short τ_{AV} (<40 ps), indicating a φPSI higher than 98% and consistent with similar analysis performed on PSI-LHCI complexes purified from other organisms [442]. The photosynthetic machinery is reorganized when *H. pluvialis* cells are stressed and astaxanthin is accumulated. Oxidative stress and ROS accumulation are indeed the triggers for activation of the astaxanthin biosynthetic pathway, with β-carotene over-production in the chloroplast followed by export to the cytosol and conversion to astaxanthin. In particular, while the different enzymes involved in β-carotene accumulation are localized in the plastids, the key enzyme β-carotene oxygenase (CRTO), which produces astaxanthin from β-carotene or zeaxanthin, was found both in the plastid and in lipid vesicles in the cytosol, despite its activity only having been previously reported in the cytosol compartment [445]. Our findings of traces of astaxanthin in the plastids suggests that a low activity of CRTO was present also in these organelles. The photosynthetic machinery continues to work even in cysts [419], but the chloroplasts reduce their volume and the thylakoid membranes become degraded [428,446]. In this work, we demonstrated that acclimation to high light induced a destabilization of the PSI-LHCI supercomplex and PSII core, especially after six days of high irradiance (**Figure 3.1.1**). Rapid turnover of PSII core subunits is likely to be the reason for the rapid destabilization observed for the PSII core. In addition, isolated PSII cores from O cells were characterized by a slower excitation energy transfer to the reaction center. In the PSII core complex, β-carotene molecules are in close contact with Chls and are required for effective quenching of ^{3}Chl* and scavenging of $^1O_2$ produced during charge recombination. Therefore, depletion of β-carotene produces a strong photooxidation in both PSII and PSI core complexes [447]. In the case of PSI-LHCI, high light acclimation caused a destabilization of the interaction between peripheral antenna complexes and PSI core, as demonstrated by both 77 K steady state and time resolved fluorescence. Moreover, the reduced energy connection between antenna proteins and PSI reaction center decreased the photochemical quenching of the LHCI proteins, exposing them to a higher risk of photooxidation, as measured using SOSG (**Figure 3.1.7**). The molecular mechanism by which PSII core and PSI-LHCI are destabilized cannot be easily identified and additional work is required to elucidate this point. The loss and partial substitution of β-carotene with astaxanthin in PSII core and PSI-LHCI could however be involved in the destabilization of Photosystems. Astaxanthin binding to Photosystems I been reported for *Chlrophyceae* species such as *Eremosphaera viridis* [448], however no information was available for the main species used in astaxanthin production, *H. pluvialis*. Astaxanthin binding complexes were not more photoprotected as compared to the control samples and their excitation energy transfer dynamics were even slower when compared to the same complexes isolated in the absence of astaxanthin. It is thus difficult to claim that astaxanthin binding to PSI or PSII has a photoprotective role. However, considering the higher level of $^1O_2$ produced in astaxanthin binding PSI-LHCI and the similar $^1O_2$ production observed in isolated membranes, it cannot be excluded that astaxanthin found free in the thylakoid membranes could have a role as scavenger of $^1O_2$ produced by Photosystems. Rather, considering the important role of β-carotene for the assembly and function of PSI and PSII [42,449], its substitution by astaxanthin could be the key to core complex destabilization. Indeed, astaxanthin was found in PSI and PSII cores even in its esterified form. Interactions between the fatty acids esterified to astaxanthin and the protein subunits of photosystems could impact the interactions at the base of the PSI and PSII assemblies. These results are indeed consistent with the observation of reduced photochemical efficiency in higher plants engineered to accumulate astaxanthin [432,433,450]. Considering the ratio between astaxanthin and Chls in whole cells and in isolated fractions, less than 1% of the total astaxanthin accumulated in *H. pluvialis* was found bound to PSI or PSII, while almost all astaxanthin is accumulated in the cytoplasm. Astaxanthin rich oil droplets accumulated in the cytoplasm could have a specific role as antioxidants to protect the nucleus. Moreover, the astaxanthin oil droplets act as a light filter, reducing the excitation pressure on photosynthetic subunits and their risk of photodamage (**Figure 3.1.8**) [419]. The presence of astaxanthin in *H. pluvialis*, even in photosynthetic pigment binding complexes, raises the question whether these astaxanthin molecules are synthetized in the plastid or, perhaps more likely, in the cytoplasm and then imported back to the plastid.

Material and methods

Strain and culture conditions

Haematococcus pluvialis strain K-0084 was obtained from Scandinavian Culture Collection of Algae & Protozoa. Liquid cultures were grown photoautotrophically at 40 µmol photons $m^{-2}s^{-1}$ on BG-11 medium at 22 °C in flasks [419]. Culture mixing was provided by bubbling filtered (0,2 µm) air. High light treatment at 400 µmol photons $m^{-2}s^{-1}$ was applied to cell cultures in their exponential phase (approximately 5 × 10^5 cells ml^{-1}). Each experiment was repeated in at least five independent experiments with three biological replicates for each sample.

Cell concentration and pigment analysis

Cell concentrations (cells ml^{-1}) were determined manually using a Neubauer counting chamber as described in [419]. Pigment analysis were performed by reverse phase HPLC as described in [231]. In particular, pigment extracts in acetone 80% were analyzed by Thermo-Fisher HPLC system equipped with a C18 column using a 15-min gradient of ethyl acetate (0 to 100%) in acetonitrile-water-triethylamine (9:1:0.01, vol/vol/vol) at a flow rate of 1.5 ml/min. Only in the case of whole cells pigmentation extraction was performed in DMSO as described in [419]. Pigment detection was done by a Thermo-Fisher 350–750 nm diode array detector.

Thylakoid membranes and pigment binding complexes isolation

Thylakoid membranes were isolated from *H. pluvialis* cells as described in [185], with some modifications. *H. pluvialis* cells, were harvested by centrifugation (1500 g, 3 min) and resuspended in B1 buffer (50 mM tricine pH 7.9, 0.35 M sorbitol, 10 mM NaCl, 5 mM $MgCl_2$, 0.5% dried powdered milk, 1 mM aminocaproic acid, 0.2 mM aminobenzamidine, and 0.2 mM phenylmethylsulfonyl fluoride) at a final concentration of 10^6 cells/ml and then passed through a prechilled (4 °C) Cell-disrupter (Constant Systems, Northants, UK) at 2.5 kbar. The resulting homogenate was subsequently centrifuged at 1500 g for 3 min at 4 °C, to remove intact cells. The supernatant was collected and centrifuged at 12000 g for 15 minutes at 4 °C. The resulting thylakoid membrane pellet was resuspended in B2 buffer (20 mM tricina pH 7.9, 50% glycerol, 10 mM NaCl, 5 mM $MgCl_2$, 1 mM aminocaproic acid, 0.2 mM aminobenzamidine, and 0.2 mM phenylmethylsulfonyl fluoride) and immediately used for analysis, or stored at −80 °C, after freezing it in liquid nitrogen. Isolated thylakoids were cleaned by ultracentrifugation in a sucrose step gradient formed by 1.9 M, 1.3 M and 1.14 M sucrose, 25 mM Hepes pH 7.0 and 10 mM EDTA. Clean thylakoid membranes were recovered from the 1.3 M layer, diluted to reduced sucrose concentration and precipitated by centrifugation. Isolated thylakoids were then solubilized at a concentration of 1 mg/ml of Chls (200 µg of Chls in total), with β-DM 1% and loaded onto a sucrose gradient (0.1–1 M) in presence of 0.06% β-DM and 10 mM Hepes pH 7.5. Protein fractions were isolated upon ultracentrifugation, collected from sucrose gradient and then cleaned by anion exchange chromatography as described in [220]. Anion exchange chromatography was performed on TOYOPEARL DEAE-650S resin (Sigma-Aldritch) equilibrated with 0.06% β-DM and 10 mM Hepes pH 7.5: protein elution was achieved using an elution buffer composed by 0.5 M NaCl, 0.06% β-DM and 10 mM Hepes pH 7.5.

Absorption and fluorescence spectroscopy

Absorption spectra were measured by DW2000 Aminco spectrophotometer as described in [451]. 77 K steady state emission spectra were recorded using a Fluoromax3 equipped with an optical fiber (Horiba Jobin Yvon) as described in [434]. Emission spectra were performed by exciting the sample at 440 nm with an excitation bandwidth of 5 nm and recording emission in the 650–800-nm range (emission bandwidth of 1 nm). Excitation spectra at 77 K were performed upon excitation in the 400–550 nm range (excitation bandwidth of 2 nm) measuring the fluorescence emitted at 680 or 715 nm (emission bandwidth of 3 nm) as described in the text.

SDS-PAGE analysis

Denaturing SDS-PAGE was performed with Tris-Tricine buffer systems [232].

PSI functional antenna size

Relative PSI antenna size was estimated from kinetics of P700 oxidation in limiting orange light (12 µE $m^{-2}s^{-1}$) in

whole cells treated with DCMU (3-(3,4-dichlorophenyl)−1,1-dimethylurea), DBMIB (2,5-dibromo-3-methyl-6-isopropylbenzoquinone), ascorbate and methyl-viologen, as described in [126].

Time resolved fluorescence measurements

Time-resolved fluorescence measurements were performed using a femtosecond laser excitation at 440 nm and a streak camera detection system, as reported in [228]. Briefly, an unamplified Ti:sapphire laser (Coherent Chameleon Ultra II) operating at 80 MHz was tuned to provide pulses with central wavelengths of 880 nm, energies of 30 nJ, and temporal and spectral bandwidths of 140 fs and 5 nm, respectively. A β-barium borate crystal provided type I phase-matched second harmonic generation, leading to pulses with central wavelengths of 440 nm. These were focused onto the sample, maintaining a low fluence (<30 mJ/cm2, 100 mm spot diameter) in order to avoid saturation and degradation effects in the sample. The samples were kept at a constant temperature of 11 °C by a temperature controlled cuvette cooled by a peltier system. The resulting collected emission was analyzed by a spectrograph (Princeton Instruments Acton SP2300) coupled to a streak camera (Hamamatsu C5680) equipped with a synchro scan voltage sweep module. In this way, measurements of photoluminescence intensity as a function of both wavelength and time were obtained with spectral and temporal resolutions of ~1 nm and ~3 ps respectively. Temporal broadening of the pump pulses caused by dispersive elements was confirmed to be well below the response time of the detection system.

Global analysis

Streak camera fluorescence decay maps were globally fitted with exponential functions as previously reported [228,272]. Briefly, the experimental datasets were fitted using a multi-exponential function as described by equation (1)

$$I(\lambda, t) = \sum_{i=1}^{n} A_i(\lambda) e - t / \tau_i$$

with $I(\lambda, t)$ the wavelength- and time-resolved fluorescence intensity, and A_i the amplitude of the exponential decay $e^{-t/\tau i}$. Whilst the amplitudes were treated as wavelength dependent ($A_i = A_i(\lambda)$), the exponential decay constants were assumed to be wavelength independent $\tau_i \neq \tau_i(\lambda)$. The resulting wavelength dependent amplitudes, $A_i(\lambda)$, are referred to as Decay Associated Spectra (DAS), with each DAS being associated with a particular exponential decay constant, τ_i. It is important to note that DAS are simply parameterizations of a time-resolved fluorescence dataset in a multi-exponential temporal basis, and so most often cannot be assigned a physical origin. Average fluorescence lifetimes were calculated as described by equation (2):

$$\tau_{AV} = \sum_{i=1}^{n} A_i \tau_i / \sum_{i=1}^{n} A_i$$

where A_i is the spectrally integrated amplitude over the spectral range 650–780 nm.

Singlet oxygen production

Singlet oxygen production was measured *in vivo* by following the 532 nm fluorescence emission of a singlet oxygen sensor green probe [396]. In particular, samples were diluted to in order to reach the same maximum at 0.15 OD in the Qy region and Singlet Oxygen Sensor Green was added to a final concentration of 5 μM. Samples were then illuminated with red light (2000 μE $m^{-2}s^{-1}$ in the case of isolated complexes, 6000 μE $m^{-2}s^{-1}$ in the case of thylakoids) and a regular time intervals, fluorescence at 532 nm was registered. Data were analyzed as increase in percentage of fluorescence, compared to time 0. Experimental data were then fitted with exponential functions.

Supporting information

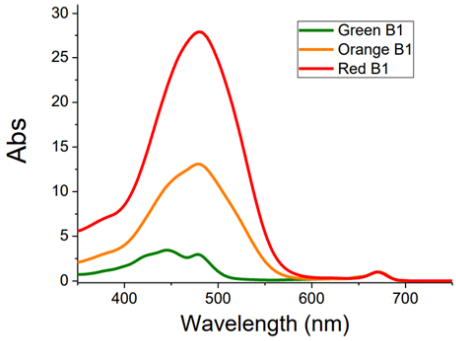

Figure S 3.1.1 *Absorption spectra of B1 fraction isolated from H. pluvialis. Absorption spectra of B1, fractions (Figure 1d) were normalized to the maximum absorption peak in the 600 nm and 700 nm region.*

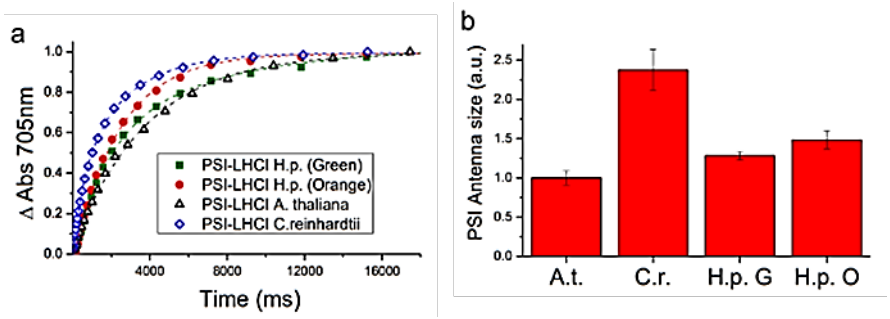

Figure S 3.1.2 *Functional antenna size of Photosystem I in H. pluvialis compared to Arabidopsis thaliana and Chlamydomonas reinhardtii. Panel a: P700 oxidation kinetics measured on whole cells in presence of DCMU and DBMIB, in order to block linear and cyclic electron transfer, and ascorbate and methyl viologen as electron donor and acceptor. Measurements were performed at 12 µmol m-2 s - 1 . Traces representative of 5 independent biological replicates are reported. Panel b: functional antenna size of PSI-LHCI calculated as 1/τ2/3, where τ2/3 is the time required to reach 2/3 of the maximum P700 oxidation. A.t.: Arabidopsis thaliana; C.r.: Chlamydomonas reinhardtii. H.p. G/O: H. pluvialis in Green/Orange stage as in Figure 1 main text. Standard deviations are indicated (n=5).*

3.2

Turning a green alga red: engineering astaxanthin biosynthesis by intragenic pseudogene revival in *Chlamydomonas reinhardtii*

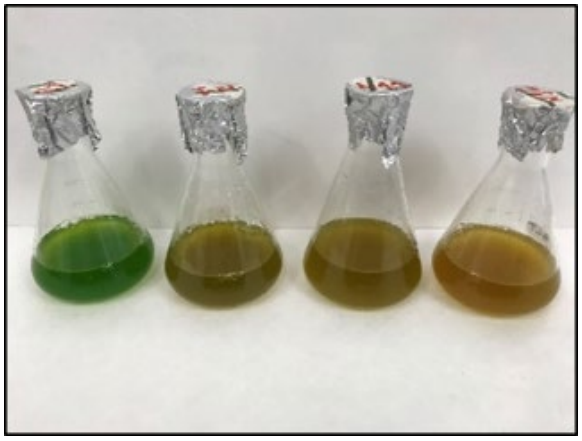

This section is based on the published article: Perozeni, F. *et al.* Turning a green alga red: engineering astaxanthin biosynthesis by intragenic pseudogene revival in Chlamydomonas reinhardtii. *Plant biotechnology journal*, doi:10.1111/pbi.13364 (2020).

Author Contributions: M.B. conceived the work. Ballottari M., Wobbe L. and Lauersen KJ. supervised experiments. Perozeni F. performed or contributed to all the experiments herein reported. Cazzaniga S. contributed to experiments reported in Table 1, figures 3-6 and S2-4. Wobbe L. and Baier T. designed strategies for BKT overexpression in *C. reinhardtii* and contributed to generation and selection of overexpressing *C. reinhardtii* strains. Zoccatelli G. and Zanoni F. contributed to experiments reported in Figure 6. Cazzaniga S. and Ballottari M. wrote the manuscript with contributions from all the authors. All the authors discussed the results, contributed to data interpretation and commented on the manuscript.

Turning a green alga red: engineering astaxanthin biosynthesis by intragenic pseudogene revival in Chlamydomonas reinhardtii.

Federico Perozeni[1], Stefano Cazzaniga[1], Thomas Baier[2], Francesca Zanoni[1], Gianni Zoccatelli[1], Kyle J. Lauersen[2], Lutz Wobbe[2], Matteo Ballottari[1*]

[1] Department of Biotechnology, University of Verona, Strada le Grazie 15, 37134 Verona, Italy
[2] Bielefeld University, Faculty of Biology, Center for Biotechnology (CeBiTec), Universitätsstrasse 27, Bielefeld, Germany.

Abstract

The green alga *Chlamydomonas reinhardtii* does not synthesize high-value ketocarotenoids like canthaxanthin and astaxanthin, however, a β-carotene ketolase (*Cr*BKT) can be found in its genome. *Cr*BKT is poorly expressed, contains a long C-terminal extension not found in homologues and likely represents a pseudogene in this alga. Here, we used synthetic redesign of this gene to enable its constitutive overexpression from the nuclear genome of *C. reinhardtii*. Overexpression of the optimized *Cr*BKT extended native carotenoid biosynthesis to generate ketocarotenoids in the algal host causing noticeable changes the green algal color to reddish-brown. We found that up to 50% of native carotenoids could be converted into astaxanthin and more than 70% into other ketocarotenoids by robust *Cr*BKT overexpression. Modification of the carotenoid metabolism did not impair growth or biomass productivity of *C. reinhardtii*, even at high light intensities. Under different growth conditions, the best performing *Cr*BKT overexpression strain was found to reach ketocarotenoid productivities up to 4.3 mg/L/day. Astaxanthin productivity in engineered *C. reinhardtii* shown here might be competitive with that reported for *Haematococcus lacustris* (formerly *pluvialis*) which is currently the main organism cultivated for industrial astaxanthin production. In addition, the extractability and bio-accessibility of these pigments were much higher in cell wall deficient *C. reinhardtii* than the resting cysts of *H. lacustris*. Engineered *C. reinhardtii* strains could thus be a promising alternative to natural astaxanthin producing algal strains and may open the possibility of other tailor-made pigments from this host.

Introduction

Carotenoids constitute a widely distributed group of lipid soluble pigments that are synthesized by plants and microorganisms [20] and fulfil several important functions in photosynthetic organisms such as light harvesting, light perception, and photoprotection [452], [82]. Carotenoids are tetraterpenes, derived from eight isoprene units, [21] containing an extended system of conjugated double bonds that are responsible for their light harvesting and free radical scavenging capacities [453]. Non-oxygenated carotenoids are named carotenes and this subgroup contains linear (e.g. lycopene) as well as cyclic (e.g. α/β-carotene) structures. Oxygenated derivatives of α- and β-carotene are named xanthophylls. Due to their strong color and antioxidant properties, these compounds are widely used in industry as 'natural' food colorants, feed additives in aquaculture, and in cosmetics as well as pharmaceuticals [414,454,455]. Animals have not been found to synthetize carotenoids naturally, however, they can structurally modify those taken up from their diet [456].

Among the carotenoids, the secondary ketocarotenoid astaxanthin (3,3′-dihydroxy-β,β-carotene-4,4′-dione) shows superior activity against reactive oxygen species (ROS) and is one of the most powerful natural antioxidants [161]. Astaxanthin synthesis proceeds through oxidation of both rings of β-carotene into canthaxanthin followed by its hydroxylation [457,458]. Alternatively, keto groups can be added to the rings of zeaxanthin, which is derived from the hydroxylation of β-carotene. The enzymes involved in astaxanthin synthesis are 3,3′-β-hydroxylase (*crtz* gene in microalgae) and 4,4′-β-ketolase (BKT, *crtO* gene in microalgae) [457,459]. Astaxanthin has multiple purported

health benefits on biological systems due to its action against ROS [460,461]. Astaxanthin has potential uses as an antitumor agent [162,462,463], the prevention of cardiovascular as well as neurological diseases, and diabetes [163,164,464]. Moreover, astaxanthin can be used as human dietary supplement and in aquaculture to improve fish color [414,454,455]. Other ketocarotenoids like canthaxanthin, an intermediate of astaxanthin synthesis, has properties similar to astaxanthin, with high potential for use in human health applications [465,466]. With few exceptions, higher-plants do not synthetize astaxanthin [467], which is currently produced industrially from unicellular photosynthetic microalgae such as *Haematococcus lacustris* (recently renamed from *H. pluvialis* [165,468]) or, to a lesser-extent, *Chromochloris zofingiensis* [469]. *H. lacustris*, is currently the main natural source of astaxanthin as it can accumulate to up to 90% of total carotenoids and 4% of cell dry weight [166] under certain environmental conditions. Astaxanthin accumulation in this alga is induced by stress conditions such as nitrogen or phosphorus starvation, high light, salt stress and elevated temperature [165] which stimulate the transition from motile zoospores (macrozooids) to immotile spores (aplanospores) [470]. These changes are accompanied by a degradation of the photosynthetic machinery and cessation of growth [167] as well as the formation of thick and resistant cell walls (cysts) [165]. The complexities of cellular changes to generate astaxanthin accumulation in *H. lacustris* require a two-stage cultivation and result in a low overall productivity for the whole process. Moreover, the recalcitrance of aplanospore cell walls reduces the bio-accessibility of astaxanthin and makes mechanical disruption necessary in order to release astaxanthin for human or animal consumption [450], a process which increases production process costs.

Given these limitations, genetic engineering approaches have been undertaken to enable astaxanthin production in different biotechnological host organisms in order to generate suitable alternatives to traditional *H. lacustris* production processes. Astaxanthin synthesis has indeed been demonstrated in many different organisms such as fermentative bacteria [471,472] as well as photosynthetic cyanobacteria [473], and eukaryotic hosts including yeasts [474, 475] and higher plants [476], [477 478]. [450], [431 479 169,480] by the transgenic expression of keto- and hydroxylases. The results obtained were promising but with limited, industrial relevance due to the high costs of cultivation of these organisms and/or low productivity. Even if high production yields of astaxanthin have been reported upon heterotrophic cultivation of different microorganisms, the possibility to produce ketocarotenoids in photoautotrophic systems has a strong advantage in terms of sustainability, by consuming CO_2 and avoiding the costs of reduced carbon sources used in heterotrophic cultivation. In order to develop a sustainable alternative to traditional astaxanthin production, we sought to engineer the common freshwater microalga *Chlamydomonas reinhardtii* to constitutively produce astaxanthin and canthaxanthin. In contrast to previous attempts by others [403,481,482], our approach is based on the synthetic redesign and revival of an endogenous yet inactive (pseudogene) β-carotene ketolase sequence present in the nuclear genome of *C. reinhardtii*. Strains resulting from the application of this strategy generated astaxanthin, exhibited reddish-brown phenotypes, and reached productivities comparable to *H. lacustris* cultivation without many of its natural process constraints.

Results

Analysis of *Chlamydomonas reinhardtii* bkt gene

Pathways for the synthesis of carotenoids and xanthophylls in *C. reinhardtii* have already been characterized in previous studies and are depicted in **Figure 3.2.1** [483]. Although, astaxanthin accumulation has never been reported in *C. reinhardtii* in any condition [483], a putative *Cr*BKT enzyme (Uniprot Q4VKB4) can be found in its nuclear genome [118]. CrBKT has indeed been previously reported to efficiently convert β-carotene and zeaxanthin into astaxanthin when expressed in engineered *Escherichia. coli* cells, even in the absence of the CrtZ hydroxylase [431,471,479]. The native expression level of *Cr*BKT gene was thus analyzed over a wide range of growth conditions using *C. reinhardtii* RNAseq databases [484]. These investigations revealed a very low expression level in any of the tested conditions compared to other genes involved in carotenoid biosynthesis (**Figure 3.2.1b**). An *in-silico* analysis of the *Cr*BKT amino acid sequence revealed an overall high degree of conservation, when compared to other BKT enzymes. A peculiarity of the sequence, however, is the presence of a 116 amino acid C-terminal extension, which is not present

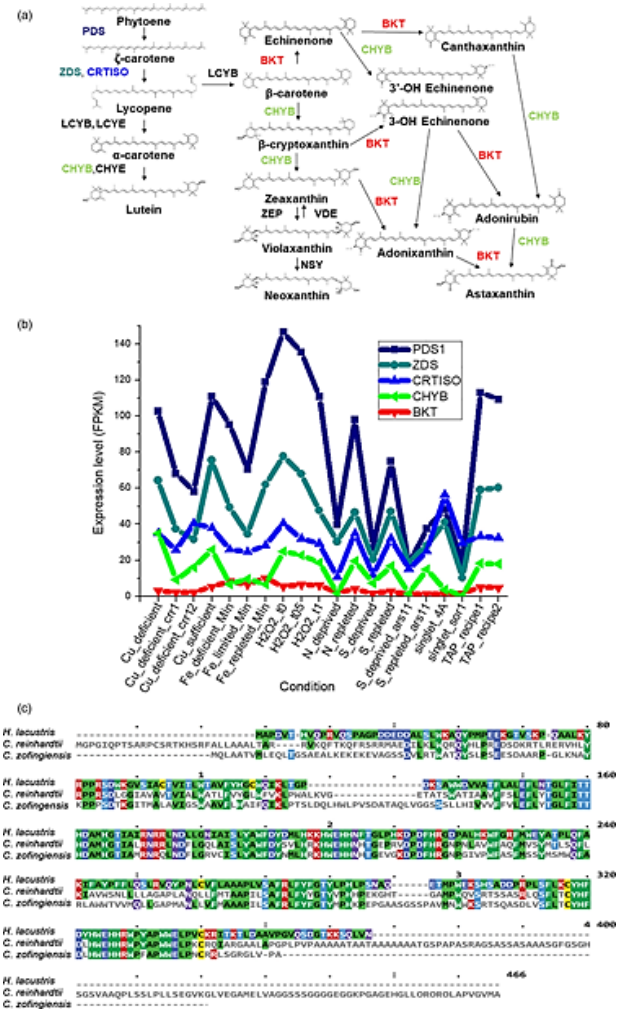

Figure 3.2.1 *The native BKT of C. reinhardtii and its potential role in astaxanthin production. (a) Schematic of the carotenoid pathway towards astaxanthin biosynthesis, according to (Misawa et al., 1995) and (Alvarez et al., 2006). Only major carotenoids are indicated. Name of enzymes are reported. PDS: phytoene desaturase, ZDS: ζ-carotene desaturase, CRTISO: carotenoid isomerase, LCYB: lycopene β-cyclase, LCYE: lycopene ε-cyclase, CHYB:Carotene β-hydoxylase, CHYE: carotene ε-hydoxylase, BKT: carotene β-ketolase, ZEP: zeaxanthin epoxidase, VDE: violaxanthin de-epoxidase, NSY: neoxanthin synthase. (b) Gene expression level of CrBKT native gene compared to other carotenoid biosynthetic genes. Expression levels in different conditions were retrieved from ChlamyNET database http://viridiplantae.ibvf.csic.es/ChlamyNet/. (c): Protein sequence alignment of BKT from different algae. BKT protein sequences from C. reinhardtii, H. lacustris and C. zofingensis were aligned by multiple alignment highlighting the long C-terminal amino acid extension of CrBKT. Colour code is on the base of consensus.*

in other BKT sequences from other organisms [483] (**Figure 3.2.1c**). A putative chloroplast transit peptide was predicted on the N-terminus of the *Cr*BKT, which was tested for its ability to enable chloroplast import of recombinant mVenus yellow fluorescent protein (hereafter, YFP) in *C. reinhardtii*. While the first 40 N-terminal residues of *Cr*BKT were sufficient for the import of YFP into the chloroplast, a smaller sequence only comprising the first 34 residues from the N-terminus was not (**Figure 3.2.2a**).

Intragenic expression of C. reinhardtii β-ketolase

The low native expression rates of *Cr*BKT led us to consider this may be a pseudogene with a residual expression level too low to have an impact on cellular physiology or expression only under some condition not known specific to its habitat or lifecycle. Given that the gene had been successfully expressed in *E. coli* and was shown to functionally convert carotenoids into astaxanthin [431], we decided to investigate whether the gene could be revived by synthetic redesign. Recently, we demonstrated that transgenes could be optimized for expression from the algal nuclear genome by codon optimization and systematic incorporation of the first intron of the *C. reinhardtii* RuBisCO small subunit II gene to mimic host regulatory structures [485]. We have recently used this strategy for overexpression of numerous foreign genes[486-488], as well as re-coding and overexpression of the endogenous photodecarboxylase (*Cr*FAP) [489] for various metabolic engineering activities in this host. Here, the amino acid sequence of the *Cr*BKT was used to generate an optimized synthetic algal transgene, employing the same optimization strategy (**Figure 3.2.2b**). The optimized gene was first generated by omitting the 116 aa C-terminal extension as this is absent from all other gene homologues in other organisms (**Figure 3.2.1c**) and may influence its activity. The optimized synthetic *Cr*BKT was then cloned into the pOpt2_PsaD_mVenus_Paro vector for expression (**Figure 3.2.2c**) [488]. In order to facilitate chloroplast import, the N-terminus of the BKT coding sequence was fused to the chloroplast transit peptide from photosystem I subunit D (PsaD), which has been already reported to be functional for chloroplast import in different conditions [490,491]. The coding sequence of YFP was left in the vector to generate a fusion at the 3' end of *Cr*BKT. The construct obtained (PsaD_BKT_YFP, **Figure 3.2.2c**) was then used to transform *C. reinhardtii* UVM4, a strain which has been mutated to enable more reliable transgene expression from the nuclear genome [492].

Chlamydomonas reinhardtii colonies recovered on plates after transformation using the PsaD_BKT_YFP construct exhibited clear changes in colour, from its native green to reddish-brown (**Figure 3.2.2d**). The accumulation of

recombinant *Cr*BKT protein in transformed cells was verified by immunoblot developed using an antibody recognizing the fused YFP (**Figure S 3.2.1**). *Chlamydomonas reinhardtii* cells expressing *Cr*BKT appeared similar in shape and size under microscopy analysis compared to the parental strain UVM4, but with a reddish color (**Figure S 3.2.2**). PsaD_BKT_YFP expression lines were screened for the highest accumulation of ketocarotenoids, first by selection of colonies based on intensity of red color, and then by acetone extraction and spectral analysis (**Figure 3.2.2e-f**). Spectra of pigments from *bkt* lines, extracted with acetone, were found to exhibit a shoulder above 500 nm which was not present in the parental control. This shoulder corresponds to the absorption peak of ketocarotenoids, as astaxanthin (**Figure 3.2.2f**). Three lines exhibiting the darkest red phenotype and the largest shoulder in spectral analysis were *bkt1*, *bkt5* and *bkt36*. The content of total

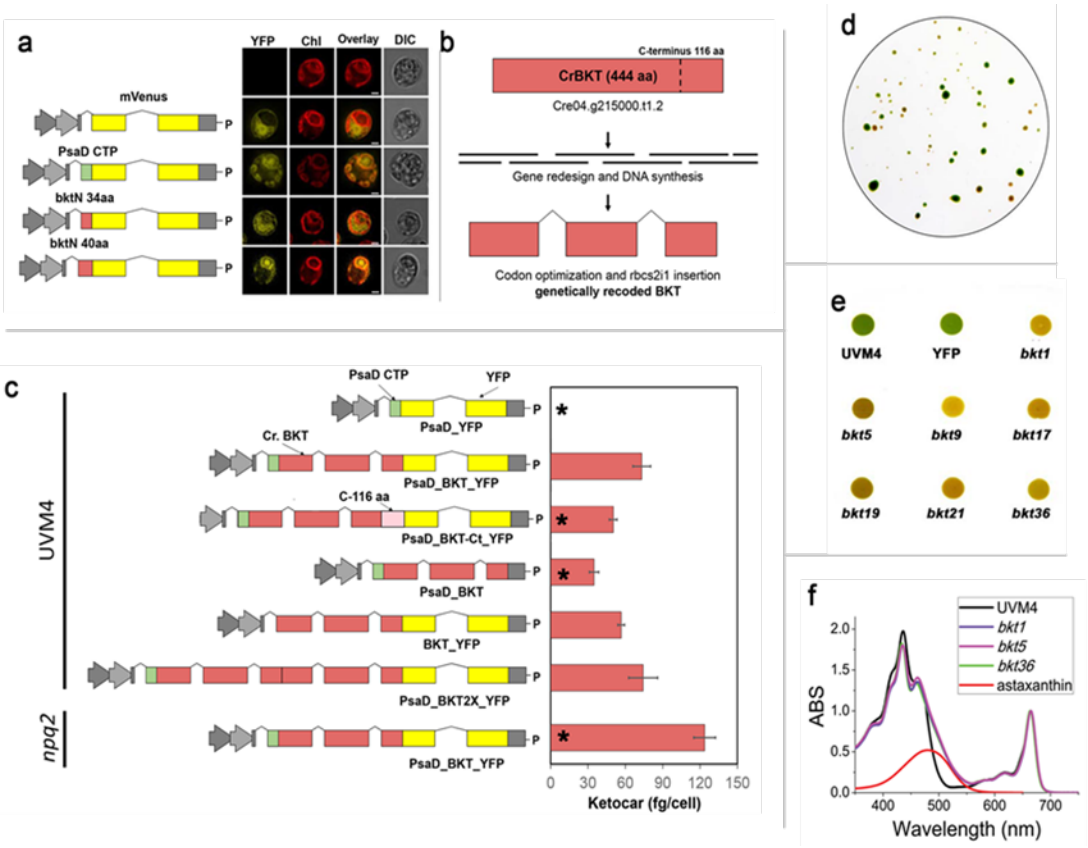

Figure 3.2.2 *Synthetic CrBKT redesign, expression vectors for C. reinhardtii transformation, and phenotypic change in expression lines. (**a**) Analysis of endogenous CrBKT transit peptide was performed by fusion of two different amino acid lengths of the targeting peptide to the YFP reporter. 40 amino acids from the N-terminus of CrBKT was enough to mediate chloroplast import of the reporter. A cytoplasmic and chloroplast targeted control are shown, the latter is mediated by the previously characterized PsaD chloroplast targeting peptide. YFP fluorescence (YFP), chlorophyll autofluorescence (Chl), merger of these two channels and differential interference contrast (DIC) images are shown. Scale bar represents 2 µm. (**b**) The optimized CrBKT sequence was built by gene synthesis after in silico design using codon optimization and systematic spreading of the rbcs2 intron 1 sequence to minimize exon lengths as previously described to enable robust transgene expression from the nuclear genome of this alga (Baier et al., 2018b). (**c**) Schematic overview of all expression vectors used in this work and their respective ketocarotenoid accumulation efficiencies. All gene expression cassettes use the Hsp70A/Rbcs2 hybrid promoter containing rbcs2 intron 1 and its 5' untranslated region as previously described (Lauersen et al., 2015). PsaD_YFP: YFP localized to the chloroplast by the PsaD transit peptide. PsaD_BKT_YFP: BKT fused to YFP targeted by PsaD transit peptide. PsaD_BKT_cterm_YFP_Paro: same as previous vector with the addition of the 116 C-terminal amino acid coding extension of the CrBKT gene. BKT_YFP_Paro: BKT fused to YFP targeted by endogenous transit peptide. PsaD_BKT: CrBKT targeted into chloroplast by PsaD transit peptide without the YFP reporter. PsaD_2xBKT_YFP: Two copies of BKT coding sequence were put in frame in order to generate a fused protein carrying two BKT and YFP. For both BKT copies, sequence coding for first 40 aa was removed. All proteins expressed carry a strepII affinity tag (WSHPQFEK*) on the C-terminus. All the constructs were used to transform UVM4 strain, a strain previously selected for having an efficiency of expression of heterologous gene (Neupert et al., 2009a). Construct was used to transform the npq2 mutant strain, a C. reinhardtii strain mutated on the gene encoding for zeaxanthin epoxidase, resulting into constitutive accumulation of zeaxanthin (Niyogi et al., 1997a). Selection was achieved for all constructs with the AphVIII paromomycin (P) resistance cassette of the pOpt vector backbone. Ketocarotenoid accumulation per cell are expressed as mean ± s.d. (n = 5). The significantly different value from the one obtained with PsaD BKT_YFP construct are marked with an asterisk (*) (P < 0.05). (**d**) Orange/red phenotypes of C. reinhardtii cells expressing CrBKT_YFP recovered after transformation and selection on solid medium. (**e**) Image of UVM4 and transformed cells spotted on TAP agar and grown at 100 µmol m^{-2} s^{-1}; YFP represents a strain transformed with PsaD_YFP as a control, bkt are lines transformed with CrBKT_YFP. (**F**) Spectra of acetone-extracted pigments from UVM4 and three select bkt lines. Spectra are normalized to absorption in Qy region. Spectrum of astaxanthin is shown as reference in red.*

ketocarotenoids accumulated in the cells was estimated to be up to 73.2 ± 3.7 fg/cell by spectral analysis (see Methods section for further details). In order to possibly improve the expression and activity, further constructs were generated with modifications in the orientation and extensions of the BKT (**Figure 3.2.2c**; UVM4). Many variations of this original expression construct were implemented, however, none resulted in improved astaxanthin production over the PsaD_BKT_YFP vectors (**Figure 3.2.2c**). First, the 116 aa extension removed at the C-terminus of *Cr*BKT was reinserted in the vector PsaD_BKT-Ct_YFP, and this resulted in an average level of ketocarotenoids ~35% lower compared to the complete version of *Cr*BKT. The YFP coding sequence was also removed from the C-terminus of *Cr*BKT (PsaD_BKT), in order to evaluate a possible negative effect due to the presence of YFP at the C-terminus of the protein. The mutants obtained showed a pale red coloration and ketocarotenoids were present although to a much lower level than in the mutants obtained with *Cr*BKT fused with YFP. A vector coding for a truncated *Cr*BKT C-terminus fused with YFP and only using the native *Cr*BKT chloroplast targeting sequence without the PsaD-CTP was also prepared (BKT-YFP) resulting in ~20% lower ketocarotenoid production to the original construct. Finally, two *Cr*BKT gene copies were fused together in order to enhance the number of catalytic sites (PsaD_BKT2x_YFP) as this strategy had been previously shown beneficial for a sesquiterpene synthase in this host [487]. However, the strains obtained from this construct, showed similar amounts of ketocarotenoids as the single *Cr*BKT construct (**Figure 3.2.2c**).

The *C. reinhardtii npq2* mutant contains a knockout mutation in the zeaxanthin epoxidase (ZEP, **Figure 3.2.1a**) and is unable to synthetize violaxanthin and neoxanthin, therefore, it accumulates zeaxanthin as a terminal carotenoid species. Zeaxanthin is one of the carotenoid substrates for the *Cr*BKT enzyme [431]. Therefore, to determine if whether ketocarotenoid yields might be higher in this host, the PsaD_BKT_YFP vector was used to transform the *npq2* mutant (**Figure 3.2.2c**; *npq2*). After transformation and selection, three lines (n2*bkt1*, n2*bkt1*1, and *n2bkt12*), were selected for strong reddish phenotype and analyzed with the same procedure used for *bkt* lines. The ketocarotenoid content per cell of these strains were indeed increased compared to the *bkt* lines obtained in UVM4 background (**Figure 3.2.2c**). Therefore, strains *bkt1*/5/36 and n2*bkt1*/11/12, obtained by transformation with construct PsaD_BKT_YFP in the UVM4 and *npq2* backgrounds, respectively, were used for further investigations.

The presence of ketocarotenoids does not perturb algal growth

The influence of the presence of astaxanthin and ketocarotenoids in *C. reinhardtii* was evaluated by cultivating selected transformant lines and their parental strains (UVM4, *npq2*) in 20 ml flasks for one week in photoautotrophy (CO_2) or mixotrophy (acetate) [299] at 100 or 500 µmol m^{-2} s^{-1}. Although *bkt* and *n2bkt* lines exhibited reddish-brown phenotypes, they were nevertheless able to grow even in photoautotrophic conditions (**Figure 3.2.3a**). Both *bkt* and *n2bkt* lines are indeed photosynthetically active: in the case of *bkt5* a similar quantum yield of photosystem II (Fv/Fm) was measured compared to its parental strain (UVM4), while in the case of only *n2bkt*, a slight decrease of Fv/Fm was evident compared to its background *npq2*. Reduced Fv/Fm in *npq2* background compared to UVM4 is consistent with previous findings owing to the overaccumulation of zeaxanthin in this strain [493]: further decrease of Fv/Fm in *n2bkt12* might be related to a partial destabilization of photosynthetic apparatus due to substitution of xanthophylls with ketocarotenoids, as previously reported in the case of *H. lacustris* [167]. In order to investigate a possible effect in biomass productivity related to ketocarotenoid accumulation, this was evaluated in autotrophic and mixotrophic conditions (**Figure 3.2.3c-f**). At either light intensity tested, growth in mixotrophy was faster compared to the autotrophic cultivation for any strain tested (**Figure 3.2.3c-f**). Cell dry weight was measured at stationary phase for all the genotypes (**Table 3.2.1**). In both TAP and HS medium, growth of *npq2* strains were slower compared to UVM4, even if the final biomass harvested was similar although in some cases statistically different (**Table 3.2.1**). Transformant lines exhibited biomass accumulation similar to their respective parental lines, with the only exception of an increased biomass yield in the case of *bkt5* grown in control light in mixotrophy, when compared to its background UVM4. Similar photoautotrophic biomass accumulation in strains containing astaxanthin and

parentals indicated that the presence of astaxanthin does not impair algal growth.

Yield of astaxanthin in different growth conditions

Pigments accumulated in *bkt* and *n2bkt* lines were further analyzed by high-performance liquid chromatography (HPLC) to verify the accumulation of astaxanthin and other ketocarotenoids. HPLC chromatograms of UVM4 parental strain contain prominent peaks of chlorophylls *a* and *b* as well as of the carotenoids neoxanthin, violaxanthin, lutein and β-carotene (**Figure 3.2.3g**). The transformed lines exhibit additional peaks (**Figure 3.2.3g**) due to the activity of the introduced CrBKT enzyme. The additional peaks present in HPLC chromatograms in transformed lines were thus analyzed by mass spectroscopy (**Figure S 3.2.3** and **Table S 3.2.2**) identifying three astaxanthin isoforms (peaks 8, 9 and 10), which according to elution time and absorption spectra (**Figure S 3.2.4**) can be tentatively attributed identified to 3S,3'S trans-astaxanthin, 3S,3'S 9-cis-astaxanthin and 3S,3'S-13-cis-astaxanthin[494,495]. Traces of other ketocarotenoids as adonirubin and canthaxanthin could also be identified by mass spectroscopy being eluted in peaks 11 and 12 respectively (**Figure S 3.2.3**): canthaxanthin is produced by CrBKT using β-carotene as substrate (**Figure 3.2.1**), while adonirubin is an intermediate being formed during hydroxylation of canthaxanthin to astaxanthin or by CrBKT using 3'OH-echinenone as substrate [496]. Other possible ketocarotenoids produced by CrBKT catalytic activity such as echinenone, 3'OH-echinenone or adonixanthin could not be detected in *bkt5* or *n2bkt12* lines. In both parental strains, ketocarotenoids were never detected while in *bkt5* and *n2bkt12* lines they represent ~70% of the total cellular carotenoids, with astaxanthin as the major compound (**Table 3.2.1**). For all conditions tested with strain *bkt5*, reduced levels of other cellular carotenoids were observed. Violaxanthin underwent the most pronounced reduction of ~ 80%, and β-carotene and neoxanthin were reduced by 65% and lutein 45%. Zeaxanthin was not decreased in *bkt5* although the amount of this carotenoid was low even in the parental strain (**Table 3.2.1**). *npq2* lines expressing CrBKT exhibited strong reductions in zeaxanthin and β-carotene contents, being both substrates from CrBKT enzyme. In both, *bkt* and *n2bkt* lines, a clear decrease of the chlorophyll amount was evident with the strongest effect in autotrophy and high

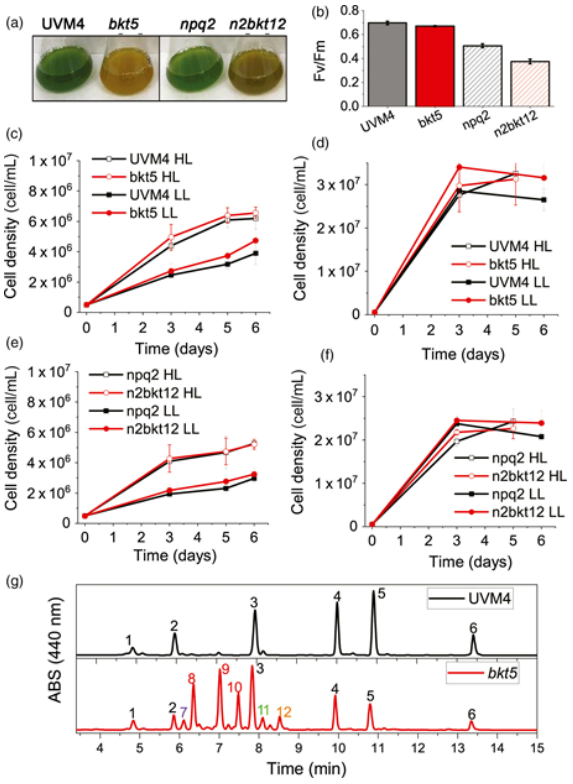

Figure 3.2.3 *Impact of astaxanthin accumulation in Chlamydomonas reinhardtii UVM4 and npq2 backgrounds on growth (a) Cultures of UVM4, bkt5, npq2 and n2bkt12 grown in autotrophy at 100 µmol/m²/s exhibit striking differences in colour. (b) Fv/Fm of UVM4, bkt5, npq2 and n2bkt12 grown in autotrophy at 100 µmol/m²/s. (c,d) Growth curves of UVM4 and bkt5 strain in autotrophy (c, HS medium) or mixotrophy (d, TAP medium) in low light (LL, 100 µmol/m²/s) or high light (HL, 500 µmol/m²/s) conditions. (e,f) Growth curves of npq2 and n2bkt5 strain in autotrophy (e, HS medium) or mixotrophy (f, TAP medium) in low light (LL, 100 µmol/m²/s) or high light (HL, 500 µmol/m²/s) conditions. (g) Representative HPLC of pigments from UVM4 (black) and mutant bkt5 (red). 1: neoxanthin, 2: violaxanthin; 3: lutein; 4: chlorophyll b; 5: chlorophyll a; 6 β-carotene; 7: unidentified; 8: 3S,3'S trans-astaxanthin, 9: 3S,3'S 9-cis-astaxanthin, 10: 3S,3'S 13-cis-astaxanthin11: adonirubin, 12: canthaxanthin;. Data are expressed as mean ± standard deviation (n = 3). In panels b–f, statistically different values comparing UVM4 vs. bkt5and npq2vs. n2bkt12are indicated with *(P < 0.05).*

light conditions (in HS medium at 500 µmol m^{-2} s^{-1}, **Table 3.2.1**) This result suggests that xanthophyll and β-carotene reduction in favor of astaxanthin accumulation destabilize the chlorophyll content of photosynthetic complexes, similar to findings previously reported for *H. lacustris* [167]. The highest ketocarotenoid content per cell was detected in *n2bkt* lines grown in mixotrophy at 100 or 500 µmol m^{-2} s^{-1}, while mixotrophic growth at 500 µmol m^{-2} s^{-1} promoted the highest values in *bkt* lines (**Table 3.2.1**). To further measure productivity of mutants expressing CrBKT in different conditions, one line with the highest level of astaxanthin for each background, *bkt5* and *n2bkt12*, was selected for astaxanthin productivity analysis in small scale (80 mL) airlift photobioreactors.

growth	genotype	chl pg/cell	chl/car	asta/car	keto/car	asta fg/cell	keto fg/cell	dry weight (g/l)	neo	viola	lute	zea	b car	asta	keto
LL HS	UVM4	0,95 ± 0,09^{a}	2,70 ± 0,21^{a}	-	-	-	-	0,14 ± 0,01^{a}	3,8 ± 0,5^{a}	7,5 ± 1,3^{a}	21,4 ± 3,9^{a}	-	4,3 ± 0,2^{a}	-	-
	bkt5	0,19 ± 0,04^{b}	1,81 ± 0,14^{b,c}	0,49 ± 0,02^{a}	0,75 ± 0,02^{a}	34,7 ± 3,3^{a}	52,1 ± 5,8^{a}	0,19 ± 0,02^{b}	1,5 ± 0,2^{b}	1,2 ± 0,2^{b}	9,0 ± 1,5^{b}	-	2,1 ± 0,1^{b}	27,2 ± 3,1^{a}	41,5 ± 4,1^{a}
	npq2	0,67 ± 0,20^{c}	2,49 ± 0,67^{b}	-	-	-	-	0,15 ± 0,02^{a}	-	-	18,6 ± 4,5^{a}	16,0 ± 4,3^{a}	5,6 ± 0,5^{c}	-	-
	n2bkt12	0,25 ± 0,07^{b}	1,42 ± 0,38^{c}	0,62 ± 0,11^{a}	0,80 ± 0,09^{a}	72,5 ± 14,5^{b}	92,7 ± 12,2^{b}	0,14 ± 0,03^{a}	-	-	11,3 ± 2,5^{b}	3,5 ± 0,9^{b}	1,8 ± 0,1^{d}	46,6 ± 17,7^{a}	59,6 ± 19,3^{a}
LL TAP	UVM4	1,41 ± 0,34^{a}	2,81 ± 0,11^{a}	-	-	-	-	0,56 ± 0,05^{a}	4,9 ± 2,1^{a}	8,7 ± 2,9^{a}	16,8 ± 1,1^{a}	-	5,3 ± 2,1^{a}	-	-
	bkt5	0,38 ± 0,08^{b}	2,39 ± 0,09^{b}	0,37 ± 0,03^{a}	0,69 ± 0,03^{a}	40,6 ± 3,6^{a}	72,9 ± 3,5^{a}	0,65 ± 0,01^{b}	1,5 ± 0,6^{b}	2,1 ± 0,6^{b}	8,6 ± 0,5^{b}	-	1,0 ± 0,3^{b}	15,6 ± 1,3^{a}	28,8 ± 1,3^{a}
	npq2	1,26 ± 0,49^{a}	2,80 ± 0,03^{a}	-	-	-	-	0,69 ± 0,04^{b}	-	-	12,3 ± 1,3^{c}	19,3 ± 2,0^{a}	4,0 ± 1,2^{a}	-	-
	n2bkt12	0,72 ± 0,09^{c}	2,45 ± 0,03^{b}	0,42 ± 0,03^{a}	0,65 ± 0,03^{a}	87,3 ± 2,0^{b}	130,4 ± 0,7^{b}	0,65 ± 0,01^{b}	-	-	13,1 ± 1,2^{c}	1,6 ± 0,2^{b}	0,6 ± 0,2^{b}	17,3 ± 0,9^{a}	26,6 ± 0,9^{a}
HL HS	UVM4	0,87 ± 0,21^{a}	2,54 ± 0,24^{a}	-	-	-		0,14 ± 0,01^{a}	3,7 ± 0,9^{a}	7,5 ± 1,8^{a}	21,2 ± 8,3^{a}	2,8 ± 0,4^{a}	4,2 ± 1,1^{a}	-	-
	bkt5	0,09 ± 0,02^{b}	0,93 ± 0,09^{b}	0,47 ± 0,10^{a}	0,75 ± 0,07^{a}	30,9 ± 10,7^{a}	47,5 ± 11,4^{a}	0,13 ± 0,06^{a}	2,5 ± 0,5^{a}	2,1 ± 0,5^{b}	16,0 ± 5,7^{a}	6,0 ± 0,7^{b}	2,3 ± 1,0^{b}	51,5 ± 14,4^{a}	81,5 ± 13,1^{a}
	npq2	0,60 ± 0,24^{a}	2,12 ± 0,73^{a}	-	-	-	-	0,18 ± 0,04^{a}	-	-	20,2 ± 8,0^{a}	22,0 ± 4,2^{c}	4,9 ± 1,6^{a,c}	-	-
	n2bkt12	0,08 ± 0,03^{b}	0,66 ± 0,22^{b}	0,39 ± 0,07^{a}	0,76 ± 0,04^{a}	53,1 ± 9,4^{b}	99,0 ± 8,2^{b}	0,14 ± 0,03^{a}	-	-	17,2 ± 7,4^{a}	4,7 ± 2,1^{b}	2,8 ± 0,4^{b,c}	42,2 ± 8,1^{a}	80,2 ± 11,5^{a}
HL TAP	UVM4	1,04 ± 0,17^{a}	2,51 ± 0,34^{a}	-	-	-	-	0,71 ± 0,05^{a}	4,8 ± 1,1^{a}	10,4 ± 2,3^{a}	17,7 ± 3,2^{a}	1,6 ± 0,6^{a,b}	5,4 ± 1,6^{a}	-	-
	bkt5	0,21 ± 0,03^{b}	1,80 ± 0,24^{b}	0,42 ± 0,01^{a}	0,74 ± 0,01^{a}	33,6 ± 4,7^{a}	57,3 ± 7,5^{a}	0,68 ± 0,03^{a,b}	1,7 ± 0,4^{a}	1,8 ± 0,3^{b}	9,6 ± 1,6^{b}	1,3 ± 0,4^{a}	1,2 ± 0,3^{b}	23,8 ± 2,8^{a}	41,5 ± 5,3^{a}
	npq2	0,98 ± 0,16^{a}	2,39 ± 0,29^{a}	-	-	-	-	0,64 ± 0,07^{b,c}	-	-	14,7 ± 2,4^{c}	22,2 ± 5,4^{c}	5,0 ± 0,2^{a}	-	-
	n2bkt12	0,47 ± 0,07^{c}	1,67 ± 0,20^{b}	0,49 ± 0,08^{a}	0,73 ± 0,07^{a}	94,9 ± 16,3^{b}	137,5 ± 17,2^{b}	0,62 ± 0,02^{c}	-	-	14,7 ± 2,2^{c}	2,2 ± 0,5^{b}	0,9 ± 0,1^{b}	30,0 ± 8,1^{a}	44,1 ± 9,4^{a}

Table 3.2.1 *Pigment content determined in cells grown at 100 (LL) or 500 (HL) µmol/m/s in HS and TAP medium for 1 week starting from 5 × 10^5 cells/mL. Acronyms indicate chlorophyll (chl), total carotenoid (car), astaxanthin (asta), total ketocarotenoid (keto), neoxanthin (neo), violaxanthin (viola), zeaxanthin (zea) and β-carotene (β car). Chlorophyll per cell is expressed as picograms (pg), and astaxanthin and ketocarotenoids as femtograms (fg). Single carotenoids are normalized to 100 chlorophylls molecules. Data are expressed as means ± SD (n = 4). Statistical analysis was performed for each growth conditions: values marked with the same letters do not differ significantly (P < 0.05).*

These two strains were cultivated at different light regimes (500 µmol and 1000 m^{-2} s^{-1}), in autotrophy (HS medium) or mixotrophy (TAP medium) and bubbling with air or 3% CO_2. These experiments were performed in a semi-continuous manner, with harvesting and culture dilution when stationary phase was reached (**Figure 3.2.4**). The experiment was continued until three cycles of dilution were repeated and the productivity of astaxanthin and ketocarotenoids was quantified as mg of pigments per liter per day of culture. In general, for both strains, mixotrophy was found to result in higher productivities compared to autotrophy **Figure 3.2.4a-d**). Supplying CO_2 to the culture clearly increased the productivity in all the different conditions especially when acetate was present (**Figure 3.2.4a-d**). For example, *bkt5* grown in TAP exhibited approximately double productivity rates of astaxanthin and ketocarotenoids when CO_2 was added to TAP cultures at 500 and 1000 µmol m^{-2} s^{-1} (**Figure 3.2.4d**). Light was observed to be important for the accumulation of astaxanthin in both *bkt5* and *n2bkt12* strains, overall ketocarotenoid production increases were observed at 1000 µmol m^{-2} s^{-1} compared to cells grown at 500 µmol m^{-2} s^{-1} (**Figure 3.2.4**). The highest volumetric productivities obtained in these experiments were obtained for *bkt5* grown in TAP at 1000 µmol m^{-2} s^{-1} with CO_2 which produced ~2.07 mg ± 0.13 mg astaxanthin $L^{-1}day^{-1}$ and 3.21 ± 0.10 mg total ketocarotenoids $L^{-1}day^{-1}$. The productivities in mg L^{-1} d^{-1} observed for *n2bkt12* were similar compared to the *bkt5* in these conditions (**Figure 3.2.4d**).

An additional experiment was performed in 600 ml stirred flasks with TAP at 500 µmol m^{-2} s^{-1}, in order to study the scalability of the productivity obtained with this mutant. The experiment was conducted for 3 weeks in continuous light (**Figure 3.2.4e-f**) and again the productivity of astaxanthin and total ketocarotenoids were determined from the system during the cultivations (**Figure 3.2.4g-h**). Pigment productivities were quantified at every dilution, which was performed when the cells reached stationary phase. Both strains exhibited an adaption phase in the first days of growth in this system, followed by a phase where repetitive dilutions could be maintained for 3 weeks (**Figure 3.2.4e-f**). For strain *bkt5*, productivity values reached 3.88 ± 0.20 mg ketocarotenoids $L^{-1}d^{-1}$ and 2.5 ± 0.18 mg astaxanthin $L^{-1}d^{-1}$ (**Figure 3.2.4g**). A slower growth rate of *n2bkt12* led to a lower overall yield of ketocarotenoids and astaxanthin (**Figure 3.2.4h**). Although *n2bkt12* exhibited increased astaxanthin and ketocarotenoid productivity per cell, its slower growth rate hindered its competitiveness with the more rapid-growing *bkt* line. Therefore, further productivity analyses focused only on *bkt5*.

The productivity of astaxanthin and ketocarotenoid of the *bkt* strain was further investigated in 80 mL airlift photobioreactors using conditions of autotrophy or mixotrophy, in the presence of 3% CO_2, and with increasing irradiance up to 3000 µmol m^{-1} s^{-1} (**Figure 3.2.5**). In autotrophy, astaxanthin accumulation was reduced when irradiance was increased past 500 µmol $m^{-1}s^{-1}$, yet total ketocarotenoid amounts increased,

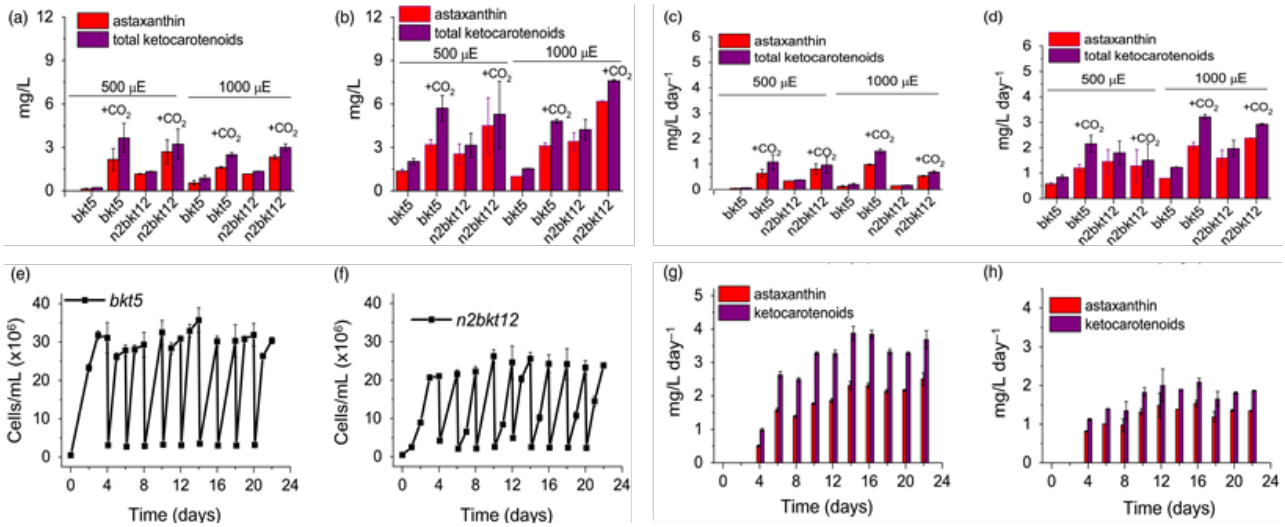

Figure 3.2.5 *Astaxanthin and ketocarotenoid productivity in different growth conditions. Productivities of astaxanthin (red) and ketocarotenoids (purple) are presented as volumetric (mg/L) (a,b) and daily volumetric (mg/L/day) (c,d) productivities obtained from bkt5 and n2bkt12 mutants in autotrophic (a,c) or mixotrophic (b,d) growth. Cells were grown in HS or TAP media for autotrophic or mixotrophic growth, respectively, at 500 or 1000 µmol photons/m²/s with air bubbling or air plus 3% CO2 bubbling (CO2). Data were obtained by HPLC analysis. (e,f) Cell density of bkt5 (e) or n2bkt12 (f) strains cultivated in semi-continuous mode in 500-mL flasks at 500 µmol photons/m2/s in TAP with 3% CO2 bubbling and stirring. Cells were manually counted and diluted 10-fold where they reached stationary phase. (g,h) Astaxanthin (red) and ketocarotenoid (purple) productivities obtained in semi-continuous cultivation of bkt5 (g) or n2bkt12 (h) strains, as determined by HPLC analysis. Data are expressed as means ± standard deviation (n = 4).*

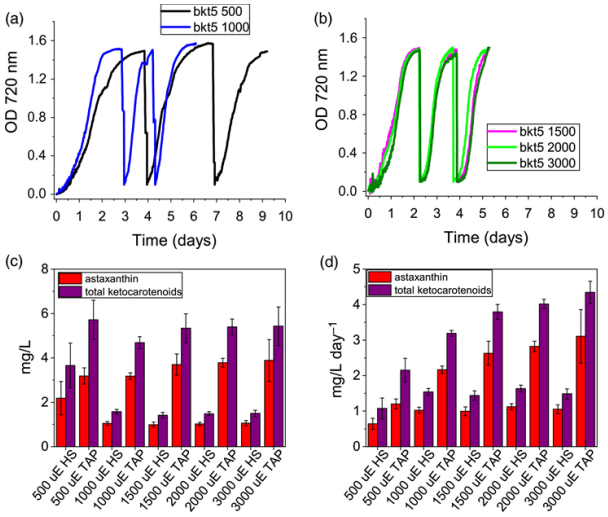

Figure 3.2.4 *Astaxanthin and ketocarotenoids production by bkt lines in very high light conditions. (a,b) Growth curves of bkt lines cultivated with 3% CO2 bubbling at 500, 1000, 1500, 2000 or 3000 µmol photons/m²/s in mixotrophy conditions (TAP medium). Cells were manually diluted 10-fold when the stationary phase was reached. Volumetric (c) and volumetric per day (d) productivities of astaxanthin (red) and ketocarotenoids (purple) obtained from bkt5 mutant grown as reported in panels a and b. Data are expressed as means ± standard deviation (n = 4).*

suggesting different carotenogenesis dynamics in very high light conditions (**Figure 3.2.5**). In mixotrophy, both astaxanthin and total ketocarotenoid accumulation were higher compared to autotrophy conditions and partitioning between these carotenoid types was largely conserved across all irradiances (**Figure 3.2.5c**). Astaxanthin and ketocarotenoid productivity was similar at the different irradiances under autotrophic conditions: ~1 mg astaxanthin L^{-1} day^{-1} and ~1.5 mg ketocarotenoids L^{-1} d^{-1}. Mixotrophy was found to yield 2.6 -3.1 mg astaxanthin L^{-1} day^{-1} and 3,7 – 4.3 mg ketocarotenoid L^{-1} day^{-1} at irradiances between 1500and 3000 µmol m^{-1} s^{-1}.

Extractability and bio-accessibility of ketocarotenoids from cells

One of the limitations in natural astaxanthin production from H. lacustris microalgae is the difficulty of pigment extraction from the cells which is hindered by the tough cell wall of the aplanospore cysts. These walls also limit the bio-accessibility of *H. lacustris* astaxanthin as they are largely resistant to digestion [497]. In order to evaluate a possible benefit in using *C. reinhardtii* for astaxanthin production over *H. lacustris*, the extractability of carotenoids from *C. reinhardtii bkt5* cells and *H. lacustris* cysts was compared by treating cells with solvent (ethyl acetate) or with mineral oil, a generally recognized as safe (GRAS) agent (**Figure 3.2.6**). Extraction with dimethyl sulphoxide (DMSO) was also used as a control as it has been previously reported to be the most effective method for total pigment extraction from *H. lacustris* [498]. Treating *H. lacustris* cells with either ethyl acetate or mineral oil gave an extremely low efficiency of astaxanthin extraction; less than 2% of total pigments could be extracted with

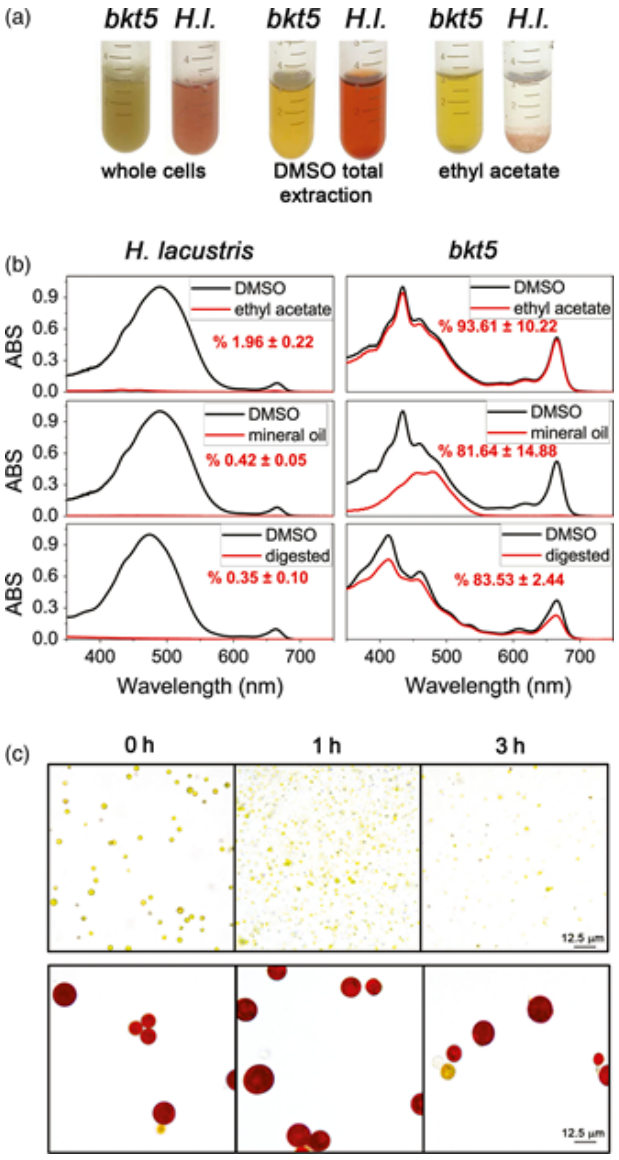

Figure 3.2.6 *Extractability and bio-accessibility of astaxanthin from Haematococcus lacustris and Chlamydomonas reinhardtii cells. (a) Aplanospore cysts of H. lacustris in 'red phase' and C. reinhardtii bkt5 in liquid medium (left) were compared using different pigment extraction methods. DMSO is used as a control from total extraction of pigments from both hosts (centre) and ethyl acetate (right) or mineral oil were used. (b) Absorption spectra of pigments extracted from H. lacustris in red phase and bkt5 with different solvents. Black traces are the absorption spectra of pigments obtained upon extraction in DMSO (positive control: maximum extraction); red traces show the pigments extracted with different methods. Spectra are normalized to the maximum absorption of the DMSO control. Inserts indicate the percentage of carotenoids extracted calculated from fitting analysis of the absorption spectra as described in Croce et al. (2000). Data are expressed as mean ± SD (n = 3). (c) Images of cells of bkt5 and H. lacustris before (0 h) and after simulated gastro-intestinal digestion (1 or 3 h).*

these agents (**Figure 3.2.6a-b**). With *C. reinhardtii bkt5*, however, ethyl acetate extracted more than 93% of pigments from C. *reinhardtii* cells and the treatment with mineral oil extracted more than 80% of the carotenoids (**Figure 3.2.6a-b**). These experiments confirmed that extractability of pigments from the transformed *C. reinhardtii* cells is more readily achieved than from *H. lacustris*. Finally, the bio-accessibility of astaxanthin produced in *C. reinhardtii* was compared to *H. lacustris* by simulating gastro-intestinal digestion *in vitro* [499] (**Figure 3.2.6b-c**). Cells were treated with simulated digestion fluids containing buffered solutions and enzymes, that is pepsin for the gastric phase and pancreatin for the intestinal phase. After 3h, almost no pigment was extracted from *H. pluvialis* cysts by this method while more than 80% of the pigments were extracted from *C. reinhardtii bkt5* (**Figure 3.2.6b**). These results indicate that cell wall deficient *C. reinhardtii* is a promising host organism for astaxanthin production as it is readily digestible and, consequently, the produced astaxanthin is more bio-accessible.

Discussion

The green microalga *C. reinhardtii* does not naturally accumulate ketocarotenoids, however, a beta-carotene ketolase (*Cr*BKT) is found in its genome. *Cr*BKT has been shown to catalyze the conversion of carotenes into ketocarotenoids when heterologous expression of this gene was performed in other organisms, however, this sequence shows almost no detectible expression in the algal host itself (**Figure 3.2.1b**). Compared to BKT from other organisms, the *Cr*BKT contains a long peptide extension on its C-terminus (**Figure 3.2.1c**), which appears to be an unfolded peptide region. Here, we took the *Cr*BKT sequence and used our recently developed transgene optimization strategy [485] to enable its re-integration into the algal nuclear genome and overexpression. When *Cr*BKT was expressed, it caused the green algal cells to noticeably change color from green to red, indicating the conversion of carotenoids to ketocarotenoids, with astaxanthin representing a major component of these. Our overexpression strategy of *Cr*BKT enzyme yielded better results compared to previous attempt where the BKT enzyme from *H. lacustris* expressed in *C. reinhardtii*: in the latter case indeed, only traces of ketocarotenoids as keto-lutein or keto-zeaxanthin were found [403]. We found the best combination of fusion partners and targeting peptides to be a fusion of the native gene, including its chloroplast targeting peptide, with the PsaD chloroplast targeting peptide and replacement of the

C-terminal amino acid extension with a GSG-linker and YFP reporter (**Figure 3.2.2c**). The 116 amino acid-long C-terminal extension of the *Cr*BKT reduced overall astaxanthin productivity when included in expression constructs, however, did not completely abolish astaxanthin formation (**Figure 3.2.2c**). This suggests that the presence of this peptide alone is not responsible for its lack of expression in the algal host and that its low transcription rates, likely, play a larger role. Interestingly, the fusion of truncated BKT with YFP at the C-terminus increased the production of ketocarotenoids (**Figure 3.2.2c**): likely, the presence of YFP at the C-terminus somehow facilitates *Cr*BKT protein folding and/or further stabilizes it, although further work is required to verify this hypothesis. As the presence of astaxanthin did not perturb growth rates of either *UVM4-bkt* or *npq2-bkt* expression strains, at least in the conditions tested here (**Figure 3.2.3**), it is unclear what advantage repression of this native gene has given to the algal host. It is possible that a condition could exist where it is expressed: indeed, *Chlamydomonas nivalis*, a relative of *C. reinhardtii*, is known to produce astaxanthin as a photoprotective pigment under variable high-light conditions on snow [500]. However, we did not find a condition where this gene was expressed to notable levels (based on FPKM) in the transcriptome databases investigated here (**Figure 3.2.1b**). Due to the very low rates of transcription, and the clear lack of ketocarotenoids in *C. reinhardtii*, we have called *Cr*BKT a pseudogene in this work.

Astaxanthin biosynthesis requires both a ketolase (BKT) and a hydroxylase (CHYB) (**Figure 3.2.1a**). A *CHYB* gene is present in the nuclear genome of *C. reinhardtii* (Cre04.g215050) and it is expressed, even if to a lower extent compared to other genes related to carotenoid biosynthesis (**Figure 3.2.1**) [483]. Re-insertion of only *Cr*BKT, into the nuclear genome of *C. reinhardtii* allowed the synthesis of high amounts of astaxanthin and other ketocarotenoids that normally do not accumulate in this organism (**Figure 3.2.2**). In contrast to previous work [482], the overexpression of *Cr*BKT alone was sufficient to induce ketocarotenoid formation in *C. reinhardtii*: these findings indicate that the native *Cr*CHYB is highly functional and able to participate in ketocarotenoid biosynthesis. When *Cr*BKT was overexpressed in the alga, astaxanthin became the major carotenoid (up to 50% of total carotenoids) with ketocarotenoids corresponding to ~70% of total carotenoids (**Table 3.2.1**). As the major substrate of *Cr*BKT is zeaxanthin, *Cr*BKT overexpression was also attempted in the *npq2* mutant, which is deficient in the zeaxanthin epoxidase and accumulates this as a terminal carotenoid [203]. Indeed, astaxanthin accumulation per cell was higher in *npq2* than UVM4 derived *bkt* lines (**Table 3.2.1**). However, *npq2* exhibits a slower growth rate than UVM4 (**Figure 3.2.3**), and although the growth was not affected by the presence of astaxanthin, overall volumetric productivities were higher with faster-growing UVM4 derived *bkt* lines (**Figure 3.2.4**).

The *bkt* mutants show a strong reduction of chlorophyll content of ~80% with respect to the parental line although remain photosynthetically active (**Table 3.2.1**, **Figure 3.2.3b** and **Figure 3.2.4**). The xanthophylls lutein, violaxanthin and neoxanthin are ligands for the photosystem antenna subunits, β-carotene is a ligand for both photosystem core complexes and antenna, while astaxanthin, in *H. lacustris*, is manly accumulated as a free form in the membrane, although it has been reported to bind photosystems [167] . In a photosynthetic cell, the absence of carotenoids hinders photosystem assembly and reduces chlorophyll content [501]. It is possible that by rapidly converting carotenoids into ketocarotenoids, photosystem assembly is hindered, and lower chlorophyll amounts accumulate in the algal cell. Another possible reason for the observed decrease of chlorophyll contents in cells expressing *Cr*BKT could be that photosynthetic complexes, assembled without proper carotenoids, generate more ROS that damage photosynthetic membrane [501], however, this hypothesis is less probable as no perturbation in growth rates were observed. In addition, high-light intensities were tolerated by cells, and ketocarotenoids exhibit high antioxidant capacities which would likely protect membranes from ROS damage. In engineered plants, strains with an almost complete conversion of carotenoid to ketocarotenoids have been generated and showed slower growth rates, reduced photosynthetic parameters and increased photoinhibition [431,433,450]. In *C. reinhardtii bkt* expression strains, ~30% of standard carotenoid and ~10-20% of the standard chlorophyll were left in engineered strains and seemingly were enough to enable light energy absorption needed photosynthetic growth. The reddish-brown phenotype (**Figure 3.2.3a**) of *bkt* transformants could be interesting for industrial application, as they are characterized by a

decreased chlorophyll content which may allow better light penetration into dense algal cultures. Indeed, reduced antennae and chlorophyll containing phenotypes have previously been reported to promote increased algal culture productivity [185,502].

H. lacustris is currently considered the best natural source and the main commercial producing organism for astaxanthin as this alga can accumulate up to 4% of its dry weight as astaxanthin [165]. Although *C. reinhardtii* strains presented in this work accumulate ketocarotenoids up to only 0.2 % of their biomass, by investigating even minimal optimization of growth conditions, productivities of ketocarotenoids and astaxanthin could be reached up to 4.3 mg L^{-1} day^{-1} and 3.1 mg L^{-1} day^{-1} respectively when cells were grown in mixotrophy at irradiance 3000 µmol m^{-2} s^{-1} bubbling 3% of CO_2. *Chlamydomonas reinhardtii bkt5* reached high productivity even in autotrophic conditions, bubbling 3% of CO_2, with ketocarotenoids and astaxanthin productivity of ~ 1.5 mg L^{-1} day^{-1} and ~ 1.0 mg L^{-1} day^{-1} respectively at irradiances between 1000 and 3000 µmol m^{-2} s^{-1}. Due to the need of a two-phase growth and astaxanthin induction, as well as a strong recalcitrant cell wall of astaxanthin containing aplanospores, the yield of astaxanthin from *H. lacustris* has been reported from 0.12 to 15 mg L^{-1} day^{-1} [503,504]. Therefore, ketocarotenoid production for *C. reinhardtii bkt* mutants is within in the same range of that of *H. lacustris*, however, requiring significantly fewer process parameters or extraction techniques, enabling also semi-continuous or continuous production processes. Indeed, stable productivity of up to 3.88 mg ketocarotenoids L^{-1} day^{-1} and 2.5 mg astaxanthin L^{-1} day^{-1} was reached when *C. reinhardtii bkt5* cells were cultivated in semi-continuous mode (**Figure 3.2.4**). Further optimization of *C. reinhardtii* cultivation, for example, in higher-density reactor concepts, will likely improve this efficiency.

Different techniques have been developed to disrupt *H. lacustris* cell walls and recover astaxanthin, these involve mechanical processes like high pressure or bead milling as well as the use of solvents, supercritical carbon dioxide, or enzymatic digestion [408]. All these procedures increase the cost of astaxanthin bio-production processes and exhibit a variable range of extraction efficiencies. *C. reinhardtii* strains commonly used for transformation and expression experiments generally lack cell walls. These strains still produce cell wall proteins, however, they are not able to assemble them on the cell surface and the proteinaceous wall proteins are instead secreted into the culture medium [197]. Here, we used the UVM4 strain which is a derivative of the *cw15* line of cell-wall deficient mutants. Due to the reduced cell wall, this strain is readily disrupted, enhancing the relative ease of pigment extraction from *bkt* expression lines. Astaxanthin extractability of *H. lacustris* aplanospores using ethyl acetate or mineral oil was below 1% while pigments in *C. reinhardtii bkt* lines could be completely extracted under similar conditions (**Figure 3.2.6**). This increased extractability also means that pigments within engineered *C. reinhardtii* are more bio-accessible, as the cyst state of astaxanthin containing *H. lacustris* may not be readily digested in target organisms (fish, livestock, or humans). *In vitro* simulated digestion showed enhanced pigment extraction from *C. reinhardtii bkt5* compared to *H. lacustris*, indicating the engineered alga could be used directly in aquaculture and nutraceutical feed, without the need for prior pigment extraction (**Figure 3.2.6b**). It has been previously reported that astaxanthin produced in maize could be delivered to trout fillet when extracted in ethanol and vegetal oil, even if zeaxanthin and keto-zeaxanthin were preferentially absorbed in the fish fillet [505]. Direct use of algal biomass as a source of ketocarotenoid pigments for livestock and aquaculture could also benefit the quality of pigments delivered to these organisms as storage of carotenoids can lead to their degradation or oxidation. Further experimental work is required to investigate the possibility of using *C. reinhardtii* cells overexpressing BKT as a feed supplement.

Given it only requires the overexpression of a single ketolase to generate constitutive astaxanthin and ketocarotenoid generation in *C. reinhardtii*, it will likely be possible to transfer this biosynthesis rapidly into other more industrially cultivated algal strains. For example, certain *Chlorella* species have demonstrated robust outdoor growth, or the genetically amenable *Nannochloropsis* sp. may be alternatives where the production of astaxanthin can be scaled in existing infrastructures [506,507]. However, both of these algae also exhibit robust cell walls, which may limit overall process productivity. Indeed, *C. reinhardtii* has been shown amenable to scale up in air-lift bioreactors even under outdoor conditions [508] and it may be that cultivation of cell-

wall deficient astaxanthin producing *C. reinhardtii* presents the best case of rapid growth and ease of pigment extractability. Moreover, additional biotechnological modifications can be attempted in *C. reinhardtii* in order to further boost carotenogenesis and astaxanthin productivity [509]. Given the robust activity of the *Cr*BKT, it may be likely that further customizations of the carotenoid biosynthesis can be readily achieved in this alga. Future engineering targets may seek to use existing carotenoids, or these new populations of ketocarotenoids, as even further targets for bioengineering optimization in this versatile algal host.

Material and methods

Algal cultivation and strain maintenance

Chlamydomonas reinhardtii strain UVM4 was graciously provided by Prof. Dr. Ralph Bock and *npq2* (CC-4101) was obtained by Chlamydomonas Resource Center (https://www.chlamycollection.org). Both strains were maintained on TAP agar plates or in liquid shake flasks at 25 C with 100-150 µmol photons m^{-2} s^{-1} of continuous white light. Growth tests were conducted using different systems: shaking flasks, stirring flasks or Multi-Cultivator MC-1000 (Photon Systems Instruments, Drasov, Czech Republic). Temperature was controlled to 25 °C while light intensities were varied as indicated in the text. Tris-acetate-phosphate (TAP) or high salts minimal (HS) media were used for mixotrophic or photoautotrophic conditions, respectively as described in the text [299]. *H. lacustris* strain K-0084 was obtained from Scandinavian Culture Collection of Algae & Protozoa and cultivated on BG-11 medium as previously described [419].

Design and cloning of expression cassettes

The *Cr*BKT (AY860820.1) found within the genome of *C. reinhardtii* was synthetically redesigned with codon optimization and intron spreading as recently described [197]. The synthetic optimized *Cr*BKT gene coding sequence (CDS) was deprived of the last 345 bp and cloned into pOpt2_PsaD_mVenus_Paro vector [488] to generate a protein which contains the *C. reinhardtii* photosystem I reaction centre subunit II (PsaD) chloroplast targeting peptide and a C-terminal mVenus (YFP) fusion. Variations on this construct were generated by successive cloning within the pOpt2_PsaD_CrBKT_YFP_Paro vector as described in the text. For subcellular localization determination mediated of the BKT N-terminal chloroplast targeting peptide, 102 and 120 bp from the 5′ region of the BKT coding for its N-terminus was amplified and cloned into *Nde*I-*Bgl*II sites of the pOpt2_PsaD_BKT_YFP_Paro. Additional details about design and cloning of expression cassettes can be found in Methods S1.

C. reinhardtii transformation and mutant screening

Nuclear transformation was carried out by glass bead agitation as previously described [404] using 10 µg of linearized plasmid DNA. Selection of transformants was done on TAP agar plates supplied by paromomycin (10 mg l^{-1}) for 5-7 days. Expressing colonies were pre-screened visually for red coloration before further quantification.

Fluorescence microscopy localization

Yellow fluorescent protein fluorescence imaging was performed as previously described [487].

Growth analysis

Parameters used for monitor growth were cell density and cell dry mass. Cell densities were measured using Countess II FL Automated Cell Counter (Thermo Fisher Scientific, Waltham, Massachusetts). Dry biomass was evaluated by overnight lyophilization of washed cell pellets and gravimetric determination.

Pigment analyses

Pigments were extracted from intact cells using 80% acetone buffered with Na_2CO_3 and analyzed by absorption spectra followed by curve fitting or by reverse phase HPLC. Absorption spectra were measured with Jasco V-550 UV/VIS spectrophotometer as described in [451]. Spectra were fitted as described in [70] introducing in the fitting method the astaxanthin absorption form in acetone 80%: considering the similar absorption of astaxanthin and canthaxanthin, the results obtained by fitting of pigment extracts absorption spectra were considered as representative to total ketocarotenoids. Reverse phase HPLC was conducted as described in [231,419]. HPLC system equipped with a C18 column using a 15-min gradient of ethyl acetate (0%-100%) in acetonitrile-water-

triethylamine (9:1:0.01, vol/vol/vol) at a flow rate of 1.5 mL/min was used. Pigment detection was conducted with a Thermo-Fisher 350–750 nm diode array detector. Ketocarotenoids peaks were identified by comparing retention times and spectra to commercially available standards (CaroteNature GmbHas, Münsingen, Switzerland). Different astaxanthins isomers were identified according to literature [494,495].

For LC mass spectroscopy measurements, single peaks were collected from HPLC separation. Sample were dried and resuspended in acetonitrile and loaded on HPLC 1260 (Agilent Technologies, Waldbronn, Germany) in tandem with a QTOF mass spectrometer used for the analysis. The QTOF-MS was implemented with an electrospray ion source with Agilent Jet Stream technology operating in positive ionization mode. Data acquisition was performed in full scan mode in the mass range of 200–1000 m/z.

Extractability and simulated digestion of ketocarotenoids in *H. lacustris* and *C. reinhardtii*

Same weight of dried cells of *H. lacustris* and *bkt5* were resuspended in water and treated with ethyl acetate or mineral oil for 20 min at room temperature and subsequently subject to centrifugation. Extracted pigments present in the supernatant were recovered and spectra were recorded to determine relative extractability. Treatment was repeated once for ethyl acetate and three times for mineral oil. The simulate digestion was performed following the protocol described by [499] with some modification. 0,1 gr of freeze-dried cells (LIO-5P, five pascal) were resuspended in 1 mL of simulated gastric fluid and stirred for 1 hour at 37° C, then 2 mL of simulated intestinal fluid was added to the samples. After further 2 h at as above, samples were centrifuged for 3 min at 3000 g to pellet intact cells and isolate the supernatant digested fraction. Pigments were extracted with acetone from the digested fraction and spectra recorded. .

Supporting information

Method S1

The CrBKT (AY860820.1) found within the genome of C. reinhardtii was synthetically redesigned with codon optimization and intron spreading as recently described (Baier et al., 2018b). The synthetic optimized CrBKT gene coding sequence (CDS) was deprived of the last 345 bp and a small region was added to make a C-terminal GSG-linker prior to optimization and the synthetic gene produced by GeneArt (Germany). The synthetic CrBKT sequence was cloned between BamHI-BglII into the pOpt2_PsaD_mVenus_Paro vector (Wichmann et al., 2018) to generate a protein which contains the C. reinhardtii photosystem I reaction centre subunit II (PsaD) chloroplast targeting peptide and a C-terminal mVenus (YFP) fusion. The empty vector served as a control. The vector confers resistance to paromomycin from a second aphVIII expression cassette (Lauersen et al., 2015). Variations on this construct were generated by successive cloning within the pOpt2_PsaD_CrBKT_YFP_Paro vector. The CrBKT was cloned into the same vector but without PsaD target peptide in order to obtain a CrBKT protein targeted with endogenous transit peptide. To test the C-terminal amino acid extension, the whole protein was generated by PCR fusion of a 345 bp region to its C-terminus. First, the C-terminal region was chemically synthesized including last 30 bp of BKT previously generated in order to allow primer binding. Then two different fragments were amplified: one containing BKT sequence using pOpt2_PsaD_BKT_YFP as template (primer: for: 5'-GGCCGGATCCGGCCCCGGCATCCAGCCCACCAGCG-3', rev: 5'-CCGCGGTCGCGGCAGCCGCGGCGGGCACGGGCAGGGGGCCGGGGGCCAGGGCGGCGC CGCGGGCGATC-3') while the second contained the BKT C-terminal region using synthetic sequence as template (primer for: 5'-GATCGCCCGCGGCGCCGCCCTG-3', rev: 5'- GGCCAGATCTGCCGCTGCCGGCCATCACGCCCACGGGGGCCAGC-3'). The two fragments were then used as template for an additional amplification to fuse these elements using additional primers for: 5'-GGCCGGATCCGGCCCCGGCATCCAGCCCACCAGCG-3' and rev: 5'-GGCCAGATCTGCCGCTGCCGGCCATCACGCCCACGGGGGCCAGC-3'. The amplified sequence was cloned into pOpt2_PsaD_BKT_YFP_Paro in the BamHI-BglII position. pOpt2_PsaD_BKT without YFP was generated by removing YFP sequence using ZraI and EcoRV enzymes from pOpt2_PsaD_BKT_YFP. pOpt_PsaD_BKT2x_YFP was generated by first PCR amplification of BKT sequence to remove the 5' 150 nucleotides coding for the N-terminal targeting peptide using pOpt2_PsaD_BKT_YFP_Paro as template (primer: for 5'-GGCCGGATCCAAGCTGTGGCAGCGCCAGTACCACCTG-3', rev: 5'-GGCCAGATCTGCCGCTGCCGGCCATCACGCCCACGGGGGCCAGC-3'). This sequence was inserted into a pOpt2 vector generating pOpt2_PsaD_-50aaBKT_YFP which could then be combined with the pOpt2_PsaD_BKT_YFP_Paro vector by compatible BamHI-BglII overhangs to generate the pOpt2_PsaD_2xBKT_YFP_Paro. For subcellular localization

determination mediated of the BKT Nterminal chloroplast targeting peptide, 102 and 120 bp from the 5' region of the BKT coding for its N-terminus was amplified and cloned into NdeI-BglII sites of the pOpt2_PsaD_BKT_YFP_Paro (primer for: 5'-GGCCGGATCCGGCCCCGGCATCCAGCCCACCAGCG-3' rev:amino acid 34 for 102bp and rev:amino acid 40 for 120bp). All cloning described here was performed using FastDigest restriction enzymes (Thermo Scientific) and the Rapid DNA Dephos & Ligation Kit (Roche) following manufacturer's instructions. PCR was conducted using Q5® High Fidelity DNAPolymerase (NEB). DNA fragments were separated in 2% (w/v) agarose gels and purified using the peqGOLD Gel Extraction Kit (VWR). Heat-shock transformation of chemically competent Escherichia coli DH5α cells was performed for all vectors followed by selection on LB-agar plates with ampicillin as a selection marker. Colonies were evaluated by colony PCR followed by plasmid isolation from overnight culture using peqGOLD Plasmid Miniprep Kit I (VWR). All sequences were confirmed by Sanger sequencing (Sequencing Core Facility, CeBiTec, Bielefeld University).

	vector	altered color/total		
UVM4	PsaD_YFP	0,00%	±	0,00%
	PsaD_BKT_YFP	16,40%	±	0,80%
	PsaD_BKT_Ct_YFP	14,50%	±	3,50%
	PsaD_BKT	13,30%	±	9,20%
	BKT_YFP	17,70%	±	6,50%
	PsaD_BKT2x_YFP	16,00%	±	12,00%
npq2	PsaD_YFP	0,00%	±	0,00%
	PsaD_BKT_YFP	17,95%	±	8,00%

Table S 3.2.1 *Percentage of colonies with visible phenotype upon transformation with bkt expression vectors. The percentage of colonies on plates with visible phenotype upon transformation with the different expression vectors carrying bkt gene was calculated from the ratio between brown/green colonies among the colonies surviving the antibiotic selection. Negative control with expression vectors carrying yfp gene only are reported. Errors are reported as standard deviations*

	HPLC peak	HPLC RT (min)	λ max (nm)	LC-MS RT (min)	m/z	chemical formula generated by LC-MS	Δ (ppm)
neoxanthin	1	4.83	415,438,466	-	-	-	-
violaxanthin	2	5.85	418,442,470	-	-	-	-
*3S 3S' trans astaxanthin	8	6.35	478	1.60	597.4	$C_{40}H_{52}O_4$	0.77
*3S 3S' 9 cis astaxanthin	9	7.01	470	1.60	597.4	$C_{40}H_{52}O_4$	0.52
*3S 3S' 13 cis astaxanthin	10	7.48	371,468	1.60	597.4	$C_{40}H_{52}O_4$	0.33
lutein	3	7.83	420,447,475	-	-	-	
*adonirubin (Phoenicoxanthin)	11	8.09	474	2.02	581,4	$C_{40}H_{52}O_3$	-1.24
*cantaxanthin	12	8.52	476	2.42	565.4	$C_{40}H_{53}O_2$	0.15
β carotene	6	13.35	428,455,478	-	-	-	-

Table S 3.2.2 *Chromatographic, spectroscopic and mass properties of identified carotenoids. First three columns indicate peak numbers, retention times (RT) and absorption peaks (λ max) of different carotenoids analysed by HPLC as shown in figure 3g. Single purified ketocarotenoids (indicated with *) were further analysed by LC Mass spectroscopy. Retention times for LC-MS, m/z value (corresponding to [M+H]+ values), chemical formula generated and the difference between the theoretical and measured mass value (Δ ppm) are reported.*

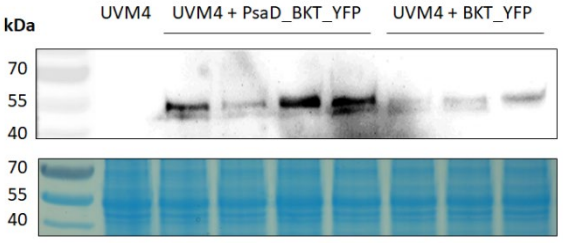

Figure S 3.2.1 *Western blot and immunodetection of BKT proteins fused with YFP. Protein extracts from transformant lines, as reported on the top of figure, we loaded in SDS-PAGE gel. Proteins were separated by 12% Tris-glycine-SDS-PAGE. Separated proteins were stained using colloidal Coomassie. Brilliant Blue G-250 or analyzed by immunodetection on nitrocellulose membranes using a HRP-linked rabbit-anti-GFP antibody (Thermo Scientific, A10260) and Pierce™ ECL Western Blotting substrates (Thermo Scientific). Coomassie staining is reported on the bottom of the figure as loading control.*

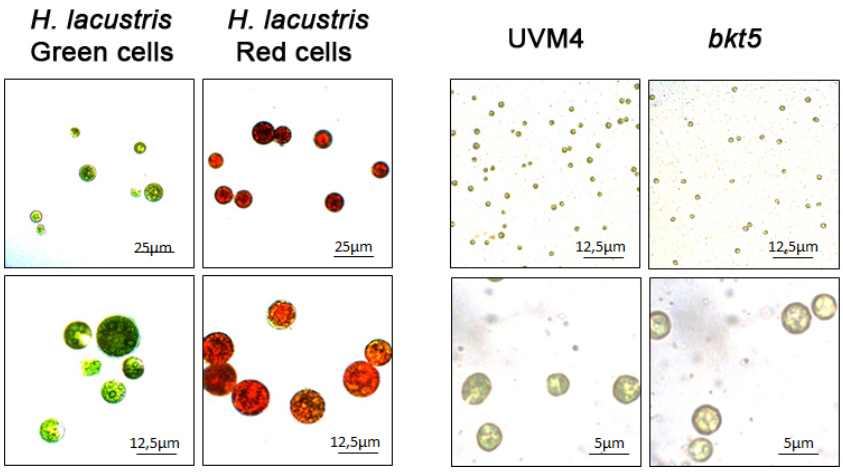

Figure S 3.2.2 *Microscopy images of H. lacustris and C. reinhardtii BKT overexpressing strain (bkt5). bkt5 strain was generated by transforming C. reinhardtii UVM4 strain with PsaD_BKT_YFP construct (Figure 2). H. lacustris cells are presented in green and red phases. Red phase was obtained by high light treatment and nitrogen starvation for 5 days.*

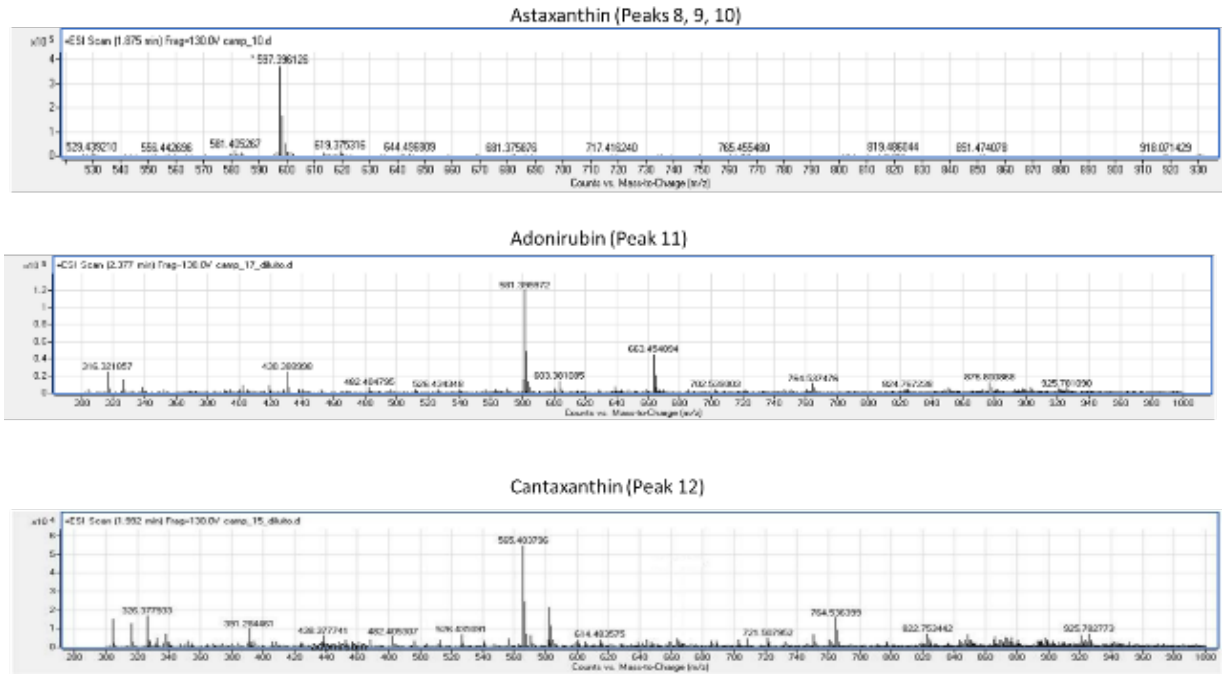

Figure S 3.2.3 *Mass spectroscopy of ketocarotenoids accumulated in bkt strains. Mass spectra of major ketocarotenoids present in bkt mutants. Peak numbers correspond to those present on HPLC chromatogram in Figure 3.*

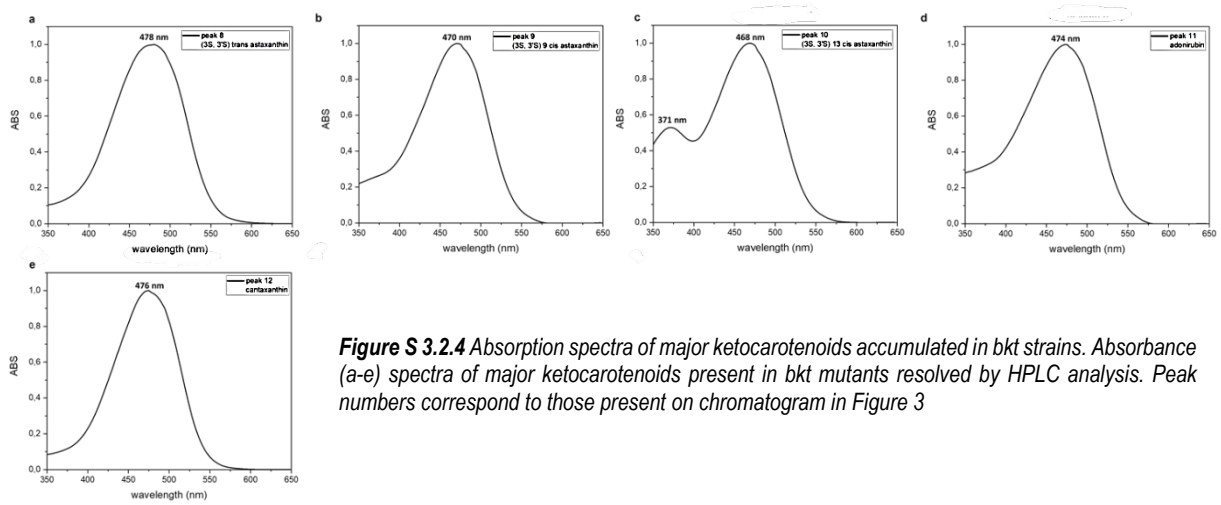

Figure S 3.2.4 *Absorption spectra of major ketocarotenoids accumulated in bkt strains. Absorbance (a-e) spectra of major ketocarotenoids present in bkt mutants resolved by HPLC analysis. Peak numbers correspond to those present on chromatogram in Figure 3*

.

Conclusions

The potential of microalgae for the development of sustainable industrial processes is high but not fully exploited yet. Indeed, a domestication of algal strains is, inevitably needed in order to fully exploit them. This thesis, with this aim, focuses the attention, first on energy dissipation process as a possible target to improve productivity, and later on the development of microalgae as green factories for the production of ketocarotenoids.

In the first part we tried to disentangle the long-debated question of non-photochemical quenching (NPQ) mechanisms in microalgae. The study is mainly focused on *Chlamydomonas reinhardtii,* model organism for green algae. LHCSR(s) proteins trigger NPQ in *Chlamydomonas reinhardtii* and, for that reason, these subunits were the main subject of our studies; in the most cases a multi-level approach combining *in vivo* and *in vitro* was used to solve the unknown aspects of NPQ mechanism. New traits of NPQ were thus revealed and can summarized as follow.

NPQ is a multi-level mechanism which is able to thermally dissipate excess energy; is triggered by LHCSR proteins among which LHCSR3 plays the major role. Beside the well-known PSII quenching we demonstrated the presence of a PSI quenching, also. LHCSR3 is, indeed, a quencher of both photosystems and can interact with several sites: PSII supercomplex, LHCI-PSI complex and “mobile” LHCII pool.

Moreover, this mechanism, differently to higher plants, require the presence of minor antennae CP26 and CP29 without which NPQ cannot be activated. Monomeric antennae resulted to be essential for energy transfer to reaction center, for supercomplex stabilization and for state transition induction.

Several mechanisms were active in quenching energy in LHCSR3: population of Car S1 state, Car-Chl energy transfer as well as Car radical cation formation. All these mechanisms are always active; however, in quenching conditions triggered by low pH they are enhanced. It is worth to note that when LHCSR3 proteins was induced to an aggregation state a strong quenching was measured, being essentially independent from the carotenoids activity. An aggregation dependent quenching is thus proposed; likely, after protonation LHCSR protein change conformation inducing a different aggregation with LHCII proteins.

Elucidation of spectroscopic proprieties of LHCSR3 allow to identify Chl *a* 612 as the chlorophyll with the lowest energy, but not essential in the quenching process, while the cluster Chl613-CarL1 can be proposed as a possible site of quenching. *In vitro* results also suggested the involvement of Chl 603 in the LHCSR3 quenching activity but the impossibility to obtain *in vivo* a mutant lacking this chlorophyll leads impossible to confirm or exclude the contribution of the cluster Chl603-CarL2. Moreover, mutant lacking Chl *a* 613 both *in vivo* and *in vitro*, even if reduced, is still able to active NPQ suggesting the presence of cooperating quenching sites.

The long debated question of zeaxanthin role in microalgae was also investigated. In *Chlamydomonas reinhardtii*, distinct quenching mechanisms were here identified: Zea, however, plays a minor role compared to the pH depedent quenching mechanism. Interestingly, in a mutant of *C. reinhardtii* with constitutive Zea accumulation, a constitutive energy dissipation mechanism was revealed, not specifically located in LHCSR subunits, but in general in LHC proteins.

Xanthophyll cycle was also investigated in another non-model microalga, *C. vulgaris*. We demonstrated the presence, differently to *C. reinhardtii* of a plant like-VDE with a conserved mechanism compared to higher plants. Moreover, similarity to plants were also found in the presence of a Zea-dependent quenching observed in C. vulgaris.

The results herein described can lay the basis for biotechnological manipulation of microalgae as reported in last part of chapter 2. Mutants with reduced and constitutive accumulation of LHCSR3, not triggered by high light exposure, were characterized by a lower NPQ and by a reorganization of photosynthetic machinery, resulting in a higher photosynthetic rate and thus higher biomass accumulation. Elucidation of the NPQ mechanism can thus lead biotechnological strategies to tune this process to produce strains with characteristics more suitable for industrial applications.

Second part of this thesis try to present a possible solution to overcome problems related to ketocarotenoids production. Indeed, currently the global request of astaxanthin is satisfied by *H. lacustris* cultivation. Despite the enormous accumulation of this ketocarotenoids, its production is complicated and expensive. Most of the problems are related to the stress requirements for biosynthesis of ketocarotenoids in *H. lacustris* leading to a block of cells division. We clearly demonstrate as this shift induce a destabilization of both photosystems by substitution of β-Car with astaxanthin. Moreover, the presence of astaxanthin bound to complexes, does not improves the photoprotection and reduces the efficiency of excitation energy transfer.

Considering the acquired importance obtained by ketocarotenoids (in particular astaxanthin) and considering also the constrains related to its production, it is evident the need of an alternative source for this antioxidant molecule. Here we present a *Chlamydomonas reinhardtii* based system, generated by over expression of a fully re-designed *bkt* pseudo gene, able to achieve the same astaxanthin daily productivity of *H. lacustris*. Beside the amount of ketocarotenoids produced, *C. reinhardtii* system ensures also a higher extractability. Considering the possible consumption of astaxanthin as dried whole cell, the bio-availability for human, of ketocarotenoids contained in our strains with respect to *H. lacustris* cells was evaluated; results show a 250 folds higher value for *Chlamydomonas* cells. These results underline the possibility to use *Chlamydomonas*, and in general microalgae, as hosts for the bio-production of molecules of interest: proteins, pigments, drugs or high value molecules. Combining the bacterial simplicity of usage with the complexity of this organisms (being eukaryotic), microalgae represents a promising platform for the development of industrial sustainable processes. The strategy reported here allows to obtain high amount of ketocarotenoid without expensive cultivation/extraction and for that reason is suitable for being combined with the cultivation for animal feeding or biofuels production; the integration of high value products allows to break down costs, leading, for example, to obtain bio fuels more competitive with respect to fossil fuels.

Both chapters of this thesis, the first with an enlargement of knowledge about energy dissipation mechanisms, the latter with a more applicative approach, show that domestication of microalgae is easily and quickly reachable with actual biotechnological techniques. Once domesticated, microalgae can provide a low cost, accessible, and sustainable source of food, drugs or high value molecule for mankind.

Appendix

In this appendix is reported a technological approach aimed to fill the gap in between photosynthesis research and industrial application. In order to effectively use PSI in light-dependent redox reaction in an extracellular context, stability in crucial. In this section we show an innovative solution by encapsulation of isolated PSI complexes in PLGA (poly lactic-co-glycolic acid) organic microparticles able to catalyze light-dependent redox reactions and characterized by a higher stability compared with PSI complexes in detergent solution.

This section is based on published article: Cherubin, A. *et al.* Encapsulation of Photosystem I in Organic Microparticles Increases Its Photochemical Activity and Stability for Ex Vivo Photocatalysis. *ACS sustainable chemistry & engineering* **7**, 10435-10444, doi:10.1021/acssuschemeng.9b00738 (2019).

Author contributions: Perduca M. and Ballottari M. conceived the work; Perduca M. supervised the nanoparticles synthesis; Ballottari M. supervised the purification and spectroscopic characterization of PSI; Cherubin A., DeStefanis L., and Bovi M. performed the nanoparticle synthesis and characterization; Romeo A. performed the AFM experiments and analyzed the data; Perozeni F., Bargigia I., and D'Andrea C. performed the time-resolved fluorescence analysis; Ballottari M. and Perduca M. wrote the paper; all the authors discussed the results and commented on the manuscript.

Encapsulation of Photosystem I in organic microparticles increases its photochemical activity and stability for ex vivo photocatalysis

Arianna Cherubin,[1] Laura Destefanis[1], Michele Bovi [1], Federico Perozeni[1], Ilaria Bargigia [2,3], Cosimo D'Andrea [2,4], Alessandro Romeo [5], Matteo Ballottari [1], Massimiliano Perduca [1]

[1]Department of Biotechnology, University of Verona, Strada Le Grazie 15, 37134 Verona, Italy
[2] Center for Nano Science and Technology @PoliMi, Istituto Italiano di Tecnologia, via Pascoli 70/3, 20133 Milano, Italy
[3] Georgia Institute of Technology, School of Chemistry and Biochemistry, 901 Atlantic Drive, Atlanta GA 30332-0400
[4] Department of Physics, Politecnico di Milano, P.za L. da Vinci 32, 20133 Milano, Italy
[5] Department of Computer Science, University of Verona, Strada Le Grazie 15, 37134 Verona, Italy

Abstract

Photosystem I (PSI) is a pigment binding multisubunit protein complex involved in the light phase of photosynthesis, catalyzing a light-dependent electron transfer reaction from plastocyanin to ferredoxin. PSI is characterized by a photochemical efficiency close to one, suggesting its possible application in light-dependent redox reaction in an extracellular context. The stability of PSI complexes isolated from plant cells is however limited if not embedded in a protective environment. Here we show an innovative solution for exploiting the photochemical properties of PSI, by encapsulation of isolated PSI complexes in PLGA (poly lactic-co-glycolic acid) organic microparticles. These encapsulated PSI complexes were able to catalyze light-dependent redox reactions with electron acceptors and donors outside the PLGA microparticles. Moreover, PSI complexes encapsulated in PLGA microparticles were characterized by a higher photochemical activity and stability compared with PSI complexes in detergent solution, suggesting their possible application for ex vivo photocatalysis.

Introduction

Photosystems (PS) are membrane protein complexes that bind pigments and are responsible for light harvesting and its conversion into chemical energy by promoting a light dependent electron transport chain across the photosynthetic membranes [32,40,55,379]. In eukaryotic photosynthetic organisms, two photosystems work in series, photosystem I (PSI) [40,43,254] and photosystem II (PSII) [32], with PSI being a plastocyaninferredoxin light-dependent oxidoreductase and PSII a light-dependent water-plastoquinone oxidoreductase [379]. PSI and PSII are then connected by the protein complex called Cytochrome b_6f which oxidizes plastoquinones and reduces plastocyanin [380]. Both PSI and PSII are composed of a core complex hosting the reaction center where charge separation occurs and an outer antenna system made of light-harvesting complexes [219,355]. In eukaryotic organisms, PSI is present in the thylakoid membrane as a monomer carrying its antenna moiety on one side in a "half-moon" shaped structure [40]. The reaction-center core complex is made up of the heterodimeric PsaA and PsaB subunits, containing the primary electron donor, a chlorophyll dimer called P700, which undergoes light-induced charge separation and transfers an electron through the sequential carriers A_0, A_1, FX being respectively a monomeric chlorophyll *a*, two phylloquinones, and a [4Fe−4S] iron− sulfur center [40]. The final acceptors, FA and FB, two other [4Fe−4S] iron−sulfur center, are located on another subunit, PsaC [40]. The redox potential of the primary donor, P700, is +0.43 V and that of the final acceptor, FB, is −0.53 V, producing a redox difference of −1.0 V. PSI absorbs in the 350−500 nm and 620−710 nm wavelength range: photochemical properties of PSI have been extensively studied either in intact cells or in detergent solution, revealing its extremely high quantum efficiency, close to 1, with a very short trapping time of excitation energy at the reaction center (30−70 ps) [355,442,510], and an energy yield of ~58% [511]. The extremely

high photochemical properties of PSI suggested its possible application in extracellular artificial devices as light convertor for the generation of electron transport chain [511-520] or for *ex vivo* photocatalysis of redox reactions [520,521](Krassen et al. 2009; Zhao et al. 2018). Moreover, PSI photochemical properties could also be potentially used for photoactivation of mammalian cells [522]: optical stimulation of living cells and tissues by means of micro and nanoparticles is an extremely promising tool in medicine and biology in order to control neuronal networks or physiological functions [523]. The different applications of PSI require its assembly in stable systems. Previous reports demonstrated the importance of the environment for the photochemical properties of PSI [524,525], which was reported to be successfully improved upon encapsulation in various organic/inorganic interfaces [512,526-535]. In order to design an environmentally friendly photocatalytic system which could be also used for applications in mammalian cells, a biocompatible formulation of PSI is required. Micro- or nanoparticles can be applied, thanks to their small size and the protected environment they offer, to fibers, sensors, wires, sheaf, meshes, cosmetic, medical, diagnostic, and therapeutic fields [536]. Among the organic polymers for particles synthesis, chitosan and PLGA are interesting for their safety and biocompatibility [536-542]. Chitosan is a cationic amino polysaccharide copolymer of β-(1−4) linked D-glucosamine and N-acetyl-glucosamine derived from chitin by alkaline or enzymatic partial deacetylation [542]. PLGA is a biocompatible copolymer of poly lactic acid (PLA) and poly glycol acid (PGA) that is used to synthesize biodegradable micro or nanoparticles [536,538,540,541,543]. Thanks to the rapid degradation without negative side effects on the human body and the absence of significant toxicity, the U.S. Food and Drug Administration (FDA) and the European Medicine Agency (EMA) have approved both chitosan and PLGA particles as delivery vehicle for drugs, proteins, and other molecules such as DNA, RNA, and peptides [536,538,541]. These kinds of micro and nanoparticles offer a nonpolar environment protecting hydrophobic compounds from water contact and mimicking what happens in cellular membranes and organelles. In this work, we investigated the possibility to encapsulate PSI complexes isolated from spinach leaves in organic microparticles (MPs) in order to obtain a stable and efficient light-dependent redox catalyst.

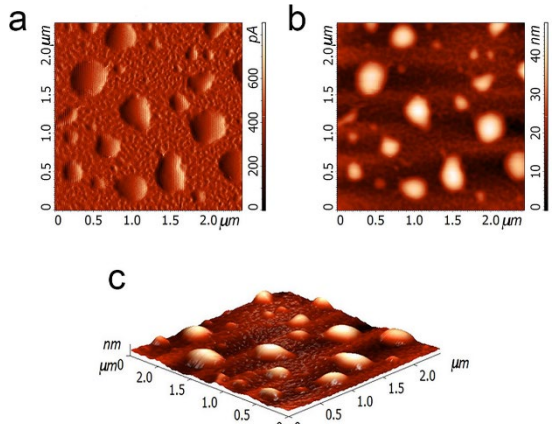

Figure App.1 *Atomic Force Microscopy (AFM) observation of PSI in PLGA microparticles. PLGA MPs visualized in three different modes: (A) Error-mode; (B) Semi-contact; (C) 3D. The images have been acquired in dry mode.*

Results

Photosystem I encapsulation in PLGA microparticles

PSI supercomplexes were purified from spinach leaves as described in [438]. Isolated PSI complexes were then encapsulated in PLGA microparticles (MPs) as described in the Methods section **Figure S App.1**). PLGA polymer was initially chosen for MPs production because of the negative charges present in this molecule, which could potentially interact with oxidized P700+. The resulting MPs, after several washing steps, were green, and the pigment composition of this MPs was investigated by HPLC. As reported in **Table S App.1**, the pigment content of PSI in PLGA MPs was like the pigments identified in PSI in detergent solution, suggesting the encapsulation procedure did not significantly alter the pigment binding properties of the PSI complex. Encapsulation efficiency, calculated on the basis of the analysis on the content of chlorophylls in microparticles, was 47.2%, indicating that the microparticles offer a suitable environment to the PSI encapsulation. In addition, from the chlorophyll content per gram of PLGA MPs, it was possible to calculate a PSI content per gram of PLGA MPs of 99 μmol PSI/g particles. Size and superficial charge of PLGA MPs containing PSI were then investigated by dynamic light scattering (DLS) compared to PSI in detergent. PSI in detergent solution was quite homogeneous with an average size of about 55 nm and a PDI (polydispersity index) of 0.06 (**Table S App.2**). It is important to note that DLS measurements of PSI in detergent give information about the detergent

micelles formed around PSI complexes, increasing the apparent diameter of the complexes from ~20 nm (isolated PSI) [40] to 55 nm (PSI in detergent micelles). The empty microparticles suspension was homogeneous with an average size of 402 nm and a PDI of 0.02, thus confirming the uniformity of the suspension. Not surprisingly, the suspension of PSI containing PLGA MPs was inhomogeneous, with an average size of 1700 nm and a PDI of 0.5: encapsulated PSI might establish different interactions with the PLGA matrix and different MPs might contain different numbers of PSI complexes, giving rise to particles having inhomogeneous size. Moreover, microparticles can aggregate together, and this can affect DLS analysis. The superficial charge measured for PLGA MPs was negative, strictly connected to the chemical characteristics of the polymeric PLGA (**Table S App.2**). Indeed, the amphiphilic nature of the PLGA monomers forces the polar carboxylic groups of PLGA to be exposed at the water solvent during the microparticles synthesis. The encapsulation of PSI in PLGA MPs was further confirmed by AFM measurements, showing that the empty PLGA MPs were much smaller compared with PLGA MPs containing PSI (**Figure S App.2**). Moreover, PSI containing PLGA MPs looked like spheres with well-defined outlines and smooth surface (**Figure App.1**), suggesting that all the PSI was encapsulated and not attached outside the shell. This finding is also consistent with the hydrophobicity of PSI complexes, leading to a reduced exposure to the water solvent.

Photosystem I encapsulation in PLGA microparticles: absorption and fluorescence emission spectra

To verify the presence of PSI in PLGA MPs and their optical properties, absorption and fluorescence emission spectra were acquired. PLGA MPs assembled in the presence of PSI were clearly characterized by absorption peaks in the 350−500 nm and 615−720 nm, as expected in the presence of chlorophyll binding complexes (**Figure App.2**). When the absorption spectrum of PSI in PLGA MPs was corrected for the scattering due to the dimension of the MPs, subtracting the signal obtained for empty PLGA MPs, it was possible to compare the absorption of encapsulated PSI vs PSI in detergent solution: PSI in PLGA MPs presented similar absorption characteristics of

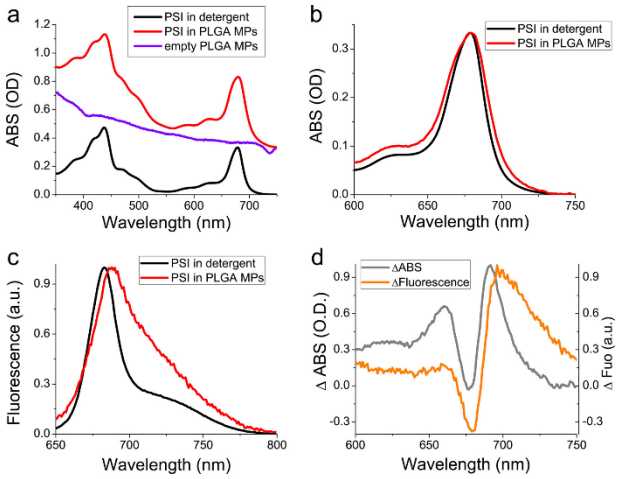

Figure App.2 *Absorption and fluorescence emission spectra of PSI in detergent and in PLGA microparticles. (a) Absorption spectra of isolated PSI in detergent solution (black) or in MPs (red). The scattering traces of empty PLGA MPs is also reported in blue. (b) Absorption spectra of PSI in detergent solution vs. PSI in PLGA MPs in the 600-750 nm range. Absorption spectrum of PSI in PLGA MPs was obtained after subtraction of the scattering trace of empty MPs. (c) Fluorescence emission spectra of PSI in detergent vs. PSI in PLGA MPs upon excitation at 440 nm (similar results were obtained upon excitation at 475 or 500nm). (d) difference absorption (grey) or fluorescence (orange) spectra obtained as PSI in PLGA MPs minus PSI in detergent*

the PSI in detergent but exhibiting a broader peak in the 600−750 nm region, indicating the formation of stronger Chl-Chl interaction in PLGA MPs, which is likely due to a protein aggregation, with a consequent enlargement of the absorption spectrum [223]. In agreement with this observation, fluorescence emission spectra of PSI were characterized by a red-shift of the peak from 684 nm (in detergent) to 689 nm (in PLGA MPs) and by a stronger emission in the 700−750 nm region for PSI in PLGA MPs compared with PSI in detergent. The fluorescence emission above 700 nm in PSI complexes is due to energy transfer to low energy chlorophylls commonly named “red forms” which are strongly coupled forming a charge transfer state [544]: the red-shifted absorption and increased emission above 700 nm in PLGA MPs (**Figure App.2**) might thus be attributed to a stronger Chl−Chl interaction likely caused by protein aggregation in MPs.

Photochemistry in PLGA microparticles

PSI photochemical activity was measured in detergent and in PLGA MPs to evaluate the possible charge separation at the level of its reaction center, P700. Photochemical activity of PSI can be measured following the kinetics of P700 oxidation upon light exposure. Reduced P700 indeed has a maximum absorption peak at ~705 nm, while

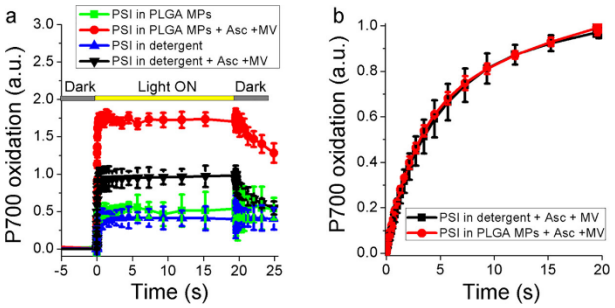

Figure App.3 *Photochemical activity of PSI. (a) light dependent P700 oxidation of PSI in detergent or in PLGA MPs measured as transient absorption at 705 nm. Ascorbate (Asc) and Methyl-viologen (MV) were added where indicated as electron donor and acceptor respectively. Orange actinic light at 940 µmol $m^{-2}s^{-1}$ were used to induce P700 oxidation (b) light dependent P700 oxidation measured under limiting light (12 µmol $m^{-2}s^{-1}$) in presence of electron donors and acceptors. Kinetics traces were in this case normalized to the maximum value. In these conditions the kinetics of P700 oxidation are inversely proportional to PSI light harvesting properties.*

the oxidized form P700+ has red-shifted absorption with a peak at ~830 nm: kinetics of P700 oxidation can thus be obtained following the transient absorption decrease at 705 nm upon exposure of PSI to an actinic light [545]. As reported in **Figure App.3a**, both PSI in detergent solution and in PLGA MPs exhibited a significant P700 oxidation in actinic light, which was further increased in the presence of ascorbate and methyl viologen (MV) in solution as electron donor and electron acceptor, respectively. When the actinic light was switched off, P700+ was re-reduced only in the presence of ascorbate. Interestingly, upon normalization of P700 oxidation kinetics to the total chlorophyll content, PSI in PLGA MPs was characterized by a P700+ formation increase of ~75% compared with the same complex in detergent solution. To evaluate possible different light-harvesting properties of PSI in PLGA MPs compared to detergent, the functional antenna size of PSI was evaluated by measuring the kinetics of P700 oxidation in limiting light [126], where the light-harvesting efficiency and the rate of P700 oxidation are inversely related. As reported in **Figure App.3b**, the kinetics of P700 oxidation in limiting light, normalized to the maximum P700+ value, were similar for PSI in detergent or in PLGA MPs, indicating similar light-harvesting properties. The photochemical efficiency of PSI in PLGA MPs was then investigated by measuring fluorescence lifetimes: an increased photochemical efficiency will decrease the fluorescence lifetime and fluorescence quantum yield because of increased nonradiative de-excitation. Time-resolved fluorescence for

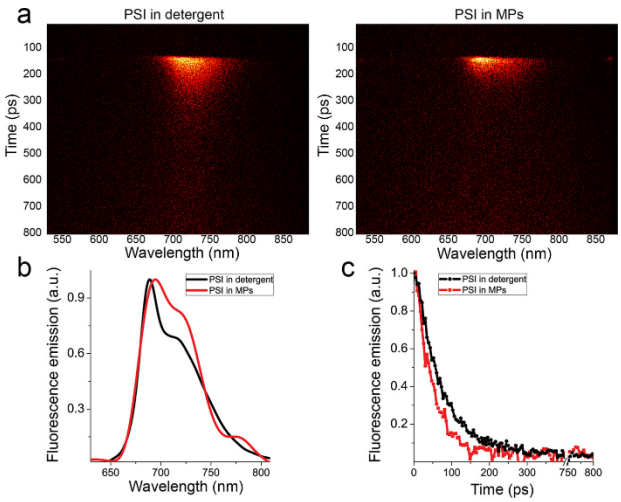

Figure App.4 *Time resolved analysis of PSI in detergent or in PLGA microparticles. (a) Fluorescence decay maps obtained upon laser excitation (440 nm) of PSI in detergent or in MPs; (b) integrated spectra in the 0-1800ps time range. (c) integrated kinetics in the 650-800 nm wavelength range*

PSI in detergent solution or in PLGA MPs were acquired by a time-resolved fluorescence spectroscopy system based on a Streak Camera detector by which the fluorescence emission kinetics are acquired at different wavelengths of emission, with the resulting 2D fluorescence maps reported in **Figure App.4a**. The fluorescence emission spectra integrated in the time range 0−800 ps confirmed the red-shifted emission for PSI in MPs compared to PSI in detergent (**Figure App.4b**). As reported in **Figure App.4c**, the integrated emission kinetics in the 650−800 nm emission range were faster in the case of PSI in PLGA MPs. Measurements of time-resolved fluorescence at different power intensity showed that the faster decay of fluorescence kinetics of PSI in PLGA MPs was not due to annihilation effect as reported in **Figure S App.3**. Average fluorescence lifetimes (τ_{AV}) calculated from exponential fitting of the decay traces resulted as 48.7 ps in the case of PSI in detergent and 31.5 ps for encapsulated PSI (**Table S App.3**). These values can be approximated to the trapping time, the time required for the excitation energy to reach the reaction center, and can be used to calculate the photochemical efficiency of PSI as previously described [546], resulting in 98.5% and 99.1% photochemical efficiency for PSI in detergent and in PLGA MPs, respectively.

Stability of Photosystem I in PLGA microparticles

The potential advantage of having a PSI complex encapsulated in MPs is an increased stability due to a shell effect of the organic matrix. The stability of PSI in PLGA

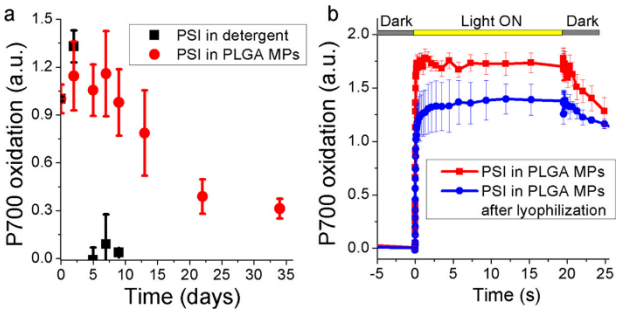

Figure App.5 *Stability of PSI in PLGA MPs to light exposure and lyophilization. (a) maximum P700 activity measured at different time (days) of exposure to 1500 µmol $m^{-2}s^{-1}$. (b) P700 oxidation measured in PSI in PLGA MPs before and after lyophilization, with the latter being resuspended in the same initial volume. Ascorbate and Methyl-viologen were added in all cases as described in Material and Methods section*

MPs was thus investigated by DSC and compared to PSI in detergent solution. As reported in **Figure S App.4**, a negative signal was measured for either PSI in detergent or in PLGA MPs, indicating that the disruption of PSI complexes is an exothermic event. Clearly, this negative peak was delayed in time when PSI was encapsulated in PLGA MPs compared with PSI in detergent solution: this result indicates that the presence of the PLGA shell conferred a longer stability to PSI. The increased stability of PSI in PLGA MPs was then evaluated measuring the PSI photochemical activity after different times of illumination with strong white light (1500 µmol m^{-2} s^{-1}). As reported in **Figure App.5**, PSI in detergent solution completely lost its photochemical activity after 5 days of illumination, while PSI in PLGA MPs exhibited an almost unaltered photochemical activity for at least 10 days. A residual 30% photochemical activity was still measured in PSI in PLGA MPs after 34 days of illumination.

Encapsulation of PSI in chitosan microparticles

To evaluate if the increased photochemical activity and increased stabilization effect were specifically related to the chemical properties of the PLGA matrix, PSI encapsulation was also performed in chitosan MPs (**Figure S App.5**). As reported in **Table S App.2**, chitosan MPs were half the size compared with PLGA MPs but with a positive superficial charge. AFM observation of PSI in chitosan MPs yielded similar results compared to PLGA MPs (**Figure S App.6**). Differently, the redshifted absorption spectrum and fluorescence emission above 700 nm were less pronounced compared with PLGA encapsulation, even if still evident (**Figure S App.7**). Photochemical activity of PSI measured as P700+ oxidation was increased compared with PSI in detergent but lower compared with PSI in PLGA MPs (**Figure S App.8**). Stability of PSI in chitosan MPs was then evaluated as described above after different times of illumination with strong white light (1500 µmol m^{-2} s^{-1}): differently from the case of PSI in PLGA MPs, encapsulation in chitosan MPs did not increase its stability during light exposure (**Figure S App. 9**). The result obtained demonstrate that encapsulation in PLGA MPs is more efficient for preserving PSI photochemical activity and stability.

Photosystem I in PLGA microparticles is resistant to lyophilization

An important parameter to be considered for possible applications of PSI MPs is the stability to lyophilization since in many cases MPs need to be dried to extend their shelf life and/or for convenient storage/transportation. PLGA MPs containing PSI complexes were thus lyophilized, and the residual PSI photochemical activity was measured on both dried and resuspended PLGA MPs. As reported in **Figure S App.10**, P700 oxidation was still detectable even on lyophilized PLGA MPs. Moreover, when lyophilized PLGA MPs were resuspended in water, the same absorption spectra (**Figure S App.11**) were obtained comparing PSI in PLGA MPs before and after lyophilization. The photochemical activity of encapsulated PSI resuspended after lyophilization was then measured, upon addition of ascorbate and methylviologen as electron donor and acceptor, observing only a slight decrease compared to the PSI in PLGA MPs before lyophilization (**Figure App.5b**): this result indicates that when PSI is encapsulated in the PLGA matrix, it can be lyophilized preserving most of its photochemical activity.

Photosystem I in PLGA microparticles can catalyze redox reaction

Light-dependent P700 oxidation observed in PSI suggests its possible application as light-dependent catalyst for redox reaction. To prove this concept, encapsulated PSI in PLGA matrix was tested for possible reduction of methylene blue (**Figure App.6**). Methylene blue is indeed commonly used as redox indicator, since its absorption in the 500−700 nm range decreases in the reduced form [547]. When PSI in PLGA MPs were incubated with ascorbate as

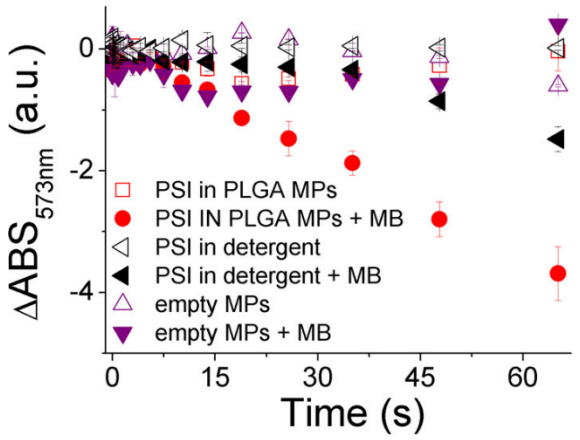

Figure App.6 *Light dependent reduction of methylene blue mediated by PSI microparticles. Samples were illuminated at 940 µmol $m^{-2}s^{-1}$. Transient absorption data are reported as the difference in absorbance at 537 nm (ΔABS537nm), setting as 0 the ΔABS537nm value at time 0.*

electron donor and methylene blue as electron acceptor, a decrease absorption at 537 nm was evident when light was turned on, indicating the formation of reduced methylene blue. Reduction of methylene blue was substantially higher when PSI was encapsulated in PLGA MPs compared with the case of PSI in detergent, consistently with the increased photochemical activity of PSI in PLGA MPs (**Figure App.3**). Even if at this stage it was not possible to assess if methylene blue reduction occurs inside the MPs, by a direct interaction of PSI with the probe, or outside the PLGA MPs through interaction with the PLGA matrix, this result indicates that the encapsulated PSI could be adopted to catalyze light-dependent redox reactions.

Discussion

In this work the potential use of PSI in extracellular context as a light-dependent redox catalyst was investigated, exploiting the possibility to encapsulate this chlorophyll binding complex in an organic matrix formed by a PLGA polymer. PSI is indeed the photosynthetic complex with the highest quantum efficiency, and it is characterized by fast trapping time of tens of ps [355]: this complex could thus be considered as an extremely efficient nanomachine that can convert light energy into chemical energy by charge separation [355,526]. The results herein presented demonstrate that it is possible to encapsulate PSI in PLGA microparticles (**Figure App.1** and **Figure App.2**) maintaining its high photochemical efficiency close to 1 (**Table S App.3**). Moreover, PSI encapsulated in PLGA microparticles was characterized by a stronger photochemical activity compared to the detergent solution case (**Figure App.3**), being able to exchange electrons with donors and acceptors added to the MPs mixture. The increased PSI photochemical activity observed in PLGA MPs compared with the detergent case is intriguing because from one side it supports the possible applications of this MPs for the exploitation of PSI photochemical properties, and from the other side, it stimulates a possible hypothesis explaining the effect of PLGA encapsulation on PSI activity. The reason(s) at the base of the increased photochemical activity of PSI in PLGA MPs might be several: the protein−protein interaction formed by PSI in the PLGA MPs might favor electron transfer process and/or PLGA matrix could allow for a more efficient electron transfer to and from the PSI complex. Encapsulation of PSI in PLGA MPs did not alter the light-harvesting properties of PSI but caused a broadening of the absorption spectrum with a stronger emission above 700 nm compared to PSI in detergent solution. This spectroscopic feature is usually related to a partial aggregation state of chlorophyll binding complexes [223]: in this condition, the different PSI complexes could thus be more interconnected creating an environment where charge separation at the level of P700 reaction centers is facilitated compared to the PSI monomers found in detergent solutions. A partial aggregation state of PSI could also be more similar to the *in vivo* condition, where the PSI complexes are present in the thylakoid membranes, which have been reported to be densely crowded by photosynthetic proteins [548]. Alternatively, since PSI is a membrane complex, formed by protein subunits with several hydrophobic domains, the protein−protein interaction induced in PLGA MPs could stabilize the complex conformation to a more photochemical active state compared with PSI in detergent. PSI in PLGA MPs catalyze a light dependent electron transport chain from electron donors to electron acceptors: ascorbate was successfully adopted as electron donor, while both methyl-viologen and methylene blue were used as electron acceptors. Considering the porous structure of the PLGA matrix [539], it is likely that electron acceptors and donors can diffuse inside the MPs and that the redox reactions occur upon direct contact with encapsulated PSI. However, it cannot be excluded that the PLGA matrix surrounding PSI could mediate the electron

exchange between PSI and electron donors and/or acceptors. The PLGA matrix forming the MPs herein investigated is indeed characterized by negative charges, which could be the source of electrons for re-reduction of P700 reaction center and/or reduction of the electron acceptors when electrons transported by PSI are available for regenerating the negative charges on the organic layer. Further investigations are required to evaluate the possible role of PLGA on the electron transport induced by light-dependent charge separation at the level of P700. Additionally, the encapsulation of PSI in chitosan MPs, characterized by positive superficial charges, did not increase PSI photochemical activity and stability as in the case of PLGA matrix, suggesting that the presence of negative charge on the MPs surface might be important for activity and stability of the encapsulated PSI. Indeed, encapsulation of PSI complexes in PLGA matrix conferred an additional stability compared with PSI in detergent solution. This enhanced stability for PSI embedded in PLGA MPs is likely ascribable to the amphiphilic nature of the polymer itself ensuring a hydrophobic environment as experienced by PSI in the thylakoid membranes. Conversely, chitosan MPs are not able to ensure a hydrophobic environment and PSI complexes even if embedded in the MPs and in a hydrophilic environment, leading to a possible easiest destabilization due to loss of protein conformation. PSI PLGA MPs maintained the same photochemical efficiency after 10 days of strong illumination, and after more than 30 days, a residual 30% photochemical activity was still detectable. Moreover, encapsulated PSI could be safely lyophilized with a minor reduction of its photochemical properties, observing P700 oxidation even in lyophilized PLGA MPs. The preservation of a functional PSI complex functionality after lyophilization represents an important achievement for the applications of PSI in PLGA MPs and for their storage and transportation. Furthermore, these microstructures might represent new potential items to produce energy: they could be employed in photovoltaic panels and/or they could be used in the H_2 production if coupled with a hydrogenase enzyme [521], exploiting electron transport induced by PSI photochemistry to produce H_2 from H_+. In addition, it is important to note that a disadvantage in using MPs is that efficient coupling of PSI complexes with photovoltaic devices require proper orientation of PSI [511], which is difficult to achieve in MPs. Several previous works reported the application of PSI in an extracellular environment coupled with artificial devices [512-515,518,522], carbon nanotubes[549], metal oxide nanowires [550], plasmonic nanostructures [527,529,533], conductive polymers [551], redox hydrogel [519,552], or assembled in metal−organic framework [526]. The advantage of the technology herein proposed, in addition to the increased photochemical activity and increased stability of PSI, consists of the organic matrix used for PSI encapsulation: PLGA polymers are environmental friendly compounds since they are biocompatible [540,541] and their ester linkages are rapidly hydrolyzed once they enter a cell to produce the monomers, lactic acid and glycolic acid, which are then easily metabolized via the Krebs cycle. PLGA-based MPs have been indeed approved by U.S. Food and Drug Administration (FDA) and by the European Medicine Agency (EMA) [541] as a delivery vehicle for drugs, proteins, and other molecules such as DNA, RNA, and peptides. In this context, it is possible to conceive a potential application of PSI MPs interacting with animal/ human cells or biomimetic system to specifically deliver light-dependent redox reactions.

Material and methods

Photosystem I purification

Photosystem I complexes were purified from spinach leaves as described in [228]. In particular, thylakoid membranes were purified from spinach leaves and then solubilized in 0.8% dodecyl β-D-maltoside, and the solubilized membranes were loaded on sucrose gradient in order to separate the different pigment binding complexes by ultracentrifugation. Isolated PSI were kept in 0.5 M sucrose, Hepes 20 mM pH 7.5, and 0.03% dodecyl β-D-maltoside: this buffer was also adopted for all the measurement of PSI in detergent conditions.

Synthesis of poly lactic-co-glycolic acid microparticle

The modified solvent displacement method (MSD) was used in PLGA microparticles preparation [543] (**Figure S App.1**): a polymeric phase containing 500 µL of PEG 400 (Merck-Schuchardt), 500 µL of poly(vinyl alcohol) (PVA) 1% solution, 2 mL of PSI (chlorophylls concentration 89.1 µg/mL in the sample), and 20 mg of PLGA 75:25 (Sigma) was sonicated for 1 min (5 s of sonication alternated to 5

s of time pausing) and slowly added dropwise to an aqueous phase of 12 mL of 1% PVA (Sigma). Sonication power used was 8 W. The mixture was sonicated 4 min at the same rate. The whole preparation was kept under magnetic stirring for 6 h, and the solution obtained was centrifuged for 20 min at 12000g; the pellet was resuspended in 15 mL of Milli-Q water, and the solution was dialyzed against deionized water overnight, with a cellulose membrane, cutoff 10−14 kDa (Sigma), to eliminate the excess PEG [537]. Two washing cycles with Milli-Q water were done to eliminate the excess PEG and the PSI, which has not been encapsulated; hence, microparticle solution was washed by centrifugation for 15−20 min at 12000g, until the supernatant was transparent because of the absence of PSI (as confirmed by absorption measurements at 680 nm). Empty microparticles were prepared following the same protocol, but the volume of PSI solution was replaced by PVA 1%. All samples were lyophilized and resuspended in Milli-Q water at the proper concentration required for each experiment.

Synthesis of chitosan microparticles

Chitosan microparticles were prepared via the ionic cross-linking method [542], in which an anionic cross-linker, such as tripolyphosphate (TPP, Sigma), is used (**Figure S App.5**). In particular, 3 mL of TPP solution at 0.028% was added dropwise in 5 mL of chitosan solution 0.1%, in which 100 µg (chlorophylls concentration of 89.1 µg/mL) of PSI were added, under magnetic-stirring. Magnetic-stirring was then kept constant for half an hour, and a solution of microparticles was then washed twice by centrifugation for 15 min at 12000g, while the pellet was suspended in 500 µL of Milli-Q water. All samples were lyophilized and resuspended in Milli-Q water at the proper concentration required for each experiment.

Dynamic light scattering analysis

The PLGA MPs size and the Z-potential were estimated using the DLS technique (Nano ZetaSizer ZS, ZEN3600, Malvern Instruments, Malvern, Worcestershire, U.K.). All the analyses were performed at 25 °C by resuspending the synthesized microparticles in distilled water.

Differential scanning calorimetry (DSC) analysis

Differential scanning calorimetry (DSC) experiments were performed on a NanoDSC, TA Instruments (New Castle, Delaware, U.S.A.). Isothermal mode was used to evaluate the heat release due to the breakdown of the PLGA shell or due to the dissolution of the protein structure of the PSI. The experiments were run at a fixed temperature of 4 °C maintained overnight for the PSI samples and over the weekend for the encapsulated PSI. Experimental setup and data collections were managed with the DSCRun software (TA Instruments).

Atomic force microscopy (AFM)

The synthesized microparticles were analyzed and characterized using the atomic force microscope (NT-MDT Solver Pro microscope, NT-MDT Spectrum Instruments, Zelenograd, Moscow, RU), with a single-crystal silicon−antimony-doped probe and a gold-coated base (NSG-01 from NTMDT). To reduce nonlinearity and hysteresis in the measurements, prior to the AFM analyses the microscope was calibrated by a calibration grid (TGQ1 from NT-MDT). The analyses were performed using the tapping mode where the cantilever is driven to oscillate vertically near its resonance frequency. The lyophilized sample was resuspended in Milli-Q water, deposited on a mica substrate, and dried under a flux of argon. All the data were collected using the software Nova (NT-MDT). The resolution of the images acquired was 15 nm.

P700 activity

PSI photochemical activity was measured following the kinetics of P700 oxidation. In particular, P700 oxidation upon actinic light illumination was analyzed measuring pump−probe transient absorption at 705 nm as previously described, using a JTS 10-LED pump−probe spectrometer (Bio-Logic SAS, Claix, France) [438]. P700 oxidation kinetics were measured on PSI complexes in detergent (0.5 M sucrose, Hepes 20 mM pH 7.5, and 0.03% dodecyl β-Dmaltoside) or in MPs (resuspended in water) at a chlorophyll concentration of 20 µg/mL applying an actinic orange light at 940 $\mu mol \cdot m^{-2} \cdot s^{-1}$. In the specific cases described in the text, electron donor and acceptor molecules (ascorbate and methyl-viologen respectively) were added to the MPs at a concentration of 1 mM. Ascorbate was used as electron donor because of its

slower rate of P700+ reduction compared to electron transfer to methyl-viologen or charge recombination: in this way, the extent of P700+ was determined by the efficiency of PSI to donate electron to acceptors.

Fluorescence lifetime measurements

Time-resolved fluorescence measurements were performed using a femtosecond laser excitation at 440 nm and a streak camera detection system, as reported in [228]. Briefly, laser pulsed at 440 nm operating at 80 MHz with temporal and spectral bandwidths of 140 fs and 5 nm, respectively, were focused onto the sample, maintaining a low laser power intensity (50 µW, 100 µm spot diameter). The samples were kept at a constant temperature of 11 °C by a temperature-controlled cuvette cooled by a Peltier system. The resulting collected emission was analyzed by a spectrograph (Princeton Instruments Acton SP2300) coupled to a streak camera (Hamamatsu C5680) equipped with a synchroscan voltage sweep module with spectral and temporal resolutions of ~1 nm and ~3 ps, respectively. Temporal broadening of the pump pulses caused by dispersive elements was confirmed to be well below the response time of the detection system. Fluorescence decay maps were then integrated in the 0−1800 ps time range in order to obtain the integrated spectra and in the 600−800 nm wavelength range for determining the integrated decay kinetics. Integrated decay kinetics were fitted with two (PSI in MPs) or three (PSI in detergent) exponential forms, whose amplitudes (A_x) and decay constants (τ_x) were used to calculate the average fluorescence decay, τ_{AV} as $\tau_{AV}=\Sigma\delta_x * \tau_x/\Sigma A_x$. In the case of PSI in detergent, the long decaying component with time constant in the ns time range was not considered for τ_{AV} calculation, as previously reported, being related to free chlorophylls or antenna proteins in the PSI sample. Photochemical efficiency of PSI was calculated from τ_{AV} as reported in [546].

PSI stability

PSI stability was measured in terms of maximum P700 oxidation level during high light (1500 µmol m^{-2} s^{-1}) exposure for several days. PSI in detergent or in MPs were kept at room temperature in agitation exposed to LED white light (1500 µmol m^{-2} s^{-1}) for up to 34 days. No volume loss was observed during treatment. P700 photochemical activity was measured as described above in the presence of ascorbate and methyl-viologen (1 mM) added fresh for each measurement.

Pigments analysis

The composition of the pigments present in PSI samples was analyzed after extraction with acetone 80%; microparticles were lyophilized and then resuspended in 400 µL of DMSO (DMSO temperature was about 65 °C) to extract the pigments of interest. The extracts were analyzed by RP-HPLC as described in [231].

Statistical analysis

All the synthesis and measurements reported in this work were performed in three independent replicates with three technical replicates each. Error bars are reported as standard deviation.

Supporting information

	Chl	Chla/b	Chla	Chlb	Chl/car	Neo	Viola	Antera	Lute	Zea	βcar
PSI in detergent	156.00	6.44	135.05	20.95	5.12	1.22	4.76	0.00	9.25	0.00	15.24
s.d.	*0.00*	*0.01*	*0.03*	*0.03*	*0.07*	*0.31*	*0.16*	*0.00*	*0.10*	*0.00*	*0.98*
PSI in PLGA MPs	156.00	6.47	135.09	20.91	6.27	0.52	4.18	0.00	7.52	0.00	12.68
s.d.	*0.00*	*0.39*	*1.07*	*1.07*	*0.31*	*0.17*	*0.13*	*0.00*	*0.48*	*0.00*	*0.79*

Table S App.1 *HPLC analysis of PSI in detergent and in PLGA MPs. Summary table of HPLC analysis conducted on PSI complexes in detergent and encapsulated in PLGA microparticles (MPs). The names of the pigments extracted are in their short form: Chlorophylls (Chl); Carotenoid (Car); Neoxanthin (Neo); Violaxanthin (Viola); Anteraxanthin (Antera); Lutein (Lute); Zeaxanthin (Zea); β-Carotene (βCar). Standard deviation (s.d.) are reported for each value.*

	PSI in detergent	Empty PLGA microparticles	PSI in PLGA microparticles	Empty CS microparticles	PSI in CS microparticles
Z-Average values (nm)	54.87 ±10.0	402.4 ±97.7	1698 ±66.6	196.20 ±59.0	539.5 ±70.4
PDI (× 10–3)	55 ±9	16 ±6	542 ±23	212 ±2	518 ±7
Superficial charge (mV)	-9.01 ±3.2	-0.327 ±2.7	-5.48 ±4.9	+25.3 ±4.7	+16 ±3.5

Table S App.2 *Average value, polydispersity index (PDI) and superficial charge of PLGA and chitosan microparticles. Data reported in the table were obtained by Dynamic Light Scattering measurements. Error range are reported as standard deviation. CS: chitosan*

	PSI in PLGA MPs	PSI in detergent
A_1 (%)	41.4%	15.3%
τ_1 (ps)	9.0	9.2
A_2 (%)	58.6%	81.3%
τ_2 (ps)	47.3	58.1
A_3 (%)	/	3.4%
τ_3 (ps)	/	1000.0
τ_{AVG} (ps)	31.5	48.7
Φ_{PSI}	99.1%	98.5%

Table S App.3 *Fitting analysis of florescence decay integrated kinetics. Fluorescence decay kinetics reported in Fig. 4 were analysed by exponential fitting, two exponential functions were sufficient for best fit in the case of PSI in PLGA MPS, while three exponentials were required in the case of PSI in detergent.* τ_{AVG} *was calculated as* $\tau_{AV} = \Sigma A_x * \tau_x / \Sigma A_x$ *. The long component in the ns range obtained in the case of PSI in detergent was not used for* τ_{AVG} *calculation, as previously reported, being related to free chlorophyll or antenna proteins in the sample. The photochemical efficiency of PSI (ΦPSI) was calculated from* τ_{AVG} *as described in Galka et al, Plant Cell, Vol. 24: 2963–2978, 2012.*

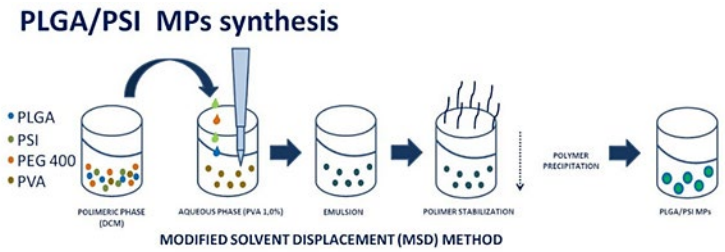

Figure S App.1 *PSI encapsulation in PLGA MPs. The modified Solvent Displacement Method is represented.*

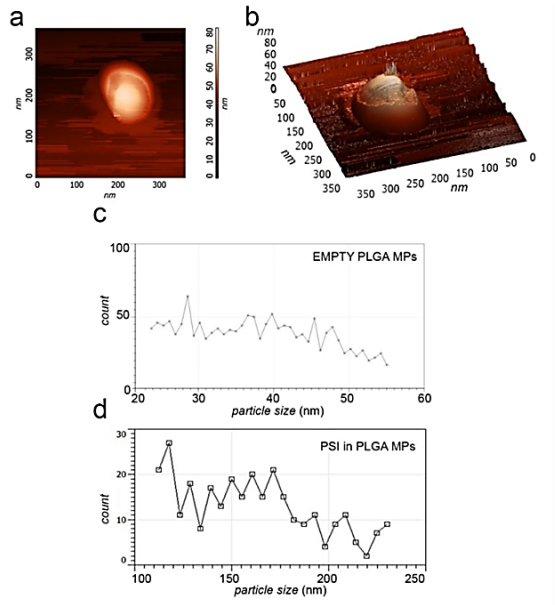

Figure S App.2 *Atomic Force Microscopy (AFM) observation of PLGA empty microparticles and particle size distribution. PLGA MPs visualized in semi-contact (A) and in 3D mode (B). The images have been acquired in dry mode. The images acquired were then used to determine the distribution of the particles size using Gwyddion software as reported in (C) and (D) for empty PLGA MPs and PLGA MPs containing PSI respectively.*

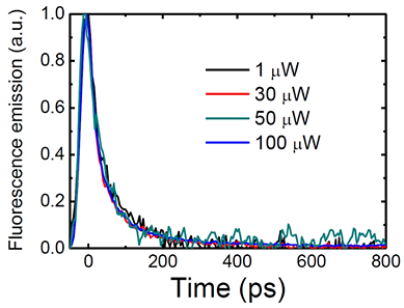

Figure S App.3 *Power dependency of fluorescence kinetics of PSI in PLGA MPs. In order to evaluate possible effects of annihilation in fluorescence decay kinetics of PSI in PLGA MPs, time resolved fluorescence was measured at different laser power intensities.*

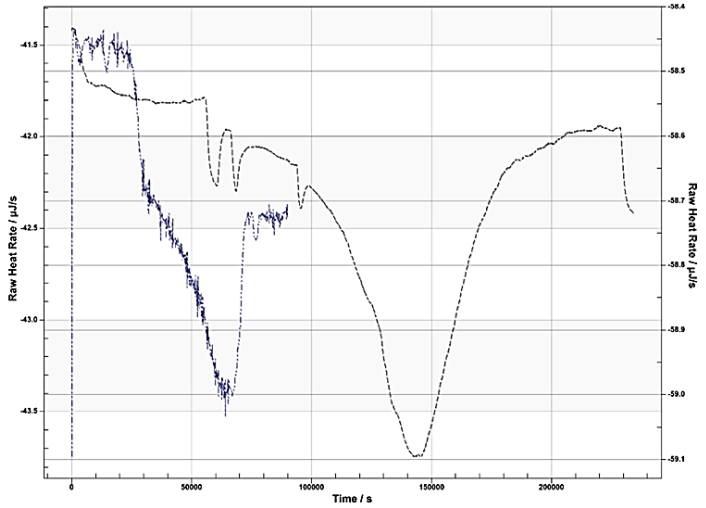

Figure S App.4 *Isothermal DSC analysis. Experiment temperature: 4°C. The blue line represents the PSI in buffer; the grey line represents the PSI in PLGA microparticles.*

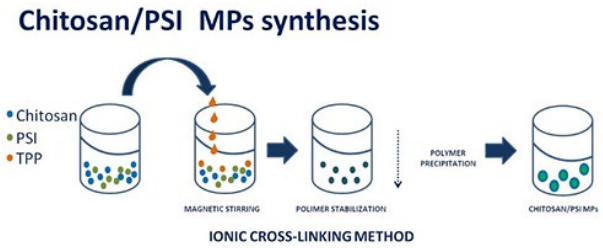

Figure S App.5 **PSI encapsulation in chitosan MPs.** The method for PSI encapsulation in chitosan (CS) microparticles is represented.

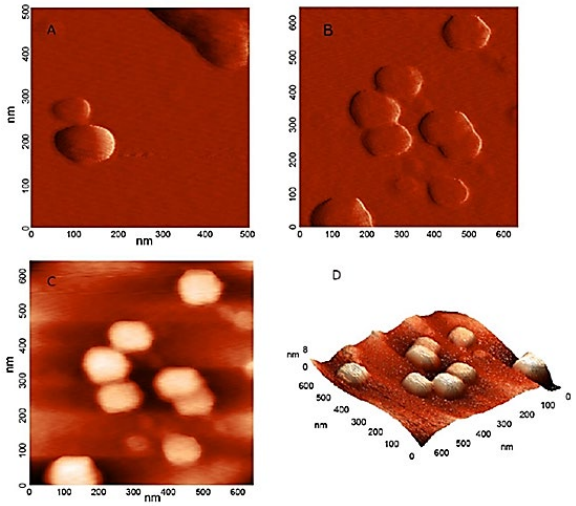

Figure S App.6 *Atomic Force Microscopy (AFM) observation of PSI in chitosan microparticles. PSI chitosan MPs visualized in three different modes: (A, B) Error-mode; (C) Semi-contact; (D) 3D. The images have been acquired in dry mode*

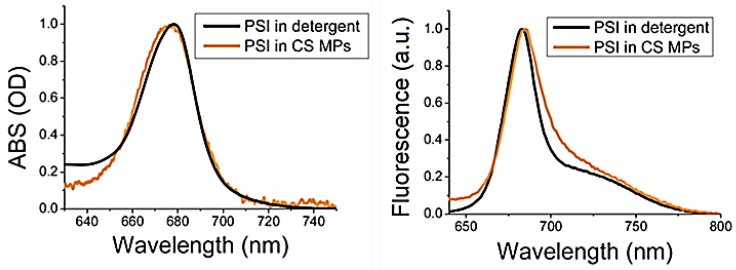

Figure S App.7 *Absorption and fluorescence emission spectra of PSI in detergent and in chitosan MPs. (A) Absorption spectra of isolated PSI in detergent solution (black) or in chitosan (CS) MPs (orange). (B) Fluorescence emission spectra of PSI in detergent and in chitosan MPs upon excitation at 440 nm (similar results were obtained upon excitation at 475 or 500 nm).*

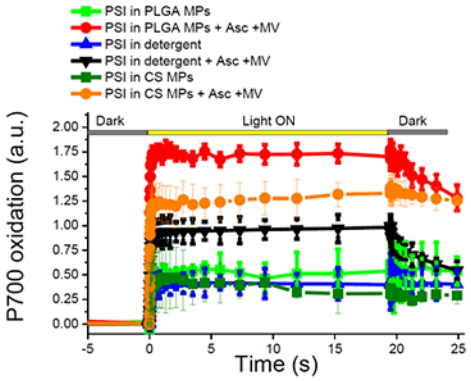

Figure S App.8 *Photochemical activity of PSI in detergent vs. PLGA or chitosan microparticles. Light dependent P700 oxidation of PSI in detergent or in PLGA or chitosan (CS) MPs were measured as transient absorption at 705 nm. Ascorbate (Asc) and Methyl-viologen (MV) were added where indicated as electron donor and acceptor respectively. Orange actinic light at 940 µmol $m^{-2}s^{-1}$ were used to induce P700 oxidation.*

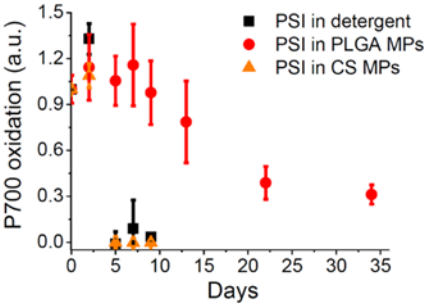

Figure S App. 9 *Stability of PSI to light exposure. Maximum P700 activity of PSI in detergent or in PLGA or chitosan (CS) measured at different time (days) of exposure to 1500 µmol $m^{-2}s^{-1}$.*

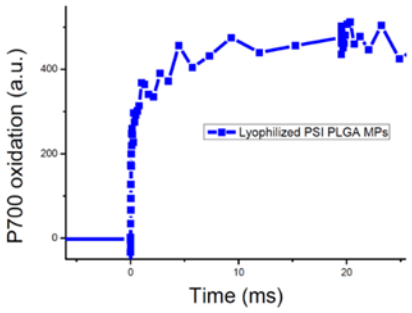

Figure S App.10 *P700 oxidation of lyophilized microparticles containing Photosystem I. P700 oxidation kinetic was measured depositing the lyophilized MPs on a 1mm quartz cuvette.*

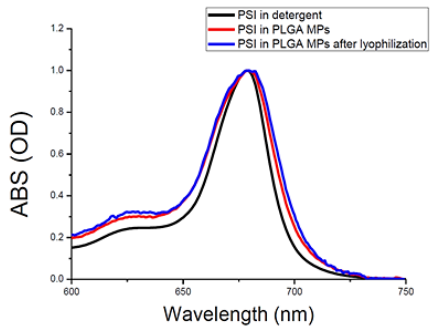

Figure S App.11 *Absorption spectrum of PSI microparticles before and after lyophilization. Absorption spectra of PSI in MPs are reported after subtraction of the scattering obtained by measuring the scattering traces of empty MPs.*

Bibliography

1 Stroebel, D., Choquet, Y., Popot, J. L. & Picot, D. An atypical haem in the cytochrome b(6)f complex. *Nature* **426**, 413-418, doi:10.1038/nature02155 (2003).

2 Barber, J. Membrane surface charges and potentials in relation to photosynthesis. *Biochim Biophys Acta* **594**, 253-308, doi:10.1016/0304-4173(80)90003-8 (1980).

3 Hill, R. & Bendall, F. A. Y. Function of the Two Cytochrome Components in Chloroplasts: A Working Hypothesis. *Nature* **186**, 136-137, doi:10.1038/186136a0 (1960).

4 McCarty, R. E., Evron, Y. & Johnson, E. A. THE CHLOROPLAST ATP SYNTHASE: A Rotary Enzyme? *Annual review of plant physiology and plant molecular biology* **51**, 83-109, doi:10.1146/annurev.arplant.51.1.83 (2000).

5 Harbinson, J. & Foyer, C. H. Relationships between the Efficiencies of Photosystems I and II and Stromal Redox State in CO(2)-Free Air : Evidence for Cyclic Electron Flow in Vivo. *Plant Physiol* **97**, 41-49, doi:10.1104/pp.97.1.41 (1991).

6 Bailey, S. & Grossman, A. Photoprotection in cyanobacteria: regulation of light harvesting. *Photochemistry and photobiology* **84**, 1410-1420, doi:10.1111/j.1751-1097.2008.00453.x (2008).

7 Benson, A. A. & Calvin, M. Carbon Dioxide Fixation By Green Plants. *Annual Review of Plant Physiology* **1**, 25-42, doi:10.1146/annurev.pp.01.060150.000325 (1950).

8 Chen, M. *et al.* A red-shifted chlorophyll. *Science* **329**, 1318-1319, doi:10.1126/science.1191127 (2010).

9 Von Wettstein, D., Gough, S. & Kannangara, C. G. Chlorophyll Biosynthesis. *Plant Cell* **7**, 1039-1057, doi:10.1105/tpc.7.7.1039 (1995).

10 Oster, U., Tanaka, R., Tanaka, A. & Rudiger, W. Cloning and functional expression of the gene encoding the key enzyme for chlorophyll b biosynthesis (CAO) from Arabidopsis thaliana. *Plant J* **21**, 305-310, doi:10.1046/j.1365-313x.2000.00672.x (2000).

11 Larkum, A. W. D. & Kühl, M. Chlorophyll d: The puzzle resolved. *Trends Plant Sci*, doi:10.1016/j.tplants.2005.06.005 (2005).

12 Willows, R. D., Li, Y., Scheer, H. & Chen, M. Structure of chlorophyll f. *Organic letters* **15**, 1588-1590, doi:10.1021/ol400327j (2013).

13 Dougherty, R. C., Strain, H. H., Svec, W. A., Uphaus, R. A. & Katz, J. J. The structure, properties, and distribution of chlorophyll c. *Journal of the American Chemical Society* **92**, 2826-2833, doi:10.1021/ja00712a037 (1970).

14 Blankenship, R. E. Molecular Mechanisms of Photosynthesis. *Molecular Mechanisms of Photosynthesis*, doi:10.1002/9780470758472 (2002).

15 Liu, Z. *et al.* Crystal structure of spinach major light-harvesting complex at 2.72 A resolution. *Nature* **428**, 287-292, doi:10.1038/nature02373 (2004).

16 Neilson, J. A. & Durnford, D. G. Structural and functional diversification of the light-harvesting complexes in photosynthetic eukaryotes. *Photosynth Res* **106**, 57-71, doi:10.1007/s11120-010-9576-2 (2010).

17 Ritz, T., Damjanovic, A., Schulten, K., Zhang, J. P. & Koyama, Y. Efficient light harvesting through carotenoids. *Photosynth Res* **66**, 125-144, doi:10.1023/A:1010750332320 (2000).

18 Harvaux, M. & Kloppstech, K. The protective functions of carotenoid and flavonoid pigments against excess visible radiation at chilling temperature investigated in Arabidopsis npq and tt mutants. *Planta* **213**, 953-966, doi:10.1007/s004250100572 (2001).

19 Plumley, F. G. & Schmidt, G. W. Reconstitution of chlorophyll a/b light-harvesting complexes: Xanthophyll-dependent assembly and energy transfer. *Proceedings of the National Academy of Sciences of the United States of America* **84**, 146-150, doi:10.1073/pnas.84.1.146 (1987).

20 Kull, O. & Pfander, H. in *Carotenoids: Isolation and Analysis* (ed S.Liaaen-Jensen G.Britton, and H.Pfander,eds.) Ch. 8, 295-317 (Birkauser Publishing, 1995).

21 Britton, G. Structure and properties of carotenoids in relation to function. *FASEB journal : official publication of the Federation of American Societies for Experimental Biology* **9**, 1551-1558 (1995).

22 Gastaldelli, M., Canino, G., Croce, R. & Bassi, R. Xanthophyll binding sites of the CP29 (Lhcb4) subunit of higher plant photosystem II investigated by domain swapping and mutation analysis. *The Journal of biological chemistry* **278**, 19190-19198, doi:10.1074/jbc.M212125200 (2003).

23 Caffarri, S., Croce, R., Breton, J. & Bassi, R. The major antenna complex of photosystem II has a xanthophyll binding site not involved in light harvesting. *The Journal of biological chemistry* **276**, 35924-35933, doi:10.1074/jbc.M105199200 (2001).

24 Ruban, A. V., Lee, P. J., Wentworth, M., Young, A. J. & Horton, P. Determination of the stoichiometry and strength of binding of xanthophylls to the photosystem II light harvesting complexes. *The Journal of biological chemistry* **274**, 10458-10465, doi:10.1074/jbc.274.15.10458 (1999).

25 Andersson, P. O., Gillbro, T., Ferguson, L. & Cogdell, R. J. Absorption Spectral Shifts of Carotenoids Related to Medium Polarizability. *Photochemistry and photobiology* **54**, 353-360, doi:DOI 10.1111/j.1751-1097.1991.tb02027.x (1991).

26 Dall'Osto, L., Caffarri, S. & Bassi, R. A mechanism of nonphotochemical energy dissipation, independent from PsbS, revealed by a conformational change in the antenna protein CP26. *Plant Cell* **17**, 1217-1232, doi:10.1105/tpc.104.030601 (2005).

27 Gilmore, A. M. & Yamamoto, H. Y. Dark induction of zeaxanthin-dependent nonphotochemical fluorescence quenching mediated by ATP. *Proceedings of the National Academy of Sciences of the United States of America* **89**, 1899-1903, doi:10.1073/pnas.89.5.1899 (1992).

28 Yamamoto, H. Y. & Kamite, L. The effects of dithiothreitol on violaxanthin de-epoxidation and absorbance changes in the 500-nm region. *Biochim Biophys Acta* **267**, 538-543, doi:10.1016/0005-2728(72)90182-x (1972).

29 Li, Z. *et al.* Evolution of an atypical de-epoxidase for photoprotection in the green lineage. *Nat Plants* **2**, 16140, doi:10.1038/nplants.2016.140 (2016).

30 Ballottari, M., Girardon, J., Dall'osto, L. & Bassi, R. Evolution and functional properties of photosystem II light harvesting complexes in eukaryotes. *Biochim Biophys Acta* **1817**, 143-157, doi:10.1016/j.bbabio.2011.06.005 (2012).

31 Nield, J., Funk, C. & Barber, J. Supermolecular structure of photosystem II and location of the PsbS protein. *Philosophical transactions of the Royal Society of London. Series B, Biological sciences* **355**, 1337-1344, doi:10.1098/rstb.2000.0695 (2000).

32 Wei, X. *et al.* Structure of spinach photosystem II-LHCII supercomplex at 3.2 A resolution. *Nature* **534**, 69-74, doi:10.1038/nature18020 (2016).

33 Shen, L. *et al.* Structure of a C2S2M2N2-type PSII-LHCII supercomplex from the green alga Chlamydomonas reinhardtii. *Proceedings of the National Academy of Sciences of the United States of America* **116**, 21246-21255, doi:10.1073/pnas.1912462116 (2019).

34 Suga, M. *et al.* Structure of the green algal photosystem I supercomplex with a decameric light-harvesting complex I. *Nat Plants* **5**, 626-636, doi:10.1038/s41477-019-0438-4 (2019).

35 Drop, B. *et al.* Photosystem I of Chlamydomonas reinhardtii contains nine light-harvesting complexes (Lhca) located on one side of the core. *The Journal of biological chemistry* **286**, 44878-44887, doi:10.1074/jbc.M111.301101 (2011).

36 Drop, B. *et al.* Light-harvesting complex II (LHCII) and its supramolecular organization in Chlamydomonas reinhardtii. *Biochim Biophys Acta* **1837**, 63-72, doi:10.1016/j.bbabio.2013.07.012 (2014).

37 Stauber, E. J., Busch, A., Naumann, B., Svatos, A. & Hippler, M. Proteotypic profiling of LHCI from Chlamydomonas reinhardtii provides new insights into structure and function of the complex. *Proteomics* **9**, 398-408, doi:10.1002/pmic.200700620 (2009).

38 Nelson, N. Plant photosystem I--the most efficient nano-photochemical machine. *Journal of nanoscience and nanotechnology* **9**, 1709-1713, doi:10.1166/jnn.2009.si01 (2009).

39 Scheller, H. V., Jensen, P. E., Haldrup, A., Lunde, C. & Knoetzel, J. Role of subunits in eukaryotic Photosystem I. *Biochim Biophys Acta* **1507**, 41-60, doi:10.1016/s0005-2728(01)00196-7 (2001).

40 Ben-Shem, A., Frolow, F. & Nelson, N. Crystal structure of plant photosystem I. *Nature* **426**, 630-635, doi:10.1038/nature02200 (2003).

41 Jansson, S. A guide to the Lhc genes and their relatives in Arabidopsis. *Trends Plant Sci* **4**, 236-240, doi:Doi 10.1016/S1360-1385(99)01419-3 (1999).

42 Mazor, Y., Borovikova, A., Caspy, I. & Nelson, N. Structure of the plant photosystem I supercomplex at 2.6 A resolution. *Nat Plants* **3**, 17014, doi:10.1038/nplants.2017.14 (2017).

43 Qin, X., Suga, M., Kuang, T. & Shen, J. R. Photosynthesis. Structural basis for energy transfer pathways in the plant PSI-LHCI supercomplex. *Science* **348**, 989-995, doi:10.1126/science.aab0214 (2015).

44 Su, X. *et al.* Antenna arrangement and energy transfer pathways of a green algal photosystem-I-LHCI supercomplex. *Nat Plants* **5**, 273-281, doi:10.1038/s41477-019-0380-5 (2019).

45 Gobets, B. & Van Grondelle, R. Energy transfer and trapping in photosystem I. *Biochimica et Biophysica Acta - Bioenergetics*, doi:10.1016/S0005-2728(01)00203-1 (2001).

46 Mozzo, M. *et al.* Functional analysis of Photosystem I light-harvesting complexes (Lhca) gene products of Chlamydomonas reinhardtii. *Biochim Biophys Acta* **1797**, 212-221, doi:10.1016/j.bbabio.2009.10.005 (2010).

47 Zouni, A. *et al.* Biochemical characterization and crystal structure of water oxidizing photosystem II from Synechococcus elongatus. *12th International congress on photosynthesis*, doi:10.1071/sa0403136 (2001).

48 Trumpower, B. L. The protonmotive Q cycle. Energy transduction by coupling of proton translocation to electron transfer by the cytochrome bc1 complex. *The Journal of biological chemistry* **265**, 11409-11412 (1990).

49 Boekema, E. J., Van Roon, H., Van Breemen, J. F. & Dekker, J. P. Supramolecular organization of photosystem II and its light-harvesting antenna in partially solubilized photosystem II membranes. *European journal of biochemistry* **266**, 444-452, doi:10.1046/j.1432-1327.1999.00876.x (1999).

50 Pagliano, C., Saracco, G. & Barber, J. Structural, functional and auxiliary proteins of photosystem II. *Photosynth Res* **116**, 167-188, doi:10.1007/s11120-013-9803-8 (2013).

51 Kouril, R., Dekker, J. P. & Boekema, E. J. Supramolecular organization of photosystem II in green plants. *Biochim Biophys Acta* **1817**, 2-12, doi:10.1016/j.bbabio.2011.05.024 (2012).

52 Su, X. *et al.* Structure and assembly mechanism of plant C2S2M2-type PSII-LHCII supercomplex. *Science* **357**, 815-820, doi:10.1126/science.aan0327 (2017).

53 Suga, M. *et al.* Native structure of photosystem II at 1.95 A resolution viewed by femtosecond X-ray pulses. *Nature* **517**, 99-103, doi:10.1038/nature13991 (2015).

54 Ago, H. *et al.* Novel Features of Eukaryotic Photosystem II Revealed by Its Crystal Structure Analysis from a Red Alga. *The Journal of biological chemistry* **291**, 5676-5687, doi:10.1074/jbc.M115.711689 (2016).

55 Umena, Y., Kawakami, K., Shen, J. R. & Kamiya, N. Crystal structure of oxygen-evolving photosystem II at a resolution of 1.9 A. *Nature* **473**, 55-60, doi:10.1038/nature09913 (2011).

56 Thornber, J. P. Comparison of a chlorophyll a-protein complex isolated from a blue-green alga with chlorophyll-protein complexes obtained from green bacteria and higher plants. *Biochimica et Biophysica Acta (BBA) - Bioenergetics* **172**, 230-241, doi:10.1016/0005-2728(69)90066-8 (1969).

57 Bassi, R., Giuffra, E., Croce, R., Dainese, P. & Bergantino, E. Biochemistry and molecular biology of pigment binding proteins. *Nato Adv Sci Inst Se* **287**, 41-63, doi:10.1007/978-1-4613-0409-8_4 (1996).

58 Bassi, R., Hoyer-Hansen, G., Barbato, R., Giacometti, G. M. & Simpson, D. J. Chlorophyll-proteins of the photosystem II antenna system. *The Journal of biological chemistry* **262**, 13333-13341 (1987).

59 Minagawa, J. & Takahashi, Y. Structure, function and assembly of Photosystem II and its light-harvesting proteins. *Photosynth Res* **82**, 241-263, doi:10.1007/s11120-004-2079-2 (2004).

60 van Oort, B. *et al.* Effect of antenna-depletion in Photosystem II on excitation energy transfer in Arabidopsis thaliana. *Biophysical journal* **98**, 922-931, doi:10.1016/j.bpj.2009.11.012 (2010).

61 Caffarri, S., Kouril, R., Kereiche, S., Boekema, E. J. & Croce, R. Functional architecture of higher plant photosystem II supercomplexes. *The EMBO journal* **28**, 3052-3063, doi:10.1038/emboj.2009.232 (2009).

62 de Bianchi, S. *et al.* *Arabidopsis* mutants deleted in the light-harvesting protein Lhcb4 have a disrupted Photosystem II macrostructure and are defective in photoprotection. *Plant Cell* **23**, 2659-2679 (2011).

63 Tokutsu, R., Iwai, M. & Minagawa, J. CP29, a monomeric light-harvesting complex II protein, is essential for state transitions in Chlamydomonas reinhardtii. *The Journal of biological chemistry* **284**, 7777-7782, doi:10.1074/jbc.M809360200 (2009).

64 Pan, X. *et al.* Structural insights into energy regulation of light-harvesting complex CP29 from spinach. *Nature structural & molecular biology* **18**, 309-315, doi:10.1038/nsmb.2008 (2011).

65 Pan, X., Liu, Z., Li, M. & Chang, W. Architecture and function of plant light-harvesting complexes II. *Current opinion in structural biology* **23**, 515-525, doi:10.1016/j.sbi.2013.04.004 (2013).

66 Ahn, T. K. *et al.* Architecture of a charge-transfer state regulating light harvesting in a plant antenna protein. *Science* **320**, 794-797, doi:10.1126/science.1154800 (2008).

67 Mozzo, M., Passarini, F., Bassi, R., van Amerongen, H. & Croce, R. Photoprotection in higher plants: the putative quenching site is conserved in all outer light-harvesting complexes of Photosystem II. *Biochim Biophys Acta* **1777**, 1263-1267, doi:10.1016/j.bbabio.2008.04.036 (2008).

68 Ruban, A. V. *et al.* Identification of a mechanism of photoprotective energy dissipation in higher plants. *Nature* **450**, 575-578, doi:10.1038/nature06262 (2007).

69 Klimmek, F., Sjodin, A., Noutsos, C., Leister, D. & Jansson, S. Abundantly and rarely expressed Lhc protein genes exhibit distinct regulation patterns in plants. *Plant Physiol* **140**, 793-804, doi:10.1104/pp.105.073304 (2006).

70 Croce, R., Canino, G., Ros, F. & Bassi, R. Chromophore organization in the higher-plant photosystem II antenna protein CP26. *Biochemistry* **41**, 7334-7343, doi:10.1021/bi0257437 (2002).

71 Dekker, J. P. & Boekema, E. J. Supramolecular organization of thylakoid membrane proteins in green plants. *Biochim Biophys Acta* **1706**, 12-39, doi:10.1016/j.bbabio.2004.09.009 (2005).

72 Kovacs, L. *et al.* Lack of the light-harvesting complex CP24 affects the structure and function of the grana membranes of higher plant chloroplasts. *Plant Cell* **18**, 3106-3120, doi:10.1105/tpc.106.045641 (2006).

73 Koziol, A. G. *et al.* Tracing the evolution of the light-harvesting antennae in chlorophyll a/b-containing organisms. *Plant Physiol* **143**, 1802-1816, doi:10.1104/pp.106.092536 (2007).

74 de Bianchi, S., Dall'Osto, L., Tognon, G., Morosinotto, T. & Bassi, R. Minor antenna proteins CP24 and CP26 affect the interactions between photosystem II subunits and the electron transport rate in grana membranes of Arabidopsis. *Plant Cell* **20**, 1012-1028, doi:10.1105/tpc.107.055749 (2008).

75 Alboresi, A., Caffarri, S., Nogue, F., Bassi, R. & Morosinotto, T. In silico and biochemical analysis of Physcomitrella patens photosynthetic antenna: identification of subunits which evolved upon land adaptation. *PloS one* **3**, e2033, doi:10.1371/journal.pone.0002033 (2008).

76 Morosinotto, T., Baronio, R. & Bassi, R. Dynamics of chromophore binding to Lhc proteins in vivo and in vitro during operation of the xanthophyll cycle. *The Journal of biological chemistry* **277**, 36913-36920, doi:10.1074/jbc.M205339200 (2002).

77 van Bezouwen, L. S. *et al.* Subunit and chlorophyll organization of the plant photosystem II supercomplex. *Nat Plants* **3**, 17080, doi:10.1038/nplants.2017.80 (2017).

78 Aro, E. M., Virgin, I. & Andersson, B. Photoinhibition of Photosystem II. Inactivation, protein damage and turnover. *BBA - Bioenergetics*, doi:10.1016/0005-2728(93)90134-2 (1993).

79 Tjus, S. E., Moller, B. L. & Scheller, H. V. Photosystem I is an early target of photoinhibition in barley illuminated at chilling temperatures. *Plant Physiology* **116**, 755-764 (1998).

80 Tjus, S. E., Scheller, H. V., Andersson, B. & Moller, B. L. Active oxygen produced during selective excitation of photosystem I is damaging not only to photosystem I, but also to photosystem II. *Plant Physiol* **125**, 2007-2015, doi:10.1104/pp.125.4.2007 (2001).

81 Knox, J. P. & Dodge, A. D. Singlet Oxygen and Plants. *Phytochemistry* **24**, 889-896, doi:Doi 10.1016/S0031-9422(00)83147-7 (1985).

82 Krieger-Liszkay, A. Singlet oxygen production in photosynthesis. *Journal of experimental botany* **56**, 337-346, doi:10.1093/jxb/erh237 (2005).

83 Tardy, F. & Havaux, M. Photosynthesis, chlorophyll fluorescence, light-harvesting system and photoinhibition resistance of a zeaxanthin-accumulating mutant of Arabidopsis thaliana. *Journal of photochemistry and photobiology. B, Biology* **34**, 87-94, doi:10.1016/1011-1344(95)07272-1 (1996).

84 Formaggio, E., Cinque, G. & Bassi, R. Functional architecture of the major light-harvesting complex from higher plants. *Journal of molecular biology* **314**, 1157-1166, doi:10.1006/jmbi.2000.5179 (2001).

85 Havaux, M. & Niyogi, K. K. The violaxanthin cycle protects plants from photooxidative damage by more than one mechanism. *Proceedings of the National Academy of Sciences of the United States of America* **96**, 8762-8767, doi:10.1073/pnas.96.15.8762 (1999).

86 Mellis, A. Photosystem-II damage and repair cycle in chloroplasts: What modulates the rate of photodamage in vivo? *Trends Plant Sci*, doi:10.1016/S1360-1385(99)01387-4 (1999).

87 Dau, H. Molecular Mechanisms and Quantitative Models of Variable Photosystem-Ii Fluorescence. *Photochemistry and photobiology* **60**, 1-23, doi:10.1111/j.1751-1097.1994.tb03937.x (1994).

88 Mehler, A. H. Studies on reactions of illuminated chloroplasts. *Archives of biochemistry and biophysics* **33**, 65-77, doi:10.1016/0003-9861(51)90082-3 (1951).

89 Papageorgiou, G. C. & Govindjee. in *Non-Photochemical Quenching and Energy Dissipation in Plants, Algae and Cyanobacteria* (eds Barbara Demmig-Adams, Gyozo Garab, William Adams Iii, & Govindjee) 1-44 (Springer Netherlands, 2014).

90 Horton, P. Nonphotochemical quenching of chlorophyll fluorescence. *Nato Adv Sci Inst Se* **287**, 99-111, doi:10.1007/978-1-4613-0409-8_8 (1996).

91 Genty, B., Briantais, J. M. & Baker, N. R. The Relationship between the Quantum Yield of Photosynthetic Electron-Transport and Quenching of Chlorophyll Fluorescence. *Biochimica Et Biophysica Acta* **990**, 87-92, doi:Doi 10.1016/S0304-4165(89)80016-9 (1989).

92 Muller, P., Li, X. P. & Niyogi, K. K. Non-photochemical quenching. A response to excess light energy. *Plant Physiol* **125**, 1558-1566, doi:10.1104/pp.125.4.1558 (2001).

93 Minagawa, J. State transitions--the molecular remodeling of photosynthetic supercomplexes that controls energy flow in the chloroplast. *Biochim Biophys Acta* **1807**, 897-905, doi:10.1016/j.bbabio.2010.11.005 (2011).

94 Nilkens, M. *et al.* Identification of a slowly inducible zeaxanthin-dependent component of non-photochemical quenching of chlorophyll fluorescence generated under steady-state conditions in Arabidopsis. *Biochim Biophys Acta* **1797**, 466-475, doi:10.1016/j.bbabio.2010.01.001 (2010).

95 Niyogi, K. K. Safety valves for photosynthesis. *Current opinion in plant biology* **3**, 455-460, doi:10.1016/s1369-5266(00)00113-8 (2000).

96 Shikanai, T., Munekage, Y., Shimizu, K., Endo, T. & Hashimoto, T. Identification and characterization of Arabidopsis mutants with reduced quenching of chlorophyll fluorescence. *Plant & cell physiology* **40**, 1134-1142, doi:10.1093/oxfordjournals.pcp.a029498 (1999).

97 Magdaong, N. C. M. & Blankenship, R. E. Photoprotective, excited-state quenching mechanisms in diverse photosynthetic organisms. *The Journal of biological chemistry* **293**, 5018-5025, doi:10.1074/jbc.TM117.000233 (2018).

98 Kramer, D. M., Sacksteder, C. A. & Cruz, J. A. How acidic is the lumen? *Photosynthesis Research* **60**, 151-163, doi:10.1023/a:1006212014787 (1999).

99 Virgin, I., Styring, S. & Andersson, B. Photosystem-Ii Disorganization and Manganese Release after Photoinhibition of Isolated Spinach Thylakoid Membranes. *FEBS letters* **233**, 408-412, doi:Doi 10.1016/0014-5793(88)80472-1 (1988).

100 Wilson, A. *et al.* A soluble carotenoid protein involved in phycobilisome-related energy dissipation in cyanobacteria. *Plant Cell* **18**, 992-1007, doi:10.1105/tpc.105.040121 (2006).

101 Peers, G. *et al.* An ancient light-harvesting protein is critical for the regulation of algal photosynthesis. *Nature* **462**, 518-521, doi:10.1038/nature08587 (2009).

102 Li, X. P. *et al.* A pigment-binding protein essential for regulation of photosynthetic light harvesting. *Nature* **403**, 391-395, doi:10.1038/35000131 (2000).

103 Demmig-Adams, B. Carotenoids and photoprotection in plants: A role for the xanthophyll zeaxanthin. *Biochimica et Biophysica Acta (BBA) - Bioenergetics* **1020**, 1-24, doi:10.1016/0005-2728(90)90088-l (1990).

104 Niyogi, K. K. PHOTOPROTECTION REVISITED: Genetic and Molecular Approaches. *Annual review of plant physiology and plant molecular biology* **50**, 333-359, doi:10.1146/annurev.arplant.50.1.333 (1999).

105 Niyogi, K. K. *et al.* Photoprotection in a zeaxanthin- and lutein-deficient double mutant of Arabidopsis. *Photosynth Res* **67**, 139-145, doi:10.1023/A:1010661102365 (2001).

106 Bonente, G. *et al.* Analysis of LhcSR3, a protein essential for feedback de-excitation in the green alga Chlamydomonas reinhardtii. *PLoS biology* **9**, e1000577, doi:10.1371/journal.pbio.1000577 (2011).

107 Engelken, J., Brinkmann, H. & Adamska, I. Taxonomic distribution and origins of the extended LHC (light-harvesting complex) antenna protein superfamily. *BMC evolutionary biology* **10**, 233, doi:10.1186/1471-2148-10-233 (2010).

108 Li, X. P. *et al.* Regulation of photosynthetic light harvesting involves intrathylakoid lumen pH sensing by the PsbS protein. *The Journal of biological chemistry* **279**, 22866-22874, doi:10.1074/jbc.M402461200 (2004).

109 Bonente, G. *et al.* The occurrence of the psbS gene product in Chlamydomonas reinhardtii and in other photosynthetic organisms and its correlation with energy quenching. *Photochemistry and photobiology* **84**, 1359-1370, doi:10.1111/j.1751-1097.2008.00456.x (2008).

110 Dominici, P. *et al.* Biochemical properties of the PsbS subunit of photosystem II either purified from chloroplast or recombinant. *The Journal of biological chemistry* **277**, 22750-22758, doi:10.1074/jbc.M200604200 (2002).

111 Fan, M. *et al.* Crystal structures of the PsbS protein essential for photoprotection in plants. *Nature structural & molecular biology* **22**, 729-735, doi:10.1038/nsmb.3068 (2015).

112 Betterle, N. *et al.* Light-induced dissociation of an antenna hetero-oligomer is needed for non-photochemical quenching induction. *The Journal of biological chemistry* **284**, 15255-15266, doi:10.1074/jbc.M808625200 (2009).

113 Johnson, M. P., Brain, A. P. & Ruban, A. V. Changes in thylakoid membrane thickness associated with the reorganization of photosystem II light harvesting complexes during photoprotective energy dissipation. *Plant signaling & behavior* **6**, 1386-1390, doi:10.4161/psb.6.9.16503 (2011).

114 Miloslavina, Y., de Bianchi, S., Dall'Osto, L., Bassi, R. & Holzwarth, A. R. Quenching in Arabidopsis thaliana mutants lacking monomeric antenna proteins of photosystem II. *The Journal of biological chemistry* **286**, 36830-36840, doi:10.1074/jbc.M111.273227 (2011).

115 Dall'Osto, L. *et al.* Two mechanisms for dissipation of excess light in monomeric and trimeric light-harvesting complexes. *Nat Plants* **3**, 17033, doi:10.1038/nplants.2017.33 (2017).

116 Tibiletti, T., Auroy, P., Peltier, G. & Caffarri, S. Chlamydomonas reinhardtii PsbS Protein Is Functional and Accumulates Rapidly and Transiently under High Light. *Plant Physiol* **171**, 2717-2730, doi:10.1104/pp.16.00572 (2016).

117 Alboresi, A., Gerotto, C., Giacometti, G. M., Bassi, R. & Morosinotto, T. Physcomitrella patens mutants affected on heat dissipation clarify the evolution of photoprotection mechanisms upon land colonization. *Proceedings of the National Academy of Sciences of the United States of America* **107**, 11128-11133, doi:10.1073/pnas.1002873107 (2010).

118 Merchant, S. S. *et al.* The Chlamydomonas genome reveals the evolution of key animal and plant functions. *Science* **318**, 245-250, doi:10.1126/science.1143609 (2007).

119 Zhu, S. H. & Green, B. R. Photoprotection in the diatom Thalassiosira pseudonana: role of LI818-like proteins in response to high light stress. *Biochim Biophys Acta* **1797**, 1449-1457, doi:10.1016/j.bbabio.2010.04.003 (2010).

120 Maruyama, S., Tokutsu, R. & Minagawa, J. Transcriptional regulation of the stress-responsive light harvesting complex genes in Chlamydomonas reinhardtii. *Plant & cell physiology* **55**, 1304-1310, doi:10.1093/pcp/pcu068 (2014).

121 Ballottari, M. *et al.* Identification of pH-sensing Sites in the Light Harvesting Complex Stress-related 3 Protein Essential for Triggering Non-photochemical Quenching in Chlamydomonas reinhardtii. *The Journal of biological chemistry* **291**, 7334-7346, doi:10.1074/jbc.M115.704601 (2016).

122 Liguori, N., Roy, L. M., Opacic, M., Durand, G. & Croce, R. Regulation of light harvesting in the green alga Chlamydomonas reinhardtii: the C-terminus of LHCSR is the knob of a dimmer switch. *Journal of the American Chemical Society* **135**, 18339-18342, doi:10.1021/ja4107463 (2013).

123 Tokutsu, R. & Minagawa, J. Energy-dissipative supercomplex of photosystem II associated with LHCSR3 in Chlamydomonas reinhardtii. *Proceedings of the National Academy of Sciences of the United States of America* **110**, 10016-10021, doi:10.1073/pnas.1222606110 (2013).

124 Elrad, D., Niyogi, K. K. & Grossman, A. R. A major light-harvesting polypeptide of photosystem II functions in thermal dissipation. *Plant Cell* **14**, 1801-1816, doi:10.1105/tpc.002154 (2002).

125 Ballottari, M., Dall'Osto, L., Morosinotto, T. & Bassi, R. Contrasting behavior of higher plant photosystem I and II antenna systems during acclimation. *The Journal of biological chemistry* **282**, 8947-8958, doi:10.1074/jbc.M606417200 (2007).

126 Bonente, G., Pippa, S., Castellano, S., Bassi, R. & Ballottari, M. Acclimation of Chlamydomonas reinhardtii to different growth irradiances. *The Journal of biological chemistry* **287**, 5833-5847, doi:10.1074/jbc.M111.304279 (2012).

127 Delosme, R., Olive, J. & Wollman, F. A. Changes in light energy distribution upon state transitions: An in vivo photoacoustic study of the wild type and photosynthesis mutants from Chlamydomonas reinhardtii. *Biochimica Et Biophysica Acta-Bioenergetics* **1273**, 150-158, doi:Doi 10.1016/0005-2728(95)00143-3 (1996).

128 Finazzi, G. The central role of the green alga Chlamydomonas reinhardtii in revealing the mechanism of state transitions. *Journal of experimental botany* **56**, 383-388, doi:10.1093/jxb/erh230 (2005).

129 Allen, J. F. Protein phosphorylation in regulation of photosynthesis. *Biochim Biophys Acta* **1098**, 275-335, doi:10.1016/s0005-2728(09)91014-3 (1992).

130 Tikkanen, M., Mekala, N. R. & Aro, E. M. Photosystem II photoinhibition-repair cycle protects Photosystem I from irreversible damage. *Biochim Biophys Acta* **1837**, 210-215, doi:10.1016/j.bbabio.2013.10.001 (2014).

131 Bennoun, P. The present model for chlororespiration. *Photosynth Res* **73**, 273-277, doi:10.1023/A:1020479920622 (2002).

132 Raghavendra, A. S. & Padmasree, K. Beneficial interactions of mitochondrial metabolism with photosynthetic carbon assimilation. *Trends Plant Sci* **8**, 546-553, doi:10.1016/j.tplants.2003.09.015 (2003).

133 Escoubas, J. M., Lomas, M., LaRoche, J. & Falkowski, P. G. Light intensity regulation of cab gene transcription is signaled by the redox state of the plastoquinone pool. *Proceedings of the National Academy of Sciences of the United States of America* **92**, 10237-10241, doi:10.1073/pnas.92.22.10237 (1995).

134 Foyer, C. H., Descourvieres, P. & Kunert, K. J. Protection against Oxygen Radicals - an Important Defense-Mechanism Studied in Transgenic Plants. *Plant Cell and Environment* **17**, 507-523, doi:DOI 10.1111/j.1365-3040.1994.tb00146.x (1994).

135 Dall'Osto, L. *et al.* Zeaxanthin protects plant photosynthesis by modulating chlorophyll triplet yield in specific light-harvesting antenna subunits. *The Journal of biological chemistry* **287**, 41820-41834, doi:10.1074/jbc.M112.405498 (2012).

136 Mathis, P., Butler, W. L. & Satoh, K. Carotenoid Triplet State and Chlorophyll Fluorescence Quenching in Chloroplasts and Subchloroplast Particles. *Photochemistry and photobiology* **30**, 603-614, doi:10.1111/j.1751-1097.1979.tb07187.x (1979).

137 El-Agamey, A. *et al.* Carotenoid radical chemistry and antioxidant/pro-oxidant properties. *Archives of biochemistry and biophysics* **430**, 37-48, doi:10.1016/j.abb.2004.03.007 (2004).

138 Niyogi, K. K., Grossman, A. R. & Bjorkman, O. Arabidopsis mutants define a central role for the xanthophyll cycle in the regulation of photosynthetic energy conversion. *Plant Cell* **10**, 1121-1134, doi:10.1105/tpc.10.7.1121 (1998).

139 Havaux, M., Eymery, F., Porfirova, S., Rey, P. & Dormann, P. Vitamin E protects against photoinhibition and photooxidative stress in Arabidopsis thaliana. *Plant Cell* **17**, 3451-3469, doi:10.1105/tpc.105.037036 (2005).

140 Muller-Moule, P., Havaux, M. & Niyogi, K. K. Zeaxanthin deficiency enhances the high light sensitivity of an ascorbate-deficient mutant of Arabidopsis. *Plant Physiol* **133**, 748-760, doi:10.1104/pp.103.026252 (2003).

141 Guiry, M. D. How Many Species of Algae Are There? *J Phycol* **48**, 1057-1063, doi:10.1111/j.1529-8817.2012.01222.x (2012).

142 Borowitzka, M. A. High-value products from microalgae—their development and commercialisation. *Journal of Applied Phycology* **25**, 743-756, doi:10.1007/s10811-013-9983-9 (2013).

143 Scranton, M. A., Ostrand, J. T., Fields, F. J. & Mayfield, S. P. Chlamydomonas as a model for biofuels and bio-products production. *Plant J* **82**, 523-531, doi:10.1111/tpj.12780 (2015).

144 Sutherland, D. L., Howard-Williams, C., Turnbull, M. H., Broady, P. A. & Craggs, R. J. Enhancing microalgal photosynthesis and productivity in wastewater treatment high rate algal ponds for biofuel production. *Bioresour Technol* **184**, 222-229, doi:10.1016/j.biortech.2014.10.074 (2015).

145 Rodolfi, L. *et al.* Microalgae for oil: strain selection, induction of lipid synthesis and outdoor mass cultivation in a low-cost photobioreactor. *Biotechnology and bioengineering* **102**, 100-112, doi:10.1002/bit.22033 (2009).

146 Macedo, I. C., Seabra, J. E. A. & Silva, J. E. A. R. Green house gases emissions in the production and use of ethanol from sugarcane in Brazil: The 2005/2006 averages and a prediction for 2020. *Biomass Bioenerg* **32**, 582-595, doi:10.1016/j.biombioe.2007.12.006 (2008).

147 Mitra, D., van Leeuwen, J. & Lamsal, B. Heterotrophic/mixotrophic cultivation of oleaginous Chlorella vulgaris on industrial co-products. *Algal Research-Biomass Biofuels and Bioproducts* **1**, 40-48, doi:10.1016/j.algal.2012.03.002 (2012).

148 Al-Dhabi, N. A. & Valan Arasu, M. Quantification of Phytochemicals from Commercial Spirulina Products and Their Antioxidant Activities. *Evidence-based complementary and alternative medicine : eCAM* **2016**, 7631864, doi:10.1155/2016/7631864 (2016).

149 Wu, Q. *et al.* The antioxidant, immunomodulatory, and anti-inflammatory activities of Spirulina: an overview. *Archives of toxicology* **90**, 1817-1840, doi:10.1007/s00204-016-1744-5 (2016).

150 Lupatini, A. L., Colla, L. M., Canan, C. & Colla, E. Potential application of microalga Spirulina platensis as a protein source. *Journal of the science of food and agriculture* **97**, 724-732, doi:10.1002/jsfa.7987 (2017).

151 Hynstova, V. *et al.* Separation, identification and quantification of carotenoids and chlorophylls in dietary supplements containing Chlorella vulgaris and Spirulina platensis using High Performance Thin Layer Chromatography. *Journal of pharmaceutical and biomedical analysis* **148**, 108-118, doi:10.1016/j.jpba.2017.09.018 (2018).

152 Li, T. *et al.* Regulation of starch and lipid accumulation in a microalga Chlorella sorokiniana. *Bioresour Technol* **180**, 250-257, doi:10.1016/j.biortech.2015.01.005 (2015).

153 Garcia, J. L., de Vicente, M. & Galan, B. Microalgae, old sustainable food and fashion nutraceuticals. *Microbial biotechnology* **10**, 1017-1024, doi:10.1111/1751-7915.12800 (2017).

154 Norambuena, F. *et al.* Algae in fish feed: performances and fatty acid metabolism in juvenile Atlantic Salmon. *PloS one* **10**, e0124042, doi:10.1371/journal.pone.0124042 (2015).

155 Madeira, M. S. *et al.* Microalgae as feed ingredients for livestock production and meat quality: A review. *Livestock Science* **205**, 111-121, doi:10.1016/j.livsci.2017.09.020 (2017).

156 Vilchez, C. *et al.* Marine carotenoids: biological functions and commercial applications. *Marine drugs* **9**, 319-333, doi:10.3390/md9030319 (2011).

157 Young, A. J. & Lowe, G. L. Carotenoids-Antioxidant Properties. *Antioxidants* **7**, doi:10.3390/antiox7020028 (2018).

158 Dufosse, L., Galaup, P., Yaron, A. & Arad, S. M. Microorganisms and microalgae as sources of pigments for food use: a scientific oddity or an industrial reality? *Trends Food Sci Tech* **16**, 389-406, doi:10.1016/j.tifs.2005.02.006 (2005).

159 Manayi, A. *et al.* Lutein and cataract: from bench to bedside. *Critical reviews in biotechnology* **36**, 829-839, doi:10.3109/07388551.2015.1049510 (2016).

160 Zhang, J., Sun, Z., Sun, P., Chen, T. & Chen, F. Microalgal carotenoids: beneficial effects and potential in human health. *Food & function* **5**, 413-425, doi:10.1039/c3fo60607d (2014).

161 Naguib, Y. M. Antioxidant activities of astaxanthin and related carotenoids. *Journal of agricultural and food chemistry* **48**, 1150-1154, doi:10.1021/jf991106k (2000).

162 Palozza, P. *et al.* Growth-inhibitory effects of the astaxanthin-rich alga Haematococcus pluvialis in human colon cancer cells. *Cancer letters* **283**, 108-117, doi:10.1016/j.canlet.2009.03.031 (2009).

163 Uchiyama, K. *et al.* Astaxanthin protects beta-cells against glucose toxicity in diabetic db/db mice. *Redox report : communications in free radical research* **7**, 290-293, doi:10.1179/135100002125000811 (2002).

164 Wu, H. *et al.* Astaxanthin as a Potential Neuroprotective Agent for Neurological Diseases. *Marine drugs* **13**, 5750-5766, doi:10.3390/md13095750 (2015).

165 Boussiba, S. & Vonshak, A. Astaxanthin Accumulation in the Green Alga Haematococcus pluvialis1. *Plant and Cell Physiology* **32**, 1077-1082, doi:10.1093/oxfordjournals.pcp.a078171 (1991).

166 Bubrick, P. Production of Astaxanthin from Haematococcus. *Bioresource Technology* **38**, 237-239, doi:Doi 10.1016/0960-8524(91)90161-C (1991).

167 Mascia, F. *et al.* Functional analysis of photosynthetic pigment binding complexes in the green alga Haematococcus pluvialis reveals distribution of astaxanthin in Photosystems. *Scientific reports* **7**, 16319, doi:10.1038/s41598-017-16641-6 (2017).

168 Kang, C. D. & Sim, S. J. Direct extraction of astaxanthin from Haematococcus culture using vegetable oils. *Biotechnol Lett* **30**, 441-444, doi:10.1007/s10529-007-9578-0 (2008).

169 Harada, H. *et al.* Construction of transplastomic lettuce (Lactuca sativa) dominantly producing astaxanthin fatty acid esters and detailed chemical analysis of generated carotenoids. *Transgenic research* **23**, 303-315, doi:10.1007/s11248-013-9750-3 (2014).

170 Ji, X. J., Ren, L. J. & Huang, H. Omega-3 Biotechnology: A Green and Sustainable Process for Omega-3 Fatty Acids Production. *Frontiers in bioengineering and biotechnology* **3**, 158, doi:10.3389/fbioe.2015.00158 (2015).

171 Ruxton, C. H., Reed, S. C., Simpson, M. J. & Millington, K. J. The health benefits of omega-3 polyunsaturated fatty acids: a review of the evidence. *Journal of human nutrition and dietetics : the official journal of the British Dietetic Association* **17**, 449-459, doi:10.1111/j.1365-277X.2004.00552.x (2004).

172 Zarate, R., El Jaber-Vazdekis, N., Tejera, N., Perez, J. A. & Rodriguez, C. Significance of long chain polyunsaturated fatty acids in human health. *Clinical and translational medicine* **6**, 25, doi:10.1186/s40169-017-0153-6 (2017).

173 Ma, X. N., Chen, T. P., Yang, B., Liu, J. & Chen, F. Lipid Production from Nannochloropsis. *Marine drugs* **14**, doi:10.3390/md14040061 (2016).

174 Shuba, E. S. & Kifle, D. Microalgae to biofuels: 'Promising' alternative and renewable energy, review. *Renewable and Sustainable Energy Reviews* **81**, 743-755, doi:10.1016/j.rser.2017.08.042 (2018).

175 Montingelli, M. E., Tedesco, S. & Olabi, A. G. Biogas production from algal biomass: A review. *Renewable and Sustainable Energy Reviews*, doi:10.1016/j.rser.2014.11.052 (2015).

176 Shokrkar, H., Ebrahimi, S. & Zamani, M. Bioethanol production from acidic and enzymatic hydrolysates of mixed microalgae culture. *Fuel* **200**, 380-386, doi:10.1016/j.fuel.2017.03.090 (2017).

177 Mohan, S. V., Devi, M. P., Subhash, G. V. & Chandra, R. Algae Oils as Fuels. *Biofuels from Algae*, 155-187, doi:10.1016/b978-0-444-59558-4.00008-5 (2014).

178 Benvenuti, G. *et al.* Towards microalgal triglycerides in the commodity markets. *Biotechnol Biofuels* **10**, 188, doi:10.1186/s13068-017-0873-2 (2017).

179 Dubini, A. & Ghirardi, M. L. Engineering photosynthetic organisms for the production of biohydrogen. *Photosynth Res* **123**, 241-253, doi:10.1007/s11120-014-9991-x (2015).

180 Khush, G. S. Green revolution: the way forward. *Nature reviews. Genetics* **2**, 815-822, doi:10.1038/35093585 (2001).

181 Beckmann, J. *et al.* Improvement of light to biomass conversion by de-regulation of light-harvesting protein translation in Chlamydomonas reinhardtii. *Journal of biotechnology* **142**, 70-77, doi:10.1016/j.jbiotec.2009.02.015 (2009).

182 Bonente, G. *et al.* Mutagenesis and phenotypic selection as a strategy toward domestication of Chlamydomonas reinhardtii strains for improved performance in photobioreactors. *Photosynth Res* **108**, 107-120, doi:10.1007/s11120-011-9660-2 (2011).

183 Mitra, M., Kirst, H., Dewez, D. & Melis, A. Modulation of the light-harvesting chlorophyll antenna size in Chlamydomonas reinhardtii by TLA1 gene over-expression and RNA interference. *Philosophical transactions of the Royal Society of London. Series B, Biological sciences* **367**, 3430-3443, doi:10.1098/rstb.2012.0229 (2012).

184 Perrine, Z., Negi, S. & Sayre, R. T. Optimization of photosynthetic light energy utilization by microalgae. *Algal Research-Biomass Biofuels and Bioproducts* **1**, 134-142, doi:10.1016/j.algal.2012.07.002 (2012).

185 Cazzaniga, S. *et al.* Domestication of the green alga Chlorella sorokiniana: reduction of antenna size improves light-use efficiency in a photobioreactor. *Biotechnol Biofuels* **7**, 157, doi:10.1186/s13068-014-0157-z (2014).

186 Perin, G. *et al.* Generation of random mutants to improve light-use efficiency of Nannochloropsis gaditana cultures for biofuel production. *Biotechnol Biofuels* **8**, 161, doi:10.1186/s13068-015-0337-5 (2015).

187 Glowacka, K. *et al.* Photosystem II Subunit S overexpression increases the efficiency of water use in a field-grown crop. *Nature communications* **9**, 868, doi:10.1038/s41467-018-03231-x (2018).

188 Kromdijk, J. *et al.* Improving photosynthesis and crop productivity by accelerating recovery from photoprotection. *Science* **354**, 857-861, doi:10.1126/science.aai8878 (2016).

189 Peers, G. Enhancement Of Biomass Production By Disruption Of Light Energy Dissipation Pathways. US patent US 8940508 B2 (2015).

190 Berteotti, S., Ballottari, M. & Bassi, R. Increased biomass productivity in green algae by tuning non-photochemical quenching. *Scientific reports* **6**, 21339, doi:10.1038/srep21339 (2016).

191 Cantrell, M. & Peers, G. A mutant of Chlamydomonas without LHCSR maintains high rates of photosynthesis, but has reduced cell division rates in sinusoidal light conditions. *PloS one* **12**, e0179395, doi:10.1371/journal.pone.0179395 (2017).

192 Wei, L., Wang, Q. T., Xin, Y., Lu, Y. D. & Xu, J. Enhancing photosynthetic biomass productivity of industrial oleaginous microalgae by overexpression of RuBisCO activase. *Algal Research-Biomass Biofuels and Bioproducts* **27**, 366-375, doi:10.1016/j.algal.2017.07.023 (2017).

193 Loera-Quezada, M. M. *et al.* A novel genetic engineering platform for the effective management of biological contaminants for the production of microalgae. *Plant biotechnology journal* **14**, 2066-2076, doi:10.1111/pbi.12564 (2016).

194 Griesbeck, C., Kobl, I. & Heitzer, M. Chlamydomonas reinhardtii: a protein expression system for pharmaceutical and biotechnological proteins. *Molecular biotechnology* **34**, 213-223, doi:10.1385/MB:34:2:213 (2006).

195 Lauersen, K. J. *et al.* Investigating the dynamics of recombinant protein secretion from a microalgal host. *Journal of biotechnology* **215**, 62-71, doi:10.1016/j.jbiotec.2015.05.001 (2015).

196 Doron, L., Segal, N. & Shapira, M. Transgene Expression in Microalgae-From Tools to Applications. *Front Plant Sci* **7**, 505, doi:10.3389/fpls.2016.00505 (2016).

197 Baier, T. *et al.* Engineered Fusion Proteins for Efficient Protein Secretion and Purification of a Human Growth Factor from the Green Microalga Chlamydomonas reinhardtii. *ACS synthetic biology* **7**, 2547-2557, doi:10.1021/acssynbio.8b00226 (2018).

198 Eichler-Stahlberg, A., Weisheit, W., Ruecker, O. & Heitzer, M. Strategies to facilitate transgene expression in Chlamydomonas reinhardtii. *Planta* **229**, 873-883, doi:10.1007/s00425-008-0879-x (2009).

199 Mergulhao, F. J., Summers, D. K. & Monteiro, G. A. Recombinant protein secretion in Escherichia coli. *Biotechnology advances* **23**, 177-202, doi:10.1016/j.biotechadv.2004.11.003 (2005).

200 Belgio, E. *et al.* Economic photoprotection in photosystem II that retains a complete light-harvesting system with slow energy traps. *Nature communications* **5**, 4433, doi:10.1038/ncomms5433 (2014).

201 Ruban, A. V., Johnson, M. P. & Duffy, C. D. The photoprotective molecular switch in the photosystem II antenna. *Biochim Biophys Acta* **1817**, 167-181, doi:10.1016/j.bbabio.2011.04.007 (2012).

202 Demmig-Adams, B. *et al.* Using chlorophyll fluorescence to assess the fraction of absorbed light allocated to thermal dissipation of excess excitation. *Physiol Plantarum* **98**, 253-264, doi:10.1034/j.1399-3054.1996.980206.x (1996).

203 Niyogi, K. K., Bjorkman, O. & Grossman, A. R. Chlamydomonas Xanthophyll Cycle Mutants Identified by Video Imaging of Chlorophyll Fluorescence Quenching. *Plant Cell* **9**, 1369-1380, doi:10.1105/tpc.9.8.1369 (1997).

204 Olaizola, M., La Roche, J., Kolber, Z. & Falkowski, P. G. Non-photochemical fluorescence quenching and the diadinoxanthin cycle in a marine diatom. *Photosynth Res* **41**, 357-370, doi:10.1007/BF00019413 (1994).

205 Ruban, A. *et al.* The super-excess energy dissipation in diatom algae: comparative analysis with higher plants. *Photosynth Res* **82**, 165-175, doi:10.1007/s11120-004-1456-1 (2004).

206 Demmig-Adams, B. & Adams, W. W., 3rd. Harvesting sunlight safely. *Nature* **403**, 371, 373-374, doi:10.1038/35000315 (2000).

207 Rees, D. *et al.* pH dependent chlorophyll fluorescence quenching in spinach thylakoids from light treated or dark adapted leaves. *Photosynth Res* **31**, 11-19, doi:10.1007/BF00049532 (1992).

208 Dinc, E. *et al.* LHCSR1 induces a fast and reversible pH-dependent fluorescence quenching in LHCII in Chlamydomonas reinhardtii cells. *Proceedings of the National Academy of Sciences of the United States of America* **113**, 7673-7678, doi:10.1073/pnas.1605380113 (2016).

209 Kim, E., Akimoto, S., Tokutsu, R., Yokono, M. & Minagawa, J. Fluorescence lifetime analyses reveal how the high light-responsive protein LHCSR3 transforms PSII light-harvesting complexes into an energy-dissipative state. *The Journal of biological chemistry* **292**, 18951-18960, doi:10.1074/jbc.M117.805192 (2017).

210 Kosuge, K. *et al.* LHCSR1-dependent fluorescence quenching is mediated by excitation energy transfer from LHCII to photosystem I in Chlamydomonas reinhardtii. *Proceedings of the National Academy of Sciences of the United States of America* **115**, 3722-3727, doi:10.1073/pnas.1720574115 (2018).

211 Correa-Galvis, V. *et al.* Photosystem II Subunit PsbS Is Involved in the Induction of LHCSR Protein-dependent Energy Dissipation in Chlamydomonas reinhardtii. *The Journal of biological chemistry* **291**, 17478-17487, doi:10.1074/jbc.M116.737312 (2016).

212 Liu, C. *et al.* Simultaneous refolding of denatured PsbS and reconstitution with LHCII into liposomes of thylakoid lipids. *Photosynth Res* **127**, 109-116, doi:10.1007/s11120-015-0176-z (2016).

213 Ware, M. A., Giovagnetti, V., Belgio, E. & Ruban, A. V. PsbS protein modulates non-photochemical chlorophyll fluorescence quenching in membranes depleted of photosystems. *Journal of photochemistry and photobiology. B, Biology* **152**, 301-307, doi:10.1016/j.jphotobiol.2015.07.016 (2015).

214 Bode, S. *et al.* On the regulation of photosynthesis by excitonic interactions between carotenoids and chlorophylls. *Proceedings of the National Academy of Sciences of the United States of America* **106**, 12311-12316, doi:10.1073/pnas.0903536106 (2009).

215 Liguori, N. *et al.* Different carotenoid conformations have distinct functions in light-harvesting regulation in plants. *Nature communications* **8**, 1994, doi:10.1038/s41467-017-02239-z (2017).

216 Muller, M. G. *et al.* Singlet energy dissipation in the photosystem II light-harvesting complex does not involve energy transfer to carotenoids. *Chemphyschem : a European journal of chemical physics and physical chemistry* **11**, 1289-1296, doi:10.1002/cphc.200900852 (2010).

217 Holt, N. E. *et al.* Carotenoid cation formation and the regulation of photosynthetic light harvesting. *Science* **307**, 433-436, doi:10.1126/science.1105833 (2005).

218 Liguori, N., Novoderezhkin, V., Roy, L. M., van Grondelle, R. & Croce, R. Excitation dynamics and structural implication of the stress-related complex LHCSR3 from the green alga Chlamydomonas reinhardtii. *Biochim Biophys Acta* **1857**, 1514-1523, doi:10.1016/j.bbabio.2016.04.285 (2016).

219 van Amerongen, H. & Croce, R. Light harvesting in photosystem II. *Photosynth Res* **116**, 251-263, doi:10.1007/s11120-013-9824-3 (2013).

220 Ballottari, M., Mozzo, M., Croce, R., Morosinotto, T. & Bassi, R. Occupancy and functional architecture of the pigment binding sites of photosystem II antenna complex Lhcb5. *The Journal of biological chemistry* **284**, 8103-8113, doi:10.1074/jbc.M808326200 (2009).

221 Bassi, R., Croce, R., Cugini, D. & Sandona, D. Mutational analysis of a higher plant antenna protein provides identification of chromophores bound into multiple sites. *Proceedings of the National Academy of Sciences of the United States of America* **96**, 10056-10061, doi:10.1073/pnas.96.18.10056 (1999).

222 Remelli, R., Varotto, C., Sandona, D., Croce, R. & Bassi, R. Chlorophyll binding to monomeric light-harvesting complex. A mutation analysis of chromophore-binding residues. *The Journal of biological chemistry* **274**, 33510-33521, doi:10.1074/jbc.274.47.33510 (1999).

223 Horton, P. *et al.* Control of the light-harvesting function of chloroplast membranes by aggregation of the LHCII chlorophyll-protein complex. *FEBS letters* **292**, 1-4, doi:10.1016/0014-5793(91)80819-o (1991).

224 Nyhus, K. J., Thiel, T. & Pakrasi, H. B. Targeted interruption of the psaA and psaB genes encoding the reaction-centre proteins of photosystem I in the filamentous cyanobacterium Anabaena variabilis ATCC 29413. *Molecular microbiology* **9**, 979-988, doi:10.1111/j.1365-2958.1993.tb01227.x (1993).

225 Girolomoni, L. *et al.* LHCSR3 is a nonphotochemical quencher of both photosystems in Chlamydomonas reinhardtii. *Proceedings of the National Academy of Sciences of the United States of America* **116**, 4212-4217, doi:10.1073/pnas.1809812116 (2019).

226 Ballottari, M., Girardon, J., Betterle, N., Morosinotto, T. & Bassi, R. Identification of the chromophores involved in aggregation-dependent energy quenching of the monomeric photosystem II antenna protein Lhcb5. *The Journal of biological chemistry* **285**, 28309-28321, doi:10.1074/jbc.M110.124115 (2010).

227 Ballottari, M., Mozzo, M., Girardon, J., Hienerwadel, R. & Bassi, R. Chlorophyll triplet quenching and photoprotection in the higher plant monomeric antenna protein Lhcb5. *The journal of physical chemistry. B* **117**, 11337-11348, doi:10.1021/jp402977y (2013).

228 Ballottari, M. *et al.* Regulation of photosystem I light harvesting by zeaxanthin. *Proceedings of the National Academy of Sciences of the United States of America* **111**, E2431-2438, doi:10.1073/pnas.1404377111 (2014).

229 Girolomoni, L. *et al.* The function of LHCBM4/6/8 antenna proteins in Chlamydomonas reinhardtii. *Journal of experimental botany* **68**, 627-641, doi:10.1093/jxb/erw462 (2017).

230 Semchonok, D. A. *et al.* Interaction between the photoprotective protein LHCSR3 and C2S2 Photosystem II supercomplex in Chlamydomonas reinhardtii. *Biochimica et biophysica acta. Bioenergetics* **1858**, 379-385, doi:10.1016/j.bbabio.2017.02.015 (2017).

231 Lagarde, D., Beuf, L. & Vermaas, W. Increased production of zeaxanthin and other pigments by application of genetic engineering techniques to Synechocystis sp. strain PCC 6803. *Appl Environ Microbiol* **66**, 64-72, doi:10.1128/aem.66.1.64-72.2000 (2000).

232 Schagger, H. & Vonjagow, G. Tricine Sodium Dodecyl-Sulfate Polyacrylamide-Gel Electrophoresis for the Separation of Proteins in the Range from 1-Kda to 100-Kda. *Anal Biochem* **166**, 368-379, doi:Doi 10.1016/0003-2697(87)90587-2 (1987).

233 Barber, J. & Andersson, B. Too much of a good thing: light can be bad for photosynthesis. *Trends in Biochemical Sciences*, doi:10.1016/0968-0004(92)90503-2 (1992).

234 Takahashi, S. & Murata, N. How do environmental stresses accelerate photoinhibition? *Trends Plant Sci* **13**, 178-182, doi:10.1016/j.tplants.2008.01.005 (2008).

235 Allahverdiyeva, Y., Suorsa, M., Tikkanen, M. & Aro, E. M. Photoprotection of photosystems in fluctuating light intensities. *Journal of experimental botany*, doi:10.1093/jxb/eru463 (2015).

236 Frank, H. A. *et al.* Photophysics of the carotenoids associated with the xanthophyll cycle in photosynthesis. *Photosynth Res* **41**, 389-395, doi:10.1007/BF02183041 (1994).

237 Polivka, T. & Frank, H. A. Molecular factors controlling photosynthetic light harvesting by carotenoids. *Accounts of chemical research* **43**, 1125-1134, doi:10.1021/ar100030m (2010).

238 Niedzwiedzki, D. M. *et al.* Carotenoid-induced non-photochemical quenching in the cyanobacterial chlorophyll synthase-HliC/D complex. *Biochim Biophys Acta* **1857**, 1430-1439, doi:10.1016/j.bbabio.2016.04.280 (2016).

239 Staleva, H. *et al.* Mechanism of photoprotection in the cyanobacterial ancestor of plant antenna proteins. *Nature chemical biology* **11**, 287-291, doi:10.1038/nchembio.1755 (2015).

240 Avenson, T. J. *et al.* Zeaxanthin radical cation formation in minor light-harvesting complexes of higher plant antenna. *The Journal of biological chemistry* **283**, 3550-3558, doi:10.1074/jbc.M705645200 (2008).

241 Li, Z. *et al.* Lutein accumulation in the absence of zeaxanthin restores nonphotochemical quenching in the Arabidopsis thaliana npq1 mutant. *Plant Cell* **21**, 1798-1812, doi:10.1105/tpc.109.066571 (2009).

242 Arnoux, P., Morosinotto, T., Saga, G., Bassi, R. & Pignol, D. A structural basis for the pH-dependent xanthophyll cycle in Arabidopsis thaliana. *Plant Cell* **21**, 2036-2044, doi:10.1105/tpc.109.068007 (2009).

243 Pinnola, A. *et al.* Electron transfer between carotenoid and chlorophyll contributes to quenching in the LHCSR1 protein from Physcomitrella patens. *Biochim Biophys Acta* **1857**, 1870-1878, doi:10.1016/j.bbabio.2016.09.001 (2016).

244 Niedzwiedzki, D. M., Sullivan, J. O., Polivka, T., Birge, R. R. & Frank, H. A. Femtosecond time-resolved transient absorption spectroscopy of xanthophylls. *The journal of physical chemistry. B* **110**, 22872-22885, doi:10.1021/jp0622738 (2006).

245 Mou, S. *et al.* Cloning and expression analysis of two different LhcSR genes involved in stress adaptation in an Antarctic microalga, Chlamydomonas sp. ICE-L. *Extremophiles : life under extreme conditions* **16**, 193-203, doi:10.1007/s00792-011-0419-7 (2012).

246 Park, S. *et al.* Chlorophyll-carotenoid excitation energy transfer and charge transfer in Nannochloropsis oceanica for the regulation of photosynthesis. *Proceedings of the National Academy of Sciences of the United States of America* **116**, 3385-3390, doi:10.1073/pnas.1819011116 (2019).

247 Amarnath, K., Zaks, J., Park, S. D., Niyogi, K. K. & Fleming, G. R. Fluorescence lifetime snapshots reveal two rapidly reversible mechanisms of photoprotection in live cells of Chlamydomonas reinhardtii. *Proceedings of the National Academy of Sciences of the United States of America* **109**, 8405-8410, doi:10.1073/pnas.1205303109 (2012).

248 Pinnola, A. *et al.* Functional modulation of LHCSR1 protein from Physcomitrella patens by zeaxanthin binding and low pH. *Scientific reports* **7**, 11158, doi:10.1038/s41598-017-11101-7 (2017).

249 van Oort, B. *et al.* Revisiting the Role of Xanthophylls in Nonphotochemical Quenching. *The journal of physical chemistry letters* **9**, 346-352, doi:10.1021/acs.jpclett.7b03049 (2018).

250 Polivka, T. & Sundstrom, V. Ultrafast dynamics of carotenoid excited States-from solution to natural and artificial systems. *Chemical reviews* **104**, 2021-2071, doi:10.1021/cr020674n (2004).

251 Snellenburg, J. J., Laptenok, S. P., Seger, R., Mullen, K. M. & van Stokkum, I. H. M. Glotaran: A Java-Based Graphical User Interface for the R Package TIMP. *J Stat Softw* **49**, 1-22, doi:Doi 10.18637/Jss.V049.I03 (2012).

252 Amarie, S. *et al.* Carotenoid radical cations as a probe for the molecular mechanism of nonphotochemical quenching in oxygenic photosynthesis. *The journal of physical chemistry. B* **111**, 3481-3487, doi:10.1021/jp066458q (2007).

253 Holleboom, C. P. *et al.* Carotenoid-chlorophyll coupling and fluorescence quenching in aggregated minor PSII proteins CP24 and CP29. *Photosynth Res* **124**, 171-180, doi:10.1007/s11120-015-0113-1 (2015).

254 Mazor, Y., Borovikova, A. & Nelson, N. The structure of plant photosystem I super-complex at 2.8 A resolution. *eLife* **4**, e07433, doi:10.7554/eLife.07433 (2015).

255 Petroutsos, D. *et al.* A blue-light photoreceptor mediates the feedback regulation of photosynthesis. *Nature* **537**, 563-566, doi:10.1038/nature19358 (2016).

256 Ware, M. A., Belgio, E. & Ruban, A. V. Comparison of the protective effectiveness of NPQ in Arabidopsis plants deficient in PsbS protein and zeaxanthin. *Journal of experimental botany* **66**, 1259-1270, doi:10.1093/jxb/eru477 (2015).

257 Bellafiore, S., Barneche, F., Peltier, G. & Rochaix, J. D. State transitions and light adaptation require chloroplast thylakoid protein kinase STN7. *Nature* **433**, 892-895, doi:10.1038/nature03286 (2005).

258 Depege, N., Bellafiore, S. & Rochaix, J. D. Role of chloroplast protein kinase Stt7 in LHCII phosphorylation and state transition in Chlamydomonas. *Science* **299**, 1572-1575, doi:10.1126/science.1081397 (2003).

259 Dumas, L. *et al.* A stromal region of cytochrome b6f subunit IV is involved in the activation of the Stt7 kinase in Chlamydomonas. *Proceedings of the National Academy of Sciences of the United States of America* **114**, 12063-12068, doi:10.1073/pnas.1713343114 (2017).

260 Lemeille, S. *et al.* Analysis of the chloroplast protein kinase Stt7 during state transitions. *PLoS biology* **7**, e45, doi:10.1371/journal.pbio.1000045 (2009).

261 Shapiguzov, A. *et al.* Activation of the Stt7/STN7 Kinase through Dynamic Interactions with the Cytochrome b6f Complex. *Plant Physiol* **171**, 82-92, doi:10.1104/pp.15.01893 (2016).

262 Allorent, G. *et al.* A dual strategy to cope with high light in Chlamydomonas reinhardtii. *Plant Cell* **25**, 545-557, doi:10.1105/tpc.112.108274 (2013).

263 Bergner, S. V. *et al.* STATE TRANSITION7-Dependent Phosphorylation Is Modulated by Changing Environmental Conditions, and Its Absence Triggers Remodeling of Photosynthetic Protein Complexes. *Plant Physiol* **168**, 615-634, doi:10.1104/pp.15.00072 (2015).

264 Roach, T. & Na, C. S. LHCSR3 affects de-coupling and re-coupling of LHCII to PSII during state transitions in Chlamydomonas reinhardtii. *Scientific reports* **7**, 43145, doi:10.1038/srep43145 (2017).

265 Xue, H. *et al.* PHOTOSYSTEM II SUBUNIT R is required for efficient binding of LIGHT-HARVESTING COMPLEX STRESS-RELATED PROTEIN3 to photosystem II-light-harvesting supercomplexes in Chlamydomonas reinhardtii. *Plant Physiol* **167**, 1566-1578, doi:10.1104/pp.15.00094 (2015).

266 Pinnola, A. *et al.* Light-Harvesting Complex Stress-Related Proteins Catalyze Excess Energy Dissipation in Both Photosystems of Physcomitrella patens. *Plant Cell* **27**, 3213-3227, doi:10.1105/tpc.15.00443 (2015).

267 Cho, F. & Govindjee. Low-temperature (4-77 degrees K) spectroscopy of Anacystis: temperature dependence of energy transfer efficiency. *Biochim Biophys Acta* **216**, 151-161, doi:10.1016/0005-2728(70)90167-2 (1970).

268 Lee, H., Bingham, S. E. & Webber, A. N. Function of 3' non-coding sequences and stop codon usage in expression of the chloroplast psaB gene in Chlamydomonas reinhardtii. *Plant molecular biology* **31**, 337-354, doi:10.1007/bf00021794 (1996).

269 Erickson, J. M. *et al.* Lack of the D2 protein in a Chlamydomonas reinhardtii psbD mutant affects photosystem II stability and D1 expression. *The EMBO journal* **5**, 1745-1754, doi:10.1002/j.1460-2075.1986.tb04422.x (1986).

270 Tanaka, A. *et al.* Chlorophyll a oxygenase (CAO) is involved in chlorophyll b formation from chlorophyll a. *Proceedings of the National Academy of Sciences of the United States of America* **95**, 12719-12723, doi:10.1073/pnas.95.21.12719 (1998).

271 Finazzi, G. & Rappaport, F. In vivo characterization of the electrochemical proton gradient generated in darkness in green algae and its kinetic effects on cytochrome b6f turnover. *Biochemistry* **37**, 9999-10005, doi:10.1021/bi980320j (1998).

272 van Stokkum, I. H., Larsen, D. S. & van Grondelle, R. Global and target analysis of time-resolved spectra. *Biochim Biophys Acta* **1657**, 82-104, doi:10.1016/j.bbabio.2004.04.011 (2004).

273 Chukhutsina, V. U., Buchel, C. & van Amerongen, H. Disentangling two non-photochemical quenching processes in Cyclotella meneghiniana by spectrally-resolved picosecond fluorescence at 77K. *Biochim Biophys Acta* **1837**, 899-907, doi:10.1016/j.bbabio.2014.02.021 (2014).

274 Wlodarczyk, L. M., Dinc, E., Croce, R. & Dekker, J. P. Excitation energy transfer in Chlamydomonas reinhardtii deficient in the PSI core or the PSII core under conditions mimicking state transitions. *Biochim Biophys Acta* **1857**, 625-633, doi:10.1016/j.bbabio.2016.03.002 (2016).

275 Wlodarczyk, L. M., Snellenburg, J. J., Dekker, J. P. & Stokkum, I. H. M. Development of fluorescence quenching in Chlamydomonas reinhardtii upon prolonged illumination at 77 K. *Photosynth Res* **137**, 503-513, doi:10.1007/s11120-018-0534-8 (2018).

276 Rochaix, J. D. Regulation and dynamics of the light-harvesting system. *Annual review of plant biology* **65**, 287-309, doi:10.1146/annurev-arplant-050213-040226 (2014).

277 Wijffels, R. H. & Barbosa, M. J. An outlook on microalgal biofuels. *Science* **329**, 796-799, doi:10.1126/science.1189003 (2010).

278 Lum, K. K., Kim, J. & Lei, X. G. Dual potential of microalgae as a sustainable biofuel feedstock and animal feed. *Journal of animal science and biotechnology* **4**, 53, doi:10.1186/2049-1891-4-53 (2013).
279 Liao, P. N., Holleboom, C. P., Wilk, L., Kuhlbrandt, W. & Walla, P. J. Correlation of Car S(1) --> Chl with Chl --> Car S(1) energy transfer supports the excitonic model in quenched light harvesting complex II. *The journal of physical chemistry. B* **114**, 15650-15655, doi:10.1021/jp1034163 (2010).
280 Ma, Y. Z., Holt, N. E., Li, X. P., Niyogi, K. K. & Fleming, G. R. Evidence for direct carotenoid involvement in the regulation of photosynthetic light harvesting. *Proceedings of the National Academy of Sciences of the United States of America* **100**, 4377-4382, doi:10.1073/pnas.0736959100 (2003).
281 Eskling, M., Arvidsson, P. O. & Akerlund, H. E. The xanthophyll cycle, its regulation and components. *Physiol Plantarum* **100**, 806-816, doi:DOI 10.1034/j.1399-3054.1997.1000407.x (1997).
282 Nicol, L., Nawrocki, W. J. & Croce, R. Disentangling the sites of non-photochemical quenching in vascular plants. *Nat Plants* **5**, 1177-1183, doi:10.1038/s41477-019-0526-5 (2019).
283 Jahns, P. & Holzwarth, A. R. The role of the xanthophyll cycle and of lutein in photoprotection of photosystem II. *Biochim Biophys Acta* **1817**, 182-193, doi:10.1016/j.bbabio.2011.04.012 (2012).
284 Sacharz, J., Giovagnetti, V., Ungerer, P., Mastroianni, G. & Ruban, A. V. The xanthophyll cycle affects reversible interactions between PsbS and light-harvesting complex II to control non-photochemical quenching. *Nat Plants* **3**, 16225, doi:10.1038/nplants.2016.225 (2017).
285 Pinnola, A. *et al.* Zeaxanthin binds to light-harvesting complex stress-related protein to enhance nonphotochemical quenching in Physcomitrella patens. *Plant Cell* **25**, 3519-3534, doi:10.1105/tpc.113.114538 (2013).
286 Tian, L. *et al.* pH dependence, kinetics and light-harvesting regulation of nonphotochemical quenching in Chlamydomonas. *Proceedings of the National Academy of Sciences of the United States of America* **116**, 8320-8325, doi:10.1073/pnas.1817796116 (2019).
287 Vidal-Meireles, A., Toth, D., Kovacs, L., Neupert, J. & Toth, S. Z. Ascorbate Deficiency Does Not Limit Nonphotochemical Quenching in Chlamydomonas reinhardtii. *Plant Physiol* **182**, 597-611, doi:10.1104/pp.19.00916 (2020).
288 Ishii, K. & Tahara, T. Two-dimensional fluorescence lifetime correlation spectroscopy. 1. Principle. *The journal of physical chemistry. B* **117**, 11414-11422, doi:10.1021/jp406861u (2013).
289 Baek, K. *et al.* DNA-free two-gene knockout in Chlamydomonas reinhardtii via CRISPR-Cas9 ribonucleoproteins. *Scientific reports* **6**, 30620, doi:10.1038/srep30620 (2016).
290 Kondo, T. *et al.* Microsecond and millisecond dynamics in the photosynthetic protein LHCSR1 observed by single-molecule correlation spectroscopy. *Proceedings of the National Academy of Sciences of the United States of America* **116**, 11247-11252, doi:10.1073/pnas.1821207116 (2019).
291 de la Cruz Valbuena, G. *et al.* Molecular Mechanisms of Nonphotochemical Quenching in the LHCSR3 Protein of Chlamydomonas reinhardtii. *The journal of physical chemistry letters* **10**, 2500-2505, doi:10.1021/acs.jpclett.9b01184 (2019).
292 Muh, F., Madjet Mel, A. & Renger, T. Structure-based identification of energy sinks in plant light-harvesting complex II. *The journal of physical chemistry. B* **114**, 13517-13535, doi:10.1021/jp106323e (2010).
293 Schlau-Cohen, G. S. *et al.* Pathways of energy flow in LHCII from two-dimensional electronic spectroscopy. *The journal of physical chemistry. B* **113**, 15352-15363, doi:10.1021/jp9066586 (2009).
294 Novoderezhkin, V., Marin, A. & van Grondelle, R. Intra- and inter-monomeric transfers in the light harvesting LHCII complex: the Redfield-Forster picture. *Physical chemistry chemical physics : PCCP* **13**, 17093-17103, doi:10.1039/c1cp21079c (2011).
295 Liguori, N., Periole, X., Marrink, S. J. & Croce, R. From light-harvesting to photoprotection: structural basis of the dynamic switch of the major antenna complex of plants (LHCII). *Scientific reports* **5**, 15661, doi:10.1038/srep15661 (2015).
296 Perozeni, F., Cazzaniga, S. & Ballottari, M. In vitro and in vivo investigation of chlorophyll binding sites involved in non-photochemical quenching in Chlamydomonas reinhardtii. *Plant, cell & environment* **42**, 2522-2535, doi:10.1111/pce.13566 (2019).
297 Di Valentin, M., Biasibetti, F., Ceola, S. & Carbonera, D. Identification of the sites of chlorophyll triplet quenching in relation to the structure of LHC-II from higher plants. Evidence from EPR spectroscopy. *The journal of physical chemistry. B* **113**, 13071-13078, doi:10.1021/jp904012j (2009).
298 Lampoura, S. S., Barzda, V., Owen, G. M., Hoff, A. J. & van Amerongen, H. Aggregation of LHCII Leads to a Redistribution of the Triplets over the Central Xanthophylls in LHCII. *Biochemistry* **41**, 9139-9144, doi:10.1021/bi025724x (2002).
299 Harris, E. H. & Harris. *Introduction to Chlamydomonas and its laboratory use*. Vol. 1 (Academic press, 2008).

300 Aitken, C. E., Marshall, R. A. & Puglisi, J. D. An oxygen scavenging system for improvement of dye stability in single-molecule fluorescence experiments. *Biophysical journal* **94**, 1826-1835, doi:10.1529/biophysj.107.117689 (2008).

301 Swoboda, M. *et al.* Enzymatic oxygen scavenging for photostability without pH drop in single-molecule experiments. *ACS nano* **6**, 6364-6369, doi:10.1021/nn301895c (2012).

302 Schlau-Cohen, G. S. *et al.* Single-Molecule Identification of Quenched and Unquenched States of LHCII. *The journal of physical chemistry letters* **6**, 860-867, doi:10.1021/acs.jpclett.5b00034 (2015).

303 Ishii, K. & Tahara, T. Extracting decay curves of the correlated fluorescence photons measured in fluorescence correlation spectroscopy. *Chem Phys Lett* **519-20**, 130-133, doi:10.1016/j.cplett.2011.11.024 (2012).

304 Ishii, K. & Tahara, T. Two-dimensional fluorescence lifetime correlation spectroscopy. 2. Application. *The journal of physical chemistry. B* **117**, 11423-11432, doi:10.1021/jp406864e (2013).

305 Wollman, F. A. State transitions reveal the dynamics and flexibility of the photosynthetic apparatus. *The EMBO journal* **20**, 3623-3630, doi:10.1093/emboj/20.14.3623 (2001).

306 Li, Z., Wakao, S., Fischer, B. B. & Niyogi, K. K. Sensing and responding to excess light. *Annual review of plant biology* **60**, 239-260, doi:10.1146/annurev.arplant.58.032806.103844 (2009).

307 Greer, D. H. & Thorpe, M. R. Leaf photosynthetic and solar-tracking responses of mallow, Malva parviflora, to photon flux density. *Plant physiology and biochemistry : PPB* **47**, 946-953, doi:10.1016/j.plaphy.2009.06.002 (2009).

308 Xu, P., Tian, L., Kloz, M. & Croce, R. Molecular insights into Zeaxanthin-dependent quenching in higher plants. *Scientific reports* **5**, 13679, doi:10.1038/srep13679 (2015).

309 Tian, L., Xu, P., Chukhutsina, V. U., Holzwarth, A. R. & Croce, R. Zeaxanthin-dependent nonphotochemical quenching does not occur in photosystem I in the higher plant Arabidopsis thaliana. *Proceedings of the National Academy of Sciences of the United States of America* **114**, 4828-4832, doi:10.1073/pnas.1621051114 (2017).

310 Rockholm, D. C. & Yamamoto, H. Y. Violaxanthin de-epoxidase. *Plant Physiol* **110**, 697-703, doi:10.1104/pp.110.2.697 (1996).

311 Betterle, N., Ballottari, M., Hienerwadel, R., Dall'Osto, L. & Bassi, R. Dynamics of zeaxanthin binding to the photosystem II monomeric antenna protein Lhcb6 (CP24) and modulation of its photoprotection properties. *Archives of biochemistry and biophysics* **504**, 67-77, doi:10.1016/j.abb.2010.05.016 (2010).

312 Gilmore, A. M. & Yamamoto, H. Y. Linear models relating xanthophylls and lumen acidity to non-photochemical fluorescence quenching. Evidence that antheraxanthin explains zeaxanthin-independent quenching. *Photosynth Res* **35**, 67-78, doi:10.1007/BF02185412 (1993).

313 Simionato, D. *et al.* Protein redox regulation in the thylakoid lumen: the importance of disulfide bonds for violaxanthin de-epoxidase. *FEBS letters* **589**, 919-923, doi:10.1016/j.febslet.2015.02.033 (2015).

314 Saga, G. *et al.* Mutation analysis of violaxanthin de-epoxidase identifies substrate-binding sites and residues involved in catalysis. *The Journal of biological chemistry* **285**, 23763-23770, doi:10.1074/jbc.M110.115097 (2010).

315 Emanuelsson, A., Eskling, M. & Akerlund, H. E. Chemical and mutational modification of histidines in violaxanthin de-epoxidase from Spinacia oleracea. *Physiol Plantarum* **119**, 97-104, doi:10.1034/j.1399-3054.2003.00151.x (2003).

316 Gisselsson, A., Szilágyi, A. & Åkerlund, H. E. Role of histidines in the binding of violaxanthin de-epoxidase to the thylakoid membrane as studied by site-directed mutagenesis. *Physiol Plantarum* **122**, 337-343, doi:10.1111/j.1399-3054.2004.00415.x (2004).

317 Fufezan, C., Simionato, D. & Morosinotto, T. Identification of key residues for pH dependent activation of violaxanthin de-epoxidase from Arabidopsis thaliana. *PloS one* **7**, e35669, doi:10.1371/journal.pone.0035669 (2012).

318 Quaas, T. *et al.* Non-photochemical quenching and xanthophyll cycle activities in six green algal species suggest mechanistic differences in the process of excess energy dissipation. *Journal of plant physiology* **172**, 92-103, doi:10.1016/j.jplph.2014.07.023 (2015).

319 Garcia-Mendoza, E. & Colombo-Pallotta, M. F. The giant kelp Macrocystis pyrifera presents a different nonphotochemical quenching control than higher plants. *The New phytologist* **173**, 526-536, doi:10.1111/j.1469-8137.2006.01951.x (2007).

320 Lavaud, J., Materna, A. C., Sturm, S., Vugrinec, S. & Kroth, P. G. Silencing of the violaxanthin de-epoxidase gene in the diatom Phaeodactylum tricornutum reduces diatoxanthin synthesis and non-photochemical quenching. *PloS one* **7**, e36806, doi:10.1371/journal.pone.0036806 (2012).

321 Chukhutsina, V. U., Fristedt, R., Morosinotto, T. & Croce, R. Photoprotection strategies of the alga Nannochloropsis gaditana. *Biochimica et biophysica acta. Bioenergetics* **1858**, 544-552, doi:10.1016/j.bbabio.2017.05.003 (2017).

322 Kana, R. *et al.* Violaxanthin inhibits nonphotochemical quenching in light-harvesting antenna of Chromera velia. *FEBS letters* **590**, 1076-1085, doi:10.1002/1873-3468.12130 (2016).

323 Bertrand, M. Carotenoid biosynthesis in diatoms. *Photosynth Res* **106**, 89-102, doi:10.1007/s11120-010-9589-x (2010).

324 Roth, M. S. *et al.* Chromosome-level genome assembly and transcriptome of the green alga Chromochloris zofingiensis illuminates astaxanthin production. *Proceedings of the National Academy of Sciences of the United States of America* **114**, E4296-E4305, doi:10.1073/pnas.1619928114 (2017).

325 Cecchin, M. *et al.* Chlorella vulgaris genome assembly and annotation reveals the molecular basis for metabolic acclimation to high light conditions. *Plant J* **100**, 1289-1305, doi:10.1111/tpj.14508 (2019).

326 Lowrey, J., Brooks, M. S. & McGinn, P. J. Heterotrophic and mixotrophic cultivation of microalgae for biodiesel production in agricultural wastewaters and associated challenges—a critical review. *Journal of Applied Phycology* **27**, 1485-1498, doi:10.1007/s10811-014-0459-3 (2015).

327 Zuniga, C. *et al.* Genome-Scale Metabolic Model for the Green Alga Chlorella vulgaris UTEX 395 Accurately Predicts Phenotypes under Autotrophic, Heterotrophic, and Mixotrophic Growth Conditions. *Plant Physiol* **172**, 589-602, doi:10.1104/pp.16.00593 (2016).

328 Sarayloo, E. *et al.* Enhancement of the lipid productivity and fatty acid methyl ester profile of Chlorella vulgaris by two rounds of mutagenesis. *Bioresour Technol* **250**, 764-769, doi:10.1016/j.biortech.2017.11.105 (2018).

329 Guarnieri, M. T. *et al.* Genome Sequence of the Oleaginous Green Alga, Chlorella vulgaris UTEX 395. *Frontiers in bioengineering and biotechnology* **6**, 37, doi:10.3389/fbioe.2018.00037 (2018).

330 Treves, H. *et al.* A newly isolated Chlorella sp. from desert sand crusts exhibits a unique resistance to excess light intensity. *FEMS microbiology ecology* **86**, 373-380, doi:10.1111/1574-6941.12162 (2013).

331 Treves, H. *et al.* The mechanisms whereby the green alga Chlorella ohadii, isolated from desert soil crust, exhibits unparalleled photodamage resistance. *The New phytologist* **210**, 1229-1243, doi:10.1111/nph.13870 (2016).

332 Dall'Osto, L. *et al.* Combined resistance to oxidative stress and reduced antenna size enhance light-to-biomass conversion efficiency in Chlorella vulgaris cultures. *Biotechnol Biofuels* **12**, 221, doi:10.1186/s13068-019-1566-9 (2019).

333 Adams, W. W., Demmig-Adams, B. & Winter, K. Relative contributions of zeaxanthin-related and zeaxanthin-unrelated types of ;high-energy-state' quenching of chlorophyll fluorescence in spinach leaves exposed to various environmental conditions. *Plant Physiol* **92**, 302-309, doi:10.1104/pp.92.2.302 (1990).

334 Goss, R., Lepetit, B. & Wilhelm, C. Evidence for a rebinding of antheraxanthin to the light-harvesting complex during the epoxidation reaction of the violaxanthin cycle. *Journal of plant physiology* **163**, 585-590, doi:10.1016/j.jplph.2005.07.009 (2006).

335 Neubauer, C. Multiple Effects of Dithiothreitol on Nonphotochemical Fluorescence Quenching in Intact Chloroplasts (Influence on Violaxanthin De-epoxidase and Ascorbate Peroxidase Activity). *Plant Physiol* **103**, 575-583, doi:10.1104/pp.103.2.575 (1993).

336 Dreyfuss, B. W. & Thornber, J. P. Organization of the Light-Harvesting Complex of Photosystem I and Its Assembly during Plastid Development. *Plant Physiol* **106**, 841-848, doi:10.1104/pp.106.3.841 (1994).

337 Le Quiniou, C. *et al.* PSI-LHCI of Chlamydomonas reinhardtii: Increasing the absorption cross section without losing efficiency. *Biochim Biophys Acta* **1847**, 458-467, doi:10.1016/j.bbabio.2015.02.001 (2015).

338 Liang, Y., Sarkany, N. & Cui, Y. Biomass and lipid productivities of Chlorella vulgaris under autotrophic, heterotrophic and mixotrophic growth conditions. *Biotechnol Lett* **31**, 1043-1049, doi:10.1007/s10529-009-9975-7 (2009).

339 Du, Z. *et al.* Cultivation of a microalga Chlorella vulgaris using recycled aqueous phase nutrients from hydrothermal carbonization process. *Bioresour Technol* **126**, 354-357, doi:10.1016/j.biortech.2012.09.062 (2012).

340 Zuliani, L. *et al.* Microalgae Cultivation on Anaerobic Digestate of Municipal Wastewater, Sewage Sludge and Agro-Waste. *International journal of molecular sciences* **17**, doi:10.3390/ijms17101692 (2016).

341 Sarayloo, E. *et al.* Understanding lipid metabolism in high-lipid-producing Chlorella vulgaris mutants at the genome-wide level. *Algal Research* **28**, 244-252, doi:10.1016/j.algal.2017.11.009 (2017).

342 Baroli, I. & Niyogi, K. K. Molecular genetics of xanthophyll-dependent photoprotection in green algae and plants. *Philosophical transactions of the Royal Society of London. Series B, Biological sciences* **355**, 1385-1394, doi:10.1098/rstb.2000.0700 (2000).

343 Li, X. P., Muller-Moule, P., Gilmore, A. M. & Niyogi, K. K. PsbS-dependent enhancement of feedback de-excitation protects photosystem II from photoinhibition. *Proceedings of the National Academy of Sciences of the United States of America* **99**, 15222-15227, doi:10.1073/pnas.232447699 (2002).

344 Berne, N., Fabryova, T., Istaz, B., Cardol, P. & Bailleul, B. The peculiar NPQ regulation in the stramenopile Phaeomonas sp. challenges the xanthophyll cycle dogma. *Biochimica et biophysica acta. Bioenergetics* **1859**, 491-500, doi:10.1016/j.bbabio.2018.03.013 (2018).

345 Walters, R. G., Ruban, A. V. & Horton, P. Identification of proton-active residues in a higher plant light-harvesting complex. *Proceedings of the National Academy of Sciences of the United States of America* **93**, 14204-14209, doi:10.1073/pnas.93.24.14204 (1996).

346 Wehner, A., Storf, S., Jahns, P. & Schmid, V. H. De-epoxidation of violaxanthin in light-harvesting complex I proteins. *The Journal of biological chemistry* **279**, 26823-26829, doi:10.1074/jbc.M402399200 (2004).

347 Leliaert, F. *et al.* Phylogeny and Molecular Evolution of the Green Algae. *Critical Reviews in Plant Sciences* **31**, 1-46, doi:10.1080/07352689.2011.615705 (2012).

348 Allen, M. M. & Stanier, R. Y. Selective isolation of blue-green algae from water and soil. *Journal of general microbiology* **51**, 203-209, doi:10.1099/00221287-51-2-203 (1968).

349 Kropat, J. *et al.* A revised mineral nutrient supplement increases biomass and growth rate in Chlamydomonas reinhardtii. *Plant J* **66**, 770-780, doi:10.1111/j.1365-313X.2011.04537.x (2011).

350 Huerta-Cepas, J., Serra, F. & Bork, P. ETE 3: Reconstruction, Analysis, and Visualization of Phylogenomic Data. *Molecular biology and evolution* **33**, 1635-1638, doi:10.1093/molbev/msw046 (2016).

351 Hieber, A. D., Bugos, R. C., Verhoeven, A. S. & Yamamoto, H. Y. Overexpression of violaxanthin de-epoxidase: properties of C-terminal deletions on activity and pH-dependent lipid binding. *Planta* **214**, 476-483, doi:10.1007/s00425-001-0704-2 (2002).

352 Laemmli, U. K. Cleavage of structural proteins during the assembly of the head of bacteriophage T4. *Nature* **227**, 680-685, doi:10.1038/227680a0 (1970).

353 Bilger, W. & Bjorkman, O. Role of the xanthophyll cycle in photoprotection elucidated by measurements of light-induced absorbance changes, fluorescence and photosynthesis in leaves of Hedera canariensis. *Photosynth Res* **25**, 173-185, doi:10.1007/BF00033159 (1990).

354 Hill, R. & Scarisbrick, R. Production of Oxygen by Illuminated Chloroplasts. *Nature* **146**, 61-62, doi:10.1038/146061a0 (1940).

355 Croce, R. & van Amerongen, H. Light-harvesting in photosystem I. *Photosynth Res* **116**, 153-166, doi:10.1007/s11120-013-9838-x (2013).

356 Murchie, E. H. & Niyogi, K. K. Manipulation of photoprotection to improve plant photosynthesis. *Plant Physiol* **155**, 86-92, doi:10.1104/pp.110.168831 (2011).

357 Vass, I. *et al.* Reversible and irreversible intermediates during photoinhibition of photosystem II: stable reduced QA species promote chlorophyll triplet formation. *Proceedings of the National Academy of Sciences of the United States of America* **89**, 1408-1412, doi:10.1073/pnas.89.4.1408 (1992).

358 Tokutsu, R., Kato, N., Bui, K. H., Ishikawa, T. & Minagawa, J. Revisiting the supramolecular organization of photosystem II in Chlamydomonas reinhardtii. *The Journal of biological chemistry* **287**, 31574-31581, doi:10.1074/jbc.M111.331991 (2012).

359 Allorent, G. *et al.* UV-B photoreceptor-mediated protection of the photosynthetic machinery in Chlamydomonas reinhardtii. *Proceedings of the National Academy of Sciences of the United States of America* **113**, 14864-14869, doi:10.1073/pnas.1607695114 (2016).

360 Scholz, M. *et al.* Light-dependent N-terminal phosphorylation of LHCSR3 and LHCB4 are interlinked in Chlamydomonas reinhardtii. *Plant J* **99**, 877-894, doi:10.1111/tpj.14368 (2019).

361 Townsend, A. J. *et al.* The causes of altered chlorophyll fluorescence quenching induction in the Arabidopsis mutant lacking all minor antenna complexes. *Biochimica et biophysica acta. Bioenergetics* **1859**, 666-675, doi:10.1016/j.bbabio.2018.03.005 (2018).

362 Malkin, S., Armond, P. A., Mooney, H. A. & Fork, D. C. Photosystem II Photosynthetic Unit Sizes from Fluorescence Induction in Leaves : CORRELATION TO PHOTOSYNTHETIC CAPACITY. *Plant Physiol* **67**, 570-579, doi:10.1104/pp.67.3.570 (1981).

363 Butler, W. L. Primary photochemistry of photosystem II in photosynthesis. *Acc.Chem.Res.* **6**, 177-183 (1973).

364 Garnier, J., Maroc, J. & Guyon, D. Low-temperature fluorescence emission spectra and chlorophyll-protein complexes in mutants of Chlamydomonas reinhardtii: Evidence for a new chlorophyll-a-protein complex related to photosystem I. *Biochim.Biophys.Acta* **851**, 395-406 (1986).

365 Drop, B., Yadav, K. N. S., Boekema, E. J. & Croce, R. Consequences of state transitions on the structural and functional organization of photosystem I in the green alga Chlamydomonas reinhardtii. *Plant J* **78**, 181-191, doi:10.1111/tpj.12459 (2014).

366 Bailleul, B., Cardol, P., Breyton, C. & Finazzi, G. Electrochromism: a useful probe to study algal photosynthesis. *Photosynth.Res.* **106**, 179-189 (2010).

367 Lucker, B. & Kramer, D. M. Regulation of cyclic electron flow in Chlamydomonas reinhardtii under fluctuating carbon availability. *Photosynth Res* **117**, 449-459, doi:10.1007/s11120-013-9932-0 (2013).

368 Dall'Osto, L., Unlu, C., Cazzaniga, S. & van Amerongen, H. Disturbed excitation energy transfer in Arabidopsis thaliana mutants lacking minor antenna complexes of photosystem II. *Biochim Biophys Acta* **1837**, 1981-1988, doi:10.1016/j.bbabio.2014.09.011 (2014).

369 Kouril, R., Wientjes, E., Bultema, J. B., Croce, R. & Boekema, E. J. High-light vs. low-light: effect of light acclimation on photosystem II composition and organization in Arabidopsis thaliana. *Biochim Biophys Acta* **1827**, 411-419, doi:10.1016/j.bbabio.2012.12.003 (2013).

370 Kargul, J. *et al.* Light-harvesting complex II protein CP29 binds to photosystem I of Chlamydomonas reinhardtii under State 2 conditions. *FEBS J* **272**, 4797-4806, doi:10.1111/j.1742-4658.2005.04894.x (2005).

371 Takahashi, H., Iwai, M., Takahashi, Y. & Minagawa, J. Identification of the mobile light-harvesting complex II polypeptides for state transitions in Chlamydomonas reinhardtii. *Proceedings of the National Academy of Sciences of the United States of America* **103**, 477-482, doi:10.1073/pnas.0509952103 (2006).

372 Furukawa, R. *et al.* Formation of a PSI-PSII megacomplex containing LHCSR and PsbS in the moss Physcomitrella patens. *J Plant Res* **132**, 867-880, doi:10.1007/s10265-019-01138-2 (2019).

373 Shin, Y. S. *et al.* Targeted knockout of phospholipase A2 to increase lipid productivity in Chlamydomonas reinhardtii for biodiesel production. *Bioresour Technol* **271**, 368-374, doi:10.1016/j.biortech.2018.09.121 (2019).

374 Tanksley, S. D. *et al.* High density molecular linkage maps of the tomato and potato genomes. *Genetics* **132**, 1141-1160 (1992).

375 Van Kooten, O. & Snel, J. F. H. The use of chlorophyll fluorescence nomenclature in plant stress physiology. *Photosynt.Res.* **25**, 147-150 (1990).

376 Baker, N. R. Chlorophyll fluorescence: a probe of photosynthesis in vivo. *Annual review of plant biology* **59**, 89-113, doi:10.1146/annurev.arplant.59.032607.092759 (2008).

377 Kuhlgert, S. *et al.* MultispeQ Beta: a tool for large-scale plant phenotyping connected to the open PhotosynQ network. *Royal Society Open Science* **3**, doi:10.1098/rsos.160592 (2016).

378 Hope, A. B. Electron transfers amongst cytochrome f, plastocyanin and photosystem I: kinetics and mechanisms. *Biochim Biophys Acta* **1456**, 5-26, doi:10.1016/s0005-2728(99)00101-2 (2000).

379 Caffarri, S., Tibiletti, T., Jennings, R. C. & Santabarbara, S. A comparison between plant photosystem I and photosystem II architecture and functioning. *Current protein & peptide science* **15**, 296-331, doi:10.2174/1389203715666140327102218 (2014).

380 Tikhonov, A. N. The cytochrome b6f complex at the crossroad of photosynthetic electron transport pathways. *Plant physiology and biochemistry : PPB* **81**, 163-183, doi:10.1016/j.plaphy.2013.12.011 (2014).

381 Erickson, E., Wakao, S. & Niyogi, K. K. Light stress and photoprotection in Chlamydomonas reinhardtii. *Plant J* **82**, 449-465, doi:10.1111/tpj.12825 (2015).

382 Campbell, D., Hurry, V., Clarke, A. K., Gustafsson, P. & Oquist, G. Chlorophyll fluorescence analysis of cyanobacterial photosynthesis and acclimation. *Microbiology and molecular biology reviews : MMBR* **62**, 667-683 (1998).

383 Brestic, M., Zivcak, M., Kunderlikova, K. & Allakhverdiev, S. I. High temperature specifically affects the photoprotective responses of chlorophyll b-deficient wheat mutant lines. *Photosynth Res* **130**, 251-266, doi:10.1007/s11120-016-0249-7 (2016).

384 Kalaji, H. M. *et al.* Chlorophyll a fluorescence as a tool to monitor physiological status of plants under abiotic stress conditions. *Acta Physiol Plant* **38**, doi:Artn 10210.1007/S11738-016-2113-Y (2016).

385 Demmig-Adams, B. & Adams, W. W., 3rd. Photoprotection in an ecological context: the remarkable complexity of thermal energy dissipation. *The New phytologist* **172**, 11-21, doi:10.1111/j.1469-8137.2006.01835.x (2006).

386 Demmig-Adams, B., Cohu, C. M., Muller, O. & Adams, W. W., 3rd. Modulation of photosynthetic energy conversion efficiency in nature: from seconds to seasons. *Photosynth Res* **113**, 75-88, doi:10.1007/s11120-012-9761-6 (2012).

387 Lepetit, B. *et al.* High light acclimation in the secondary plastids containing diatom Phaeodactylum tricornutum is triggered by the redox state of the plastoquinone pool. *Plant Physiol* **161**, 853-865, doi:10.1104/pp.112.207811 (2013).

388 Kirst, H., Gabilly, S. T., Niyogi, K. K., Lemaux, P. G. & Melis, A. Photosynthetic antenna engineering to improve crop yields. *Planta* **245**, 1009-1020, doi:10.1007/s00425-017-2659-y (2017).

389 Chisti, Y. Biodiesel from microalgae. *Biotechnology advances* **25**, 294-306, doi:10.1016/j.biotechadv.2007.02.001 (2007).

390 Chisti, Y. Biodiesel from microalgae beats bioethanol. *Trends in biotechnology* **26**, 126-131, doi:10.1016/j.tibtech.2007.12.002 (2008).

391 Akbari, F., Eskandani, M. & Khosroushahi, A. Y. The potential of transgenic green microalgae; a robust photobioreactor to produce recombinant therapeutic proteins. *World Journal of Microbiology and Biotechnology*, doi:10.1007/s11274-014-1714-0 (2014).

392 Stephens, E. *et al.* Future prospects of microalgal biofuel production systems. *Trends Plant Sci* **15**, 554-564, doi:10.1016/j.tplants.2010.06.003 (2010).

393 Petroutsos, D. *et al.* The chloroplast calcium sensor CAS is required for photoacclimation in Chlamydomonas reinhardtii. *Plant Cell* **23**, 2950-2963, doi:10.1105/tpc.111.087973 (2011).

394 Schroda, M., Blocker, D. & Beck, C. F. The HSP70A promoter as a tool for the improved expression of transgenes in Chlamydomonas. *Plant J* **21**, 121-131, doi:10.1046/j.1365-313x.2000.00652.x (2000).

395 Kim, S. *et al.* Arabidopsis thaliana Rubisco small subunit transit peptide increases the accumulation of Thermotoga maritima endoglucanase Cel5A in chloroplasts of transgenic tobacco plants. *Transgenic research* **19**, 489-497, doi:10.1007/s11248-009-9330-8 (2010).

396 Flors, C. *et al.* Imaging the production of singlet oxygen in vivo using a new fluorescent sensor, Singlet Oxygen Sensor Green. *Journal of experimental botany* **57**, 1725-1734, doi:10.1093/jxb/erj181 (2006).

397 Giordano, M., Norici, A., Forssen, M., Eriksson, M. & Raven, J. A. An anaplerotic role for mitochondrial carbonic anhydrase in Chlamydomonas reinhardtii. *Plant Physiol* **132**, 2126-2134, doi:10.1104/pp.103.023424 (2003).

398 Langner, U., Jakob, T., Stehfest, K. & Wilhelm, C. An energy balance from absorbed photons to new biomass for Chlamydomonas reinhardtii and Chlamydomonas acidophila under neutral and extremely acidic growth conditions. *Plant, cell & environment* **32**, 250-258, doi:10.1111/j.1365-3040.2008.01917.x (2009).

399 Vitova, M. *et al.* Chlamydomonas reinhardtii: duration of its cell cycle and phases at growth rates affected by temperature. *Planta* **234**, 599-608, doi:10.1007/s00425-011-1427-7 (2011).

400 Kliphuis, A. M. *et al.* Metabolic modeling of Chlamydomonas reinhardtii: energy requirements for photoautotrophic growth and maintenance. *J Appl Phycol* **24**, 253-266, doi:10.1007/s10811-011-9674-3 (2012).

401 Carbonera, D., Gerotto, C., Posocco, B., Giacometti, G. M. & Morosinotto, T. NPQ activation reduces chlorophyll triplet state formation in the moss Physcomitrella patens. *Biochim Biophys Acta* **1817**, 1608-1615, doi:10.1016/j.bbabio.2012.05.007 (2012).

402 Chaux, F. *et al.* PGRL1 and LHCSR3 Compensate for Each Other in Controlling Photosynthesis and Avoiding Photosystem I Photoinhibition during High Light Acclimation of Chlamydomonas Cells. *Molecular plant* **10**, 216-218, doi:10.1016/j.molp.2016.09.005 (2017).

403 Leon, R., Couso, I. & Fernandez, E. Metabolic engineering of ketocarotenoids biosynthesis in the unicelullar microalga Chlamydomonas reinhardtii. *Journal of biotechnology* **130**, 143-152, doi:10.1016/j.jbiotec.2007.03.005 (2007).

404 Kindle, K. L. High-frequency nuclear transformation of Chlamydomonas reinhardtii. *Proceedings of the National Academy of Sciences of the United States of America* **87**, 1228-1232, doi:10.1073/pnas.87.3.1228 (1990).

405 Ferrante, P., Ballottari, M., Bonente, G., Giuliano, G. & Bassi, R. LHCBM1 and LHCBM2/7 polypeptides, components of major LHCII complex, have distinct functional roles in photosynthetic antenna system of Chlamydomonas reinhardtii. *The Journal of biological chemistry* **287**, 16276-16288, doi:10.1074/jbc.M111.316729 (2012).

406 Lemoine, Y. & Schoefs, B. Secondary ketocarotenoid astaxanthin biosynthesis in algae: a multifunctional response to stress. *Photosynth Res* **106**, 155-177, doi:10.1007/s11120-010-9583-3 (2010).

407 Ambati, R. R., Moi, P. S., Ravi, S. & Aswathanarayana, R. G. Astaxanthin: Sources, extraction, stability, biological activities and its commercial applications - A review. *Marine drugs*, doi:10.3390/md12010128 (2014).

408 Shah, M. M., Liang, Y., Cheng, J. J. & Daroch, M. Astaxanthin-Producing Green Microalga Haematococcus pluvialis: From Single Cell to High Value Commercial Products. *Front Plant Sci* **7**, 531, doi:10.3389/fpls.2016.00531 (2016).

409 Terao, J. Antioxidant activity of beta-carotene-related carotenoids in solution. *Lipids* **24**, 659-661, doi:10.1007/bf02535085 (1989).

410 Kurashige, M., Okimasu, E., Inoue, M. & Utsumi, K. Inhibition of oxidative injury of biological membranes by astaxanthin. *Physiological chemistry and physics and medical NMR* **22**, 27-38 (1990).

411 Guerin, M., Huntley, M. E. & Olaizola, M. Haematococcus astaxanthin: applications for human health and nutrition. *Trends in biotechnology* **21**, 210-216, doi:10.1016/S0167-7799(03)00078-7 (2003).

412 Stahl, W. & Sies, H. Bioactivity and protective effects of natural carotenoids. *Biochim Biophys Acta* **1740**, 101-107, doi:10.1016/j.bbadis.2004.12.006 (2005).

413 Daubrawa, F., Sies, H. & Stahl, W. Astaxanthin diminishes gap junctional intercellular communication in primary human fibroblasts. *The Journal of nutrition* **135**, 2507-2511, doi:10.1093/jn/135.11.2507 (2005).
414 Yuan, J. P., Peng, J., Yin, K. & Wang, J. H. Potential health-promoting effects of astaxanthin: a high-value carotenoid mostly from microalgae. *Molecular nutrition & food research* **55**, 150-165, doi:10.1002/mnfr.201000414 (2011).
415 Kobayashi, M., Katsuragi, T. & Tani, Y. Enlarged and astaxanthin-accumulating cyst cells of the green alga Haematococcus pluvialis. *Journal of bioscience and bioengineering* **92**, 565-568, doi:10.1263/jbb.92.565 (2001).
416 Wang, S. B., Chen, F., Sommerfeld, M. & Hu, Q. Proteomic analysis of molecular response to oxidative stress by the green alga Haematococcus pluvialis (Chlorophyceae). *Planta* **220**, 17-29, doi:10.1007/s00425-004-1323-5 (2004).
417 Gao, Z. *et al.* Differential expression of carotenogenic genes, associated changes on astaxanthin production and photosynthesis features induced by JA in H. pluvialis. *PloS one* **7**, e42243, doi:10.1371/journal.pone.0042243 (2012).
418 Gao, Z. *et al.* Induction of salicylic acid (SA) on transcriptional expression of eight carotenoid genes and astaxanthin accumulation in Haematococcus pluvialis. *Enzyme and microbial technology* **51**, 225-230, doi:10.1016/j.enzmictec.2012.07.001 (2012).
419 Scibilia, L., Girolomoni, L., Berteotti, S., Alboresi, A. & Ballottari, M. Photosynthetic response to nitrogen starvation and high light in Haematococcus pluvialis. *Algal Research-Biomass Biofuels and Bioproducts* **12**, 170-181, doi:10.1016/j.algal.2015.08.024 (2015).
420 Li, K. *et al.* In vivo kinetics of lipids and astaxanthin evolution in Haematococcus pluvialis mutant under 15% CO2 using Raman microspectroscopy. *Bioresour Technol* **244**, 1439-1444, doi:10.1016/j.biortech.2017.04.116 (2017).
421 Wang, J., Sommerfeld, M. & Hu, Q. Occurrence and environmental stress responses of two plastid terminal oxidases in Haematococcus pluvialis (Chlorophyceae). *Planta* **230**, 191-203, doi:10.1007/s00425-009-0932-4 (2009).
422 Hong, M. E. *et al.* Enhanced autotrophic astaxanthin production from Haematococcus pluvialis under high temperature via heat stress-driven Haber-Weiss reaction. *Applied microbiology and biotechnology* **99**, 5203-5215, doi:10.1007/s00253-015-6440-5 (2015).
423 Aflalo, C., Meshulam, Y., Zarka, A. & Boussiba, S. On the relative efficiency of two- vs. one-stage production of astaxanthin by the green alga Haematococcus pluvialis. *Biotechnology and bioengineering* **98**, 300-305, doi:10.1002/bit.21391 (2007).
424 Grunewald, K., Eckert, M., Hirschberg, J. & Hagen, C. Phytoene desaturase is localized exclusively in the chloroplast and up-regulated at the mRNA level during accumulation of secondary carotenoids in Haematococcus pluvialis (Volvocales, chlorophyceae). *Plant Physiol* **122**, 1261-1268, doi:10.1104/pp.122.4.1261 (2000).
425 Fan, L., Vonshak, A., Zarka, A. & Boussiba, S. Does astaxanthin protect Haematococcus against light damage? *Zeitschrift fur Naturforschung - Section C Journal of Biosciences* (1998).
426 Su, Y. *et al.* Metabolomic and network analysis of astaxanthin-producing Haematococcus pluvialis under various stress conditions. *Bioresour Technol* **170**, 522-529, doi:10.1016/j.biortech.2014.08.018 (2014).
427 Wan, M. *et al.* The effect of temperature on cell growth and astaxanthin accumulation of Haematococcus pluvialis during a light-dark cyclic cultivation. *Bioresour Technol* **167**, 276-283, doi:10.1016/j.biortech.2014.06.030 (2014).
428 Collins, A. M. *et al.* Carotenoid distribution in living cells of Haematococcus pluvialis (Chlorophyceae). *PloS one* **6**, e24302, doi:10.1371/journal.pone.0024302 (2011).
429 Gu, W. *et al.* Comparison of different cells of Haematococcus pluvialis reveals an extensive acclimation mechanism during its aging process: from a perspective of photosynthesis. *PloS one* **8**, e67028, doi:10.1371/journal.pone.0067028 (2013).
430 Gu, W. *et al.* Quantitative proteomic analysis of thylakoid from two microalgae (Haematococcus pluvialis and Dunaliella salina) reveals two different high light-responsive strategies. *Scientific reports* **4**, 6661, doi:10.1038/srep06661 (2014).
431 Zhong, Y. J. *et al.* Functional characterization of various algal carotenoid ketolases reveals that ketolating zeaxanthin efficiently is essential for high production of astaxanthin in transgenic Arabidopsis. *Journal of experimental botany* **62**, 3659-3669, doi:10.1093/jxb/err070 (2011).
432 Roding, A. *et al.* Production of ketocarotenoids in tobacco alters the photosynthetic efficiency by reducing photosystem II supercomplex and LHCII trimer stability. *Photosynth Res* **123**, 157-165, doi:10.1007/s11120-014-0055-z (2015).
433 Fujii, R., Yamano, N., Hashimoto, H., Misawa, N. & Ifuku, K. Photoprotection vs. Photoinhibition of Photosystem II in Transplastomic Lettuce (Lactuca sativa) Dominantly Accumulating Astaxanthin. *Plant & cell physiology* **57**, 1518-1529, doi:10.1093/pcp/pcv187 (2016).

434 Grewe, S. *et al.* Light-Harvesting Complex Protein LHCBM9 Is Critical for Photosystem II Activity and Hydrogen Production in Chlamydomonas reinhardtii. *Plant Cell* **26**, 1598-1611, doi:10.1105/tpc.114.124198 (2014).

435 Johnson, M. P. *et al.* Elevated zeaxanthin bound to oligomeric LHCII enhances the resistance of Arabidopsis to photooxidative stress by a lipid-protective, antioxidant mechanism. *The Journal of biological chemistry* **282**, 22605-22618, doi:10.1074/jbc.M702831200 (2007).

436 Fiore, A. *et al.* A quadruple mutant of Arabidopsis reveals a beta-carotene hydroxylation activity for LUT1/CYP97C1 and a regulatory role of xanthophylls on determination of the PSI/PSII ratio. *BMC plant biology* **12**, 50, doi:10.1186/1471-2229-12-50 (2012).

437 Phillip, D. *et al.* The binding of Xanthophylls to the bulk light-harvesting complex of photosystem II of higher plants. A specific requirement for carotenoids with a 3-hydroxy-beta-end group. *The Journal of biological chemistry* **277**, 25160-25169, doi:10.1074/jbc.M202002200 (2002).

438 Ballottari, M., Govoni, C., Caffarri, S. & Morosinotto, T. Stoichiometry of LHCI antenna polypeptides and characterization of gap and linker pigments in higher plants Photosystem I. *European journal of biochemistry* **271**, 4659-4665, doi:10.1111/j.1432-1033.2004.04426.x (2004).

439 Jordan, P. *et al.* Three-dimensional structure of cyanobacterial photosystem I at 2.5 A resolution. *Nature* **411**, 909-917, doi:10.1038/35082000 (2001).

440 Moya, I., Silvestri, M., Vallon, O., Cinque, G. & Bassi, R. Time-resolved fluorescence analysis of the photosystem II antenna proteins in detergent micelles and liposomes. *Biochemistry* **40**, 12552-12561, doi:10.1021/bi010342x (2001).

441 Caffarri, S., Broess, K., Croce, R. & van Amerongen, H. Excitation energy transfer and trapping in higher plant Photosystem II complexes with different antenna sizes. *Biophysical journal* **100**, 2094-2103, doi:10.1016/j.bpj.2011.03.049 (2011).

442 Wientjes, E., van Stokkum, I. H., van Amerongen, H. & Croce, R. Excitation-energy transfer dynamics of higher plant photosystem I light-harvesting complexes. *Biophysical journal* **100**, 1372-1380, doi:10.1016/j.bpj.2011.01.030 (2011).

443 Jennings, R. C., Zucchelli, G. & Santabarbara, S. Photochemical trapping heterogeneity as a function of wavelength, in plant photosystem I (PSI-LHCI). *Biochim Biophys Acta* **1827**, 779-785, doi:10.1016/j.bbabio.2013.03.008 (2013).

444 Le Quiniou, C., van Oort, B., Drop, B., van Stokkum, I. H. & Croce, R. The High Efficiency of Photosystem I in the Green Alga Chlamydomonas reinhardtii Is Maintained after the Antenna Size Is Substantially Increased by the Association of Light-harvesting Complexes II. *The Journal of biological chemistry* **290**, 30587-30595, doi:10.1074/jbc.M115.687970 (2015).

445 Grunewald, K., Hirschberg, J. & Hagen, C. Ketocarotenoid biosynthesis outside of plastids in the unicellular green alga Haematococcus pluvialis. *The Journal of biological chemistry* **276**, 6023-6029, doi:10.1074/jbc.M006400200 (2001).

446 Wayama, M. *et al.* Three-dimensional ultrastructural study of oil and astaxanthin accumulation during encystment in the green alga Haematococcus pluvialis. *PloS one* **8**, e53618, doi:10.1371/journal.pone.0053618 (2013).

447 Cazzaniga, S., Li, Z., Niyogi, K. K., Bassi, R. & Dall'Osto, L. The Arabidopsis szl1 mutant reveals a critical role of beta-carotene in photosystem I photoprotection. *Plant Physiol* **159**, 1745-1758, doi:10.1104/pp.112.201137 (2012).

448 Vechtel, B., Pistorius, E. K. & Ruppel, H. G. Occurrence of Secondary Carotenoids in PS I Complexes Isolated from Eremosphaera viridis De Bary (Chlorophyceae). *Zeitschrift für Naturforschung C* **47**, 51-56, doi:10.1515/znc-1992-1-210 (1992).

449 Telfer, A. Too much light? How beta-carotene protects the photosystem II reaction centre. *Photochemical & photobiological sciences : Official journal of the European Photochemistry Association and the European Society for Photobiology* **4**, 950-956, doi:10.1039/b507888c (2005).

450 Hasunuma, T. *et al.* Biosynthesis of astaxanthin in tobacco leaves by transplastomic engineering. *Plant J* **55**, 857-868, doi:10.1111/j.1365-313X.2008.03559.x (2008).

451 Cinque, G., Croce, R. & Bassi, R. Absorption spectra of chlorophyll a and b in Lhcb protein environment. *Photosynth Res* **64**, 233-242, doi:10.1023/A:1006467617697 (2000).

452 Mimuro, M. & Katoh, T. Carotenoids in Photosynthesis - Absorption, Transfer and Dissipation of Light Energy. *Pure and Applied Chemistry* **63**, 123-130, doi:DOI 10.1351/pac199163010123 (1991).

453 Edge, R., McGarvey, D. J. & Truscott, T. G. The carotenoids as anti-oxidants — a review. *Journal of Photochemistry and Photobiology B: Biology* **41**, 189-200, doi:10.1016/s1011-1344(97)00092-4 (1997).

454 Hussein, G., Sankawa, U., Goto, H., Matsumoto, K. & Watanabe, H. Astaxanthin, a carotenoid with potential in human health and nutrition. *J Nat Prod* **69**, 443-449, doi:10.1021/np050354+ (2006).

455 Li, J., Zhu, D., Niu, J., Shen, S. & Wang, G. An economic assessment of astaxanthin production by large scale cultivation of Haematococcus pluvialis. *Biotechnology advances* **29**, 568-574, doi:10.1016/j.biotechadv.2011.04.001 (2011).

456 Gerster, H. The potential role of lycopene for human health. *Journal of the American College of Nutrition* **16**, 109-126, doi:10.1080/07315724.1997.10718661 (1997).

457 Lotan, T. & Hirschberg, J. Cloning and expression in Escherichia coli of the gene encoding beta-C-4-oxygenase, that converts beta-carotene to the ketocarotenoid canthaxanthin in Haematococcus pluvialis. *FEBS letters* **364**, 125-128, doi:10.1016/0014-5793(95)00368-j (1995).

458 Cunningham, F. X. & Gantt, E. Genes and Enzymes of Carotenoid Biosynthesis in Plants. *Annual review of plant physiology and plant molecular biology* **49**, 557-583, doi:10.1146/annurev.arplant.49.1.557 (1998).

459 Grossman, A. R., Lohr, M. & Im, C. S. Chlamydomonas reinhardtii in the landscape of pigments. *Annual review of genetics* **38**, 119-173, doi:10.1146/annurev.genet.38.072902.092328 (2004).

460 Jyonouchi, H., Sun, S. & Gross, M. Effect of carotenoids on in vitro immunoglobulin production by human peripheral blood mononuclear cells: astaxanthin, a carotenoid without vitamin A activity, enhances in vitro immunoglobulin production in response to a T-dependent stimulant and antigen. *Nutrition and cancer* **23**, 171-183, doi:10.1080/01635589509514373 (1995).

461 Bennedsen, M., Wang, X., Willen, R., Wadstrom, T. & Andersen, L. P. Treatment of H. pylori infected mice with antioxidant astaxanthin reduces gastric inflammation, bacterial load and modulates cytokine release by splenocytes. *Immunology letters* **70**, 185-189, doi:10.1016/s0165-2478(99)00145-5 (1999).

462 Zhang, L. & Wang, H. Multiple Mechanisms of Anti-Cancer Effects Exerted by Astaxanthin. *Marine drugs* **13**, 4310-4330, doi:10.3390/md13074310 (2015).

463 Kim, J. H. *et al.* Astaxanthin Inhibits Proliferation of Human Gastric Cancer Cell Lines by Interrupting Cell Cycle Progression. *Gut and liver* **10**, 369-374, doi:10.5009/gnl15208 (2016).

464 Gross, G. J. & Lockwood, S. F. Cardioprotection and myocardial salvage by a disodium disuccinate astaxanthin derivative (Cardax). *Life sciences* **75**, 215-224, doi:10.1016/j.lfs.2003.12.006 (2004).

465 Møller, A. P. *et al.* Carotenoid-dependent signals: indicators of foraging efficiency, immunocompetence or detoxification ability? *Avian and Poultry Biology Reviews* **11**, 137-159 (2000).

466 Miki, W. Biological Functions and Activities of Animal Carotenoids. *Pure and Applied Chemistry* **63**, 141-146, doi:DOI 10.1351/pac199163010141 (1991).

467 Cunningham, F. X., Jr. & Gantt, E. Elucidation of the pathway to astaxanthin in the flowers of Adonis aestivalis. *Plant Cell* **23**, 3055-3069, doi:10.1105/tpc.111.086827 (2011).

468 Nakada, T. & Ota, S. What is the correct name for the type of Haematococcus Flot. (Volvocales, Chlorophyceae)? *Taxon* **65**, 343-348, doi:Doi 10.12705/652.11 (2016).

469 Chen, J. H., Liu, L. & Wei, D. Enhanced production of astaxanthin by Chromochloris zofingiensis in a microplate-based culture system under high light irradiation. *Bioresour Technol* **245**, 518-529, doi:10.1016/j.biortech.2017.08.102 (2017).

470 Kobayashi, M., Kurimura, Y., Kakizono, T., Nishio, N. & Tsuji, Y. Morphological changes in the life cycle of the green alga Haematococcus pluvialis. *Journal of Fermentation and Bioengineering* **84**, 94-97, doi:Doi 10.1016/S0922-338x(97)82794-8 (1997).

471 Park, S. Y., Binkley, R. M., Kim, W. J., Lee, M. H. & Lee, S. Y. Metabolic engineering of Escherichia coli for high-level astaxanthin production with high productivity. *Metabolic engineering* **49**, 105-115, doi:10.1016/j.ymben.2018.08.002 (2018).

472 Henke, N. A., Heider, S. A., Peters-Wendisch, P. & Wendisch, V. F. Production of the Marine Carotenoid Astaxanthin by Metabolically Engineered Corynebacterium glutamicum. *Marine drugs* **14**, doi:10.3390/md14070124 (2016).

473 Harker, M. & Hirschberg, J. Biosynthesis of ketocarotenoids in transgenic cyanobacteria expressing the algal gene for beta-C-4-oxygenase, crtO. *FEBS letters* **404**, 129-134, doi:10.1016/s0014-5793(97)00110-5 (1997).

474 Kildegaard, K. R. *et al.* Engineering of Yarrowia lipolytica for production of astaxanthin. *Synthetic and systems biotechnology* **2**, 287-294, doi:10.1016/j.synbio.2017.10.002 (2017).

475 Miura, Y. *et al.* Production of the carotenoids lycopene, beta-carotene, and astaxanthin in the food yeast Candida utilis. *Appl Environ Microbiol* **64**, 1226-1229 (1998).

476 Mann, V., Harker, M., Pecker, I. & Hirschberg, J. Metabolic engineering of astaxanthin production in tobacco flowers. *Nature biotechnology* **18**, 888-892, doi:10.1038/78515 (2000).

477 Stalberg, K., Lindgren, O., Ek, B. & Hoglund, A. S. Synthesis of ketocarotenoids in the seed of Arabidopsis thaliana. *Plant J* **36**, 771-779, doi:10.1046/j.1365-313x.2003.01919.x (2003).

478 Jayaraj, J., Devlin, R. & Punja, Z. Metabolic engineering of novel ketocarotenoid production in carrot plants. *Transgenic research* **17**, 489-501, doi:10.1007/s11248-007-9120-0 (2008).

479 Huang, J. C., Zhong, Y. J., Liu, J., Sandmann, G. & Chen, F. Metabolic engineering of tomato for high-yield production of astaxanthin. *Metabolic engineering* **17**, 59-67, doi:10.1016/j.ymben.2013.02.005 (2013).

480 Nogueira, M. *et al.* Engineering of tomato for the sustainable production of ketocarotenoids and its evaluation in aquaculture feed. *Proceedings of the National Academy of Sciences of the United States of America* **114**, 10876-10881, doi:10.1073/pnas.1708349114 (2017).
481 Tan, C.-P., Zhao, F.-Q., Su, Z.-L., Liang, C.-W. & Qin, S. Expression of β-carotene hydroxylase gene (crtR-B) from the green alga Haematococcus pluvialis in chloroplasts of Chlamydomonas reinhardtii. *Journal of Applied Phycology* **19**, 347-355, doi:10.1007/s10811-006-9141-8 (2007).
482 Zheng, K. *et al.* Expression of bkt and bch genes from Haematococcus pluvialis in transgenic Chlamydomonas. *Science China. Life sciences* **57**, 1028-1033, doi:10.1007/s11427-014-4729-8 (2014).
483 Lohr, M., Im, C. S. & Grossman, A. R. Genome-based examination of chlorophyll and carotenoid biosynthesis in Chlamydomonas reinhardtii. *Plant Physiol* **138**, 490-515, doi:10.1104/pp.104.056069 (2005).
484 Romero-Campero, F. J., Perez-Hurtado, I., Lucas-Reina, E., Romero, J. M. & Valverde, F. ChlamyNET: a Chlamydomonas gene co-expression network reveals global properties of the transcriptome and the early setup of key co-expression patterns in the green lineage. *BMC genomics* **17**, 227, doi:10.1186/s12864-016-2564-y (2016).
485 Baier, T., Wichmann, J., Kruse, O. & Lauersen, K. J. Intron-containing algal transgenes mediate efficient recombinant gene expression in the green microalga Chlamydomonas reinhardtii. *Nucleic acids research* **46**, 6909-6919, doi:10.1093/nar/gky532 (2018).
486 Lauersen, K. J. *et al.* Phototrophic production of heterologous diterpenoids and a hydroxy-functionalized derivative from Chlamydomonas reinhardtii. *Metabolic engineering* **49**, 116-127, doi:10.1016/j.ymben.2018.07.005 (2018).
487 Lauersen, K. J. *et al.* Efficient phototrophic production of a high-value sesquiterpenoid from the eukaryotic microalga Chlamydomonas reinhardtii. *Metabolic engineering* **38**, 331-343, doi:10.1016/j.ymben.2016.07.013 (2016).
488 Wichmann, J., Baier, T., Wentnagel, E., Lauersen, K. J. & Kruse, O. Tailored carbon partitioning for phototrophic production of (E)-alpha-bisabolene from the green microalga Chlamydomonas reinhardtii. *Metabolic engineering* **45**, 211-222, doi:10.1016/j.ymben.2017.12.010 (2018).
489 Yunus, I. S. *et al.* Synthetic metabolic pathways for photobiological conversion of CO2 into hydrocarbon fuel. *Metabolic engineering* **49**, 201-211, doi:10.1016/j.ymben.2018.08.008 (2018).
490 Lauersen, K. J., Kruse, O. & Mussgnug, J. H. Targeted expression of nuclear transgenes in Chlamydomonas reinhardtii with a versatile, modular vector toolkit. *Applied microbiology and biotechnology* **99**, 3491-3503, doi:10.1007/s00253-014-6354-7 (2015).
491 Rasala, B. A. *et al.* Expanding the spectral palette of fluorescent proteins for the green microalga Chlamydomonas reinhardtii. *Plant J* **74**, 545-556, doi:10.1111/tpj.12165 (2013).
492 Neupert, J., Karcher, D. & Bock, R. Generation of Chlamydomonas strains that efficiently express nuclear transgenes. *Plant J* **57**, 1140-1150, doi:10.1111/j.1365-313X.2008.03746.x (2009).
493 Couso, I., Cordero, B. F., Vargas, M. A. & Rodriguez, H. Efficient heterologous transformation of Chlamydomonas reinhardtii npq2 mutant with the zeaxanthin epoxidase gene isolated and characterized from Chlorella zofingiensis. *Marine drugs* **10**, 1955-1976, doi:10.3390/md10091955 (2012).
494 Holtin, K. *et al.* Determination of astaxanthin and astaxanthin esters in the microalgae Haematococcus pluvialis by LC-(APCI)MS and characterization of predominant carotenoid isomers by NMR spectroscopy. *Analytical and bioanalytical chemistry* **395**, 1613-1622, doi:10.1007/s00216-009-2837-2 (2009).
495 Yuan, J.-P. & Chen, F. Identification of astaxanthin isomers in Haematococcus lacustrisby HPLC-photodiode array detection. *Biotechnology Techniques* **11**, 455-459, doi:10.1023/a:1018441411746 (1997).
496 Ye, R. W. *et al.* Construction of the astaxanthin biosynthetic pathway in a methanotrophic bacterium Methylomonas sp. strain 16a. *J Ind Microbiol Biotechnol* **34**, 289-299, doi:10.1007/s10295-006-0197-x (2007).
497 Sommer, T. R., Potts, W. T. & Morrissy, N. M. Utilization of Microalgal Astaxanthin by Rainbow-Trout (Oncorhynchus-Mykiss). *Aquaculture* **94**, 79-88, doi:Doi 10.1016/0044-8486(91)90130-Y (1991).
498 Zhekisheva, M., Boussiba, S., Khozin-Goldberg, I., Zarka, A. & Cohen, Z. Accumulation of oleic acid in Haematococcus pluvialis (Chlorophyceae) under nitrogen starvation or high light is correlated with that of astaxanthin esters. *Journal of Phycology* **38**, 325-331, doi:DOI 10.1046/j.1529-8817.2002.01107.x (2002).
499 Minekus, M. *et al.* A standardised static in vitro digestion method suitable for food - an international consensus. *Food & function* **5**, 1113-1124, doi:10.1039/c3fo60702j (2014).
500 Rezanka, T., Nedbalova, L., Sigler, K. & Cepak, V. Identification of astaxanthin diglucoside diesters from snow alga Chlamydomonas nivalis by liquid chromatography-atmospheric pressure chemical

ionization mass spectrometry. *Phytochemistry* **69**, 479-490, doi:10.1016/j.phytochem.2007.06.025 (2008).
501 Cazzaniga, S., Bressan, M., Carbonera, D., Agostini, A. & Dall'Osto, L. Differential Roles of Carotenes and Xanthophylls in Photosystem I Photoprotection. *Biochemistry* **55**, 3636-3649, doi:10.1021/acs.biochem.6b00425 (2016).
502 Melis, A. Solar energy conversion efficiencies in photosynthesis: Minimizing the chlorophyll antennae to maximize efficiency. *Plant Sci* **177**, 272-280, doi:10.1016/j.plantsci.2009.06.005 (2009).
503 Lopez, M. C. *et al.* Comparative analysis of the outdoor culture of Haematococcus pluvialis in tubular and bubble column photobioreactors. *Journal of biotechnology* **123**, 329-342, doi:10.1016/j.jbiotec.2005.11.010 (2006).
504 Park, J. C., Choi, S. P., Hong, M. E. & Sim, S. J. Enhanced astaxanthin production from microalga, Haematococcus pluvialis by two-stage perfusion culture with stepwise light irradiation. *Bioprocess and biosystems engineering* **37**, 2039-2047, doi:10.1007/s00449-014-1180-y (2014).
505 Breitenbach, J. *et al.* Engineered maize as a source of astaxanthin: processing and application as fish feed. *Transgenic research* **25**, 785-793, doi:10.1007/s11248-016-9971-3 (2016).
506 Liu, J. *et al.* Chlorella zofingiensis as an alternative microalgal producer of astaxanthin: biology and industrial potential. *Marine drugs* **12**, 3487-3515, doi:10.3390/md12063487 (2014).
507 Lubian, L. M. *et al.* Nannochloropsis (Eustigmatophyceae) as source of commercially valuable pigments. *Journal of Applied Phycology* **12**, 249-255, doi:Doi 10.1023/A:1008170915932 (2000).
508 Lauersen, K. J. Eukaryotic microalgae as hosts for light-driven heterologous isoprenoid production. *Planta* **249**, 155-180, doi:10.1007/s00425-018-3048-x (2019).
509 Morikawa, T., Uraguchi, Y., Sanda, S., Nakagawa, S. & Sawayama, S. Overexpression of DnaJ-Like Chaperone Enhances Carotenoid Synthesis in Chlamydomonas reinhardtii. *Appl Biochem Biotechnol* **184**, 80-91, doi:10.1007/s12010-017-2521-5 (2018).
510 Werst, M., Jia, Y., Mets, L. & Fleming, G. R. Energy transfer and trapping in the photosystem I core antenna. A temperature study. *Biophysical journal* **61**, 868-878, doi:10.1016/S0006-3495(92)81894-5 (1992).
511 Frolov, L., Rosenwaks, Y., Carmeli, C. & Carmeli, I. Fabrication of a photoelectronic device by direct chemical binding of the photosynthetic reaction center protein to metal surfaces. *Adv Mater* **17**, 2434-+, doi:10.1002/adma.200500295 (2005).
512 Carmeli, I. *et al.* A photosynthetic reaction center covalently bound to carbon nanotubes. *Adv Mater* **19**, 3901-+, doi:10.1002/adma.200700536 (2007).
513 Das, R. *et al.* Integration of photosynthetic protein molecular complexes in solid-state electronic devices. *Nano letters* **4**, 1079-1083, doi:10.1021/nl049579f (2004).
514 Gerster, D. *et al.* Photocurrent of a single photosynthetic protein. *Nature nanotechnology* **7**, 673-676, doi:10.1038/nnano.2012.165 (2012).
515 Gunther, D. *et al.* Photosystem I on graphene as a highly transparent, photoactive electrode. *Langmuir : the ACS journal of surfaces and colloids* **29**, 4177-4180, doi:10.1021/la305020c (2013).
516 Kaniber, S. M., Simmel, F. C., Holleitner, A. W. & Carmeli, I. The optoelectronic properties of a photosystem I-carbon nanotube hybrid system. *Nanotechnology* **20**, 345701, doi:10.1088/0957-4484/20/34/345701 (2009).
517 Kothe, T. *et al.* Engineered electron-transfer chain in photosystem 1 based photocathodes outperforms electron-transfer rates in natural photosynthesis. *Chemistry* **20**, 11029-11034, doi:10.1002/chem.201402585 (2014).
518 Zeynali, A., Ghiasi, T. S., Riazi, G. & Ajeian, R. Organic solar cell based on photosystem I pigment-protein complex, fabrication and optimization. *Org Electron* **51**, 341-348, doi:10.1016/j.orgel.2017.09.032 (2017).
519 Zhao, F. *et al.* Light Induced H2 Evolution from a Biophotocathode Based on Photosystem 1--Pt Nanoparticles Complexes Integrated in Solvated Redox Polymers Films. *The journal of physical chemistry. B* **119**, 13726-13731, doi:10.1021/acs.jpcb.5b03511 (2015).
520 Zhao, F. *et al.* Light-induced formation of partially reduced oxygen species limits the lifetime of photosystem 1-based biocathodes. *Nature communications* **9**, 1973, doi:10.1038/s41467-018-04433-z (2018).
521 Krassen, H. *et al.* Photosynthetic hydrogen production by a hybrid complex of photosystem I and [NiFe]-hydrogenase. *ACS nano* **3**, 4055-4061, doi:10.1021/nn900748j (2009).
522 Kuritz, T., Lee, I., Owens, E. T., Humayun, M. & Greenbaum, E. Molecular photovoltaics and the photoactivation of mammalian cells. *IEEE transactions on nanobioscience* **4**, 196-200, doi:10.1109/tnb.2005.850480 (2005).
523 Di Maria, F., Lodola, F., Zucchetti, E., Benfenati, F. & Lanzani, G. The evolution of artificial light actuators in living systems: from planar to nanostructured interfaces. *Chemical Society reviews* **47**, 4757-4780, doi:10.1039/c7cs00860k (2018).

524 Saboe, P. O. *et al.* Biomimetic wiring and stabilization of photosynthetic membrane proteins with block copolymer interfaces. *J Mater Chem A* **4**, 15457-15463, doi:10.1039/c6ta07148a (2016).
525 Saboe, P., Conte, E., Farell, M., Bazan, G. & Kumar, M. Biomimetic and bioinspired approaches for wiring enzymes to electrode interfaces. *Energ Environ Sci* **10**, 14-42, doi:10.1039/C6EE02801B (2017).
526 Bennett, T. H. *et al.* Jolly green MOF: confinement and photoactivation of photosystem I in a metal-organic framework. *Nanoscale Adv* **1**, 94-104, doi:10.1039/c8na00093j (2019).
527 Brecht, M., Hussels, M., Nieder, J. B., Fang, H. & Elsässer, C. Plasmonic interactions of photosystem I with Fischer patterns made of Gold and Silver. *Chemical Physics* **406**, 15-20, doi:https://doi.org/10.1016/j.chemphys.2012.05.005 (2012).
528 Carmeli, I. *et al.* Broad band enhancement of light absorption in photosystem I by metal nanoparticle antennas. *Nano letters* **10**, 2069-2074, doi:10.1021/nl100254j (2010).
529 Czechowski, N. *et al.* Large plasmonic fluorescence enhancement of cyanobacterial photosystem I coupled to silver island films. *Appl Phys Lett* **105**, doi:Artn 04370110.1063/1.4891856 (2014).
530 Kim, I. *et al.* Metal nanoparticle plasmon-enhanced light-harvesting in a photosystem I thin film. *Nano letters* **11**, 3091-3098, doi:10.1021/nl2010109 (2011).
531 Niroomand, H., Pamu, R., Mukherjee, D. & Khomami, B. Microenvironment alterations enhance photocurrents from photosystem I confined in supported lipid bilayers. *J Mater Chem A* **6**, 12281-12290, doi:10.1039/c8ta00898a (2018).
532 Niroomand, H., Pamu, R., Mukherjee, D. & Khomami, B. Tuning the photocurrent generations from photosystem I assembled in tailored biotic–abiotic interfaces. *MRS Communications* **8**, 823-829, doi:10.1557/mrc.2018.83 (2018).
533 Pamu, R., Sandireddy, V. P., Kalyanaraman, R., Khomami, B. & Mukherjee, D. Plasmon-Enhanced Photocurrent from Photosystem I Assembled on Ag Nanopyramids. *The journal of physical chemistry letters* **9**, 970-977, doi:10.1021/acs.jpclett.7b03255 (2018).
534 Niroomand, H., Mukherjee, D. & Khomami, B. Tuning the photoexcitation response of cyanobacterial Photosystem I via reconstitution into Proteoliposomes. *Scientific reports* **7**, 2492, doi:10.1038/s41598-017-02746-5 (2017).
535 Saboe, P. O. *et al.* Two-dimensional protein crystals for solar energy conversion. *Adv Mater* **26**, 7064-7069, doi:10.1002/adma.201402375 (2014).
536 Lu, J. M. *et al.* Current advances in research and clinical applications of PLGA-based nanotechnology. *Expert review of molecular diagnostics* **9**, 325-341, doi:10.1586/erm.09.15 (2009).
537 Ali, M. E. & Lamprecht, A. Polyethylene glycol as an alternative polymer solvent for nanoparticle preparation. *International journal of pharmaceutics* **456**, 135-142, doi:10.1016/j.ijpharm.2013.07.077 (2013).
538 Danhier, F. *et al.* PLGA-based nanoparticles: an overview of biomedical applications. *Journal of controlled release : official journal of the Controlled Release Society* **161**, 505-522, doi:10.1016/j.jconrel.2012.01.043 (2012).
539 Klose, D., Siepmann, F., Elkharraz, K., Krenzlin, S. & Siepmann, J. How porosity and size affect the drug release mechanisms from PLGA-based microparticles. *International journal of pharmaceutics* **314**, 198-206, doi:10.1016/j.ijpharm.2005.07.031 (2006).
540 Kumari, A., Yadav, S. K. & Yadav, S. C. Biodegradable polymeric nanoparticles based drug delivery systems. *Colloids and surfaces. B, Biointerfaces* **75**, 1-18, doi:10.1016/j.colsurfb.2009.09.001 (2010).
541 Makadia, H. K. & Siegel, S. J. Poly Lactic-co-Glycolic Acid (PLGA) as Biodegradable Controlled Drug Delivery Carrier. *Polymers* **3**, 1377-1397, doi:10.3390/polym3031377 (2011).
542 Wang, L. Y. *et al.* Preparation and characterization of uniform-sized chitosan microspheres containing insulin by membrane emulsification and a two-step solidification process. *Colloids and surfaces. B, Biointerfaces* **50**, 126-135, doi:10.1016/j.colsurfb.2006.05.006 (2006).
543 Barichello, J. M., Morishita, M., Takayama, K. & Nagai, T. Encapsulation of hydrophilic and lipophilic drugs in PLGA nanoparticles by the nanoprecipitation method. *Drug development and industrial pharmacy* **25**, 471-476, doi:10.1081/ddc-100102197 (1999).
544 Novoderezhkin, V. I. *et al.* Mixing of exciton and charge-transfer states in light-harvesting complex Lhca4. *Physical chemistry chemical physics : PCCP* **18**, 19368-19377, doi:10.1039/c6cp02225a (2016).
545 Joliot, P. & Johnson, G. N. Regulation of cyclic and linear electron flow in higher plants. *Proceedings of the National Academy of Sciences of the United States of America* **108**, 13317-13322, doi:10.1073/pnas.1110189108 (2011).
546 Galka, P. *et al.* Functional analyses of the plant photosystem I-light-harvesting complex II supercomplex reveal that light-harvesting complex II loosely bound to photosystem II is a very efficient antenna for photosystem I in state II. *Plant Cell* **24**, 2963-2978, doi:10.1105/tpc.112.100339 (2012).

547 Edison, T. J. I. & Sethuraman, M. G. Instant green synthesis of silver nanoparticles using Terminalia chebula fruit extract and evaluation of their catalytic activity on reduction of methylene blue. *Process Biochemistry* **47**, 1351-1357, doi:https://doi.org/10.1016/j.procbio.2012.04.025 (2012).

548 Goral, T. K. *et al.* Visualizing the mobility and distribution of chlorophyll proteins in higher plant thylakoid membranes: effects of photoinhibition and protein phosphorylation. *Plant J* **62**, 948-959, doi:10.1111/j.0960-7412.2010.04207.x (2010).

549 Kaniber, S. M., Brandstetter, M., Simmel, F. C., Carmeli, I. & Holleitner, A. W. On-chip functionalization of carbon nanotubes with photosystem I. *Journal of the American Chemical Society* **132**, 2872-2873, doi:10.1021/ja910790x (2010).

550 Mershin, A. *et al.* Self-assembled photosystem-I biophotovoltaics on nanostructured TiO(2)and ZnO. *Scientific reports* **2**, 234, doi:10.1038/srep00234 (2012).

551 Robinson, M. T., Simons, C. E., Cliffel, D. E. & Jennings, G. K. Photocatalytic photosystem I/PEDOT composite films prepared by vapor-phase polymerization. *Nanoscale* **9**, 6158-6166, doi:10.1039/c7nr01158j (2017).

552 Badura, A. *et al.* Photocurrent generation by photosystem 1 integrated in crosslinked redox hydrogels. *Energ Environ Sci* **4**, 2435-2440, doi:10.1039/c1ee01126j (2011).